VORTEX BREAKDOWN IN DUST-COLLECTING RETURN-FLOW CYCLONES

Ross Francis Wakelin

A thesis presented in partial fulfilment of the
requirements of the degree of Doctor of Philosophy

Chemical and Process Engineering Department
University of Canterbury

1992

Acknowledgements:

I am very grateful to Dr John Abrahamson for his guidance and supervision of the work for this thesis. He was always patient, persistent when needed, and a consistent source of ideas for overcoming apparent blocks. Many of the techniques that have yielded useful results were ones that I had initially rejected as unpromising. Apart from the academic supervision I am also grateful for John's efforts to obtain funding and contract work to give me income.

The work would not have been possible without the skilled technical assistance of the technicians in the Chemical and Process Engineering Department. In particular, the construction of the perspex cones and cyclone were essential to the success of the project, so many thanks are due to David Brown for his skill and dedication in solving the multitude of problems that arose. I am relieved that I managed to finish the experimental work without dropping the cone!

The problems encountered with obtaining photographs of the fast, faint and fleeting movements of the tracers were solved with the assistance of Trevor Berry, who also printed the photographs in this report. Leicester Cheeseman and Graham Harris from the Mechanical Engineering Department were most helpful in allowing the use of the windtunnel for calibration work, and assistance with problems associated with tracers and anemometry. The video was recorded with equipment borrowed from the Audio Visual Department of the University of Canterbury, and the editing of the segments was carried out with the assistance of Alan Bright.

The access to the industrial scale cyclones was by courtesy of the management and staff of Canterbury Timber Products, Rangiora and Scotts Engineering, Christchurch. Further practical enlightenment (and entertainment) was also gratefully received from the late Charles Martin, who acted as an associate supervisor for part of this study.

For financial support I am very grateful for the assistance received from the Chemical and Process & Engineering Department through the efforts of Brian Earl and Miles Kennedy, for teaching assistant work as well as bursaries. Separation Processes Service, Harwell, U.K. also provided funding for one year with a contract for work that was related to the thesis. In the final analysis, the completion of this thesis would not have been possible without the support of my parents - both in securing the bank loan that proved necessary to make ends meet, and also in providing the steady encouragement needed.

A good number of people have combined to make the completion of this work possible, others have helped make it enjoyable, and particular thanks go to the South Island orienteering 'fraternity' for mental exercise away from a desk, and the Engineering school lunchtime runners for a regular source of escapism, exercise & endorphins to face the second three-quarters of the day.

Chapter 1

SUMMARY:

This thesis presents the results of an experimental study of the airflows in reverse-flow dust collecting cyclones. Measurements and flow visualisation techniques were used to examine both the 'paired vortex breakdown' theory that was proposed by Abrahamson & Allen (1986), and the 'natural vortex length' that was identified by Alexander (1949) and which has been widely used in predictive models of the collection efficiency. The object of this study was to improve the assumptions concerning the vortex structure that are used in the collection efficiency models. The models available at present are unable to account for the variation in the slope of the grade efficiency curve. The effect of the geometry on the flow was examined for variations on the Stairmand High Efficiency design cyclone, which is a commonly used design with an anomalous grade efficiency curve.

The results that are presented in this thesis show that in conical cyclones the vortex is stabilised over cyclone lengths that are far greater than are used in industrial designs. A descriptive theory of the vortex structure was developed that included three types of 'vortex breakdown' phenomena, resulting from different mechanisms. These breakdowns were found to be strongly dependent on the cyclone geometry. Assisted by the stabilising effect of the cone, the vortex reaches the dust exit but forms a recirculating breakdown under the influence of the pressure increase and the diverging streamlines that result from the expansion into the bin. It is proposed that in geometries where the expansion into the bin is delayed the vortex terminates before the dust exit due to the separation of the boundary layer from the wall. Simple measurement techniques were found that could identify the occurrence of the vortex termination.

The susceptibility of the vortex to this termination before reaching the bin was found to be determined by the length of the apex end of the cone rather than the length of the barrel section or the overall length. This is consistent with the proposed mechanism involving ejections from, and separation of, the boundary layer at the wall as the instability of the boundary layer increases with smaller radius of curvature. In addition, the ratio of the

boundary layer flow to the main vortex flow increases while the proximity of the boundary layer to the core decreases.

The proposed theory also features a recirculating bubble-type vortex breakdown of the core vortex as it left the cyclone through the gas exit. This was of the type that has been widely studied in connection with the trailing vortices generated by wings. The location of this breakdown depended on the geometry of the gas exit, was well as upstream disturbances. In exits consisting of a short tube before a sudden expansion, the vortex breakdown was located at the expansion. In long tubes the vortex breakdown moved from the initial point of breakdown to become stabilised a short distance downstream of the gas exit lip. This vortex breakdown was permanently present and under certain conditions a subsidiary vortex breakdown could move upstream along the core vortex and become stabilised on the bin base. This resulted in the establishment of a fast reverse flow from the gas exit to the bin, which featured multiple breakdowns along its length, in a dynamic fashion. This feature will serve as a useful test for the validity of numerical simulations of the cyclone flowfield. Another aspect of the dynamic behaviour of the vortex was the non-uniformity of the radial inflow.

The majority of the experiments that led to the development of this vortex structure theory were carried out in a 140mmØ laboratory cyclone that was constructed from perspex. An extensive set of time averaged velocity profiles were also obtained in this cyclone for several variants on the Stairmand High Efficiency geometry, over inlet velocities ranging from 8 - 23m/s as well as in two industrial scale cyclones that were also of the Stairmand High Efficiency design with barrel diameters of 750mmØ and 2090mmØ. The four-hole Pitot cylinder probe that was used yielded total and static pressure and tangential, axial and radial velocity profiles. The radial velocity was not able to be measured accurately because of the high radial pressure gradients and limitations of the probe calibration. The total velocity profiles were also measured with a 45° Hot film anemometer in the 140mmØ cyclone, and these profiles were in reasonable agreement with the Pitot cylinder results. The ten traverse locations along the length of the cyclones represent a more comprehensive set of measurements than previously has been available.

The profiles of the time-averaged tangential and axial velocity components scaled well between the 140mmØ and 750mmØ diameter cyclones and between inlet velocities of 8 and 22m/s. The profiles were compared with several models, of which the Burgers (1949) and Batchelor(1964) equations were found to be the most suitable. These theories give expressions of a simple form for the velocity components that apply to both the outer and inner vortices (except near the wall and the axis). The expressions are:

Tangential velocity (Burgers, 1948): $$V_\theta = \frac{\Gamma_o}{r} \cdot \left[1 - \exp\left(\frac{-a\,r^2}{2.\nu_{Tr\theta}}\right)\right]$$

Axial velocity (Batchelor, 1964): $$V_X = W\_\left[1 - W_{ex}.\exp\left\{\frac{-a\,r^2}{2.\nu_{Trz}}\right\}\right]$$

Relationships to predict the value of the model parameters were determined that gave good agreement over the range of cyclones diameters studied, from 0.14mØ to 2.09mØ. The fitted parameter in the model were the turbulent viscosity parameters $\nu_{Tr\theta}$ and ν_{Trz}, which

demonstrated an anisotropy of the cyclone vortex. The fitting of the tangential velocity maximum required a dependence of $v_{Tr\theta}$ on the Reynolds number of:

$$\left(\frac{v_{Tr\theta}}{v}\right) = 0.0645 \times (Re)^{0.921}$$

for $Re = \left(\frac{Q}{Lv}\right)$ ranging from $5X10^3$ to $65X10^3$ for the three cyclones studied. The axial velocity required a value of $v_{Trz} = 5.9.v_{Tr\theta}$ in order to satisfy the mass balance requirement.

These expressions describing the velocity in the cyclone will prove useful in the prediction of the cyclone collection efficiency, as will the improved understanding of the relation of the vortex structure to the cyclone geometry, and the nature of the cyclone dynamic behaviour.

Table of Contents:

FIGURES:

Note: The figures are not cross-referenced by their page number, but they are given a label which has the chapter, and where applicable the section letter, as the first two digits.

Chapter

2

INTRODUCTION:

2.A: GENERAL BACKGROUND:

Cyclones as air-dust separators are an old technology, having been first patented in 1884. They are simple and cheap to construct and maintain, have no moving parts, and are capable of operating over a wide range of temperatures and pressures. Although they are not capable of high efficiencies much below particle sizes of 5μm, the ability to operate at high temperature ensures a continued interest in their use as an industrial separator.

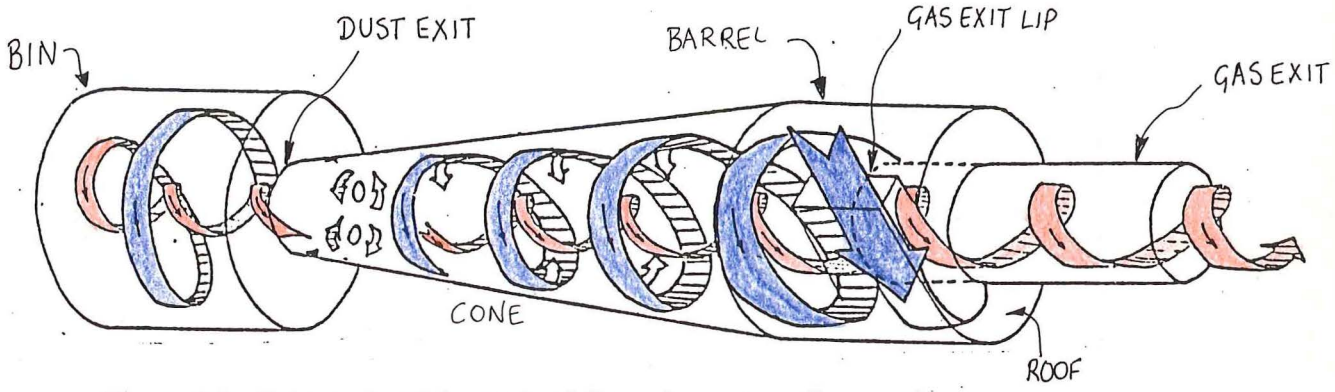

Figure 2.1: Schematic of the main airflows in a return-flow cyclone

In the reverse-flow type of cyclone that is the subject of this study, the vortex produced by the tangential inlet travels towards the cone apex before reversing back on itself and travelling out of the cyclone via the core, carrying a reduced dust loading of predominantly fine dust. The separation of the dust from the air is achieved by the swirling air in the cyclone, which sets up a centrifugal force field that acts radially outwards on particles that are heavier than the suspending fluid (air). This tends to move the heavier dust particles towards the wall, from where they are carried into the bin at the apex end of the cone by a secondary flow in the boundary layer along the cone wall. In the absence of leaks about 10% of the inlet flow enters

the bin, but this carries 90% or more of the inlet dust. The larger diameter of the bin results in a reduction in the velocity, enabling the particles to settle out as the air turns to leave the bin. Agglomeration of the particles has also been identified by Abrahamson et al (1978) as a necessary mechanism for the collection of the dust.

There is a radial inflow of gas from the outer to the inner vortex that occurs along the cyclone length and this tends to carry the particles into the core vortex, and out of the cyclone. The separation of particles from the air is affected by the density, size and shape of the particle. If the particle density is approximately the same for all particles, then it is the larger particles that will experience a stronger separating force, enhancing their collection. Apart from the centrifugal and aerodynamic drag forces there are other, smaller, forces acting on the particles, including a lift force. The lift force is the force that causes the flight path of a spinning object to curve. Franko (1987) reports that the direction of the lift force changes between the outer and inner vortices, being directed outwards in the potential vortex of the outer, while in the forced vortex of the core it is directed inwards. Particles of greater specific surface area will be more subject to aerodynamic drag, opposing their collection, and the lift force is also greater for higher specific surface area. The starting position of the particle, and the turbulence will also have an effect.

The performance is represented by a 'Grade Efficiency curve', where the collection efficiency of each particle size (or size band) is plotted against a suitable dimension characterising that size band. This grade efficiency curve is found experimentally to have a sigmoid shape, approaching asymptotic limits of 100% collection at large particles, and 0% collection for very small particles. Different cyclone geometries and sizes show different characteristic grade efficiency curves, with both the relative position, and the slope of the curve changing. A typical curve is shown below:

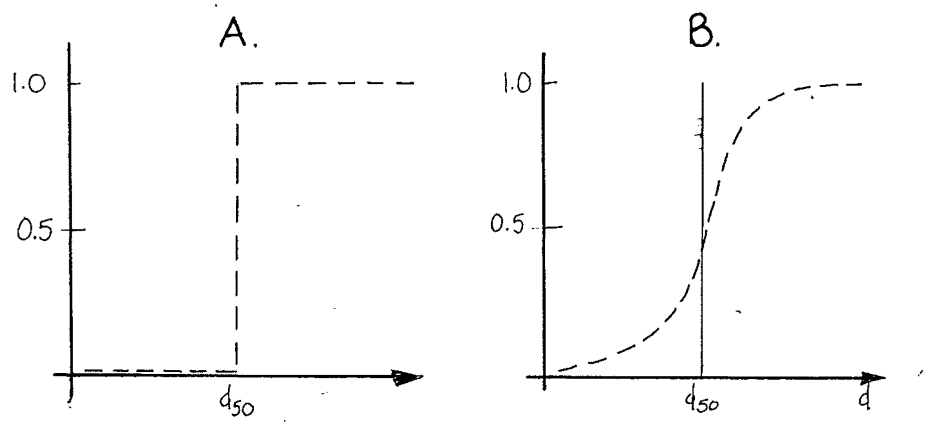

Figure 2.2: Theoretical and actual grade efficiency curves

The long history of use, and the apparent simplicity of operation would suggest that the principles underlying the performance would be well understood. In fact the flow inside the cyclone is complex, and research has tended to take an empirical, 'black-box' approach.

Cyclone design has consequently involved the scaling within limits of the results from measurements made on an existing cyclone. Studies of cyclone performance have concentrated

on the measurement of the collection efficiency for various designs, resulting in an empirically determined 'optimum' design, but adding little to the understanding of the collection mechanism. It has not been possible to generalise the empirical correlations of cyclone performance to fit the wide range of geometrical parameters. The prediction of the efficiency for new designs is not possible, nor is it possible to suggest (with confidence) remedies for cyclones with poor performance. To optimise the cyclone design at present involves the testing of a large number of cyclones to cover the possible variations of the geometrical parameters. These parameters can have conflicting effects and confuse the findings.

While the empirical approach is still being used (Iozia & Leith, 1989b; Zhou et al, 1987), increasingly research is aimed at predicting the grade efficiency collection performance using models of the flowfield. The optimisation of the design has been attempted (Iozia and Leith (1989b) and Ramachandran et al (1991)) using the existing models capable of predicting the efficiency and pressure drop, but the low accuracy of these models has meant the results have not been successful.

The poor agreement between the experimental grade efficiency and the predictions of the best performed models has been attributed to the unrealistic assumptions concerning the flowfield. Fitting models to experimentally determined velocity profiles will help to improve assumptions made about the flow but the results are likely to be still specific to the geometries that were examined. To generalise the results, an improvement in the understanding of the flowfield structure is needed - including knowledge of the mechanisms that form it and the effect that changes in the cyclone geometry have on it. Only then will it be possible to predict the collection efficiency and pressure drop for an arbitrary design, and hence optimise the cyclone design.

The current models of the flow have assumed a steady-state flow, with turbulent effects superimposed on this. The radial inflow of air is assumed to be uniform over the vortex length, and the dust is assumed to be collected once it reaches the wall. Assumptions are made about the rate-determining step in the collection process, and refinements to the models are often made as "add-ons" to improve the agreement. The vortex length used is either equated to the cyclone length, or estimated by the 'Natural length' equation proposed by Alexander (1949), which depends on the geometry.

A more fundamentally based description of the vortex structure was made by Abrahamson and Allen (1986) that explained the observed differences in the slopes of the grade efficiency curves. They proposed that the vortex was capped at each end by breakdowns that featured a recirculating region of gas (or 'gas bubble'). The upper one would be stabilised in the gas exit and the spacing between the two breakdowns would be determined by Alexander's (1949) 'natural' length. The position of the lower breakdown relative to the dust exit would then vary as the cyclone length was varied, and for short lengths and large dust exit diameters (relative to the gas exit diameter) the breakdown could enter the bin. Abrahamson & Allen (1986) used this to account for the effect of cyclone geometry on the classification number (a measure of the steepness of the grade efficiency curve).

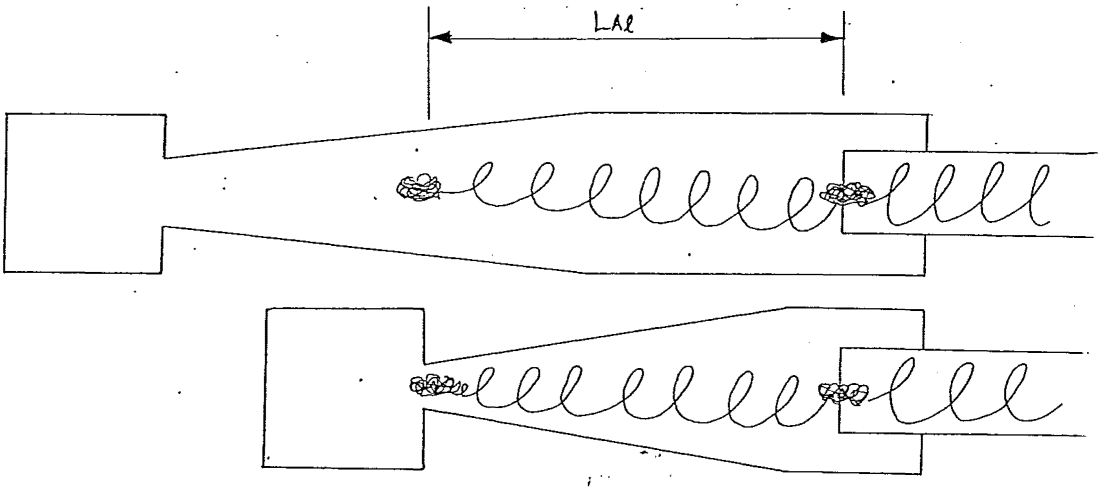

Figure 2.3: The proposed dependence of vortex structure on the geometry, by Abrahamson & Allen (1986).

Cyclones for which the lower breakdown bubble was predicted to be close to the small end of the cone (cyclone lengths 10% to 50% longer than the natural length) showed a much less sharp classification than cyclones longer or shorter. This was thought to be due to increased radial transport of dust at the bubble location, resulting in enhanced losses of larger particles from the wall and also an increased residence time for finer particles through the recirculating action, giving improved chances for agglomeration.

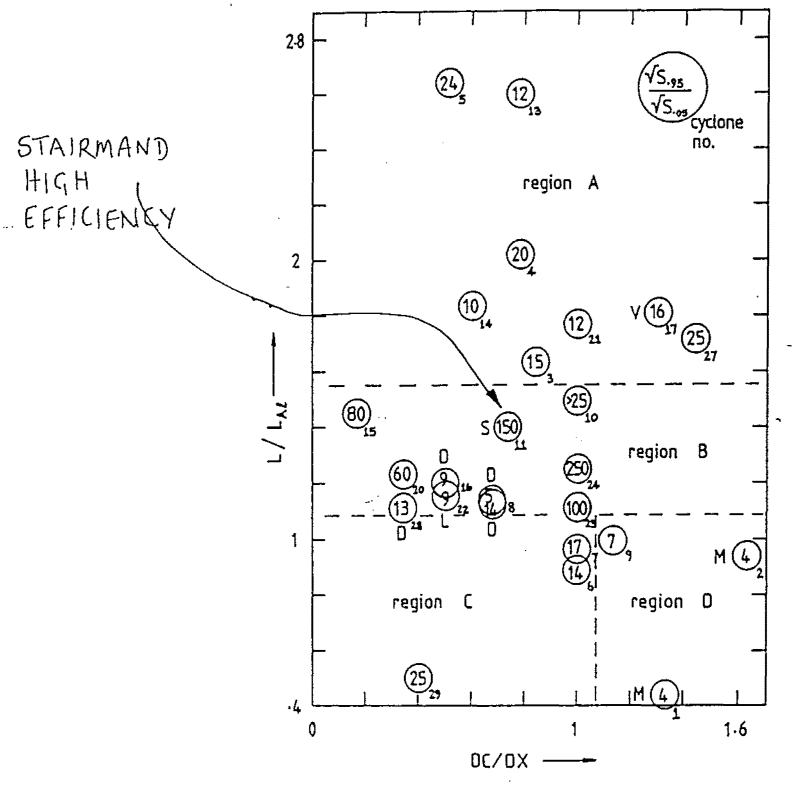

Figure 2.4: Variation of the classification sharpness with geometry, from Abrahamson & Allen, 1986)

On the other hand, the theory that an improvement in efficiency is gained by keeping the vortex out of the bin is supported by Svarovsky (1984). For a relatively short, wide cyclone the extension of the dust exit by 3 dust exit diameters resulted in the elimination of the drop off in efficiency found at high flowrates in the unmodified cyclone.

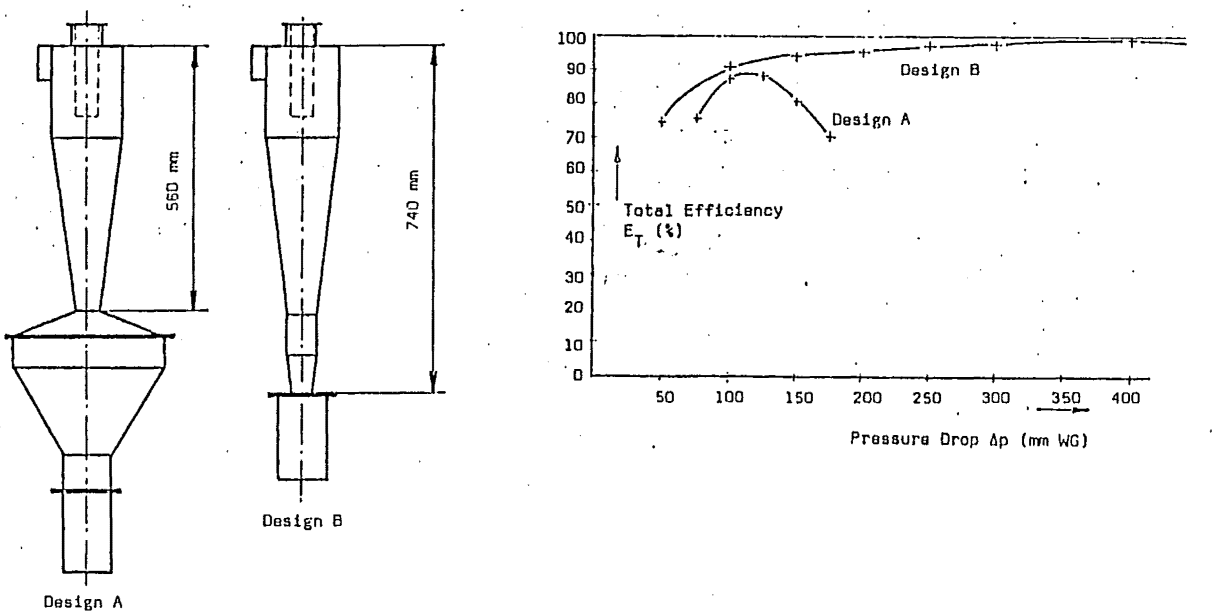

Figure 2.5: Variation of gross efficiency with flowrate (expressed by ΔP) for two types of cyclone geometries, from Svarovsky (1984)

The Stairmand high efficiency geometry is a commonly used design, with a very low sharpness of classification. By Abrahamson and Allen's (1986) analysis the breakdown is predicted to be situated in the lower cone region in this design. Hence it was chosen as the starting point for this study. The geometry is shown below:

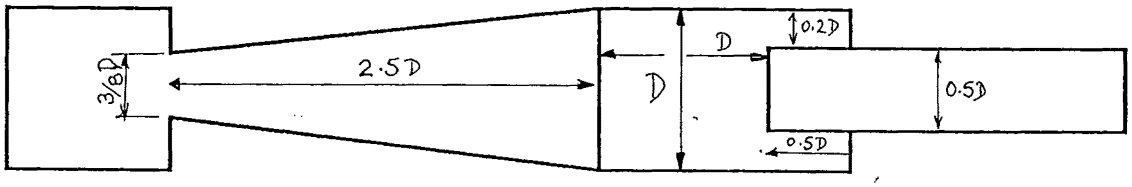

Figure 2.6: Standard Stairmand High efficiency cyclone geometry

The approach that has been taken was to examine the flow in a 140mmØ transparent cyclone in search of evidence for the occurrence of vortex breakdown. A variety of flow visualisation techniques were used and the geometry was varied from the standard design by adding sections to the barrel or cone. Steady-state velocity and pressure profiles were determined at a large number of locations to form a quantitative picture of the flow, which was compared between different scales of cyclones of the same geometry. The steady state velocity profiles were

modelled using theories from the literature. Theories of possible structures of the vortex flow were then developed to account for the observations, including the dynamic behaviour.

The long term aim is to improve the understanding of the flow structure to the point where the influence of geometrical changes on the flow, the efficiency and the pressure drop can be predicted. The numerous studies of the effects of the geometry on the efficiency could then be used to optimise the design. This thesis concentrates on the first part of this path: the understanding of the vortex structure and the relation of the vortex structure to the geometry. The flow and pressure measurements were made with dust free air, which introduces an approximation since the presence of dust has been reported to improve the efficiency, lower the pressure drop, and cause changes to the flow structure. The pressure drop of the cyclone can be as important as the efficiency and generally one cannot be improved without a reduction in the other (although in some cases, extending the length of a cyclone does both). The results from this study have been incorporated into a report by Abrahamson (1992) on 'Predicting pressure drop in cyclones' for Separation Processes Service, Harwell, U.K. Hence, details about the pressure drop characteristics of cyclones will not be dealt with at length in this report.

2.B: LITERATURE REVIEW

The components of previous research on cyclones from the literature are reviewed briefly in the following sections in this introduction:

2.B.1 Measurement of the time-averaged velocity profiles
2.B.2 Existing cyclone vortex structure theories
2.B.3 Measurement of the fractional collection efficiency
2.B.4 Attempts to empirically predict the grade efficiency
2.B.5 Predictions of grade efficiency with models of the flowfield
2.B.6 Refinements to the models to take account of secondary flows and dynamic behaviour

2.B.1 Measurements of the velocity profiles:

The cyclone was first used in the 1880s, and although it was found to be a robust and generally reliable device for removing large particles from airstreams, the 'black box' design approach was unsatisfactory, particularly when dealing with finer particles near the limit of performance. Research to determine the operating mechanism was commenced by examining the structure of the flowfield and determining the velocity profiles. An indication of the complexity of the cyclone is that this initial step has not been completed, and studies are still being carried out on the measurement of the velocity profiles.

The gross structure of the cyclone vortex can be seen in simple visualisation experiments, and is generally agreed to consist of an outer vortex spiralling towards the bin, with a core vortex spiralling towards the gas exit. The velocity is usually resolved into cylindrical components in the tangential, axial and radial directions. The tangential component is found to be the dominant

one, and rises to nearly twice the inlet velocity away from the walls and the axis. The axial velocity is of the order of one half of the inlet velocity. If a sign convention is adopted for the axial velocity of negative velocities in the direction of the cone apex, then the axial velocity changes from negative values near the wall, to positive values near the axis, passing through zero at a radius that can be taken as characteristic of the imaginary boundary between the vortices.

The radial velocity component is the smallest of the three, and is often comparable to the magnitude of the velocity fluctuations. The precession of the vortex away from the axis also complicates the measurement of the radial velocity, and it seems unlikely that techniques will be found that can cope with these problems. The best estimates are obtained by applying a mass balance to the axial velocity profiles, as has been done by Knowles et al (1973), Dabir & Petty (1986) and Grabek & Meirzwinski (1980). Radial velocities were measured by Pervov (1974), Hejma (1971) and ter Linden (1953), and found to be directed inwards in the outer region, but outwards in the core, These local measurements of the radial velocity are reported to be 10-20% of the inlet velocity, which is 3-10 times the value that would be expected if the radial inflow was uniform over the cyclone length. Pervov (1974) reported much higher radial velocities just below the lip of the gas exit.

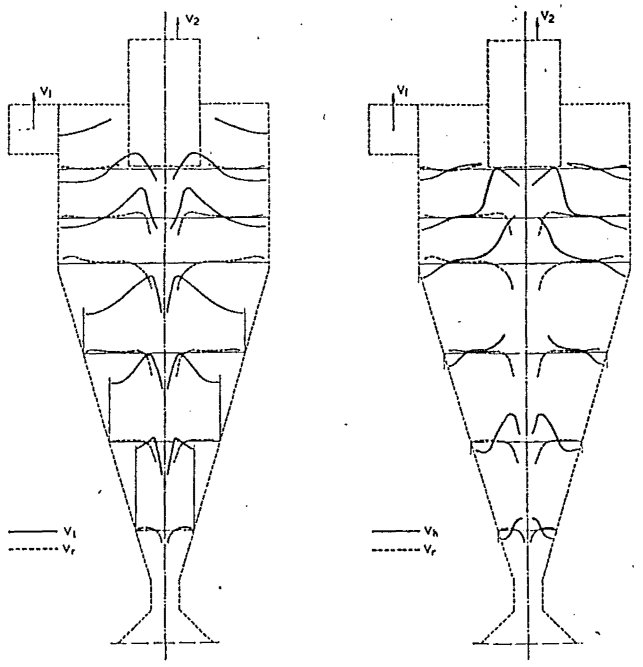

FIG. 8 TANGENTIAL VELOCITY v_t AND RADIAL VELOCITY v_r OF GASES AT DIFFERENT POINTS IN CYCLONE

FIG. 9 RADIAL VELOCITY v_r AND VERTICAL VELOCITY v_h OF GASES AT DIFFERENT POINTS IN CYCLONE

Figure 2.7: Velocity profiles from ter Linden (1953)

The understanding of the structure of the cyclone vortex has not improved greatly since the early studies of Shepherd & Lapple (1939) and ter Linden (1949, 1953), who found most of the features described above. Shepherd & Lapple (1939) observed the movements of streamers, smoke and dust in a 285mmØ diameter glass reverse-flow cyclone, and made traverses with a pitot tube to measure velocity components. Ter Linden (1949, 1953) measured tangential, axial and radial velocity components as well as total and static pressure using a "Globe pitot meter developed by Dr van der Hegge Zijnen", about which no further details are

given. The cyclone diameter is not given, but it would appear to be about 400mmØ. For an inlet velocity of 10m/s the radial velocities were found to be 1 - 2 m/s inwards for the outer vortex over most of the length, whereas in the core the radial velocities were found to be directed outwards.

Other visualisation studies have been made by Smith (1962a); van Schaick (1970) and Kessler & Leith (1991) to gain an understanding of the flow, but the fast, dynamic nature of the flow and the high turbulence have made this difficult. To reduce the disturbance that the probes have on the flow many different designs of probes have been used. Different sizes of cyclones will change the extent of the interference of the flow by the probe. Smith (1962a) used a 'cobra probe' to measure the flow direction and a pitot-static tube to measure the velocity magnitude in a 140mmØ cylindrical cyclone. The probes were less than 1mm in diameter and were kept symmetrically aligned across the cyclone. Uspenskii et al (1972) used a 5 channel spherical probe to obtain the velocity component profiles in cyclones of diameters 200, 300, 400, 500, and 600mmØ, each of length 2.5m.

A thorough investigation of the flow in a 140mmØ cylindrical reverse-flow cyclone was made by Ogawa et al (1990) using a 3mmØ cylindrical pitot probe. Traverses were made at seven heights, and along six different radii at different azimuthal angles at each height, This shows that the azimuthal variation of the velocity is negligible. These measurements were repeated at three different inlet velocities. The axial profiles reveal negative values near the axis, suggesting a reversal flow inside the core vortex.

The tubulence measured (by unspecified means) by Hejma (1971) was 10%, in a 315mmØ cyclone. In comparison, radial velocities were 1 - 3 m/s for an inlet velocity of 17m/s, showing the radial velocity to be of comparable magnitude to the turbulent fluctuations. The wall boundary layer was approximately 12mm, and the radial position of the zero axial velocity was found to vary slightly in position. In the cylindrical section this crossover occurred at $0.64R_B$ while in the cone it varied from 0.54 to $0.65R_B$ where R_B is the radius of the cyclone barrel.

In the past, the determination of the velocity profiles by probe traverses has been discredited because of the sensitivity of the vortex flow to disturbance by probes. Despite this, the profiles obtained are still at least qualitatively useful and the errors are to some extent compensated for by the fact that the probe yields only a time-averaged representation of the flow. More sophisticated measurement techniques also suffer from difficulties. The precession of the vortex axis off the centreline complicates the measurement of velocities with Laser Doppler velocimetry apparatus (LDA), and the inability to sample all regions at once means that the picture of the flow that results will be a time averaged, or statistical representation. The dynamic behaviour of the flow as well as the secondary flows such as the cone boundary layer also need to be addressed, as they may have a large impact on the dust collection flows.

The modern approaches include the continued development of Laser Doppler anemometer techniques, and computer modelling and simulation. Zhou and Soo (1990) used a Laser Doppler velocimeter in a 300mmØ cyclone with inlet tangential velocity of 21m/s. This cyclone was somewhat shorter than a Stairmand H.E. geometry, with a barrel length of 0.95D and a cone length of 2.3D. They found that the radial distribution of tangential velocity could be fitted by an equation that was similar to the Burgers (1948) vortex solution, and an equation to predict the radius of the core was given. The flow patterns in hydrocyclones have been

examined in many studies using tracers, LDA and computer simulations. Examples include Kelsall (1953), Bradley & Pulling (1959), Knowles et al (1973), Dabir & Petty (1986), and Hsieh & Rajamani (1991). The modelling of the flowfield received treatment, by Bloor and Ingham (1973, 1975a, 1975b, 1987), Rhodes et al (1987) and Hsieh & Rajamani (1991).

To minimise the interference to the flow, and to get a more continuous view of the flowfield, the use of tracers looks promising. This has been used successfully in hydrocyclones, but visible tracers that are close to the density of air is more difficult. Near-neutrally buoyant helium bubble tracers have been used in this study, and are also reported by Kessler and Leith (1991). They used the tracers to measure the tangential and radial velocity components in a transparent 250mmØ Stairmand H.E. cyclone, and estimated the axial velocity from the conservation of mass. The radial velocities obtained had to be smoothed before being considered usable.

2.B.2: Existing cyclone vortex structure theories:

The double vortex described earlier is generally accepted as the structure of the cyclone vortex, and this can be observed by simple visualisation experiments. The axial and tangential velocity are found experimentally to be roughly constant over the cyclone height, but since the remaining axial flow measured at the entrance to the bin represents only 10% of the inlet flow there must be a radial inflow. The measurements of radial velocity are reported to be approximately uniform over the cyclone height, and although these measurements are subject to inaccuracies due to the turbulence, the probe interference, and the precession of vortex about the axis, the concept of uniform radial inflow has been adopted in the models of the vortex structure.

The progression of the models of the cyclone collection mechanism by Barth (1956), Muschelknautz (1972), Leith and Licht (1972, Dietz (1981) and Mothes & Loffler (1984) all use the same basic vortex structure, but differ in the refinements that they make to the model. These theories represent the best prediction methods at present, but they still fall short. The assumed vortex structure could be modified to allow for the localised variations of the inflow that were observed in certain regions of the cyclone, but such a model provides no explanation of the mechanism that causes the inflow to vary. The vortex could be expected to demonstrate dynamic variations rather than the steady-state picture used to date.

The three more recent models models (Deitz, 1981; Leith & Licht, 1972; Mothes & Loffler, 1984) allow for a finite length of the vortex, by adopting the 'natural length' determined empirically by Alexander (1949). Rather than spreading the radial inflow over the entire cyclone length, this allows for the vortex length to be less than the cyclone length.

The 'Natural length' of a vortex:

Descriptions of the flowfield arising from flow visualisation often involve mention of a discontinuation of the vortex at some point before the dust exit, particularly for long or cylindrical cyclones. While the concept of a natural length for a vortex had been raised as early as da Vinci in the 17th Century, the equation for predicting this length in return-flow cyclones was developed more recently by Alexander (1949). This remains to date the only means of estimating the natural length of a cyclone type vortex. The equation was developed from

experiments on what was in essence a cylindrical cyclone, as the cone (closed, with no bin) was progressively withdrawn in the axial direction (Alexander, 1986). The location of the termination of the vortex was observed by introducing water droplets through the inlet, giving streaks of water on the walls. The termination was revealed by these streaks losing their axial component. The distance from the gas exit lip at which the termination occurred was found to be:

$$L_{Al} = 2.3\, D_X \left(\frac{D^2}{Fen}\right)^{\frac{1}{3}} \qquad \text{--- (2.1)}$$

where D_X is the gas exit diameter; D is the barrel diameter and F_{en} is the entrance area

Abrahamson and Allen (1986) report that this closely predicts the position of the lower stagnation region found by ter Linden (1949) with velocity probe measurements. Some dependence on velocity or Reynolds number would also be expected, but this dependence has not been demonstrated. For the standard Stairmand High Efficiency cyclone geometry the distance from the gas exit lip to the dust exit is 1.4 times the natural turning length as calculated from equation 2.1. This would suggest that unless the contraction of the cone prolongs the vortex beyond the distance observed in the cylindrical case, the vortex terminates before the bin entrance.

The vortex is expected to have some means of capping the low pressure core. Possible forms of the termination of the vortex are:

(a) the vortex attaching to the wall and precessing;
(b) an axially symmetric breakdown on the axis at a stagnation point with a region of recirculating gas;
(c) a breakdown into multiple vortex cores,
(d) or a separation of the boundary layer from the wall.

The attachment of the vortex to the wall has been observed in many confined vortex flows, including those reported by Muschelknautz & Krambrock (1970), Krambrock (1979), and Smith (1962a). The diagrams from the former article are reproduced below:

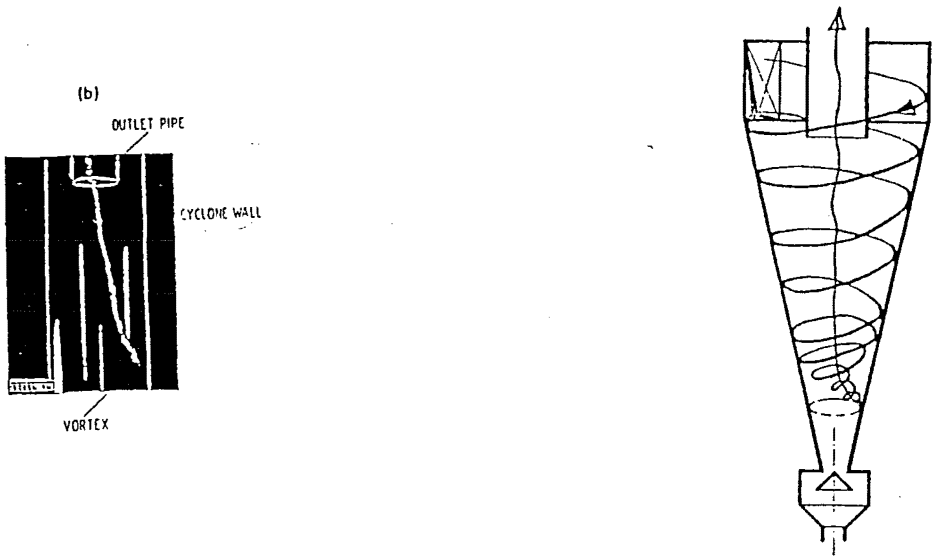

Figure 2.8: Vortex breakdown observations of Muschelknautz & Krambrock (1970)

Muschelknautz & Krambrock (1970) determined the vortex length by inserting a screw propeller axially in a 2 metre long cyclone tube of 100mm diameter. This was reported to show that the vortex always has a limited length, and in very long tubes it always ends on the wall.

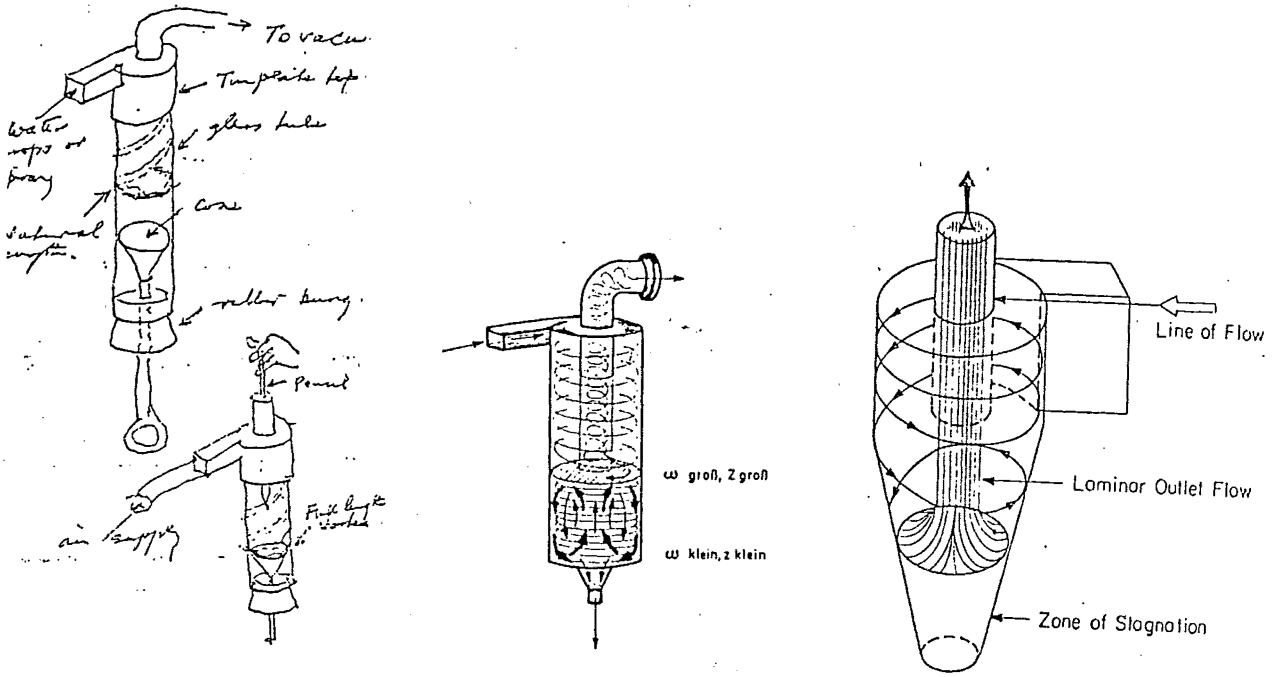

Alexander (1986) Trawinski (1981) Ayer & Hochstrasser (1976)

Figure 2.9: Vortex breakdown observations of Alexander (1986), Trawinski (1981) and Ayer & Hochstrasser (1976)

The rotation of the point of attachment around the wall in the axial plane is mentioned by Smith, and this could explain the observations of Alexander (1949,1986), Trawinski (1981) and Ayer & Hochstrasser (1976) which are also shown in figure 2.9. Dust deposits on the wall in these latter studies ended abruptly at a plane, below which considerable turbulence and mixing were observed, and according to Alexander (1986) there was "no remnant of the vortex flow". Only Ayer & Hochstrasser (1976) observed the termination occurring in a conical cyclone, and this was for a 19mmØ Stairmand H.E. sampling cyclone, with "laminar" conditions in the exit. They reported that below the ring of dust deposits there was "no further change in the pressure inside the cyclone", and the phenomenon was not observed when the conditions in the gas exit were turbulent.

Bryant et al (1983) set out to verify Alexander's natural vortex length concept, which predicted a length of 2.0 barrel diameters for the standard design that they considered. Dust was observed to adhere to the walls below a certain level, and this demarcation was found to be 1.6D for a range of cyclone geometries including straight cylindrical cyclones, and those with cones of different angles, as shown in figure 2.10.

Bryant et al (1983) considered this to be evidence that the actual length over which the core vortex could exert a positive driving force was 1.6D rather than the 2D predicted by Alexander for their geometry. To further test this, the behaviour of a bed of particles on the cyclone base was observed as the base was advanced and retracted.

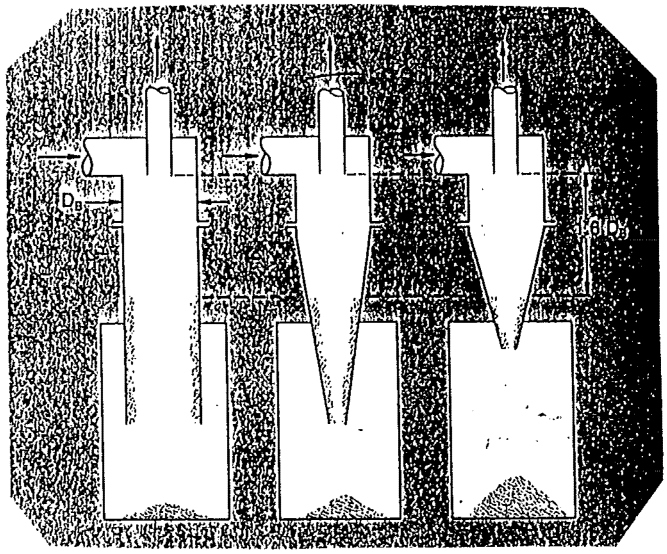

Figure 2.10: Dust deposits on the walls of cyclones, from Bryant et al (1983)

It was found that the particles were first entrained from the bed by the core vortex when the surface was 1.6D from the gas exit lip, but this behaviour could be stretched to a separation of 2D upon retraction. While the particles were being entrained by the vortex the static pressure at the base was considerably less than the pressure observed at greater separations, suggesting a connection with the low pressure core. These experiments were carried out in a cylindrical cyclone, which was effectively the case in Alexander's (1949) measurements.

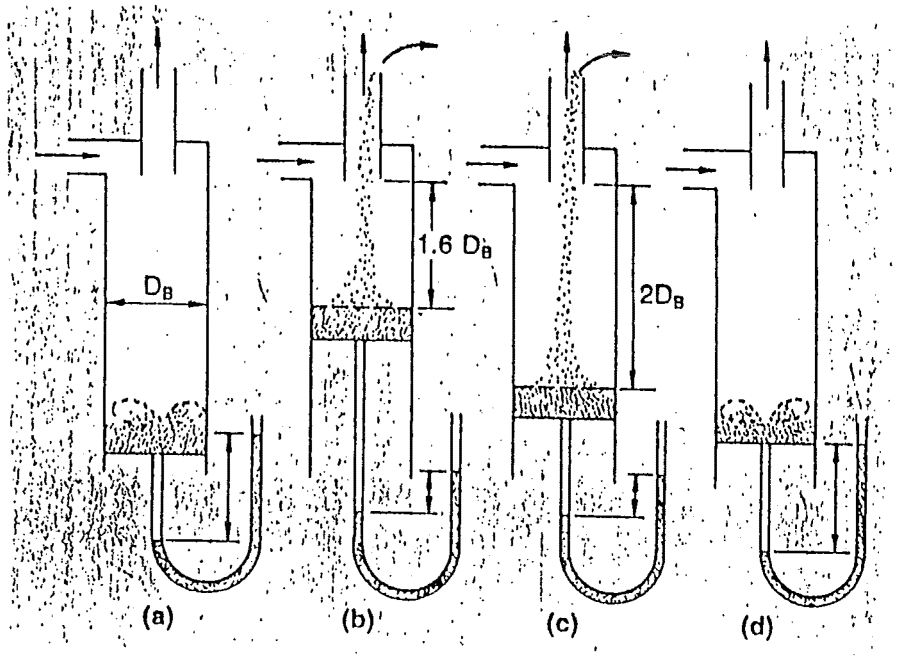

Figure 2.11: Entrainment from the bin base indicating vortex length, from Bryant et al (1983)

Alexander had a cone of length 2D, but this was withdrawn until the cylindrical barrel length was sufficient (about 3D) to bring about the observed change in flow pattern. The attachment of the vortex to the wall that was observed by Smith (1962a) was also in a cylindrical cyclone,

and it was never observed for lengths less than 4D and was always observed for lengths longer than 12D. The vortex would jump to attach to the centre of the base when the base was within 2 diameters of the point of attachment. The reservation about all of these length criteria that are based on cylindrical cyclones is that it is expected that a cone can stabilise the vortex over an increase in length of several diameters compared with the cylinder.

A periodic motion of the core similar to that observed by Smith (1962a) was reported by Chanaud (1965) in a hydrocyclone. As well as cylindrical geometries, three cylinder/cone combinations were examined with different cone lengths and angles. These also showed the periodic motion, but the extent of this behaviour was less with the longest cone. The cone length was reported to have no effect on the velocity dependence of the phenomenon.

The results of Muschelknautz & Krambrock (1970) and Smith (1962a) clearly show the vortex core attached to the wall of the cylinder. The other observations mentioned above are based on the abrupt end to the dust wall deposits. These deposits could be interpreted as due to the influence on the dust flow at the wall by other flow structures, including the 'gas bubbles' proposed by Abrahamson & Allen (1986). van Schaick (1970) set out to record visual evidence of the Alexander natural length in a Stairmand High efficiency geometry design, but no support was found. The observations on which the natural length equation is based, as shown in figure 2.9 (Alexander, 1986) could be due to other mechanisms.

Allowing for dynamic behaviour the flow may involve vortex breakdowns forming and dispersing and the vortex stretching and retracting between meta-stable positions. The core vortex after the reversal is often assumed to be a steady flow towards the gas exit, but could be subject to further breakdowns and flow reversals. Such 3 celled vortices have been observed in hydrocyclones by Dabir & Petty (1986). A downdraft at the centre of the gas exit is often recorded, for example by Weber & Keenan (1956) and Smith (1962a). The investigation of the existence of a natural length for vortices in conical cyclones is the major aim of this thesis.

2.B.3 Measurements of cyclone collection efficiency

In the absence of the means to theoretically predict the efficiency of a cyclone, progress has been made by experimentally determining the efficiency for a range of geometries and identifying the best one. This is unable to predict the performance of new designs, but it was shown by Stairmand (1951) that for a given geometry the efficiency for different operating conditions of velocity, dust density, dust size distribution or cyclone diameter could be predicted.

Stairmand (1951) reported grade efficiencies for his 200mmØ Stairmand High Efficiency. cyclone at an inlet velocity of 15.2m/s with a dust of density 2000kg/m^3. These have been widely used to compare the performance of models of cyclone efficiency. To transform the grade efficiency curve to other conditions Stairmand suggested using the Stokes number as a scaling parameter:

$$d_2 = d_1 \cdot \sqrt{\frac{\rho_{p1} \cdot V_{i1} \cdot D_2}{\rho_{p2} \cdot V_{i2} \cdot D_1}} \qquad \text{--- (2.2)}$$

where the particle diameters d_2 and d_1 correspond to the same efficiency.

van Schaick (1970) measured the grade efficiency at three different flowrates (inlet velocities of 7.8, 12.8 and 15.2m/s) in a 200mmØ Stairmand H.E. cyclone. The test dust had a density of 2600kg/m^3 and 50% was larger than 10mm. The grade efficiency curve agreed well with the results of Stairmand (1951) when adjusted for the different test conditions.

In determining the efficiency of dust collection the size distribution must be measured, and for irregularly shaped dust there is no unique number to describe the size. The aerodynamic diameter is considered the most relevant, and sizing methods are generally selected which yield values related to this. van Schaick (1970) fractionated the particles according to their aerodynamic diameters using a 6 stage Andersen sampler, whereas Tengbergen (1965) used a Bahco classifier for the size analysis, which yielded the terminal velocity of the particles. Tengbergen (1965) used dried clay (50% larger than 19μm) and foundry dust (50% larger than 30μm) to investigate the grade efficiency in 5 cyclone geometries ranging in diameter from 280 to 370mmØ.

Mothes et al (1981) determined the grade efficiency curves by means of a light-scattering particle size analyser for a variety of cyclone geometries. The barrel diameters were all 190mmØ and the height was varied from 290mm to 650mm with flowrates from 0.028 to 0.063m^3/s (giving inlet velocities from 9.8 to 20.8m/s). Limestone dust (with a d_{50} of 1.4μm and no particles over 10μm) was used at loadings of 0.5 to 20 g/m^3.

The determination of the efficiency using dust encounters problems ensuring that the dust is fully dispersed in the inlet stream, as compaction and agglomeration occur in the feed hopper. It is also suspected (such as by Stairmand (1951)) that the bouncing of larger particles off the walls causes re-entrainment of 'already collected' particles, with a consequent shift in the slope of the grade efficiency curve. For this reason, many studies have used oil aerosols at low concentrations. The low concentrations reduce the likelihood of agglomeration and are below the level at which the particle presence would be expected to influence the gas flow. The aerosol particles are spherical, and once they reach the wall they are unlikely top be re-entrained.

In comparing different grade efficiency curves with each other, and with predictions from the models the technique used to obtain the data should be noted. Aerosols have been used widely because they fit assumptions made in developing the models. However, the results obtained with aerosols may not agree with the collection characteristics of dust. Dusts are generally used at feed concentrations of 5-10g/m^3 whereas aerosols are typically used up to 0.05g/m^3. Peterson and Whitby (1965) examined the grade efficiency of a 305mmØ cyclone with two standardised test dusts of irregular shapes as well as monodisperse aerosols of between 0.065 and 5μm diameter. The concentration of the aerosols was measured by tagging them with a fluorescing dye, a technique that has been used subsequently by a number of workers.

Beeckmans and Kim (1977) measured the collection efficiency in two cyclones, of diameters 152mmØ and 76mmØ, with inlet velocities in the range 6.1 - 15.5 m/s. They used monodispersed dye (specific gravity of 1.42) aerosols of sizes 0.6 to 4.7μm. Electrical charges on the aerosol were neutralised, and the inside surfaces of the cyclone were coated with conducting paint and were grounded. The aerosol was collected on slides and sized with a

microscope at 800 times magnification. The cyclone was washed down with water at the end of each run, and the concentration of the dye was measured fluorometrically to determine the amount of aerosol captured. The log-log plot of efficiency versus particle size was found to fall on a straight line.

Iozia & Leith (1989a) tested eleven cyclone configurations based on the standard Stairmand design, with diameter 250mmØ. One geometrical parameter was altered at a time and a mineral oil aerosol with specific gravity 0.876 was used. The effect of particle charging was found to be negligible by performing tests with and without a charge neutraliser. A light-scattering spectrophotometer was used to determine the concentration and size distribution of the aerosol particles. Dirgo and Leith (1985a) used a mineral oil aerosol of density 860kg/m^3 to examine the grade efficiency in a 305mmØ Stairmand H.E. cyclone at inlet velocities of 5, 10, 15, 20, and 25 m/s. The particles over 1μm were sized and counted into size intervals of 0.75μm using an aerosol scattering spectrometer. Comparing their results with those of Stairmand (1951) they found higher efficiencies for particles greater than 3.5μm, and lower efficiencies for smaller particles.

Other studies using aerosol particles include DeOtte (1990b); Kim and Lee (1990) for 9 geometries of cyclones with diameters from 22mmØ to 41mmØ, and Burkholz (1985) who examined the fractional efficiencies of 14 different cyclone geometries of diameters 30mmØ to 600mmØ.

Abrahamson and Allen (1986) list 24 studies that present grade efficiencies of 29 different cyclone geometries of industrial size (see figure 2.4). The sharpness of classification for these is summarised in their figure 4. The variation of the gross efficiency with changes in geometrical parameters or operating conditions has also shown interesting trends, such as reported by Svarovsky (1984), Zhou, Zhang and Yu (1987) and Petroll and Langhammer (1962).

2.B.4 Empirical Predictions of the grade efficiency:

Cyclones are characterised by the cut size d_{50}, the size of particle that is collected with 50% efficiency. However the slope of the grade efficiency curve also varies, and although the cut size has been predicted reasonably well, the slope has proven more difficult to account for. Instead, empirical descriptions have had to be resorted to, which are specific to the cyclone geometry on which the measurements were carried out. Using the approach of Barth (1956), Muschelknautz (1972) or Stairmand (1951), an experimental efficiency curve can be adapted to the conditions of a geometrically similar cyclone of interest. Attempts have been made to generalise the results to other geometries, but the large number of possible combinations of the geometrical parameters makes this approach difficult.

Rietema (1961) proposed a hydrocyclone correlation number, Cy_{50} based on the idea that both the separation and the pressure drop depended on the centrifugal acceleration field. Hence for a certain cyclone a relation was proposed between the static pressure drop and the separation achieved expressed in terms of the 50% separation diameter. The effect of the turbulent eddy

diffusivity on the separation was ignored, and Stokes law was assumed. This resulted in the expression:

$$C_{y50} = \frac{d_{50}^2.\Delta\rho}{\eta}.L\frac{(\Delta P)_t}{\rho Q} \qquad \text{--- (2.3)}$$

where η is the dynamic liquid viscosity
$\Delta\rho$ is the density difference between the solid and liquid phases
ρ is the liquid density
Q is the throughput
and $(\Delta P)_t$ is the total pressure drop.

The cyclone correlation number C_{y50} was thought to be a constant for a cyclone of a given shape. It could be expressed as a combination of the cyclone dimension and velocity ratios:

$$C_{y50} = \frac{72C_1}{\pi}\frac{R_1}{b^2}\left(\frac{U}{W}L - R_1\right) \qquad \text{--- (2.4)}$$

where C_1 is the ratio of the axial velocity to the inlet velocity $= \frac{W}{V_i}$
U is the radial velocity
L is the Length
R_1 is the radius of the wall, less the radius of the air core
b is the diameter of the inlet.

However, Rietema (1961) did not calculate the value of C_{y50} as the velocity ratios were not readily available. Instead he fitted the value to experimental values of the separation of cyclones. Values of approximately 10 were obtained, and plots of the correlation number versus the geometry ratios were presented.

Beeckmans and Kim (1977) correlated their experimental results with a function of the cyclone Stokes number and the cyclone Reynolds number. They found that the cyclone efficiency had a Reynolds number dependence, whereas previous studies had claimed that it was solely a function of the Stokes number. They acknowledged that the range of the parameters in their study (cyclones of 152mmØ and 76mmØ) was considerably less than values for industrial cyclones, and there may be a critical Reynolds number above which the efficiency becomes a function of the Stokes number only. This could be related to the development of the low Reynolds number flowfield to a constant structure at higher Reynolds number.

Lapple (1951) used the concept of the effective number of turns (N_e) of the vortex in the length of the cyclone, with the efficiency predicted to increase in the ratio of d_p/d_{pc}. Here the cyclone cut size d_{pc} is given by:

$$d_{pc} = \sqrt{\left[\frac{\mu_G b}{2\pi\,\rho\,V_g\,N_e}\right]} \qquad \text{--- (2.5)}$$

Lapple (1951) estimated the value of N_e by fitting the equation empirically. N_e is reported by Friedlander et al (1952) to vary from 0.5 to 10 for various cyclone geometries. Dirgo and Leith (1985a) found with their Stairmand High Efficiency design that the number of turns was 10 to 12 for inlet velocities up to 15 m/s, and approximately 20 to 25 for inlet velocities up to 25m/s. DeOtte (1990b) found Lapple's prediction of the cutpoint agreed within 0.3% of the experimental measurements in a 89mmØ cylindrical multiple inlet cyclone, at a single inlet

velocity. The number of turns of the vortex was measured by attaching a thread to the inlet and this also demonstrated good agreement with the prediction of Lapple. However, N_e is an unknown function of geometry and Reynolds number and therefore must be measured for each case.

van Schaick (1970) observed the number of turns of the dust rope on the wall in a transparent Stairmand H.E. cyclone and found Lapple's equation for N_e underpredicted the number of turns. The discrepancy was higher for lower velocities, but even at an inlet velocity of 15m/s the prediction was for 5 turns, whereas 9 turns were observed. The number of turns of the dust rope need not necessarily equal the number of turns of the gas, but replacing N_e by the observed number of turns in Lapple's prediction of efficiency for the Stairmand H.E. geometry improved the agreement with the experimental results.

The cyclone cut size d_{50} can be estimated by balancing the centrifugal force on a particle with the drag on the particle due to the radial gas velocity, calculated at the radius of the gas exit. This yields the Stokes number $N_{stk} = \frac{\rho_p d_p^2 V_g}{\mu D}$ as a parameter, and for geometrically similar cyclones the experimental data can be scaled using this approach, which is explained in more detail in section 2.B.5. This gives a reasonable estimate of the cut size, but not the shape of the grade efficiency curve, for which the classification is less steep, as the efficiency for larger particles is lower than expected, and the collection of fine particles is enhanced. These deviations are thought to be due to agglomeration, re-entrainment, particle bounce (off the walls), and secondary by-pass flows.

For the Stoke number parameter to be valid the particle Reynolds number for relative motion (air-particle) must be less than 1. Abrahamson and Allen (1986) point out that this is exceeded in many cyclones, and hence used a more general drag law that reduces to the Stokes law at low Reynolds number. The Abraham (1970) drag coefficient was used, which is accurate to 6% for Reynolds numbers up to 6000. The radial sink velocity V_{rp} can then be calculated from the radial drift Reynolds number Re_r. where:

$$Re_r = 20.5\left[\sqrt{\left[\left(\frac{Ga^{0.5}}{9.61} + 1\right)\right] - 1}\right]^2 \qquad \text{--- (2.6)}$$

and the Galileo number Ga, evaluated at the exit tube radius R_x:

$$Ga = \frac{\rho_g V_{\theta x}^2 D_p^3 \rho_p}{R_x \mu^2} \qquad \text{--- (2.7)}$$

with the radial drift Reynolds number then yielding the radial sink velocity from:

$$Re_r = \frac{V_{rp} D_p \rho_g}{\mu} \qquad \text{--- (2.8)}$$

In these expressions the particle diameter is D_p, ρ is the density for the particle or the gas depending on the subscript, and μ is the gas viscosity. $V_{\theta x}$ is the tangential velocity at the particular radius R_x.

The sigmoid shape of the grade efficiency curve can be approximated by a logistic equation, allowing the efficiency to be predicted by:

$$\eta = \frac{1}{(1 + (d_{50}/d)^{\beta})} \qquad \text{--- (2.9)}$$

where d is the particle size.

To predict efficiencies for particles with sizes other than d_{50} the slope parameter (β) must be known - however, no method is available to predict β. This approach has been used by Theodore & De Paola (1980) to fit the data of Lapple (1951) with a value of $\beta = 2$. (Lapple's data had apparently already been smoothed). Dirgo & Leith (1985) similarly described the data of Barth with $\beta = 3.2$. DeOtte (1990b) found $\beta = 6.4$ to fit the slope of the grade efficiency curve for his cylindrical multi-inlet sampling cyclone

These values of β for the logistic equation were specific to the cyclone geometry and experimental conditions. Iozia & Leith (1990) made measurements with a mineral oil aerosol in a 250mmØ Stairmand H.E. cyclone and proposed an empirical equation for the prediction of the parameter β :

$$\ln(\beta) = 0.62 - 0.87 \ln(d_{50}) + 5.21 \ln\left(\frac{ab}{D^2}\right) + 1.05\left(\ln\left(\frac{ab}{D^2}\right)\right)^2 \qquad \text{--- (2.10)}$$

For the Stairmand H.E. cyclone, the inlet area $ab = 0.1\ D^2$ and the equation simplifies to

$$\ln(\beta) = -5.81 - 0.87 \ln(d_{50})$$

where d_{50} is given in centimetres. (The fitting coefficient, adjusted for the number of degrees of freedom is 0.833). This predicted β well for the cyclones used in Iozia & Leith's (1990) study, but did not agree well with the results of Dirgo and Leith (1985b).

2.B.5 Efficiency prediction based on the flow field

In order to generalise the method of predicting the efficiency of a cyclone, other workers (Barth (1956), Leith and Licht (1972), Dietz (1981), Mothes & Loffler (1984)) have made assumptions about the flow that allow direct calculation of the entire fractional efficiency curve.

The static particle theory was developed by Stairmand (1951) and Barth (1956). This theory suggests that for a critical particle size (d_{50}) a balance is achieved between the centrifugal force given to the particles by the spinning gas, and the drag force caused by the inward flowing gas. The critical particle will theoretically remain spinning forever at the radius at which this balance occurs. Given some diffusive movement, smaller particles will be more likely to escape the cyclone, while larger particles will be more likely to be captured. The critical size will be collected with 50% efficiency. Applying the equation for the force balance at the radius of the core r_c (where the tangential velocity is a maximum, $V_{\theta max}$) requires:

$$\frac{\tau(V_{\theta max})^2}{r_c} = V_r \qquad \text{--- (2.11)}$$

where τ is the particle relaxation time: $\frac{d^2 \rho_p}{18u}$ --- (2.12)

Barth (1956) neglects the non uniformity in the distribution of axial velocity and assumes that the radial and tangential velocity components are independent of the height in the cyclone. The

average (inwards) radial velocity of the gas is obtained by assuming the inlet flow Q is evenly distributed over the length of the cyclone, z_c :

$$V_r = \frac{Q}{(2\pi\, r_c\, z_c)} \qquad \text{---- (2.13)}$$

This yields the expression of the cut diameter: d_{50}

$$d_{50} = \sqrt{\left\{\frac{9\mu Q}{\pi\, z_c\, \rho_p\, (V_{\theta max})^2}\right\}} \qquad \text{--- (2.14)}$$

Barth calculates the terminal settling velocity for the 'static particle' as

$$V_{ts}^* = \frac{Q.g}{2\pi.z_c.V_{\theta max}^2} \qquad \text{--- (2.15)}$$

and the collection efficiency for any other particle size is determined by the ratio of its settling velocity to V_{ts}^* .

This expression can be used to calculate d_{50} for any cyclone geometry and operating conditions providing the tangential velocity and the core length are known. Iozia and Leith (1989a) used their empirical correlation for the maximum tangential velocity (equation 3.B.5) to predict the cut size. This thesis presents results that will be useful in improving this estimate, and for evaluating the other assumptions made about the structure of the flow and the mechanism of particle collection.

Dirgo and Leith (1985a) compared the predictions of Barth (1956), Lapple (1951), Leith & Licht (1972) and Dietz (1981) with aerosol collection data from a Stairmand H.E. cyclone. They found that theory of Barth gave the best prediction of the slope of the grade efficiency curve, but the curves were displaced to higher particle sizes. To achieve a better fit to the data Dirgo and Leith treated the ratio of the terminal settling velocities as an adjustable parameter, and a good fit was found if the velocity ratio was quadrupled. Kim and Lee (1990) found good agreement between Barth's (1956) predictions and their measurements on small cyclones of 22 to 41mmØ, without the modification of Barth's equation that Dirgo and Leith used.

Ayer and Hochstrasser (1976) found that the approach of Barth predicted the grade efficiency well in their 19mmØ sampling cyclone. On moderate sized cyclones the theory of Leith-Licht performs better. Burkholz (1985) examined 14 different geometries ranging from 30mmØ to 600mmØ and reported that the theory of Barth agreed well with the results.

Dietz (1981) used the experimental observations of ter Linden (1949) to propose a model for the collection of particles in a cyclone. In the study of ter Linden (1949) dust was released at various points in the cyclone, and collection was still found even when dust was released into the inner vortex region (see figure 8.1). This supports the idea of a turbulent redistribution of dust within the cyclone. Dietz (1981) divided the cyclone up into three regions: the entrance region, the outer vortex (the annular regions travelling downwards), and the inner vortex or core (travelling upwards). The exchange of particles between the outer and inner vortices was allowed, and rapid turbulent mixing is assumed to keep the radial dust concentration profiles uniform within each region. This was to allow for the loss of particles by both short gas residence times and by mixing into the core region.

The particle flux between the outer and inner vortices was viewed as being composed of two components. The first was due to the drag of the radial velocity which carries particles from the

outer to the inner vortex, and the second was the propulsion of particles out of the core under the action of the centrifugal force. The velocity of particles crossing the boundary between the vortices was calculated by equating the centrifugal and drag forces at that location. The model results in different particle concentrations on either side of the separating surface (the imaginary extension of the gas exit). This physical discontinuity in the concentration is unrealistic. In addition, the particles are assumed to move radially into the core at the same velocity as the gas, whereas some slip would be expected. The predicted grade efficiency curve is lower than the experimental measurements.

The assumptions made by Dietz (1981) about the flow pattern inside the cyclone were:
- The radial inflow from the outer to the inner vortex is constant:

$$U_r(z) = U_{ro} = \frac{Q}{2\pi R_c L} \qquad \text{--- (2.16)}$$

- The axial flow rate is given by $Q(z) = Q_o(1 - z/L)$ --- (2.17)

- The tangential velocity does not vary axially (as suggested by Stairmand, 1951)

- The radial variation of the tangential velocity is given by a modified free vortex as in equation 3.B.1 with n between 0.5 and 1.0

- The radius of the core region is the same as the radius of the gas exit tube. (Although Stairmand (1951) states that the maximum separative region is somewhat smaller than this radius).

The cyclone efficiency is calculated as:

$$\eta = 1 - \left[K_o - (K_1^2 + K_2)^{0.5}\right] \times \exp\left[\frac{-\pi(2S - a)\rho_p d^2 V_i}{18\mu\, ab}\right] \qquad \text{--- (2.18)}$$

K_o, K_1, K_2 are functions of the particle and gas properties as well as the cyclone dimensions. S is the length of the gas exit below the roof, and a and b are the height and width of the inlet, respectively.

Leith & Licht (1972) used the concept of a residence time and found the efficiency was dependent on the Stokes number (as used by Stairmand for scaling purposes) and a geometrical parameter. The resulting equation for predicting the cyclone efficiency is:

$$\eta = 1 - \exp\left[-2(C\Psi)^{1/(2n+2)}\right] \qquad \text{--- (2.19)}$$

where: C is a function of the cyclone dimension ratios only, which takes into account the natural vortex length predicted by Alexander (1949)

Ψ is a modified inertia parameter, which depends on the properties of the gas/particle system to be treated: $\Psi = \frac{\rho_p d_p^2 V_i}{18\,\mu_G\, D}(n+1)$ --- (2.20)

with n being the vortex exponent calculated by Alexander (1949) in equation 2.2:

This agrees very well with the experimental results of Stairmand (1951) and Peterson and Whitby (1965), but not for generalised geometries. This approach has been discounted by Abrahamson (1985) and Clift, Ghadiri & Hoffman (1985,1992) as being unrealistic and based on erroneous mass balance concepts. Although Leith & Licht recognised that there was a

distribution of gas residence times in the cyclone, only the average residence time was utilised in their analysis. The model also assumes that gas passing from the outer vortex to the inner vortex contains no particles, and particles enter the inner vortex only at the end of the collection region (at the natural length of the inner vortex). The shorter residence times that actually occur can result in a significant loss of particles. In addition, the uniform mixing of the particles across the cross-section of the cyclone and the flow becoming progressively cleaner as the residence time increases may be appropriate for an axial flow cyclone, but it neglects the effect of the reverse flow. Clift et al (1985) indicated how some of the inconsistencies could be removed, but felt that this was effectively converting this to the model of Dietz (1981).

Abrahamson et al (1978) showed that the velocity of radial redistribution of the dust that was assumed by Leith and Licht (1972) was unrealistically high. Instead, the mixing was proposed to be related to the large convective eddies, and hence would be dependent on the cyclone Reynolds number. This led to a modification to the Stokes number scaling parameter, yielding:

$$N_{Ab} = \frac{\rho_p d_p^2 V_i^{17/16} \rho^{1/16} g}{\mu^{17/16} D^{15/16}} = N_{Stk} \cdot (N_{Re})^{1/16} \qquad \text{--- (2.21)}$$

The possibility of a Reynolds number dependence of efficiency was raised by Beeckmans & Kim (1977)

Aslami & Licht (1978) adjusted the approach of Leith and Licht (1972) by using an empirically determined 'effective residence time' and an 'effective operating parameter', which allowed for factors such as re-entrainment from the walls and the bin base, agglomeration of the dust as well as any errors in the assumptions inherent in Leith and Licht's analysis. The central core was also assumed to be conical rather than cylindrical.

Both Leith and Licht, and Dietz (1981) underestimate the residence time of the gas in the inlet section, according to Clift et al (1985). This arises from the assumption that all of the gas enters the cyclone at mid-height in the inlet. Clift et al showed that the correct average residence time for a distributed inlet according to Danckwerts (1953) is simply the volume divided by the throughput. This result also applies to the distributed exit as the gas moves from the outer to the inner vortex.

Beeckmans (1973) took the turbulence in the cyclone into account, using a mean turbulent diffusivity in the cyclone. The turbulent diffusion was assumed to be the predominant mechanism determining the efficiency. Axial migration and diffusion of dust was allowed, but the radial velocity towards the axis was underestimated, and re-entrainment from the walls was not allowed for. These assumptions were identified by Beeckmans (1973) as the limitations that resulted in the model overpredicting the collection efficiency when compared with the experimental data of Stairmand (1951).

Mothes and Loffler (1984) took a similar approach to that of Dietz (1981) but limited the turbulent diffusion of the particles in the radial direction, to provide a more realistic radial exchange. Allowance was also made of the fraction of the inlet flow that enters the bin. This approach at present is the most realistic generalised representation of the flow used for modelling the grade efficiency.

Boysan, Ayers and Swithenbank (1982) derived a fundamentally based mathematical model of the gas and particle flows in the cyclone. An algebraic turbulence model was used for the highly swirling flow and good agreement was achieved between the computed flow and the

experimentally observed gas flows in a Stairmand H.E. cyclone. A stochastic particle tracking technique was used to predict grade efficiency curves, which also were reported to agree well with experimental measurements.

Kessler and Leith (1991) used the gas velocities in the cyclone that had been obtained by photographing the movements of helium bubble tracers. The spline-smoothed velocities were used in the numerical solution of the equations of motion, which were reduced to three first order non-linear differential equations. This allowed the paths of particles in the cyclone to be predicted. It was assumed that particles reaching the inside of the exit duct were lost, and particles impinging on the cyclone walls were collected. The turbulence was modelled using a radial velocity fluctuation of 14% for radial velocities above $4ms^{-1}$ and a constant value of 0.56 ms^{-1} for radial velocities below this.

The resulting predicted grade efficiency curve was compared with the experimental grade efficiency measurements of Iozia & Leith (1990) which had been carried out in the same cyclone. The model performed better than the models of Barth (1956), Dietz (1981) and Iozia & Leith (1990) for particle sizes below 5μm. The prediction was within experimental error of the experimental data for these small particles, but for particles above 5μm the model overestimated the collection efficiency. This difference was attributed by the authors to an incomplete description of turbulence, or from errors in the measured velocity profiles. The difference could also be attributed to secondary flows not considered in this approach, and the possibilities for this will be examined in this research.

DeOtte (1990b) predicted the collection efficiency of 88.9mmØ and 44.5mmØ cylindrical multi-inlet sampling cyclones on the basis of numerically calculated particle paths using three dimensional velocity profiles determined with a laser doppler velocimeter (DeOtte, 1990a). He made experimental measurements of the collection efficiency using an oil aerosol tagged with sodium fluorescin. The numerical predictions gave a good estimate of the cut size, but the slope of the efficiency curve was far too steep.

2.B.6 Refinements of the efficiency models

Turbulence in the cyclone has been suggested as the cause of the difference in the slope between the predicted and measured grade efficiency curves. The presence of turbulence flattens the curve, and models that incorporate turbulence (Dietz, 1981; Mothes & Loffler 1984) generally perform better than those that do not. However, other factors would appear to be contributing as well, as the effect of turbulence is not consistent with all of the observed differences. Some researchers (Rietema, 1961; Li et al, 1987) have suggested that the influence of turbulent diffusion on the particle separation is negligible, but this was for flows in hydrocyclones. Rietema suggests that the turbulent viscosity and diffusion increase less rapidly than the flow velocity, hence the influence of turbulence becomes less pronounced at high velocity. This would suggest that turbulence is not the cause of the reduction of the efficiency at high velocities.

Hejma (1971) observed that the dust in the boundary layer became coarser closer to the dust exit, suggesting that fine dust was being redistributed. Mothes et al (1985) measured the radial distribution of particle sizes and concentrations in the cyclone and found the particle size distributions became finer as the sampling location was moved from the wall towards the axis. The size distribution near the wall ($r/R_W = 0.96$) was only slightly finer than the feed. This suggested that some of the already collected particles were being re-entrained from the wall.

Abrahamson et al (1978) argue that the agglomeration of particles is a primary effect, and necessary for the collection of fine particles. Abrahamson (1975) and Mothes & Loffler (1985) made a comparison between the possible mechanisms for agglomeration, and this indicated that the particle agglomeration due to different settling velocities was dominant in the cyclone. Large particles sweep smaller ones out of the gas stream as they migrate to the wall. Mothes and Loffler (1985) found that the separation efficiency due to agglomeration with the larger particles reached a maximum with particles of 2 to 3μm in size. They calculated that for an inlet dust concentration of $1000g/m^3$ of 15μm particles, more than 50% of the 2 to 3 μm particles are collected in the cyclone by agglomeration with the big particles. Tackie et al (1989) found that saltation of large particles across a bed of particles was an important agglomeration process.

Tengbergen (1965) considered the agglomeration to take place once particles entered the boundary layer, and considered further calculation of the dust movements 'impossible' because the size of the agglomerates was unknown. More recent studies of the boundary layer have yielded more information. Tengbergen (1965) considered that the degree of agglomeration was a function only of the inlet dust concentration, and not of the inlet velocity. The re-entrainment of agglomerates from the boundary layer was also considered to be a function only of the dust concentration. In this way, the agglomeration was assumed to be independent of the conditions in the main flow. This is not supported by the results of later work, such as that of Mothes and Loffler (1985) as mentioned earlier.

The models of the collection efficiency commonly assume that once the particle reaches the wall it is collected. However, the dust may bounce and become reentrained or there may be removal of the boundary layer. Measurements of the collection efficiency using a mineral oil aerosol (Dirgo & Leith, 1985a; Iozia & Leith, 1990a; DeOtte, 1990b) generally avoids these problems, and hence have been used to compare with the predicted collection efficiency of the model. When collecting dust the effects of bouncing and reentrainment may need to be taken into account.

Kalen and Zenz (1974) proposed the application of a saltation velocity analogous to that for dusty flow in pipes to account for the reduction in efficiency at higher velocities. The maximum cyclone collection efficiency was predicted to occur for inlet velocities 25% greater than the saltation velocity, while re-entrainment occurs for inlet velocities 36% greater than the saltation velocity. However, this does not explain the variation of the effect with different geometries at the same wall velocity, as pointed out by Abrahamson (1981), citing the results of Petroll and Langhammer (1962).

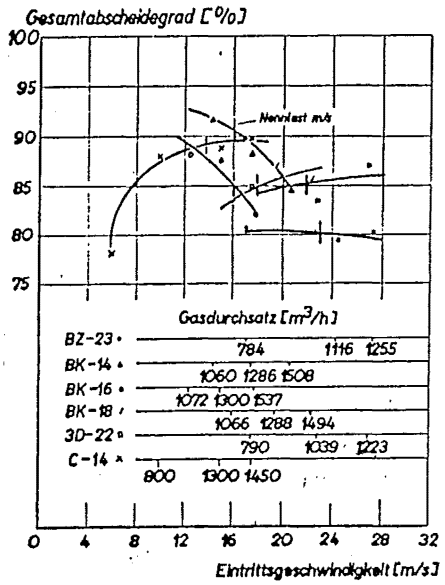

Figure 2.12: Dependence of the gross efficiency on the inlet velocity for various cyclone geometries, from Petroll & Langhammer (1962)

Ranz (1985) considered the effects of particle concentration on the collection efficiency and the contribution of the dust ropes or 'dunes' that form on the walls of the cyclone. The hold-up time of the particles in the dune flow was estimated to somewhat more than twice the residence time of the gas in the cyclone. Ranz developed a dynamic simulation of the movement of these dunes.

Zhou and Soo (1991) calculated a collection efficiency that incorporated boundary conditions for the continuity and momentum equations for the particle phase in the cyclone. This made it possible to predict the influence of the vortex motion turbulence on the collection efficiency. This suggested that the collection efficiency will be reduced by strong particle turbulence. The collection efficiency was reported to be improved by increasing both the cyclone length and the inlet velocity, and decreasing the cyclone radius. It was also desirable to reduce the gradient of the tangential velocity near the wall to reduce the particle turbulence.

The prediction of the collection efficiency of particles based on velocity measurements made on dust-free flows may result in error. Dust loading is known to reduce the pressure drop (Briggs, 1946) and increase the efficiency (Tengbergen, 1965) significantly and a number of explanations for this have been suggested. Crowe & Pratt (1974) made a numerical study of the flowfield in an axial flow cyclone. They found that the introduction of dust reduced the inwards radial velocity of the gas, presumably due to collective drag. This was suggested as an explanation of the observed increase in efficiency at higher dust loadings.

The static particle theory assumes that inflow occurs uniformly over the length of the vortex. Dietz (1981) uses the 'natural length' of the vortex that was proposed by Alexander (1949). This length depends only on the gas inlet and outlet dimensions, and the predicted efficiency is not very sensitive to this length. This 'natural length' determined the location of the attachment of the vortex core to the cyclone wall, which would be expected to have a larger effect on the efficiency than simply fixing the length over which the average radial inflow is calculated. For example, the assumption that once the particles reach the wall they are collected would need to

be adjusted. The structure and behaviour of the vortex could alter the radial flow in other ways, such as the separation of the boundary layer flow from the wall, or by axial variation of the strength of the vortex. The value of z_c used in the critical state efficiency equation above would need to be varied.

Similarly, the vortex length could be determined by the occurrence of vortex breakdown in the cyclone, which could also give rise to large variations in the local radial inflow of gas and particles. Research into vortex breakdown has concentrated on the vortices associated with aerofoils. Confined vortex flow breakdown has received attention because of the ease of control in laboratory studies. The apparatus in some studies, particularly that of Escudier & Zehnder (1982) has similarities to the geometry of the hydrocyclone, and suggest that vortex breakdown could be associated with the hydrocyclone. Disturbances in the flow in gas cyclones have been observed, but chiefly in cylindrical cyclones and of the form of an attachment of the vortex core to the wall. This study applies the concept of vortex breakdown to the flow in gas cyclones and looks for evidence of a natural vortex length, as suggested by Alexander (1949).

Chapter

3

FLUID DYNAMICS THEORY (of vortices and cyclones)

3.A FLUID DYNAMICAL CONCEPTS

Vortices are an important feature of fluid motion, and they occur widely in nature as well as in industrial flows. Lugt (1983) gives a highly readable, entertaining and informative overview of the history of the study of vortices in nature and technology. This should be consulted for an introduction to the concepts of vortex motion.

Observations and theories regarding vortices predate history - it can be assumed that the earliest humans were aware of the destructive power of tornadoes, and vortices play a central role in myths and legends from civilisations all over the world. Life was thought to have started 'in the water of the primaeval vortex', the celestial vortex was the source of all energy, and souls departed earth on a whirlwind.

Vortices have often been employed in explanatory scientific theories, including the attempt by Lord Kelvin in 1867 to interpret the structure of atoms as being knotted and linked vortex rings. The variety of combinations would account for the different elements and compounds and the vibrations and kinetic energy of atoms were also reproduced. However it became clear that since the natural fate of vortices is instability and decay the theory was unsuitable as an atomic model. Even today vortex concepts are being invoked to explain phenomena such as ball-lightning (Coleman, 1990) or crop circles (Meaden, 1990).

On a more general level, vortices play an essential role in the study of fluid motion, as expressed by Kuchemann (1963): "*vortices are the sinews and muscles of fluid motion*". Vortices are important in the transition of boundary layers to turbulence, the occurrence of coherent structures in turbulent flows, aerodynamic lift; propeller and turbine flows, combustion chambers meteorology acoustics and astronomy.

Despite, or perhaps because of, their prevalence, there is no simple nor unique definition of what a vortex is. Lugt (1983) proposes a definition as:
" *a vortex is the rotating motion of a multitude of material particles about a common centre*".
This is valid only in a reference frame which does not move relative to the vortex centre and the identification of a vortex in an unsteady flow requires the knowledge of the history of motion. This section presents a brief introduction to some of the concepts of fluid dynamics, but for fuller details reference should be made to Batchelor (1967), (or at a more elementary level, Lugt (1983)).

Closely allied to the concept of a vortex is the vorticity, which is an important feature of all 'real' flows. Fluid motion can be decomposed into translation, deformation and rotation, and the vorticity describes the rotation of the fluid at a point in space. There is no vortex without vorticity, but the presence of vorticity does not imply a vortex, as vorticity may be generated in a planar shear flow. Vorticity is mathematically defined as the curl of the velocity vector ($\nabla \times \mathbf{v}$), which for solid body rotation is shown to be equal to twice the angular velocity. A physical interpretation for this factor of two was given by Lindgren (1980): "*the vorticity is the sum of the microscopic and macroscopic rotations.*" The vorticity is a vector normal to the plane of rotation (thus it coincides with the axis of rotation). The positive direction may be found from

the right-hand rule: with the fingers curled in the direction of the velocity the thumb points in the positive direction.

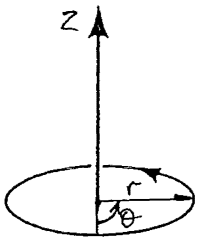

Figure 3.A.1: The vector of the angular velocity is normal to the plane of rotation

In cylindrical polar coordinates of r, θ, z with velocity components v_r, v_θ, v_z the vorticity vectors are: $\omega_r = \frac{1}{r}\frac{\partial v_r}{\partial \theta} - \frac{\partial v_\theta}{\partial z}$ $\omega_\theta = \frac{\partial v_r}{\partial z} - \frac{\partial z}{\partial r}$ $\omega_z = \frac{1}{r}\frac{\partial (r.v_\theta)}{\partial \rho} - \frac{1}{r}\frac{\partial vr}{\partial \theta}$ --- (3.A.1)

Vorticity is generated by shearing of the flow, such as at a wall, and it is conserved on a particle path. Vorticity can only be transferred to an adjacent particle path through the action of diffusion.

The 'div' and 'curl' of a vector function of position are fundamental differential operators in vector analysis, and they yield quantities that are independent of the choice of the coordinate system.

div **u** = ∇.**u** is a scalar that indicates the source intensity of **u** at the corresponding point, (where ∇ is the differential operator: $(\partial/\partial x_1, \partial/\partial x_2, \partial/\partial x_3)$).

curl **u** = ∇x**u** is a vector describing the rotation of fluid about a point P_o

Applied to the velocity field of a steady, incompressible flow div **u** is the net outward flow per unit volume (or the local rate of expansion), while curl **u** is the local vorticity.

$$\nabla.\mathbf{u} = \left(\frac{\partial u_1}{\partial x_1} + \frac{\partial u_2}{\partial x_2} + \frac{\partial u_3}{\partial x_3}\right) \quad \text{--- (3.A.2)}$$

$$\nabla x\mathbf{u} = \left(\left(\frac{\partial u_3}{\partial x_2} - \frac{\partial u_2}{\partial x_3}\right), \left(\frac{\partial u_1}{\partial x_3} - \frac{\partial u_3}{\partial x_1}\right), \left(\frac{\partial u_2}{\partial x_1} - \frac{\partial u_1}{\partial x_2}\right)\right) \quad \text{--- (3.A.3)}$$

One further mathematical relationship of use in the study of fluid motion is the circulation, which is the line integral of the fluid velocity around a closed curve. This is equal to the integral of the vorticity over an open surface bounded by the curve, and is equal to the strength of the vortex tube.

$$\int \omega . ndA = \oint \mathbf{u}.d\mathbf{x} \quad \text{--- (3.A.4)}$$

The integral of vorticity over an open surface A that cuts the vortex tube is thus independent of the choice of A and is termed the strength of the vortex tube.

The motion of fluids is governed by the laws of conservation of mass, momentum and energy. For all of these a distinction must be made between the Lagrangian frame of reference (which moves with the fluid) and the Eulerian frame (which is fixed to an external point). The material

derivative D/Dt is the rate of change observed in the Lagrangian frame. The partial derivative $\partial/\partial t$ is the local rate of change observed from a fixed point in the Eulerian reference frame. These are related by

$$D/Dt = \partial/\partial t + (\mathbf{u}.\nabla), \qquad \text{--- (3.A.5)}$$

where the second term represents the convection.

For a homogeneous and incompressible fluid the conservation of mass is expressed by the continuity equation:

$$\text{div } \mathbf{v} = 0 = \nabla . \mathbf{v} \qquad \text{--- (3.A.6)}$$

The conservation of momentum requires that the rate of change of the momentum of a volume of fluid is equal to the sum of all the forces acting on that fluid. For constant (isotropic) viscosity the equation of motion are termed the Navier-Stokes equations and can be expressed (in vector notation) as:

$$\frac{\partial \mathbf{v}}{\partial t} + (\mathbf{v}.\nabla)\mathbf{v} = \frac{-1}{\rho}\nabla p + \nu\nabla^2 \mathbf{v} + \mathbf{F} \qquad \text{--- (3.A.7)}$$

(For inviscid flow the equations reduce to the Euler equations). For the vortex flows that will be examined here the Navier-Stokes equations are best expressed in cylindrical polar coordinates, which can then be simplified by assuming axisymmetry ($\partial/\partial\theta = 0$). The resulting equations are:.

$$\frac{\partial v_r}{\partial t} + v_r\frac{\partial v_r}{\partial r} + v_z\frac{\partial v_r}{\partial z} - \frac{v_\theta^2}{r} = \frac{-1}{\rho}\frac{\partial p}{\partial r} + \nu\left[\frac{\partial^2 v_r}{\partial r^2} + \frac{\partial}{\partial r}\left(\frac{v_r}{r}\right) + \frac{\partial^2 v_r}{\partial z^2}\right] + F_r \qquad \text{--- (3.A.8)}$$

$$\frac{\partial v_\theta}{\partial t} + v_r\frac{\partial v_\theta}{\partial r} + v_z\frac{\partial v_\theta}{\partial z} + \frac{v_r . v_\theta}{r} = \nu\left[\frac{\partial^2 v_\theta}{\partial r^2} + \frac{\partial}{\partial r}\left(\frac{v_\theta}{r}\right) + \frac{\partial^2 v_\theta}{\partial z^2}\right] + F_\theta \qquad \text{--- (3.A.9)}$$

$$\frac{\partial v_z}{\partial t} + v_r\frac{\partial v_z}{\partial r} + v_z\frac{\partial v_z}{\partial z} = \frac{-1}{\rho}\frac{\partial p}{\partial z} + \nu\left[\frac{\partial^2 v_z}{\partial r^2} + \frac{1}{r}\left(\frac{\partial v_z}{\partial r}\right) + \frac{\partial^2 v_z}{\partial z^2}\right] + F_z \qquad \text{--- (3.A.10)}$$

and the continuity equation: $\frac{\partial v_z}{\partial r} + \frac{v_r}{r} + \frac{\partial v_z}{\partial z} = 0$ --- (3.A.11)

Another form of the Navier-Stokes equations that is frequently used is the vorticity transport equation, which is obtained by taking the curl of both sides of the Navier-Stokes equations and substituting the vorticity vector: $\omega = \nabla \mathbf{x} \mathbf{u}$. For an incompressible fluid the vorticity equation is:

$$\frac{\partial \omega}{\partial t} + (\mathbf{v}.\nabla)\omega - (\omega.\nabla) = \nu\nabla^2\omega + (\nabla \mathbf{x} \mathbf{F}) \qquad \text{--- (3.A.12)}$$

It is often useful to describe fluid flow at large Reynolds numbers in terms of the distribution of vorticity. The net viscous force on an element of incompressible fluid is determined by the local gradients of vorticity. When the fluid viscosity is small the net viscous force is significant only at places where the vorticity gradients are large.

The vorticity of a material element increases (as far as non-viscous effects are concerned) when the element is extended in the direction of the local vortex line. This suggests that the net total 'amount' of vorticity in a body of fluid can be increased by stretching of the vorticity line. The extension of the vortex lines arising from thermal up-currents is the cause of the intensification of tornadoes, and the bathplug vortex is a steady concentrated distribution of vorticity resulting

from the extension due to the draining motion of the vortex lines associated with the initial motion.

One advantage of a description of flow changes in terms of vorticity is the elimination of an explicit dependence on the pressure. An analogy can be drawn between the vorticity equation for two dimensional flow and the heat transfer equation, suggesting that vorticity is transported in a similar manner to heat: by convection and diffusion. This similarity was further utilised by Batchelor (1964) in proposing a model for the axial velocity in a trailing vortex, which will be examined further in section 3.B.

The vorticity equation is often combined with the use of a single stream function ψ chosen to satisfy the continuity equation. This is possible for flows which are either two-dimensional, or possess axial symmetry, and the latter can often be assumed for the study of vortices. In cylindrical coordinates z,r,θ with velocity components w,u,v and axisymmetry about the axis r = 0 the velocity components are related to the stream function by:

$$\text{axial } w = \frac{1}{r}\left(\frac{\partial \psi}{\partial r}\right) \qquad \text{and radial } = \frac{-1}{r}\left(\frac{\partial \psi}{\partial z}\right) \qquad \text{--- (3.A.13)}$$

It will be noticed that the tangential (or azimuthal) component of velocity v does not enter the mass conservation equation in an axisymmetric flowfield, and hence v cannot be obtained from the stream function ψ.

This lack of coupling between the tangential and the meridional flow components is also found in the vortex solutions of Burgers (1948) and Sullivan (1959). This has been pointed out as a flaw, as in practice the tangential velocity does exert an influence on the meridional flow components. The mechanism by which the axial and azimuthal components of motion in a steady line vortex are coupled via the pressure is described by Batchelor (1964):. "*The radial pressure gradient balances the centrifugal force, and any change in azimuthal motion with distance downstream produces an axial pressure gradient and consequently axial acceleration.*" Hall (1966) shows that substantial swirls cause pressure gradients imposed at the edge of the vortex core to be amplified on the centreline, making the flow on the axis highly sensitive to the environment.

The stream function ψ (called the Stokes stream function) can be interpreted both as a measure of volume flux and as one component of a vector potential. Lines in an axial plane on which ψ is constant are everywhere parallel to the vector (w,u,0) and can be described as the 'streamlines of the flow in an axial plane'.

The viscosity appearing in the Navier-Stokes equation is the kinematic viscosity, related to the dynamic viscosity by $\nu = \mu/\rho$. The kinematic viscosity determines the contribution made by viscous stresses to the acceleration of a fluid volume by a given rate of strain. The viscosity represents the diffusion of momentum by random interaction of molecules and acts to reduce the non-uniformity of fluid velocity. The importance of viscosity to the fluid motion is characterised by the Reynolds number, which is the ratio of a characteristic length multiplied by a characteristic velocity divided by the kinematic viscosity.

The requirement of zero slip of the fluid at a rigid, impermeable boundary gives rise to the boundary layer. This is the layer of fluid close to a wall in which the fluid velocity makes a transition from the required value of zero at the boundary, to the free stream value outside the boundary layer. As the Reynolds number tends to infinity the thickness of the boundary layer

tends to zero, but no matter how small the viscosity becomes the no slip condition must be satisfied. Boundary layer approximations are used to simplify the analysis, by assuming that axial gradients are negligble in comparison with radial gradients. There is an analogy with the quasi-cylindrical approximations used to simplify the study of vortices. The boundary layer is obviously very important to the characteristics of vortices in cyclones, accounting for the dust rope and the source of vorticity). At the same time, vortices (on a microscale) are important in the study of boundary layers. Both of these will be discussed further in section 3.D. Since the circumferential velocity must be zero on the axis of symmetry, viscous effects will also be important in the core of the vortex.

The study of fluid motion generally falls into one of three classes, depending on the restricting assumptions that the equations are formulated under:

-Potential or Irrotational flow:	Vorticity is zero and viscous forces are neglected
-Ideal, inviscid or frictionless flow	Vorticity is present but viscous forces are neglected (hence no diffusion of vorticity)
-Real or viscous flow	No restricting assumptions on vorticity or viscous forces.

A potential or irrotational flow is defined by having zero vorticity, except at some singular points (for example at the axis of a potential vortex). Having $\omega = (\nabla \times \mathbf{v}) = 0$ implies that a potential function exists such that $\mathbf{v} = \nabla\phi = (\frac{d\phi}{dx}, \frac{d\phi}{dy}, \frac{d\phi}{dz})$. This considerably simplifies the analysis of the flow, (but is only realised for ideal fluids which have zero viscosity). Although the equation of motion is non-linear in the velocity, the potential flow assumption allows the velocity distribution to be determined by a linear equation, which simplifies the calculation of the flowfield.

Bernouilli's theorem states that for an incompressible, inviscid fluid of uniform density on which gravity acts, the total head is constant on any streamline of constant flow. In irrotational, inviscid flow the total head is constant throughout the fluid. Although irrotational flow may appear to be a special case of limited applicability, Kelvin's circulation theorem shows that material elements of a uniform fluid set into motion from rest remains without rotation unless they move into a region where viscous forces are significant. A body of inviscid fluid in irrotational motion continues to move irrotationally.

Helmholtz's vortex law states that in an inviscid fluid of uniform density a vortex tube moves with the fluid and its strength remains constant. Vortex strength or circulation cannot be created in the interior of a fluid, but once it has been convected there it is spread by the action of viscosity. Vorticity cannot be created nor destroyed in the interior of a homogeneous fluid under normal conditions, and is only produced at boundaries.

The fluid motion can be visualised by pathlines, streaklines or streamlines. In steady flow these are all the same, but they may not be in time-dependent flow. A pathline is the record of the position of a particle over a specific time interval, which is of interest when dealing in a Lagrangian reference frame. The streamline is a curve such that the tangent to it at any point P is parallel to the velocity of the fluid at P at the instant considered. The whole set of streamlines gives a representation of the direction of the flow at all points at one instant. In visualisation

experiments where tracers are continuously released into the fluid at a point the observed path is a streakline. In a time-varying flow the pathlines of successive tracers are different, and hence the streakline differs from the pathline. In time-independent flows the pathlines do not change, and pathlines, streamlines and streaklines coincide.

The two basic types of planar vortices are the potential vortex, and solid body rotation. In the latter the velocity increases linearly with the distance from the centre, hence the angular velocity (and the vorticity) are constant throughout. Fluids can exhibit this motion, for example the fluid inside a hollow cylinder that is rotating steadily, since the fluid must have zero slip at the wall

A potential vortex is formed by the rotation (at constant angular velocity) of a solid rod in a fluid. Again the fluid adheres to the rod, but with increasing distance from the rod the velocity decreases in inverse proportion to the distance. The fluid has no vorticity, except at the centre of rotation (the rod must be in solid body rotation and hence has constant vorticity). In a potential vortex adjacent concentric layers rub against each other causing shear and hence a dissipation of energy.

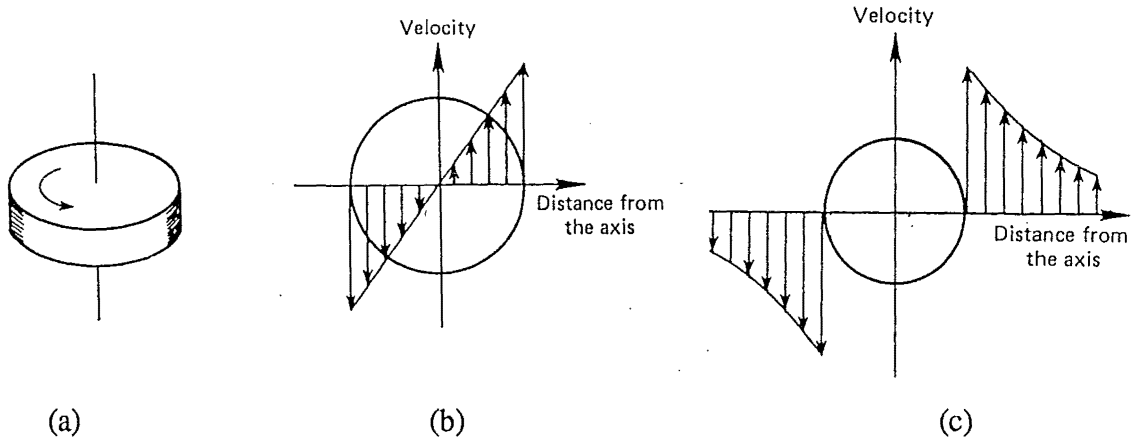

(a) Every rotating solid body is a vortex
(b) Velocity distribution in a solid body vortex
(c) Potential vortex velocity distribution

Figure 3.A.2: Velocity profiles in Solid body rotation and Potential vortices

A steady vortex flow requires that the decay in the tangential velocity at any radius due to dissipation must be balanced by the tangential velocity increase resulting from the inwards convection of fluid with higher angular momentum. When the radial inflow is insufficient the vortex core will diffuse radially outwards with increasing time and the flow will be unsteady. A vortex can only be time independent if it has a radial velocity component, and hence by continuity, an axial velocity.

If the potential vortex was generated by a thin walled cylinder, which itself was filled with fluid a combined vortex profile would be obtained - with a solid body rotating vortex embedded in a potential vortex. This combined vortex is called a Rankine vortex, and for a steady circular motion without a velocity component perpendicular to the plane of rotation it is the only vortex that can have zero velocity at the centre as well as far away from it. Rankine's vortex has a

discontinuity of the velocity derivatives at the point of transition from free to forced modes and overestimates the velocity near the core.

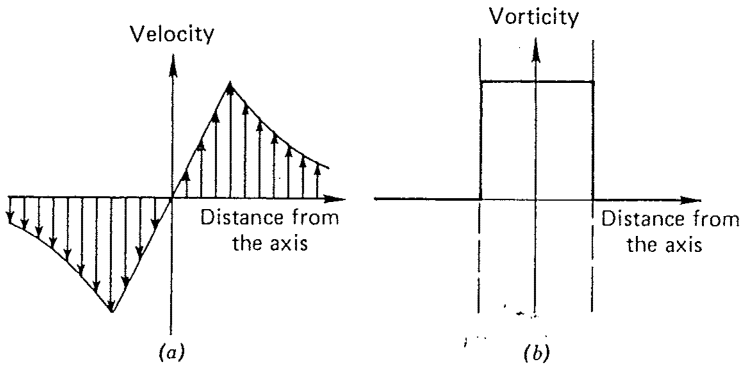

Figure 3.A.3: The velocity and vorticity distributions in a Rankine vortex

The shear between adjacent layers can be visualised by floating tiny rods on the surface. In solid body rotation these rods turn once around their own axes at each revolution of the fluid. In a potential vortex the rods do not change their direction on their path, but move with a circular translational motion. The following diagram shows the velocity profiles and movement of rods on the surface.

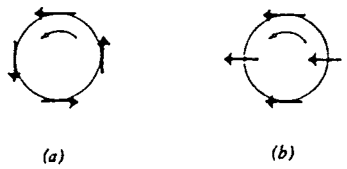

Figure 3.A.4: The movement of a rod:
(a) in solid-body rotating fluid and (b) a potential vortex

If the radius of the solid body rotation in the Rankine vortex shrinks to a point the vortex becomes a vortex line. The vortex line is a special case of a vorticity line - an isolated vorticity line with infinite vorticity at the axis. A vortex line is the analogy to a streamline for vorticity vectors: it is the curve that is everywhere parallel to the vorticity vector. A streamline is a curve in the fluid that at all times is tangent to the local velocity vector. The surface that encloses a bundle of vorticity lines is termed a vorticity tube, and the bundle of vorticity lines (which need not have infinite values) is termed a vortex filament.

Although swirl is generally used to denote the tangential component of velocity in a vortex, it has been used with more specific meanings - such as to denote a vortex with an axial velocity component. Uberoi (1979) distinguishes between vortices and swirls: a vortex convects in

angular momentum from a large radius ($\Gamma \to \Gamma_o$ for $r \to \infty$) whereas a swirl is generated in a localised radial region ($\Gamma \to 0$ for $r \to \infty$). In cyclones with tangential inlets the flow will be closer to the vortex form, whereas axial entry through vanes will approximate to the swirl form.

Much of the research on vortices has concentrated on vortices generated by wings or the atmospheric vortices such as tornadoes. The applicability of these results to the confined flow of the cyclone needs to be considered, as different vortex characteristics result from different methods of production. Leading edge vortices are generated at the leading edges of delta wings and they are distinguished by axial velocities in the core which exceed the freestream velocity: $W_o(Y) = 1 + e^{-Y}$. The trailing vortex is generated at the tips of a straight wing and has a wake-like axial velocity distribution with a core velocity smaller than the freestream velocity $W_o(Y) = 1 - e^{-(Y/2)}$. Garg and Leibovich (1979) used an exponential profile to model the axial velocity in a confined vortex similar to that generated at a wing tip. The form of the equation was: $W = W_A + W_B \exp\{-\alpha r^2\}$. Upstream of the vortex breakdown a jet like axial profile was observed, with $W_B > 0$. Immediately downstream of the vortex breakdown the profile was wake-like, with $W_B < 0$ and far downstream a conventional smooth wake profile was established.

Vortex similarity:

Similarity between vortices is given by their characteristic dimensionless parameters: the Reynolds number and the swirl number. The swirl number is defined as the ratio of the flux of azimuthal momentum to the flux of axial momentum:

$$Sw = \frac{G_\phi}{G_X R} \qquad \text{--- (3.A.14)}$$

where: G_ϕ, G_X = the axial flux of angular and linear momentum respectively
R is the radius of the exit throat.

$$G_\phi = \int_0^R V_\theta . r . \rho W . 2\pi r . dr \qquad \text{--- (3.A.15)}$$

$$G_X = \int_0^R W \rho W . 2\pi r . dr + \int P . 2\pi r . dr \qquad \text{--- (3.A.16)}$$

where V_θ is the tangential velocity and W is the axial velocity.

Experiments have shown Sw to be a significant similarity criterion for swirling flows. Faler and Leibovich (1977) defined a non-dimensional circulation number Ω to characterise the swirl,

$$\Omega = \frac{\Gamma}{\overline{W}.D} \qquad \text{--- (3.A.17)}$$

where $\overline{W}$ is the average axial velocity and Γ is the circulation $2\pi R_e V_\theta$.
Abrahamson (1981) shows that this is approximately equivalent to:

$$\Omega = \frac{\pi^2 . R_i . D}{2 . A_{in}} \qquad \text{--- (3.A.18)}$$

and for the Stairmand High efficiency cyclone geometry this is equal to 19.7.

Flow visualisation and static pressure measurements have been made in the laboratory on model tornado flows exhibiting vortex breakdown, such as the Purdue tornado vortex chamber or TVC (Church and Snow, 1985; Pauley, 1989).

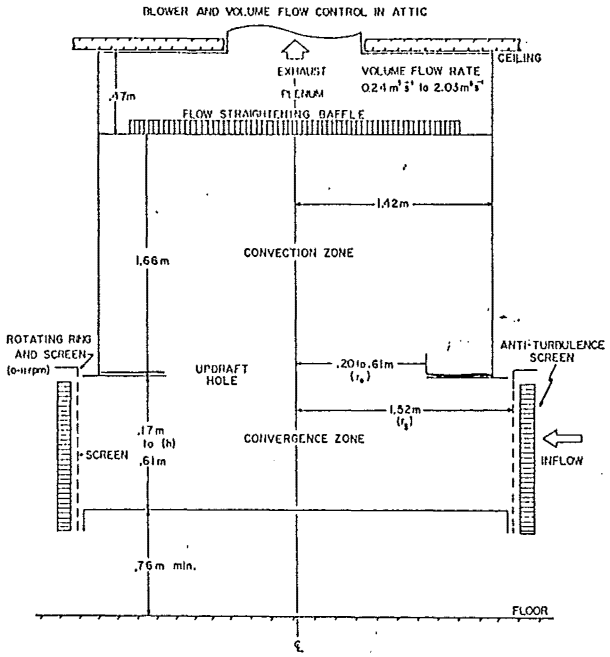

Figure 3.A.5: The Purdue Tornado Vortex Chamber, from Church et al (1979)

The TVC differs from the situation that exists in the cyclone, but has some fundamental similarities. Air is drawn radially inwards through a rotating mesh screen that extends 0.17 to 0.61m above the smooth base. The inflow conserves angular momentum as it moves inwards and then upwards through an updraft hole of 0.4 to 1.2m diameter, above this is the convection region of diameter 2.8m. A swirling column is developed along the centreline in the convergence region and this extends up through the convection region. This column simulates the tornado embedded within a rotating thunderstorm updraft. The apparatus is described more fully by Church et al (1979), who found 5 configurations of the vortex occurred as the swirl ratio S and the radial Reynolds number Re were varied. These parameters are given by:

$$S = \frac{\Gamma . r_o}{2.Q.h} \qquad Re_r = \frac{Q}{2\pi\nu} \qquad \text{--- (3.A.19)}$$

where Q is the volume flowrate scaled by the height over which the radial inflow occurs. r_o is the radius of the core. The configurations observed were:

1. a single laminar vortex
2. A single vortex with breakdown bubble separating the upper turbulent region from the lower laminar region.
3. Fully developed turbulent core where the breakdown bubble penetrates to the bottom
4. Vortex transition to two intertwined helical vortices
5. Examples of higher order multiple vortex configurations

The observed rotation of tornadoes develops by concentration of the background angular momentum present in the low level environment which feeds the updraft. The principal similarity variable is the swirl ratio S, given above.

In a closed region the conservation of matter and assumption of impermeable boundaries requires that the flow must have closed streamlines and therefore be rotary. In a simply connected region a potential flow cannot have closed streamlines.

Turbulent flow:

The flow in cyclones features a high degree of turbulence. In a turbulent flow the viscosity is modified by the action of the turbulent eddies, meaning the use of an eddy (or turbulent) viscosity is more appropriate. Turbulent viscosity values are typically found to be orders of magnitude greater than the kinematic viscosity. Ustimenko and Bukhman (1968) calculated the turbulent viscosities from experimental profiles of averaged velocity and the correlations between the fluctuating velocities. The resulting turbulent viscosities were 100 to 1000 times greater than the molecular viscosity factors in the quasi-potential outer vortex, and 1000 to 10 000 times greater in the quasi solid inner vortex.

The intensity of turbulence is characterised by: $tu = \frac{\sqrt{\overline{u'^2}}}{\overline{u}}$ --- (3.A.20)

Schowalter and Johnstone (1960) report that the intensity of turbulence in a cyclone is at least 10%. The scale of turbulence was given as Dc/4 by Ranz (1985), or a minimum of 1mm was suggested by Hinze (1959). The generation of turbulence by the boundary layer also suggests that the characteristic scale of turbulence will be related to the boundary layer thickness.

Analytical solutions for the Navier-Stokes equations are not possible in turbulent flows, where the effects of viscosity cannot be neglected. One approach is to smooth the equation of motion by writing the velocity as the sum of an averaged value, and a fluctuating or turbulent component. This gives rise to the nine components of the Reynolds stresses of the form $\tilde{\tau}^t_{xx} = \rho \overline{v_x'.v_x'}$. This results in an excess of 6 unknowns over equations for which empirical expressions or models must be found.

Eddy viscosity, ν_T turbulence models are based on a generalised Boussinesq hypothesis relating the stress, $\overline{u_i u_j}$ to the rate of strain, $\frac{\partial U}{\partial x}$, as given by Truelove & Mahmud (1986):

$$\overline{u_i u_j} = \tfrac{2}{3} k \delta_{ij} - \nu_T \left[\frac{\partial U_i}{\partial x_j} + \frac{\partial U_j}{\partial x_i}\right] \quad \text{--- (3.A.21)}$$

where ν_T is the kinematic turbulent viscosity.

Another approach is the Prandtl mixing length:

$$\tilde{\tau}^t_{xx} = -\rho l^2 \left|\frac{\partial \bar{v}_x}{\partial y}\right| . \frac{\partial \bar{v}_x}{\partial y} \quad \text{--- (3.A.22)}$$

where l is the mixing length. So & Mellor (1975) summarise the approach of Prandtl, who also used an extension of the analogy between buoyancy and curvature effects to the turbulent rotating flow. A flow is stable if a fluid particle is prevented from further displacement by a net restoring force in the flow. While convex flow should be stable, concave flows will be unstable. Prandtl proposed to account for the curvature effect by multiplying the mixing length

by a factor f which is a function of the dimensionless curvature parameter K:

$$f = 1 - \frac{1}{4} \frac{KU}{\partial u/\partial y} \qquad \text{--- (3.A.23)}$$

In the k-ε model (Launder & Spalding, 1974) the turbulent viscosity is expressed in terms of the turbulence energy k and its dissipation rate ε by:

$$\nu_T = C_\mu k^2/\varepsilon \qquad \text{--- (3.A.24)}$$

where C_μ is an empirical constant

It has been pointed out by Duggins & Frith (1987) that the internal flow in cyclones has a special turbulence character caused by the strong swirl. The swirl causes a reduction in the net energy transfer from large eddies to small ones. This has the effect of decreasing the rate of dissipation of turbulence and increasing the length scales especially along the axis of rotation. Turbulence modelling is reported by Rodi (1992) to require a turbulent viscosity that varies in magnitude across the flow field. Anisotropy of turbulence is present for all swirling flows according to Lilley & Chigier (1971), Lilley (1976) and Frith & Duggins (1986). This will be examined further in chapter 6.B2.

Significant forces:

The effect of gravity in cyclones is generally negligible in the cyclone compared with the high rotational velocity. The acceleration due to the tangential velocity is $a_c = \frac{v_\theta^2}{r}$, which for a 140mmØ cyclone can be 4000 times the acceleration due to gravity, and even in a 2mØ cyclone the ratio will still be in excess of 200 times.

There is an analogous result to the Archimedes principle in a gravity field for the case of a two dimensional flow field subject to steady rotation. The equation of motion in a rotating frame differs from that in an absolute frame only by the addition of a body force per unit volume. Both the centrifugal force and gravity are functions of position in space only, and the coriolis force can be treated similarly if the streamfunction ψ can be assumed to be continuous into the region occupied by the body. The additional force on unit depth of the body due to the action of the body force due to rotation is then:

$$\int \nabla \{ -2 \rho \Omega \psi + \tfrac{1}{2} \rho \Omega^2 (x^2 + y^2) \} \, dA \qquad \text{--- (3.A.25)}$$

This force is equal and opposite to the resultant centrifugal and coriolis force which would act on the displaced fluid if it were moving rigidly. It follows that a rigid body which is free to move will do so in a way which is unaffected by steady rotation of the whole system, provided that it has the same total mass and centre of mass as the displaced fluid. Since the particles are denser than the fluid they are driven towards the wall. Any particles that are lighter than the fluid will be driven towards the axis of rotation.

The drag of the walls slows the velocity down in the boundary layer, but has little effect on the pressure. This results in an imbalance in the radial forces due to centrifugal action and the pressure gradient, and this generates secondary flows along the cone generators and the roof.

Wave dynamics:

Vortices are capable of supporting travelling waves, and the interaction of the vortex with these waves has implications for the stability of the vortex. The analysis of this deals with 'solitons' which are solitary waves that retain their form after mutual interactions.

The Korteweg-de Vries equation was associated with the discovery of the soliton, and is frequently used in connection with calculations of the propagation of waves, such as those on vortex cores that are thought to be associated with vortex breakdown. The Korteweg-de Vries equation (which is usually attributed to Korteweg and de Vries (1895)), governs the propagation of weakly dispersive, weakly nonlinear water waves and serves as a model equation for any physical system for which the dispersion relation for frequency versus wavenumber is approximated by $\omega/k = c_o(1 - \beta k^2)$ and non-linearity is weak and quadratic.

3.B: VELOCITY COMPONENT MODELLING

It is desired to have models to describe the variation of the velocity components in cyclones. Since these are to be manipulated in calculations of the efficiency, pressure drop and stability, simple functional forms are desired. Some encouragement that this may be achieved is given by Vatistas (1991) who reports that "The main properties of concentrated vortices as represented by the radial distributions of azimuthal velocity and static pressure were found to be common to most vortical flows and not to depend on the method of production." Leibovich (1984), similarly finds that great stretches of vortex flows can be approximated as being columnar, with universal profiles.

The early studies of the velocity profiles described the radial distributions of tangential velocity, $V_\theta(r)$, in the outer vortex of cyclones by empirically fitting:

$$V_\theta = V_{\theta w}\left(\frac{R_w}{r}\right)^n \qquad \text{--- (3.B.1)}$$

with the subscript w indicating values at the wall. This is the form that has been used to describe the tangential velocity in efficiency prediction models, such as that of Barth (1956). It is generally agreed that values of the exponent n range from 0.5 to 0.8 (Shepherd and Lapple,1939; Alexander, 1949; ter Linden, 1953; Dabir & Petty, 1986). This places the cyclone vortex between the free vortex which has n = +1, and the forced vortex (as for solid rotation) with n = -1. Ogawa et al (1990) found that the exponent varied along the cyclone length, and was not always less than 1 in the lower region of their cylindrical vortex chamber.

Alexander (1949) proposed a correlation for the value of the vortex exponent 'n' :

$$n = 1 - \left[(1 - 0.67D^{0.14})\left(\frac{T}{283}\right)^{0.3}\right] \qquad \text{--- (3.B.2)}$$

(T is the absolute temperature, K)

Since equation 3.B.1 is applicable only to the outer vortex it is often combined with a forced vortex to describe the core region. The combined Rankine vortex is composed of solid body rotation embedded in a potential vortex, with the velocities and pressures being matched at the boundary. This approach has the disadvantage of two equations being required to describe the vortex, and discontinuous derivatives occurring at the join. Smith (1962b) used:

$$V_\theta = C.{}^{Rw}/_{r} + D.\,{}^{r}/_{Rw} \qquad \text{--- (3.B.3)}$$

and

$$V_x = A\left[{}^{r}/_{Rw} - {}^{r_{zav}}/_{Rw}\right] \qquad \text{--- (3.B.4)}$$

where: A, C, and D are functions of the axial location, z
Rw is the radius of the outer wall
r_{zav} is the radius of the zero axial velocity boundary.

The exponent n in equation 3.B.1 generally needs to be determined for each geometry, as equation 3.B.2 includes only the effect of the scale. Iozia and Leith (1989a) attempted to find a general relationship for the tangential velocity profiles in eleven geometrical variations on a 250mmØ Stairmand H.E. cyclone that were measured using a Tsi model 1650 hot film anemometer. A regression of variables was carried out to yield equations for the value of the

maximum tangential velocity, $V_{\theta max}$ and the radius of the core, r_c:

$$V_{\theta max} = 6.1 V_i \cdot \left(\frac{ab}{D^2}\right)^{0.61} \left(\frac{De}{D}\right)^{-0.74} \left(\frac{H}{D}\right)^{-0.33} \quad \text{--- (3.B.5)}$$

$$r_c = 0.26D \cdot \left(\frac{ab}{D^2}\right)^{-0.25} \left(\frac{De}{D}\right)^{1.53} \quad \text{--- (3.B.6)}$$

(The exponent of the first bracket in equation 3.B.5 was given incorrectly as -0.61 in the original paper, but corrected in Iozia & Leith, 1990). The core radius is taken as the radial location of the maximum tangential velocity, and presumably this is equated with the position of the zero axial velocity boundary, although this is not stated. The agreement is good for the Stairmand H.E. cyclone, but does not adapt to other geometries so well.

The large number of geometrical variables that affect the cyclone flowfield suggests that a simple empirical description of the flowfield will not be obtained. In any case, an empirical description is likely to be valid only over the range of geometries that it was based on. To be able to predict the flowfield in new designs analytical relationships derived from the equations of motion are desired. The equations of motion for swirling flow cannot be solved directly, but some special cases have been obtained, notably by Burgers (1948) and Bloor and Ingham (1987). The Burgers (1948) vortex provides a single expression to model the tangential velocity in both the inner and outer vortex regions. Although Abrahamson (1981) reported good agreement with the tangential velocity in cyclones it does not appear to have been used in collection efficiency modelling. Bloor and Ingham (1987)'s inviscid flow model appears to be an improvement over the simple forms usually assumed for the axial velocity. These and other descriptions of free and confined vortices will be examined in detail later.

Analytical solutions for velocity profiles:

A potential vortex decays as there is no supply of energy to counteract the action of viscosity. Oseen (1911) obtained an unsteady solution to the equations of motion for:

$$V_z = 0 \qquad V_r = 0 \qquad V_\theta = \frac{\Gamma_o}{r}\left[1 - \exp\{-r^2/(4\nu t)\right] \quad \text{--- (3.B.7)}$$

where t is the time since the supply of energy was stopped. This is found to describe detached vortices well, as they have no means of supplying energy to the core. A more accessible description of this result is contained in Lamb (1945). This equation has been utilised to describe steady vortices by Vatistas (1987) by replacing t by a constant 'a'. Govindaraju and Saffman (1971) also used it, replacing t by z/W_o. Squire (1955) suggested that a turbulent trailing vortex could be described by Lamb's solution if the kinematic viscosity was replaced by an eddy diffusivity ν_t.

One of the earliest, and perhaps the most well known and successful solution for vortex flow is that due to Burgers (1948). The velocity components in both the inner and outer vortex regions are modelled by single expressions which are of a simple form:.

$V_z = 2az \qquad V_r = -ar$

z is the axial distance from some origin; r is the radius. The solution for the tangential velocity as a function of the radius was found to be independent of time and was given by:

$$V_\theta = \frac{\Gamma_o}{r} [1 - \exp\{-ar^2/2\nu_T\}] \qquad \text{--- (3.B.8)}$$

ν_T = is the turbulent or eddy viscosity.

Γ_o is the circulation at large radius

= $\lim_{r \to \infty} (r.V_\theta)$, which in the cyclone is approximated by the maximum circulation.

The Burgers vortex is an exact solution for a viscous vortex produced by a radial inflow and axial outflow where the conditions at large radius r are irrotational. The inward radial convection of angular momentum just balances the outward diffusion so that the flow is steady. The parameter 'a' is a measure of the radial influx. The meridional flow (radial, axial) is independent of the swirl flow, as the strength of the rotation does not affect the influx and outflow. The stronger the inflow, the faster is the decay of angular momentum over the distance from the axis. The assumption of a linear variation of the radial velocity with radius means that continuity requirements restrict the axial velocity to being linear with height and constant with radius.

In the case of the cyclone, the parameter 'a' can be estimated by calculating the average radial inflow between the outer and inner vortices. If the total flowrate Q (neglecting the bin and short circuit flows) is evenly spread over the boundary between the vortices of length L (which has an area of $\pi D_x L$) then the average radial velocity at the core radius is $Q/\pi D_x L$. Since the radial velocity must be zero at the axis the gradient of the radial velocity can be calculated. If the radius of the core is taken as $D_x/2$ the expression for the parameter a is obtained:

$$a = \frac{2.Q}{\pi D_x^2 L} \qquad [s^{-1}] \qquad \text{--- (3.B.9)}$$

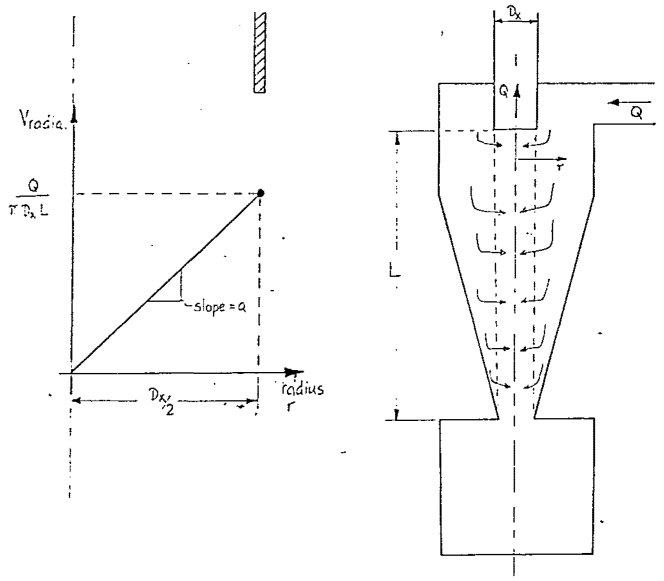

Figure 3.B.1: Relation of the parameter 'a' to the cyclone geometry and radial inflow

Ogawa (1987) developed an empirical expression for the turbulent viscosity to fit experimental pressure drops in cylindrical vortex chambers. Further work by Abrahamson (1991) has suggested that the value of the exponent needs to be reduced to predict the pressure drop in cyclones.

Ogawa's (1987) expression is:

$$\nu_T = \nu \times 0.0001841 \times \left(\frac{V_W D}{2\nu}\right)^{1.25} \qquad [m^2 s^{-1}] \qquad \text{--- (3.B.10)}$$

V_W = tangential gas velocity at cyclone wall, m/s
Q = total gas flowrate, m^3/s
D_X = vortex finder diameter, m
L = length of cyclone below vortex finder (between gas exit lip and dust exit), m
ν = kinematic viscosity, m^2/s (Taken as 1.568×10^{-5} m^2/s for air at STP)

The simple forms for the radial and axial velocities are not realistic representations of the flow, but the tangential velocity expression has been reported by Abrahamson (1981) to describe the tangential velocity in cyclones well. It has been widely used to describe a range of vortices including jets, tornadoes, confined, and free.

Phillips (1990) suggested a variation on the Burgers equation by taking the average of 2 exponential terms:

$$V_\theta = \frac{\Gamma_o}{r} \times \left(1 - \tfrac{1}{2}\left(\exp\left(\frac{-ar^2}{0.7\nu_T}\right) + \exp\left(\frac{-ar^2}{7\nu_T}\right)\right)\right) \qquad \text{--- (3.B.11)}$$

The parameters have the same definitions as for the Burgers equation above. There was no theoretical justification for this form, just that it was reported to improve the agreement with experimental profiles. The application of the tangential velocity expression to the velocities obtained in this study will be examined in sections 5.C and 6.B1.

Rott (1958) studied the development of Burgers vortex with time, and obtained solutions for the unsteady viscous vortex:

$$V_z = 2az \qquad V_r = -ar \qquad V_\theta = \frac{\Gamma_o}{r}\left[1 - \exp\left\{\left(\frac{-ar^2}{2\nu_T}\right).(1+be^{-2at})\right\}\right] \qquad \text{--- (3.B.12)}$$

For inflow towards the z axis the parameter 'a' must be positive, and Burgers steady state solution is obtained as $t \to \infty$. If the meridional flow is away from the z axis, the parameter 'a' must be negative, and the diffusion of angular momentum is in the same direction as the convection. For this case the rotation ceases for $t \to \infty$, which is the explanation for the Burgers solution being restricted to values of 'a' > 0.

Sullivan (1959) found a solution for a steady two-cell vortex that had an axial flow reversal near the axis, relative to the outer flow. The outer flow consists of a radial flow spiralling inwards and an upwards axial flow. This is separated from an inner flow by a cylindrical stream tube. The inner flow consists of a spiralling flow which is downwards near the axis and radially outwards and then upwards near the separation surface.

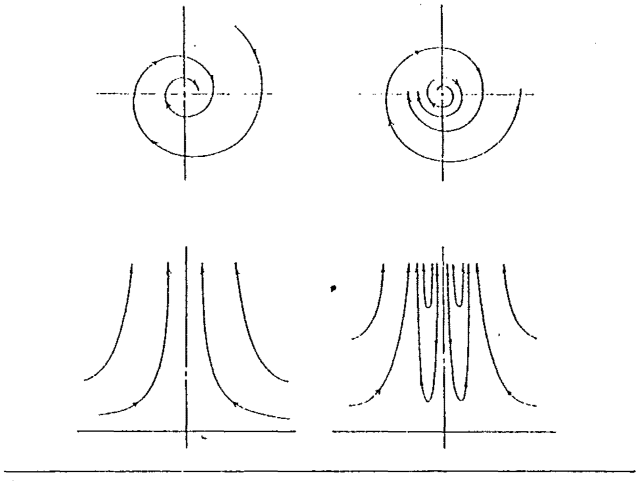

Figure 3.B.2: Diagram of the meridional flow lines for Sullivan's (1959) vortex.
Left: One-celled flow Right: Two celled flow

The expressions for the velocity components are:

Radial: $$u = -ar + \frac{6\nu}{r}\left[1 - \exp\left(-\frac{ar^2}{2\nu}\right)\right] \quad u = 0 \text{ when } r = 2.3755\sqrt{\frac{\nu}{a}} \qquad \text{--- (3.B.13)}$$

Axial $$w = 2az\left[1 - 3\exp\left(-\frac{ar^2}{2\nu}\right)\right] \qquad \text{--- (3.B.14)}$$

Tangential: $$v = \frac{K_c}{r}\left[\frac{H\left(\frac{ar^2}{2\nu}\right)}{H(\infty)}\right], \qquad \text{--- (3.B.15)}$$

where H is defined by: $$H(x) = \int_0^x \exp\left\{-t + 3\int_0^t [1 - \exp(-s)]s^{-1}ds\right\}dt \qquad \text{--- (3.B.16)}$$

Pressure:

$$p = p_o - 1/2\rho\left\{4a^2z^2 + a^2r^2 + 36(\nu^2/r^2)\left[1 - \exp\left(-\frac{ar^2}{2\nu}\right)^2\right]\right\} + \rho\int_0^r v^2 r^{-1}\,dr$$

--- (3.B.17)

The expression for V_θ features exponential integrals for which analytical solutions cannot be obtained. Leslie and Snow (1980) tabulated values of H/H(∞). Bellamy-Knights (1970) obtained the unsteady 2-cell viscous vortex solutions, which yield Sullivan's solution as t ->∞. Bellamy-Knights generalised the Sullivan vortex solution to the time-dependent case in which the separation surface between the two cells moves radially outwards with a velocity related to the diffusion of the vorticity. Kendall (1978) also proposed an unsteady two-cell similarity solution. The form of the tangential velocity profile consists of very low values of the velocity in the core region, and a maximum value outside the radius of the zero axial velocity.

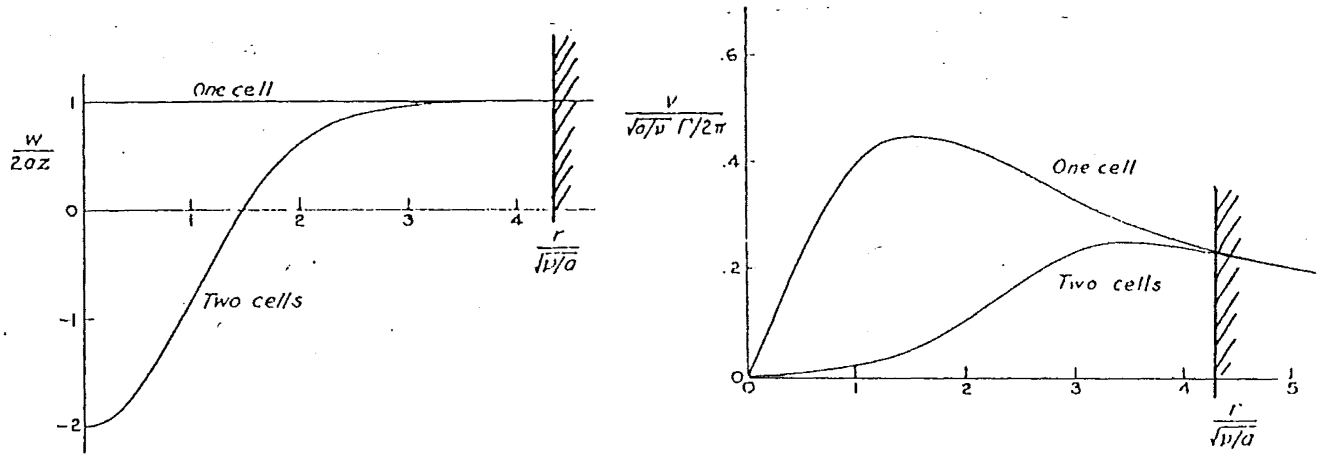

Figure 3.B.3: Diagram of the axial (w) and tangential (v) velocity component profiles for the Sullivan (Two cells) and Burgers (One cell) vortices.

Sullivan's solution approaches Burgers solution as r ->∞, and similarly has no coupling between the swirl and meridional flow. Bellamy-Knights (1974) found that for the radial momentum equation to be essentially independent of the swirl velocity requires r^2/ν_T to be sufficiently large, with the exact magnitude depending on the size of the tangential Reynolds number Γ/ν. Lugt (1983) points out that the lack of control of V_r and V_z by V_θ is contrary to observations in nature. These solutions all assume free slip on the horizontal plane z = 0 and thus neglect the boundary layer effects which are important in rotating flows above a solid surface. The nonslip condition makes the meridional flow strongly dependent on the primary rotating fluid.

In a steady three dimensional flow the existence of a vorticity extremum requires the convective transport of vorticity into the location of the extremum. Generally this requires the influx $\partial V_z/\partial z$ to be greater than zero, as is found in the Burgers solution. Examination of the meridional flow in the Sullivan's solution (shown in Figure 3.B.2 above) suggests that the extremum of the vorticity will occur away from the axis. The profiles of velocity are shown above, compared with the Burgers velocity profiles. The tangential velocity profile in the cyclone is better represented by the Burgers profile, but the Sullivan axial velocity profile allows for the axial flow reversal.

Since the meridional flow is independent of the swirl flow it may be possible to combine the Burgers tangential velocity with the axial velocity expression from the Sullivan vortex. However, both expressions for the axial velocity tend to infinity as z -> ∞, which is unrealistic, and the solutions have a stagnation point at the origin without physical justification. Batchelor's (1964) expression for the axial velocity component, featuring an exponential dependence on radius, has been utilised by other workers in a more general form, and will be examined further in later sections.

Procedure for fitting the Burgers profile:

The parameters Γ_o, a, and ν_T in the tangential velocity profile can be specified by forcing a fit to some characteristic feature of the tangential velocity profile. The location and magnitude of the maximum tangential velocity is frequently chosen for this, although other possibilities will be examined in Chapter 6.B1. The equation is simplified for manipulations by substituting $\alpha = \frac{a}{2.\nu_T}$.

The location of the maximum tangential velocity of the Burgers or Phillips profile is found by differentiating the equation for V_θ and setting the expression to zero. For example, the Burgers equation becomes:

$$\frac{\partial V_\theta}{\partial r} = (1 + 2.\alpha.r^{*2})\, e^{-\alpha.r^{*2}} - 1 = 0. \quad \text{--- (3.B.18)}$$

This shows that the radius of the maximum tangential velocity (r*) is independent of the magnitude of $V_{\theta max}$. Solving this equation gives the relationship between the parameter α and the radius r* as:

$$\alpha\, r^{*2} = 1.2564 \quad \text{or} \quad \nu_T = 0.398.\, a.r^{*2} \quad \text{--- (3.B.19)}$$

This approach suggests that for $a/(2.\nu_T)$ to remain constant over the cyclone height, the radius of the tangential velocity maximum must be constant with height. This is in fact frequently reported to be the case. For the two-term Phillips equation given by equation 3.B.11, the analogous equation to equation 3.B.19 is:

$$\nu_T = 0.9339\, a.r^{*2} \quad \text{--- (3.B.20)}$$

The magnitude of the $V_{\theta max}$ is determined by the value of Γ_o, and the relationship is found by solving the expression for V_θ at $r = r^*$:

$$\text{Burgers} \quad \Gamma_o = 1.398.(r^*.V_{\theta max}) \quad \text{--- (3.B.21)}$$

$$\text{Phillips} \quad \Gamma_o = 2.162.(r^*.V_{\theta max}) \quad \text{--- (3.B.22)}$$

An alternative form of the Burgers vortex model is given by Zhou & Soo (1990). They used the radius of the core of solid body rotation to scale the radius in the equation:

$$V_\theta = \frac{\Gamma}{r}\left[1 - e^{-\left(\frac{r}{R_c}\right)^2}\right] \quad \text{--- (3.B.23)}$$

with the radius of the core of solid body rotation, R_c, given by:

$$R_c = \left(\frac{4\, w_o\, \nu_{eff}}{1 - \left(\frac{\partial P}{\partial z}\right)/Pa}\right)^{\frac{1}{2}} \quad \text{--- (3.B.24)}$$

where the parameters are:

w_o = the average axial velocity in the gas exit = $\frac{V_{in}\, A_{in}}{A_{exit}}$

$\nu_{eff} = \nu + \nu_T$ the effective viscosity = kinematic viscosity + eddy viscosity,

$\frac{\partial \bar{P}}{\partial z} = \Delta p/L$, the pressure drop divided by the cyclone length.

L is taken as the distance between the dust exit and the roof of the cyclone, but it is not detailed where the pressure drop is measured between. In order to keep the dimensionality of the equation correct, Pa must have units of kg/m^3. The lower case p is used to denote pressure, 'Pa' is assumed to be a misprint for ρ_a, the density of the gas phase. However, this gives a negative value of the denominator, suggesting that there is another misprint in this equation. Comparison with a worked example in the appendix (of Zhou and Soo, 1990) suggests that the term '1 - ' should not be present, as the other term in the denominator is considerably greater than 1, and they do not obtain a negative value. Zhou and Soo (1990), who were studying a cyclone that was 300mm in diameter used a value for the turbulent viscosity of 0.01 m^2/s. This equation is found (see section 6.B1) to underestimate the radius of the core.

Batchelor (1964) examined the equations of motion for line vortices such as those generated from wingtips (trailing vortices). These are characterised by strong axial flows near the axis of symmetry. A similarity solution for the flow was found for the region far downstream where the departure of the axial velocity from the freestream speed is small.

In the line vortex the pressure was shown to provide the link between the azimuthal and axial components of motion through the balance between the radial pressure gradient and the centrifugal force. The slowing of the tangential velocity by viscosity leads to a positive axial pressure gradient and consequently a loss of axial momentum. The asymptotic variation of the centreline axial velocity defect with axial distance z was found to be proportional to (log z)/z.

The equations of motion were simplified by Batchelor by assuming boundary-layer type approximations $\partial/\partial z << \partial/\partial r$ and $V_r << V_x$ as well as $|w - W_o| << W_o$, the difference between the vortex axial velocity, w being much less than the free stream velocity W_o. The resulting equation for the azimuthal equation of motion is observed to be the same as the viscous decay of the circulation in two-dimensional motion, with t replaced by z/W_o and the solution for the tangential velocity is obtained by making use of the heat conduction equation, which is also satisfied by the vorticity. The asymptotic form of the solution as $z \to \infty$ is :

$$\Gamma = r.V_\theta = \Gamma_o [1 - e^{-\eta}] \qquad \text{where } \eta = \frac{W_o.r^2}{4.z.\nu} \qquad \text{--- (3.B.25)}$$

This is obviously of a similar form to the tangential velocity component of the Burgers vortex.

For the axial velocity, an analogy between the axial equation of motion and the equation for the radial conduction of heat in a two-dimensional solid (with t replaced by z/W_o) suggests that an asymptotic solution exists of the form:

$$w = W_o - \frac{\Gamma_o^2}{8.\nu.z} \log\{\frac{z.W_o}{\nu}\}. e^{-\eta} + \frac{\Gamma_o^2}{8.\nu.z}. Q_2(\eta) - L\frac{W_o^2}{8.\nu.z}. e^{-\eta} \qquad \text{--- (3.B.26)}$$

The last term (with the arbitrary constant with dimensions of area) accounts for any initial velocity defect which is independent of the circulation. The function $Q_2(\eta)$ is an exponential integral for which no analytical solution is possible. [However, Lessen et al (1974) who made use of this axial velocity expression point out that for large free flow Reynolds numbers $Re = W_o.z/\nu$ the term involving $Q_2(\eta)$ is very much smaller than the second term].

Batchelor (1964) then demonstrated the relationship of the arbitrary constant L to the drag associated with the core of a trailing vortex, D_c/ρ:

$$\frac{D_c}{\rho} = \tfrac{1}{2}\pi(LW_o^2 - \alpha\Gamma_o^2) \qquad \text{--- (3.B.27)}$$

Lessen et al (1974) utilised Batchelor's (1964) similarity solution in the development of a criterion for the inviscid stability of swirling flows to infinitesimal non-axisymmetric disturbances. By neglecting the third term in equation (3.B.26) the axial velocity profile simplifies to:

$$w = W_o - \left[\frac{\Gamma_o^2}{8.\nu.z} \log\{\frac{z.W_o}{\nu}\} - L\frac{W_o^2}{8.\nu.z} \right] . e^{-\eta} \qquad \text{--- (3.B.28)}$$

$$\eta = \frac{W_o.r^2}{4.z.\nu} \qquad \text{--- (3.B.29)}$$

In their analysis they made the profiles non-dimensional by scaling by W_s for velocities and r_s for lengths, where:

$$W_s = \frac{\Gamma_o^2}{8.\nu.z} \log\{\frac{z.W_o}{\nu}\} + L\frac{W_o^2}{8.\nu.z} \qquad r_s = \sqrt{\frac{W_o^2}{4.\nu.z}} \qquad \text{--- (3.B.30)}$$

This gives the non-dimensional profiles:

$$\overline{V_\theta} = \frac{q[1 - e^{-r^2}]}{r^2} \qquad q = \frac{\Gamma_o}{W_s.r_s} \qquad \text{--- (3.B.31)}$$

$$\overline{W} = \frac{W_o}{W_s} - e^{-r^2} \qquad r = \frac{r_o}{r_s} \qquad \text{--- (3.B.32)}$$

For the stability analysis the axial profile is then translated and inverted to $W = e^{-r^2}$ since these changes do not alter the amplification factor for the waves in question. Other workers have made use of the profiles (3.B.30) and (3.B.31), particularly in the study of vortex flows that lead to vortex breakdown. The parameter q is important in assessing the stability of vortex flows. According to Lessen et al (1974) q involves the ratio of the magnitude of the maximum swirl to that of the maximum axial velocity. However Garg and Leibovich (1979) and Escudier & Keller (1985) state (without supporting arguments or proof) that q is the ratio of axial vorticity to the azimuthal vorticity.

The experimental profiles of velocity components obtained by Faler and Leibovich (1977) in a vortex leading to breakdown were modelled by:

$$V_\theta(r) = \frac{\Gamma_o}{r}[1 - e^{-\alpha r^2}] \qquad \text{--- (3.B.33)}$$

$$W(r) = W_1 + W_2\, e^{-\alpha r^2} \qquad \text{--- (3.B.34)}$$

Although Faler and Leibovich (1977) recognised equation (3.B.32) as the Burgers vortex, they said that they " were not aware of a theoretical justification for the functional form of [equation (3.B.33)]". However it will be noted that it has the same form as the large Reynolds number approximation of equation (3.B.26) given by equation (3.B.28). Garg and Leibovich (1979), who extended Faler and Leibovich's (1977) measurements to higher Reynolds numbers, noted that equations (3.B.32) and (3.B.33) could be transformed to the profiles of Lessen et al (1974)

(equations 3.B.30 and 3.B.31), and made use of the latter's stability analysis. The Burger's model for the tangential velocity has been examined earlier in this section, and will be applied to the cyclone velocity profiles in sections 5.C and 6.B1. The generalised exponential form for the axial velocity component will be examined further in Chapter 6.B2.

The axial velocity profile assumed by Burgers (1948) is obviously not a realistic representation of the cyclone vortex axial profile. Batchelor's analysis suggests that the Burgers tangential velocity model can be combined with an exponential profile for the axial velocity. Faler and Leibovich (1977) suggest that the existence of a jet in the axial component on the axis (as opposed to uniform flow) is a necessary consequence of the constancy of the total head in a swirling flow, and that $W(0)^2 - W_1^2 = 2\,\Omega^2\,\alpha \ln 2/\pi^2$. Where W(0) is the axial velocity on the axis, and W1 is the axial velocity at large radius. The proof for this result is not given and the writer has not been able to deduce it. Faler and Leibovich (1977) report that their centreline velocity data did show the predicted trend with Ω^2 but the coefficient (presumably α) was a little too large for an accurate fit.

Turner (1966) proposed a model for the velocity profiles in vortices with strong circulation. The similarity variables were the radius, non-dimensionalised by dividing by the zero axial velocity radius ($\eta = r/r_o$); and the axial distance scaled by the length ($\zeta = z/l$). The resulting profiles are reproduced below:

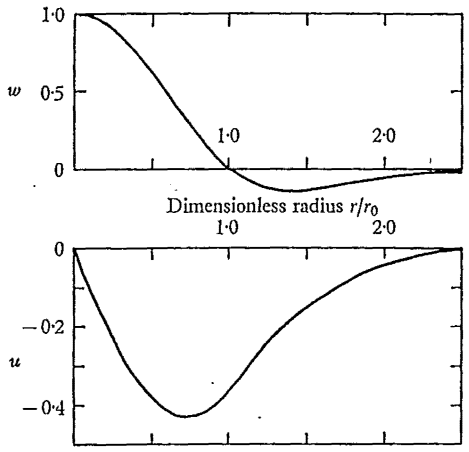

Figure 3.B.4: Axial (w) and radial (u) velocity profiles from Turner (1966)

The characteristic velocity u_o was 'e' times the radial velocity at the radius of the axial velocity crossover. The components were given by:

$$W = 2\,u_o \frac{l}{r_o}(1-\eta)\,e^{-\eta}(1+\zeta) \qquad \zeta = z/l \qquad \text{--- (3.B.35)}$$

$$U = -u_o\,\eta^{1/2}\,e^{-\eta} \qquad \eta = (r/r_o)^2 \qquad \text{--- (3.B.36)}$$

The position of the zero axial crossover was approximately 40% of the wall radius.

Another similarity form for the azimuthal motion was proposed by Hoffman and Joubert (1963). This was derived for the distribution of circulation for any turbulent vortex, not

necessarily self-similar ones.

$$\frac{\Gamma}{\Gamma_1} = [(1/H)\log_{10}(r/r_1) + 1] \qquad \text{--- (3.B.37)}$$

where Γ_1 and r_1 are the circulation and radius at the location of the maximum tangential velocity and 1/H is a universal constant given by 2.14 (and suggested by Govindaraju & Saffman (1971) to be 2.303)

Davidson (1988) obtained a similarity form for the axial velocity in the cyclone:

$$W = B\, r^n \left[\frac{2+n}{\theta_c^{2n}} - \frac{(2-n)}{(r/x)^{2n}}\right] \qquad \text{--- (3.B.38)}$$

where the parameter 'n' was determined as -0.5 from the work of Bloor and Ingham (1973). θ_c is the cone half-angle; r is the radius and x the axial distance from the origin. The 'B' parameter must be empirically determined. Similar to the Bloor and Ingham (1987) model which will be discussed below, the model predicts infinite velocities at the wall and axis, which is due to the viscosity becoming important there, according to Davidson (1988). The position of the boundary between the inner and outer vortices is found to occur at:

$$\frac{\theta_{zav}}{\alpha} = \left(\frac{2+n}{2-n}\right)^{1/2.n} = 0.6, \qquad \text{--- (3.B.39)}$$

that is at approximately 60% of the wall radius.

Bloor and Ingham (1987) developed an inviscid flow model for the small-angled conical hydrocyclone, which allowed solutions to the equations of motion to be obtained in closed form. The expression that resulted for the tangential velocity was essentially that of a free vortex, as the correction term was found to be very much less than one for conditions normally encountered. The expression for the axial velocity appeared to be the most suitable for comparison with the experimental profiles, and the results are given in Chapter 5.D.

The model considers the contributions of so-called secondary flows (arising from the entry conditions) to the generation of vorticity. A spherical polar co-ordinate system (r,θ,λ) is used with the origin at the apex of the cone. The momentum equation for the steady, axially symmetric flow is written and a stream function ψ is introduced that satisfies the continuity equation. The equations obtained for the radial and azimuthal components of vorticity include dependence on the functions $C(\psi)$ (the total angular momentum of the fluid) and $H(\psi)$ (the total head of the fluid).

The fluid is introduced to the cyclone with zero azimuthal vorticity, but with angular momentum that varies with radius (and hence an axial component of vorticity). The geometry of the system ensures that an azimuthal component of vorticity is generated (as a radial component of velocity must develop). The entry flow is expected to be three-dimensional, but the flow is assumed to become axially symmetric at some distance into the cyclone. At that location the flow is assumed to have an azimuthal velocity component with a 'top hat' profile, uniform axial velocity W, and the radial velocity is chosen to ensure that the normal velocity at the wall is zero, and the total head is constant. The inlet conditions are equivalent to the fluid being injected through the roof into the annulus around the gas exit.

This allows expressions to be derived for the stream function and the functions C and H. These are combined to yield a partial differential equation for the stream function ψ:

$$\frac{\partial^2\psi}{\partial r^2} + \frac{\sin\theta}{r^2}\frac{\partial}{\partial\theta}\left(\frac{1}{\sin\theta}\frac{\partial\psi}{\partial\theta}\right) = -\frac{V^2}{W} \qquad \text{--- (3.B.40)}$$

for a swirl velocity at inlet of V. The physical quantities are all non-dimensionalised using R_O for lengths, $Q/2\pi$ for the stream function, and hence the velocity components in the axial plane are scaled by $\frac{Q}{2\pi R_O^2}$.

R_O is the radius of the cyclone wall at the level of the gas exit lip and Q the volume flow in m^3/s. This transforms the right hand side of equation 3.B.39 to -2σ, where σ is a dimensionless geometrical parameter:

$$\sigma = -\frac{\pi R_O^2 . V^2}{Q.W} \qquad \text{--- (3.B.41)}$$

An analytical solution to the dimensionless form of 3.B.39 is obtained is obtained by choosing suitable complementary functions. The value of σ must be determined, as the velocity W is not known. This is done by noting that the streamline ψ=1 just enters the gas exit.

There are a number of errors (typographical and mathematical) in the published derivation (Bloor & Ingham, 1987), these have been corrected, yielding the velocity components:

Tangential velocity: $$\frac{q_\lambda}{V} = \frac{\sqrt{1 - \frac{Q^2\sigma\psi}{(\pi R_O^2 V)^2}}}{r.\sin\theta} \qquad \text{--- (3.B.42)}$$

The second term in the numerator is much smaller than 1 for conditions normally encountered, and hence this is essentially a free vortex of the form encountered earlier as equation 3.B.1, with n = -1.

That is: $V_\theta \propto 1/r$

Of more interest is the expression that was obtained for the dimensionless axial velocity,w. The corrected form:

$$w/\sigma = -\left[\frac{(2\theta+2\theta^2\tan\theta).\ln(\theta/\alpha) + \theta}{\tan\theta}\right] \qquad \text{--- (3.B.43)}$$

where α is the cone half-angle; and θ is the polar angle.

This can be acceptably approximated to:

$$w/\sigma = -\left[(2+2\theta^2).\ln(\theta/\alpha) + 1\right] \qquad \text{--- (3.B.44)}$$

and for small angles θ, α only a small error is introduced by a further simplification to:

$$w/\sigma = -\left[2.\ln(\theta/\alpha) + 1\right] \qquad \text{--- (3.B.45)}$$

(The small angle approximation fails near the wall, resulting in a 1.3% increase in the outer vortex volume flow). The dimensional axial velocity is given by:

$$W = \frac{-Q}{\pi . R_B^2} . \left[2 \ln\left(\theta/\alpha\right) + 1\right] \qquad \text{--- (3.B.46)}$$

This model is expected to be the most applicable to the cyclone vortex. While many of the other approaches are being developed for the unconfined vortices of aerodynamics, this theory is aimed at the confined flow case of the return-flow, conical hydrocyclone. The two-cell return flow structure is allowed for and a mass balance is made between the outer and inner vortices. Since the flow is assumed to be inviscid it will apply equally well to the gas cyclone as to the hydrocyclone. The model is plotted alongside the experimental profiles in section 5.D, and its performance is further examined in chapter 6.B2.

Research into other analytical solutions for vortex flows is continuing. Yih et al (1982) divide the known exact solutions of the Navier-Stokes equations for steady axially symmetric flows with swirl into three classes:
(i) Solutions with radial and azimuthal components that only depend on the radius (in cylindrical coordinates). Special cases had been discovered by Burgers and Rott and Bellamy Knights, and the entire class has been explored by Donaldson & Sullivan (1960)
(ii) Vortices with arbitrary stream surfaces for which the azimuthal velocity $v = \lambda r^{-1} \Psi$ and the azimuthal vorticity $\zeta = \lambda v$ where λ is a constant and Ψ is the Stokes stream function. This class is not in similarity form, and the swirl component decays with $\exp\{-\nu\lambda^2\tau\}$
(iii) The third class is the family of conical vortices. These are stated to be the only similarity solutions that allow the azimuthal velocity to vary along the axis of symmetry.

Hence, further developments in the solutions to the Navier-Stokes equations are concentrating on conical vortex solutions. These allow exact vortex solutions and show promise in the satisfaction of physical boundary conditions. The laminar solutions of Yih et al (1982) have been extended to turbulent vortices by Wu (1986), who allowed the viscosity to vary across the radius. Of the similarity solutions of the axially symmetric Navier-Stokes solutions only conical ones have bounded velocity at infinity. Wu (1986) also states that conical vortices are the only admissible solutions to the Navier-Stokes equations that satisfy both the adherence condition and the regularity condition. Hence the conical solutions may approach the reality more closely than columnar ones if the interaction between the vortex and a wall is to be considered.

The intractability of the solution of the equations of motion for swirling flow has lead to various polynomial approximations to the experimentally measured velocity profiles in vortex cores. Reyna and Menne (1988) made a study of the high Reynolds number behaviour of quasi-cylindrical vortex cores leading to vortex breakdown. They described the velocity profiles using the polynomial distributions below, which were also used by Mager (1972), Grabowski and Berger (1976), and Lopez (1986). The initial profiles were taken as:

$$V_o = 1 + \alpha . f(r) \quad \text{where} \quad f(r) = 1 - 6r^2 + 8r^3 - r^4 \quad \text{for } r < 1 \qquad \text{--- (3.B.47)}$$
$$f(r) = 0 \quad \text{for } r > 1$$

$$W_o = \beta . g(r) \quad \text{where} \quad g(r) = r(2 - r^2) \quad \text{for } r < 1 \qquad \text{--- (3.B.48)}$$
$$g(r) = 1/r \quad \text{for } r > 1$$

The parameter α controls the shape of the axial velocity profile: the flow being uniform for $\alpha = 0$; jet-like for $\alpha > 0$ and wake-like for $\alpha < 0$. Solid body rotation occurs for $r < 1$ and potential flow outside of this. The polynomials describe a symmetric flow and there is a smooth transition from the core to the outer flow. The parameter β is the ratio of the tangential velocity at the edge of the vortex core to the axial velocity at infinity at the initial station.

Tran (1981) described the axial velocity by a general quartic function, by specifying suitable boundary conditions. The form of the similarity equation is:

$$W = a.V_{in}\left(\left(\frac{r}{R_w}\right)^4 + b.\left(\frac{r}{R_w}\right)^3 + c.\left(\frac{r}{R_w}\right)^2 + d.\left(\frac{r}{R_w}\right) + e\right) \quad \text{--- (3.B.49)}$$

Where a,b,c,d,e are the parameters to be determined and V_{in} is the inlet velocity. (Section 5.B shows that the axial velocities scale well with the inlet velocity, and wall radius). The boundary conditions applied were:

1. The radial gradient of the axial velocity at the axis should be zero.
2. The radial gradient of the axial velocity at the wall should be zero.
3. The integration of the axial velocity between the axis and the core boundary should be equal to the inlet flow to the cyclone (at the level of the gas exit lip).
4. Similarly the integration of the axial velocity in the outer vortex annulus should also be equal to the inlet flow.

The form of the velocity profiles are shown below (Case 2), compared with a simple profile (Case 1) which takes two constant axial velocity values in the outer and inner vortices.:

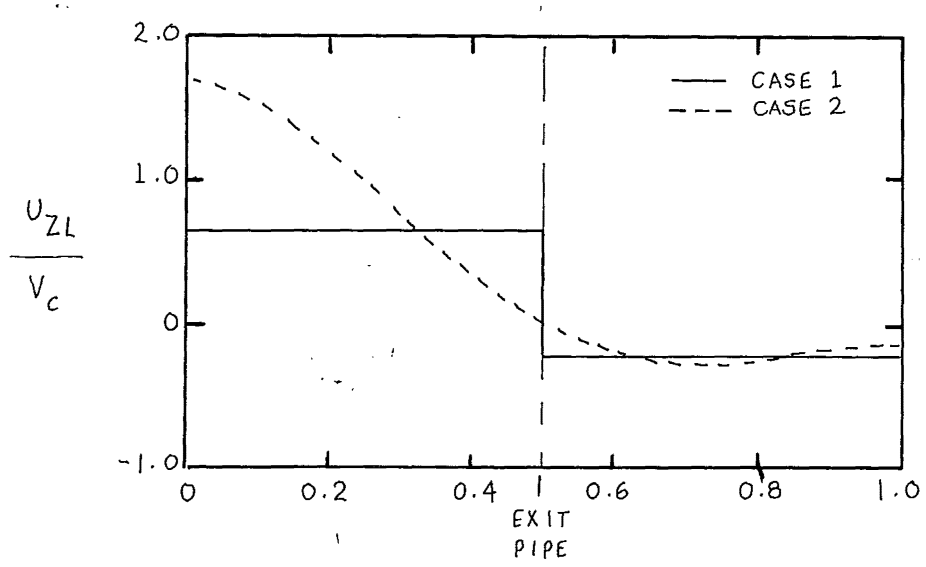

Figure 3.B.5: Shape of the axial velocity profile obtained from the polynomial approach, of Tran (1981)

Tran (1981) fitted the equation only at the gas exit lip, but a description of the axial velocity is sought that can be applied throughout the cyclone volume. To do this it is necessary to ensure that the total flow decreases down the cyclone, as the radial inflow takes place. This model will be examined further in Chapter 6.B2

Zhou and Soo (1990) also used a polynomial expression for the axial velocity after scaling by the mean axial velocity:

$$w^* = \frac{w}{\bar{w}} = z^* f(r^*) \qquad \text{--- (3.B.50)}$$

where: $\bar{w} = \frac{Q}{\pi R_o^2}$ $\qquad z^* = 1 - z/z_o \qquad r^* = r/Rw(z)$ $\qquad$ --- (3.B.51)

Rw = is the wall radius, which varies with length z.

and f(r*) is given by a polynomial: $f(r^*) = a_o + a_1 r^{*2} + a_2 r^{*4} a_3 r^{*6}$

The coefficients a_o to a_3 are determined by:

$$a_o = \alpha_1(1 - 0.5 r_1^{*2}) \qquad a_1 = \alpha_1(-3 + 2r_1^{*2}) \qquad a_2 = -1.5\,\alpha_1 r_1^{*2} \qquad a_3 = 2\alpha_1$$

where: $\alpha_1 = \frac{1}{r_1^{*2}(1 - r_1^{*2})^2}$ and $r_1^* = r_1/R_o$ $\qquad$ --- (3.B.52)

A different approach to the modelling of axial velocities in swirling flow was taken by Kuroda, Ogawa and Inoue (1981). The axial velocity W(r,z) at an arbitrary position was assumed to be divided into a fully developed non-swirling pipe flow velocity $\hat{W}_Z(r)$ and the velocity difference from $\hat{W}_Z(r)$ which is $\Delta W_Z(r,z)$. The latter is expected to decrease towards zero as z increases. The velocities are then normalised by the maximum value of $\hat{W}_Z(r)$. The profiles of U_Z^* can then be obtained from a single characteristic curve by appropriate choice of the scaling velocity. The resulting expression for U_Z^* is then:

$$U_Z^* = (1-r^*)^{\frac{1}{2}} + k(1-r^*)^{\frac{1}{2}}\left(\frac{B(4,1.5)}{B(2,1.5)} + r^{*2}\right) \qquad \text{--- (3.B.53)}$$

B() indicates the Beta function. The parameter 'k' was found to have an exponential dependence on: $\frac{z}{R} \cdot \frac{\nu}{R^2\omega_i}$

where ω_i is the initial angular velocity at the inlet (the tangential inflow velocity /R)

The exponential dependence suggests a similarity to the Burgers equation for the tangential velocity in the previous section, but the expression is cumbersome to use and this approach was not pursued further.

Vatistas (1991) also recognised the universality of the vortex profiles and proposed an empirical formula for the tangential velocity. This empirical equation is reported to give results that are very close to those from the Burgers equation, but it has the advantage of being easily integrated, enabling the static pressure distribution to be easily obtained. The other velocity components were then derived from the equations of motion. The tangential velocity, V_θ, was made dimensionless by scaling by $\frac{\Gamma_\infty}{2\pi r_c}$ and the radius was scaled by r_c. The proposed empirical expression for the tangential velocity was :

$$\overline{V_\theta} = \frac{\overline{r}}{(1 + \overline{r}^{an})^{1/n}}$$, where a and n are general constants. --- (3.B.54)

In order for the maximum tangential velocity to occur at $\overline{r} = 1$ the parameter 'a' must equal 2. By assuming that the tangential velocity does not vary significantly in the axial direction Vatistas (1991) was able to obtain an expression for the radial velocity component from the θ-momentum equation. The axial velocity component was then derived from the equation of continuity. Both the radial and axial velocities were scaled by ν/r_c, where ν was the kinematic viscosity. The dimensionless radial and axial velocity components were given by:

$$\overline{V_r} = -2(1+n)\frac{\overline{r}^{(2n-1)}}{(1 + \overline{r}^{2n})}$$ --- (3.B.55)

$$\frac{\overline{V_z}}{\overline{z}} = 4n(1+n)\frac{\overline{r}}{(1 + \overline{r}^{2n})^2}$$ --- (3.B.56)

where $\overline{z}$ is the axial distance scaled by r_c.

The profiles are shown below for various values of n.

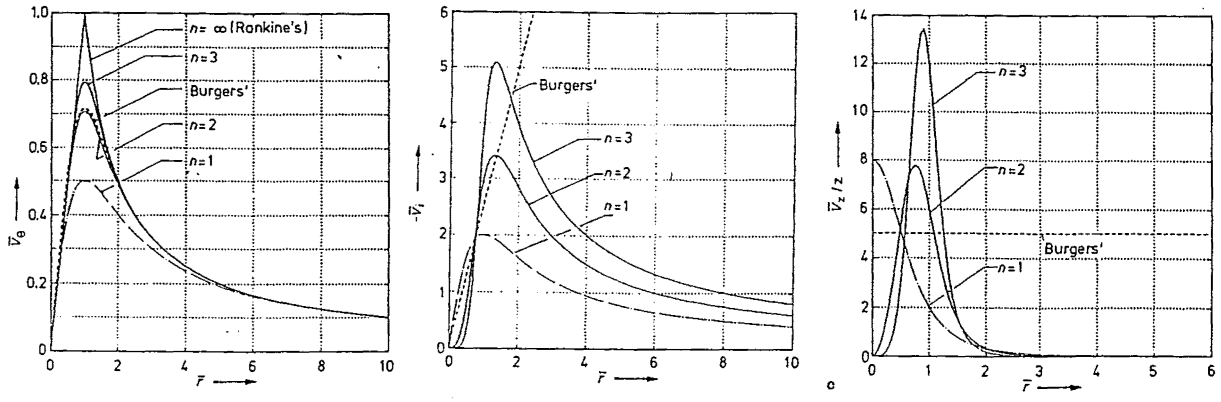

Figure 3.B.6: Velocity profiles from the model of Vatistas (1991).

The tangential velocity approaches the Rankine vortex profile as n ->∞. The parameter n is restricted to n > 1 to avoid singularities in the radial and axial profiles on the axis. Vatistas found that the best fit to experimental tangential velocities was obtained for 'n' = 2, if 'n' is restricted to integer values (no reason is given for why 'n' should be an integer). The non-dimensional static pressure distribution is given by:

$$\overline{\Delta P} = \frac{2}{\pi}\arctan(\overline{r})^2$$ where $\overline{\Delta P} = P - P_o/P_\infty - P_o$. --- (3.B.57)

Radial velocity measurement and modelling:

Comparatively little attention has been paid to the modelling of the radial component of velocity. It is also very difficult to measure and hence there is little data available for comparison with the models.

The results obtained by Ohasi & Maeda (1958) suggested that the radial velocity was relatively small and directed inwards near the centreline and wall, and was directed outwards in a small region in the mid zone of a hydrocyclone. Measurements with tracer particles by Kelsall (1952) showed a linear dependence on the radius for the radial velocity. The radial velocity profiles were calculated from the axial velocity profiles using:

$$V_r = \frac{Q_z|_1 - Q_z|_2}{2\pi\bar{R}(z_2 - z_1)} \qquad \text{--- (3.B.58)}$$

where $\bar{R}$ = the arithmetic average of the radius of the cyclone at the axial locations z_1 and z_2.

The results of Kelsall (1952) have been criticised for having an unusually long gas exit to achieve axially symmetric flow. Knowles et al (1973) pointed out that there was a 30% discrepancy in the mass balance, and made their own measurements using the same method. They reported that the radial velocities are small and are directed outwards near the axis and inwards near the wall.

Tran (1981) used a wire to indicate the direction of the radial velocity, and found that the radial velocity near the wall was directed inwards at all axial levels in the cyclone, as would be expected from mass balance requirements. Generally the radial profile is assumed to be constant with height. Abrahamson (1992) found that the only experimental profile of the radial velocity in a cyclone was obtained by Grabek & Meirzwinski (1980), who obtained the radial profile of the radial velocity by a mass balance on the axial velocity. The analytical solution of Bloor and Ingham (1987) yielded a radial velocity model, which is presented along with the measurements made in this study in section 5.D.

Summary of velocity modelling:

The Burgers (1948) tangential velocity profile and the Bloor and Ingham (1987) axial velocity profile will be compared with the experimental measurements in section 5.C and 5.D. Other possibilities for the modelling will be examined in chapter 6.B.

The models of the velocity components can be used in steady state predictions for the efficiency and pressure drop, but the dynamic behaviour is not taken into account, and may have a significant effect on the cyclone performance. The fitting of the tangential and axial velocity models to the time averaged experimental profiles will be examined further in sections 5.C and 6.B. As mentioned earlier, the structure of the vortex in the cyclone has not been conclusively determined. In this thesis, the applicability of the phenomenon of vortex breakdown to the cyclone flowfield is examined, and the background theory to this is reviewed in the next section.

3.C: CORE-TYPE VORTEX BREAKDOWN:

Although for the purposes of this thesis the term 'vortex breakdown' has been broadened to include any discontinuity of the vortex flow, the definition generally accepted in the literature is rather more specific. The following section will review the literature concerned with the type of vortex breakdown phenomenon that is characterised by an abrupt expansion in space of the vortex core, and which often leads to a stagnation point (on the axis) and regions of reversed axial flow. This "core-type breakdown" will be the scope for the following sections, and forms an important part of the theory proposed for the cyclone vortex structure in Chapter 7. Other mechanisms of disruption to the vortex, such as boundary layer separation, will be considered in sections 3.D and 6.C.

Peckham and Atkinson (1957) were the first to experimentally observe vortex breakdown, in a study of the vortices shed from the wingtips of aircraft. Since then considerable effort has been devoted to the understanding of the phenomenon. In some cases the presence of vortices is beneficial to lift and stability, but the trailing vortices generated behind large aircraft are a hazard to smaller craft, and are cited as the limitation to the traffic densities that airports can handle. Hence in some cases the maintenance of the breakdown is desirable, while in others the promotion of the decay is preferred.

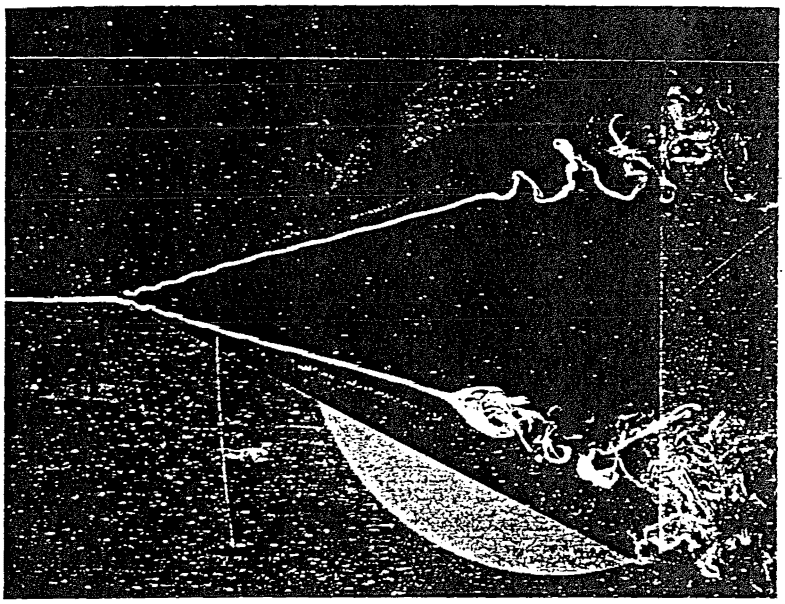

Figure 3.C.1: Bubble and spiral types of vortex breakdown behind a delta wing from Lambourne & Bryer (1961)

However, the phenomenon is not restricted to aircraft, but may occur in any flow featuring longitudinal vortices. Vortex breakdown has been observed in swirling flows in straight pipes, nozzles, diffusers, combustion chambers, within boundary layers, and in tornadoes. The study of vortex breakdown may thus predate the observations of Peckham and Atkinson. Lugt (1989) has given historical evidence that it may have been recognised in atmospheric vortices centuries ago. It also seems likely that Leonardo da Vinci may have been observing

breakdown when he described vortices in rivers: " *some which are faster at the centre than the sides, while others turn back upon themselves*". As an example of a modern application, vortex breakdown is utilised in combustion chambers as a means of stabilising the flame and recirculating hot gases around the base of the flame. In some applications the interest centres on simply the position of the breakdown and how to predict or control it, while in others the internal structure of the breakdown is of interest.

Harvey (1962) recognised the transition between forward and reverse core flow as the vortex breakdown phenomenon. He then made an important advance by reproducing the wingtip vortex phenomenon in a tube, and thus isolating it from the complicating factors of wing geometry and external influences. This has proved useful, as the unconfined vortices have some fundamental differences from the cyclone vortex - such as the ability to entrain fluid from the surroundings, and to spread at the natural angle. The vortices in the confined geometries will be more closely related to the cyclone vortex, but there are still significant differences between the experimental arrangements. Escudier and Zehnder (1982), Escudier et al (1980, 1982) and Chanaud (1965) all used a tangential entry to generate the swirl, but most other studies use a vane entry, which sheds a boundary layer into the core. All studies use through-flow conditions rather than the reverse-flow arrangement present in the cyclone, and cylindrical or diverging tubes are used to promote the breakdown. Flow visualisation has generally been made using water or water/glycerol as the fluid, although Harvey (1962) and Smith (1962a) used smoke in air. To facilitate observations and measurements, many studies have been limited to laminar upstream conditions, which is also not a good approximation to the cyclone conditions.

Perhaps the most applicable results are to be found in the research on hydrocyclones, which operate with water or water/glycerol as the fluid. Reverse flows inside the core vortex have been observed (Dabir & Petty, 1986; Hsieh & Rajamani, 1991; Ohtake, 1987), but the flow does not appear to have been described in terms of vortex breakdown.

Vortex breakdown has also been produced in closed cylinders with a rotating lid by Vogel (1968) and Escudier (1984). This geometry is easier to analyse and model because axial symmetry is improved and there are no inflow or outflow boundary conditions to be set.

The theory is covered in reviews by Hall (1966, 1972), Leibovich (1978, 1984) and Escudier (1987). The applicability of the vortex breakdown to gas return flow cyclones was first suggested by Abrahamson (1981). This section is divided up as follows:

3.C.1: Vortex breakdown characteristics
3.C.2: Possible Breakdown mechanisms
3.C.3: Criteria for breakdown

3.C.1: Vortex breakdown characteristics:

Once again, there is some debate on what features constitute the core-type vortex breakdown. Weak forms of vortex breakdown may only involve the abrupt expansion in space of the core, but in stronger forms this is associated with stagnation of the flow and regions of reverse velocity. Generally it is accepted that what sets vortex breakdown apart from other vortex flows are the appreciable axial gradients of pressure or velocity, the abrupt expansion of the streamlines and the free stagnation point on the axis. Vortex breakdown occurs in laminar and turbulent flow, but the downstream flow is always turbulent, and generally has a larger scale of turbulence than the upstream flow.

Upstream of the vortex breakdown the flow varies slowly in the axial direction compared with the radial gradients. As the breakdown is approached there is a retardation of the flow in the axial direction leading up to a stagnation point on the axis and an enlargement of the core diameter around a disturbance that often takes the form of a region of recirculating gas or flow reversal. This 'gas bubble' caps or seals the low pressure core of the vortex against the inflow of high pressure flow from the outer regions.

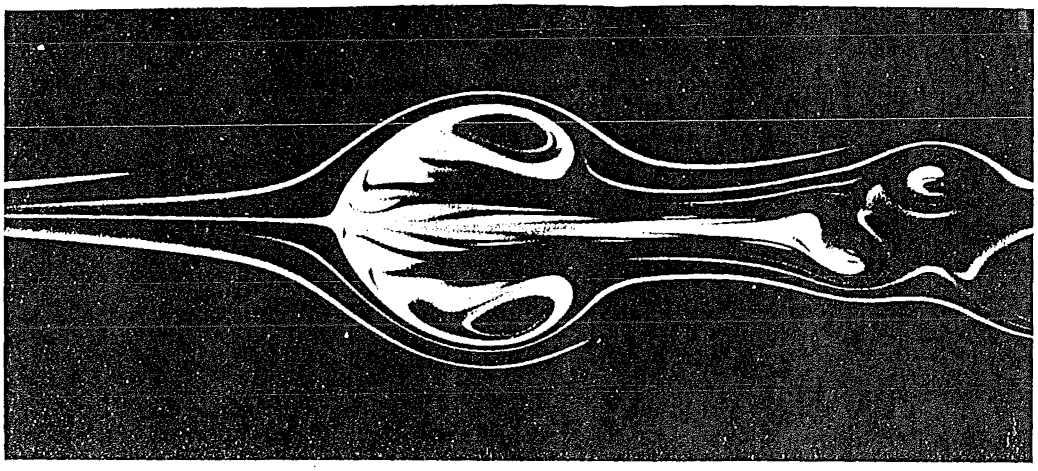

(a) $Ur_t/v = 575$

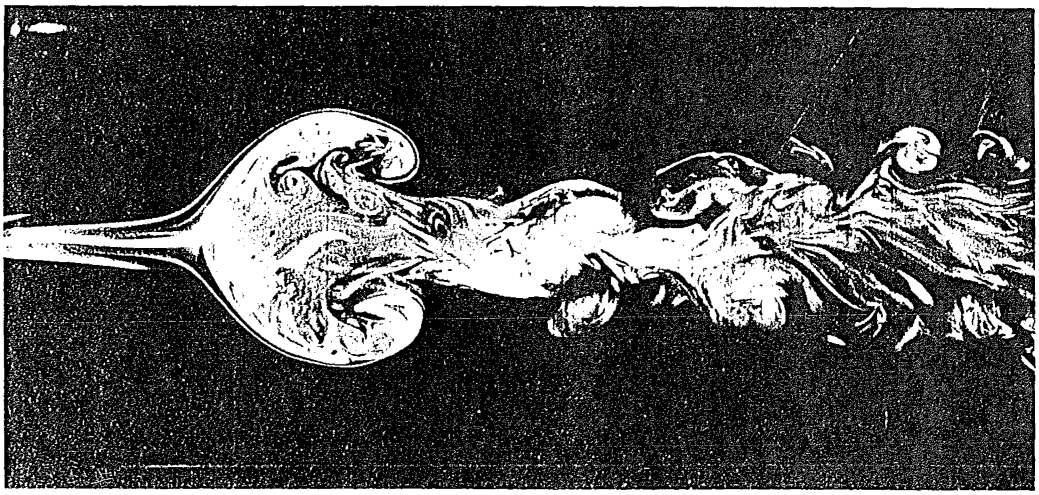

(b) $Ur_t/v = 1650$

Figure 3.C.2: Examples of vortex breakdown in a cylindrical tube, flow from left to right from Escudier & Keller (1983)

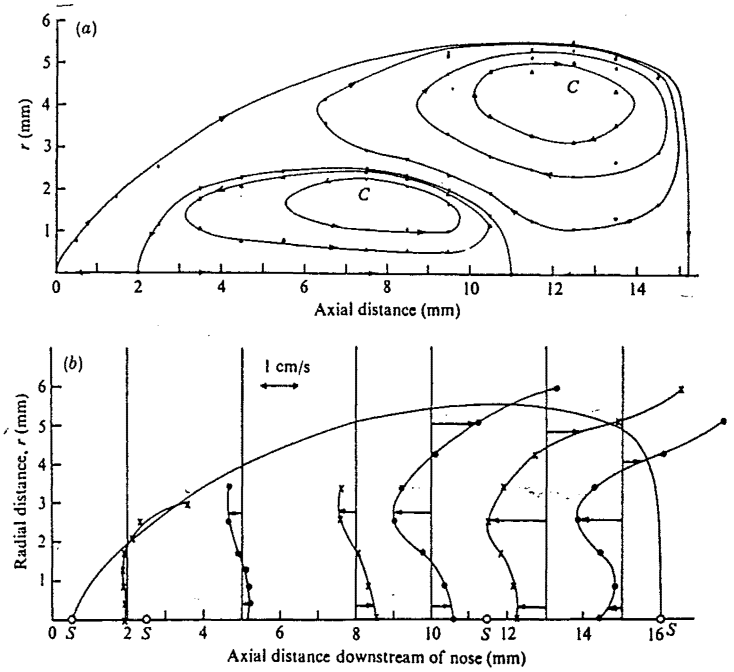

Figure 3.C.3: The internal structure of a breakdown bubble, as revealed by Faler & Leibovich (1978).

In the absence of a downstream supply of rotational energy the natural decay of the vortex results in a decrease in the tangential velocity downstream. The flow is stable provided that the pressure also decreases in the downstream direction, however the decreasing velocity and the spreading core tend to increase the pressure. The increase of pressure along the axis acts to decelerate the flow along the axis and a stagnation point may form - indicating zero axial flow. The change of the core from a jet-like flow to one with an axial velocity defect at the axis does not occur smoothly, but is associated with vortex breakdown. The vorticity tube abruptly expands and forms a closed egg shaped recirculating region, or a spiral - this is the 'vortex breakdown'.

Sarpkaya (1971) found that the position and occurrence of vortex breakdown was a function of both swirl and Reynolds number. Vortex breakdown is found to be promoted by the presence of a positive (adverse) axial pressure gradient. The swirl must also be sufficiently large and the streamlines near the axis must also diverge. Many studies have employed diverging walls to manipulate the vortex breakdown. Vortex breakdown is also very sensitive to disturbances - even from downstream.

Many forms of the breakdown have been described and it is commonly accepted that there are two extremes: an asymmetric 'spiral' type and an axisymmetric or 'bubble' type. The spiral type is obtained under low swirl conditions and is more commonly found in unconfined vortices such as those shed by wing tips. The spiral breakdown is variously described as having a sense of spiral that is opposite to the vortex it is embedded in (Leibovich,1982), or the same sense (Hall, 1967). As the swirl is increased the breakdown passes through as many as 6 different states, becoming more axisymmetric, until the bubble type is obtained. Further increase of swirl results in the breakdown bubble moving upstream, until it reaches the upper boundary of the swirl chamber as reported by Church et al (1979) and others. This results in a columnar vortex, with backflow reported by Harvey (1962) along the entire axis of the tube.

Leibovich (1978) states that reversed axial flows are common in theory and often observed in rapidly swirling flows in devices like 'cyclone chambers'. Leibovich however considered that vortex breakdown is set apart from such flows by its free stagnation point and region of flow reversal embedded within the flow. Leibovich (1982) therefore assigns vortex breakdown an intermediate status between weak swirls with no flow reversals and strong swirl with reversed axial flows of nearly columnar nature.

The diameter of the breakdown bubble examined by Faler & Leibovich (1978) was 1/4 of the tube diameter, and the length of the breakdown transition region was less than 5 bubble diameters, meaning the extent of the reversals is relatively short compared with the columnar reversal. The columnar reversal is often 0.5D in diameter, where D is the diameter of the confining tube. Leibovich (1984) stresses that the phenomenon is not due to viscous wall effects, as the wall is assumed to be far enough away to prevent frictional influences of the wall to penetrate to the vortex core (as must be the case in unconfined vortex breakdown). The wall boundary conditions do exert an influence on the core, as the action of the swirl is to magnify the effect that disturbances at the boundary have on the core as detailed by Hall (1966).

Faler and Leibovich (1978) observed as many as four stagnation points along the axis, however as Lopez (1986) points out, Faler and Leibovich redefined the position of the axis to achieve this, and Lopez has identified the formation of pseudo stagnation points just off the axis.

Although the form of the bubble-type breakdown is axisymmetric on the outside, the internal flow may be decidedly asymmetric, as suggested by the LDA measurements of Faler & Leibovich (1978), or the numerical calculations of Spall, Gatski & Ash (1990). Inside the breakdown bubble the velocities are reported by Escudier & Zehnder (1982) to be small. Velocities obtained with a LDA in the recirculating zone were up to 15% of the axial velocity in the approach flow, and in the inner cell only 4%.

The breakdown of the vortex into many vortex 'fingers' has been proposed by various authors including Stefferns (1988) and Church et al (1979) who found up to 6 subsidiary vortices in a tornado simulator. This geometry has a large cross-sectional area and is short compared with the cyclone. These fingers could be rotating or twisted about each other, presenting a complicated flow structure. Leslie (1977) describes the transitions from a single vortex to paired helical vortices and on to multiple vortices. The transitions were reported to occur not by simply adding another vortex to the ensemble, but rather the new state emerged as the flow pattern gradually recognised from the chaotic state that the previous pattern had degenerated to.

From the above studies,the breakdown is found to depend on:

- the presence of a sufficiently high degree of swirl - typically swirl angles ($\tan^{-1} v/w$) of over 40° are required. The swirl number defined for the cyclone depends only on the geometry - for the Stairmand H.E. geometry this is equal to 19.6, indicating very high swirl (as expected for a cyclone)
- sufficient length for the breakdown to develop.
- the presence of a positive pressure gradient. An adverse pressure gradient can precipitate a breakdown which would otherwise not occur.
- the divergence of the streamtubes in the vortex core immediately upstream of the breakdown - this can produce an adverse pressure gradient in the interior of the vortex core even when the exterior gradient is not adverse.

- the vortex breakdown is very sensitive to interference by probes. This was supported by our flow visualisation observations. This lead to more reliance on the Helium bubble tracers (HBT) than probes. The HBT could also show the time dependent nature of the flow.
- The influence of the Reynolds number is reported to be small compared with the other parameters such as the swirl. .
- The phenomenon is basically inviscid.

Breakdown Dynamics:

The breakdown flowfield is modified by changes in the flow parameters such as the swirl or Reynolds number, but there are also temporal fluctuations in behaviour that occur at fixed values of these parameters. Leibovich (1982) reports that the breakdown may be bi-stable, with transitions occurring spontaneously between adjacent flow states. This is not a true hysteresis as the phenomena are seen to occur in the same way regardless of how the flow settings are arrived at. In addition to having regular oscillations, the entire breakdown form is generally unsteady in position, moving back and forth in a unpredictable way along the axis. These movements are reported to be of the order of a few core diameters around an average position. Church et al (1979) noted that a free stagnation point is inherently very unstable, and the breakdown point is expected to oscillate about a mean position.

Under certain conditions, a spiral type may change to a bubble type without any alteration in the experimental conditions. When this happens, the mean position of the resulting bubble is always several vortex core diameters upstream of the original spiral. These transformations can be reversible at a certain range of swirl levels. The breakdown could also disperse and reform periodically.

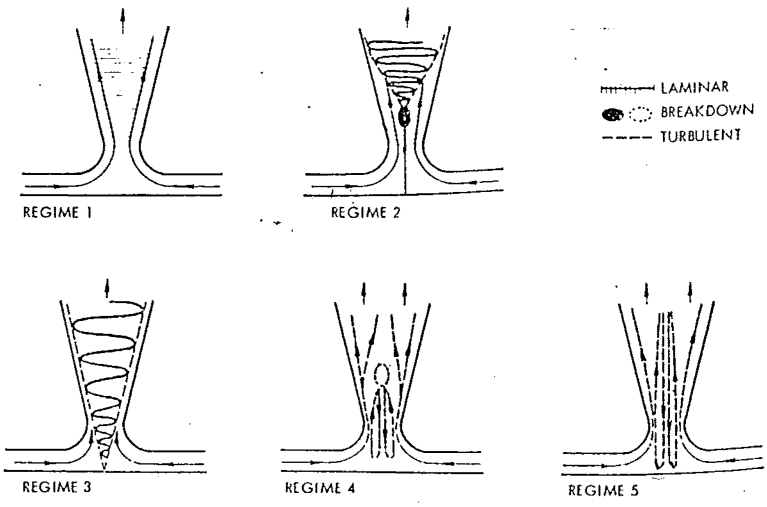

Figure 3.C.4: Movement of vortex breakdown in a conical diffuser as the velocity is increased, from So (1967)

The bubble is not closed at the rear end, and the flow at the rear is markedly unsteady and asymmetric. Fluid passing over the bubble can be entrained at the rear into the recirculating zone (Faler & Leibovich, 1978). Fluid also leaves the bubble at the rear end, and is reported to form a new vortex core that persists for only about 1 bubble length before breaking down. Fluctuations that are not axially symmetric are found downstream even if the upstream flow is axisymmetric. Leibovich (1984) suggests that the expansion of the core in the wake is due to the mixing associated with the instabilities and turbulence, indicating that instabilities play an essential role in shaping the global structure.

Escudier (1984) observed multiple recirculation bubbles along the axis that were produced in a closed cylinder with a rotating lid for length to diameter ratios of greater than 1.25. Lopez (1990) reproduced this feature in numerical simulations of the flow and was able to elucidate the dynamic movements of the bubbles. As the swirl was increased the two bubbles coalesced and separated repeatedly. Lopez (1990) reports that none of the flows that resulted in recirculations ever settled down to steady state. At the highest Reynolds number flow examined the regions of recirculations continued to move back and forwards on the axis.

Experimental observations of vortex breakdown flows are hampered by the rapidly fluctuating behaviour and the sensitivity to disturbances. Numerical simulations of the flow can avoid some of these problems and show features of the breakdown in a clean, controlled environment. With the increase in computing power the accuracy of the simulations has improved.

Early numerical simulations of the vortex breakdown were not able to cope with the tendency of the vortex breakdown to move upstream and become modified by the specified boundary conditions at the inlet. The inlet boundary condition is avoided altogether by studying the vortex breakdown in a closed container such as that observed by Escudier (1984). Numerical simulations of closed cylinder flows have been made by Lugt and Abboud (1987) and Lopez (1988). Both used an axisymmetric form for the flow and good agreement was obtained between these numerical results and the experimental results of Escudier (1984). However when the breakdown has been modelled numerically for through-flow situations the agreement has been unsatisfactory. Spall et al (1990) have avoided this by controlling the location of the vortex breakdown by manipulating the side boundary conditions. Bruer and Hanel (1989) were able to keep the breakdown from moving upstream to the inlet by controlling the static pressure at the wall. The type of breakdown changed from bubble to the spiral type.

Spall et al (1990, 1991) found numerical results for fully three-dimensional unsteady Navier-Stokes equations and the computed internal flow structure compared favourably with the observations of Faler and Leibovich (1978). Both spiral and bubble forms of breakdown were demonstrated by the flows, and the computations are being extended to turbulent conditions.

Dependence on geometry:

The major influence of the geometry on the breakdown is its effect on the pressure gradient. Diverging tubes give a positive pressure gradient in the direction of flow, whereas straight or converging tubes will have a negative gradient. The converging walls of the cone of the cyclone clearly help to delay the onset of vortex breakdown by restricting the divergence of the

streamlines, maintaining a high tangential velocity and helping to maintain negative pressure gradient. Even so, an adverse (positive) gradient along the core can occur despite negative gradients existing in the outer flow. Hall (1972) gives the example of a parallel sided duct with a negative pressure gradient at the wall when the swirl was just less than that needed for breakdown. A slight increase in swirl caused breakdown to occur in the tube and a region of positive pressure gradient was then observed along the wall, beginning upstream of the breakdown. When an adverse gradient is increased, less swirl is needed to maintain a breakdown, according to Leibovich (1982)

Pressure gradients may be impressed upon the vortex core by a deceleration of the outer flow, or from pressure differences caused by the sudden expansion of the flow (such as at the dust exit) or by leaks into the bin (raising the bin pressure). Chanaud (1965) found a conically decreasing section caused the critical Reynolds number that was required for breakdown to increase "beyond the range of their instrumentation", which had been adequate for cylindrical flow. Hall (1966) found that in most vortex flows a change in axial velocity along the outside of the streamtube is accompanied by a more pronounced change along the axis, which Leibovich (1978) attributed to the amplification on the axis of pressure gradients at the edge of the core.

Escudier & Zehnder (1982) reportedly obtained a well defined and relatively stable breakdown bubble in a sudden downstream constriction similar to the geometry of the gas exit tube in the cyclone. Lavan et al (1969) studied the case of a swirling flow (generated by a rotating cylinder) entering a stationary tube and found that a region of reversed flow tended to form on the axis, which was in contrast to the behaviour observed when the flow entered a rotating tube.

Kirkpatrick (1964) measured the wall pressures in a tube with a parallel/diverging transition with swirling flow and found a steeper negative gradient opposite a breakdown in the straight tube section. This is also demonstrated in figure 3.C.5 from Sarpkaya (1971a) where the prevailing positive pressure gradient in a diverging tube changes to a negative gradient opposite the breakdown location:

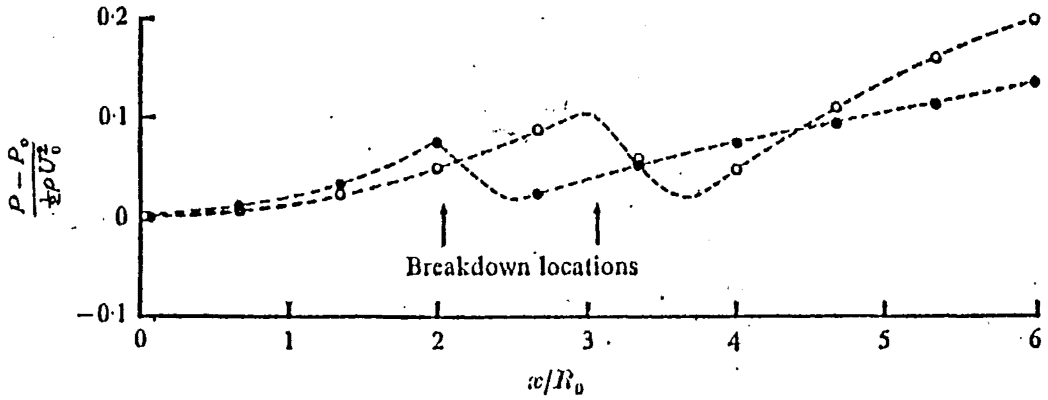

Representative wall-pressure distributions. P_0 denotes the pressure at the start of the diverging tube. ○, for $Re = 7500$ and $\Omega = 1{\cdot}5$; and ●, for $Re = 4000$ and $\Omega = 1{\cdot}75$.

Figure 3.C.5. Relationship between the wall pressure gradient and the vortex breakdown location, (from Sarpkaya, 1971a)

It should be noted that the majority of observations of vortex breakdown were for vortex flow in tubes, for which the breakdown occurs in the core of the vortex - the region up to the radius of maximum swirl velocity. Typically these experimental arrangements were for straight-through flow, with no exit or draw-off that would allow for the reverse flow, unlike the case of the return-flow cyclone. Care must be taken when applying the results from unconfined vortices to confined vortices, as the confining walls may alter the natural sink flow of the vortex. In addition there may be differences between different scales of cyclones. There may be fundamental differences between flow in closed cylinder flow exhibiting vortex breakdown; vortex breakdown in confined through-flow and reverse-flow apparatus, and vortex breakdown in unconfined flow.

The vortex flow studied by Church et al (1979) in a tornado vortex chamber is essentially unconfined, as the walls are at a large distance from the core. The vortex does demonstrate a similar conical structure and at large swirl the breakdown was observed to penetrate upstream to the 'lower' surface, with an associated downflow following. After this the core was reported to consist of an outer, slightly conical shear zone of spiralling upflow surrounding an inner subcore of downward flow.

Lopez (1990) examined the vortex breakdown in a swirling flow in a cylinder with a rotating endwall. The experimental visualisation of the flow reported by Escudier (1984) was compared with numerical simulations. Of particular interest, (because of the resemblance to features of the cyclone flowfield) are the existence of multiple recirculations along the axis. These were promoted at high length to diameter ratios and for higher Reynolds numbers. This suggests that the multiple recirculations will be even more prevalent in the cyclone geometry than the cylinder studied by Lopez. Also of interest in the computations was the observation that none of the cases that lead to a recirculation bubble ever settled down to a steady state. The bubble would migrate upstream until halted by the influence of the time-independent upstream boundary conditions.

The rotating endwall flow is deemed particularly suitable for the examination of the vortex breakdown phenomenon because it has easily applied boundary conditions, is essentially axisymmetric and is dependent on 4 parameters which are easily measured (and controlled). As a closed system, there are no inflow or outflow boundary conditions to consider. The earliest observations of the breakdown in the rotating endwall cylinder were by Wilcke (1780) and Vettin (1857). The first systematic experiments on the phenomenon were by Vogel in 1968. Escudier (1984) extended the measurements and observations and was the first to report the occurrence of multiple breakdown bubbles.

Steady, axisymmetric solutions to the Navier-Stokes equations have been found for flows exhibiting vortex breakdown by Kopecky and Torrance (1973); Grabowski and Berger (1976) and Lopez (1986, 1990). There is some debate as to whether these are fully representative of the vortex breakdown phenomenon. Leibovich (1984) suggests that both the spiral and bubble forms of breakdown evolve from flows that are clearly not axisymmetric, since bubble types are observed to evolve from spiral types. Leibovich (1984) suggests that axially symmetric breakdowns are physically realisable only at sufficiently low Reynolds numbers in wall-dominated flows. Since then Lopez has extended results to higher Reynolds number.

3.C.2. Vortex breakdown mechanisms

The explanation of the mechanism of vortex breakdown does not appear to have been resolved in the literature. Hall (1972) considered three main proposals:
1. The failure of the axial gradient assumption. (Hall (1967))
2. Instability of the vortex to perturbations. (Ludwieg (1962, 1965))
3. The existence of a critical state. (Squire (1960), Benjamin (1962))

A more recent review by Leibovich (1984) still considered that proposals could be classified into one of these three categories. However there seem to be some proposals that do not fit into this scheme, as they treat vortex breakdown as a natural development of the flowfield rather than special condition or state. Hence a fourth proposed mechanism will be considered:
4. Positive feedback of streamline divergence. (Bossel (1969), Lugt (1983), Brown & Lopez (1990)

These proposals are outlined in more detail below:

1. Failure of axial gradient assumption:

Hall (1967) proposed that the vortex breakdown is analogous to the separation of a 2 dimensional boundary layer from a wall, in that breakdown is predicted at the point when the quasi-cylindrical approximations fail because of sizeable axial gradients. Upstream of the breakdown the flow varies slowly in an axial direction compared with the radial gradients and the stream surfaces are approximately cylindrical. The equations of motion are formulated with approximations which are termed 'quasi-cylindrical' and the flow pattern is then calculated progressively downstream from the inlet. In the course of the calculation if appreciable axial gradients are found, then the quasi-cylindrical approximations fail. It is conjectured that this point corresponds to the onset of vortex breakdown, where appreciable axial gradients are found in practice. This approach is analogous to the case of boundary layer separation, where flow calculations assume that flow is parallel to the wall. When the calculated flow deviates from the wall the flow equations are no longer valid, but the location of this deviation corresponds with the experimentally determined point of separation of the real boundary layer.

Ludwieg (1970) has shown that the failure of the quasi-cylindrical approximation for inviscid flow coincides with the vortex breakdown critical state suggested by Benjamin (1962) such that Hall's criterion is equivalent to the criticality criterion of Benjamin. However, it is obvious that Hall's approach can not yield information about the flow downstream of the breakdown point. Bossel (1969) also mentions the work of Strscheletzky (1957) who treated vortex breakdown as a centrifugal separation phenomenon. This work is not readily available, and Bossel dismisses it as imposing a definition of vortex breakdown that is too narrow.

2. Instability to perturbations:

Ludwieg (1962, 1965) proposed that the phenomenon is a consequence of hydrodynamic instability, with perturbations travelling on the vortex and growing to the point where breakdown is induced. Different studies have examined different forms of perturbations including axi- and asymmetric and using both phase- and group velocity approaches.

The hydrodynamic instability explanation of vortex breakdown appears to be more applicable to unconfined flows such as wing-tip vortices rather than the axisymmetric type of breakdown. Most versions of this criterion assume the perturbation waves to be present along the entire vortex, as observed with vortices in long (L/D >4) cylinders (Smith, 1962a; van Dyke, 1982). However, other studies of vortices in tubes report that the waves are only observed below the breakdown (Leibovich, 1978). If this is the case then the third proposal, which is outlined below, is more relevant.

3. The existence of a critical state:

Squire (1960) was one of the first to offer an explanation for the phenomenon of vortex breakdown, by proposing a critical condition for breakdown. Taking three alternative descriptions of the basic flow, he reduced the steady and inviscid non-linear equations of motion to a linear disturbance equation. This could then be solved to yield the conditions that were required for the existence of a steady perturbation on the flow (a standing wave). This resulted in the definition of a swirl ratio, at which breakdown was proposed to occur.

Benjamin (1962) arrived at a similar condition for criticality although he disagreed with Squire's approach. Benjamin (1960) viewed vortex breakdown as a finite transition between two dynamically conjugate states of flow, which were differentiated by their ability to support standing waves. Squire's (1960) criterion effectively marked the transition between these two states. According to Benjamin, the flow upstream of the breakdown is supercritical and cannot support standing waves, whereas downstream the flow is sub-critical and can support waves.

The interpretation of super- or sub-criticality is based on the wave propagation characteristics of the mean flows. The upstream mean and instantaneous flows coincide, but there is a difference in the downstream mean and instantaneous flows. Increasing the swirl reduces the minimum value of the negative wave speed, c_- so that increasing the swirl drives super-critical flows to the sub-critical condition. Leibovich (1984) points out that the group velocity should have been used rather than the phase velocity, but this error is not important if the analysis is restricted to axisymmetric waves.

Escudier & Keller (1985) claim that the critical state theory is now generally accepted as the explanation for the phenomenon. The term 'Critical' refers to "a flow for which long inertia waves (that is those with the highest phase speed) are stationary with respect to the flow" (Escudier & Keller (1985)). In supercritical flow these waves are swept downstream from the original disturbance, whereas in subcritical flow the waves propagate upstream against the flow. Benjamin (1962), Garg & Leibovich (1979) and Escudier et al (1982) claim that it is the state of criticality which determines the breakdown, and the waves are a superimposed, but important fine detail.

The upstream propagation of wave energy in subcritical regions is permitted for infinitesimal waves, but these waves cannot penetrate upstream of the point at which criticality starts. This suggests the possibility that the disturbances could become trapped at this barrier and build up to the large disturbance that causes, or is, the vortex breakdown. The wave propagation characteristics of the vortex change as a vortex evolves or responds to an imposed pressure gradient or geometrical constraints.

As with the Instability mechanism outlined above, different forms of the waves have been proposed by various authors. Squire (1960) considered linear waves, while Benjamin (1962), Leibovich (1970), Randall & Leibovich (1973) and Leibovich and Randall (1973) have extended this to non-linear waves. The trapping of waves by phase-velocity considerations was extended to group-velocity considerations by Tsai & Widnall (1980).

In cases of high swirl, the breakdown moves upstream to the upstream endwall - the whole flow will then become subcritical, indicating that waves can travel upstream throughout the flow. One other indicator of whether the flow is sub- or supercritical is the effect of changing the vortex tube diameter on the vortex core diameter. The changes are of the same sign for supercritical flow and of opposite sign for subcritical flow according to Benjamin (1962). This criterion will be difficult to apply to the cyclone vortex because of the effect of radial inflow swelling the inner vortex.

Experimental studies (Kirkpatrick (1964), Faler & Leibovich (1977, 1978)) have identified supercritical flow upstream and subcritical flow downstream of the breakdown in accord with the travelling wave theories of Squire (1960) and the finite transition theory of Benjamin (1962). From their observations, Escudier and Keller (1985) proposed a two-stage transition between the super- and sub-critical regions.

4. Positive feedback of streamline divergence.

Although the above theories are frequently cited as the three main alternative theories , there have been attempts to link them into a unified theory, such as by Lugt (1983). Lugt's arguments are similar to proposals advanced by Bossel (1969) and Lopez (1990) in that the development of the breakdown is considered as a natural development of the flow, not one that requires distinct states between upstream and downstream regions.

Bossel (1969)'s theory was classified by Reyna & Menne (1988) as a 'critical state' approach. However Bossel rejects the concept of a finite transition from super- to sub critical states of flow, and instead regards vortex breakdown as a necessary feature of supercritical flows which have high swirl, rigid initial rotation and some axial flow retardation at and near the axis.

Whereas the failure of the quasi-cylindrical approximations can only be used to predict the breakdown location, Bossel makes further approximations for the flowfield regions around and downstream of the breakdown region to enable the flowfield inside the breakdown to be estimated. Benjamin (1967) showed that a stationary wave requires a non-linear statement of the stream function. Bossel assumes the *a priori* existence of conditions leading to the retardation of the flow on the axis, which then allows stationary solutions to the linear problem.

Bossel's proposal starts by reducing the Navier-Stokes equations for viscous, incompressible flow at fairly high core Reynolds numbers (c 10 000) to three different approximating systems for a vortex with high swirl. These approximations are then applied in four distinct regions of the flow. The approximations are:

1. A viscous parabolic set in regions of quasi-cylindrical flow
2. An inviscid elliptic equation, which is applied in regions where the flow is expanding or contracting and also near or at the axis of such flows
3. The Stokes equations in a very small region surrounding a free stagnation point.

Initial rigid rotation of the inner core is taken as a valid approximation to the upstream conditions. Downstream, the stream function is approximated by an expansion in even powers of the radius R, which yields bulges and bubbles on the axis for high swirl values. The four regions that the vortex breakdown flowfield is broken down into are:

1. A region of quasi-cylindrical flow upstream and possibly downstream and surrounding the breakdown - where the angle between the stream surfaces and the axis is zero or small.
2. A region of expanding or contracting flow (excluding the regions of stagnation) where the axial velocity gradients are appreciable, as is the stream surface angle.
3. A region next to the axis and inside the breakdown where axial gradients are large and the radius tends to zero.
4. The region surrounding the stagnation points where both the radius and the velocities tend to zero.

Bossel uses an order of magnitude analysis to show that region 1 is viscous, and region 2 is dominated by inertia and pressure terms when terms of order $(\nu/w_o r_c)$ are neglected. Region 2 then can be described by the equations for inviscid rotating flow. Region 3 is the interior of region 2, as the radius tends to zero. Once again, the viscous terms can be neglected for large core Reynolds numbers and the same inviscid rotating flow equations apply. Region 4 concerns the region around a stagnation point, where since the inertial terms vanish (the velocities go to zero) the viscous terms must dominate. It is shown that the viscous terms become of the same order as inertia terms only when $W' = O(\nu/w_o r_c)$ which shows that this region is extremely small, and is consequently neglected.

This analysis suggests that the inner breakdown region (including the stagnation point) can be approximated well by the inviscid equations of rotating flow. This inner inviscid region is imbedded in a viscous quasi-cylindrical region. The appearance of the breakdown bubbles is a continuous phenomenon. Vortex breakdown is thus said to be fully explainable by supercritical solutions to the inviscid equation to which the Navier-Stokes equations approximate in the breakdown region. The weakness of this theory is that the retardation of the flow at the axis is prescribed rather than described, and is attributed to the presence of an exterior pressure gradient or an object on the axis. In the absence of either of these there is no explanation for the initiation of the breakdown.

Lugt's (1983) unified mechanism starts with the spread of vorticity away from the axis by diffusion and convection. This leads to an increase in pressure along the axis, diverging streamlines and a deceleration of the axial flow which can lead to a stagnation point on the axis with flow reversal.

The divergence of streamlines near the stagnation point requires a reduction in the tangential velocity along the streamlines due to conservation of angular momentum. This reduction "overshoots" the balance between the centrifugal acceleration and the radial pressure gradient, resulting in converging streamlines and hence increasing tangential velocity. The separation region closes, but the wave may be repeated along the vortex length.

Brown and Lopez (1990) have proposed a mechanism for the breakdown of the vortex in a closed cylinder with a rotating endwall. This was shown to be consistent with experimental observations of Escudier (1984), as well as numerical simulations of the flow by Lopez (1988,

1990). Brown and Lopez then generalised the mechanism to swirling flow in pipes, again backed up by comparisons with numerical simulations of the time-dependent flowfield, by Lopez (1988).

Brown and Lopez (1990) found that swirling pipe flow required the presence of viscosity to initiate the divergence of the streamlines, but the subsequent development of the flow was inviscid. The assumption of inviscid flow for the breakdown region has been widely supported in the literature, from both experimental observations and from numerical modelling. Reyna & Menne (1988) report that numerical solutions of the slender vortex approximations show that the viscous forces are really small compared with the pressure and inertia forces near the breakdown of the slender vortex equations.

Spall et al (1991) from their numerical studies suggest that the mechanism of the vortex breakdown is analogous to boundary-layer separation in that the initial divergence of the streamlines is caused by an axial pressure increase in the direction of flow. This convects vorticity away from the vortex axis, and if convection is greater than diffusion the vorticity may be larger off the centreline. The reduction of the axial vorticity must lead to an increase in other vorticity components. Spall et al (1990, 1991) only consider laminar flows and are extending this to turbulent flow conditions in further research.

3.C.3 Criteria for Vortex Breakdown

Many criteria to predict the occurrence of breakdown have been proposed, generally based on one of the mechanisms outlined above, but also from empirical studies or from the results of numerical simulations. Where possible, these have been related to the case of the cyclone vortex, and a selection of these are presented below, grouped under the following headings:

Perturbation instability
Critical state
Failure of approximations
Empirical relationships
Numerical studies

3.C.3a Instability to perturbations:

The **Rayleigh** (1917) criterion considers the simple type of inviscid rotational instability that results when the balance of the centrifugal force and the radial pressure gradient is upset in an axisymmetric motion. Karman (1934) provided a clear physical description of this by considering the effect of an axisymmetric disturbance in an inviscid region of a rotating fluid where the principal balance of the forces is between the centrifugal and radial pressure gradient. If fluid elements at radii r_o and r_1 are swapped by the disturbance then the flow is inherently stable if the force field tends to restore the particles to their original positions, and is unstable otherwise. The criterion for instability is obtained by consideration of the conservation of angular momentum:

For $r_o > r_1$ the flow is unstable if $(r_o v_o)^2 < (r_1 v_1)^2$

$$\text{that is, } \Gamma_o^2 < \Gamma_1^2 \qquad \text{--- (3.C.1)}$$

as the slight deviations are accentuated by the force imbalance. Thus Rayleigh's criterion predicts that a steady, laminar motion is unstable when the square of the absolute circulation about the rotation axis decreases with increasing cylindrical radius. The requirement for the flow to be laminar obviously limits the applicability of this criterion, in addition the criterion is for flows with one velocity component only. A similar result is arrived at by Uberoi (1979), who noted that Rayleigh's criterion applies for axisymmetric disturbances only. Nevertheless, the Rayleigh criterion forms the basis for other stability criteria.

Belousov & Gupta (1986) suggest that a natural instability caused by the radial pressure gradients is the reason for the axial reversal of the vortex in cyclone type devices. The flow reversal on the axis is necessary to form a vortex core that behaves like a solid body on the axis, with V_θ/r = constant rather than the $V_\theta.r$ = constant found in the outer vortex. If $V_\theta.r$ = constant then an increase in radius r must decrease V_θ, however according to Bernouilli's equation this will cause the static pressure to decrease in order to conserve the total pressure, and hence the radial pressure gradient.

Shivamoggi & Uberoi (1981) give a criterion based on the density gradient, with a positive stratification (density increasing away from the axis) found to postpone the vortex breakdown.

Howard & Gupta (1962) examined inviscid flows between cylinders and gave a necessary (but not sufficient) condition for stability, based on a local Richardson number. For the flow to be stable to axisymmetric perturbations the local Richardson number, J(r), should nowhere be less than 1/4, where

$$J(r) = \frac{r^{-3}\,\frac{d(r^2V^2)}{dr}}{\left(\frac{dW}{dr}\right)^2} \qquad \text{--- (3.C.2)}$$

where W is the axial velocity and V the tangential or azimuthal velocity. This result is used in several of the criteria below.

Stewartson (1982) restated Howard and Gupta's (1962) criterion as

$$-2\,\Gamma\frac{d\Gamma}{dr} + \frac{1}{4}r^3\left(\frac{dW}{dr}\right)^2 > 0 \qquad \text{--- (3.C.3)}$$

Ludweig (1962) emphasised the asymmetrical features of the vortex breakdown, citing the instability to non-axisymmetric disturbances as the principal mechanism of vortex breakdown, and not a secondary effect. Ludwieg's stability criterion however, was derived for a geometry that differed greatly from that encountered in vortex breakdown flows, being inviscid flow spiralling in a narrow annulus.

The model is a direct extension of Rayleigh's classical model (1917), to allow radial gradients of axial velocity. In terms of the dimensionless velocity gradients

$v_r^* = \frac{r_m}{v_m}\cdot\frac{\partial v}{\partial r}$ and $w_r^* = \frac{r_m}{v_m}\cdot\frac{\partial w}{\partial r}$. the condition for stability is:

$$(1 - v_r^*)\,(1-v_r^{*2}) - (\tfrac{5}{3} - v_r^*)\,w_r^{*2} > 0$$

The stability boundary is shown below as a curve in the v_r^*, w_r^* -plane.

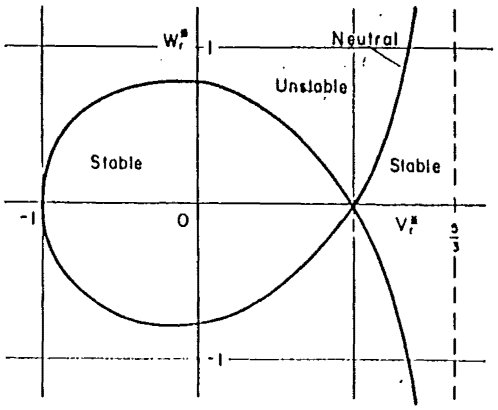

Figure 3.C.6: Stability boundary for spiralling flow (From Ludwieg, 1962)

The figure illustrates the strong destabilising effect of a radial gradient in axial velocity. Ludwieg (1962) applied the criterion to profiles of leading edge vortices and predicted the flow to be unstable if v/w was greater than 1.12, or the helix angle of a streamline was less than 42°. The theory is valid only for infinitesimal disturbances, but Ludwieg proposes that after the onset of instability, amplification of the disturbances leads to breakdown. Instability was predicted for all approach flows examined by Hall (1966) and Leibovich (1978) using this criterion. It should be noted that the onset of instability need not imply breakdown, and the criterion is not expected to apply to near-axisymmetric flows.

The geometry used by **Lessen, Singh & Paillet** (1974) is more suitable for many vortex geometries. They examined the inviscid stability to infinitesimal non-axisymmetric disturbances and calculated the magnitude of swirl needed to stabilise jets and wakes against non-axisymmetric disturbances on a flow with an idealised velocity profile. They superimposed a profile for a convecting and diffusing vortex onto the ordinary axisymmetric far wake profile. This flow is characterised by a swirl parameter q which involves the ratio of the magnitude of the maximum swirl velocity to the maximum axial velocity. Only the non-axisymmetric disturbances were considered as the swirl stabilises the axisymmetric ones.

Velocities in cylindrical coordinates (r,θ,z) were non-dimensionalised with respect to an axial velocity scale W_S:

$$W_S = \frac{\Gamma_o^2}{8.\nu.x}\log\frac{W_o.x}{\nu} + L.\frac{W_o^2}{8.\nu.x} \qquad \text{and the radius scaled by } r_S = \left(\frac{W_o^2}{4.\nu.x}\right)^{\frac{1}{2}} \qquad \text{--- (3.C.4)}$$

W, V are the axial and azimuthal velocity profiles respectively
W_o is the free axial velocity
ν is the kinematic viscosity
Γ_o is the constant circulation at large radius r_o
L is a constant depending on the induced drag or initial velocity defect.

This gives the non-dimensionalised mean velocity profiles:

$$V = q\frac{(1 - e^{-r^2})}{r} \qquad W = \frac{W_o}{W_S} - e^{-r^2} \qquad \text{where } q = \frac{\Gamma_o}{W_S.r_S} \qquad \text{and } r = \frac{r_o}{r_S}$$

--- (3.C.5)

They use $W = e^{-r^2}$ as the mean axial velocity distribution.

This form of columnar vortex velocity profile (termed the Q-vortex) has been widely used in studying the stability of vortex flows, particularly in modelling the leading edge and trailing vortices in aerodynamics. Lessen et al found that the Q-vortex was unstable to three dimensional Fourier disturbances of the form: $e^{i(kz+n\theta-\alpha ct)}$. Where n = azimuthal wave number, α is the axial wave number and $c = c_r + ic_i$ is the complex phase velocity. θ is the azimuthal coordinate.

The phase speed is inversely proportional to the magnitude of the wave vector and the waves are in general dispersive, dissipative and anisotropic. The long waves (small n) travel fastest

and the short waves slowest. The group velocity is the velocity of energy propagation and may be determined by calculating the energy flux.

A wavenumber n = 0 indicates axisymmetric perturbations, but attention was focused here on asymmetric perturbations. The presence of swirl was found to create a distinction between positive and negative azimuthal wavenumbers. The n = +1 mode is stabilised by the addition of small amounts of swirl - as little as q = 0.07. However the addition of a small amount of swirl lead to enhanced instability of the negative azimuthal modes. In the case of n less than or equal to -2 the flow is completely stable without swirl but unstable with q = 0.07. The disturbances eventually become damped out and the flow completely stabilised at a value of q slightly greater than 1.58

The growth rate of the disturbance is given by the product of the axial wave number and the imaginary part of the phase speed. This appears to increase continuously with |n|, a feature that was examined by Leibovich and Stewartson (1983) and will be discussed further below.

The swirl parameter q can be expressed as: $1.56\frac{V_{max}}{\Delta W}$ where ΔW is the axial velocity deficit (for the velocity profile in the cyclone ΔW will be the difference between the peak axial velocities in the core and the outer, or the sum of the absolute values). Since for the 140mmØ cyclone V_{max} is about 36m/s, and ΔW of at most 20m/s this approach suggests that approach flows are stable to all infinitesimal disturbances, including asymmetric ones. The method of estimating the axial velocity deficit in both jet and wake type vortices is given by the following figure from Escudier, Bornstein and Maxworthy (1982):

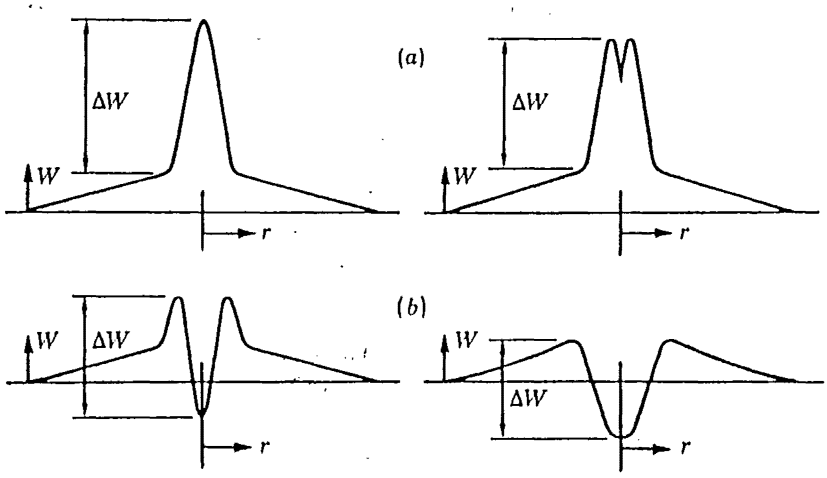

Figure 3.C.7: Definition of characteristic axial velocity deficit for stability analysis for (a) jet-like and (b) wake-like vortices (from Escudier et al (1982)

The Q-vortex has been used by a number of workers (Garg and Leibovich (1979), Leibovich and Stewartson (1983), Escudier, Bornstein and Maxworthy (1982)) to fit experimental profiles or to model the vortex flow when examining the stability to perturbations.

Stewartson (1982) developed an asymptotic theory describing the stability of a swirling axial flow at high Re when subject to large azimuthal wavenumber n. The disturbance is concentrated on a narrow band at a finite distance from the axis, decaying exponentially on either side. The analysis is applied to a trailing vortex and results in the swirl parameter q that defines the intensity of the rotational velocity in relation to the axial flow. The stability of the flow requires that q be greater than 1.4.

Leibovich & Stewartson (1983) found a sufficient condition for instability to three-dimensional perturbations in unbounded domains. This arose from considering the limit to the increase of the disturbance growth rate with |n| that was found by Lessen et al (1974) and mentioned above. On energy stability grounds it was shown that the growth rate could not exceed the maximum rate of strain, s, of the basic flow:

$$s = \left(\left(r \frac{d\Omega}{dr} \right)^2 + \left(\frac{dW}{dr} \right)^2 \right)^{\frac{1}{2}} \qquad \text{--- (3.C.6)}$$

Ω is the angular velocity of the basic flow = V/r and W is the axial velocity. Consideration of the behaviour as n approached infinity revealed that the growth rate approached a limit from below. The theory was valid for wavenumbers down as low as n = 3. The result was able to be generalised to hold for arbitrary inviscid profiles V(r) and W(r), yielding a local Richardson number-type criterion, based on the geometric mean of the angular velocity gradient and the circulation gradient. It can be compared with the Richardson number that was obtained by Howard and Gupta above. The condition is a sufficient one for the instability of a columnar vortex, with instability predicted if:

$$V \cdot \frac{d\Omega}{dr} \left(\frac{d\Omega}{dr} \frac{d\Gamma}{dr} + \left(\frac{dW}{dr} \right)^2 \right) < 0 \qquad \text{--- (3.C.7)}$$

Ω = angular velocity = V/r
V = azimuthal velocity
w = axial velocity
Γ = circulation (r V)

The one-parameter model of the trailing vortex was used to illustrate the stability criterion, with the components used being: Swirl $V(r) = \frac{q}{r} . (1 - e^{-r^2})$ and Axial $W(r) = e^{-r^2}$ with scaling of the velocities and length as detailed above.

The analysis results in a sufficient condition for the instability of the swirling flow if $q < \sqrt{2}$. The parameter q is stated to be 'essentially the maximum pitch angle of the helices on which the fluid particles move in the flow', and the flow is stable if q is greater than about 1.6. That is $q = \tan^{-1} (V/W)$). In the 140mmØ and 750mmØ cyclones the angle of the outer flow to the axial plane was never more than 30° (hence the pitch of the helix is greater than 60° and q > 1.73) and was typically less than 20° (q > 2.7) at the wall. Larger angles were found in the core vortex, approaching 60° (q = 0.6).

Garg & Leibovich (1979) use the inviscid stability criteria of Howard and Gupta (1962) and Lessen et al (1974) for the time-averaged velocity profiles described by:

an axial velocity $W(r) = W_1 + W_2\exp(-\alpha r^2)$ --- (3.C.8)

and a tangential velocity given by $V(r) = \Gamma_o r^{-1} [1 - \exp(-\alpha r^2)]$ --- (3.C.9)

These equations are transformed to the form adopted by Lessen et al (1974) by non-dimensionalising by the magnitude of the axial velocity deficit $|W_2|$, and substituting the parameter

$q = \frac{\Gamma_o \sqrt{\alpha}}{|W_2|}$. q is a measure of the ratio of axial to azimuthal vorticity components in the vortex core and equals $1.57 \frac{V_{max}}{|W_2|}$, where V_{max} is the maximum swirl velocity. The radius r^* of Lessen et al is obtained from the radius used here by $r^* = r\sqrt{\alpha}$.

the scaled axial velocity is $\bar{W} = \frac{W(r)}{|W_2|} = \frac{W_1}{|W_2|} + \frac{W_2}{|W_2|} \exp(-\alpha r^2)$ --- (3.C.10)

and the scaled tangential velocity is $\bar{V} = \frac{V(r)}{|W_2|} = \frac{q}{\sqrt{\alpha}\, r} [1 - \exp(-\alpha r^2)]$ --- (3.C.11)

and q and α are parameters to be adjusted to achieve the fit to their experimental profiles. The experiments were obtained with a laser Doppler anemometer for a vane-generated vortex in a slightly diverging tube. Velocities in the wake downstream of the vortex breakdown were time-averaged before fitting.

For the Q-vortex, the Howard and Gupta (1962) criterion for stability to axisymmetric disturbances requires $q > 0.402$ for the flow to be stable. This was satisfied for the flows both upstream and downstream of the vortex breakdown.

Application of Lessen et al's (1974) criterion indicates complete stabilisation to all infinitesimal inviscid asymmetric disturbances when $q > 1.5$. All flows resulting in vortex breakdown had values of q greater than 1.5 upstream of the breakdown, and hence were stable. Far downstream in the wake the profiles were stable to axisymmetric (azimuthal wavenumber $m = 0$) disturbances but were unstable to non-axisymmetric ($m \neq 0$) disturbances.

The Q-vortex was also fitted to the profiles just upstream of the vortex breakdown, although the columnar profile is not strictly valid for regions of high axial gradients such as in the region of the breakdown. The results suggested enhanced stability of the flow just before the breakdown, although the accuracy of this is questionable.

The frequency of oscillations in the wake of the breakdown matched the frequency calculated from

$$f = \frac{k((W_1/W_2) - C_r)\, |W_2| \sqrt{\alpha}}{2\pi\, r_t} \quad \text{--- (3.C.12)}$$

The wave speed c_r was able to be estimated from the results of Lessen et al (1974) only for the case of the wavenumber m = ±1, but the results for this agreed well. Tsai and Widnall (1980) gave a more detailed estimate for the frequency of oscillations and showed that these oscillations were consistent with fluctuations expected from the n=1 perturbations, and the frequency could be calculated from:

$$f = (\omega_r / 2\pi) [\delta_o / R(z)] \qquad \text{--- (3.C.13)}$$

where ω_r is the real part of the complex perturbation frequency

δ_o is the (axial) velocity scale taken from the value at the inlet

and R(z) is the local tube radius

The Burgers vortex form of the tangential velocity variation was also used to fit the tangential velocity profiles in the cyclone for this study, in section 6.B1, hence the parameters are easily determined. This stability criterion will be applied to the cyclone flow in section 6.C

The problem in using this criterion is the estimate of the axial velocity deficit, which is defined for the swirling jet flows. This parameter needs to be related to an axial velocity that is characteristic of the cyclone flow, and is preferably easily determined. Examining the form of the axial velocity model used in developing this criterion it appears that the peak axial velocity in the outer or core regions of the vortex should be used. Even so, it is debatable whether the columnar vortex can be used as a representation of the cyclone vortex.

Hultgren (1988) examined the stability of inviscid swirling gas flow to small nonaxisymmetric perturbations and presented the necessary and sufficient conditions for stability. The analysis reduced the problem to the classical Sturm-Liouville form of differential equation, and applied the oscillation theorem. The criterion again takes the form of a Richardson number, and is asymptotically valid for small Brunt-Vaisala (refer to Ince, 1956) disturbance frequencies N_{BV}.

$$J(r) = \frac{N_{BV}^2 \Phi}{4g^2 W'^2} = \frac{N_{BV}^2}{W'^2}\left(1 + \frac{rg'}{2g}\right) \geq \frac{1}{4} \qquad \text{--- (3.C.14)}$$

(where W' = axial velocity

r = radius

$g = V/r + 1$

$\Phi = r^{-3}[(r^2 g)^2]'$ which is the usual Rayleigh discriminant.

Ito, Suematsu & Hayase (1985) considered stationary and unsteady vortex breakdown with the stability of a vortex (of solid body rotation in a streamtube) to small amplitude disturbances. Both axisymmetric and asymmetric disturbances are considered and the criterion is found from the requirement for the existence of solutions to their disturbance equations. Their results were incorporated into the Rossby number criterion of Spall et al (1987) which is discussed further below.

Leibovich & Kribus (1990) studied large-amplitude axisymmetric waves on columnar vortices using the Bragg-Hawthorne equation. Solutions are found to satisfy the steady, axisymmetric Euler equations, and four different solution forms are found as a function of the swirl ratio. These are:

1. Multiple columnar solutions with sub/super-critical pairing of wave characteristics
2. Solitary waves, which extend the previously known weakly nonlinear solutions to amplitudes large enough to produce flow reversals similar to the breakdown transition
3. Periodic wavetrains
4. Solitary waves superimposed on the conjugate flow that emerge from the third type as the wavelength or amplitude becomes sufficiently large.

Weakly nonlinear soliton solutions are found to be accurate even when the perturbations they cause are fairly strong.

Maslowe & Stewartson (1982) This deals with confined flow in a pipe, and studies the inviscid asymmetric disturbances to flow with rotation. The most significant variations in the perturbations occurred near the wall of the pipe.

Leibovich & Holmes (1981) studied the global stability of the Burgers' vortex:
$\mathbf{u} = (u, v, w) = \{-\alpha r, K/r[1-\exp(-\alpha r^2/2\nu)], 2\alpha z\}$
where α, K represent the axial strain rate and circulation respectively and ν is the kinematic viscosity. No finite critical viscosity was found to exist for the problem, but the lack of global stability was emphasised to be a necessary but not sufficient condition for the flow to be unstable to all perturbations. Local instability of the flow must also exist.

Lundgren and Ashurst (1989) also support the concept that instability to helical disturbances arises when the jet-like axial velocity is high enough to overcome the stabilising effect of the swirling motion. Lundgren and Ashurst (1989) consider the effect of area variation along a vortex tube. Using one dimensional flow the motion consists of waves propagating to the right and left relative to the fluid with speed $c = \Gamma/\sqrt{8\pi A} = V_{max}/\sqrt{2}$. An analogy with waves in shallow water is drawn.

Noting that shallow water theory does give a satisfactory description of bores and hydraulic jumps (steady bores) despite the shallow-water approximations ceasing to be valid when the axial derivatives are no longer small. Thus the theory of travelling waves leading to a shock discontinuity is used as a means of predicting breakdown (as done by Hall in the failure of approximations approach).

The wave speed of weak waves propagating with or against the flow were found to be $w \pm 0.707\ V_{max}$, The results from Benjamin's (1967) perturbation theory (using a Burgers vortex swirl profile and an approximately Gaussian axial flow) give $w = 0.93\ W_m \pm 0.72\ V_{max}$. Therefore Lundgren and Ashurst suggest there is only a weak dependence on the details of the swirl and axial profiles.

> Conclusion: The drawback of the instability theory is the experimental observation (Garg & Leibovich, 1979) that oscillations in vortex breakdown flows occur only downstream of the critical point, whereas the hydrodynamic instabilities would usually be expected to occur over the whole flow. Examples that exist of instabilities existing on the

entire core are predominantly in long geometries,see for example the bathtub vortex in Van Dyke (1982) or at low flow rates on the core of the long cylindrical cyclone of Smith (1962a). The presence of both spiral (asymmetric) and bubble (axisymmetric) types of breakdown in some flows, and the ability to change between them (in either direction), as shown by Harvey (1962), is given as evidence that breakdown is not due to the build up of instabilities. There was no evidence of a disturbance that propagated upstream and caused the breakdown in the numerical study of Lopez (1990).

The instability analysis is only valid for infinitesimal disturbances, whereas the vortex breakdown is a large disturbance. The breakdown must be viewed in a manner analogous to laminar - turbulent transition, with the theory predicting the location of the transition even though the resulting transition is beyond the scope of the theory. Kribus and Leibovich (1990) found support for this approach.

It is difficult to refute or test the validity of the perturbation instability approach because the velocity gradients associated with vortex breakdown make it inevitable that there will be instability. The perturbation instability theories could find application as a test for stability to propagating waves in the critical state analyses, but the stability criterion appears to disagree with that used by Squire (1960) in the critical state analysis given below.

3.C.3b Critical State:

Squire (1960) was the first to suggest a criterion for vortex breakdown, and together with the theories of Benjamin (1962, 1967) this forms the basis of the critical state theory for vortex breakdown. This is based on the ability of standing waves to propagate upstream from a downstream disturbance. This upstream propagation is generally enhanced by increasing the swirl. To characterise the flow state a Benjamin number, N_B is used (also termed a Froude-like swirl number):

$$N_B = \frac{(C_+ + C_-)}{(C_+ - C_-)} \qquad \text{--- (3.C.15)}$$

N_B is the ratio of the absolute phase velocities of long wavelength waves which propagate in the axial direction. C_+ and C_- denote the (axial) phase velocities (measured positively in the direction of the flow) at which the long waves propagate with and against the flow respectively. Hence for supercritical flow $N > 1$ and for sub critical flows it is <1. This is complicated if the flow undergoes axial reversal , as pointed out by Leibovich (1983).

Squire (1962, 1960) (as summarised in Spall et al (1987)) considered three types of vortex flow and presented a criterion for the occurrence of vortex breakdown for each, using linear long waves. Two of the vortex flows are given below as flows A and B- these have a uniform axial velocity W and tangential velocities respectively described by:

Flow A.: $V = \frac{V_o}{r}\left(1 - e^{-r^2}\right)$ --- (3.C.16)

Flow B.: $V = V_o . r$ for $0 < r < 1$ and $\frac{V_o}{r}$ for $r > 1$

In flow A, V_o is a non-dimensional parameter, whereas in flow B it is a constant. The radius is scaled by the core radius. For flow A the maximum swirl velocity is given by $V_{max} = 0.638\ V_o$

The existence of steady perturbations or standing waves on the vortex was apparently not predicted using a wave propagation approach that was similar to Lessen et al (1974), nor Howard and Gupta (1962). Squire instead used the above functional forms of the velocity component profiles to reduce the non linear equations of motion to a linear disturbance equation. The criteria for standing waves to exist on the respective flows were then obtained by solving this equation. The resulting criterion was a swirl parameter k (the ratio of the maximum swirl speed to the axial speed). For the respective flows the critical values were:

A. $\frac{V_{max}}{W} > 1$ and in the case of B. $\frac{V_{max}}{W} > 1.2$ --- (3.C.17)

This is in direct conflict with the results of Lessen et al (1974), who predict that an increase in swirl will dampen out any disturbance on the flow. A direct comparison of the disturbance equations used by Lessen et al (1974) and Squire (1960) has not been possible because Squire's theory has only been accessible through the literature reviews such as Leibovich (1983), Hall (1972) and Spall et al (1987). Experimental observations show that vortex breakdown is promoted by increasing the swirl, in accordance with the results of Squire.

If the maximum swirl velocity exceeds the axial velocity the flow is subcritical. The form of the velocity in A. is the same as the 1 term Burgers model applied to the tangential velocity profiles in section 5.C, but the experimental axial velocity profile is clearly not a good approximation to the uniform axial velocity assumption. The criterion that results (a ratio of azimuthal to axial velocity) is a common theme in the criteria developed. In our experiments for the Stairmand H.E. cyclone typical maximum tangential velocities are up to 35m/s, and axial velocities are up to 12m/s for an inlet velocity of 23m/s.

Benjamin (1962) arrived at essentially the same criterion (V_{max} / W = constant) as Squire (1960) but from a different perspective. For the vortex flow defined by:

$V = V_o r$ for $0<r<1$ $V = V_o/r$ for $1<r<R$

The value of the constant for the critical condition was found to depend on R, but lay between 1.92 for R = 1, and 1.2 when $R = \infty$, the latter being equivalent to the combined vortex studied by Squire as flow B above. Benjamin's (1962) finite transition theory cannot provide a jump condition that would allow the subcritical downstream structure to be inferred from the supercritical approach flow. Benjamin's theory is based on an inviscid quasi-cylindrical approximation which neglects all axial gradients. Salas & Kuruvila (1989) report that no consistent correlation has been found between the occurrence of breakdown in the numerical solutions of the Navier-Stokes equations and Benjamin's criticality condition.

There is a problem, pointed out by Leibovich (1984) in that Benjamin used the phase velocity, whereas the ability of perturbations to propagate upstream is determined by the group velocity, not the phase velocity. It is not known if the group velocity of non-axisymmetric modes of

perturbations is directed downstream in supercritical flows. The few special cases which have been examined so far suggest that the criticality concept is sill valid.

Escudier & Keller (1983) detail a two-stage transition for breakdown, firstly an isentropic change from the initial supercritical state to an intermediate state which is also supercritical. The second stage of the transition, to a downstream sub-critical state is non-isentropic, much like a hydraulic jump. For a given upstream structure (they used a Rankine vortex), the breakdown was predicted to occur at a unique value of the swirl number $\Gamma/\pi r_c U$ (an inverse Rossby number). For the Rankine vortex this is given as 2.4

Escudier, Bornstein & Maxworthy (1982) support the concept of the criticality of the flow being the important feature and the waves being merely fine detail. They used their experimental velocity profiles (obtained with a LDA) to determine the radial variation of streamline helicity as measured by the angle $\phi = \arctan (V/W)$, for tangential velocity V and axial velocity W. The conditions obtained by Squire's analysis for his three flow models (the third being a Rankine vortex with uniform axial velocity) gave critical angles of 45°, 48° and 50°, whereas Barcilon (1967) found an angle of 54.7° for a Rankine vortex with uniform axial velocity only in the core. This critical condition can be converted to the velocity ratio form:

$$(V/W)_{crit} = 1.0,\ 1.11,\ 1.20,\ 1.41 \quad \text{respectively}$$

Escudier et al (1982) state that it is the values of ϕ in the core flow that are important in determining the criticality of the flow, and within the core the maximum value occurs at the core's edge. This was because of the low axial velocities that were present in the outer flow in their apparatus. In the cyclone the core's edge corresponds to the reversal of the axial velocity,. hence the axial velocity can have a value of zero. This problem will be returned to under the discussion of the Rossby number criterion of Spall et al (1987) below. For the profiles obtained by Escudier et al (1982), the flow was subcritical at every location in the apparatus for Reynolds numbers of 1970 and 4080. For lower Reynolds numbers the criticality varied, but this will have less relevance to the cyclone conditions.

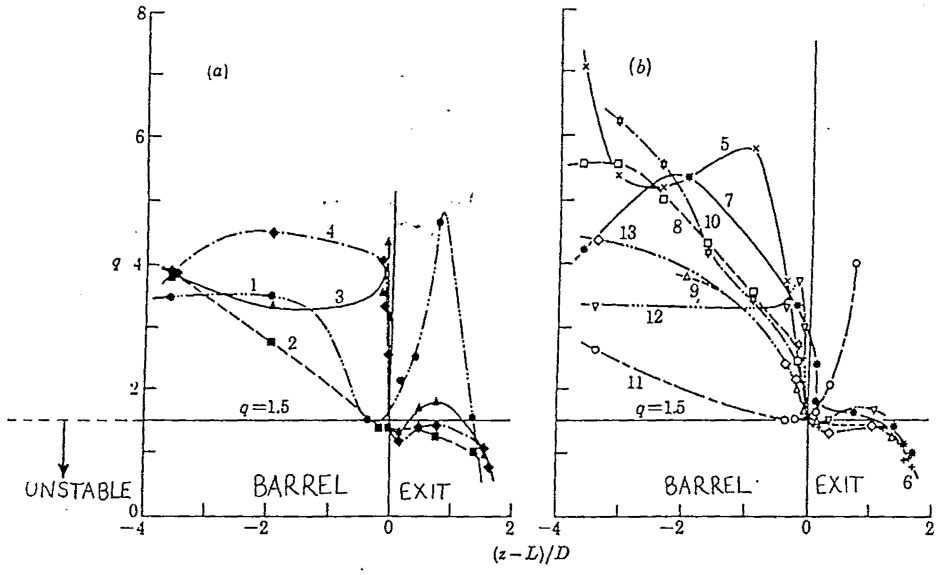

Figure 3.C.8: Stability parameter q plotted against normalised axial location, from Escudier, Bornstein & Maxworthy (1982)

Escudier et al (1982) went on to apply the stability analysis of Lessen et al (1974) to their profiles and calculated the value of q at each axial station in their flow, from experimental velocity profiles obtained with a LDA. The flow was stable for a value of $q = 1.56 \frac{V_{max}}{W_2}$ greater than 1.50, and the value of q was found to fall rapidly as the position of the experimental breakdown was approached, as shown above in figure 3.C.8.

The geometry of Escudier et al had a sharp edged contraction at the entrance to the exit tube. The flow always became unstable at the entry to this contraction, and the breakdown could occur anywhere downstream of this. The flow profiles upstream of the breakdown was also found to be unstable according to the analysis of Lessen et al (1974). The stability criterion was found not to predict the location of the breakdown, even though instability waves were observed to exist. Instead, Escudier et al (1982) suggest that it is the stability of the downstream flow field that is created by the vortex breakdown that is of prime importance.

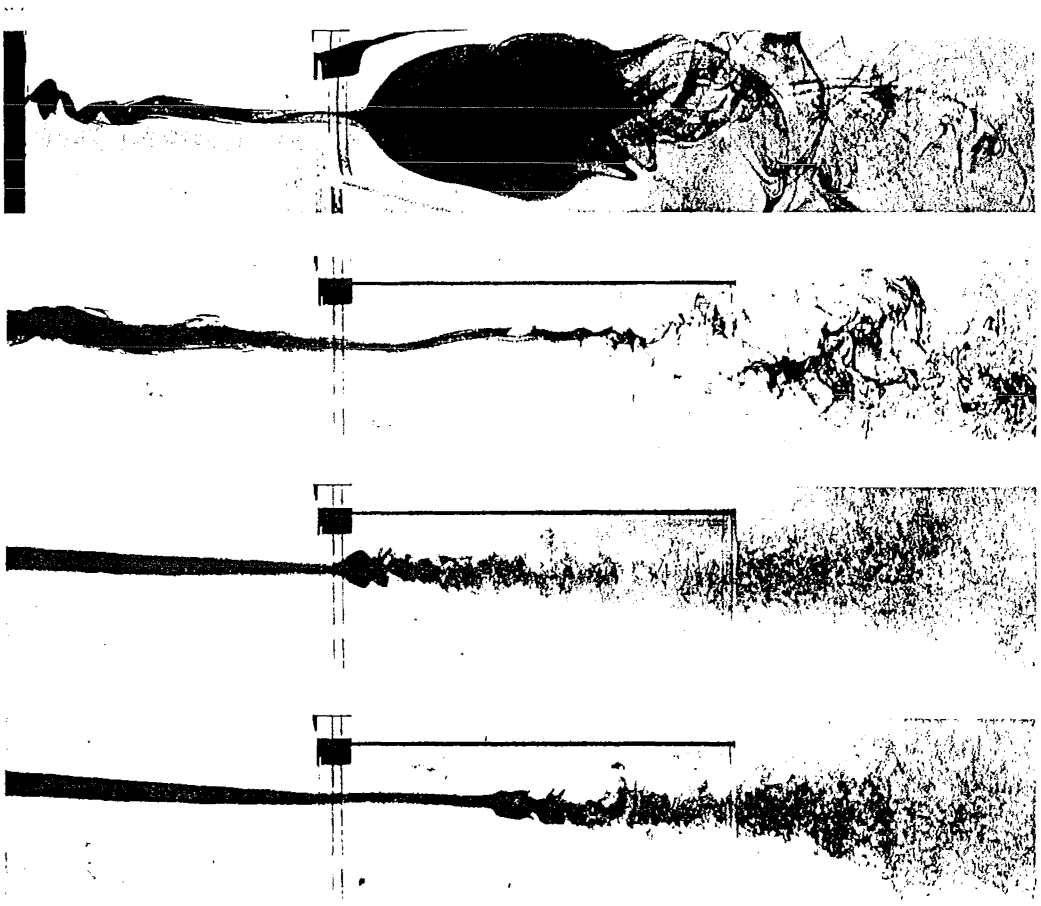

Figure 3.C.9: Photographs of vortex breakdown as a contraction is entered, from Escudier et al (1982). The flow is from left to right and the conditions were:
(A) $\Omega = 5.22$, Re = 550; (B) $\Omega = 1.46$ Re = 3300
(C) $\Omega = 1.46$ Re = 15000 (D) $\Omega = 1.46$ Re = 15000.

The occurrence of breakdown was deemed to be related to the spatial growth rate of instability waves on the vortex. A core with a jet like upstream profile may be unstable, but the waves

will propagate slowly because of the high axial velocity. After the core flow undergoes a shock-like transition and forms a lower velocity wake-type flow, the waves will be able to grow rapidly. The state of criticality determines the flow downstream, and the waves are a superimposed, but important, fine detail. The value of q just downstream of the breakdown is the important parameter. If q is just critical, the growth is slow, but if q is close to the maximum growth rate there will be rapid growth of disturbances and a large amplitude spiral breakdown will be formed. If q crosses the stability boundary for n = -2 but not n = -1 then bubbles and double spiral breakdowns will be formed.

As pointed out by Leibovich (1983) there are several flaws in this approach, including the application of the Q-vortex model (which assumes a columnar vortex) to the region of the breakdown (which is a flow region with large axial gradients). Leibovich discounts the idea that the instabilities observed were associated with vortex breakdown and suggests that they were probably due more to the design of Escudier et al's (1982) apparatus than the vortex properties.

In Escudier et al's (1982) apparatus the flow was subcritical throughout when the breakdown was located at the inlet endwall. This jump was created as the supercritical flow erupted from the endwall boundary layer. The vane-generated flows used in most other studies (Garg and Leibovich (1979), Faler and Leibovich (1977), Sarpkaya (1971), and Harvey (1962)) had a centrebody that shed the boundary layer and fed the core. The tangential entry apparatus of Escudier et al (1982) is expected to be closer to the type of vortex present in the cyclone than the vane-generated apparatus.

Escudier & Zehnder (1982) studied vortex breakdown in the apparatus depicted below in Figure 3.C.6. The tangential entry is expected to produce a vortex similar to the cyclone vortex and the exit contraction is similar to the cyclone gas exit apart from the diverging exit.

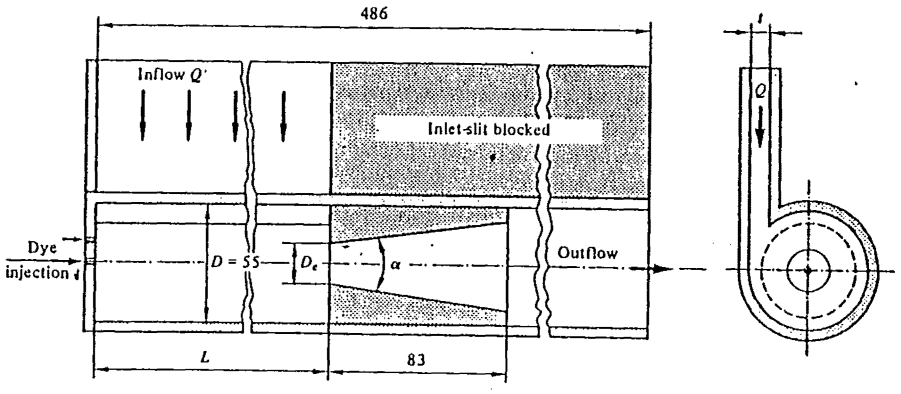

Figure 3.C.10: Experimental apparatus of Escudier and Zehnder (1982)

Escudier & Zehnder (1982) identified two dimensionless groups that were required to characterise the vortex core: $\frac{vL}{we r_c^2}$ and $\frac{\Gamma_0}{2\pi r_c we}$. --- (3.C.18)

where w_e is an average axial velocity $= \frac{4Q}{\pi D^2}$,

L is the length of the apparatus between the inlet and exit, Γ_o is the circulation at large radius, ν is the viscosity and r_c is the radius of the core.

Applying the concepts of similarity the first dimensionless group was found to provide an invariant definition of the core radius, which can then be substituted into the second, which has been shown to have a particular value that describes the onset of criticality (by the analysis of Benjamin, 1962). This leads to the criticality criterion, which correlated conditions for the occurrence of vortex breakdown in their apparatus well, and was suggested to be applicable to other experimental data. The criterion is:

$$Re_B\, \Omega^3\, R^{-1} = \text{constant, or: } Re_B \approx \Omega^{-3}\, R^{-1}$$

where Ω is the circulation number $\Omega = \frac{\Gamma}{w_e\, D_e} \approx \frac{\pi^2\, D\, D_e}{4\, L\, t}$, --- (3.C.19)

Γ	is the circulation
D, D_e	the diameters of the tube and exit
t	is the width of the inlet
L	is the length of the inlet

R is the ratio of the radial to the tangential velocities in the inflow region $R = \frac{Q}{\Gamma L}$

and Re_B is the pipe Reynolds number at which vortex breakdown occurs

$$Re_B = \frac{w_e\, D_e}{\nu} \approx \frac{4\, Q}{\pi\, D_e\, \nu} \qquad \text{--- (3.C.20)}$$

If the Reynolds number is redefined as $Re = \frac{Q}{L\nu}$ then the parameter R can be eliminated and the form becomes: $Re_B\, \Omega^2 = \text{constant}$

The later results of Escudier, Bornstein and Maxworthy (1982) suggested that the stability of the flow downstream of the breakdown also needs to be taken into account. Leibovich (1983) discounts this approach by saying that Re and Ω cannot form a universal criterion for the occurrence of breakdown at a fixed location simply because bubble and spiral types of breakdown have distinctly different locations as a function of Re and Ω. Leibovich also suggests that the breakdown is essentially governed by inviscid dynamics as the Reynolds number is above the threshold of viscous dynamics. The core diameter rather than the wall radius should be used in the Reynolds number definition, as it was shown (Faler & Leibovich (1977a), Leibovich (1978)) that the relevant dynamics in vortices scale more consistently with this dimension. In addition, when dealing with unconfined flows the core diameter is the only suitable length scale. The choice of length scale is also taken up by Spall et al (1987) in their Rossby number criterion which is discussed later.

The criterion given above from Escudier & Zehnder (1982) has been restated by Abrahamson (1985) as a gas (breakdown) bubble number BUB, given by:

$$BUB = 0.010 \frac{(R_{en}\, V_{en})^2\, D_{ex}^2}{\nu\, l\, Q} = 2.4 \times 10^{-3} \cdot \frac{D^2 V_{en}^2\, D_{ex}^2}{\nu\, l\, Q} \qquad \text{--- (3.C.21)}$$

where R_{en} = radius of the midpoint of the entrance, m
V_{en} = average inlet velocity, m/s
ν = kinematic gas viscosity

Abrahamson (1985) proposed that for values of BUB < 50 to 150 (depending on the exit Reynolds number), the vortex cannot fill the cyclone length. While the observations of Escudier & Zehnder that lead to this criterion were of bubble-type breakdowns, Abrahamson (1992) suggested the form of the termination may also resemble the vortex ending on the wall as shown by Muschelknautz (1972).

The concept of the wave trapping at the position of the breakdown was developed by **Randall & Leibovich** (1973) and Leibovich & Randall (1973). They studied the long axisymmetric waves that are valid near the critical condition. Finite amplitude wave propagation was taken to be governed by a modified Korteweg-de Vries equation (Korteweg and de Vries, 1895) with coefficients that vary slowly in the axial direction, and with a term that allows for wave amplification or damping. Deceleration of the basic flow causes energy to flow to the wave and acceleration of the basic flow has the opposite effect. A stationary wave equilibrium in which the energy gained is balanced by viscous dissipation may exist only between two well defined axial locations in decelerated portions of flow (adverse-pressure gradient). To persist the waves must remain trapped in this zone. Tsai & Widnall (1980) extended this phase-velocity wave trapping to group-velocity considerations.

The theory used to develop this analysis is valid only for weakly non-linear disturbances, but the predictions are for large disturbances. Randall & Leibovich recognised the problem and suggested that the criterion be regarded as a model, (not a theory) of vortex breakdown in a similar way to the relation of Burgers equation to weakly non-linear dissipative gas dynamics. Leibovich and Kribus (1990) found that weakly non-linear solutions were accurate even when the perturbations that they caused were fairly strong. The criterion also only deals with axisymmetric disturbances, and the upstream propagation of asymmetric waves past the critical station is not ruled out.

An approximation for the wave equilibrium position was obtained for assumptions applicable to a solitary wave. This showed that for the flow examined, breakdown could only occur for a tube diverging in the flow direction.

Tsai and Widnall (1980) examined a group velocity criterion for vortex breakdown in the slightly diverging tube that had been examined experimentally by Faler and Leibovich (1977). Upstream of breakdown the group velocity of both asymmetric and axisymmetric waves was directed downstream and hence the flow was supercritical. However, the flow downstream of the breakdown was unstable to asymmetric disturbances for a finite range of wavenumbers and hence was sub critical. The calculated frequencies of the unstable disturbances were in good agreement with the frequencies obtained from the experimental measurements.

The Q-vortex is most usually applied to the flow in swirl jets and wingtip vortices, but the similarity of the form of the model to the Burgers vortex suggests that it may also be applicable to the velocity profiles in the cyclone.

The applicability of the q-vortex stability approach is limited by the assumptions made. The simple expression of the flowfield model is not valid in regions with large axial gradients of pressure or velocity. Thus like the approach of Hall (failure of the quasi-cylindrical assumption), detailed information of the flow downstream of the initial breakdown will not be possible.

3.C.3c Failure of approximations:

Hall (1967) does not appear to have used his proposed mechanism to give an easily applied criterion for the occurrence of breakdown. However, the failure of the cylindrical approximation has been shown by Reyna & Menne (1988) to coincide with the position of the breakdown predicted by the critical state theory of Benjamin (1962) and the experimentally observed positions. A critical value of $\sqrt{2}$ is predicted for the parameter q in the Q-vortex model for the occurrence of vortex breakdown. This compares well with the values obtained from the instability theory of Lessen et al (q = 1.5) and from the critical state theory (q = 1.6).

Bossel (1968) used the results of Hall (1966) for inviscid incompressible quasi-cylindrical spiralling flow in a streamtube of radius r_c. A small retardation of the axial velocity was found to lead to further deceleration and eventual stagnation if the initial swirl parameter $v/w > \sqrt{2}$ or if the maximum swirl angle $\phi > 54.8^\circ$ anywhere within the vortex. This criterion is found to agree well with other criteria from theories and observations in experimental studies.

Mager (1972) used momentum-integral methods on the quasi-cylindrical equations in conjunction with further simplifying assumptions of uniform axial velocity and negligible pressure gradients in the outer flow. When the momentum-integral equations are integrated, algebraic equations result that depend on the axial distance only parametrically. If a dimensionless constant θ is smaller than a critical value, the vortex decays continuously with axial distance. If θ is larger than this , a singularity occurs at a well-defined point and the solution cannot be further continued. The singularity corresponds to the failure of the quasi-cylindrical approximations. Viscosity is known to be unnecessary for the existence of the singularity, and the condition for its occurrence coincides with the critical condition of Benjamin (1962).

Sarpkaya (1974) used Mager's (1972) equations to estimate the location of the breakdown, taking into account the deceleration of the outer flow. A singularity was found, and the position of this was forced to agree with the location of the breakdown by selecting suitable initial profile parameters (which were not determined experimentally). These parameters were found to give good 'prediction' of the location of the breakdown for flows with other Re and Ω values, but this is obviously well short of being a full predictive criterion.

Krause (1983) presents an analysis to allow the axial pressure gradient to be estimated. The momentum equations for the radial velocity component are integrated with respect to radius and differentiated with respect to the axial distance. An order of magnitude analysis results in an expression for the axial static pressure, this could be used to indicate where the axial gradient of pressure becomes appreciable, and hence indicate the location of the breakdown. The form of this was not easy to apply to the results in the cyclone

3.C.3d Streamline divergence:

Bossel (1969)'s analysis of the computations of viscous model vortex flow approximations found that significant retardation of the velocity near the axis first appeared near swirl angles of $\phi = 52.3^{\circ}$, while stagnation and reversed flow occurred for $\phi = 55.5^{\circ}$.

Leibovich (1978) criticises the approach of Bossel (1969), and the general approach of developing theories of the breakdown mechanism from the examination of axisymmetric closed flows. Leibovich reports that it is easy to generate steady solutions of the equations of motion with regions of closed streamlines resembling vortex breakdown, and qualitatively correct results for flow outside the bubble are easy. However, the inviscid axisymmetric equation results in the azimuthal velocity in the interior of the recirculation bubble being predicted to be in the reverse direction to that of the outer flow. In addition, the axisymmetric solutions cannot explain the occurrence of the spiral form of vortex breakdown, nor the transitions between the bubble and the spiral forms.

Brown & Lopez (1990):

A recent analysis of vortex breakdown presented by Lopez (1990) and Brown and Lopez (1990) appears to be applicable to the case of the cyclone vortex. A simple criterion for the existence of the breakdown was proposed by Brown and Lopez, and this will be examined in more detail here.

Brown and Lopez (1990)'s criterion for the occurrence of vortex breakdown was developed from the observation that the onset of the vortex breakdown is associated with the deceleration and stagnation of the axial flow. This is associated with a divergence of the streamlines, and requires the azimuthal component of vorticity to become negative. Starting with the equations for steady, inviscid axisymmetric swirling flow, Brown and Lopez (1990) showed that the radial acceleration balance:

$$u\frac{\partial u}{\partial r} + w\frac{\partial u}{\partial z} = \frac{v^2}{r} - \frac{1}{\rho}\cdot\frac{\partial p}{\partial r} \qquad \text{--- (3.C.22)}$$

could be re-expressed in terms of the angular momentum (or circulation $\Gamma = r.v$) and the total head. This in turn could be reformulated as a relationship between the azimuthal vorticity and the circulation, the head and the stream function ψ.

The axial vorticity, ζ is associated with the tangential (azimuthal) velocity since

$$\zeta = \frac{1}{r}\frac{\partial(r.v)}{\partial r} - \frac{1}{r}\cdot\frac{\partial u}{\partial \theta} \qquad \text{--- (3.C.23)}$$

where r and u are the radial distance and velocity component, and θ and v are the azimuthal position and velocity component. If it is assumed that the radial velocity does not vary significantly with the azimuthal position (which follows from the assumption of axisymmetric flow), the axial vorticity is :

$$\zeta = \frac{\partial v}{\partial r} + \frac{v}{r} \qquad \text{--- (3.C.24)}$$

The azimuthal component of vorticity is $\eta = \frac{\partial u}{\partial z} - \frac{\partial w}{\partial r}$ --- (3.C.25)

where r and u are the radial distance and velocity component, and z and w are the axial distance and velocity component.

To bring the axial velocity to zero requires the development of a negative azimuthal component of vorticity. The radial velocity is often assumed constant with axial distance, hence the azimuthal component of vorticity is associated with the axial velocity. An order of magnitude analysis shows that the contribution of $\partial u/\partial z$ can be neglected. The axial velocity ranges from 10m/s to 0 over 25mm in the 140mmØ cyclone. Even if the radial velocity switched from 2m/s inflow to outflow over a length of 60mm, its contribution to η would only be 14%. In the absence of measurements of the actual radial velocity fluctuations with length the actual contribution is expected to be no more than 14%.

By considering a particular stream surface ψ_1 at some upstream location z_0 at which the initial axial and azimuthal vorticity and velocity components are known, the development of a divergence of the stream surface downstream was shown to depend on the ratio of the helical angles of the velocity and vorticity. Brown and Lopez took this to be a necessary condition for vortex breakdown to occur that is that at some upstream location the helix angle of velocity had to be greater than the helix angle of vorticity on some stream surface.

A suitable value of the helix angle allows the development of a negative value for the azimuthal vorticity, which induces a negative axial velocity on the axis. The breakdown grows quickly from this because of a positive feedback mechanism, with the negative axial velocity leading to further divergence of the streamlines, and further generation of negative vorticity. For the divergence to continue to grow also requires the centrifugal force to exceed the radial pressure gradient. Once formed, the region of negative azimuthal vorticity was observed to propagate upstream due to its own induced velocity.

To illustrate the generality of the proposed criterion, Lopez applied it to the case of swirling flow in pipes. Lopez has obtained time-dependent numerical solutions of the Navier-Stokes equations for swirling flows in pipes (unpublished). The criterion

$$\alpha_0/\beta_0 > 1 \qquad \text{--- (3.C.26)}$$

was shown to successfully predict the occurrence of vortex breakdown, where α_0,β_0 are the helix angles for velocity and vorticity respectively, calculated at some upstream location. The initial velocity profiles used were exponential profiles similar to those that are fitted to the cyclone velocity profiles in Chapter 6.B. The form of the profiles used by Brown and Lopez (1990) results in the criterion being expressed as:

$$\frac{\alpha_o}{\beta_o} = \left(\frac{e}{e-1}\right)^2 \frac{V_e^2 r_c^2 (1 - e^{-r^2/r_c^2})}{W_e r^2 (1 + W_e e^{-r^2/r_c^2})} \qquad \text{--- (3.C.27)}$$

where $V_e = v_e/W_\infty$ is the dimensionless azimuthal velocity, and W_e is the dimensionless axial velocity excess at an initial radius r = a.

This simplifies to the following when $r = r_c$:

$$\frac{\alpha_o}{\beta_o} = \frac{W_e e^2}{(e-1)(W_e+e)} \frac{V_e^2}{W_e^2} \qquad \text{--- (3.C.28)}$$

The dependence of the stability on the parameters Ve and We is given in this figure from Brown and Lopez (1990). Circles indicate the locations in (Ve,We) space where the numerical solutions showed breakdown to occur, and stars indicate where breakdown was not found.

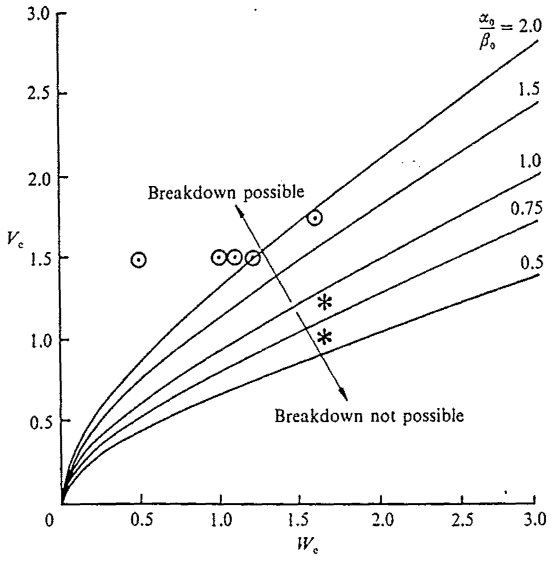

Figure 3.C.11: The dependence of the helix angle ratio on the characteristic velocity parameters, (from Brown & Lopez (1990)

In the case of the swirling pipe flow, the flow was found to initially be in cyclostropic balance, with $\rho v^2/r = \partial p/\partial r$. The breakdown mechanism proposed requires viscosity to initiate the reduction of the azimuthal component of vorticity with distance downstream and the initial divergence of the streamlines. However, the further development of the breakdown is essentially inviscid.The diffusion of axial vorticity leads to $\rho v^2/r - \partial p/\partial r$ becoming positive. The radial balance of forces is also important to allow the growth of the breakdown. The balance between the radial pressure gradient and the centrifugal 'force' has been examined in the 140mmØ cyclone in section 5.G.

To apply this criterion, the velocity profiles given by the exponential equations need to be fitted to the cyclone velocity profiles. This will be examined in Chapter 6.B, and the results discussed in Chapter 7.

3.C.3d Numerical studies:

Lavan, Nielsen & Fejer (1969) studied a low Reynolds number flow in a rotating cylinder, (that is, in rigid rotation), that entered a pipe of the same diameter. This has a resemblance to the arrangement in the cyclone gas exit. A reverse flow was observed to be initiated at the axis when the pipe was stationary, but for a rotating pipe the reversal occurred at the wall. The geometry and Reynolds number range that they studied was very different from those used in vortex breakdown experiments according to Leibovich (1984), and they do not examine the structure of the recirculation zone.

Kopecky and Torrance (1973) examined the flow in a cylindrical tube with initial velocity distribution given by the Burgers vortex swirl, and uniform axial velocity. All flows showing breakdown were initially sub-critical, by the criterion of Benjamin (1962).

Grabowski & Berger (1976) made a numerical investigation of vortex breakdown using solutions of the full, steady axisymmetric Navier-Stokes equations. The geometry was a vortex core embedded in an unconfined irrotational viscous vortex for Reynolds numbers up to 200. The upstream velocity profiles used were chosen to approximate the experimentally-measured velocity in vortex cores such as in trailing vortices, and were given by a family of polynomial profiles. Flow reversals were found to evolve from both sub and supercritical initial flows. Grabowski and Berger clearly established the existence of solutions with bubble like breakdown under the axisymmetric assumption, but difficulties were encountered in realising fully converged solutions.

Nakamura & Uchida (1981) used an 8 parameter axial velocity model as a solution that approximately satisfies the Navier-Stokes equation. This model profile is of an arbitrary form: $w = 1 + az + bz^2 + (c + dz + ez^2 + fz^3)(g + hr)r^2$ and from this the radial velocity component can be calculated directly from the continuity equation, yielding:
$u = -r(a + 2bz)/2 - (d + 2ez + 3fz^2)(g/4 + hr/5)r^3$.

The analysis results in a critical angular velocity ω_c of nearly 1.0

Stefferns (1988) found that the assumed vorticity profile was important in numerical predictions, as the vorticity profile needs to be sharply peaked at finite radius for breakdown. This may explain the influence of the bin on the flow, as a source of low vorticity air.

Salas and Kuruvila (1989) used the stream function-vorticity formulation of the incompressible, axisymmetric, steady Navier-Stokes equations and discretised, linearised and solved this for core Reynolds numbers from 100 to 1800, and swirl parameters from 0.9 to 1.1. The effect of the inflow boundary conditions, the location of the farfield and outflow boundaries were examined. The stability was examined by solving the time dependent equations for two conditions.

The vortex was confined in a cylindrical tube, with walls far enough away to give inviscid irrotational axisymmetric flow. The solutions featured multiple recirculation zones along the axis, as observed by Harvey (1962). As the Reynolds number is increased the vorticity intensifies at the spot where breakdown is to occur.

Lopez (1990) describes the time-dependent numerical solutions of the Navier-Stokes equations for vortex breakdown flow in a closed cylinder as well as various swirling flows in a

pipe. The results were found to agree well with the experimental observations and led to the development of a criterion to predict the occurrence of vortex breakdown.

Spall et al (1990, 1991) have made numerical simulations of vortex breakdown flows that revealed details of the internal structure of the bubble-type breakdown. This was made possible by controlling the boundary conditions of the flow to ensure that the breakdown did not occur in the inlet, and did not move upstream to the inlet, which had been the difficulties encountered by previous studies. The Reynolds numbers of the flows studied were low, but later studies are reported to be in progress that extend the approach to higher values, and also study the spiral-type breakdown.

The numerical experiments demonstrate that the Navier-Stokes equations do have axially symmetric solutions with embedded regions of closed stream surfaces. Leibovich (1984) disputes that these necessarily coincide with the vortex breakdown phenomenon. Leibovich (1984) suggests that the axisymmetric solutions of Navier-Stokes equations are unstable solutions and may be realised only for flows at Low Reynolds numbers in wall dominated flows. The sequence of transitions observed in experiments as the swirl is increased suggests that both the swirl and bubble forms of breakdown evolve from flows that are clearly not axially symmetric.

3.C.6e Empirical relationships:

Chigier & Chervinsky (1967) found that reverse flow in swirling jets occurred above a swirl number of 0.6. Their definition of the swirl number was $Sw = \frac{G_\phi}{G_x R}$ where

G_ϕ, G_x = the axial flux of angular and linear momentum respectively

Kuroda and Ogawa (1987) confirmed the above, and extended this to the case of a third reversal near the axis, which appeared for:

$$Re \,.\, Re_\theta^{0.4} = 7.5 \times 10^5 \qquad \text{--- (3.C.29)}$$

Re_θ = Swirl Reynolds number $= \frac{R_1^2 \, w_{i1}}{\nu}$; Re = Reynolds number $= \frac{D_1 U_a}{\nu} = \frac{2Q}{\pi \nu R_1}$

w_{i1} = characteristic angular velocity at the jet exit

The Swirl Number $= \frac{Re_\theta}{Re}$

For the 140mmØ cyclone the value of Re_θ was: $\frac{0.07^2.1000}{1.568 \times 10^{-3}} = 312\,500$

and the value of Re was $\frac{2 \times 0.043}{\pi \times \nu \times 0.07} = 25010$. This gives a value of $Re \,.\, Re_\theta^{0.4}$ of 39

$\times 10^5$ which is well in excess of the value required to give the third reversal. The visualisation of the flow, and the associated flow regimes are shown below in figure 3.C.12

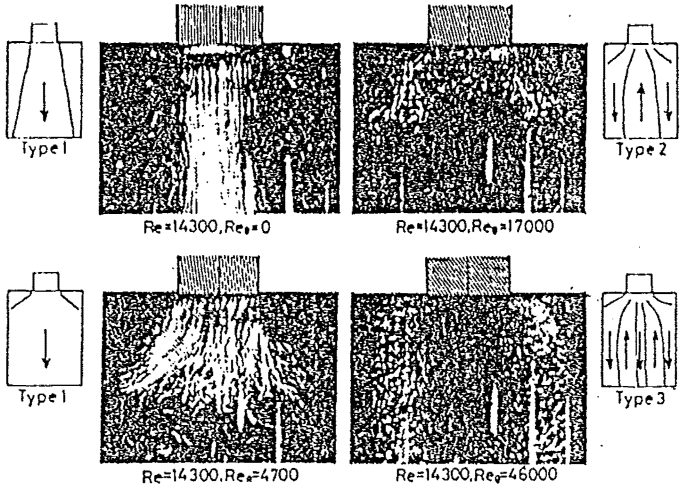

Figure 3.C.12: Visualisation of flow reversals with increasing swirl Reynolds number from Kuroda & Ogawa (1987)

Spall, Gatski & Grosch (1987) used a partly empirical approach to resolve the conflict between the various criteria given above. This was based on the simple relationship found by Ito, Suematsu & Hayase (1985) that resulted when the breakdown criterion was reduced to the dimensionless Rossby number. Spall et al (1987) examined previous studies of vortex breakdown criterion including those of Squire (1960), Benjamin (1962), Tsai & Widnall (1980) and Ito, Suematsu & Hayase (1985) and found that the nondimensionalisation of the criteria lead to the relevant parameter being the Rossby number, which is similar to an inverse swirl number, being the ratio of the axial flow to the swirl flow.

The Rossby number as defined by Spall et al (1987) used velocities defined at a specific location - the radius of the maximum tangential velocity, r^*. The axial velocity at this radius was taken as the characteristic axial velocity, W. The maximum tangential velocity was not taken as the characteristic tangential velocity, but instead the extrapolation of the core rotation rate, Ω, to the radius of the maximum tangential velocity, r^*, was used.

Hence the Rossby number is given by:

$$Ro = \frac{W}{r^*\Omega} \qquad \text{--- (3.C.30)}$$

This definition of the Rossby number was found to resolve the results of the various studies well and applied to a variety of computational and experimental as well as confined and unconfined flows. For Re>100 they found breakdown occurred for Ro < 0.65, for both unconfined and confined swirl. These definitions are shown in Figure 3.C.13 below and figure 3.C.14 shows the Rossby number-Reynolds number characterisation plots.

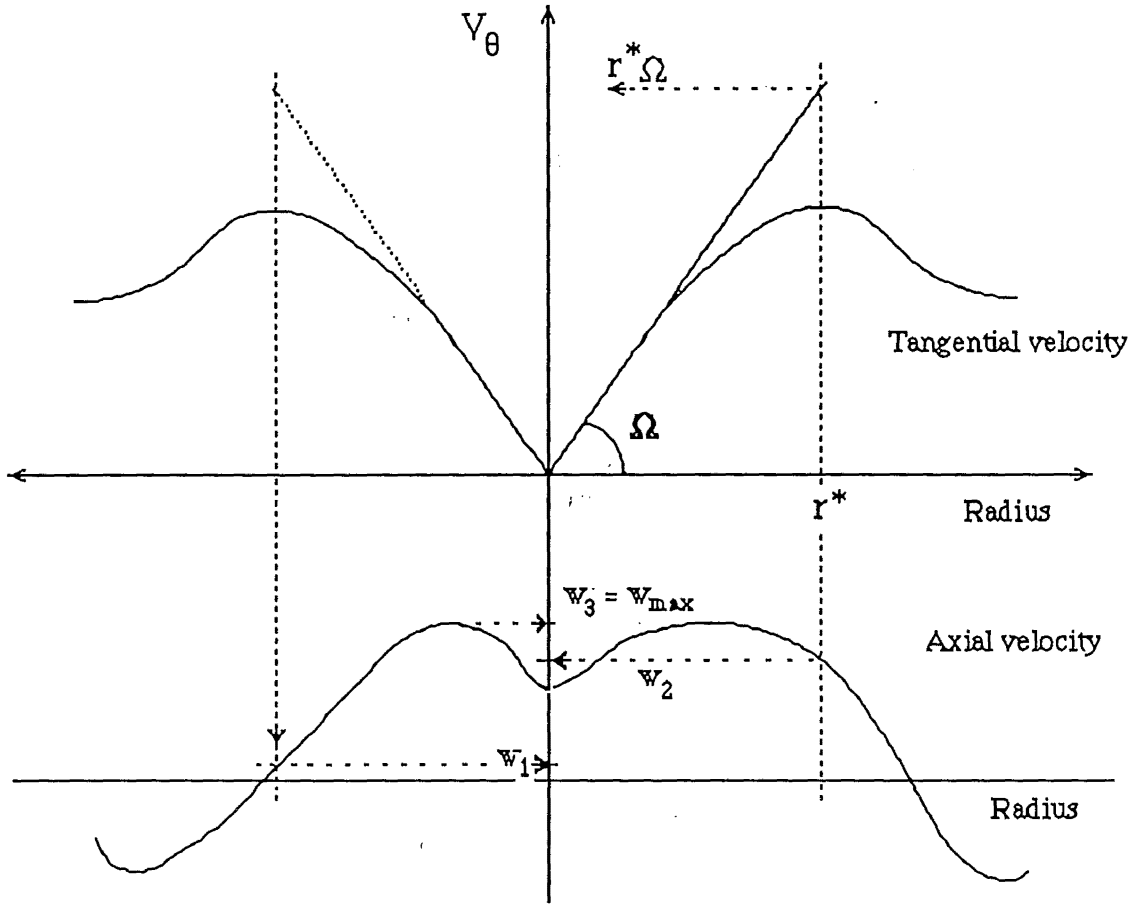

Figure 3.C.13: Characteristic velocity definitions for the Rossby number.

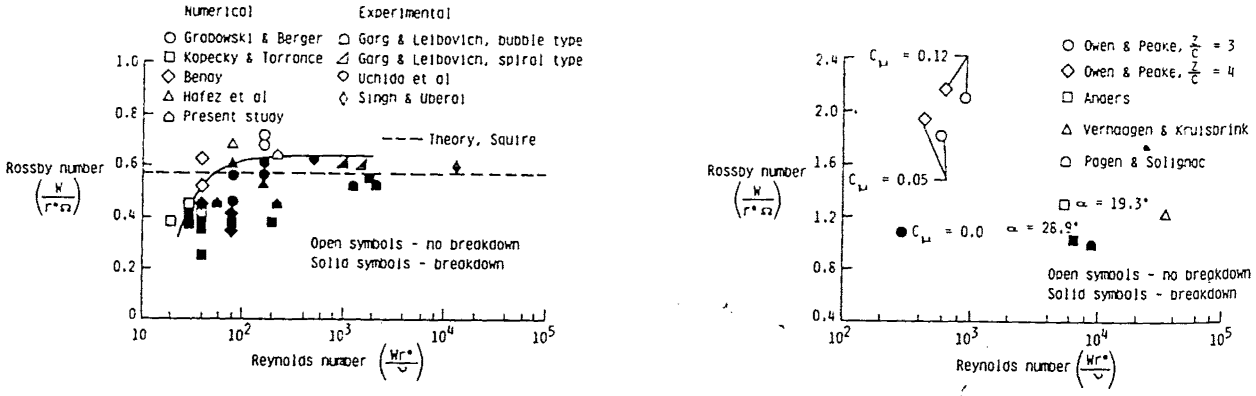

Figure 3.C.14: Rossby-number dependence of vortex breakdown in (A) Wing-tip and (B) Leading edge vortices, from Spall et al (1987)

There is a problem in the numerical modelling of vortex breakdown flows in that the breakdown is found to move upstream (under its own induced velocity) until it collides with the inflow boundary, resulting in breakdown being predicted at the inlet of the model. This problem was avoided by Spall, Gatski & Ash (1990) by applying the Rossby number criterion to the numerical modelling of vortex flow. The inflow profile was made to correspond to a

Rossby number greater than the critical value, hence preventing wavelike solutions near the inlet. The local Rossby number was then modified as the flow evolved in the streamwise direction. This can be achieved either by a mechanism inherent in the dynamics of the flow, or an externally imposed one. Spall et al (1990) introduced a Burgers vortex along the central axis of the computational domain, allowed the strength of the vortex to vary, and forced a linear deceleration of the free stream axial velocity. This was possible as the flowfield studied was that of an essentially unconfined vortex with no walls specified in the computational domain. In a confined vortex such as the cyclone such a deceleration of the freestream axial velocity would not be possible.

Spall et al (1990) found that the breakdown occurred at the location where the Rossby number reached the critical condition. The internal structure of the breakdown bubble was able to be revealed, and the instantaneous particle paths that were obtained bear a striking resemblance to the paths of the helium bubble tracers near the axis observed in this study, that are shown in Figure 5.A 2 on page 27.

Despite the claims of Spall et al (1987) that the Rossby number criterion is the most consistent and easily applied predictor of vortex breakdown there is still a problem in the definition of the characteristic variables. The criterion appears to be intended for unconfined, trailing vortices as it does not allow for large scale reversal of the vortex core, which is presumably the 'post-breakdown' condition. In the cyclone the radius of the maximum tangential velocity is close to the zero axial velocity boundary and this results in a wide variation in the magnitude of the characteristic axial velocity, and hence the Rossby number. This is shown by the profiles in the left hand side of figure 3.C.13, while the right hand side shows 'well-behaved' profiles. The axial velocity that would be obtained from a profile resembling the left hand side would not be a 'characteristic' value. Other definitions of a characteristic axial velocity may be more suitable.

3.C.3f Summary of vortex breakdown criteria:

The vortex breakdown criteria are mainly being developed for leading edge or wingtip vortices - which are unconfined flows, and usually do not feature large scale reversal of the flow. This complicates the application of the vortex breakdown criteria to the cyclone vortex. The wing-tip trailing vortex has a circumferential velocity distribution far downstream that can be approximated by the Burgers vortex. Outside the core the flow is nearly irrotational, whereas the core is nearly solid-body rotation. This is expected to be a have a similar tangential velocity profile to the cyclone vortex, but the axial profiles differ. The leading edge vortex is approximated by Spall et al (1987) by the concept of a viscous subcore near the axis surrounded by an inviscid rotational conical flow, therefore radial gradients in the core are much higher for the leading edge vortex than for the wingtip vortices, and the critical Rossby number is higher.

The velocity profiles that were obtained in this study for the Stairmand High efficiency design cyclones will be used to evaluate the stability criteria in Chapter 6.C.

3.D. BOUNDARY LAYER DYNAMICS

The boundary layers on the walls are important facets of the study of the cyclone flowfield and collection efficiency. The boundary layer is the thin layer of fluid across which the velocity increases from zero at the wall (due to the non-slip condition), to the freestream velocity. The size and volume flowrate of the boundary layers in the cyclone means that they are too large to be neglected from the description of the flowfield, but their inclusion significantly complicates the analysis. The study of the cyclone boundary layers is further complicated by the surface curvature, high turbulence and lack of knowledge of the external flow.

The importance of the boundary layers to the collection efficiency is exemplified by the cone boundary layer, which transports the dust to the bin; and the roof boundary layer which supplies the short-circuit flow that escapes from the cyclone via the outside edge of the gas exit. The high velocity gradients across the boundary layer means that the influence of viscosity is important, and the high shear is responsible for the production of vorticity. The convection and stretching of the vorticity produced in the boundary layer determines the structure of the vortex core to a large extent. It is obvious that an understanding of these flows will be an important part of a model of the collection process in the cyclone.

Boundary layers have attracted considerable attention because of their importance in heat transfer, to flow modelling boundary conditions, and to the generation of turbulence. As with the study of vortex breakdown there is a considerable volume of literature from the aerospace and tornado research fields, and from the study of the transition of boundary layers from laminar to turbulent conditions. The implications of the latter to a wide range of engineering applications has resulted in boundary layer transition becoming a field of study in its own right. Once again, there is no general agreement on the mechanisms involved in the dynamic behaviour of the boundary layer, and even the basic terms sometimes lack consistent definitions. Hence this section will not attempt a comprehensive review of the theory, but will seek to highlight some of the concepts that appear useful in the study of cyclone boundary layers.

As mentioned earlier, the boundary layer provides the match between the external freestream velocity, and the condition of zero slip at the wall, resulting in appreciable velocity gradients in the direction normal to the wall. Viscous effects are thus important in the boundary layer, even if they can be neglected in the external flow. This approach of dividing the flow into an inviscid region and a thin boundary layer was first used by Prandtl (1952) and this has allowed great advances in the calculation of flows.

3.D.1 Boundary Layer characterisation

For a simple, steady two-dimensional boundary layer formed on a thin flat plate the boundary layer thickness δ (defined in any convenient way) increases in the direction of the flow. At any position x downstream from the edge of the plate the local boundary layer thickness is proportional to $\sqrt{\nu x/U}$. It is assumed that the boundary layer thickness sufficiently small to have a negligible effect on the free stream velocity, and the streamwise gradients are taken to be

much less than the gradients normal to the surface. The equation of motion in the streamwise, x direction is:

$$\frac{\partial u}{\partial t} + u\frac{\partial u}{\partial x} + v\frac{\partial u}{\partial y} = -\frac{1}{\rho}\frac{\partial p}{\partial x} + \nu\frac{\partial^2 u}{\partial y^2} \qquad \text{--- (3.D.1)}$$

and the mass conservation equation:

$$\frac{\partial u}{\partial x} + \frac{\partial v}{\partial y} = 0 \qquad \text{--- (3.D.2)}$$

The term $\nu\frac{\partial^2 u}{\partial y^2}$ represents the viscous diffusion across the boundary layer, which is comparable in magnitude with the inertial terms. The pressure can be assumed to be uniform just outside the boundary layer, and approximately uniform throughout the boundary layer. This allows the steady flow equation to be written as:

$$u\frac{\partial u}{\partial x} + v\frac{\partial u}{\partial y} = -\frac{1}{\rho}\frac{\partial p}{\partial x} + \nu\frac{\partial^2 u}{\partial y^2} \qquad \text{--- (3.D.3)}$$

$$\frac{\partial u}{\partial x} + \frac{\partial v}{\partial y} = 0 \qquad \text{--- (3.D.4)}$$

The mass conservation equation is satisfied by using a streamfunction ψ such that $u = \frac{\partial \psi}{\partial y}$ and $v = -\frac{\partial \psi}{\partial x}$, leaving just one dependent variable ψ. The approximate equation of motion is made dimensionless by noting that the velocity distribution at a position x in the plate is independent of the total length of the plate. This leads to a stream function of the form:

$$\psi(x,y) = \sqrt{\nu U x}\, f(\eta) \qquad \text{--- (3.D.5)}$$

where $$\eta = \sqrt{\frac{U}{\nu x}}\,.\,y \qquad \text{--- (3.D.6)}$$

$$u = U f'(\eta) \qquad \text{--- (3.D.7)}$$

$$v = \tfrac{1}{2}\sqrt{\frac{U}{\nu x}}\,.\,(\eta.f' - f) \qquad \text{--- (3.D.8)}$$

f is a dimensionless function, and a prime denotes differentiation with respect to η. The velocity profiles at different streamwise locations are expected to have the same shape. Numerical integration of the equation of motion yields a solution that is able to satisfy the required boundary conditions. This profile is the Blasius boundary layer, which is shown below in figure 3.D.1.

The freestream and the boundary layer are not separated by a sharply defined layer, but rather the velocity in the boundary layer tends asymptotically to the freestream velocity. Hence the boundary layer thickness cannot be simply defined. One measure of the thickness is to specify the position at which the velocity reaches 99% of the freestream velocity.

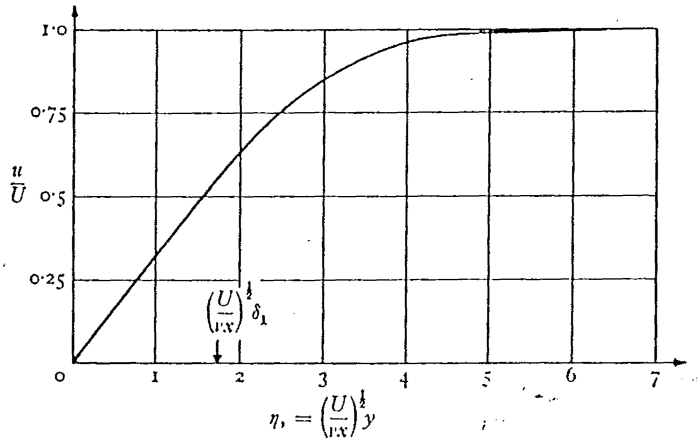

Figure 3.D.1: Blasius boundary layer profile (from Batchelor, 1967)

Other measures of the boundary layer thickness are sometimes more appropriate, such as the displacement thickness δ_d, or the momentum thickness, δ_m:

$$\delta_d = \int_0^\infty (1-v/v_\infty)dy \qquad \text{--- (3.D.9)}$$

$$\delta_m = \int_0^\infty v/v_\infty(1-v/v_\infty)dy \qquad \text{--- (3.D.10)}$$

If the displacement thickness is written as: "$v_\infty\delta_d = \int_0^\infty (v_\infty - v)dy$ ", a physical interpretation for the meaning of δ_d is obvious. If the boundary layer had a velocity equal to the freestream velocity throughout the boundary layer, the same total flux would be achieved in a distance δ_d less than that actually required. δ_d is the distance that the flow has been displaced from the wall compared with the profile without a boundary layer, as depicted below:.

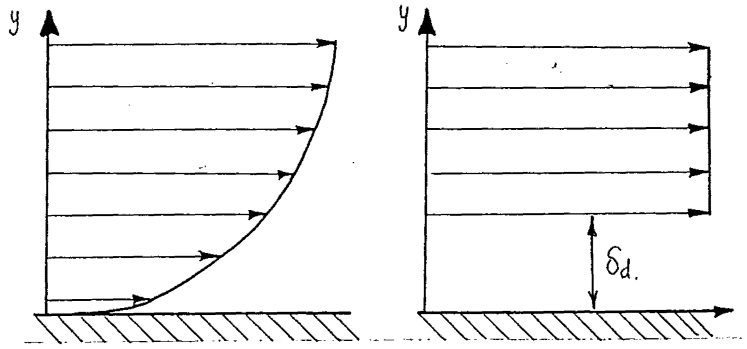

Figure 3.D.2: Displacement thickness of a boundary layer

For the Blasius boundary layer the displacement thickness is given by:

$$\delta_d = 1.72\sqrt{\frac{U}{vx}} \qquad \text{--- (3.D.11)}$$

The characteristic length scale used to non-dimensionalise dimensions in the boundary layer is the 'wall unit' defined by:

$$y* = \frac{\nu}{u*} \; ; \; u* = \text{friction velocity } \sqrt{\frac{\tau_w}{\rho}} \qquad \text{--- (3.D.12)}$$

The study of boundary layer flows has divided the flow into regions depending on the nature of the velocity profiles. (Once again, the boundaries between these regions are not sharp). The laminar sublayer is nearest the wall, and features velocity profiles that are approximately linear with distance from the wall. It extends up to 5 wall units from the wall ($y^+ < 5$). Outside of this is the buffer region $5<y^+<30$. This is bounded by the logarithmic region where the velocity can be described by $u^+ = A.\ln y^+ + B$. Further out is the law of the wake region. The wall region is the region where viscous stresses contribute more than 1% of the total stress.

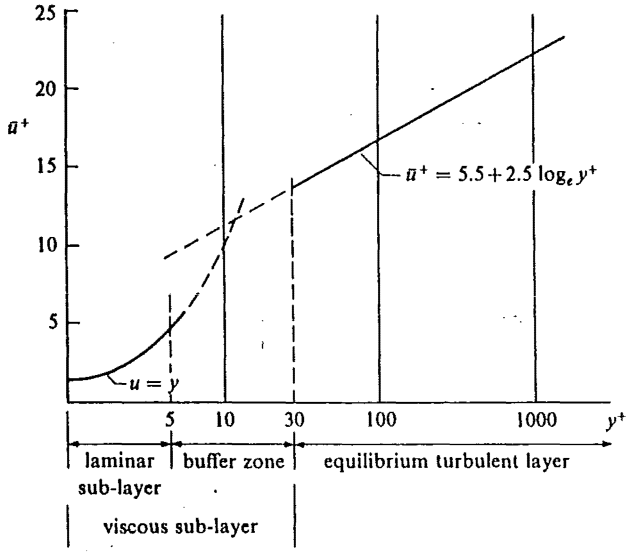

Figure 3.D.3: Variation of dimensionless velocity with dimensionless distance in a turbulent boundary layer, from Kay & Nedderman (1985).

The Blasius solution is for a steady or laminar flow. In fact the boundary layer flow becomes unstable when the local Reynolds number $\frac{\delta_d U}{\nu}$ exceeds approximately 600. Above this value disturbances grow in the boundary layer, and a transition to turbulent conditions occurs. The turbulent boundary layer is characterised by permanent and random unsteadiness although the mean velocity distribution exhibits the same general boundary layer character. The turbulent fluctuations are continually being generated, and dissipated by viscosity. The source of energy for the boundary layer and this turbulence comes from the mean flow of the freestream.

Herbert (1988) summarises the research into the transition of boundary layers to turbulence, from which it appears that the laminar boundary layer may contain two dimensional waves and still be stable. The waves represent a necessary but not sufficient condition for the breakdown of the laminar flow. The frictional force at the wall is considerably larger for turbulent flow compared with laminar flow as the random cross currents are more effective in promoting lateral transport than molecular diffusion. Leoutsakos (1987) made an experimental

investigation of the boundary layer transition on concave surfaces, and provides details of the position of the transition onset. It was found that the transition onset Reynolds number was of similar magnitude to values for flat surfaces, but the transition progressed faster than on flat surfaces.

3.D.2 Boundary layer stability

The boundary layer over a concave surface is prone to centrifugal instability, one example of which is the formation of Görtler vortices, which will be considered in further detail in section 3.D.5. The instability of rotating flows was studied by Rayleigh (1880, 1917), who developed a criterion for the stability of an inviscid fluid subject to axisymmetric disturbances, as outlined in section 3.C.3a on page 71. Rayleigh stated that a sufficient condition for stability requires that the square of the circulation increase with increasing radius to counteract the imbalance between the centrifugal forces and the radial pressure gradient. This indicates an inherent instability in the cyclone boundary layer, further consideration of which will be given in section 6.C.5.

3.D.3 Cyclone boundary layers

It is expected that the boundary layer in the cyclone will be strongly turbulent. Coles (1965) found that the lower limit for the existence of a fully developed turbulent boundary layer is $Re_\theta = 5000$, where Re_θ is the Reynolds number based on the momentum thickness and the freestream velocity.

Since the boundary layer is in effect a region of the freestream that has simply been slowed by the wall friction it could be expected that it will have a velocity vector parallel to that of the freestream. In fact, the importance of the boundary layer in the cyclone partly comes from the modification of the flow direction by the pressure gradient.

The rotating flow in the cyclone is thought to be in cyclostropic balance with the pressure field, with the outwards directed centrifugal force balanced by a radial pressure gradient. In the boundary layer on the cyclone roof the velocity is reduced, while the pressure is largely unaffected and the force imbalance that results tends to drive the boundary layer inwards to the gas exit. By flowing down the outside of the gas exit this flow can escape from the cyclone without experiencing the separating power of the cyclone. Estimates of this flow suggest that as much as 15% of the inlet flow may leave the cyclone by this path (Kelsall, 1952), with a commensurate loss of dust.

In the cone there is a component of the centrifugal force directed towards the cone-barrel junction, and the pressure gradient has a component directed towards the dust exit. Again, when the velocity is slowed by the boundary layer there is a net force towards the bin since the pressure is largely unaffected by the boundary layer. The wall pressure generally decreases towards the bin.

The theoretical analysis of boundary layer flow is still grappling with the case of infinte flat plates, but extensions to curved surfaces have been made. A selection of analyses of the boundary layer flow in cyclones will be mentioned in the following pages.

3.D.3a: The cone boundary layer flow:

One of the first studies of conical wall boundary layers was by Taylor (1950), who examined the conical swirl atomiser and considered the secondary motion through a laminar boundary layer produced by a free vortex. The Pohlhausen method was used to solve the momentum-integral equations, and this approach has been used by many subsequent authors.

Early studies assumed that the boundary layer was laminar in nature, even when the freestream was turbulent. Burggraf (1971) cites the experimental work of Kelsall (1962) who showed that the boundary layers associated with potential vortices are usually turbulent. The first analysis of boundary layer flow on the conical walls of a cyclone was by Weber (1956), who followed Taylor's approach, but considered both laminar and turbulent boundary layers. Weber assumed that the free stream flow was an ideal vortex with the tangential velocity inversely proportional to the radius, and he used a $^1/_7$th power law velocity distribution in the boundary layer. In addition the wall shear stress expression used was based on experimental data for pipe flow.

Weber's analysis gives:

$$\frac{W}{V_\theta} = 0.66\left(\left(\frac{y}{\delta}\right)^{1/7} - \left(\frac{y}{\delta}\right)\right) \qquad \text{--- (3.D.13)}$$

where W is the secondary flow velocity directed towards the cone apex
y is the distance from the wall, in a boundary layer of thickness δ.
V_θ is the swirl velocity outside the boundary layer

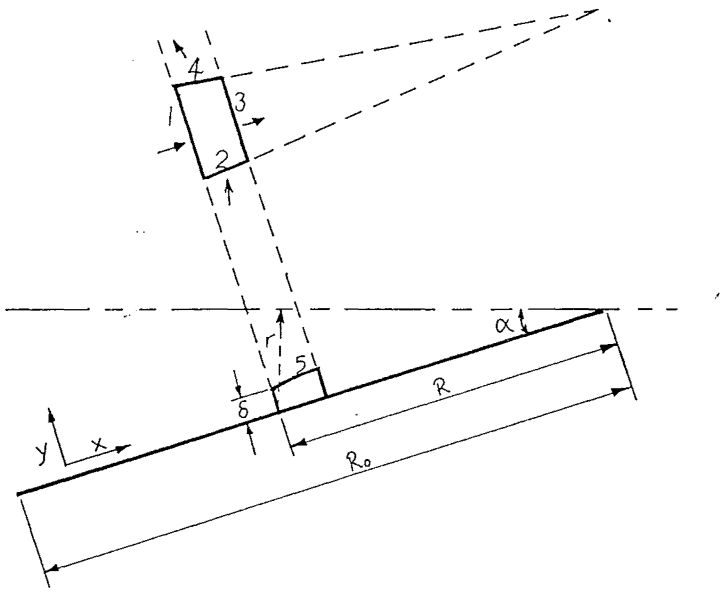

Figure 3.D.4: Coordinate system used in the analyses of Weber (1956) and Tran (1981)

The predicted maximum value of $\frac{W}{V_\theta}$ is about 0.4, and this occurs at $y/\delta = 0.1$. The thickness of the boundary layer at the same location is $\frac{\delta}{D_c} = \frac{1.4}{(V_\theta . D_c / \nu)^{0.2}}$. --- (3.D.14)

The ratio of the boundary layer flow Q_{bl} to the inflow is predicted by:

$$\frac{Q_{BL}}{Q_o} = 1.5 \frac{V_\theta}{V_c} \cdot \frac{\delta}{D_c} \qquad \text{--- (3.D.15)}$$

The assumptions made by Weber in his analysis were regarded by Tran (1981) to be unrealistic representations of the cyclone flow. Tran (1981) estimated the volume flow in the cone wall boundary layer by indirect means. The boundary layer flow into the bin was observed to result in a 'dust storm' caused by the recirculating air. By increasing the underflow that was drawn from the bin until the dust storm was eliminated, an estimate of the boundary layer flow entering the bin could be obtained. Typically 5 - 7% of the inlet flow in a 300mmØ cyclone was found to enter the bin and the thickness of the boundary layer was of the order of 10mm. Using the theory of Weber (1956) Tran found that the volume flow in the boundary layer was overpredicted by 500%, and the boundary layer thickness was similarly overestimated.

Bloor and Ingham (1976) numerically solved the equations of motion for the cone boundary layer flow using the same technique as Taylor (1950). Tran (1981) found that these predictions were only 30% of the experimentally observed values. Bloor and Ingham's approach is complicated and requires the empirical fitting of two parameters.

Tran (1981) adapted Weber's approach to use an experimental value of 'n' = 0.6 in $V_\theta \propto 1/r^n$ to describe the external swirl velocity in the cyclone. This analysis makes approximate momentum and moment of momentum balances for elements of the boundary layer on the conical surface. The cyclones that Tran used had cone half angles of $\alpha = 10.6°$, whereas the Stairmand High efficiency cyclone has $\alpha = 7°$. It is assumed that there is no momentum flux across the surface, that the thickness of the boundary layer is small compared with the radius, and the flow parallel to the cone generators is zero at the edge of the boundary layer. The simple forms that were assumed for the velocity profiles across the boundary layer were:

$$W = E.V_\theta.f(\eta)$$

$$V_{\theta\delta} = V_\theta . g(\eta)$$

where V_θ is the tangential velocity outside the boundary layer

and E is a proportional factor introduced to facilitate the numerical calculations.

$$\eta = y/\delta$$

The functions $f(\eta)$ and $g(\eta)$ are arbitrary, but should match the external flow at the boundary layer edge, and tend to zero at $\eta = 0$. Weber assumed $f(\eta) = \eta^{1/7} - \eta$ and $g(\eta) = \eta^{1/7}$, but these do not satisfy the requirement that the derivatives of both velocity components should vanish at the boundary layer edge. Instead of these, Tran used:

$$f(\eta) = \eta^{1/7} . P_1(\eta) \qquad \text{--- (3.D.16)}$$

and $$g(\eta) = \eta^{1/7} . P_2(\eta) \qquad \text{--- (3.D.17)}$$

P_1 and P_2 are polynomials with non-zero coefficients for terms of order zero. The simplest forms were adopted:

$$f(\eta) = \eta^{1/7} . (1 - 2\eta - \eta^2) \qquad \text{--- (3.D.18)}$$

and $$g(\eta) = \eta^{1/7} . \left(\frac{8-\eta}{7}\right) \qquad \text{--- (3.D.19)}$$

The equations were solved and the angle of the fluid streamlines on the cone wall calculated from:

$$\tan \psi = \lim_{\eta \to \infty} \frac{W}{V_{\theta\delta}} = \frac{E}{\beta} \qquad \text{--- (3.D.20)}$$

where ψ is the angle between the fluid streamlines on the wall, and the tangential plane. This was calculated for n = 1.0, 0.8 and 0.6 for the cyclone examined by Tran, and the results are reproduced below, plotted against the dimensionless radial distance in spherical coordinates.

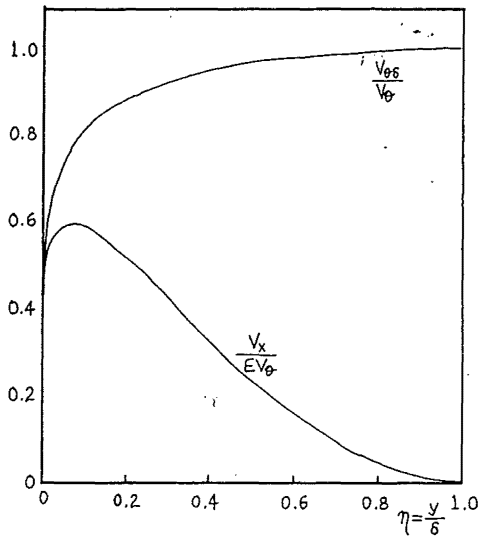

Figure 3.D.5: Calculated Boundary layer profiles from Tran (1981)

At the cone outlet the boundary layer thickness will no longer be small compared with the cyclone radius, nevertheless the calculated results were found to be in good agreement with Tran's experimental measurements.

3.D.3b Cyclone roof/gas exit boundary layer

Tran (1981) then extended the analysis to the roof boundary layer by using the same results, but with the cone half angle taken as 180° (that is, a flat plate 'cone'). The value of 'n' was taken as 0.8 to match the experimentally determined swirl profile in this region. The calculated flow path was found to agree well with the observed pattern of ink streaks. The short circuit flow was calculated to be of the order of 8% of the inlet flow. No measurements of this were obtained for comparison, but Kelsall (1952) has indicated that this boundary layer flow can be comprised of 15% of the inlet flow.

Drabner et al (1988) made an experimental study of the boundary layer flow down the outside of the exit tube, which showed that 10.6% of the inlet flow passed under the lip of the exit tube via the roof boundary layer. This flow passed under the lip within 0.1 exit diameters of the lip. By installing a conical gas exit that contracted as the gas left the cyclone the flow was halved.

The results from the calculations carried out by Tran (1981) cannot be directly applied to the Stairmand High efficiency cyclone because of the difference in geometries, and the calculations have not been repeated for the Stairmand cyclone (because of lack of reliable computer resources).

The roof short-circuit flow was also examined by Bloor and Ingham (1975b), using the Pohlhausen approach, and the modifications to the calculation of the boundary layer made by Rott and Lewellen (1966). For a turbulent boundary layer the leakage is given by:

$$Q = r_o^{9/5}.V_o^{4/5}.\mu^{1/5}\rho^{-1/5}.Q' \qquad \text{--- (3.D 21)}$$

The parameters are selected to fit the experimental profiles of Kelsall (1952) and the volume flow in the roof boundary layer was found to be of the order of 10%.

3.D.3c Bin base boundary layer

The bin base boundary layer can be related to the research on the boundary layer induced by a vortex on a plane placed perpendicular to the vortex axis. Again the initial interest in this problem was shown by Taylor (1950) in his study of swirl atomisers. The boundary layer is also of interest in the study of tornadoes. The bottom boundary is seen to have a strong influence on tornado-like vortices since the up and down flows are linked there by a rapid radial inflow in a thin boundary layer. The boundary layer acts as the source of the vorticity for the core. The description of the bin base boundary layer would provide the initial velocity profile for the vortex core for use in numerical simulations.

The action of viscosity ensures that a rotational layer develops. The balance of forces in the base boundary layer determines the direction of the axial flow in the core, according to Hatton (1975). Initially there is an axial downflow and radial outflow. As the swirl increases the radially inward pressure gradient increases to balance the increasing centrifugal force in the freestream, but in the boundary layer since the velocity doesn't correspondingly increase the radially inwards pressure gradient eventually overcomes the radial outflow in the boundary layer, thus causing a cell of reversed flow in the neighbourhood of the ground.

Phillips has made experimental investigations of the phenomenon both through surface pressure measurements (Phillips, 1984), flow visualisation (Phillips, 1985) and Laser Doppler anemometer measurements (Phillips and Khoo, 1987). The boundary layer was laminar and was observed to flow inwards and then upwards at the axis, undergoing vortex breakdown a short distance later. This breakdown would move several diameters downstream, then move back and touch the base again. The boundary layer became turbulent above a Reynolds number of about Re = 20 000, but it tended to relaminarise as it flowed inwards. The Reynolds number was based on the radius and velocity at the disk edge.

The LDA flowfield survey revealed that the boundary layer was laminar at Re = 5000, underwent transition around 10 000 and for Re > 15 000 was turbulent over some of the disk. The radial pressure gradient associated with the external flow has a stabilising effect and for 10 000 < Re , 30 000 it acts to revert the flow to laminar conditions. It was also found that the tangential velocity component of velocity at the wall in the boundary layer conformed to the same law of the wall as the streamwise component in two-dimensional turbulent boundary layers.

Experimental studies of the vortex-plane interaction are reported by Church et al (1979), Church and Snow (1985) and Pauley (1989), all of which were carried out in the same tornado vortex chamber (TVC). The vortex core formed by the radial inflow and stretching undergoes a vortex breakdown as the swirl is increased, and the vortex breakdown is observed to move upstream until it meets the bottom plane. Further increase in swirl results in the formation of multiple vortices.

Burggraf et al (1971) numerically calculated the laminar boundary layer on a fixed circular disk of radius 'a' placed perpendicular to a vortex of circulation strength Γ. The boundary layer was shown to consist of an inner layer next to the surface with thickness of order $(\sqrt{\nu/\Gamma})$ in which the flow is primarily radial. Outside this is an outer layer with thickness of order $(\sqrt{\nu/\Gamma}.\ a)$ which is predominantly inviscid in nature and in which the flow recovers to the external potential vortex field. The mass flux in the outer layer does not vanish as the radius tends to zero, indicating that it must erupt from the surface at $r = 0$. Rott and Lewellen (1966) approached the problem using the momentum integral equations, while Goldshtik (1960) investigated the existence of similarity solutions. This approach has demonstrated that there are no solutions if the Reynolds number Γ/ν was greater than 5.6. This is far below the values encountered in the cyclone.

3.D.3d Dust rope

Tran (1981) considered the cyclone to feature three important secondary flows, of which the cone wall boundary layer and the roof short-circuit flow have been considered already. The third flow was the secondary flow generated at the inlet, as described by Smith (1962a). This involved the slow moving boundary layer of the inlet walls flowing radially inwards once they entered the cyclone, leaving behind heavy particles at the outer wall which form the start of the 'dust rope'. The dust rope is a commonly observed phenomenon in cyclones, where the dust transport on the wall of the cyclone takes the form of a helical strand or 'rope' of particles, with other regions of the wall comparatively dust-free. The dust rope is observed to start from the inlet and persist to the dust exit. Ranz (1985) notes that the rope fluctuates in position and 'bounces like a spring in tension'. Observations of the dust rope are reported in the literature by ter Linden (1949), Muschelknautz (1972), Smith (1962), Ranz (1985, 1979) and Yuu et al (1978).

Tran (1981) proposed a mechanism to explain the formation of the dust bands based on Smith's description of the secondary flow caused by the inflow of the boundary layer. Once particles reached the wall they came under the influence of the secondary flow. Since momentum is transfered to the dust by the secondary flow the dust will weaken the flow. If the dust loading is too high, the dust band was predicted to disperse. It was also predicted that the dust spiral would deviate from the gas streamlines since the centrifugal force and the wall friction force oppose the particle motion toward the cone outlet.

Since the secondary flow generated by the inlet boundary layers is short lived, and certainly dies out before the conical section, Tran predicted that the band will diffuse. In fact this is not observed, and Tran found that dust released midway down the cone still formed itself into bands. A dependence on the inlet geometry was found by Hejma (1971): with a square inlet the

dust rope helix formed at the inlet and had an approximately constant pitch over the height of the cyclone, whereas for a narrow rectangular inlet the angle of the pitch was zero at the start, and the dust rope only started at the end of the cylinder.

Ranz (1985) reports the measurements of the particle concentration in the wall flow within 30mm of the wall in a 300mmØ cyclone. Because of the wave nature of the layer it was necessary to make instantaneous measurements. These were obtained by measurement of the side-scattering of light via fibre optics and photodiode circuitry. The boundary thickness at the cone outlet was found to be 10mm, while midway down the cone the dust layer appeared to be about 2.5mm thick. Yuu et al (1978) observed the behaviour of the dust rope as the inlet dust concentration was increased. The rope remained of constant width and increased in depth up to an inlet concentration of 50 g/m^3. At 50 g/m^3 the dust rope suddenly widened and spread to cover the entire outer wall.

The presence of dust in the cyclone reduces the pressure drop to 70% of the dust free level with an inlet concentration as low as 0.2 g/m^3, but further addition of dust has no effect until 50 g/m^3, where it begins to decrease again. This is consistent with the reduction of the pressure drop being in proportion to the amount of the wall covered by the dust.

Ranz (1985) then proposes a kinetic model of the fluidised layer, using a theoretical particle viscosity μ_p caused by the random particle motion. The dynamics of the dust rope is predicted by using classical surface wave theory. The dust rope is approximated by the peaks of an associated ideal wave form. The depth of the dust layer is predicted to be about one tenth of the width, and it is shown that as the inlet dust loading is increased the depth grows rapidly, suggesting a limit to the ability of the rope to move 'collected' particles from the cyclone.

Zhou and Soo (1991) considered the effect of particle and gas turbulence on the probability of wall deposition and collection in the cyclone. It is found that to enhance the collection efficiency the cyclone length and inlet velocity should be increased, and the radius decreased, In addition it is desirable to reduce the gradient of the tangential velocity near the wall in order to reduce the particle turbulence.

Muschelknautz (1972) gave an explanation of the dust rope formation that considered the dust as a moving roughness that increased the wall friction of the flow. The much faster external flow displaces the boundary layer along the wall and there is vigorous exchange between the two flows. The retarded boundary layer has a reduced centrifugal force, and flows inwards due to the radial pressure gradient. Further boundary layer fluid flows into the same point, bringing more dust to the same point. This produces the strands of dust, which will be self-sustaining by this mechanism. At moderate dust loadings the strands start from the upper and lower edges of the inlet, and these merge into a broader main strand. At high dust concentrations the boundary layer does not have sufficient energy for a distinct strand to develop.

A similar explanation for the dust rope was developed independently by Abrahamson (1981) involving the formation of Görtler vortices on the concave surfaces of the cyclone. The theory behind Görtler vortices is considered in the next section, but the essential feature utilised by Abrahamson was the generation of alternating bands of slow and fast gas flow along the wall of a cyclone. Due to centrifugal instability, the regions of higher tangential velocity will move towards the wall, while those with lower velocity will move radially inwards. It is expected

that this will result in dust being concentrated in the fast gas flow regions. This will alter the fluid density and enhance the instability. Agglomeration is thus not the only mechanism by which the speed of fine particles can be increased relative to the speed of individual particles.

The dust in the boundary layer is thought to move as swarms rather than agglomerates, as the wall breaks up the agglomerates. Abrahamson (1981) presents photographic evidence of this with very few agglomerates observed close to the wall, but more further out. Fluid forces hold the particles in a fast settling swarm.

The agglomeration of particles is thought to occur in the bin where the lower velocity makes the breakup of agglomerates by wall collisions less likely. The recirculation of dust from the bin and back into the boundary layer was described by Abrahamson (1981). When the dust feed to the cyclone was halted the dust ropes continued, and only when the bin was emptied was the wall transport of the dust halted. This recirculation helps to account for the agglomeration of the fine particles that otherwise could not be captured. Mothes and Löffler (1985) have shown that more than 50% of the 2 to 3 μm particles are collected in the cyclone by agglomeration with big particles. The removal or ejection of portions of the boundary layer similarly explains why particles larger than the theoretical cutsize are not completely collected. Thus the study of the boundary layer could contain the explanation for the slope of the grade efficiency curve, which remains a major problem in the prediction of cyclone performance.

3.D.4 Longitudinal vortices in the boundary layer

Developments in the theoretical description of boundary layer flows in the last 30 years have been centred on the visualisation of the coherent structures in the flow. Prandtl (1935) had proposed that longitudinal vorticity elements had an important role in the origin of turbulence in shear flows adjacent to walls. Later theories by Görtler (1945) and Theodorsen (1952) proposed structures for the cases of concave curved walls and flat plates respectively. The experimental support for these theories has gradually been revealed with the advent of sophisticated visualisation, velocity measurement and computational techniques. It is generally accepted that streamwise-oriented vortices are a dominant feature of the boundary layer, and a considerable amount of literature on the subject has been generated, from which a clear consensus has yet to emerge. Two areas of research will be briefly mentioned here - that of the existence of Görtler vortices on concave curved walls (3.D.5), and the more general case of coherent structures in boundary layers above flat plates (3.D.6).

3.D.5 Görtler Vortices

The first prediction of secondary vortex type motion in concave surface boundary layers was by the linear stability analysis of Görtler (1941). He predicted that a system of longitudinal vortices would be produced in the laminar boundary layers on concave walls as a consequence of the instability to small perturbations. This physical mechanism for the instability is the same as those found by Taylor (1935) for a rotating viscous fluid, and by Rayleigh (1917) for a rotating inviscid fluid. The presence of the concave surface vortices was predicted to be

governed by a Görtler parameter Gö:

$$Gö = \frac{U_1\,\theta}{\nu}\left(\frac{\theta}{R}\right)^{1/2} \qquad \text{--- (3.D.22)}$$

U_1 = The freestream velocity
θ = the momentum thickness (as defined in equation 3.D.11)
ν = the kinematic viscosity
R = the radius of curvature

The existence of the Görtler vortices has been confirmed by numerous experiments (including Swearingen & Blackwelder (1987)). Reviews of the progress have been presented by Herbert (1988) and Sabry (1992). Measurements of velocities in the boundary layer along a concave wall reveal a periodic variation in the spanwise direction (the spanwise direction is perpendicular to both the streamwise and surface normal directions). The measurements have been interpreted as the result of a system of counter-rotating vortices with their axes aligned with the streamwise direction. The basic structure is depicted below in this diagram from Floryan and Saric (1982).

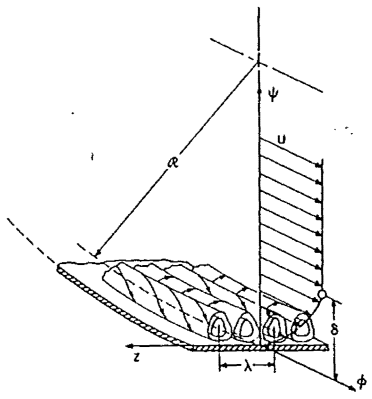

Figure 3.D.6: Görtler vortices in a boundary layer flow over a concave wall with the axes of the vortices parallel to the principal flow direction, from Floryan & Saric (1982)

Prandtl (1935) predicted that the counter rotating vortices would give rise to regions of flow that alternated between being directed towards, and away from the wall. The ejection of low momentum fluid away from the wall and into the unretarded external flow was expected to result in inflexional velocity profiles that are unstable and undergo further breakdown. This was also a feature of Görtler's theory and is found experimentally, with the unstable Görtler vortex structure apparently breaking down as it progresses downstream.

So and Mellor (1975) found that turbulent intensities inside the boundary layer were substantially increased for a concave wall. The heat transfer rate across the boundary layer was increased for concave surfaces, and decreased for convex surfaces. A convex curved wall tends to suppress the turbulence in the outer layer, as was demonstrated by So and Mellor (1975). They passed a boundary layer from a flat plate onto a convex surface, and found that the turbulence that had been present in the outer layer disappeared.

Görtler's analysis was for a laminar boundary layer. The first observations of longitudinal vortices in a turbulent boundary layer on a concave wall was by Tani (1962), who proposed a

turbulent Görtler parameter:

$$G\ddot{o}_T = \frac{U_1\,\theta}{\nu_T}\left(\frac{\theta}{R}\right)^{1/2} \qquad \text{--- (3.D.23)}$$

The symbols have the same definitions as in equation 3.D.22, but an eddy viscosity,ν_T is used in place of ν. Tani assumed a constant value of the eddy viscosity, suggested by Clauser (1956) for flow in pipes as

$$\nu_T = 0.018\,U_1.\delta_d \qquad \text{--- (3.D.24)}$$

This gives sufficiently accurate velocity profiles for 80-90% of the turbulent boundary layer, irrespective of the Reynolds number, pressure gradient or wall roughness.

Using this value for ν_T, and assuming that $\delta_d = 1.3\,\theta$ the Reynolds number can be given as:

$$\frac{U_1\,\theta}{\nu_T} = \frac{1}{0.018 \times 1.3} = 42.7 \qquad \text{--- (3.D.25)}$$

Hence the Görtler parameter for turbulent boundary layers is given by:

$$G\ddot{o}_T = 43\left(\frac{\theta}{R}\right)^{1/2} \qquad \text{--- (3.D.26)}$$

The effect of the vortices was most noticeable in the centre of the boundary layer thickness, and increased markedly in the downstream direction. This feature was reproduced by Hall (1982) using an asymptotic expansion of the linear stability equations based on small disturbance wavelengths. The Görtler vortex disturbances were located in internal viscous layers away from the wall and the freestream regions. For a surface with a curvature K(x) (= 1/R) that varies in the streamwise direction, this analysis can be generalised by multiplying the Görtler number by K(x).

Denier et al (1991) identified a new structure which is relevant for vortices with wavenumbers of order $G\ddot{o}^{1/5}$. This structure has the property that the vortices are trapped in a thin layer of thickness $O(G\ddot{o}^{-1/5})$ at the wall, in contrast to the structure identified by Hall (1982), where vortices of wavenumber $G\ddot{o}^{1/4}$ are confined to a thin layer embedded with the boundary layer at some well defined position. Denier et al (1991) showed that within the $O(G\ddot{o}^{1/5})$ wavenumber region a particular Görtler vortex arrangement existed that was the most unstable according to linear stability theory. Bassom and Hall (1991) sought to extend this to three dimensional boundary layers with crossflow.

In practice, the transition to turbulence on curved walls could be affected by both the Tollmein-Schlichting waves and Görtler vortices. Tollmein-Schlichting waves are travelling non-axisymmetric waves that occur at high Reynolds numbers. The linear development of Görtler vortices with dimensionless wavenumbers of order O(1) considered by Hall (1983) suggested that for flows with $G\ddot{o} > 10$ the transition would be dominated by the Görtler vortices, this corresponds to walls with $l/R > O(1/50)$, where l is the length scale along the wall. Daudpota et al (1988) also found a preference for Görtler vortices over the Tollmein-Sclichting waves near the critical Reynolds number. They extended the analysis to consider the interaction between Tollmein-Schlichting waves and Görtler vortices.

In many practical situations the boundary layer is three dimensional. Hall (1985) found that the critical feature that determines the vortex structure in the boundary layer is the relative size of

the crossflow and chordwise flows. If this ratio, χ, is increased from zero the first significant change occurs for $\chi \sim Re^{-1/2}$, where $Re = \frac{U_1 l}{\nu}$. After this the vortices become time-dependent and the high wavenumber modes no longer have the vortices aligned with the flow. For values of χ of order O(1) the Görtler mechanism is reportedly unimportant compared with the Tollmien-Schlichting and crossflow type instabilities. Bassom (1989) showed steady weakly non-linear vortices could only persist below a certain threshold value of the crossflow.

Shizawa and Eaton (1992) showed that the development of a three-dimensional turbulent boundary layer with an embedded longitudinal vortex is very sensitive to cross flow in the boundary layer and the sign of the vortex relative to the cross flow. If the crossflow direction is opposite to the vortex induced flow near the wall then a strong cross flow separation results. In the opposite case the crossflow separation is suppressed. Shizawa and Eaton (1992) found that longitudinal vortices attenuated very rapidly when embedded in a three dimensional boundary layer, the decay being twice as fast as for a similar vortex in a two dimensional boundary layer. They considered rotation effects to be very important in suppressing turbulence near the vortex core, and to estimate the importance of this effect they evaluated the gradient Richardson number, as proposed by Bradshaw (1973):

$$Ri = \frac{2\,\frac{V_\theta}{r^2}\,\frac{\partial (V_\theta . r)}{\partial r}}{\left(\frac{\partial U}{\partial r}\right)^2 + \left(\frac{\partial V_\theta}{\partial r}\right)^2} \qquad \text{--- (3.D.27)}$$

The curvature effects become significant for $Ri > 0.01$ with complete stabilisation of turbulence above $Ri = 0.25$.

In order for the Görtler vortices to form the wall must be sufficiently curved to overcome the viscous stabilising forces, although once formed they persist even on flat walls. Sabry & Liu (1991) point out that the growth of the Görtler vortex is driven by the Reynolds shear stress conversion mechanism, with the concave curvature effect only important in the initiation of the disturbance.

The effect of different boundary layer velocity profiles on the development of the Görtler instability was examined by Floryan (1986) using an inviscid stability analysis. It was shown that convex surface boundary layers can also be subject to Görtler instability if the velocity profile is non-monotonic (such as with a wall jet). On concave surfaces the flows with monotonic velocity distributions are expected to become unstable earlier than flows with non-monotonic velocity distributions.

On a concave surface the behaviour of a wall jet boundary layer was found by Floryan (1986) to differ from the monotonic Blasius-type boundary layer. The neutral stability wavelength parameter was considerably smaller than is the case for the monotonic Blasius type boundary layer, and the wavelength at which the maximum total amplification occurs was not constant, but increased as the Görtler number increased, In addition, a different boundary layer structure developed for a wall jet boundary layer which consisted of multiple layers. At the neutral curve a single layer is found, at Gö ~ 5 a second layer forms and at Gö ~ 17 the upper vortex splits into two, resulting in three layers of vortices. This split occurs when the vortex is compressed far enough to reach the location of the maximum of the mean flow velocity. Westphal and

Mehta (1989) observed the flattening of the vortex core shape when the vortex grew to a sufficiently large fraction of the distance of the vortex centre from the surface.

For a laminar boundary layer on a surface with radius of curvature 10m and a freestream velocity of 11 m/s Tani (1962) observed spanwise variations in the velocity of about 1m/s at 3mm from the wall. The spanwise wavelength was approximately 21mm. In the 5m radius case the spanwise wavelength was 34mm. In a turbulent boundary layer on a radius of 5 metres the wavelength was 65mm compared to 32mm on the 10m radius. The wave amplification appeared to be favoured for the laminar boundary layer, and for the smaller radius of curvature.

Liepmann (1945) found experimentally that for a constant radius of curvature of 2.5 feet the critical Görtler number was 9 for turbulent levels from 0.065% to 0.2%, but dropped to Gö = 6 for turbulent levels of 0.3%. The transition Reynolds number was very much less for concave surfaces than either convex or flat surfaces.

Swearingen and Blackwelder (1987) took care to keep the freestream turbulence level below 0.07% in their experimental study of the growth of Görtler vortices in a boundary layer. The apparatus featured a concave wall extending for 45° with a radius of curvature of 3.2m and a freestream velocity of 5m/s. Görtler numbers ranged from 0.5 to 10, and Reynolds numbers from 10 000 to 100 000. The Görtler vortices were observed to form at Gö ~ 5.6, and the breakdown to turbulence was observed to take place for Gö between 6.7 and 9, in accordance with the critical value of Liepmann (1945)

The radii of curvature used by Tani (1962) and Swearingen & Blackwelder (1987) is greater than is commonly found in cyclones. In addition, the surface described only part of the circle. Winoto and Low (1989) have examined the transition to turbulence of boundary layer flow in the presence of Görtler vortices in a curved duct of radius 1000 mm over a 90° bend with freestream velocities of 5.7, 8 and 11.8 m/s. Quantitative velocity measurements were carried out using a single sensor hot wire anemometer and transitions were observed using a frequency spectrum method. For the freestream velocities of U_1 = 8.0 m/s Winoto and Low present graphs of the spanwise variation of the streamwise velocity. The peak to trough variations are greatest in the transition region, with a ratio of velocities of 3, whereas further downstream in the turbulent conditions the variations are smaller, with a ratio of 1.25. The observed vortex spanwise wavelengths for three freestream velocities in the range 5.7 to 11 m/s were all about 15 -18mm. This appeared to be independent of the streamwise distance, but was slightly dependent on the freestream velocity.

Another commonly cited result is the critical Görtler number of 16.1 found by Schweizer & Scriven (1983). It should be noted that this was for a laminar flow of a liquid film descending on a concave surface under gravity, with the initial section vertical. The Görtler number is referred to as a modified Reynolds number, and this is transformed by making use of Nusselt's relation between the mean film thickness and q, the volumetric flowrate per unit width, in fully developed film flow on a vertical wall, yielding:

$$Re_{ss} = \left(3\, q^7.\nu^{-5}.R^{-3}.\, g^{-1}\right)^{1/6} \qquad \text{--- (3.D.28)}$$

It was assumed that the effect of the slowing and thickening of the boundary layer on initial part of the concave section could be neglected. The value of Re_{ss} at which the Görtler vortices were first detected ranged from 10.8 to 19.1, but the root-mean-square value was 16.1. The

dimensionless wavenumber $\alpha = 2\pi\delta/\lambda$ varied from 3.2 to 6.4. The concave sections examined extended for 90° and had radii of 12.7, 25.4 or 76.2mm. Although the observed features show similarity to the Görtler vortex flow it can not be determined if the higher value of the critical Görtler number is due to the smaller radius of curvature (which is an order of magnitude smaller than the other experiments) or the difference in the physical arrangement.

Richmond & Patel (1991) made a numerical simulation of the flow in a duct that curved for almost 360°, and compared the findings with the experiments of Eskinazi & Yeh (1956). The computation showed a significant difference between the measured and computed skin friction for the concave surface, which they attributed to the presence of Görtler vortices causing local three-dimensional effects. The computations were made in two-dimensions and lacked sufficient resolution close to the wall (the first grid point from the wall was at $y^+ \sim 0.3$). Eskinazi & Yeh (1956)'s experiments did not show any significant spanwise variation, although this is likely to be due to a lack of resolution in the measurement technique.

A more detailed three-dimensional computation of a flow featuring Görtler vortices was carried out by Botarro (1991) in a duct curved over 60°. It was found that an inlet perturbation was necessary for the vortices to develop, and the removal of the perturbation eliminated the vortices. Swearingen and Blackwelder (1987) found that suitable initiating disturbances were present even with turbulence levels below 0.07%.

Stability diagram:

Consideration of the amplification or decay of disturbances of the form:

$$\text{"}F(y)\, e^{\beta t} \cos az \text{"} \qquad \text{--- (3.D.29)}$$

leads to a stability diagram expressed as the Görtler number versus $a\theta$. Here 'a' is the wavenumber, equal to the number of waves contained in 2π cm in the spanwise direction; and θ is the momentum thickness. Görtler vortices are predicted to grow and develop in a concave surface if they are in the unstable region of the Görtler vortex stability diagram where the disturbance amplification factor β is greater than zero. β is a measure of the rate of growth of a disturbance as a function of the streamwise direction. A larger Görtler number is more unstable, thus a smaller radii of curvature enhances the formation of the vortices.

Experimental occurrences of the Görtler vortices are generally found to be located in the region of the stability diagram where the disturbances are predicted to be amplified. However the theory is not able to predict which wave number will actually appear for a given radius of curvature. The minimum theoretical Görtler number appears to be 0.464 at small wavenumbers. Critical values for the wavenumber α or the wavelength parameter Λ are not able to be identified. The observed spanwise wavelengths have been found to depend on the edge effects of the experimental apparatus or the oncoming disturbances, especially for measurements near the neutral stability. The position of neutral stability was found by Hall (1982) to depend on the location and mechanism by which the perturbation was introduced, so that a unique neutral curve is likely to be found only for asymptotically small wavelengths. The naturally occuring vortices are found to be those with the highest amplification rates, and effort has been directed towards determining the mechanism that selects the wavelength.

Experimentally it is found that the dimensional wavenumber is conserved in the flow direction - that is the spacing between the vortices does not change as the boundary layer evolves, and it is approximately independent of the freestream velocity. If the wavenumber (or wavelength) is

scaled by the boundary layer thickness (which increases in the downstream direction) then the dimensionless parameters will vary with the downstream distance. Instead Floryan and Saric (1982) suggest a wavelength parameter:

$$\Lambda = \frac{U_1 \lambda}{\nu_T} \left(\frac{\lambda}{R}\right)^{1/2} \qquad \text{--- (3.D.30)}$$

where λ is the dimensional wavelength in the spanwise direction. Similarly the wave number parameter

$$A = \frac{\alpha \nu_T}{U_1} (\alpha R)^{1/2} \qquad \text{--- (3.D.31)}$$

Swearingen & Blackwelder (1987) used a viscous length scale ν/u_T (commonly referred to as a 'wall unit') for scaling quantities in the boundary layer. u_T is the friction velocity given by:

$$u_T = \left(\nu . \left(\frac{\partial U}{\partial y}\right)_w\right)^{0.5} \qquad \text{--- (3.D.32)}$$

where y is the direction normal to the wall. Swearingen & Blackwelder (1987) found that the spatial scales of the temporal velocity fluctuations correlated better with the velocity gradient in the spanwise direction than with the normal velocity gradient. The spanwise spacing of vortices was 100 wall units, and the lengths were of the order of 1000 wall units.

The early analyses of the Görtler vortex phenomenon neglected the effect of boundary layer growth, and assumed that there was no variation in the streamwise direction. This is suggested by Hall (1982) to be the cause of the disagreements between the neutral stability curves calculated by these theories. The neglect of boundary layer growth is shown by Hall (1982) to be valid only in the limit of small spanwise vortex wavelengths, since the linear stability equations for vortices of wavelength comparable to the boundary layer thickness cannot be reduced to ordinary differential equations. Theoretical analyses of the stability of the Görtler vortices have been made without resorting to the parallel flow approximations in numerous papers by Floryan (1982, 1984, 1986, 1989) and Hall and coworkers (1982, 1983, 1985, 1988, 1991). An overview of the recent progress is contained in Sabry & Liu (1991) and Sabry (1992).

By assuming that the radius of curvature of the wall, the freestream velocity and the viscosity are fixed, Floryan and Saric (1984) used the Görtler number as a measure of the distance downstream. Starting in a streamwise location corresponding to G = 0.3 the flow is stable and all disturbances are damped. When the location is moved downstream and the neutral curve is crossed a whole band of wavelengths begins to grow. This band is unbounded for small wavenumbers but the neutral curve defines a boundary separating stable and unstable vortices on the side of large wavenumbers. The lower bound of the unstable wavelengths is $\Lambda = 44.29$. The reason for the elimination of the smaller vortices is that there is an increase in the gradients of the disturbance velocity fields associated with the smaller vortex, leading to higher dissipation.

When the neutral curve is crossed in the direction of increasing Görtler numbers the wavelength that is favoured from the band available is determined by the disturbance growth process. Floryan and Saric (1984) identified $\Lambda = 210$ as the most unstable wavelength since it stays closest to the line of maximum amplification, as shown in the figures below.

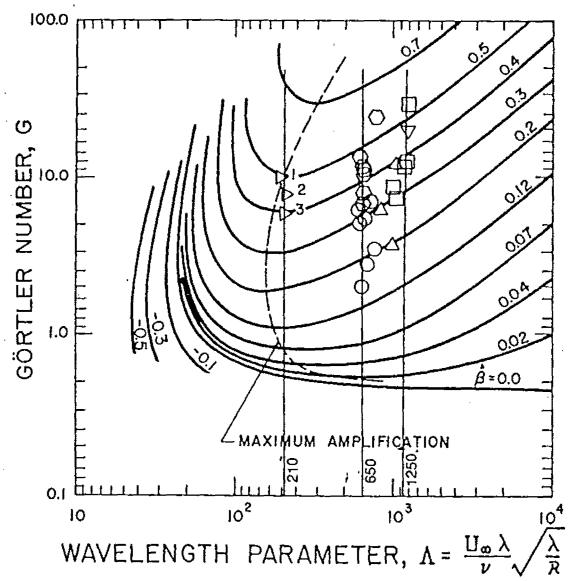

Figure 3.D.7: Curves of constant amplification rate $\hat{\beta} = \beta/Gö$ as a function of the Görtler number Gö and the wavenumber α for the Blasius boundary layer. from Floryan and Saric (1984)

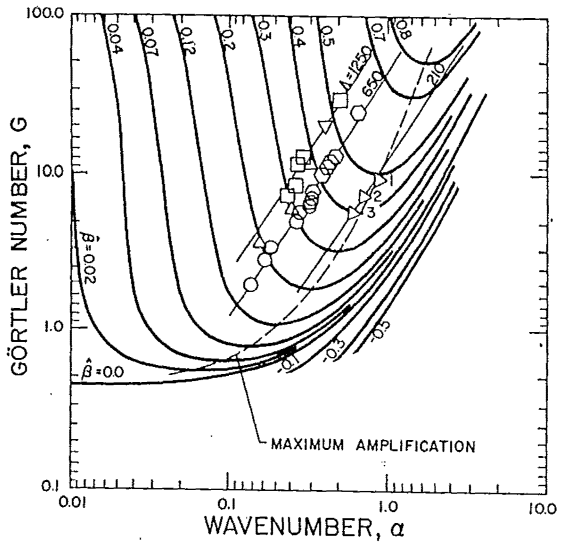

Figure 3.D.8: Curves of constant amplification rate $\hat{\beta} = \beta/Gö$ as a function of the Görtler number Gö and the wavelength parameter λ, for the Blasius boundary layer, from Floryan and Saric (1984)

Theoretical calculations of the amplification rate made by Floryan and Saric (1984) agreed with the experimental measurements of Tani (1962), but overpredicted the experimental measurements of Bippes (1972). However Bippes used disturbances artificially forced into the boundary layer, and non-linear effects may be responsible for slowing the growth.

For a boundary layer of constant curvature once the wavelength is selected it is observed to be remain downstream regardless of the growth rate. The growth of the vortices is given by the amplification parameter β:

$$\beta = \frac{1}{A^*} \frac{dA^*}{d\phi^*} \qquad \text{--- (3.D.33)}$$

where A^* is the dimensional amplitude
ϕ^* is the distance along the curve.

$$\text{The total growth is } A^* = A_o^* \exp \{ \int_{\phi_o^*}^{\phi^*} \beta^* \, d\phi^* \} \qquad \text{--- (3.D.34)}$$

where $A_o^* = A^*(\phi_o^*)$

Using dimensionless quantities this transforms to:

$$A = \exp \{ \int_{G_o}^{G} \tfrac{4}{3} \frac{\beta}{G} . \, dG \} \qquad \text{--- (3.D.35)}$$

where: $A = \frac{A^*}{A_o^*}$; $A(G_o) = 1.$ $\hat{\beta} = \frac{\beta}{G}$

The plot of the amplification rate versus the Görtler number is shown below:

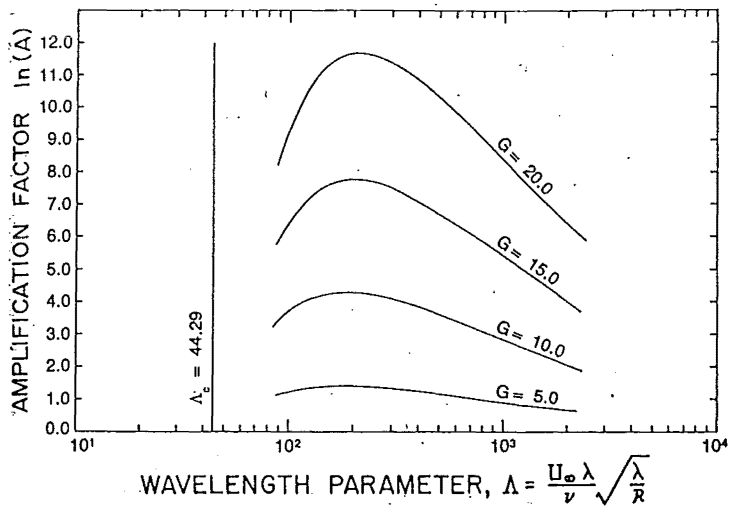

Figure 3.D.9: Amplification rate of Görtler vortices as a function of Görtler number

The position at which the Görtler vortices undergo the transition to turbulence has attracted interest because of the connection of this to the more general transition of laminar boundary layers to turbulence and the generation of turbulence in a turbulent boundary layer. Smith (1955) suggested the $\int \beta dx$ transition criteria, which can be used in conjunction with the vortex growth diagram method to predict the vortex wavelength λ. To use this criterion in general situations it is necessary to have expressions for the variation of the boundary layer thickness and freestream velocity in the streamwise (x) direction. This is reported by Winoto and Low (1989) to be a better criterion that the simple critical Görtler number criterion, and the $\int \beta \, dx = 9$ criterion was found to predict the position of the transition to within 6%.

Winoto and Low (1989) found that the theoretical $Gö_{tr}$ criterion gave values of about $Gö_{tr} = 8$, whereas the experimental value was found to be 40-50. Winoto and Low (1989) found that the

transition was initiated at the trough or upwash regions where the boundary layer is thickest. They suggested that a new transition criterion based on the value of the Görtler number at the trough or upwash section should be used.

In the 1980s Phillip Hall made a series of theoretical studies of the process of Görtler vortex instability. Starting with the asymptotic case of high wavenumbers with linear disturbances (Hall, 1982), the analysis was extended to dimensionless wavenumbers of order O(1) in Hall (1983), and the corresponding nonlinear regimes in Hall (1982b) and Hall (1988). Non-parallel flow effects were found to be particularly important at small vortex wavelengths, and the nonlinear effects were found by Hall (1988) to stabilise the flow compared with the linear case.

The non-linear evolution of streamwise vortices produces inflexional profiles which will breakdown via a secondary Rayleigh instability. The spanwise location where the profile is most inflexional (in both experiments and calculations) is at the vortex boundaries where the flow is away from the wall, and the shear stress at the wall is a minimum. This agrees with the experimental observations of So and Mellor (1975) who found that the boundary layer transition occurred at the upwash trough between vortices. Hall (1988) concludes that the major effect of Görtler vortices on the boundary layer is to make them highly receptive to rapidly growing Rayleigh modes of instability.

In the early stages of the development of Görtler vortices the disturbance field is steady and of the form of spanwise periodic counter-rotating vortices. These initial stages appear extremely sensitive to upstream flow and often the initial periodicity is fixed by some forcing mechanism at the wall. Denier et al (1991) have shown that freestream disturbances and wall roughness are both possible causes of the initial growth.

Further downstream the steady state undergoes a secondary instability to a three-dimensional time dependent disturbance, which sometimes leads to an unsteady wavy vortex flow (similar to the Taylor vortices between closely spaced rotating cylinders). In other cases the secondary instability leaves the vortex boundaries smooth but causes the generation of horseshoe vortices typical of the later stages of flat plate boundary layer transition. These constitute two distinct modes of instability to longitudinal vortex structures. If the wall curvature is small enough to postpone the Görtler vortices until sufficiently high Reynolds numbers, then the Tollmein-Schlichting waves can also be involved.

Swearingen and Blackwelder (1987) arranged their experimental apparatus to ensure that the flow became unstable to Görtler vortices before Tollmein-Schlichting waves. They observed both of the secondary instability modes mentioned above, but reported that the wavy mode was the most preferred mechanism in their experiments. The primary disturbance of the Görtler vortices was noted to have a streamwise developing stucture that was independent of time, whereas the secondary instabilities were modulated in time and in the streamwise distance.

The transition of the boundary layer is thought (for example, by So & Mellor (1975)) to be affected indirectly by the spanwise variation of the boundary layer thickness that is induced by the vortices. These peaks and troughs are then distorted by a secondary instability, and further downstream the vortices are observed to 'meander' in the transverse direction (as discussed by Westphal and Mehta 1989), especially for boundary layers on surfaces of large curvature. It is thought that this meandering might initiate the boundary layer transition, but Aihara and Koyama (1981) suggest that this inherent fluctuation grows into periodic three-dimensional

horseshoe-type vortices, and it is the breakdown of these that leads to the boundary layer transition.

3.D.6 Coherent structures in flat boundary layers

Görtler vortices are a consequence of the wall curvature, and are thus not present in flat plate boundary layers. However, research in recent years on the transition of and turbulent structures in boundary layers on flat plates has identified similarities in the structure of these two boundary layers. In particular, it has become recognised that the flat plate boundary layer is dominated by quasi-streamwise longitudinal vortices that are associated with the ejection of fluid from the wall. The following section is based on the published research carried out on flat plate boundary layers, but the same mechanisms will be expected to apply, and may even be amplified in the case of concave boundary layers. As mentioned in the previous section, recent developments in the theories of Görtler vortices have made connections between the Görtler vortices and the formation of horseshoe vortices that are also found in the flat plate boundary layer. However, it should be noted that the physical scales of Görtler vortices are much larger than the longitudinal vortices found in flat plate boundary layers, as noted by Swearingen & Blackwelder (1987).

The visualisation, description and modelling of coherent structures in the boundary layer near the wall became the new emphasis of boundary layer turbulence research in the early 1960s, supplanting the earlier statistical approach. Rather than the steady, quasi-laminar flow that had been assumed, the boundary layer was observed to contain organised motions including longitudinal vortices, 'bursts' or ejections of fluid from the boundary layer, and inwards 'sweeps' of fluid from the external flow. Experimental observations made by numerous researchers have suggested that the majority of the turbulence production occurs in the buffer region during intermittent, violent ejections of low speed fluid and inrushes of high speed fluid. Consequently this topic has attracted considerable attention and has resulted in the research concentrating on the description and explanation of these coherent structures - this interest continues unabated at present. The progress in the understanding of the dynamic structure of the boundary layer has been reviewed by Cantwell (1981), Herbert (1988), Chu and Falco (1988) and Robinson (1991).

A taxonomy of the various forms of the coherent motions that have been observed has been presented by Robinson (1991), classified into eight groups:

- Low speed streaks
- Ejections of low speed fluid outward from the wall
- Sweeps of high speed fluid inward to the wall
- Vortical structures of various forms (including quasi-streamwise, hairpin & ring-like)
- Near wall 'pockets', revealed by regions that are swept clear of near wall fluid
- Large scale motions resulting in three-dimensional bulges in the outer region
- Shear layers in the near wall, and

- in the outer region.

Currently interest is focussed on the role of the low speed streaks, the various vortical structures and the sweeps and ejections of fluid at the wall. A consensus has not been reached on the mechanisms that connect these, nor on the order in which they occur during a 'typical' burst cycle. The following section highlights some features of these structures and the mechanisms that have been proposed to explain the connection between them.

Streaks of low-speed fluid

One of the first structures to be identified in the turbulent boundary layer were the alternating long narrow streaks of high and low velocity fluid aligned approximately in the streamwise direction, as reported by Runstadler et al (1963) and Kline et al (1967). The review by Cantwell (1981) found typical spanwise spacings of 100 wall units (see equation 3.D.28b), and a streamwise extent of the order of 1000 wall units. Chu and Falco (1988) observed that long counter-rotating streamwise-oriented vortices exist in wall regions on flat plates, and act in pairs to produce a gathering of wall layer dye between them that appear as low speed streaks. A high speed streak would be the result of high speed fluid being induced towards the wall between a pair of these streamwise vortices rotating the other way.

A number of experimental studies have suggested that the streaks are consistent with the removal of low-momentum fluid from the wall by pairs of counter-rotating streamwise oriented vortices in the boundary layer. The longitudinal vortices can act as pumps, transferring fluid across velocity gradient in the boundary layer. Where the flow is downwards between them, the vortices will tend to be forced apart, while upwards flow between them will tend to pull them together. The downwards flow brings high speed fluid down and would be expected to form a high speed streak. The inflexional velocity profile resulting from the layers of low momentum fluid riding above high speed fluid gives rise to a secondary instability that results in the rapid ejection of fluid away from the wall. Models of the turbulent boundary layer featuring the quasi-streamwise vortices as the dominant structure are favoured by Swearingen & Blackwelder (1987) and Robinson (1991).

Smith (1984) proposed that the ejection of a low speed streak was due to the roll up of the vortex formed on the top and sides of the streak. This is convected in the streamwise direction and moves outwards by self-induction. The trailing legs remain in the near-wall region but are stretched, forming counter-rotating quasi-streamwise vortices that pump fluid away from the wall and accumulate low speed fluid between the legs. Although the hairpin vortices are not observed to exist for long, Smith (1984) explained the persistence of the longitudinal vortices by the coalescence of the legs of adjacent hairpins. The model proposed by Smith (1984) was based on observations of a laminar boundary layer where the symmetry was forced by the geometry, which was reflected in the structures proposed.

The vortices were observed by Guezennec et al (1989) to occur most often as single units, rather than in counter rotating pairs, and single vortices were found to be capable of producing both ejections and sweeps without the need for an equal-strength twin. The prevalence of paired vortices reported in the literature is said to be a result of the conditional averaging methods used, as these prescribe a spanwise symmetry. The high speed fluid regions are shorter in the streamwise direction than the elongated streaks of low speed fluid, but are wider

in the spanwise direction. The most common near-wall coherent motions such as the quasi-streamwise vortices travel significant distances downstream of the order of 1000 viscous lengths.

The ejections of fluid have been commonly referred to as 'bursts', but there have been conflicting definitions for this term. The term 'bursting' was originally coined by Runstadler et al (1963) to describe the production of turbulence in the boundary layer by outwards eruptions of the near wall fluid. The two main concepts now in use for the term 'bursting' are:
- A localised ejection of fluid from the wall caused by the passage of one or more quasi-streamwise vortices.
- Violent, temporally intermittent eruption of fluid away from the wall due to a local instability,

These two concepts summarise the different viewpoints of the mechanism linking the ejections and the vortical structures. In some theories, such as outlined above, the jet-like bursts are induced by the action of the longitudinal vortices; while others have proposed that the longitudinal hairpin vortices are induced at the edges of the ejection.

This second concept views the eruptions as primarily the result of a streak of low speed fluid lifting from the wall, and the longitudinal vortices are secondary features induced at the edges of the streak. The relationship between the quasi-streamwise vortices and the hairpin vortices is also subject to debate. The high speed streak can be viewed in terms of a wall jet which develops two longitudinal vortices on its two sides according to Launder and Rodi (1982). Arcarlar and Smith (1987) view the pair of streamwise vortices as secondary features induced at the edges of a low speed streak. The hairpin vortices are depicted as evolving from the low speed streak and lifting off from the wall, but the secondary vortices are not shown to lift off.

Hairpin vortices

In other theories (Cantwell, 1981) the quasi-streamwise vortices formed by the roll-up of the edges of the low-speed streaks merge due to the expansion and growth of the high speed regions in the streamwise direction. The lifting of the streak from the wall is proposed to result in hairpin-shaped vortices that are formed from the merged longitudinal vortices. Incomplete merging of the vortices explains the observation of Head and Bandyopadhyay (1981) that the coherent structures are not always perfect hairpins, but often pieces of the structure such as the legs, or arch. Falco (1991) proposes that the pinching-off and merging of the hairpin vortex results in ring-shaped eddies in the outer region, to which he gave the term 'Typical eddies'. These may also be formed by a local instability. The typical eddies interact with the near wall region and are responsible for the formation of 'pockets', which are evidenced by regions swept clear of dyed near wall fluid.

Robinson (1991) distinguishes between the hairpin vortices, which predominant at high Reynolds numbers, and the 'arch' or horseshoe vortices which occur at low Reynolds numbers. The horseshoe or arches are approximately as wide as they are high, while the hairpin vortices are more slender and feature a tighter curve and elongated trailing legs. Both the arch and hairpin vortices may be asymmetrical, and fragments of arches can account for other structures that are observed. Robinson (1991) reports that quasi-streamwise vortices are found to dominate the buffer region of the boundary layer nearest the wall, while the horseshoe and transverse vortices dominated the wake region. The transverse vortices may be viewed as

the heads of the arches, and these are less common than the quasi-streamwise vortices. The quasi-streamwise vortices may not all be legs of arches, or alternatively arches may form several legs during their lifetime. The relative scarcity of the arch heads may also be explained by faster dissipation due to the orientation, or the fact that the legs are at an earlier stage of development. Guezennec et al (1989) found that the transverse vortices of the outer region have relatively long lifetimes compared with quasi-streamwise vortices which form, evolve and dissipate in the near-wall region.

Smith et al (1991) use the hairpin vortex as the dominant element in their model of the turbulent boundary layer, with the ejections occurring as a result of its interaction with the wall. Falco (1991) regards the 'typical eddies' as the dominant feature of the boundary layer, and proposes a model in which the typical eddies are responsible for the production of the streaks, pockets and subsequent ejections from the wall. The pockets observed by Chu and Falco (1988) were a result of the local removal of wall fluid, leaving a region of low marker concentration. They are described as the "footprints of the outer region motions that interact with the wall", Falco (1980a) showed that they start out as a movement of wall layer fluid away from a location as a high speed eddy from the outer region nears the wall. The fluid is seen to lift off the wall and take on the character of a hairpin vortex. Robinson (1991) suggests that the low speed streaks and the pockets can be formed by the wake left behind by the buffer layer vortices being dragged through the wall region. The buffer layer vortices are an order of magnitude shorter than the streaks in the sublayer.

The first theoretical explanation of these features actually predated the experimental observations, but the structures proposed by Theodorsen (1952) - notably the hairpin or horseshoe vortices were subsequently identified in experiments and have remained an important concept in the description of the observed boundary layer structure. Theodorsen's model was developed from the vorticity transport form of the Navier-Stokes equations to explain the production and dissipation of turbulence in the boundary layer. In the model vortices form astride low speed zones in the near wall region and grow outwards at an angle of 45° to the wall, with spanwise dimension comparable to the distance from the wall. Willmarth and Tu (1967) also proposed a hairpin model based on spacetime correlations between wall pressure and the three dimensional velocity components in the near wall region. The dominant features were the quasi-streamwise vortices that trailed the hairpin vortex.

Swearingen & Blackwelder (1987) found that the quasi-streamwise vortices lead to a secondary instability that results in the ejections due to a localised inviscid shear layer instability. This secondary instability was reported to be associated more with the inflexional velocity gradients in the spanwise direction than with the normal gradients of the streamwise velocity. It would seem that the longitudinal vortices may contribute to the production of the streaks, but the lifting from the wall is due to the instability of the streak. The pumping of the fluid away from the wall by the longitudinal vortices is on a smaller scale than the wholesale lifting of the streak from the wall. The lifting of the low speed streak is expected in the rotating flow of the cyclone because of the Rayleigh instability, whereby layers of lower momentum fluid are unstably situated below high momentum layers.

Sweeps & Ejections

Apart from the debate over the relative importance of the features to the mechanism of the production of the ejections, the order in which the features occur is also in doubt. The sweeps of fluid towards the wall could be viewed as a compensating flow to balance the depletion of fluid near the wall caused by the ejections, however other theories favour a mechanism where the inrushes precede the ejections. This is supported by the experiments of Gad el Hak and Hussain (1986), who applied intermittent suction through pin holes on a flat surface. This was observed to result in high speed fluid being brought into the wall region and the establishment of the high speed streaks that lead to the ejections being produced between the holes. Suction at one hole was insufficient to result in a burst. The energy for the wall flow is supplied by the inrush, in contrast to the growing instability of the wall layer. Offen and Kline (1975) also observed that the "typical pattern was for sweeps to precede bursts, which in turn were followed by new sweeps further downstream". The sweeps were thought to represent the passage of an ejection from further upstream.

The sweeps or inrushes of fluid are variously reported to originate from the log law region (Offen and Kline, 1975), from the outer region (Kline and Robinson, 1989) or from outside the boundary layer (Antonia, Danh and Prabhu (1976)). Sweeps must have a significant wall-ward component of velocity, while 'gusts' of high speed fluid parallel to the wall also exist. The path of the sweeps and ejections are reported by Cantwell (1981) to lie at a shallow angle to the wall, in the range of 5 to 40°.

Although the ejections are often viewed as localised, intermittent and time periodic events, Robinson (1991) has suggested that this view has resulted from the convection past the stationary measuring station of long lived quasi streamwise vortices. Robinson (1991) notes that the analysis of the coherent structures is complicated by the fact that several of the structural elements can be formed by more than one mechanism.

Offen and Kline (1975) proposed a model to explain the structures observed during the bursting cycle from the near wall. This was based on a large number of visualisation studies and used the passage of a horseshoe vortex to account for the three varieties of oscillatory growth that had been observed. The lifting up of the wall streak from the sub-boundary layer was a consequence of an upswelling separation, or of a rollup of the vortex. The inrush or sweep that preceded the burst was thought to be the passage of a previous burst from further upstream. This begs the chicken and egg question of how the initial burst forms. The sweeps were thought to bring about the adverse pressure gradient required to bring about the lifting of the streak or to provide the outer vortex.

Praturi and Brodkey (1978) also based their model on visualisation studies, but allowed for an interaction between the outer flow motion and the wall region. Transverse vortices were formed in the outer region at the shear interface between the high and low speed regions. These outer region vortices induce near wall ejections and streamwise vortices. Bulges in the boundary layer 'interface' result in the entrainment of freestream fluid which will act as a inrush.

The interest in the phenomenon of bursting to this study is in the characteristic frequency and volume of the ejection. Rao et al (1971) found that over a large range of Reynolds numbers the characteristic value for the mean interval between bursts scales with the outer, rather than the

inner variables, even for the wall or inner layers. Rao et al (1971) made their measurements in air with hotwire anemometer techniques, in contrast to Kline et al (1967) who used hydrogen bubble visualisation in water.

Rao et al (1971) found that a scaling of the burst period with the purely outer variables U/δ^* performed well, but this was found to depend on the Reynolds number. Instead, a mixed scaling was proposed, using inner variables for the transverse spatial scale and outer for the time, leading to:

$$\frac{U\, u^*}{\nu\, \delta^*\, F} \qquad \text{--- (3.D.36)}$$

as the relevant parameter, where:

F = the burst rate per unit span
U = freestream velocity
δ^* = the displacement thickness
u^* = the friction velocity
ν = the kinematic viscosity

This was found to apply equally well to unconstrained flow and fully developed duct flow.

Blackwelder and Haritonidis (1983) determined typical burst frequency of $f^+ = 0.0041$ at $y^+ = 15$ where:

$$f^+ = \frac{f\,\nu}{u_T^{\,2}} \qquad \text{--- (3.D.37)}$$

and

$$y^+ = \frac{u_T}{\nu} \qquad \text{--- (3.D.38)}$$

Blackwelder and Haritonidis (1983) suggested that the bursting frequency scaled on inner variables (the shear velocity u_T, and the kinematic velocity ν) rather than on the outer variables of the freestream velocity and the boundary layer thickness.

Meek and Baer (1970) give the normalised period of the wall boundary layer bursting as $T^+ = 17$ at Reynolds numbers (based on the freestream velocity) of above 10^4. This was based on measurements made on air and various liquids, including ethylene glycol. The scaling was done with respect to the shear stress at the wall τ_w, the friction velocity u^* and the kinematic viscosity.

$$T^+ = u^* \sqrt{\frac{T}{\nu}} \qquad \text{--- (3.D.39)}$$

where

$$u^* = \sqrt{\frac{\tau_w}{\rho}} \qquad \text{--- (3.D.40)}$$

T is the sublayer growth period

The means of predicting the burst frequency has not been agreed on, as recently as 1991: Falco (1991) stated: "... our knowledge of the parameters that govern the period between the bursts of high Reynolds stress in the wall region, which would shed light on the mechanism that maintains the turbulence is unsatisfactory. Inner scaling is currently preferred, over the narrow range of commonly obtained laboratory Reynolds numbers but it is unlikely to hold at high Reynolds numbers"

3.E PRESSURE DROP THEORY

As has been mentioned, the performance on the cyclone is determined by both the collection efficiency and the pressure drop, with equal importance. The loss of pressure across the cyclone determines the power requirements ($H = Q.\Delta P$) and hence the operating cost. A cyclone with a high efficiency may have a high pressure drop, meaning that a less efficient geometry with a lower pressure drop may be preferred, using a smaller diameter or operating in series . This thesis does not extend to the stage of proposing improvements in the modelling of collection efficiency, instead the fundamental flowfield structure of the cyclone has been investigated, with a view to later developments. The results from this study have been incorporated in a design report on the prediction of cyclone pressure drop (Abrahamson, 1992). This section will review the literature on cyclone pressure drop prediction, and draw on the analysis of Abrahamson (1992).

The basic principle that underlies the understanding of the pressure in the cyclone is expressed by the Bernouilli equation , and this has been used in many theoretical models of the pressure drop. The total pressure is comprised of static and kinetic components:

$$\frac{P}{\rho g} + \frac{v^2}{2g} + h = \text{constant} \qquad \text{--- (3.E.1)}$$

A transferral of energy from the kinetic to the static form is possible, and this illustrates the importance of specifying the location of the pressure tappings. The position of the tappings has an effect on the measured pressure drop, which complicates the comparison between different studies. In particular, the exit flow still has a significant swirl velocity component, which is generally not recovered, and the pressure reading at the wall is not necessarily representative of the average pressure at that location. The swirl in the exit has been reported to persist for 27 diameters downstream (First, 1949), and Loeffler and Meissner (1973) have calculated that the swirl still has 1% of the original value at a distance of 146 diameters downstream.

When two cyclones of different geometries are being compared there may be a difference in the strength of the swirl in the gas exit. For example, the exit spin of a cyclone in which the vortex is stretched out may be reduced compared with that found in the exit of a cyclone with a shorter vortex length. The difference between the pressure at the wall and the centreline will be less for the long cyclone for this case, but more importantly, the position of the average pressure may be different. In the example shown below the picture that is formed of the cyclone pressure drop by comparing the wall pressure may be the opposite of the actual pressure drop.

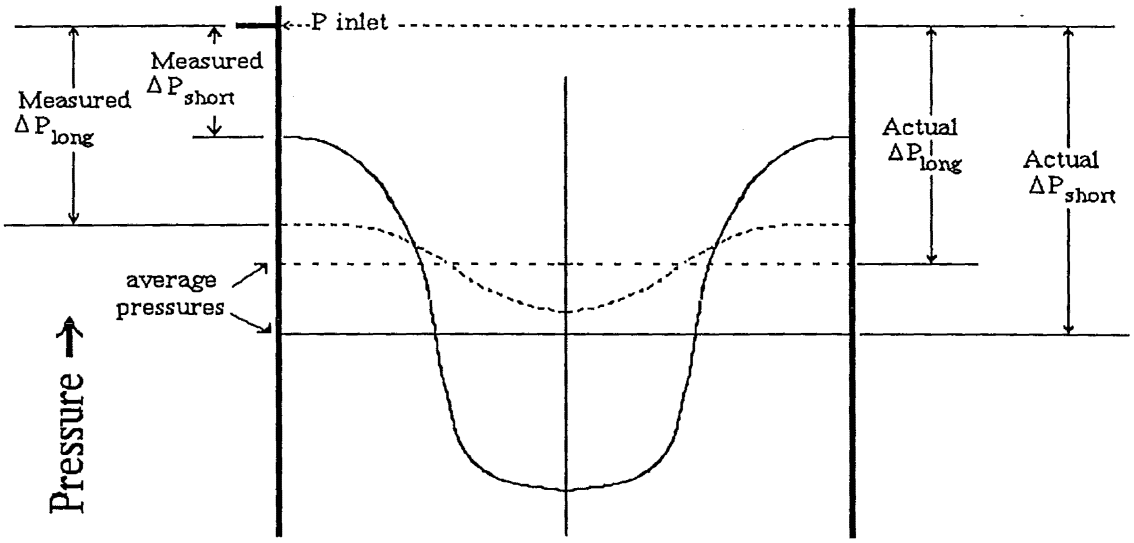

Figure 3.E.1: Effect of the gas exit pressure profiles on the apparent DP

When two different cyclone geometries are being compared there may be a difference in the strength of the swirl in the gas exit. For example, the exit spin of a cyclone where the vortex is stretched out may be reduced compared with that found in the exit of a cyclone with a short vortex. The difference between the pressure at the wall and the centreline will be less for the long cyclone in this case, but more importantly, the position of the average pressure may be different. In the example shown above the picture formed of the cyclone pressure drop by measuring the wall pressure may be the opposite of the actual pressure drop. .

The pressure drop across the cyclone has been shown by numerous workers to be dependent on the geometrical proportions of the cyclone, and on the inlet velocity. The pressure drop is found to be directly proportional to the dynamic pressure, which for convenience is based on the average inlet velocity. The dimensionless ratio of the pressure drop to the inlet velocity head is termed the Euler number, ξ:

$$\xi = \frac{\Delta P}{0.5\ \rho\ V_{in}^2} \qquad \text{--- (3.E.2)}$$

This will be used throughout this thesis to compare pressure readings made at different flowrates.

For tappings in the inlet close to the entrance, and in the exit close to the roof, the overall pressure drop Euler number was reported by ter Linden (1954) to range from 14 to 17.5 for most industrial cyclones. The Stairmand High efficiency design has a loss of 5 inlet velocity heads in the exit at roof level.

Experimental studies of the pressure drop have been reported by Shepherd and Lapple (1939, 1940), ter Linden (1949, 1954), Stairmand (1949), Alexander (1949), Barth (1954, 1956), and Muschelknautz (1972); Vatistas et al (1989); Ogawa (1987); Abrahamson (1992); Dirgo and Leith (1985) and Hoffmann et al (1992)

Kim and Lee (1990) examined a nine small cyclones, with barrel diameters of 22 to 41mmØ with flowrates of 8.8 to 18.4l/min. The investigation of the pressure drop showed good

agreement with the theory of Barth (1956). Varying the ratio of the gas exit diameter to the cyclone barrel diameter showed a minimum in the pressure drop occurred for a value of the ratio of about 0.5. Tager (1971) also noted the strong effect of this ratio on the pressure drop. A decrease of D_x/D_B from 0.45 to 0.3 leads to a doubling of the drag, while an increase from 0.45 to 0.6 halves the drag.

Troyankin and Baluev (1969) noted that the Euler number for the cyclone overall pressure drop fell with an increase in length. Troyankin and Baluev (1969) proposed an empirical formula for the Euler number that takes account of the length L, wall roughness Δ, and geometry. This was for a cyclone chamber with multiple tangential inlets down the length.

$$Eu \frac{(77/n_c + 88)\,(1.28 - 0.28\,\Delta)\,[66.7 + 2.67(h/b)^{1.63}}{L^{0.273}\,\psi^{1.43}\,(1+d)^2}) \times \left(\frac{1.9}{\sqrt[3]{Tg/Tin}} - 0.9\right) \quad \text{--- (3.E.3)}$$

ψ is the total cross sectional area of the inlets divided by the area of the cyclone.

In the published literature the most comprehensive review of the dependence of pressure drop on cyclone geometry was given by Ramachandran et al (1991). This presented data for 98 cyclones, and compared the pressure drops with the models of Shepherd and Lapple (1940), Alexander (1949), First (1949), Stairmand (1949), Barth (1956) and Dirgo (1988). The latter was an empirical model based on a statistical analysis of the entire data set, and proved to be the best performed of the six models. The earlier empirical model of First (1949) was also well-performed, despite taking account of fewer variables. The equation of Dirgo (1988) is given as:.

$$\xi = \frac{\Delta P}{0.5\,\rho\,V_{in}^2} = \Delta H = 20\left\{\frac{ab}{D_x^2}\right\}\left\{\frac{S/D}{(H_B/D)\,(H/D)\,(B/D)}\right\}^{1/3} \quad \text{--- (3.E.4)}$$

where: a, b are the inlet width and height respectively; D_x is the gas exit diameter; S is the distance that the gas exit extends into the cyclone; B is the diameter of the dust exit; H_B is the height of the cylinder and H is the overall height of the cyclone.

First (1949) had also included the length of the cyclone in the expression for the 'total pressure difference', F, after noting the decay of swirl energy along the cyclone length:

$$F = \frac{24\;a\,b\,D^{2/3}}{D_x^2\,(H_B.H_c)^{1/3}} \quad \text{--- (3.E.5)}$$

where H_c is the height of the conical section (= H-H_B). It can be seen that this neglects the dependence on the gas exit length and the dust exit diameter.

Measurements of the pressure drop are generally made in dust-free air, but the pressure drop is found to be reduced by the presence of dust. Hoffmann et al (1992) review the analyses that have been proposed to account for this. Yuu et al (1978) present measurements of the pressure drop reduction for dust concentrations between 0.2 and 300 g/m³. It was found that the pressure drop decreased to 70% of the dust-free value at the addition of the lowest dust concentration, and remained at this fraction for concentrations up to 50 g/m³. It was observed that over this range the dust rope on the wall retained the same width, and increased in depth with increasing dust loading. At about 50 g/m³ the dust rope suddenly widened to cover the

whole wall, and further decreases in the pressure drop occurred for increasing concentrations. Kelsall (1952) found that the pressure drop increases again for loadings above about 2000 g/m³, while Muschelknautz and Brunner (1967) found the minimum lay between 1000 and 10 000 g/m³. Parker et al (1981) also measured the pressure drop reduction down to low dust concentrations of 2 g/m³ but found that the decrease was less at low concentrations.

Briggs (1946) proposed an equation to empirically fit the pressure drop reduction that occurs for a given dust concentration, c g/m³:

$$\Delta P_{dust} = \frac{\Delta P}{1 + ac^b} \qquad \text{--- (3.E.6)}$$

where a and b are parameters to be fitted, and ΔP is the dust free pressure drop, that is reduced to a value of ΔP_{dust}. Comas et al (1991) fitted this equation to data they collected, as well as data from the work of Yuu et al (1978) and Parker (1981).

The mechanism by which the pressure drop is reduced is thought to be the slowing of the tangential velocity. Shepherd and Lapple (1939) attributed the slowing to the inertia of the particles passing through the gas stream having an equalising action on the momentum of adjacent layers. Yuu et al (1978) stuck particles to the walls of the cyclone and observed a similar, although less, reduction in the tangential velocity and pressure drop. Although the reduction in the tangential velocity results in A lowering of the centrifugal separating force, the efficiency does not necessarily decrease with increasing dust loadings, which has been attributed to the improvement in the agglomeration of particles.

The pressure drop has also been reduced by inserting a deswirler into the gas exit, to recover some of the swirl energy. Browne and Strauss (1978) present a design for a deswirler which was able to reduce the pressure drop of the Stairmand high throughput design by 22%.

Ramachandran et al (1991) report that the proportion of the predictions that were within 20% of the actual value was 67% for Dirgo (1988)'s equation; 64% for First (1949); 53% for Barth (1956); and 39% for Stairmand (1949). The best of these are clearly the empirical expressions, but these are still not sufficiently accurate for design purposes. The attempts to predict the pressure drop from a theoretical basis have had even less success, and these have been reviewed by Abrahamson (1992) from which the following is largely derived.

The pressure drop can be broken down into losses incurred in the inlet, the exit, that due to wall friction, the kinetic transferral between different radii, and the core dissipation. Of the total loss, Stairmand (1949) attributed one inlet velocity head to the expansion of kinetic energy at the inlet, and two velocity heads to the contraction into the outlet duct. Stairmand's simplified model indicates that 40% of the pressure drop occurs through swirl energy losses. Tager (1971) compared a range of types of cyclone chambers with gas exits at the same and opposite ends as the inlet; as well as through flow cyclones. Since a similarity dependence of the pressure drop on the exit to barrel diameter ratio was found Tager concluded that the aerodynamic drag of the cyclone chamber is determined almost entirely by the loss in the exit.

Shepherd and Lapple (1939) used Bernouilli's theorem with a term, F, to account for the mechanical energy loss due to friction.

$$\Delta H = H_{in} - H_{ex} = \frac{V_{ex}^2}{2g} - \frac{V_{in}^2}{2g} + F \qquad \text{--- (3.E.7)}$$

The exit pressure is an effective pressure, in order to take account of the presence of swirl as

noted above. The head and friction loss are expressed as velocity heads, and the friction loss is broken up into that incurred in the exit, and that in the cyclone chamber. The exit friction loss is calculated from the Fanning equation for fluid flow in a straight pipe.

$$F_{ev} = \frac{4 f L_e}{e} \left(\frac{A}{A_e}\right)^2 \qquad \text{--- (3.E.8)}$$

'e' is the cyclone exit diameter; f is the Fanning friction factor, taken as 0.0055.

The friction loss in the cyclone chamber is broken down into the following components:

- The regain of rotational kinetic energy
- Additional frictional losses in the exit (over and above straight flow)
- Wall friction in the chamber
- Inlet expansion
- The loss as kinetic energy of rotation in the chamber.

Only the latter two are considered to be significant. The inlet expansion loss is estimated from the geometry but is found to contribute only 10% to the total for most designs, and is neglected. The rotational kinetic energy loss is calculated by assuming that the transfer from the outer to the inner vortex is sufficiently gradual to incur no loss. It is assumed that none of the rotational energy in the inner vortex is recovered, and this constitutes the friction loss. Using the power law given by equation 3.B.1 with a value of 'n' = 0.5, this simplifies to:

$$F_{ev} = \frac{r_a}{\sqrt{r_o\, r_d}} \qquad \text{--- (3.E.9)}$$

where r_o is the radius of the zero axial velocity boundary; r_a is the radius at which the tangential velocity is equal to the inlet velocity; r_d is the inner radius of the inner spiral
The angle of the inner vortex helix to the tangential plane can also be calculated by:

$$\tan \alpha = \frac{0.238\ b.h}{r_a^{0.5}.r_o^{0.5}} \qquad \text{--- (3.E.10)}$$

Here b is the width of the cyclone entrance; h is the height of the cyclone entrance.

The analysis of Weber (1956) results in an expression for the cyclone Euler number:

$$Eu = \left(\frac{r_i}{r_e}\right)^2 \left(\frac{r_e}{r_c}\right)^2 + \left(\frac{a_i}{a_e}\right)^2 \left(\frac{r_e}{r_c}\right)^2 \qquad \text{--- (3.E.11)}$$

Tran (1981) estimates the energy loss attributable to shear action on the wall of the cyclone using an expression from turbulent pipe flow:

$$\tau = N_f\ (\rho/4)\ V_c^2/2 \qquad \text{--- (3.E.12)}$$

N_f is a friction factor, which is taken as 0.02 for typical wall roughness. Tran found that the wall loss makes a negligible contribution to the total mechanical energy loss. Tran suggests that the pressure drop can be attributed primarily to the transfer of kinetic energy of mean motion being lost in turbulent chaos.

Stairmand (1949) applied Bernouilli's theorem to a small control volume of fluid as it moved through the cyclone. The tangential velocity in the core was described as solid rotation, while in the outer vortex region the simple expression equation 3.B.1 was used, with the value of 'n' selected as 0.5. The energy loss that resulted from the element moving from the wall to the core radius was calculated, with the core radius taken as the position of the maximum tangential velocity . Stairmand's experiments on the cyclone vortex resulted in this core radius being taken as half of the gas exit radius, however it has been shown (for example, Iozia and Leith, 1988) that the core radius varies between cyclone geometries, particularly between those with differing inlet areas.

The description of the tangential velocity was improved by Alexander (1949) using the same equation, but with 'n' varying as a function of the cyclone size and gas viscosity. The core radius was again taken as half the exit radius, but more account was taken of the losses at the walls and in the core itself. The exit calculations allowed for the rotational energy lost through the exit.

Barth (1956) made use of detailed velocity measurements in the gas exit, although these were from a non-standard design with the diameter increasing conically in the direction of the flow. The relationship between the inlet velocity and the velocities at the wall in the barrel was determined and the frictional wall losses calculated, but the core dissipation was neglected. The losses associated with the radial inflow of gas from the wall to the radius of the exit tube was expressed as the friction on an imaginary wall placed between these two radii, and was dependent on the value of a friction factor. The treatment of the exit tube losses assumed the flow was in an infinitely annulus around a central stagnant core, which Barth had observed in his experiments. This exit tube analysis was the most realistic of the models of cyclone pressure, and it has been extended by Abrahamson (1992).

Vatistas, Lin, and Kwok (1986) proposed a model for the pressure drop in a vortex chamber, in which the gas leaves through the floor of the device at the opposite end to the tangential inlets. The analysis makes use of the energy equation to show that there must be a certain core diameter at the exit that will give a minimum for the pressure drop for given values of the flowrate, the inlet area, the exit orifice diameter and the vortex circulation. Vatistas et al (1986) go on to suggest that the flow will adjust the core radius at the exit to achieve the minimum pressure drop. The theory agrees well with the pressure drop data presented by Vatistas et al (1986), but Abrahamson (1992) found that the predicted value only agreed with 2 cases out of seven investigated. The two that agreed were for cyclones with long exits, but the theory is developed for a short exit tube. Escudier (1979) also assumed that the core size would adjust to maximise the flow for a given pressure drop.

A different approach to the previous methods was taken by Ogawa (1987), who used the mechanical energy balance equation applied to a finite control volume for a steady state flow. If the pressure is multiplied by the velocity and integrated across the cross sectional area, then the mechanical energy balance relates the net change in this area integral between the inlet and exit to the dissipation within the cyclone control volume. Abrahamson pointed out that Ogawa (1987) had neglected the flux of kinetic energy across the surface of the control volume, and that the correct pressure to use in the integral was the total pressure. The velocity component normal to the surface is used, resulting in the equation:

$$\int_{S_i}(P_i + \tfrac{1}{2}\rho_i V_i^2)\,\mathbf{V}_i.\,d\mathbf{S} \;-\; \int_{S_x}(P_x + \tfrac{1}{2}\rho_i V_x^2)\,\mathbf{V}_x.\,d\mathbf{S} \;=\; \mu \int_{vol}\gamma^2\; d(vol) \qquad \text{--- (3.E.13)}$$

It can be assumed that the inlet kinetic term can be simply calculated from the linear inlet velocity, but the exit kinetic term will have significant contributions from both the axial and the tangential velocity components. Abrahamson (1992) uses this pressure-velocity integral approach to evaluate the pressure difference across the cyclone. The dissipation in the core of the cyclone and the exit are calculated separately by modified approaches. This approach will be outlined in more detail below, taken from a report by Abrahamson (1992).

The pressure drop calculations of Abrahamson (1992)

The mechanical energy balance equation that forms the starting point is reproduced below in the corrected form given by Abrahamson (1992):

$$\int_{S_1}(P_i + \tfrac{1}{2}\rho_i V_i^2)\, \mathbf{V}_i \cdot d\mathbf{S} - \int_{S_x}(P_x + \tfrac{1}{2}\rho_i V_x^2)\, \mathbf{V}_x \cdot d\mathbf{S} = \mu \int_{vol}\gamma^2\, d(vol) \qquad \text{--- (3.E.14)}$$

To describe the tangential velocity component profile, Abrahamson uses the Burgers vortex rather than the Rankine combined vortex profile that Ogawa (1987) used. The Burgers equation is compared with the experimental velocity profiles in sections 5.C.1 and 6.B1 of this thesis. The expression can be written as:

$$V_\theta = \frac{\Gamma_o}{r}\left[1 - \exp\{\frac{-ar^2}{2\nu_T}\}\right] \qquad \text{--- (3.E.15)}$$

where: ν_T = is the turbulent or eddy viscosity.

Γ_o is the circulation at large radius, $\lim_{r \to \infty} V_\theta \cdot r$ which in the cyclone is approximated by the circulation at the wall, since this is sufficiently far from the core.

The vorticity γ that appears in the mechanical energy balance is dominated by the axial component, and the other components will be neglected. If the axial gradient of the radial velocity is neglected, the axial vorticity is a function of only the tangential velocity, and is given by:

$$\gamma = \frac{\partial V_\theta}{\partial r} + \frac{V_\theta}{r} \qquad \text{--- (3.E.16)}$$

for the Burgers vortex the axial vorticity is $\gamma = \dfrac{a.\Gamma_o}{\nu_T}\exp\{\dfrac{-ar^2}{2\nu_T}\}$ --- (6.D.5)

The vorticity for the Burger's vortex is concentrated in the core, which means that the effective volume of integration is a small part of the cyclone radius. Abrahamson assumes that the turbulent viscosity ν_T is constant over the integration volume since the turbulence is observed to be roughly uniform across the core. The tangential velocity is nearly independent of the axial location, hence the integration over the volume of the vortex is a function of the radius alone, multiplied by a constant vortex length, L. The right hand side of equation 3.E. **, which is the dissipation rate, can then be written as:

$$DS_{core} = \mu_T . L \int_0^\infty \gamma^2 .\, 2\,\pi\, r\, dr \qquad \text{--- (3.E.17)}$$

The contribution to the pressure drop Euler number is:

$$\Delta\xi_{core} = \frac{DS_{core}}{0.5\,\rho\, V_{in}^2} \cdot \frac{1}{Q} \qquad \text{--- (3.E.18)}$$

Evaluating the Burgers' profile exponential term between the radial limits gives a value of unity,

hence the pressure drop number contribution for the Burgers profile is:

$$\Delta\xi_{core} = \frac{2\,\mu_T}{Q}\,\frac{\pi\,L\,a\,\Gamma_o^2}{\nu_T\,\rho\,V_{in}^2} \qquad \text{--- (3.E.19)}$$

As shown in figure 3.B.1 the parameter 'a' in Burgers' profile can be related to the cyclone geometry and flow by considering the average radial velocity over the imaginary cylindrical extension of the vortex finder. This gives:

$$a = \frac{2\,Q}{\pi\,D_{in}^2\,L} \qquad \text{--- (3.E.20)}$$

With this substituted into the equation 3.E.19 the contribution to the Euler number is :

$$\Delta\xi_{core} = \frac{4\,\Gamma_o^2}{V_{in}^2\,.\,D_x^2} \qquad \text{--- (3.E.21)}$$

The circulation Γ_o can be estimated by the circulation at the wall (outside the boundary layer) $R_w.V_{\theta w}$ since the wall is generally far enough away from the core to act as the infinite asymptote. This circulation has been found to decrease down the length of the cyclone, in contrast to the frequently made assumption of constant vortex strength. If Γ_o is the local circulation at an axial location z, then the total dissipation becomes an integral over the length. The radial inflow may also vary along the cyclone length, expressed as a fractional flow q per metre length. The contribution to the Euler number is :

$$\Delta\xi_{core} = \frac{4\int_0^L q\,.\,z.\,\Gamma_o^2\,dz}{L\,V_{in}^2\,.\,D_x^2} \qquad \text{--- (3.E.22)}$$

The dependence of the circulation on the length is shown in section 6.B1, where the square of the circulation is plotted against the distance from the gas exit lip, z. A linear expression for this variation appears adequate, written as:

$$\Gamma_o^2 = \Gamma_{oe}^2[1 - gz] \qquad \text{--- (3.E.23)}$$

The slope g is the fractional decrease in the square of the circulation with unit length of the vortex. Values of the dimensionless group 'gD' can be obtained from the graphs in section 6.B1, and other measurements have been made by Smith (1962a) and Separation Processes Service, Harwell (unpublished). These show a dependence on the swirl Reynolds number which can be summarised as:

$$gD = 4.6 \times 10^{-5}\,Re_s^{0.71} \quad \text{for } Re_s < 1.8 \times 10^5$$
$$gD = 0.24 \quad \text{for } Re_s > 1.8 \times 10^5 \qquad \text{--- (3.E.24)}$$

These rates of spin decay are considerably higher than the values found for straight tube decay, such as the results of Ward-Smith (1980).

Allowing for the variation of the circulation and inflow down the length, as well as an amount Q_{by} in the roof short circuit flow, the expression for the Euler number contribution becomes:

$$\Delta\xi_{core} = \frac{Q_{by}}{Q}\,.\,Eu + \left(1 - \frac{Q_{by}}{Q}\right)\left(1 - \frac{g}{2}L\right)Eu \qquad \text{--- (3.E.25)}$$

where Eu is the simple expression for the Euler number given by equation 6.F.7, which can be approximated by

$$\Delta\xi_{core} = \left(\frac{D.\,V_{\theta w}}{D_x\,.\,V_{in}}\right)^2 \qquad \text{--- (3.E.26)}$$

The test of the consistency of this theory is to plot ($\Delta\xi_{core}$ /Eu) versus the length of the vortex L. If the roof short circuit flow is zero then a straight line of slope g/2 should be obtained. For non-zero bypass the slope will be a little less.

Chapter

4

EXPERIMENTAL TECHNIQUES

A brief summary is given here of the experimental techniques utilised in this study. Fuller details are contained in the Appendices in Chapter 10.

4.A. CYCLONES USED:

Most of the measurements were made on a 140mmØ cyclone in the laboratory but velocity profiles were also measured in two industrial scale cyclones with barrel diameters of 750mmØ and 2090mmØ. These cyclones were all Stairmand HE designs, although the 2090mmØ cyclone had the dust exit extended at constant diameter for $1.5D_{dx}$ and had some air taken off the base. Both of the larger cyclones were operated at positive pressure, whereas the laboratory cyclone was operated by suction at the exit. The flowrates used for most of the measurements were V_{in} =18m/s in the 750mmØ and 2090mmØ cyclones, and 23m/s in the 140mmØ cyclone.

The laboratory cyclone was made in modular form which allowed the geometry to be varied by adding in sections in the barrel, or by exchanging or extending the cone. The geometries studied are shown as scale drawings in Appendix 10.A. Initially four geometries were studied, and labelled 'Longest', 'Second Longest', 'Standard' and 'Shortest'. These were not the longest or shortest geometries examined, but the labels have been retained. As all the flanges were made to the same pattern the sections could be interchanged. A scroll exit geometry could be approximated by using one of the inlet sections inverted and attached to the exit. To investigate the effect of a diverging gas exit the long cone could be bolted to the roof of the standard geometry. Flow visualisation was made possible by constructing the cyclone out of "Perspex", a clear polymethylacrylate.

A few measurements were carried out on a 220mmØ metal Stairmand HE cyclone. This is referred to as the 'Heat exchanger cyclone' as it was attached to a laboratory heat exchanger. It was run at positive pressure. As a final check on some of the results obtained a 300mmØ Stairmand High efficiency design cyclone constructed from steel was used.

4.B. AIR SUPPLY:

So that tracers could be introduced easily into the cyclone, the laboratory cyclone was operated by inducing a low pressure at the exit. This was achieved by using air from a Rootes blower to drive a venturi air ejector, the design of which is detailed in Appendix 10.B. The larger cyclones were operated by blowing air through the inlet and exhausting to the atmosphere. Both of these cyclones featured a sharp bend in the inlet duct shortly before the entrance to the cyclone, see for example figure 10.A.3 on plate 5 in the Appendices.

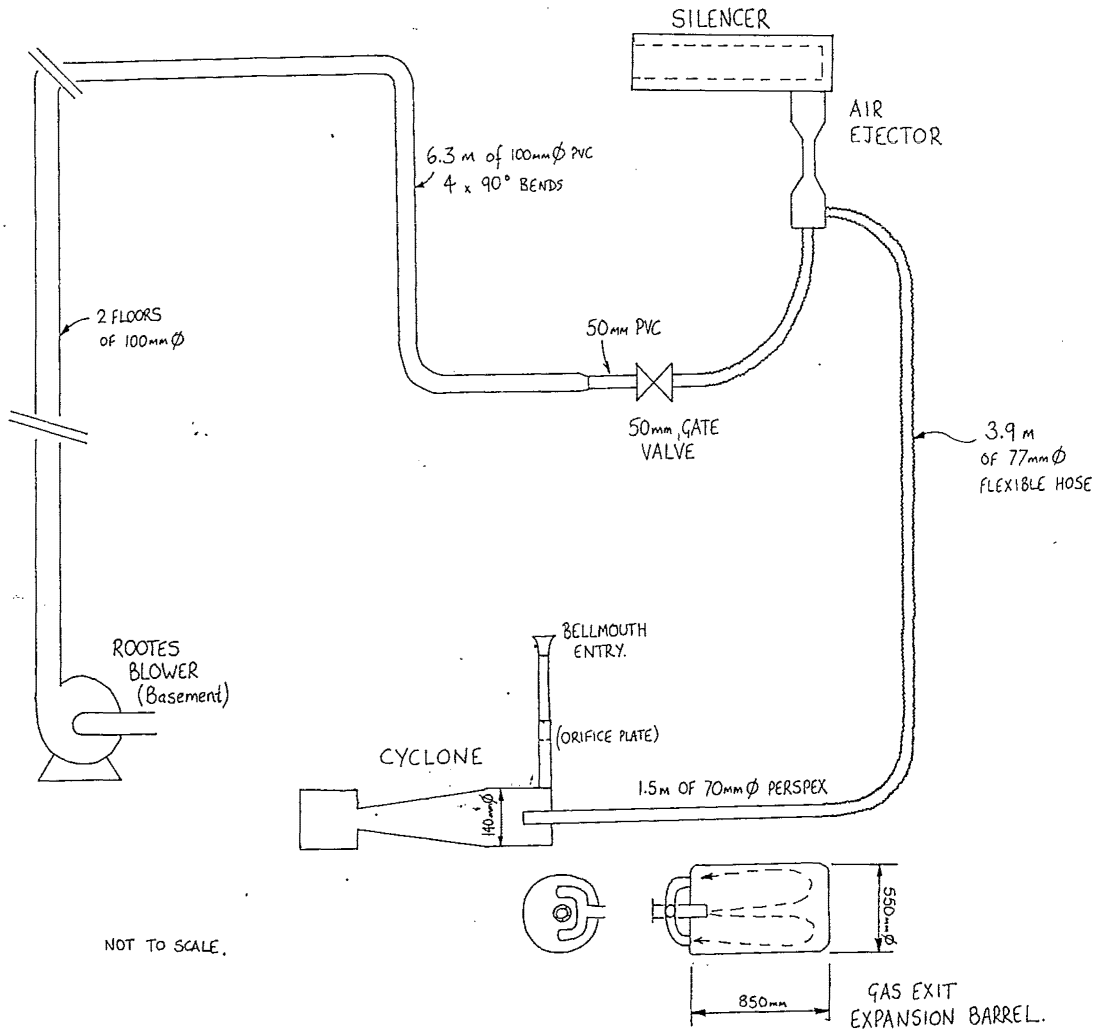

Figure 4.1: Air supply arrangement for the 140mmØ laboratory cyclone.

4.C. FLOW METERING:

In early experiments the volume flow was estimated with a square orifice plate in the inlet, constructed to a standard design. Later this was replaced by a bellmouth entry, constructed

according to the principles given by Ito, Watanabe & Shoji (1985b). To check the design flow this was calibrated against a pitot tube traverse, which gave readings that were 10% low (Abrahamson, 1988). The bellmouth entry was then used to calibrate the orifice plate, showing that the orifice plate design equations underestimated the flow by up to 40%. These flows have been corrected, and the bellmouth was used for all quantitative runs thereafter. A second bellmouth entry was constructed when the loan of the original one expired. This second bellmouth was calibrated against the re-calibrated orifice plate. The orifice plate was used for dirty experiments (such as with the Helium Bubble tracers), where the bellmouth tappings could become clogged. Pressures were measured on an Airflow Type 4 inclined tube manometer, or for some later measurements, a digital manometer (an Air Neotronics micromanometer MP6KSR).

4.D. PROBES USED:

A 4-hole Pitot cylinder was used to obtain the tangential, axial and radial velocity components of the flowfield in the various cyclones. This probe was built in the department, along the lines detailed in Winternitz & Ramsay (1963) The scatter in the radial velocity component was reduced in the larger cyclones, where the radial pressure gradient was small compared with the spacing of the probe holes in the radial direction. Insertion of the probe in to the 140mmØ cyclone caused a reduction in the cyclone pressure drop. This led to the inlet flow rising, but this had little effect on the profiles, and has been corrected for.

A Hot film anemometer and lineariser was built in this department, following the principles given by Sakao (1980), Wyngaard & Lumley (1967), Weidman & Browand (1975) and Miller (1976). The HF probes used were TSI 45° hot film probes of 60, 20 or 10 micron diameter. The total velocity obtained was not resolved to components as the yaw and pitch angles could not be obtained accurately.

A static tube was used to measure the static pressure up the axis of the 140mmØ cyclone. This probe was 5mm in diameter and had a ring of holes around the circumference 7mm back from the hemispherical tip. The probe was inserted progressively from the base and measurements were made (at 5 or 10mm intervals) of the static pressure at the axis relative to the side wall pressure of the bin, 30mm below the dust exit. Using this reference pressure kept the pressure difference within the manometer range, and the insertion of the axial probe was not observed to affect this reference pressure. For some experiments the reference pressure was taken to the cone wall near the junction with the barrel section, in order to avoid the influence of a change in the bin pressure. The pressure difference was converted to an Euler number based on the inlet velocity in order to compare results at different flowrates.

4.E. VELOCITY PROFILE TRAVERSE LOCATIONS:

Radial measurements were made through holes drilled in the walls of the cyclone. As far as possible these traverse locations were kept the same between the different scales of cyclones, and the respective positions are tabulated in Appendix 10.A. The measurement location varies by up to 2.5mm in the axial direction as the probe is rotated with the change in yaw angle across the radius. In the larger cyclones the probe was not always exactly aligned with the

geometrical diameter. Because of the type of bin employed in the 750mmØ cyclone, the traverses could not be done in the lower two locations (Ports 3 & 4).

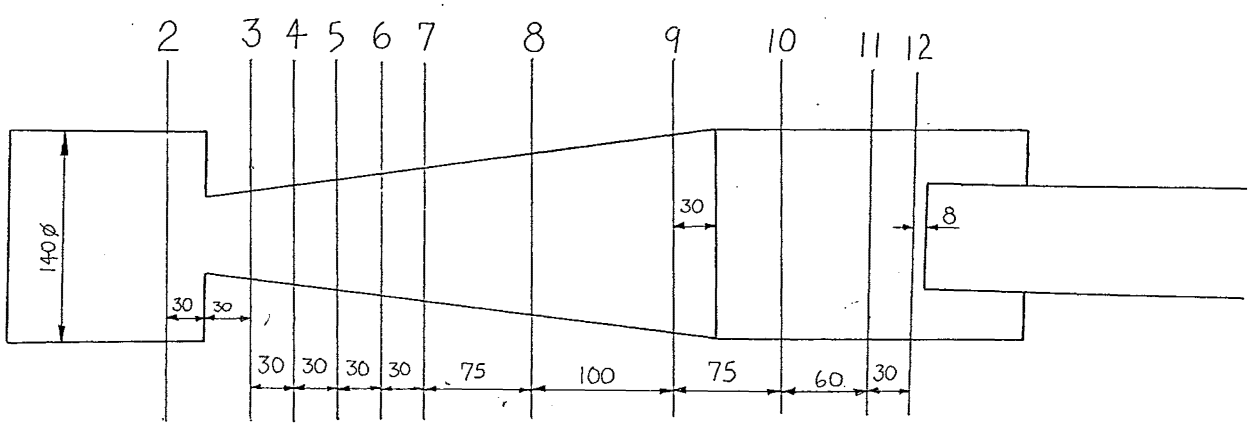

Figure 4.2: Location and labelling of the traverse locations in the cyclones.

The probes were inserted from the wall as far as the centreline from opposite sides of the cyclone and at right angles to the inlet tangent.

4.F. FLOW TRACERS:

The best results were obtained with Helium bubble tracers. These are 2-3mm soap bubbles filled with helium, such that they have close to neutral buoyancy in air. The bubble generator was built in the department, similar to the commercial unit produced by Sage Action Inc.(1986) The helium bubble tracers are robust, and follow ambient air movements well

The buoyancy varied from bubble to bubble and could not be quantified by measuring the rise rates in the atmosphere as the centrifugal acceleration in the cyclone was 1300 to 5000 times that due to gravity. Therefore it was not feasible to use a classifier relying on gravity to ensure the neutrality of the tracers' buoyancy before they were injected into the cyclone. Bubbles were produced both lighter and heavier than air at the same time. When the flow was cut abruptly tracers in the bin moved slowly along the axis, showing they were neutrally buoyant with respect to lower body accelerations such as gravity.

Because of the separating action of the cyclone those heavier than air were quickly destroyed against the wall. Some tracers were observed in the outer vortex and occasionally reached the bin by this path. The more commonly observed route was for the tracers to move in to the cyclone axis in the upper cone, or earlier. Presumably those not destroyed against the wall were slightly lighter than air and were driven to the axis more quickly than the actual air movement by the pressure gradient. Hence the radial inflow velocity could not be estimated with the Helium tracers, but once on the axis, the movements would indicate the actual, axial movements of the gas.

The tracer movements were fast, which made it difficult to record. The cyclone was illuminated axially with a slide projector to give a streak path, and also strobed with a triple flash unit to allow the velocity to be estimated. The bubble image consisted of two bright spots inside the

bubble outline, as shown in figure 10.H.3, plate 6B, with the position of the bubble centre located midway between the spots. These spots were aligned along the light path, which allowed the 3 strobe flashes to be distinguished. The streak path showed up as two parallel lines. A video was recorded to capture some of the dynamic motions of the bubble tracers, this is appended to the thesis.

Cotton streamers were constructed by threading beads on a wire and attaching 10mm long pieces of cotton. These were able to rotate and indicate the air movements.

4.G. PRESSURE FLUCTUATIONS:

Wall pressures at two locations in the cyclone were sampled simultaneously using a Macquisition unit. This is a serial-parallel data acquisition unit manufactured by Strobe Electronics of Wellington, N.Z. The data was Fast Fourier Transform analysed to show any dominant frequencies, and then the cross correlation was calculated to show if there was a connection between the locations. The correlation coefficient was close to 1.0 for all values of the lag. Moving averages and zero mean data were used to try and dampen out the noise in the data. It was found that there was a strong fluctuation of 71Hz in the suction line.

Chapter

5

RESULTS:

INDEX:

5.A. FLOW VISUALISATION:

The path of the air in the cyclone was examined with various tracers, including shredded paper, wood fibre, cotton streamers and helium filled soap bubbles. The simple, double vortex flow theory was confirmed for the steady state or time averaged flowfield, but superimposed on this were more complex motions that are not taken into account by current theories.

Air entering the tangential inlet is forced into a downwards spiral in the annulus between the barrel wall and the gas exit outer wall. This annular flow is continued below the level of the gas exit lip and demarcated by a core vortex that is spinning upwards and out the gas exit. This inner vortex is fed continuously down its length by air moving in from the outer vortex. Dust is carried into the bin along the walls by a small remainder of the flow (approximately 10% of the inlet flow enters the bin). The slowing of the air in the expanded volume of the bin allows the dust to disengage from the air. The inner vortex of clean air can be seen to start from the bin base, accumulate extra flow with height, and travel along the axis of the cyclone and out the gas exit tube.

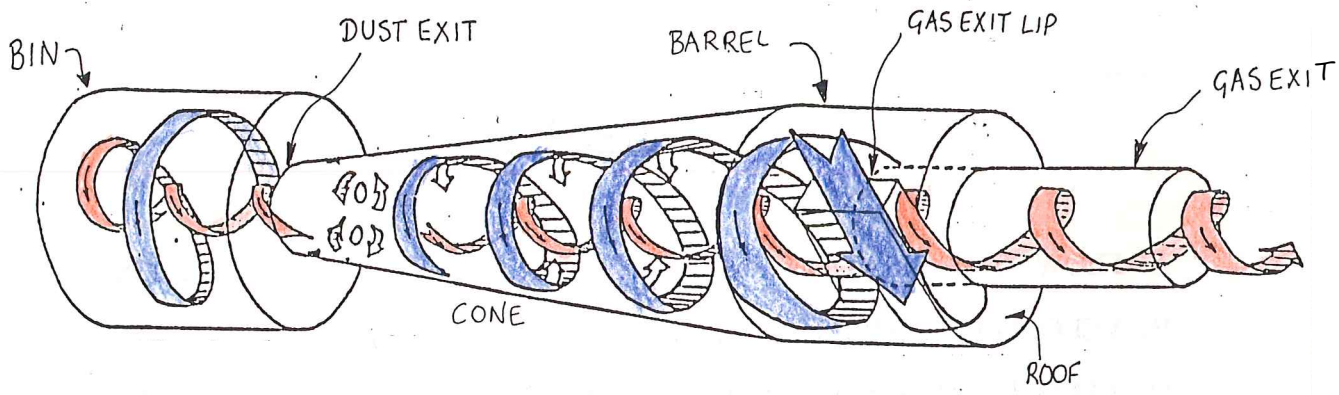

Figure 5.A.1: Schematic diagram of the airflows in a reverse flow cyclone

From steady state, as well as dynamic measurements, the core vortex was found to be larger than the gas exit in the upper barrel region and of roughly constant diameter lower in the cyclone. The boundary between the outer and inner vortices roughly corresponded to the position of the maximum tangential velocity. The core vortex was not aligned with the geometric axis, but described a helix down the cyclone for both time averaged and dynamic observations.

The most striking observation was the existence of a third vortex flow that travelled close to the geometric axis inside and against the inner vortex, connecting the far end of the gas exit and the bin base. This flow was intermittent and dependent on the cyclone geometry. The major inner vortex travels continuously towards the gas exit, around the outside of this reverse flow. Stagnation points formed and dispersed at various axial locations.

Overleaf: Figure 5.A.2 (Plate 1) and Figures 5.A.3, 5.A.4 & 5.A.5 (Plate 2). All of these show examples of the near-axis reverse flow reavealed by the helium bubble tracer technique.

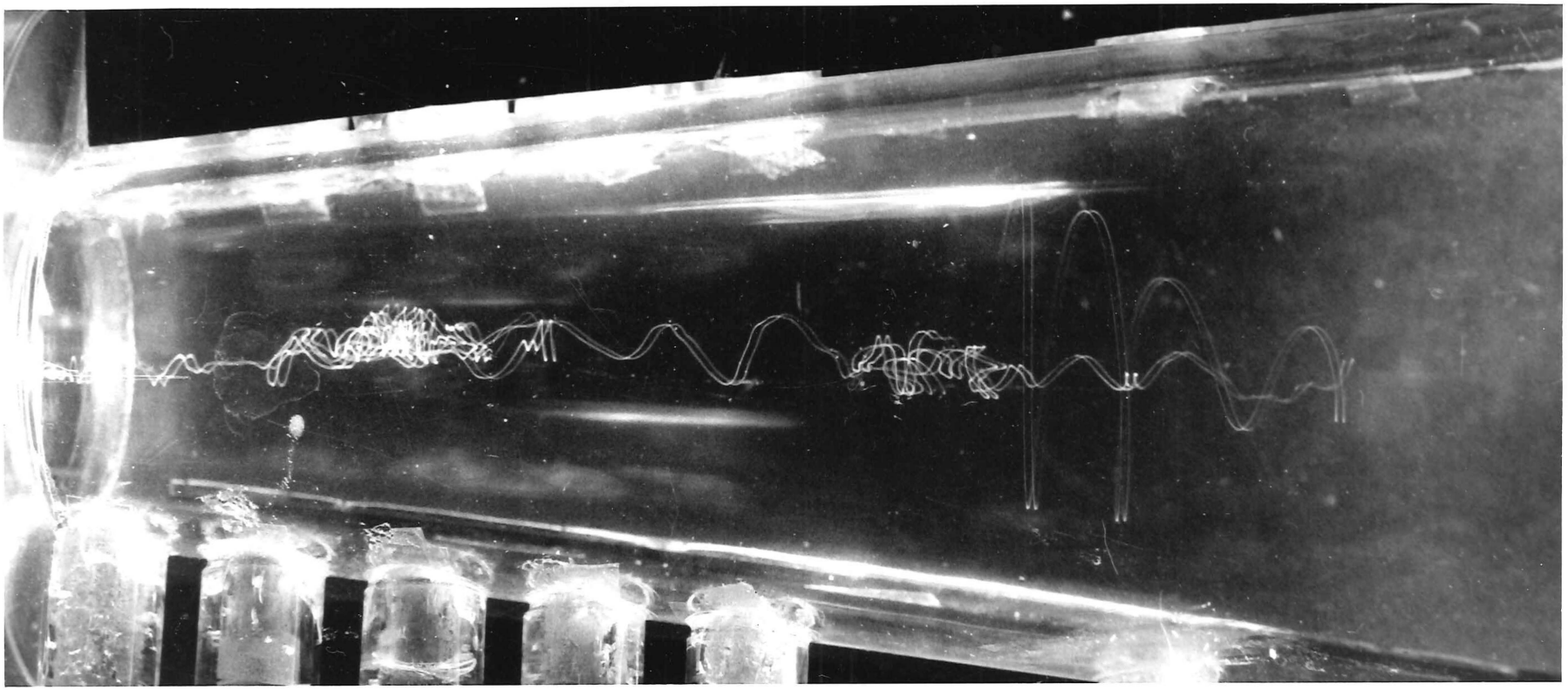

Plate 1: A helium bubble tracer demonstrating the near-axis reverse flow
in the 140mmØ Stairmand High Efficiency cyclone. (Inlet velocity: 15 m/s)

Illumination of the bubble tracer gives 2 spots of light inside the bubble outline that are aligned with the light beam, and are inside the bubble outline. The tracer path is indicated here by the twin streaks from axial illumination with a slide projector. The strobe flashes are not clearly visible in the photograph, but they establish the direction of flow near the axis as being towards the bin. The tracer initially spirals inwards in the direction of the gas exit, but then doubles back on itself. The inner spiral towards the bin is interrupted by two regions of strongly recirculating motion. The axial velocity of the tracer determined in the relatively straight section of flow is of the order of 60m/s, and as much as 90% of the time spent in this photograph was spent in the two recirculation zones.

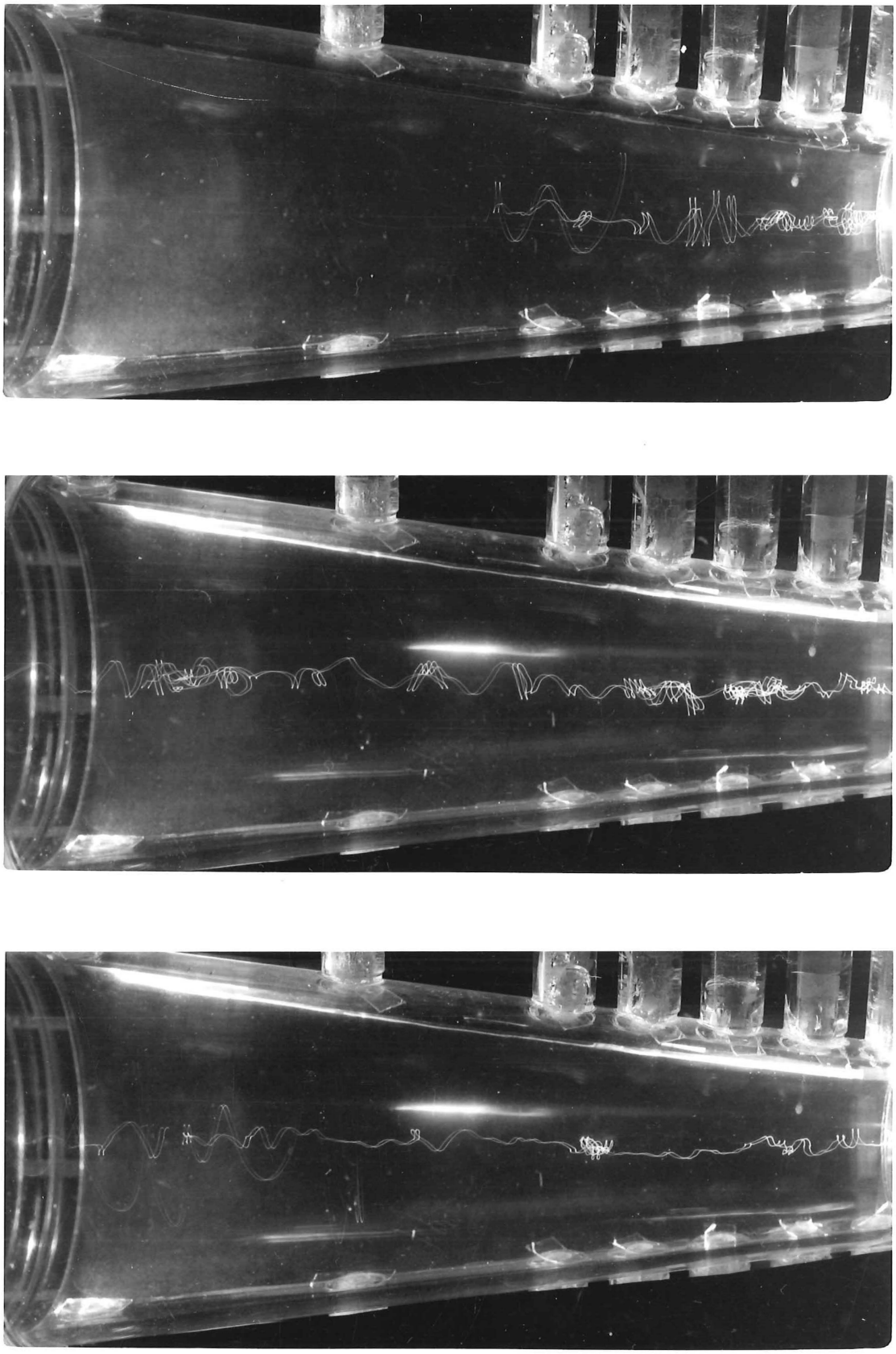

Plate 2: Further examples of the near-axis reverse flow shown by helium bubble tracers in the standard Stairmand High efficiency geometry at an average inlet velocity of 15 m/s.

Figure 5.A.2 is a typical example of this behaviour - it shows the path of a single tracer tightening in from the outer vortex, then reversing towards the bin and encountering two recirculation zones along the way. There is a similarity between the structure of these zones and the internal structure of a vortex breakdown 'bubble' as recorded by Faler and Leibovich (1977), and as simulated numerically by Spall, Gatski and Ash (1990). In Plate 1 the strobe flashes have been indicated on the mylar overlay. The flashes were strobed at 2000Hz, giving a period of 0.5 milliseconds between successive flash sequences. The interval between the triple flashes was 43 microseconds, which should give a spacing ratio of 5.8 between the flashes within a group compared with the return period of the group. The low illumination afforded by the flashes at this cycle rate means that only one of the flashes can be seen clearly. Measuring the distance between successive strobe events of this flash shows that the axial velocity in the regions of relatively straight flow is 60m/s, or four times the average inlet velocity of 15m/s.

The helium bubble tracers also revealed a more long term trap of tracers in the gas exit just above the level of the roof. This was difficult to obtain a still photograph of, as there were usually many tracers in the region at once, and the tracers overlapped. The nature of the flow is shown well by the video, which also shows the effect of inserting probes on the position of the recirculating tracers. The helium bubble tracers could not be used to indicate radial movements in the cyclone because of the high radial pressure gradients that caused the bubbles to move to the centre faster than the air velocity.

The cotton streamers showed a steady flow direction for the outer vortex, but as the axis was approached there were increasing fluctuations between the forward and reverse directions and near the axis the cottons spun continuously. An example of this behaviour is shown in Plate 3 (figures 5.A.6 and 5.A.7), which are photographs of the cotton streamers frozen by a high speed flash. Figure 5.A.6 (Plate 3A) is taken in the 140mmØ standard Stairmand High Efficiency cyclone, while figure 5.A.7 (Plate 3B) is in the same cyclone but with a conical extension of the dust exit end of the cone by 90mm. Both figures were taken at an inlet velocity of 23m/s. Near the axis in Plate 3A, on the first and third wires from the right, the cottons show a flow direction towards the bin, whilst elsewhere in the core the direction is towards the gas exit. At other times the cottons showed a more extensive reversal involving 4 or 5 of the cottons at the same instant. The cause of these results was made clear by the observation of the tight recirculation zones revealed by the helium bubble tracers in Plates 1 & 2.

Well downstream in the gas exit (17 exit diameters from the gas exit lip) the cottons showed a steady reverse flow at the axis. At $1.5D_X$ from the gas exit lip the flow direction at the axis fluctuated between forward and reverse flow. The pitot cylinder did not record a reversal when the traverse was made in this fluctuating region with the constant diameter gas exit tube. With a diverging exit tube the pitot cylinder did record a reversal.

Overleaf: Plate 3: Instantaneous flow directions shown by cotton streamers

3.A: (Figure 5.A.6): In the 140mmØ standard Stairmand High Efficiency cyclone

3.B: (Figure 5.A.7): In the 140mmØ Stairmand cyclone with a 90mm long conical extension of the cone at the dust exit end

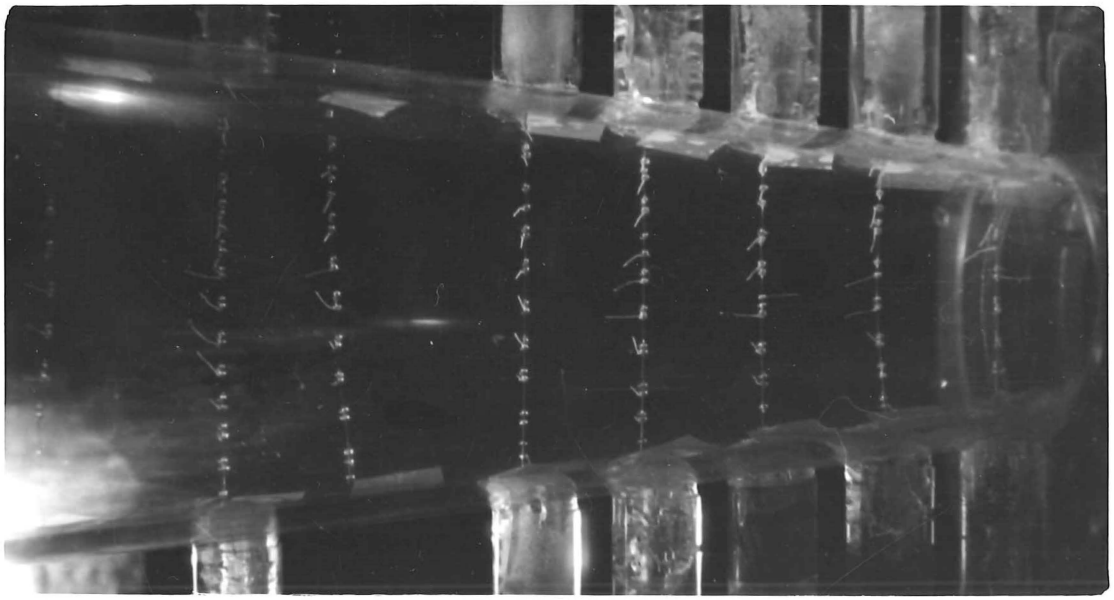

A. Standard Stairmand High Efficiency cyclone

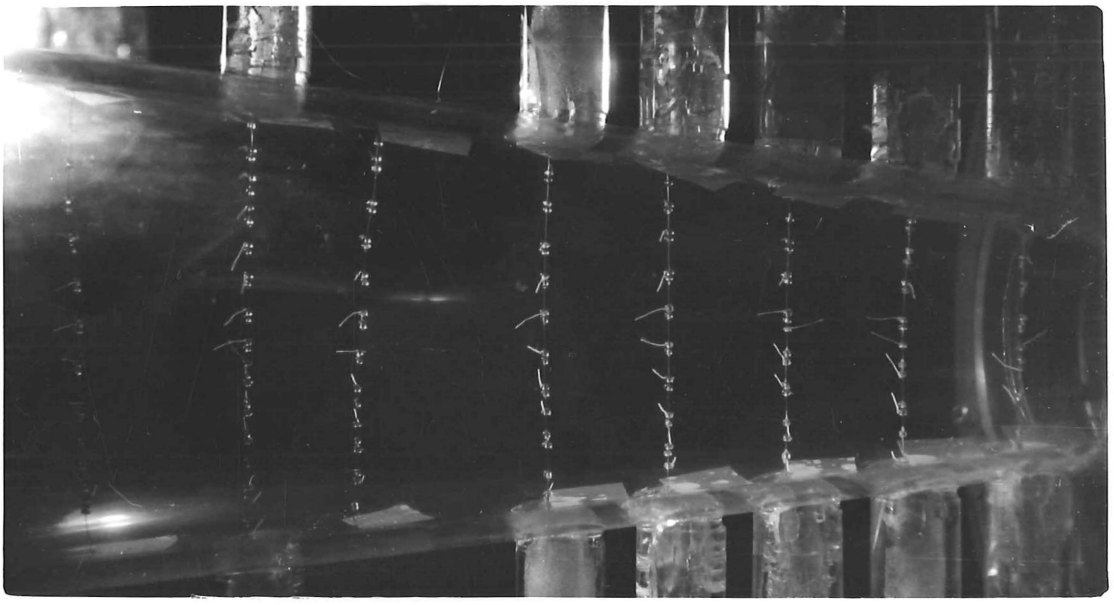

B.: Standard Stairmand H.E. cyclone with a conical extension of the dust exit

Plate 3.: Instantaneous flow direction shown by cotton streamers in 140mmØ cyclones

Positive pressure cyclones, with short tubular exits of several exit diameters in length, all showed a downdraft in the centre of the end of the gas exit. Particles (leaves etc) that were released above the centre of the exhaust were drawn down into the cyclone. Some of the leaves were collected in the bin of the cyclone - either by being reseparated or by being carried directly to the bin by this axial reverse flow. The downdraft in the exit of the heat exchanger cyclone (220mmØ barrel) was stronger when the exit was extended by 5 diameters.

Smith (1962a) observed a clear zone on the axis in a smoke-filled cylindrical cyclone in accord with a thin region of backflow from the surrounding air. This was not observed in this study as the cyclone did not exhaust to the free air and therefore could not bring in clean air along the core reversal. When a fine stream was injected at the wall some regions of the cone showed higher inward diffusivities, while in other regions the fog was kept close to the wall. As examples of this, the results from three positions in the cone are shown overleaf in Plate 4 (figures 5.A.8 - 10).

The photographs are taken through the base of the bin, at an angle slightly off the axis. In each, the fog is being injected at the wall at the top of the photo, and is swirling clockwise with the flow. The heating wire is strung across the diameter, and this enables the extent of the inflow to be observed. In figure 5.A.8 (Plate 4.A) the fog stream, after half a revolution, can be seen to have moved inwards to approximately 60% of the radius. This photograph is focussed on the wire at Port 8, about 2 barrel diameters from the gas exit lip, in the 140mmØ standard Stairmand HE geometry at an average inlet velocity of 8 m/s. In figure 5.A.9 (Plate 4.B) the injection is at Port 6, 2.7 barrel diameters below the gas exit lip, while figure 5.A.10 (Plate 4.C) is focussed on Port 4.

Overleaf: Plate 4: Axial view of the injection of a fog stream at the wall, showing radial inflow

4.A: Figure 5.A.8: Port 8 in 140mmØ standard Stairmand HE cyclone

4.B: Figure 5.A.9: Port 6 in 140mmØ standard Stairmand HE cyclone

4.C: Figure 5.A.10: Port 4 in 140mmØ standard Stairmand HE cyclone.

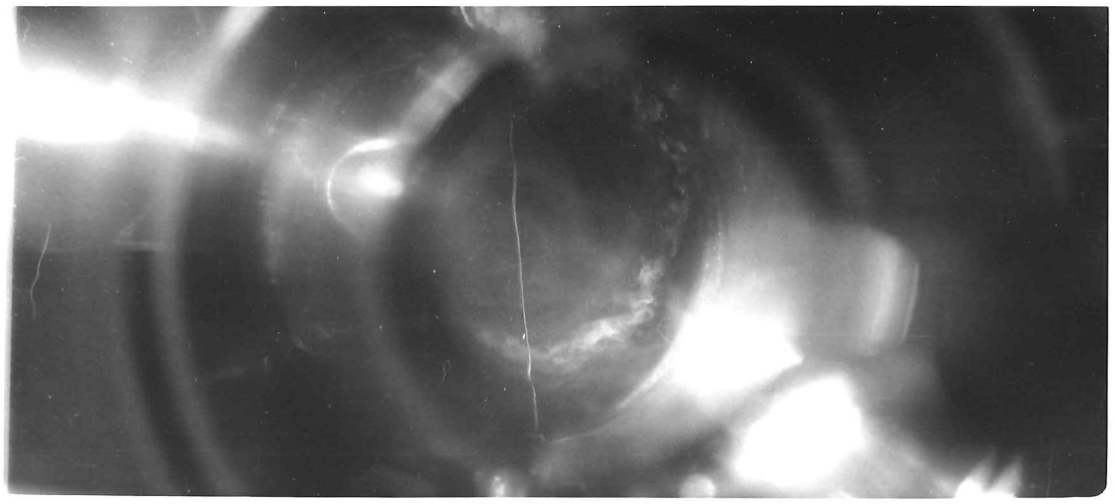

A. Port 8, located 1.95 Barrel diameters below gas exit lip.

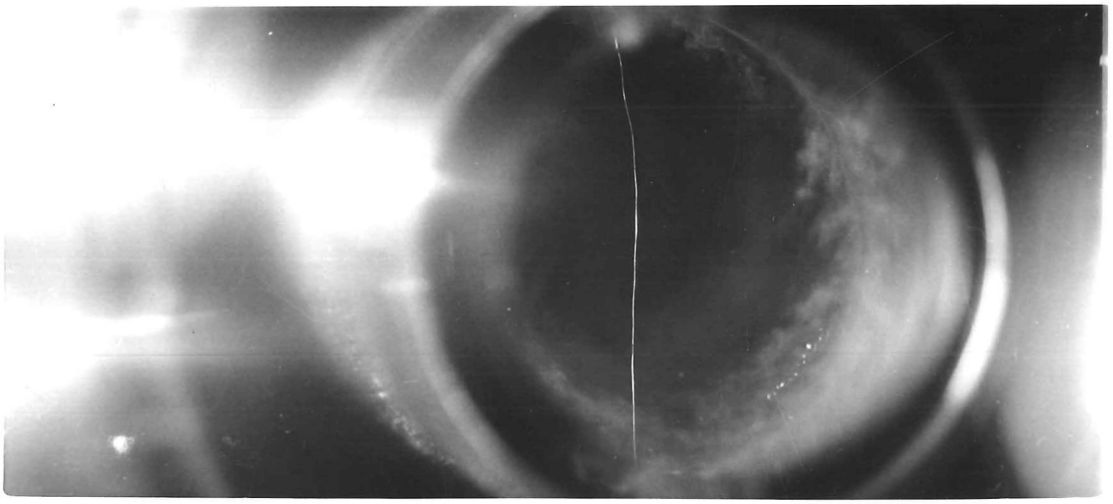

B. Port 6, located 2.7 Barrel diameters below gas exit lip.

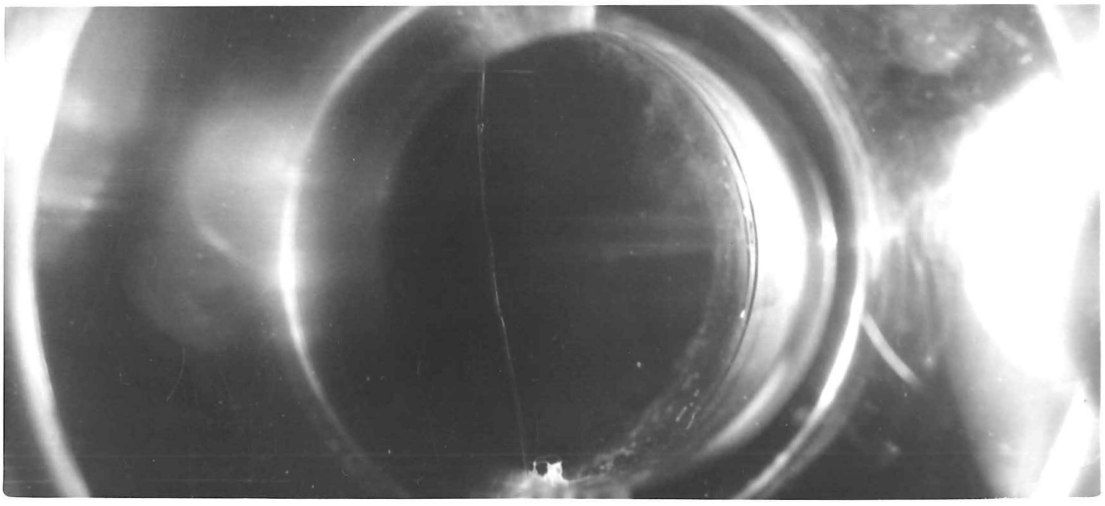

C. Port 4, located 3.1 Barrel diameters below gas exit lip.

Plate 4.: Axial views of the injection of a fog stream at the cone wall of the 140mmØ standard Stairmand High efficiency cyclone.

These three photographs demonstrate distinctive behaviour. While the average position of the fog stream at Port 6 does not appear to have moved inwards as much as at Port 8, there are several 'fingers' of fog showing sharp localised inflows. At Port 4, near the dust exit, the fog appears to have been kept pressed against the wall for the half revolution that is shown. These figures are only a sample of the results that were obtained, representing the extremes. Appendix 10.I presents details of how the photographs were used to calculate the velocity of the radial inflow, and tabulates the results. A summary of the results is presented as a histogram in figure 5.A.11 below:

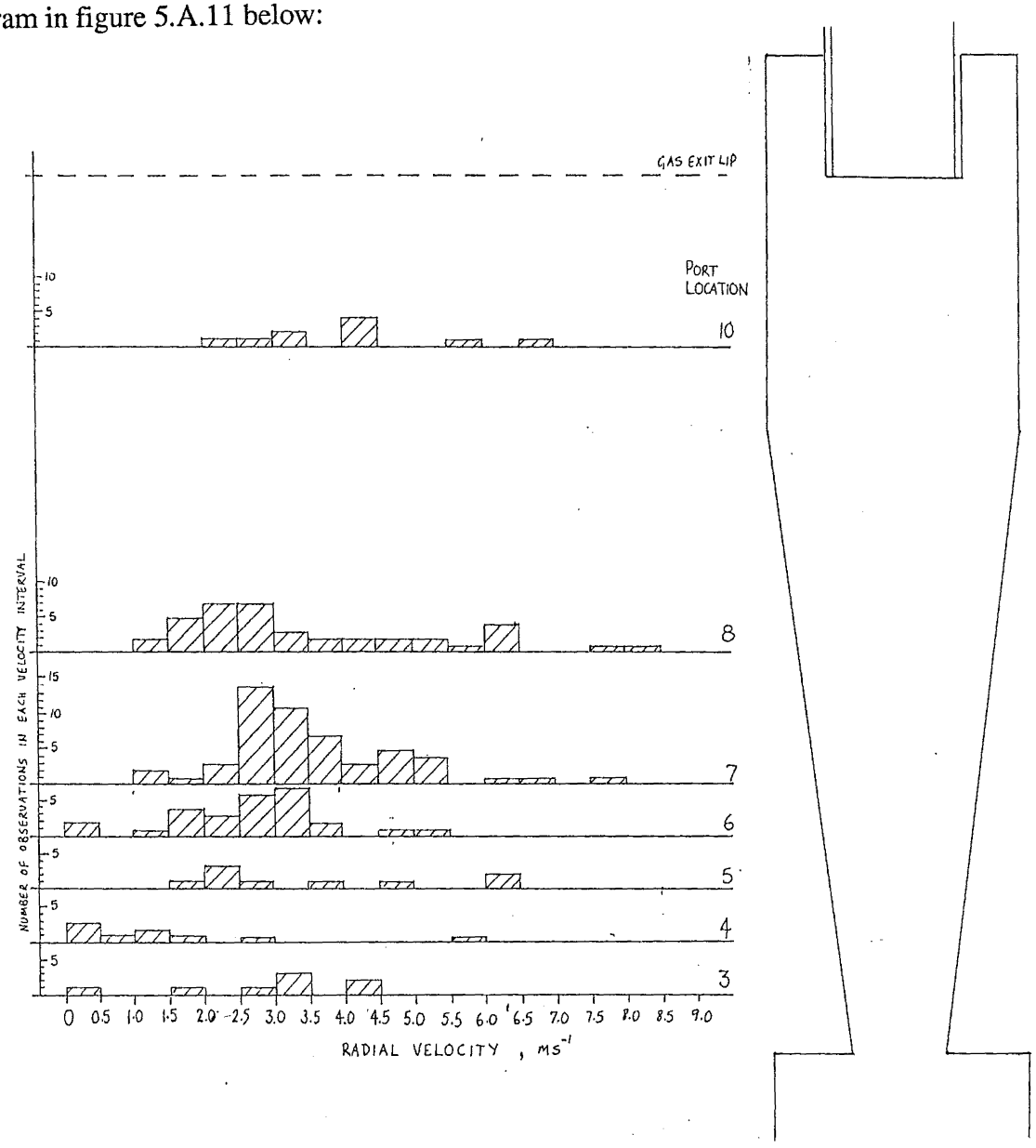

Figure 5.A.11: Histogram of the radial velocities calculated from the fog injection.

5.B. VELOCITY PROFILES:

Measurements of the velocity profiles were made with a 4-hole Pitot Cylinder in the 2090mmØ, 750mmØ and 140mmØ cyclones. Comparisons were made between the different cyclone size, low and high inlet flowrates and for various geometrical configurations, with traverses made at ten or more locations between the roof and bin base.

The profiles are presented on a scale drawing of the cyclone, in dimensionless form by scaling by the inlet velocity and the radius. For the tangential velocity profiles the traverse location is drawn through the point corresponding to 0.8 V_θ/V_i on the graph, while for the axial profiles it is drawn through the zero velocity axis. The radial position is scaled by the barrel radius. To help in identifying the profiles alternate locations use different symbols - the 'even' numbered ports have bolder or half-filled in symbols, and there are different symbols for the inlet and opposite inlet sides.

5.B.1. Varying Flowrate in 140mmØ cyclone

(a) Low flowrate V_{in} = 8.3 m/s
(b) Normal Flowrate V_{in} = 22 m/s

The plots of Tangential (Figure 5.B.1) and Axial (Figure 5.B.2) velocity profiles show good agreement between the inlet velocities of 8.3m/s and 22m/s when the velocity components are scaled by the inlet velocity. This needed to be confirmed to allow comparisons between experiments done at different flowrates. For the tangential velocity the largest discrepancies occur near the gas exit lip, whereas for the axial velocities they occur in the lower cone.

Opposite:

Figure 5.B.1 Tangential velocity profiles in 140mmØ cyclone
for inlet velocities of 8 and 22m/s

Figure 5.B.2 Axial velocity profiles in 140mmØ cyclone
for inlet velocities of 8 and 22m/s

Figure 5.B.1: Tangential velocity profiles for the 140mm∅ Stairmand H.E. geometry at V_{in} = 8.3 and 22 m/s

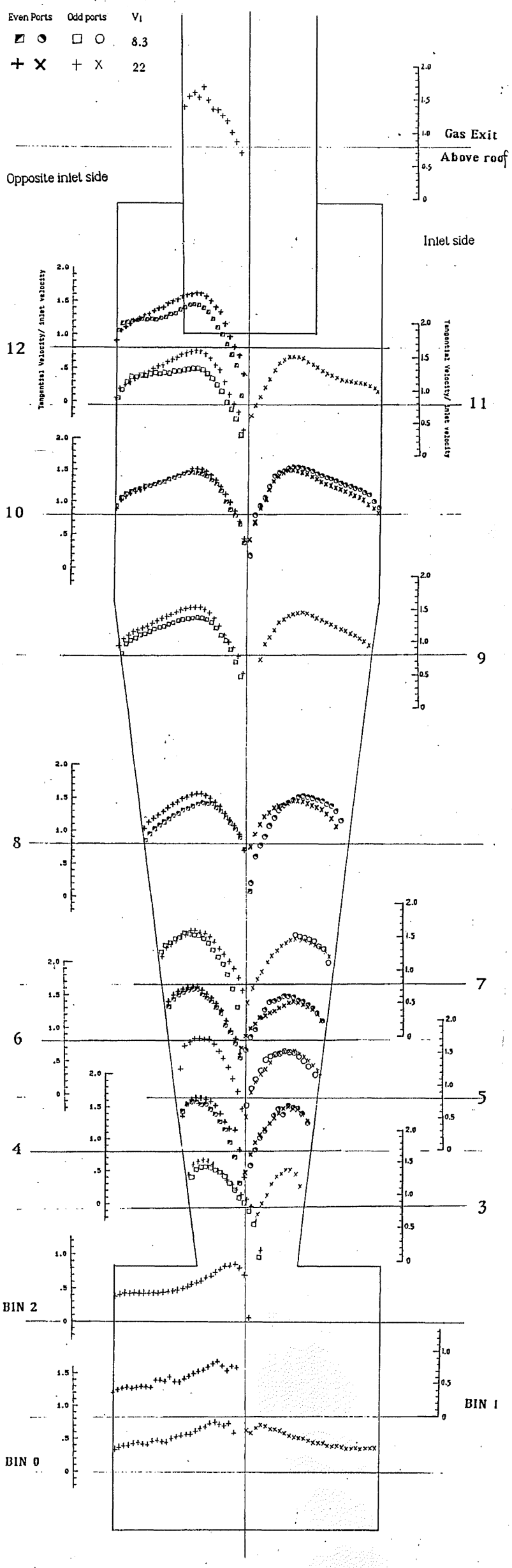

Figure 5.B.2: Axial velocity profiles for the 140mm∅ Stairmand H.E. geometry at V_{in} = 8.3 and 22 m/s

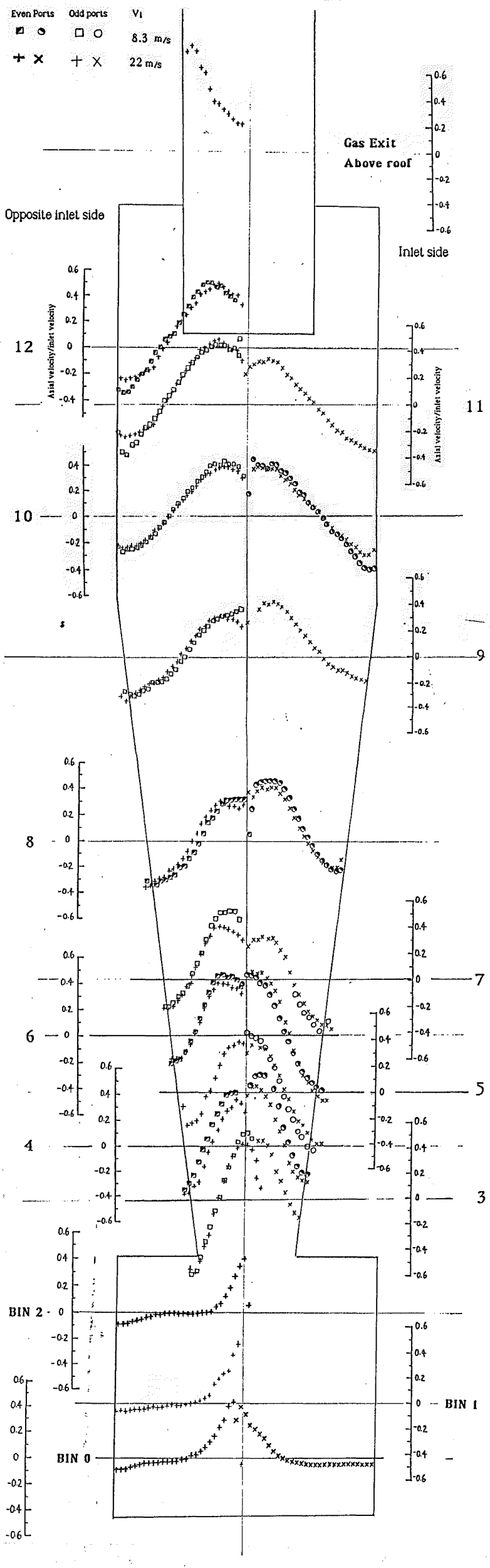

5.B.2. Varying cyclone size

(a) D = 140mmØ Perspex laboratory cyclone, University of Canterbury
(b) D = 750mmØ Industrial scale cyclone, Scotts Engineering, Christchurch
(c) D = 2090mmØ Industrial cyclone, #321, Canterbury Timber Products, Rangiora

Differences between profiles could be expected to arise from the differences in the scale of the cyclones, surface roughness, extent of the probe interference, inlet and exit configurations, or by the air supply being by positive rather than negative pressure. The 2090mmØ cyclone was a Stairmand High Efficiency geometry, but had the dust exit extended at constant diameter for 1.5 barrel diameters before entering the bin. Also there was a small offtake of air from the bin during the runs.

Plots of the velocity profiles (Figures 5.B.3 and 5.B.4) for these cyclones showed that there was significant disagreement, particularly in the axial velocity profiles, and the tangential velocity profiles on the inlet side of the lower cone. To check if this was due to the different air supply or exit arrangements, measurements were made with modifications to the 140mmØ cyclone. A large barrel was placed in the gas exit to simulate the sudden expansion, which is thought to allow the vortex to move more freely than in the straight gas exit configuration, possibly affecting the axial profiles. To attempt to stabilise the movement a plate was placed in the gas exit - just blocking the core and leaving an annulus for the flow, this simulated the "chinese hat" that was present on the 2090mmØ cyclone. The few comparisons of exit configuration shown in Figure 5.B.5 indicate a closer agreement than is found for the comparisons of cyclone scale, suggesting the exit differences are not significant. As shown above in section 5.B.1, the slightly different flowrates (18m/s in the 750 and 2090mmØ cyclones, 22m/s in the 140mmØ) are not expected to affect the scaled profiles.

If the probe interferes with the flow, the extent of interference could be expected to change as the ratio of the probe : cyclone size changes. It has been observed that the probe insertion results in an increase of the flow into the 140mmØ cyclone due to a lowering of the pressure drop. For most locations the 750mmØ cyclone velocities are higher than the 140mmØ ones, so this is not expected to be the cause of the discrepancy. The radial velocities obtained for the 750mmØ & 2090mmØ cyclones look more realistic than those obtained for the laboratory cyclone - this is due to the radial separation of the 4 holes in the pitot cylinder becoming significant compared with the pressure gradient in the smaller cyclone, and a possible response bias in strongly fluctuating flows.

Overleaf:
Figure 5.B.3: Tangential velocity profiles for 140mmØ, 750mmØ and 2090mmØ for Standard Stairmand High efficiency cyclones

Figure 5.B.4: Axial velocity profiles for 140mmØ, 750mmØ and 2090mmØ for Standard Stairmand High efficiency cyclones

Overleaf:
Figure 5.B.5: Axial velocity profiles for 140mmØ, Varying gas exit configuration

Figure 5.B.6: Axial velocity profiles for 140mmØ cyclone with a 90mm long conical extension

Figure 5.B.3: Tangential velocity profiles for the 140mm∅, 750mm∅ and 2090mm∅ Stairmand H.E. cyclones

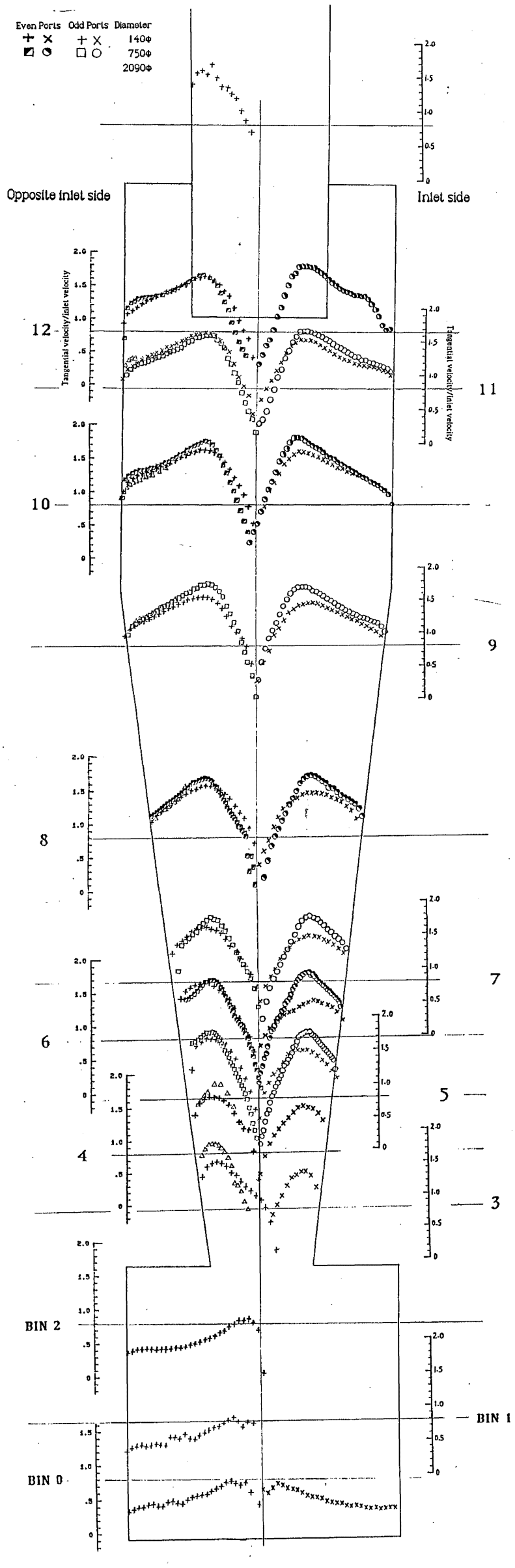

Figure 5.B.4: Axial velocity profiles for the 140mm∅, 750mm∅ and 2090mm∅ Stairmand H.E. cyclones

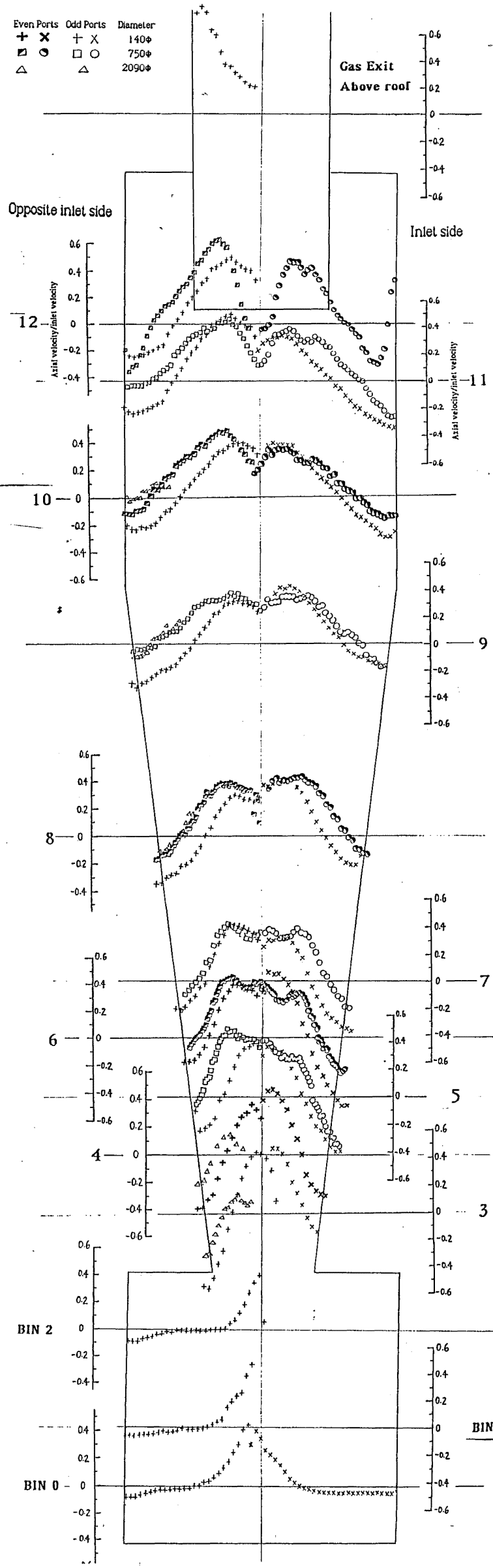

Figure 5.B.5: Axial velocity profiles for the 140mm∅ cyclone, varying gas exit configurations

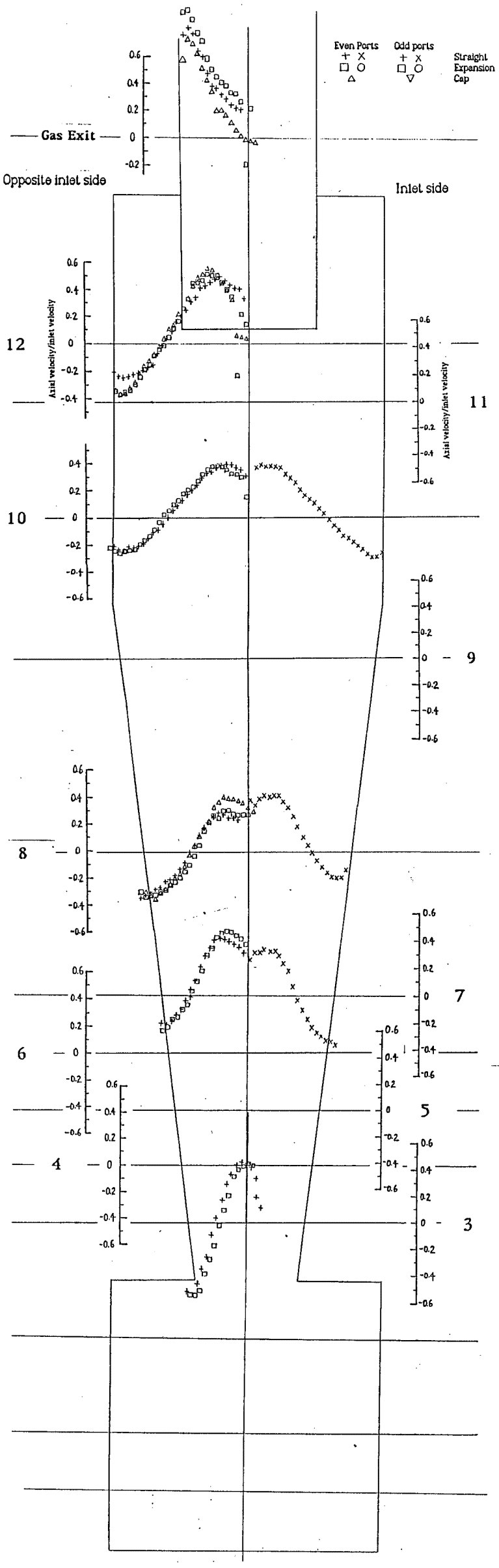

Figure 5.B.6: Axial velocity profiles for the 140mm∅ cyclone with a 90mm extension of the cone

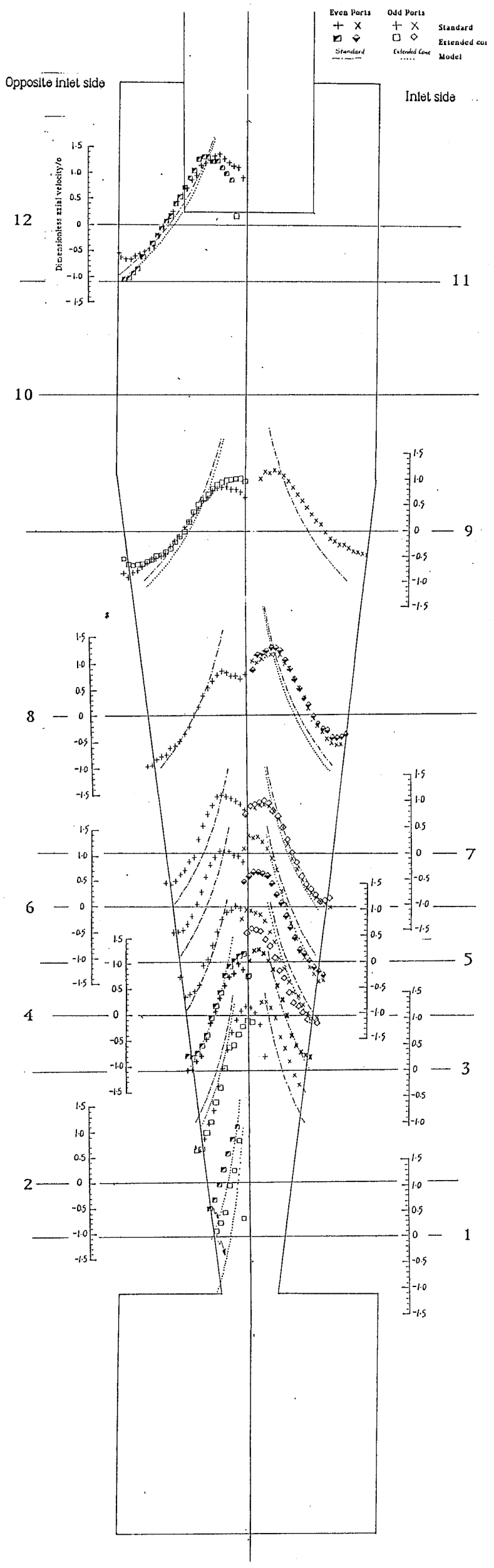

5.B.3. Varying geometry

Initial measurements from a range of techniques showed anomalous behaviour of the vortex in the lower cone region, which was thought to be related to the position of the vortex breakdown. The position of these observations was more invariant with respect to the distance from the dust exit than from the gas exit lip, for a wide range of barrel lengths. This suggested that the cone was able to stabilise the vortex.

To check this, the cone geometry of the 140mmØ cyclone was altered. Firstly, a 90mm (0.6 barrel diameters) long extension piece was made, with the same cone angle. This was added to the dust exit, reducing from the normal dust exit diameter of 53mmØ to 19mmØ, while delaying the expansion into the bin by 90mm. The axial velocity profiles for a selection of positions in the cyclone are shown in Figure 4.B.6 on the previous page, along with the traverses for the same ports with the normal cyclone geometry. For this extended cone geometry the profile of the axial velocity near the dust exit appears to show velocities all directed upwards. This is obviously inconsistent with a mass balance, and shows the difficulty of obtaining accurate velocities with the 10mmØ probe in a small diameter section. There must be some boundary layer flow that the probe does not identify because of the coarseness of the measurements. However, the general trend is for there to be less flow directed towards the bin than for the standard cone.

The effect of the barrel section was then investigated by constructing a cone that extended from the gas exit lip to the dust exit, and had the same overall length as the standard Stairmand H.E. cyclone. This is referred to as the "Long cone" cyclone, and the tangential and axial velocity components for this are compared with the standard geometry in Figures 5.B.7 and 5.B.8 respectively. The Long cone geometry is the same geometry assumed for the Bloor & Ingham (1987) axial velocity model which is applied to these profiles in section 5.D.

The vortex centreline was more off axis for the Long cone than the standard geometry

Overleaf:

Figure 5.B.7: Tangential velocity profiles for 140mmØ, Varying barrel length
Standard Stairmand H.E. geometry and Long cone geometry

Figure 5.B.8: Axial velocity profiles for 140mmØ, varying barrel length
Standard Stairmand H.E. geometry and Long cone geometry

Figure 5.B.7: Tangential velocity profiles for the 140mm∅ Standard and Long cone (no barrel) geometries

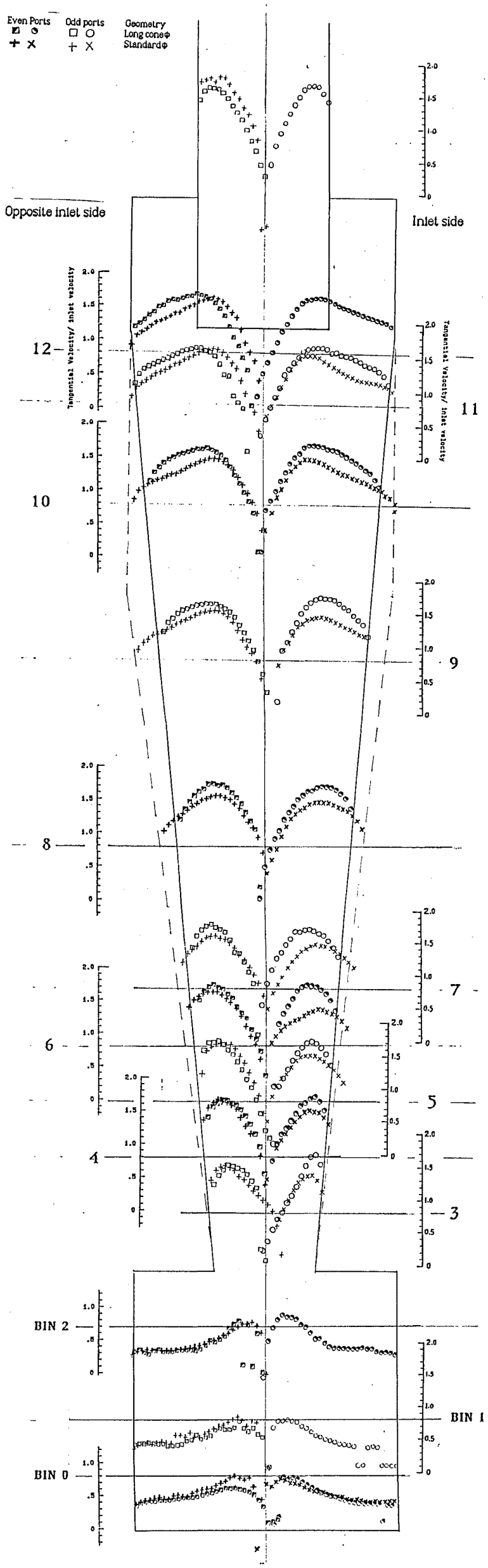

Figure 5.B.8: Axial velocity profiles for the 140mm∅ Standard and Long cone (no barrel) geometries

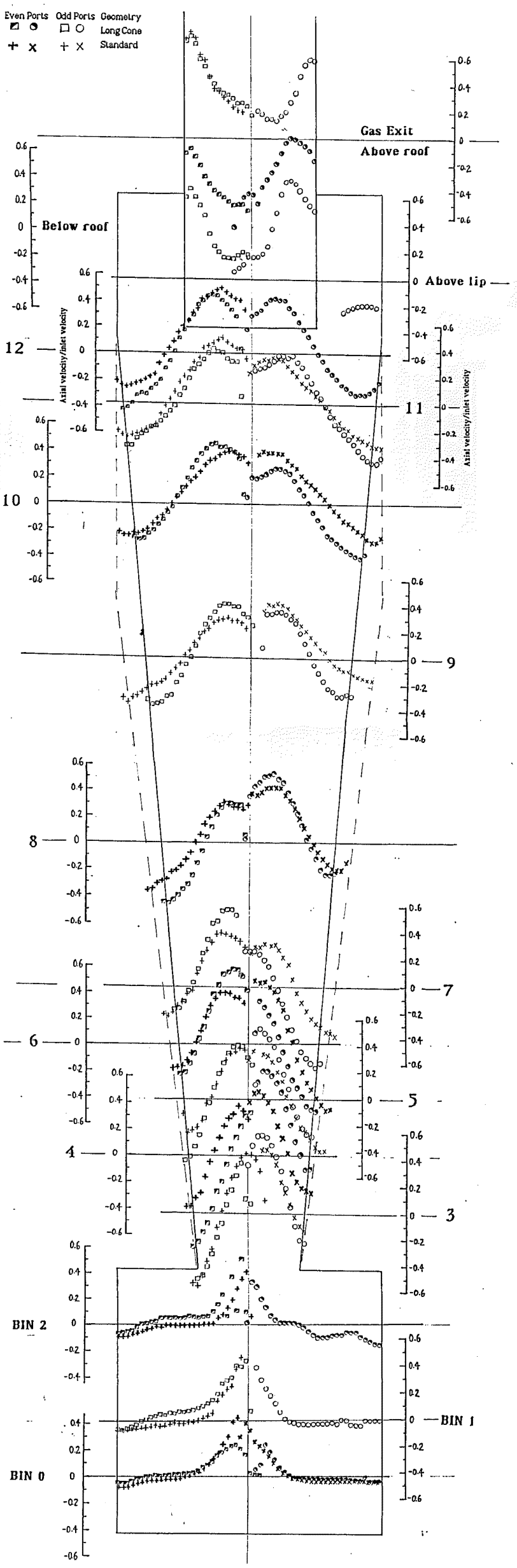

5.B.4. Varying probe scale

It was evident that the pitot cylinder probe disturbed the flow from observations of the helium bubble tracers, and the drop in the overall Euler number (by 20%) upon probe insertion. An indication of the relative scales of the cyclones and the probes is given in Figure 6.A.1 in the Discussion.

To check the effect of probe interference on the flow, the profiles obtained from the different sizes of cyclone were compared. As the differences could be due to the effect of scale on the flowfield, comparison was also made between the total velocity profiles obtained with the pitot cylinder and a hot film probe, in the 140mmØ cyclone. An example of a typical result, the comparison for Port 8oi in the Long cone geometry, is given below. For both traverses the inlet velocity was kept constant (at 23m/s) and was used to scale the total velocity. The total velocity is given here to avoid the errors of resolving into components.

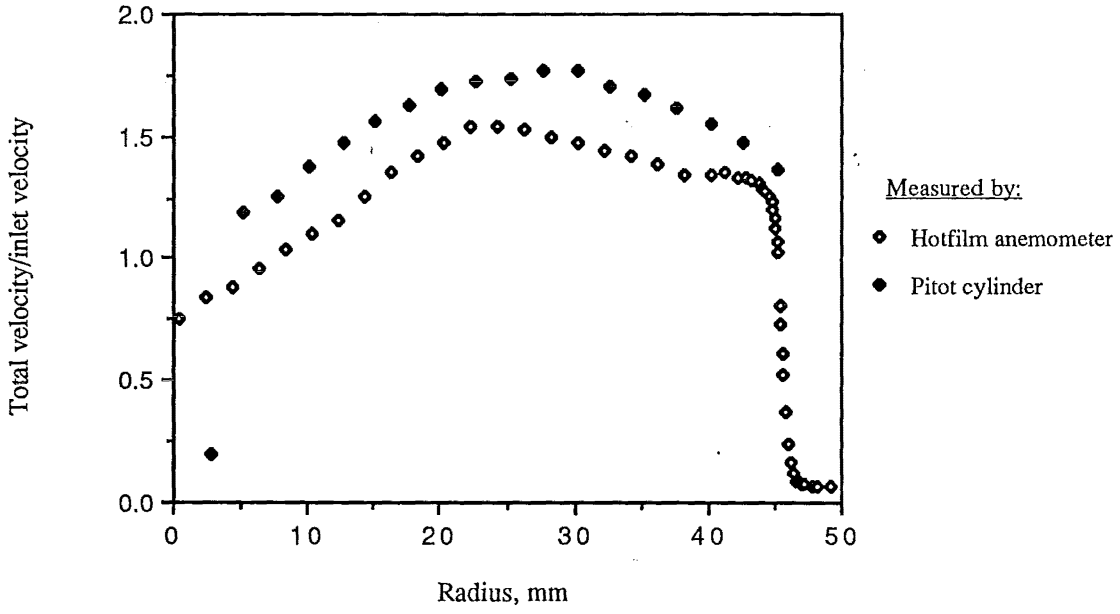

Figure 5.B.9: Hotfilm and Pitot cylinder total velocities (at Port 8 in the 140mmØ cyclone)

The velocities from the hotfilm are closest to the Pitot cylinder results near the wall and become further away near the maximum tangential velocity. This was despite allowing for the increase in velocity caused by the probe insertion. See also Figure 5.K.2 for a comparison of the velocities recorded by the hotfilm with and without the pitot cylinder probe inserted.

5.B.5. Boundary layer measurements

Sample plots of the total velocity against distance from the wall are given below for the 140mmØ cyclone.

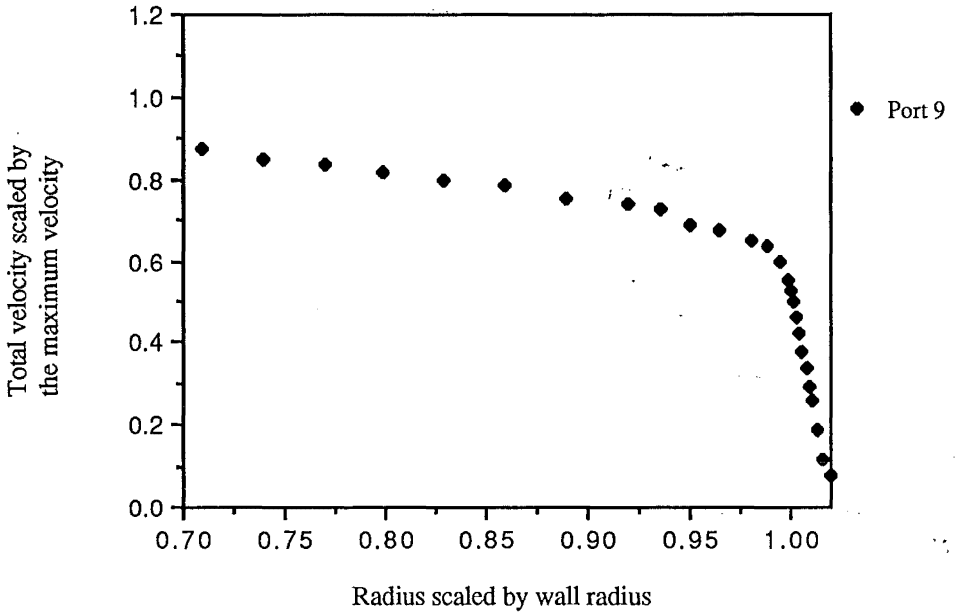

Figure 5.B.10: Profile of total velocity in Boundary layer in 140mmØ cyclone (near cone-barrel junction)

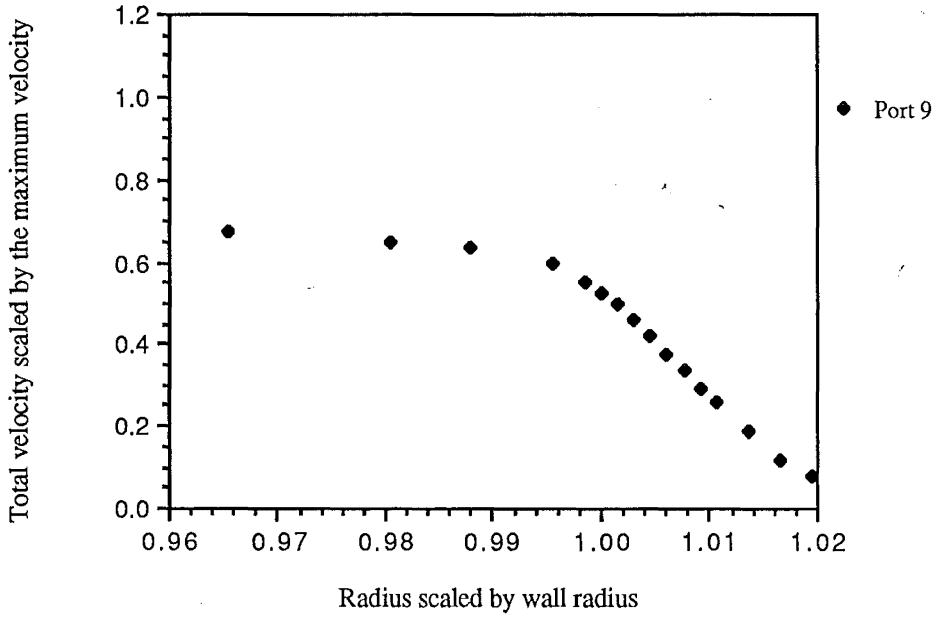

Figure 5.B.11: Detail of boundary layer profile of total velocity (in 140mmØ cyclone, near cone-barrel junction)

The 45° hot film probe used didn't allow a precise Boundary layer thickness to be determined because the radial extent of the probe was comparable to the thickness of the boundary layer. It was expected that the cone wall boundary layer would become thicker as it approached the dust exit, especially in the case of the extended cone, where the outer vortex does not appear to be reach into the bin, so that the dust transport must be achieved by the Boundary layer alone. In fact, in the 140mmØ cyclone the boundary layer thickness was found to be about 0.5 to 3mm, being a maximum at Port 7 , and reaching the minimum near the dust exit.

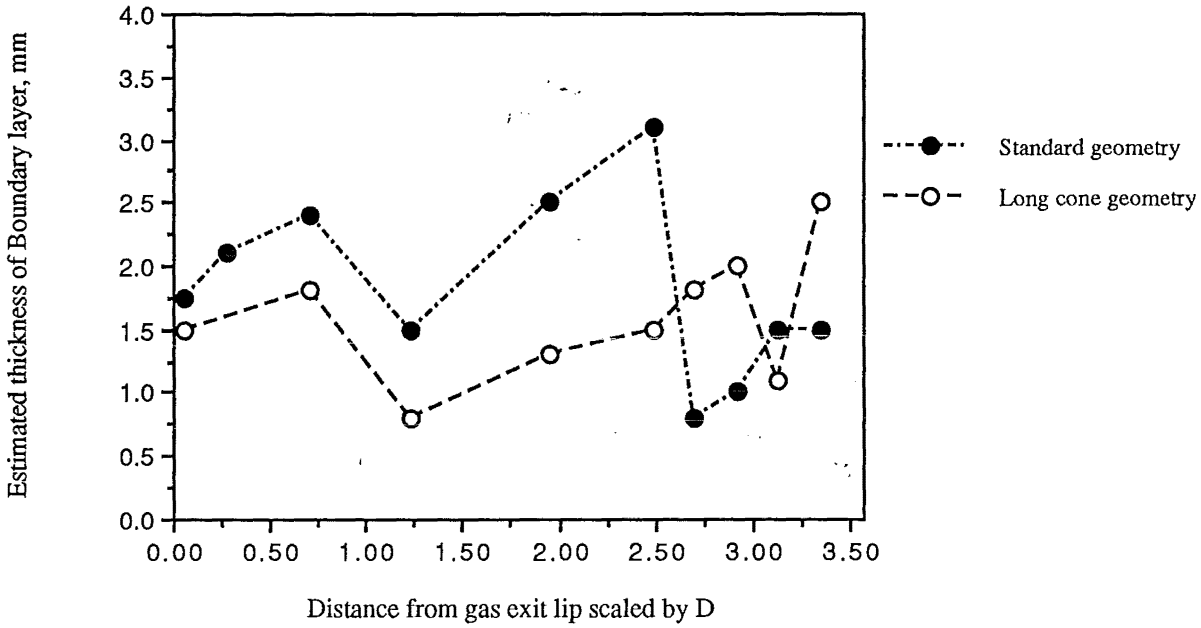

Figure 5.B.12: Thickness of boundary layer along 140mmØ cyclone length

The boundary layer thickness can also be estimated from the tangential and axial velocity profiles, where the velocity decreases near the wall due to the drag of the wall. This appears to be approximately 3mm in the 140mmØ cyclone and 15mm in the 750mmØ cyclone.

5.B.6. Symmetry of Velocity profiles:

The features of the velocity profiles that are of interest for the modelling are shown below for from the results obtained in the 750mmØ cyclone. It can be seen that the radius of the maximum tangential velocity is approximately constant along the cyclone length, whereas the zero axial velocity boundary is an approximately constant proportion of the wall radius. The vortex centreline is not exactly aligned with the geometrical axis, but the opposite sides of the cyclone agree well. The 140mmØ cyclone has a more scattered distribution along the length.

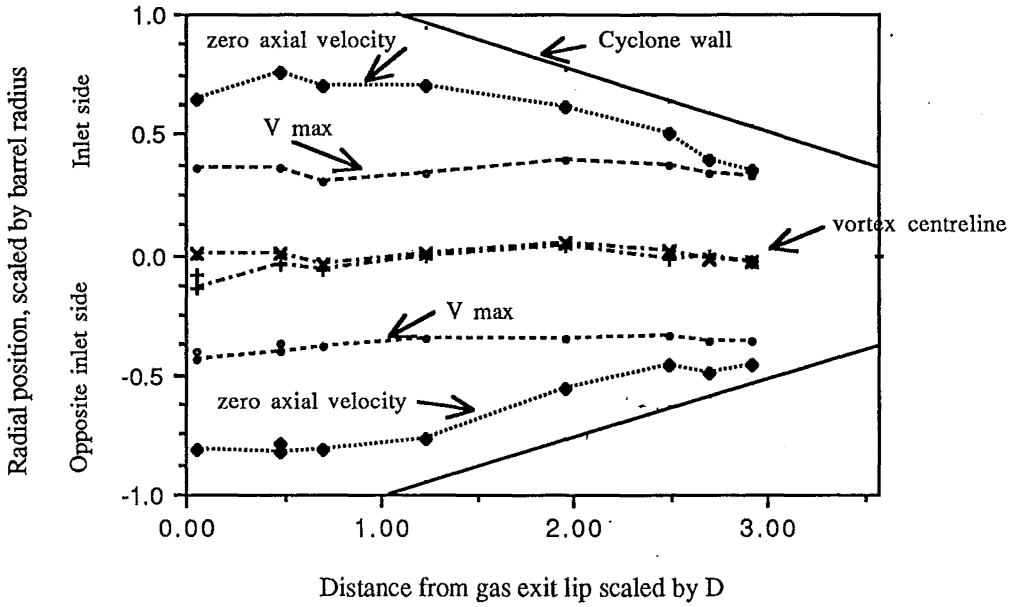

Figure 5.B.13: Variation of radial positions along the length of 750mmØ cyclone

Figure 5.B.14 shows the poor agreement that was obtained in the axial flow volume balance. The axial velocity profiles were integrated across the cyclone diameter at each axial level and the volume flow compared between the outer and inner vortices. It appears that the inner vortex measurements overestimate the volume flow, while those in the outer vortex underestimate it by a similar amount.

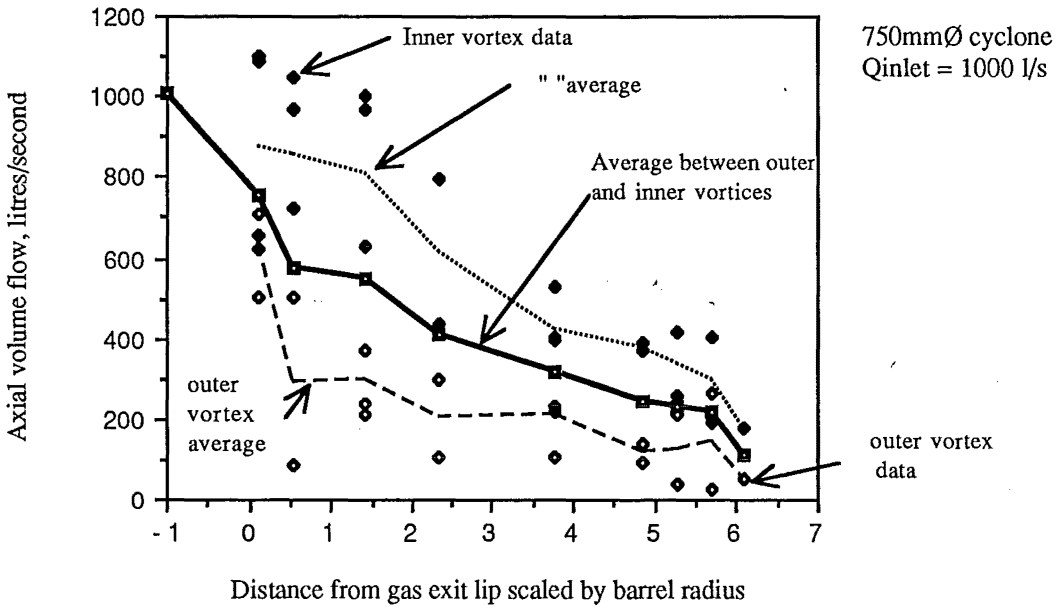

Figure 5.B.14: Area integral of the axial velocity at different locations along cyclone length

5.C. TANGENTIAL VELOCITY MODELLING

Details of the previous approaches to modelling the tangential velocity component in cyclones are given in Chapters 2 and 3. From these the Burgers (1948) and Phillips (1990) equations were selected as the most suitable, and these are compared with the experimental profiles in this section. The model equations were outlined in section 3.B along with details of the method used to select the parameters to fit the equations to the experimental profiles. The variation of the fitted parameters along the cyclone length is examined in Chapter 6.B1, with a view to finding relationships that can be used to predict the parameters. Other methods of fitting the model parameters are also examined as well as empirical relationships for the parameters.

5.C.1: The Burgers equation

The Burgers (1948) model for the tangential velocity component can be expressed as:

$$V_\theta = \frac{\Gamma_o}{r}\left[1 - e^{-\alpha . r^2}\right] \qquad \text{--- (5.C.1)}$$

where the exponential parameter 'α' $= \dfrac{a}{2\nu_T}$.

A variation on the Burgers equation was suggested by Phillips (1990) :

$$V_\theta = \frac{\Gamma_o}{r} \times \left(1 - \frac{1}{2}\left(\exp\left(\frac{-ar^2}{0.7\nu_T}\right) + \exp\left(\frac{-ar^2}{7\nu_T}\right)\right)\right) \qquad \text{--- (5.C.2)}$$

The relationship of the parameters to the physical conditions of the cyclone was detailed in Chapter 3.B, resulting in the following equations:

Radial inflow parameter: $$a = \frac{2Q}{\pi D_X{}^2 L} \quad [s^{-1}] \qquad \text{--- (5.C.4)}$$

Turbulent kinematic viscosity:

$$\nu_T = \nu \times 0.0001841 \times \left(\frac{V_W D}{2\nu}\right)^{1.25} \quad [m^2 s^{-1}] \qquad \text{--- (5.C.5)}$$

Γ_O : circulation at large radius [=] m^2/s
V_W : tangential gas velocity at cyclone wall, [=] m/s
Q : total gas flowrate, [=] m^3/s
D_X : vortex finder diameter, [=] m
L : length of cyclone below vortex finder (between gas exit lip and dust exit), [=] m
ν : kinematic viscosity, [=] m^2/s (Taken as 1.568×10^{-5} m^2/s for air at STP)

Equation 5.C.4 comes from the vortex pressure drop calculations of Abrahamson (1991), being in effect the average radial inflow velocity over the cylindrical extension of the gas exit between the gas exit lip and the dust exit. The basis of this has been detailed in Chapter 3.B on page 42.

Equation 5.C.5 is based on the empirical equation of Ogawa (1987) that was developed to fit experimental pressure drops in cylindrical vortex chambers. Further work by Abrahamson (1991) has suggested that the value of the exponent needs to be reduced to predict the pressure drop in cyclones. Rather than apply this empirical equation rigidly through the cyclone, the values of the turbulent viscosity were determined independently for each location in the cyclone, to achieve the best fit to the experimental data of this study. The resulting viscosity values are compared with the predictions of equation 5.C.5 in section 6.B1

For the three scales of cyclone at the flowrates examined, the parameters calculated by equations 5.C.4 and 5.C.5 had the values:

Diameter:	a [=] s^{-1}	ν_T [=] m^2s^{-1}
140mmØ	11.7	0.00525
750mmØ	1.4355	0.032
2090mmØ	0.61	0.131

To fit the models, the parameters 'Γ_o' and 'α' (or a/ν_T) were adjusted independently for each of the experimental profiles in the cyclone to provide the best fit to the location and magnitude of the maximum tangential velocity. The variation of the parameters will be examined in Chapter 6.B1 in order to find universal values or expressions for the fitting parameters. Alternative methods of fitting the parameters, and empirical relationships are also discussed.

5.C.2 Experimental and model V_θ profiles

In the following pages the graphs of the experimental points and the models are presented. The values of the parameters Γ_o and 'α', (or 'a' and ν_T) that were used in the model are indicated beside each traverse. These are the values used to achieve the best fit to the position and value of the maximum tangential velocity.

Figures 5.C.1A and 5.C.1B show the experimental tangential velocity profiles for the 140mmØ Standard Stairmand H.E. geometry with the Phillips and the Burgers models respectively (Equations 5.C.1 and 5.C.3). There is little difference between the two in terms of goodness of fit and the Burgers model has the advantage of simplicity. Figures 5.C.2A and 5.C.2B show the same comparisons for the 140mmØ Long cone geometry, with the Burgers and Phillips models plotted alongside the tangential velocity experimental points. Figure 5.C.3 shows the Burgers model with the 750mmØ cyclone tangential velocity measurements.

The agreement between the model and the experimental profiles is generally good, especially considering the simple form of the axial velocity that is assumed by the Burgers vortex model.

Overleaf are shown:
Figures 5.C.1A and 5.C.1B: Tangential velocity profiles and models in 140mmØ cyclone.

Figures 5.C.2A and 5.C.2B: Tangential velocity profiles and models in 140mmØ Long cone.

Figure 5.C.3: Tangential velocity profiles and models for the 750mmØ cyclone.

Figure 5.C.1A: 140mm∅ Stairmand H.E. geometry Tangential velocity profiles compared with the 2 term model of Phillips

Tangential velocity profiles scaled by the inlet velocity (22m/s) and compared with the 2-term Phillips model using distributed parameters fitted to the radius of the maximum tangential velocity $V_\theta = \frac{\Gamma_o}{r} \times \left(1 - \frac{1}{2}\left(\exp\left(\frac{-ar^2}{0.7\nu_T}\right) + \exp\left(\frac{-ar^2}{7\nu_T}\right)\right)\right)$

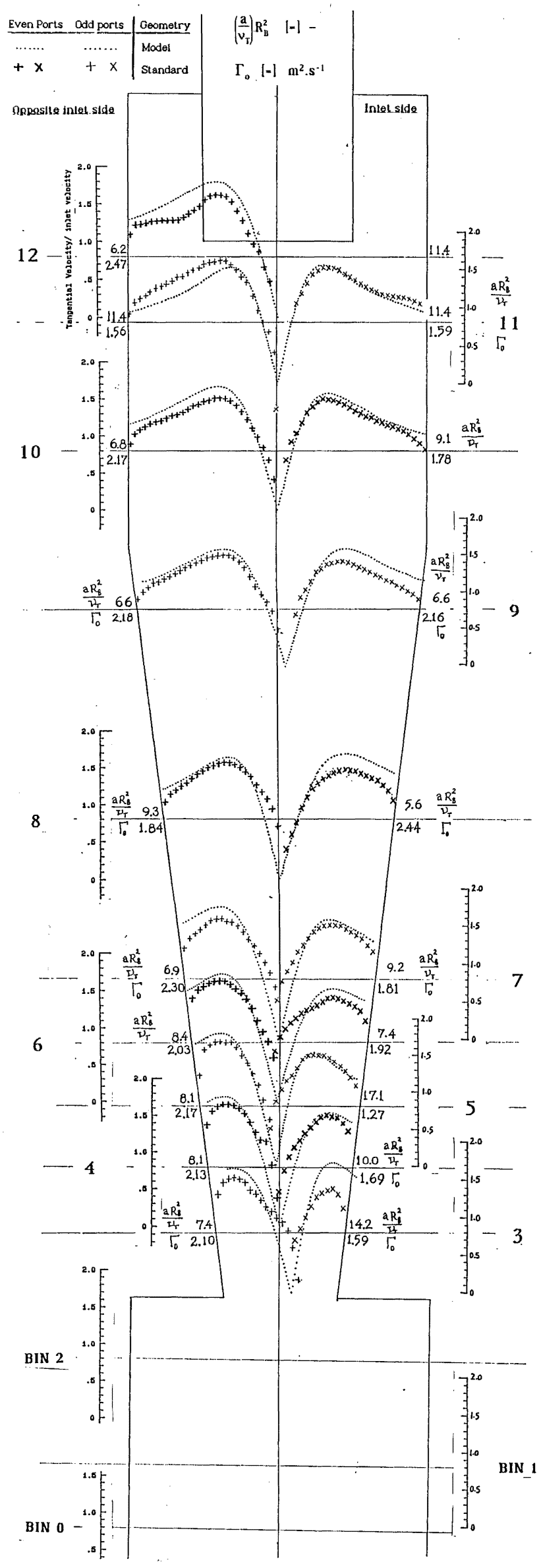

Figure 5.C.1B: 140mm∅ Stairmand H.E. geometry Tangential velocity profiles compared with Burgers 1 term model

Tangential velocity profiles scaled by the inlet velocity (22m/s) and compared with the 1-term Burgers model using distributed parameters fitted to the radius of the maximum tangential velocity

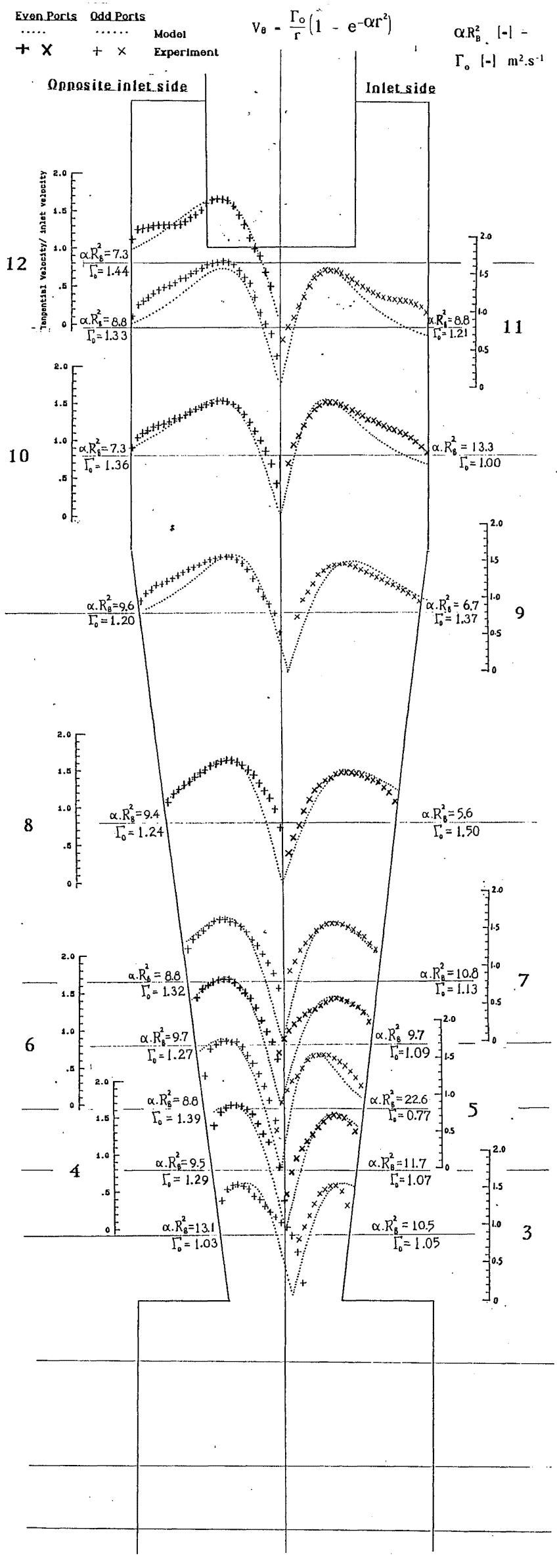

Figure 5.C.2A: 140mm∅ "Long cone". geometry Tangential velocity profiles compared with the 2 term model of Phillips

Tangential velocity profiles scaled by the inlet velocity (22m/s) and compared with the 2-term Phillips model using distributed parameters fitted to the radius of the maximum tangential velocity $V_\theta = \frac{\Gamma_o}{r} \times \left(1 - \frac{1}{2}\left(\exp\left(\frac{-ar^2}{0.7\nu_T}\right) + \exp\left(\frac{-ar^2}{7\nu_T}\right)\right)\right)$

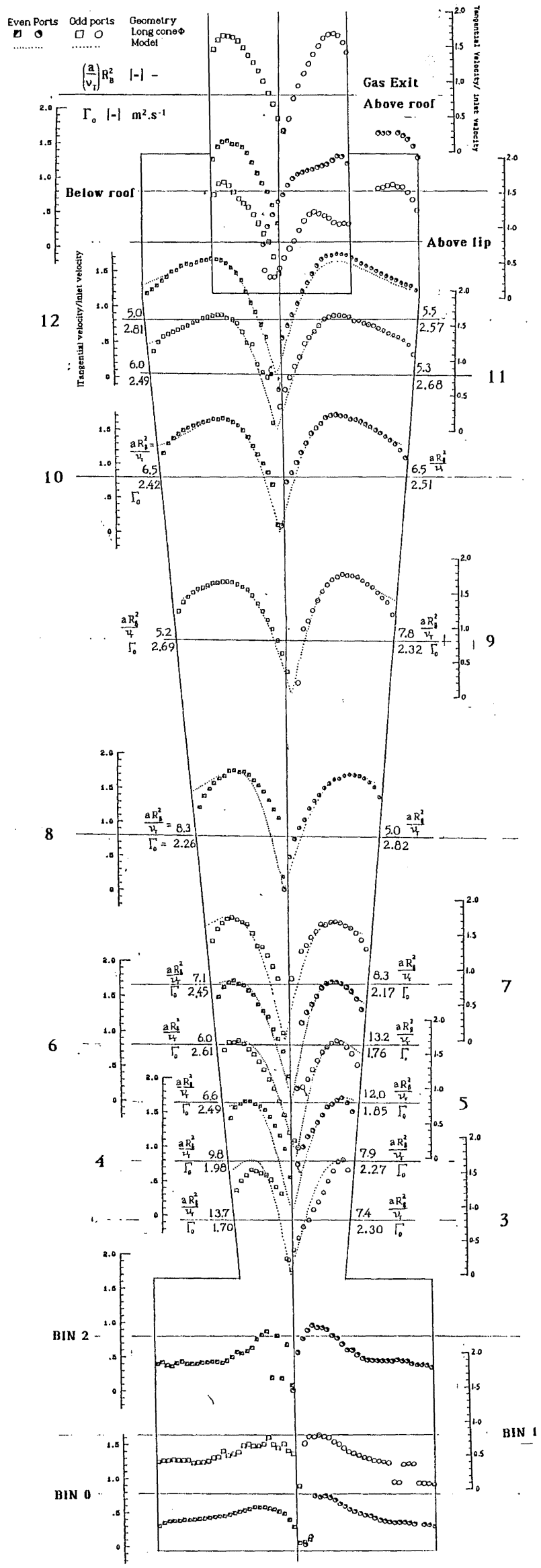

Figure 5.C.2B: 140mm∅ "Long cone". geometry Tangential velocity profiles compared with Burgers 1 term model

Tangential velocity profiles scaled by the inlet velocity (22m/s) and compared with the 1-term Burgers model using distributed parameters fitted to the radius of the maximum tangential velocity

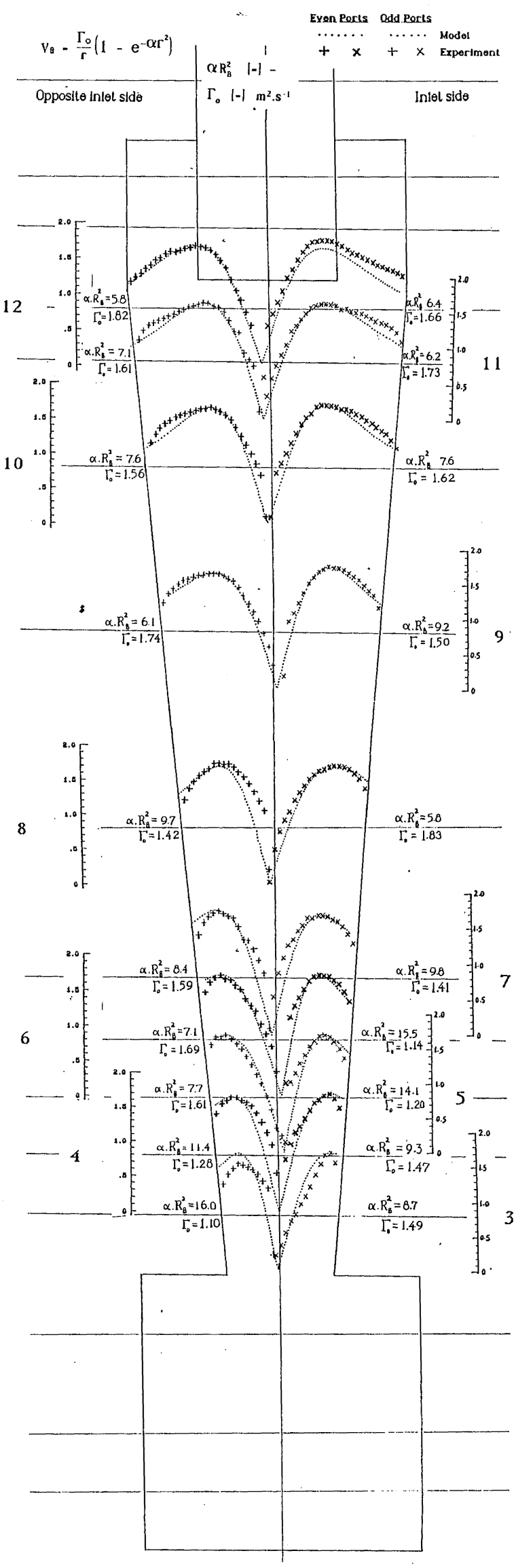

Figure 5.C.3: Tangential velocity profiles for the 750mm∅ Stairmand H.E. geometry with Burgers model

Tangential velocity profiles scaled by the inlet velocity (18m/s) and compared with the 1-term Burgers model using distributed parameters fitted to the radius of the maximum tangential velocity.

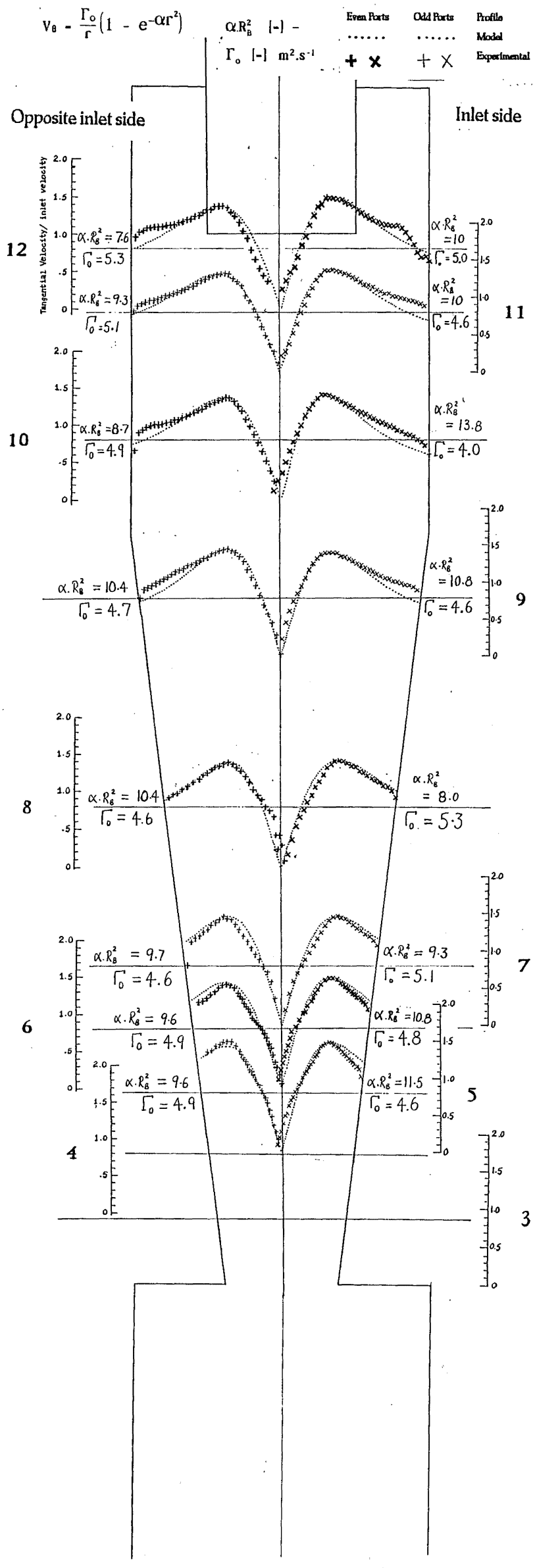

5.D AXIAL VELOCITY MODELLING

The Bloor and Ingham (1987) model was selected as the most promising for the cyclone axial velocity component. The model assumes a cone of half angle α that extends from the vortex finder to the dust exit, which is our "Long cone" geometry. The standard geometry is at most 17% different from the model wall radius, at the cone/ barrel junction. The theory behind this model was detailed in Chapter 3.B, and the correct form of the axial velocity equation can be simplified to:

$$w/\sigma = - \left[2 \ln(\theta/\alpha) + 1 \right] \qquad \text{--- (5.D.1)}$$

where : w is the dimensionless axial velocity
σ is a dimensionless geometrical parameter,
(which equals 5.746 for the Stairmand H.E. geometry)
θ is the polar angle, radians
α is the cone wall half-angle, radians

Substituting the axial velocity scaling factor: $\frac{Q}{2\pi\sigma R_O^2}$ gives the dimensional form for the axial velocity as:

$$V_X = (w/\sigma) \times \frac{Q}{2\pi R_O^2} = \frac{-Q}{2\pi . R_B^2} . \left[2\ln(\theta/\alpha) + 1 \right] \qquad \text{--- (5.D.2)}$$

where: Q is the volume flow at the inlet, m^3/s
R_B is the radius of the cyclone at the level of the gas exit lip.

For the plots of the experimental and model axial velocity profiles (Figures 5.D.1, 5.D.2 & 5.D.3) the dimensionless axial velocity w/σ is plotted.

The location of the boundary between upward and downward vortices was predicted well in the barrel, but with large errors in the cone. There was good agreement for the low flow traverses as well The inner flow is not fitted well and some traverses appear to be shifted sideways - the effect of the vortex being off axis was not allowed for these plots. This expression is a better approximation to the axial profile assumed by Burgers vortex, which has no radial dependence. Conversely, the Burgers vortex expression for the tangential velocity is markedly better than the expression obtained from this approach.

Shown overleaf:

Figure 5.D.1: Axial velocity profiles for Long cone and standard geometries together in 140mmØ cyclone with Bloor and Ingham model

Figure 5.D.2: Axial velocity profiles for Long cone (alone) in 140mmØ cyclone with Bloor and Ingham model.

and :

Figure 5.D.3: Axial velocity profile for 140mmØ and 750mmØ standard Stairmand H.E. geometry with Bloor and Ingham model.

Figure 5.D.1: Dimensionless axial velocity profiles for "Long cone" and standard geometries compared with the Bloor & Ingham model

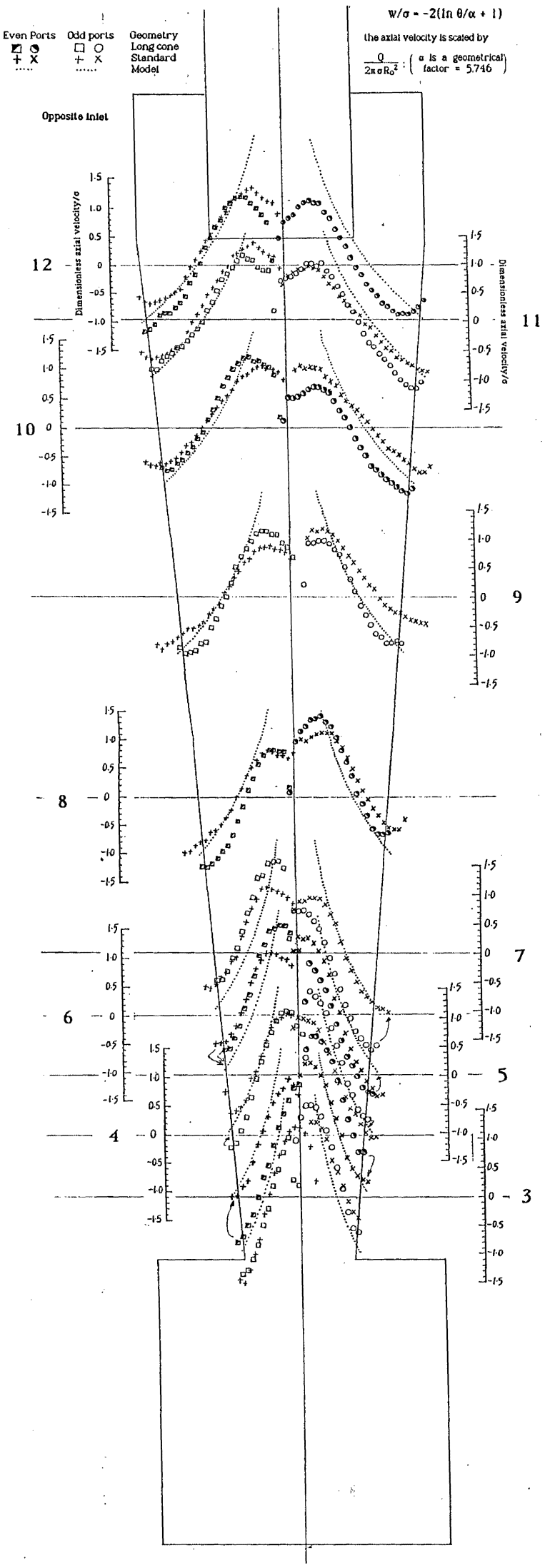

Figure 5.D.2: Dimensionless axial velocity profiles for "Long cone" and standard geometries compared with the Bloor & Ingham model

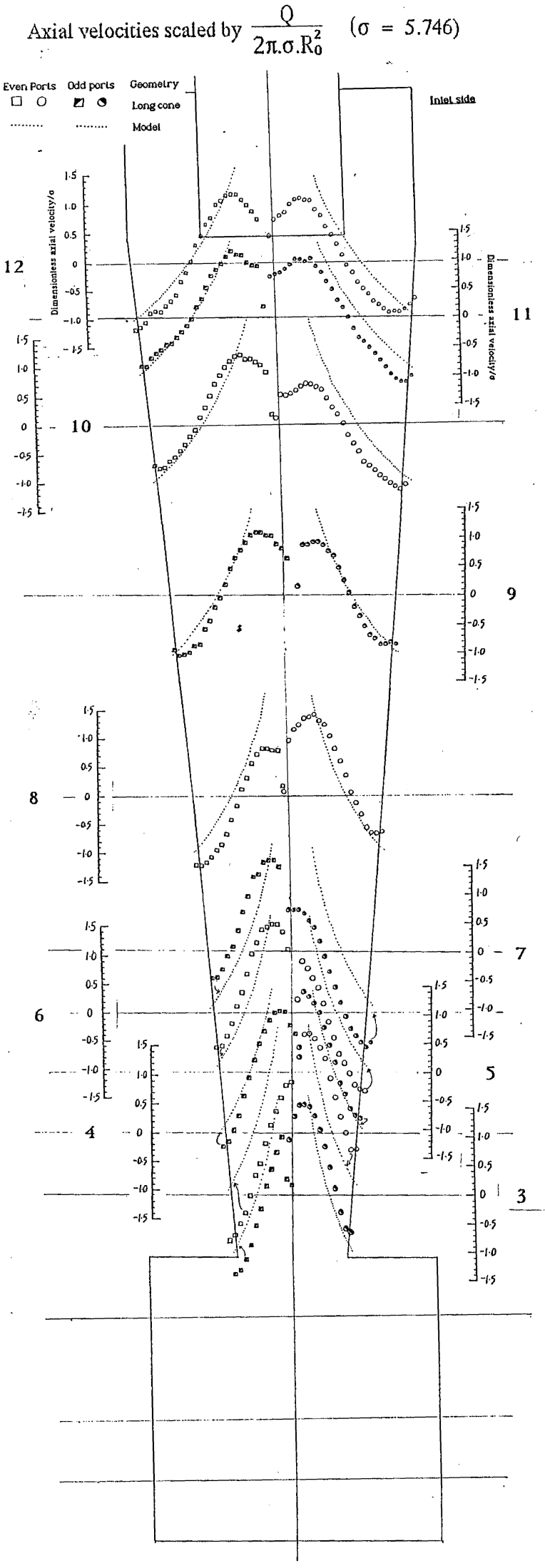

Figure 5.D.3: Dimensionless axial velocity profiles for the 140mm∅ and 750mm∅ cyclones with the Bloor & Ingham model.

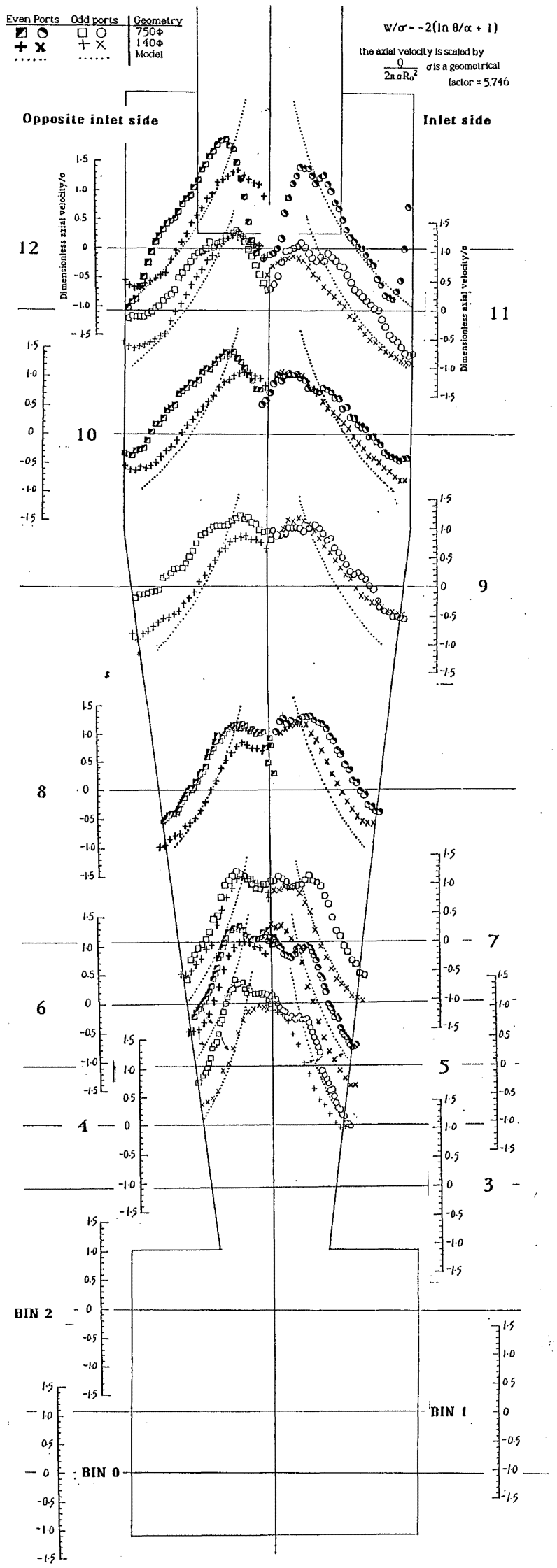

5.E RADIAL VELOCITY MODELLING

The Bloor and Ingham (1987) model used for the axial velocity has an expression for the radial velocity, which when corrected (Abrahamson, 1989) yielded the equations as :

$$V_r = q_r \sin\theta + q_\theta \cos\theta \qquad \text{--- (5.E.1)}$$

where $$q_r = \sigma\left(2 \times \frac{A}{\sigma}\cos\theta - 2(\cos\theta \times \ln(\tfrac{1}{2}\tan\theta)) - \frac{1}{\cos\theta} - 1\right) \qquad \text{--- (5.E.2)}$$

$$q_\theta = \frac{-2\psi}{r^2 \sin 2\theta} \qquad \text{--- (5.E.3)}$$

$$\psi = \sigma \times r^2 \times \left(\frac{A}{\sigma} \times \sin^2\theta - \sin^2\theta \times \ln(\tfrac{1}{2}\tan\theta)\right) \qquad \text{--- (5.E.4)}$$

The resulting radial velocity profile was found to be a simple shape and agreed only approximately with the profiles. The best agreement was found with the measurements in the 2090mmØ cyclone, which was encouraging. It gave positive radial velocities (outwards) within 25mm of the axis up to 0.1m/s, and inwards velocities elsewhere of up to -0.7m/s. The radial velocity profiles are given in Figure 5.E.4 and 5.E.5. Integration of axial velocities could give an approximate average radial inflow, but the agreement in the volume balances between ports was not good, with errors of up to 200% (see figure 5.B.14). This resulted in outward velocities being calculated for some levels. The average radial inflow calculated over the length of the cyclone is 0.41 m s^{-1}.

The results from the pitot cylinder in the 140mmØ cyclone are not reliable because of the difficulty of determining the pitch angle (the radial direction) in the high pressure gradients as well as the large difference in magnitude between the tangential and radial components of velocity. Radially outwards velocities are inconsistent with the conservation of mass and momentum. The results obtained for the larger scale cyclones had less scatter, and indicated that the inflow velocities were larger in the lower cone. The radial velocities obtained from the Pitot cylinder were an order of magnitude greater than expected from the uniform distribution of the radial inflow. The radial diffusivities found with the injection of fog at the wall at various levels in the cone were an order of magnitude larger again, and suggested that the turbulent diffusivity appears to dominate the convective inflow.

Overleaf:

Figure 5.E.1: Radial velocity profiles Ports 10, 8 and 4 for 140 mmØ, 750 mmØ and 2090 mmØ.

Figure 5.E.2: Radial velocity profiles, all locations, 750 mmØ and 2090 mmØ cyclones.

Figure 5.E.1: Radial velocity profiles in the 140mm∅, 750mm∅ and 2090mm∅ Stairmand H.E. geometry cyclones

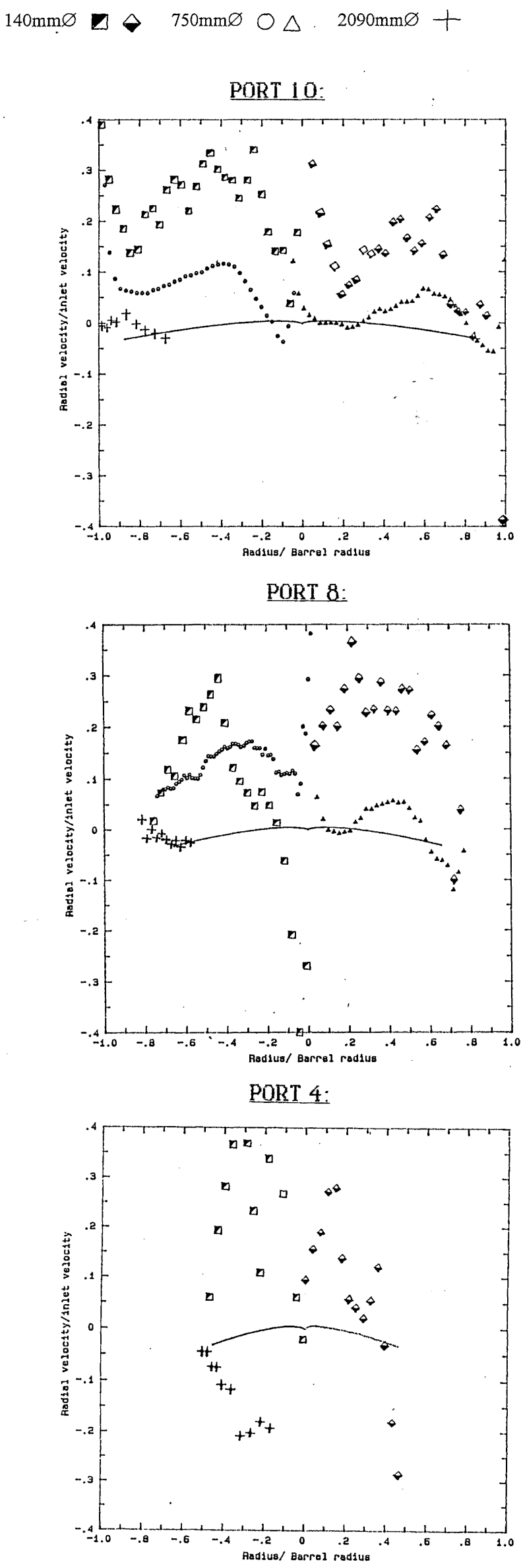

Figure 5.E.2: Radial velocity profiles from 750mm∅ and 2090mm∅ cyclones compared with Bloor & Ingham model.

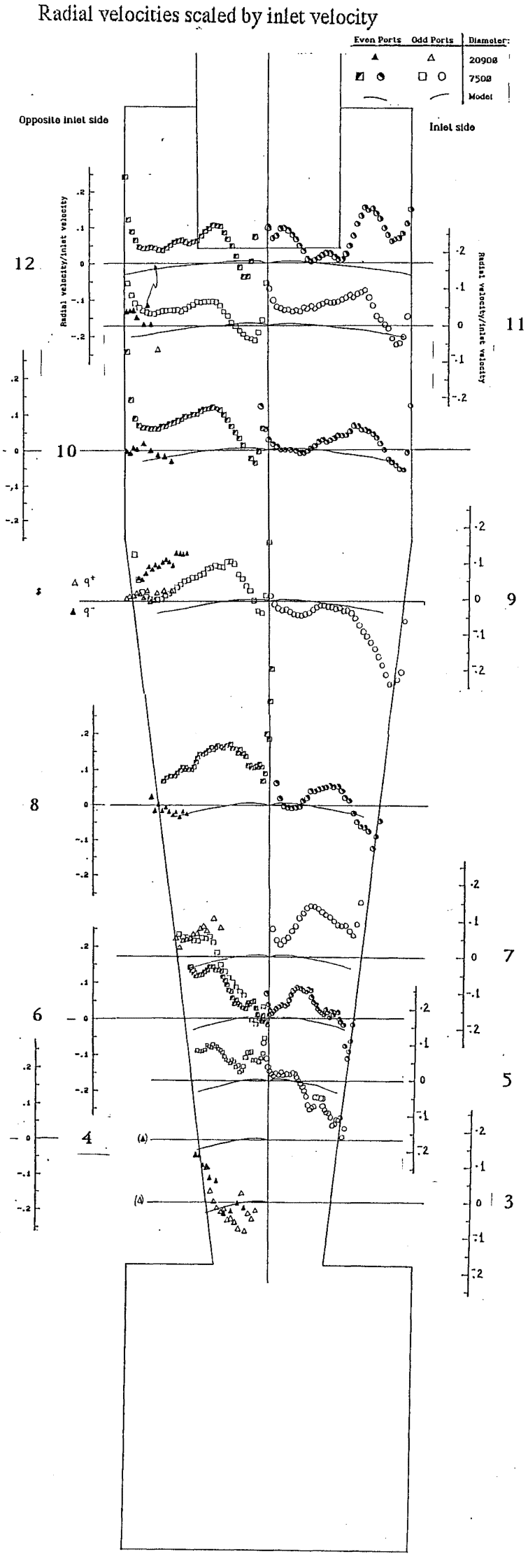

5.F. PRESSURE DROP

5.F.1. Euler number plots:

The overall cyclone pressure drop was measured in several different geometries based on the 140mmØ Stairmand High Efficiency geometry, and over inlet velocities ranging from 7 to 25m/s. The pressure drop was converted to an Euler number based on the average inlet velocity, and this Euler number was expected to be constant with velocity for a given geometry. The results in Figure 5.F.1 show a general rise in the Euler number up to an inlet velocity of about 20m/s, beyond which the Euler number is approximately constant, paralleling a similar trend in the effect of velocity on the efficiency. The axial static pressure profiles in section 5.H also show a change in the cyclone characteristics at flowrates around 10-12m/s

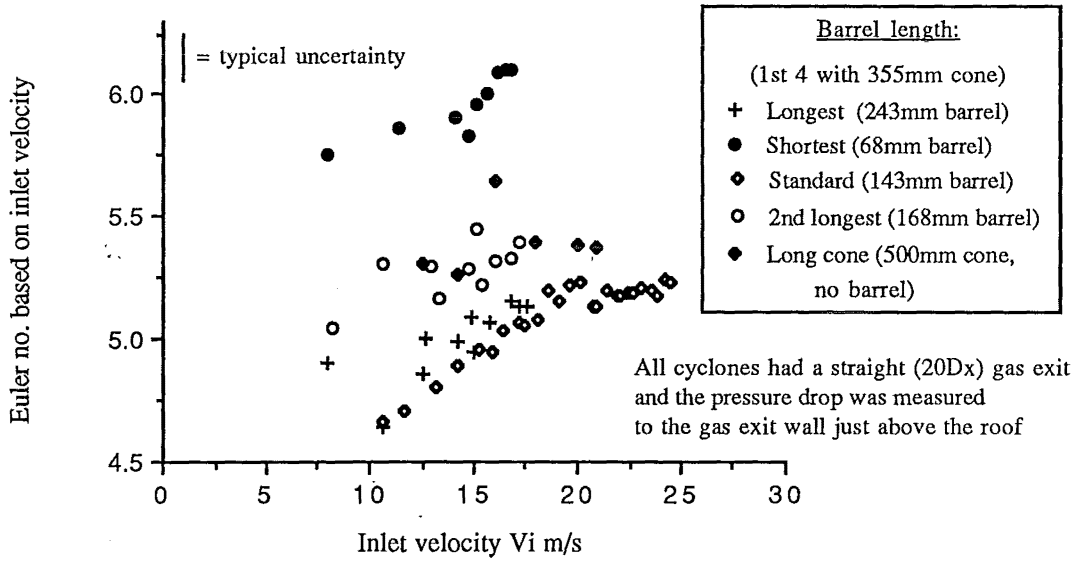

Figure 5.F.1: Cyclone overall pressure drop Euler numbers versus inlet velocity for various barrel lengths, 140mmØ cyclone

This figure also shows the effect of changing the barrel length on the Euler number. For all of the measurements in Figure 5.F.1 the cyclone pressure drop was measured between the wall of the inlet, and the wall of the gas exit just (30mm) above the cyclone roof. The gas exit in these cases was a straight cylindrical tube, 20 diameters in length.

Increasing the barrel length generally gave a lower Euler number, with the shortest geometry having the highest value. However, the standard geometry gave a lower Euler number than either of the longer geometries. The difference between the 'Standard' and 'Longest' geometries is not significant compared with the measurement uncertainty but the standard does appear to give an anomalously low Euler number. The Long cone and Standard geometries have the same distance between gas and dust exits, but the Long cone is entirely conical with no

cylindrical section. The Long cone does not appear to have an advantage of the standard in terms of pressure drop.

The effect of the cyclone length on the pressure drop was further examined by examining the extreme case presented by the "Extra Long" geometry. This has a length of 881mm, or 6.29 barrel diameters, between the gas exit lip and the dust exit. This was made up of 383mm of barrel sections, and the 498mm long "long cone" with a cone half angle of 5°. Small pieces of plastic were used as tracers to show the strength of the swirl in the bin. It was observed that at the lower velocities the airflow in the bin was usually insufficient to keep the plastic tracers in motion, and the overall pressure drop Euler number was markedly less than that obtained above an inlet velocity of 15m/s. It was possible to keep the tracers in motion at low inlet velocities by slowly reducing the flowrate from the high values. In this situation the Euler number was found to be comparable to that obtained at the higher velocities. These results are shown in figure 5.F.2.

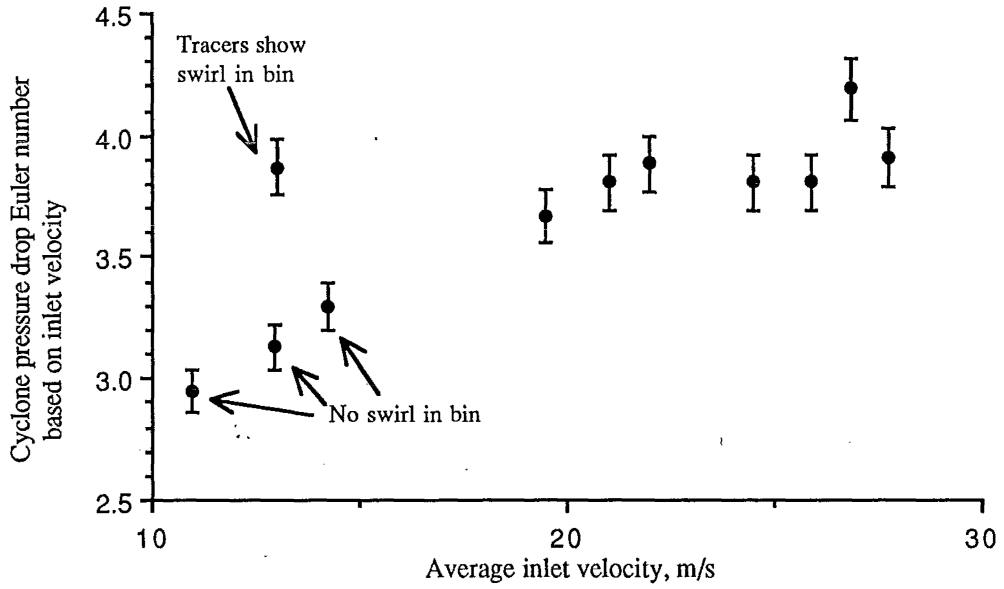

Figure 5.F.2: Overall pressure drop Euler number for the "Extra Long" geometry

The characteristic Euler number for each geometry was estimated at an inlet velocity of 20 m/s, and these are plotted against the cyclone length in figure 5.F.3 below. As well as the geometries in Figure 5.F.1 the Euler numbers for the standard and shortest geometries with the addition of an 90mm long conical extension piece to the dust exit are shown. The experimental error in the results is too high for the differences to be significant, but the Standard Stairmand HE length appears to be below the general trend.

The report on cyclone pressure drops by Abrahamson (1991) contains more details of the effect of the cyclone length on the pressure drop. It was found that Euler numbers for a wide range of cyclones were generally linear with length but there was a split between two diverging lines at around the standard Stairmand length. As the length was increased the data tended to fall more on the lower line, but there was a region where the data swapped between the two lines. It is possible that the results in figure 5.F.3 are indicating some of this behaviour.

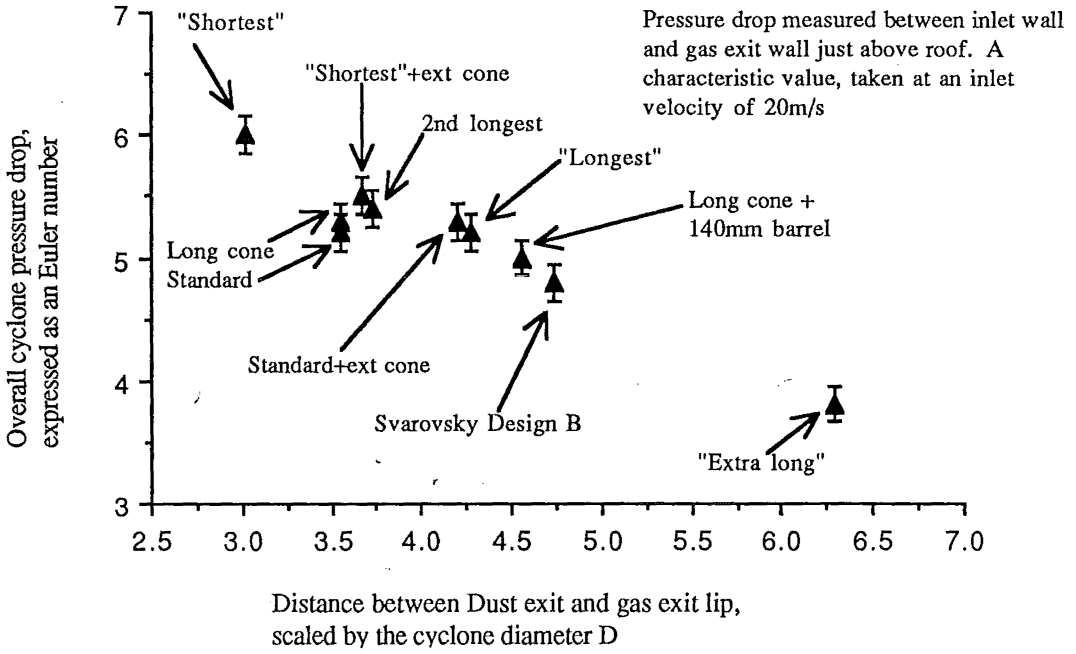

Figure 5.F.3: Effect of cyclone length on pressure drop in 140mmØ cyclone

The effect on the Euler number of increasing the cyclone length by extending the cone (to a smaller dust exit diameter) is shown in Figure 5.F.4 below. The 'Shortest' geometry Euler number is reduced by the extension, but the Standard geometry Euler number is slightly increased. Also shown in this graph is the effect of partially blocking the gas exit by placing a 35mmØ disk on the axis of the gas exit 3 diameters downstream of the gas exit lip. This results in an increase in the Euler number that is comparable to the effect of the cone extension. However neither change is significantly greater than the experimental uncertainty.

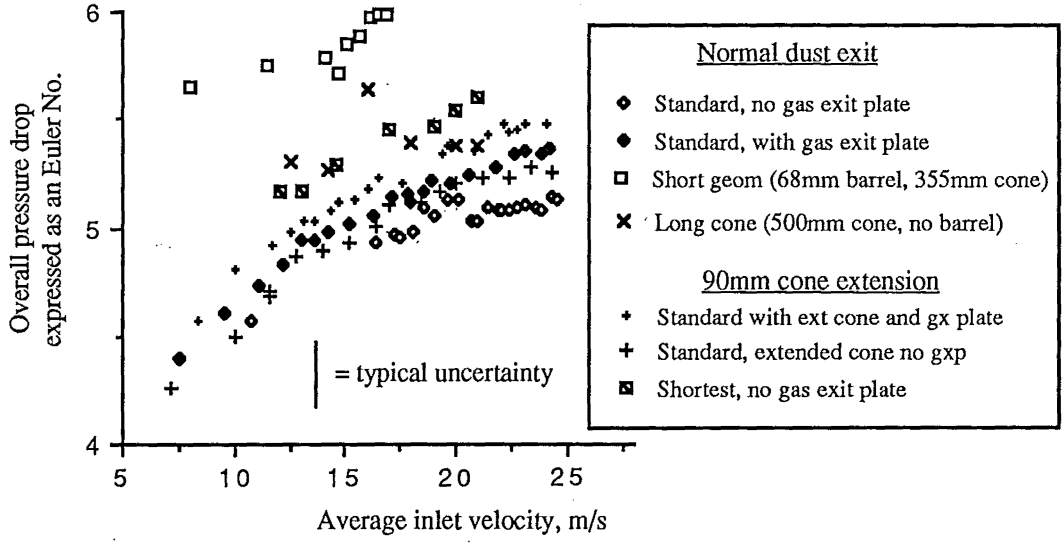

Figure 5.F.4: Variation of pressure drop Euler number with dust exit geometry

The cone extension with its smaller dust exit diameter may prevent the vortex entering the bin. The same modification to the standard geometry resulted in a slight increase in pressure drop, possibly because the vortex is already prevented from reaching the bin. The gas exit plate and a

Scroll exit were also examined to investigate the possible effect of.stabilising the axial position of the cyclone vortex.

Initially, measurements of the overall cyclone pressure drop were made with a long straight gas exit tube (L/D = 20). Cyclones commonly exhaust to the atmosphere, and the pressure drop is taken as the gauge pressure of the inlet, as was the case with the 750mmØ cyclone. To compare pressure drops with this, a sudden expansion in the gas exit was provided by means of a 0.5mØ barrel. This was placed in the gas exit 400mm above the roof of the cyclone and the pressure drop could then be measured to the base of this bin where the exit air did not have spin. The advantage of this method of measuring the cyclone pressure drop was outlined in figure 3.E.1. Figure 5.F.5 shows the variation of the pressure drop with the gas exit configuration of the 140mmØ Long cone cyclone (with 498mm long cone and no cylindrical section). The effect of adding a 140mm long cylindrical section to this cyclone is also shown, as the 'Long cone + 140mm cylinder' points.

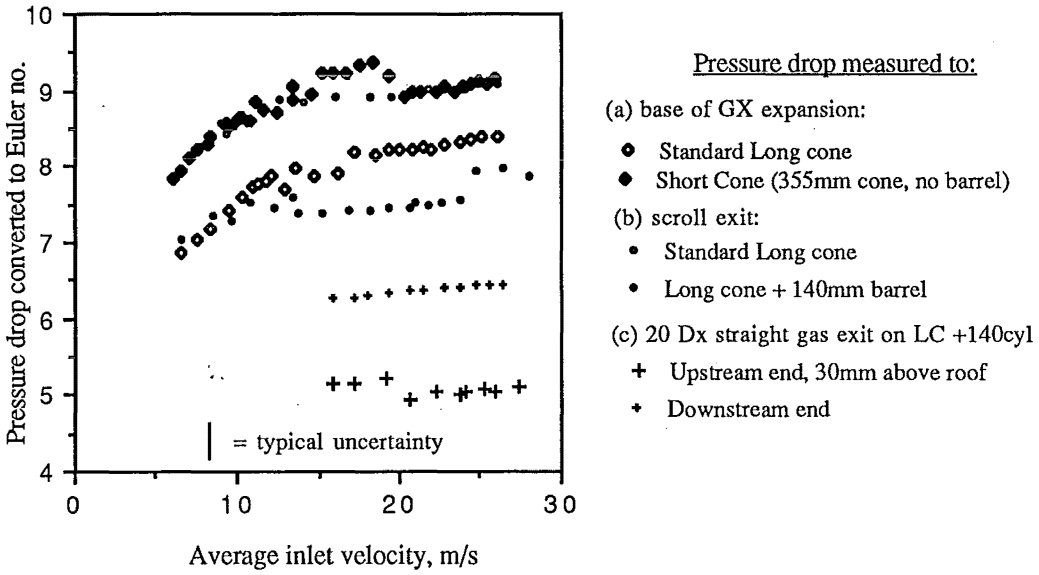

Figure 5.F.5: Overall pressure drop for variations in the gas exit configuration

These pressure drops were measured between the inlet and the base of the expansion barrel in the gas exit, hence cannot be directly compared with the results in Figures 5.F.1 - 4. The standard and long cone geometries can be compared in the gas exit Euler number profiles in figure 5.E.6 (for a inlet velocity of 23m/s). The long cone geometry pressure drop is (in Figure 5.E.6) shown to be lowered by the addition of a 140mm long barrel section,to almost the level achieved by disturbing the flow with a probe. A scroll exit added to the long cone geometry causes an increase in the pressure drop, and the resulting profile suggests that the flowfield has become similar to that of the short cone/no barrel case.

5.F.2. Gas Exit wall pressures and pressure recovery

To examine the behaviour of the vortex in the gas exit, 34 tappings were drilled along the gas exit wall. The pressure drop between the inlet and each tapping was measured for various geometries and converted to an Euler number based on the inlet velocity. These results are shown below, plotted against the distance from the gas exit lip, for an inlet velocity of 23m/s :

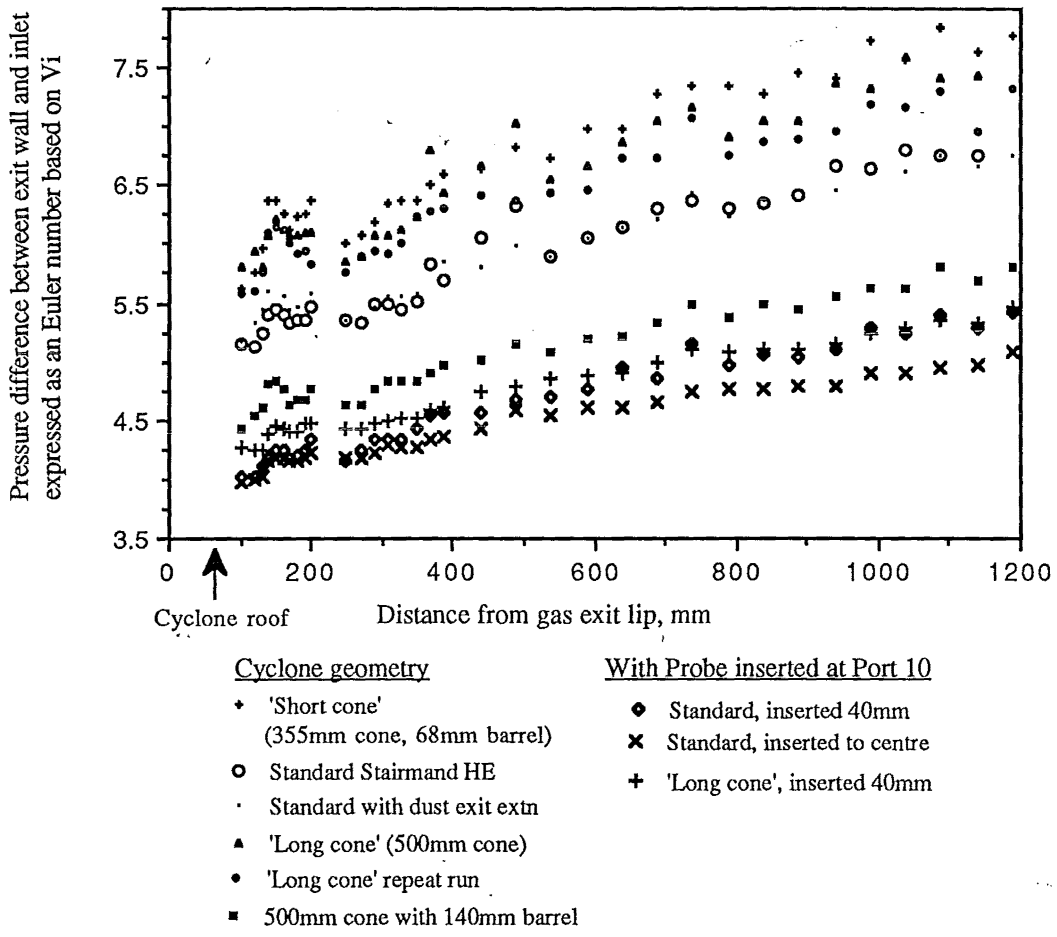

Figure 5.F.6: Profile of gas exit wall pressure relative to inlet pressure (in 140mmØ cyclone)

In the gas exit there was a region of steep wall pressure gradient just above the roof. For many profiles this was followed by a short regain in pressure followed by a more gentle pressure gradient along the rest of the gas exit. Different cyclone geometries had higher Euler numbers but showed similar slopes in the gas exit downstream of the initial regain.

The region of the regain in pressure is thought to correspond to a vortex breakdown in the exit, and this agrees well with the position of the tracer trap observed with the helium bubble tracers.

5.G. RADIAL PRESSURE GRADIENT.

The radial static pressure gradient was calculated for each profile location in the 750mmØ and 140mmØ cyclones and a selection of these are presented in the graphs in this section. The Pitot cylinder yields a radial profile of the static pressure, which could then be crudely differentiated by taking the slope between two adjacent points. These local gradients are plotted as the individual points on the graphs that follow. It can be seen that there is a lot of scatter in the data, which is in part caused by the amplification of measurement errors and the rough method of differentiation.

To reduce the amplification of scatter a 5th order polynomial was fitted to the original static pressure profile. This polynomial was then differentiated with respect to radius, giving a smoothed radial static pressure gradient. As the pressure gradient in the outer vortex was of the most interest another polynomial was fitted to just the data in the outer vortex - to avoid the inflexion in the core profile. Both of these smoothed gradients are shown in the graphs, but there is not much difference between them in the outer vortex.

These experimental static pressure gradients are to be compared with the expected radial pressure gradient due to the centrifugal effect, which is given by $\frac{\rho V\theta^2}{r}$. The experimental tangential velocities ($V\theta$) determined with the Pitot cylinder were used to estimate this, and the resulting profile of the radial pressure gradient is plotted as the dotted line. Once again, to smooth out the curves the tangential velocities obtained from the fitted Burgers vortex profile were also used to calculate a smoothed gradient.

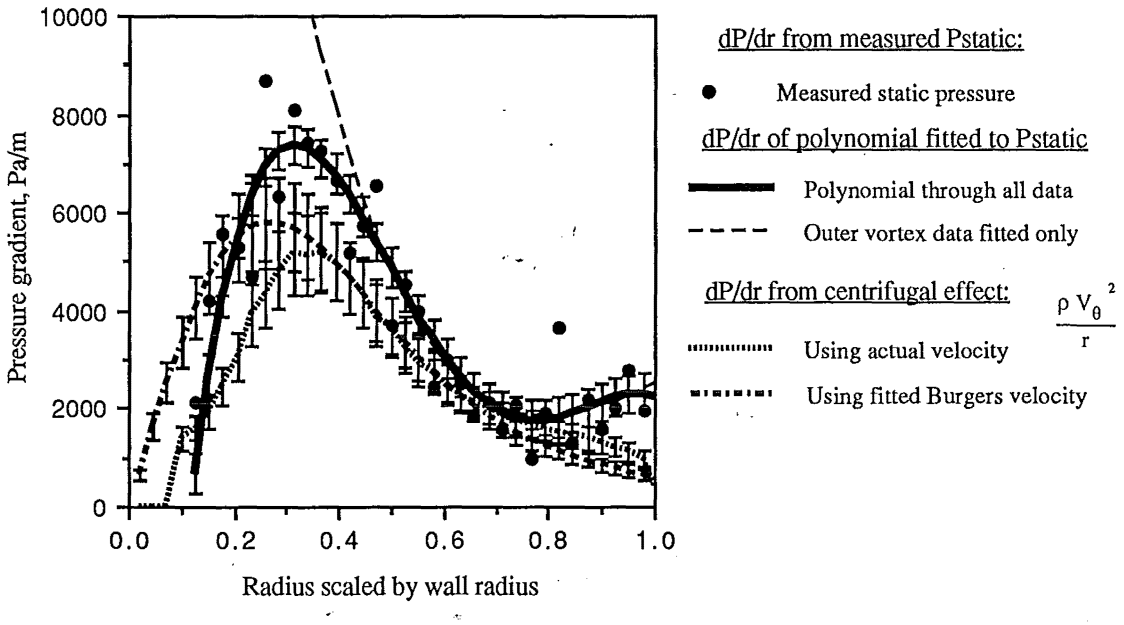

Figure 5.G.1: Radial pressure gradient at Port 12 in 750mmØ cyclone

The relationship is derived from the Navier Stokes equations for the conservation of momentum assuming a quasi-cylindrical flow. Ranz (1985) used the relationship to obtain the tangential velocity profiles from the static pressure profile in a cyclone operating with dust flowing. This was necessary, as the impact tube used to measure velocities would plug with dust whereas the static tube could be kept clear. Good agreement between the methods of determining $V\theta$ was reported for traverses made without dust flowing (Ranz, 1990)

The error bars have been included on the first graph, but left off the others to avoid cluttering the graph. Figures 5.G.1, 5.G.2, and 5.G.3 show the radial gradients in the 750mmØ cyclone at Ports 12 (just below the gas exit lip), 9 (just below the cone/barrel junction) and 6 (in the lower cone region) - all on the opposite inlet side.

The radial pressure gradient is of interest in the prediction of the stability of the cone wall boundary layer in the cyclone, this is discussed further in Chapter 6. If the gradient is greater than supported by the centrifugal effect then there exists a driving force to move the boundary layer inwards. From these graphs it appears that a driving force exists in some regions but not in others. There appears to be a significant difference in the radial pressure gradient near the inlet in the 750mmØ cyclone as shown in Figure 5.G.1, but the profiles of the gradient are closely matched at Ports 9 and 6 as shown in Figures 5.G.2 and 5.G.3 below. Further processing of results is required to clarify the trends.

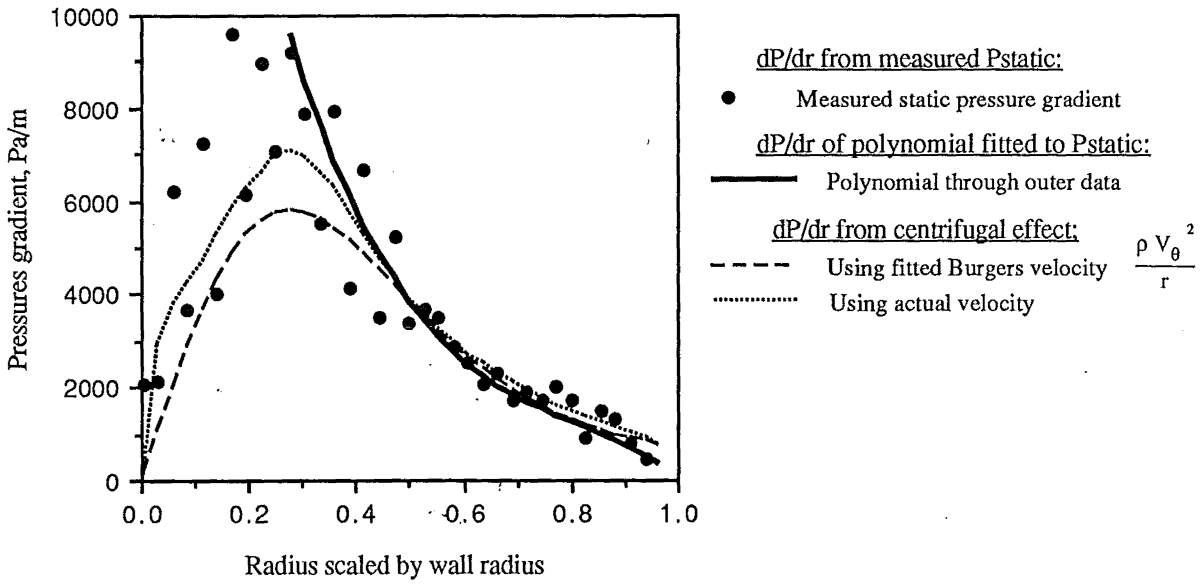

Figure 5.G.2: Radial pressure gradient in upper cone in 750mmØ cyclone (Port 9oi)

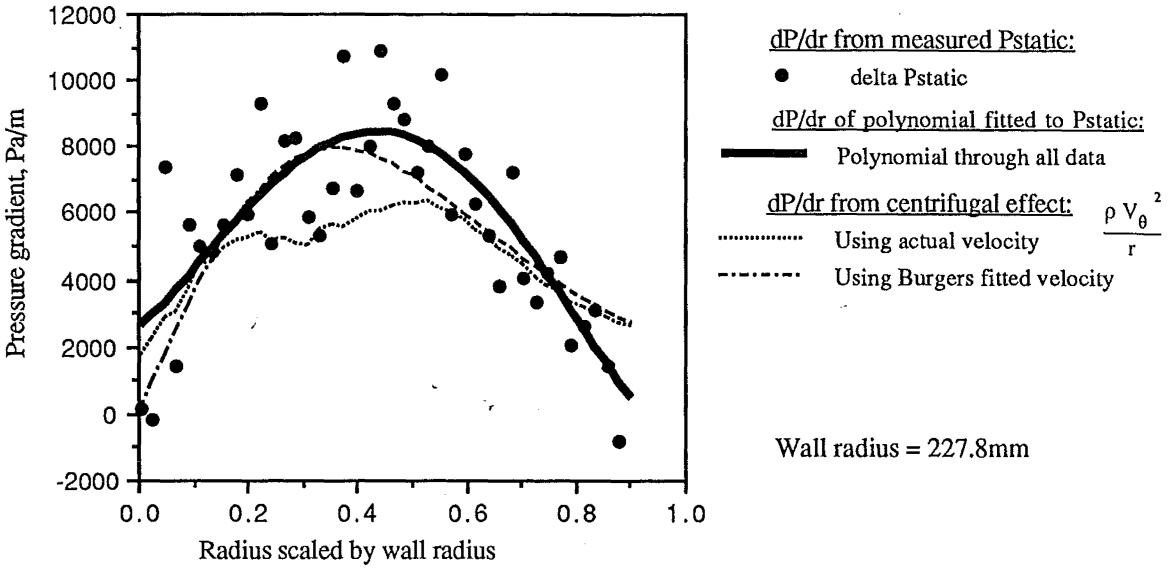

Figure 5.G.3: Radial pressure gradient in mid cone in 750mmØ cyclone (Port 6oi)

Since the lower two traverses were not accessible in the 750mmØ cyclone the same radial pressure gradients have been calculated for the 140mmø cyclone, including ports near the dust exit. These are given below:

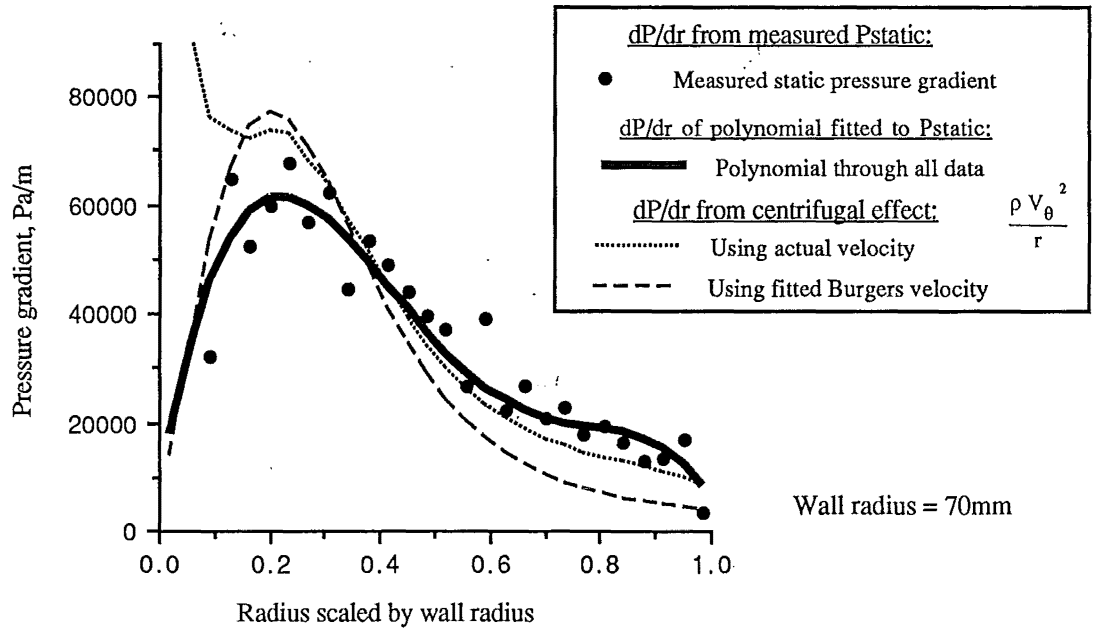

Figure 5.G.4: Radial pressure gradient near inlet in 140mmØ cyclone (Port 11i)

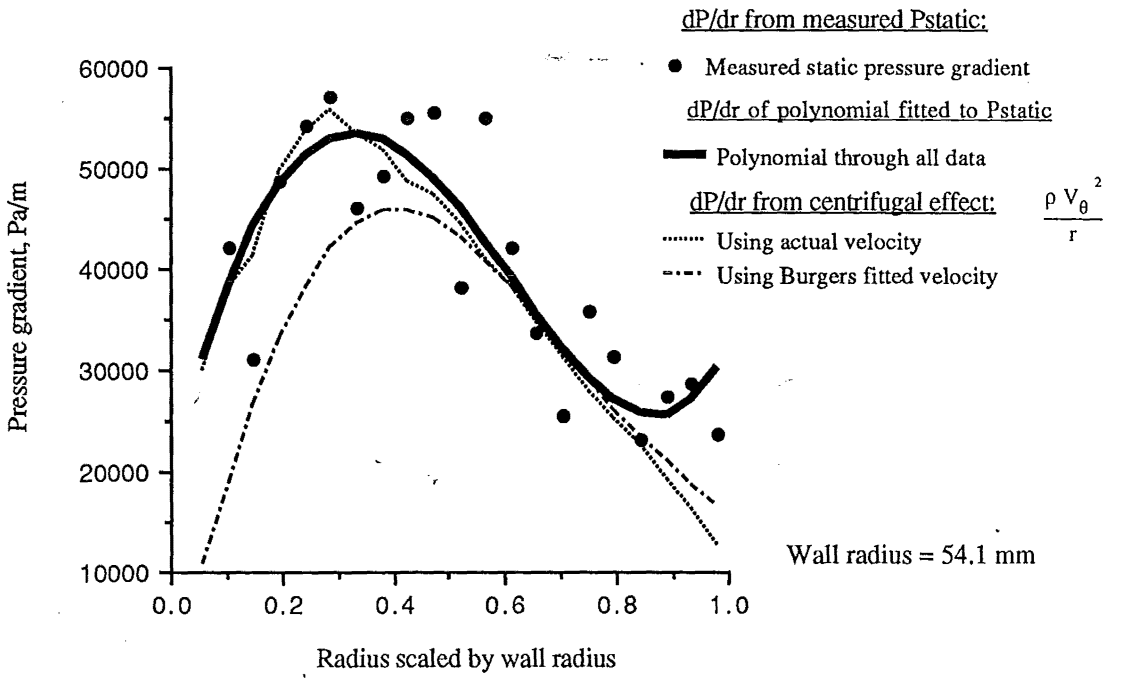

Figure 5.G.5: Radial pressure gradient in upper cone in 140mmØ cyclone (Port 8i)

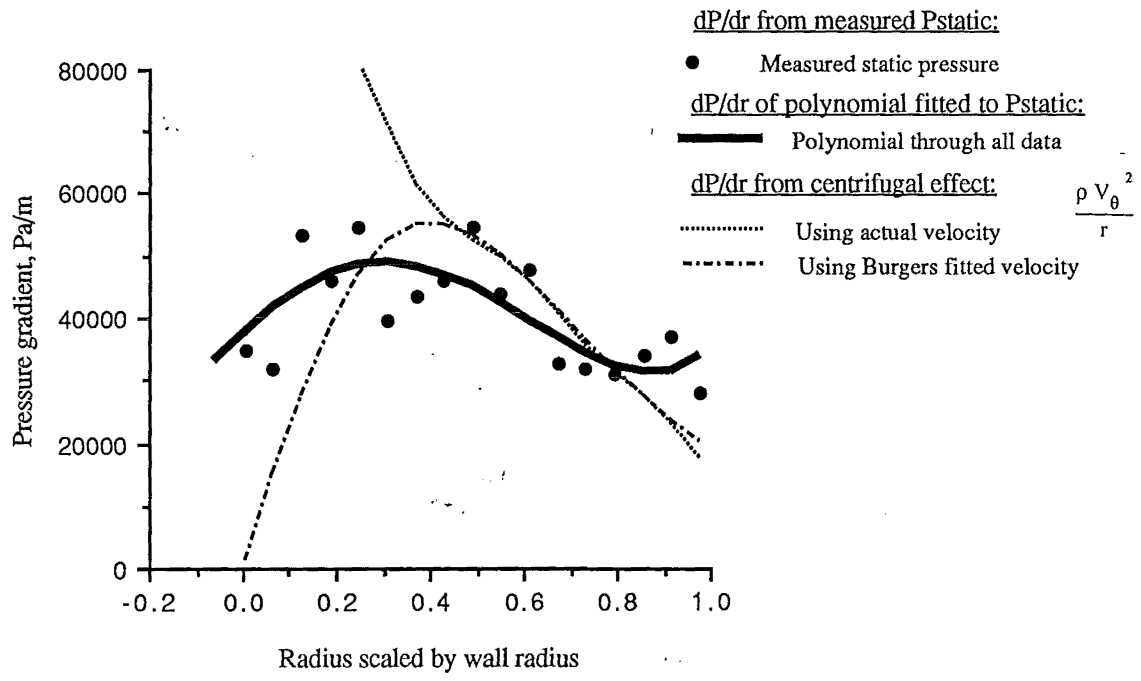

Figure 5.G.6: Radial pressure gradient in mid cone in 140mmØ cyclone (Port 6i)

When a fog tracer was injected at the wall at the location of the following graph (Port 4, 60mm above the dust exit in the 140mmø cyclone) the fog was observed to remain close to the wall, as shown in figure 5.A.10 (Plate 4C). The two radial gradients are closely matched. Other regions, such as Port 6 in figure 5.A.9 (Plate 4B) showed 'fingers' of the fog moving towards the centre faster than the average inflow.

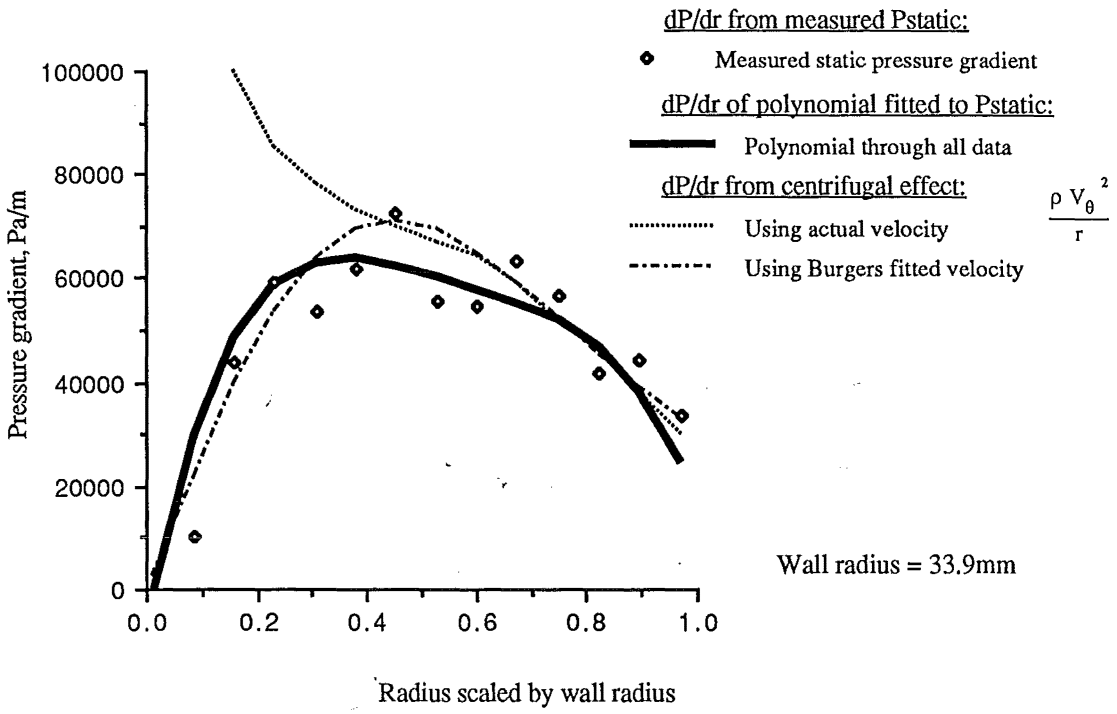

Figure 5.G.7: Radial pressure gradient in lower cone in 140mmØ cyclone (Port 4i)

The most complete profiles obtained in the bin were with the 140mmØ Long cone geometry, but the flow pattern is essentially the same as the standard geometry. The radial gradients of the pressure obtained from the pitot cylinder, and the centrifugal radial pressure gradient calculated from the pitot cylinder tangential velocities are shown below. The two local maximums of the experimental gradient were observed in other traverses just below the dust exit expansion and were thought to be characteristic of this location. The gradient away from the axis is lower than found in the cyclone cone.

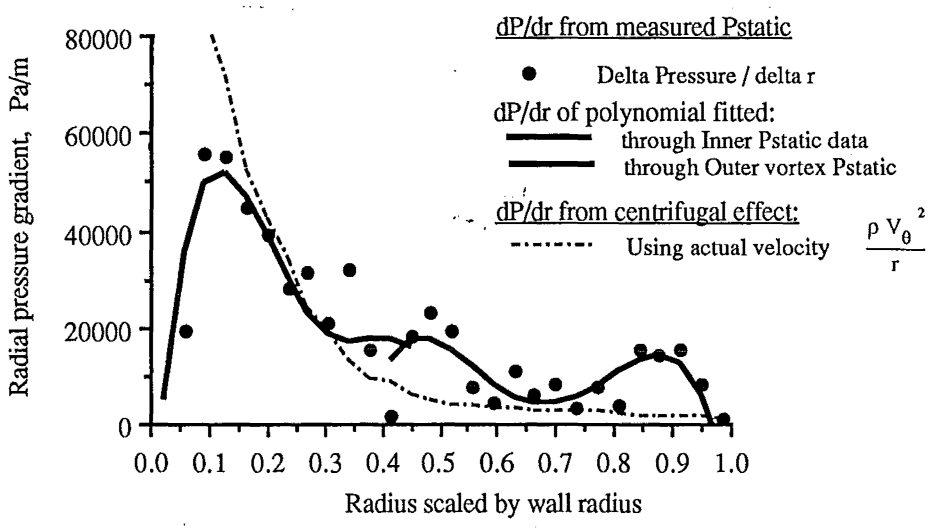

Figure 5.G.8: Radial pressure gradient in bin 0.57 dust exit diameters below dust exit in 140mmØ cyclone, inlet side

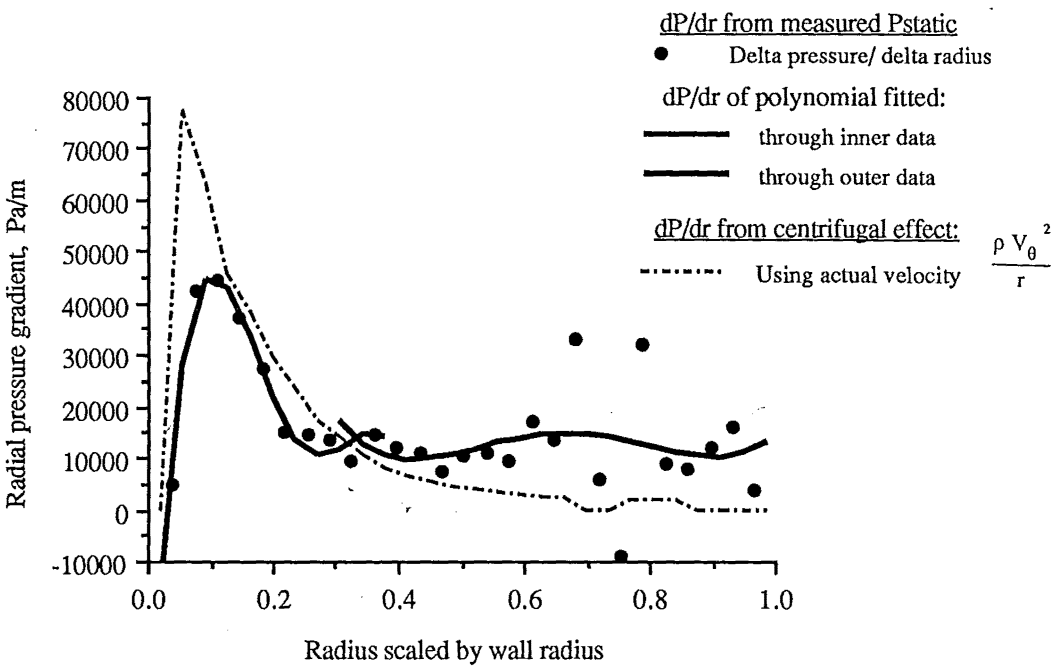

Figure 5.G.9: Radial pressure gradient in mid bin 1.1 dust exit diameters above base in 140mmØ cyclone, inlet side

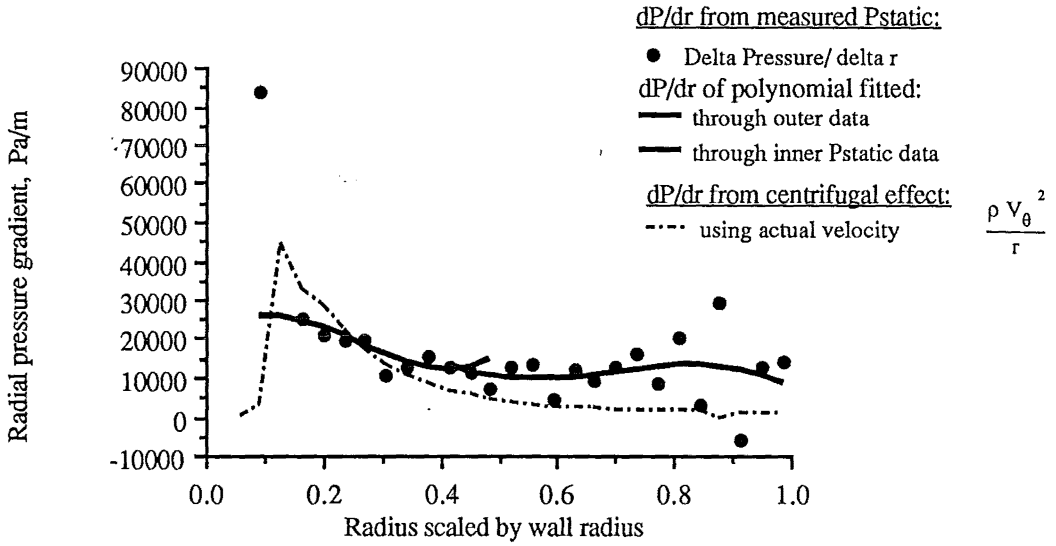

Figure 5.G.10: Radial pressure gradient 0.57 dust exit diameters above bin base in 140mmØ cyclone, inlet side

The radial pressure distribution could also be estimated by the difference between the wall and axis pressure measurements. The wall pressure was measured with a flush tapping at the wall, the pressure at the axis was obtained from the axial static pressure traverses. The difference between these, at each Port location, was then expressed as an Euler number based on the inlet velocity. This gives a measure of the wall - axis pressure difference that is easier to measure than making complete traverses, and it gives a single value for each location that can be compared with other locations. This wall-axis pressure difference is plotted against the distance

from the dust exit expansion for a range of geometries in Figure 5.G.11. In some geometries the expansion into the bin has been delayed by the addition of conical or cylindrical extensions of the dust exit. If the dust exit expansion stabilised the vortex at that position then the wall-axis pressure difference would be expected to be similar for these profiles.

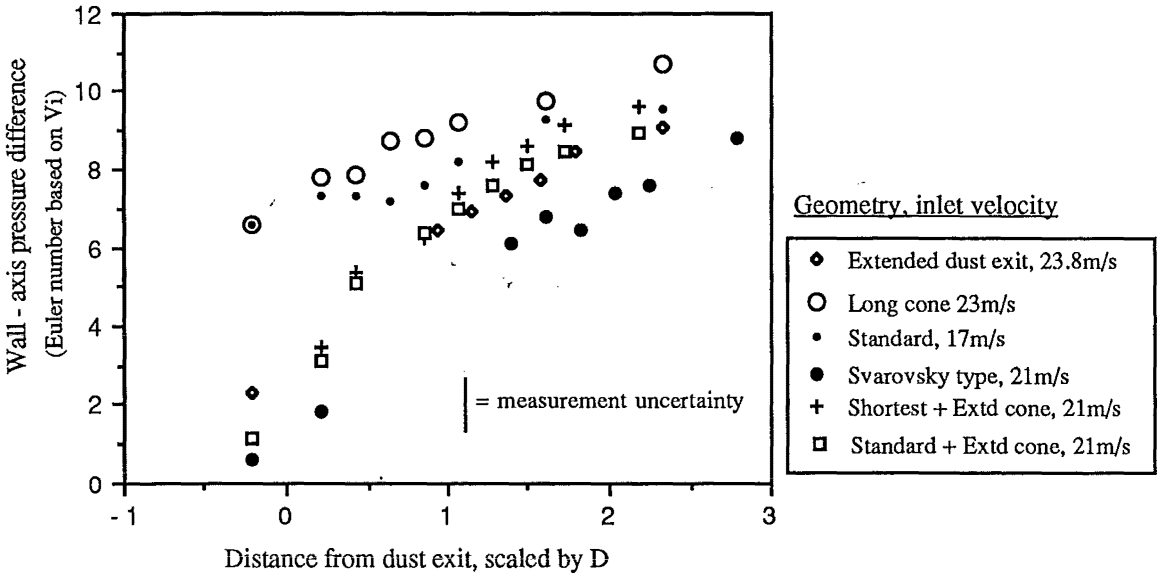

Figure 5.G.11: Wall-axis pressure difference plotted against distance from dust exit for various 140mm geometries

As shown in Figure 5.G.11 a consistent change in the wall-axis pressure difference is not obtained relative to the expansion into the bin. When these pressure differences are plotted relative to the distance from the gas exit lip, the agreement is much improved, as shown below in Figure 5.G.12.

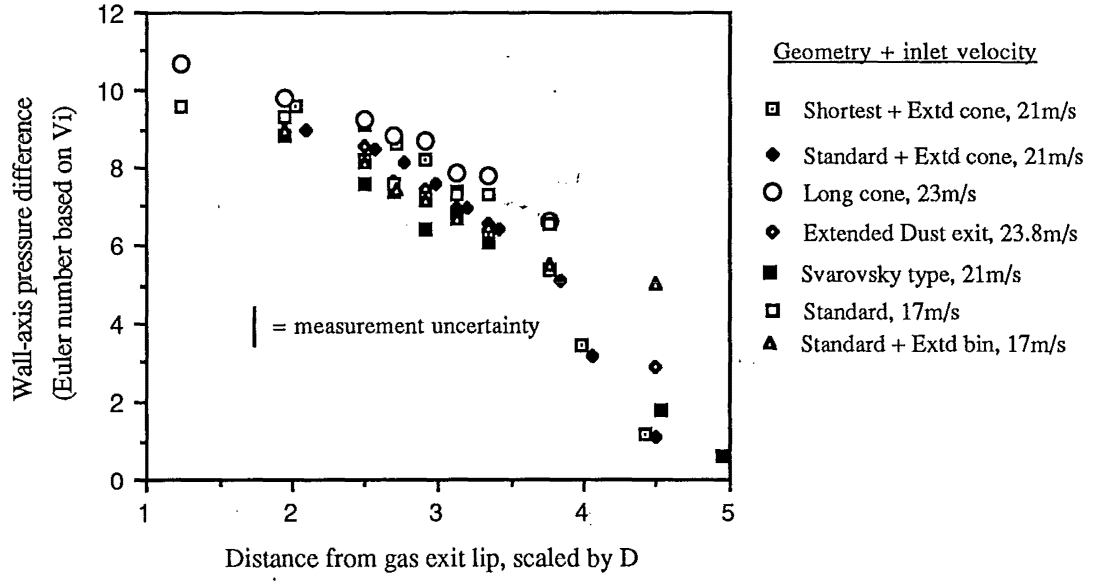

Figure 5.G.12: Wall-axis pressure difference plotted against distance from gas exit lip for various 140mmØ geometries

This suggests that the pressure difference between the wall and axis is not determined by the dust exit geometry, but by the evolution of the vortex along the cyclone length. Note that the total difference between the wall and the axis decreases with increasing distance from the gas exit, and the difference in the bin roughly fits the trend of this decline.

This wall-axis pressure difference was then converted to an average radial gradient by dividing the Euler number by the local wall radius. The variation of this down the cyclone length for a range of dust exit configurations could then be examined. As the dust exit expansion occurred at different positions relative to the gas exit lip, the results are again presented with respect to the distance from both the dust exit expansion, and from the gas exit lip.

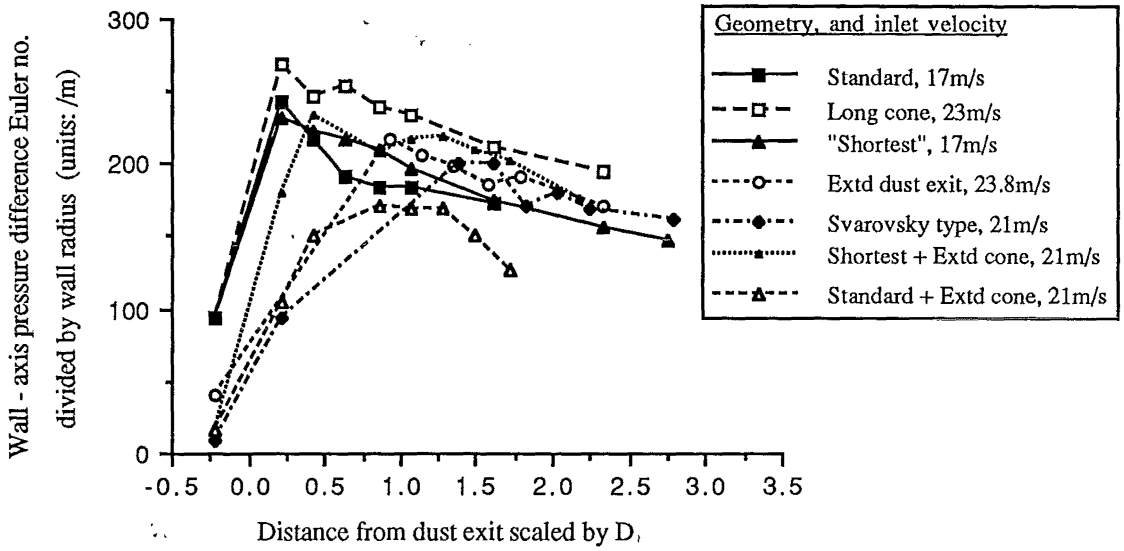

Figure 5.G.13: Variation of average radial pressure gradient in 140mmØ geometries plotted against the distance from the dust exit

One measurement between the sidewall and the axis was possible in the bin, just below the expansion. This shows that the gradient between the wall and the axis was considerably less than in the cone of the cyclone, as expected because of the low tangential velocities found in the bin. The high gradient is maintained right up to the dust exit expansion in the case of the Standard and Long cone geometries, but it appears that the steep reduction begins before the expansion in the case of the extended cone and Svarovsky type geometries.

All of the geometries had the same distance from the gas exit lip to the 53mmØ normal dust exit, except for the Shortest + extended cone. Whereas the Standard and long cone geometries then expanded into the bin, the other geometries had the expansion delayed by the addition of conical or cylindrical extensions to the dust exit.

When the pressure difference is plotted with respect to the distance from the gas exit lip the position of the start of the decline appears to be at about the same position for a wide range of dust exit geometries. This position is about the position of the end of the normal Stairmand H.E. cone at 3.5 barrel diameters from the gas exit lip. For the geometries with the dust exit expansion delayed by the addition of the conical or cylindrical extensions this decline appears to start before the expansion. The exception is the Shortest geometry with the extended cone, which manages to push the vortex further into the extension piece before the decline starts.

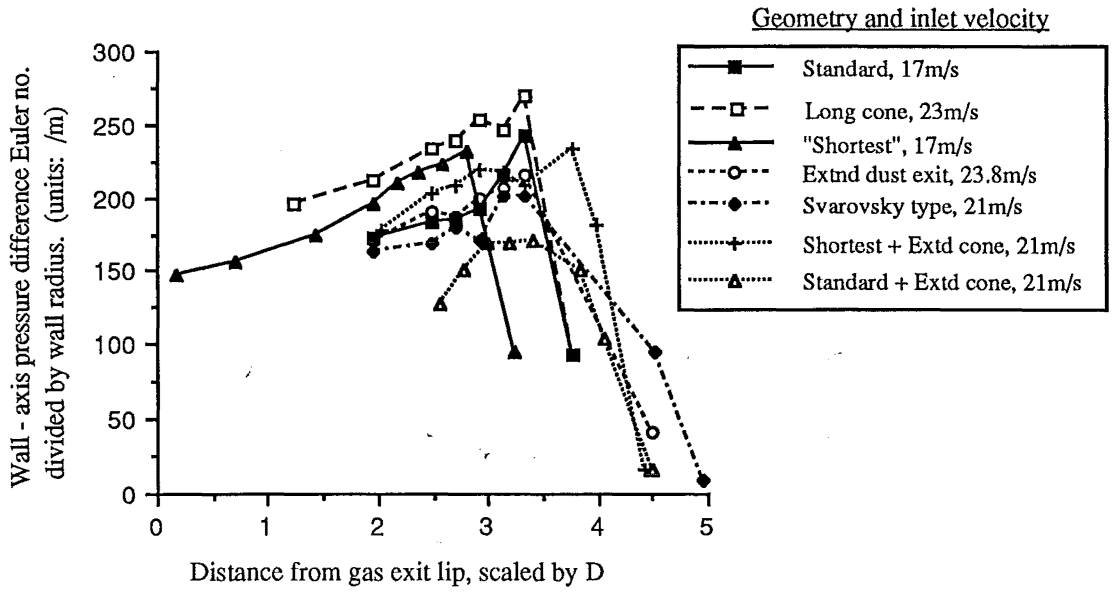

Figure 5.G.14: Variation of average radial pressure gradient in 140mmØ geometries plotted against the distance from the gas exit lip.

The sharp reduction in the radial gradient could be viewed as an indication of the ending of the vortex, which for the extended cone is brought about before the dust exit expansion. The radial gradient is supported by the opposing pressure gradient due to the centrifugal action. When the swirl of the vortex weakens, this opposing gradient is reduced and the high gradient flow becomes unstable. The reduction in the gradient is sharp, suggesting a catastrophic ending to the vortex rather than a steady decay. Alternatively, the change in the radial gradient could be interpreted as an effect of the boundary layer. In the extended cone, the boundary layer could grow to become an appreciable part of the diameter and the slower swirl in the boundary layer would not be able to support such a high pressure gradient.

This value of the gradient was an average taken between measurements at the wall and at the axis. In the above plots the wall pressure is taken with a flush pressure tapping, and the axis pressure is taken by inserting the 5mmØ static pressure probe in from the base. Since profiles of the pressure along the axis in the 750mmØ cyclone were not made, the static pressures at the wall and the axis obtained from the 4 hole Pitot cylinder had to be used. To check the agreement between these methods of measuring the pressure both methods were calculated for the 140mmØ cyclone, and these were then compared with the results from the 750mmØ cyclone. In order to compare the different scale cyclones the average Euler number gradient between the axis and the wall was multiplied by the barrel radius, giving a dimensionless quantity that ranged from 7 to 15 in the cone, as shown overleaf:

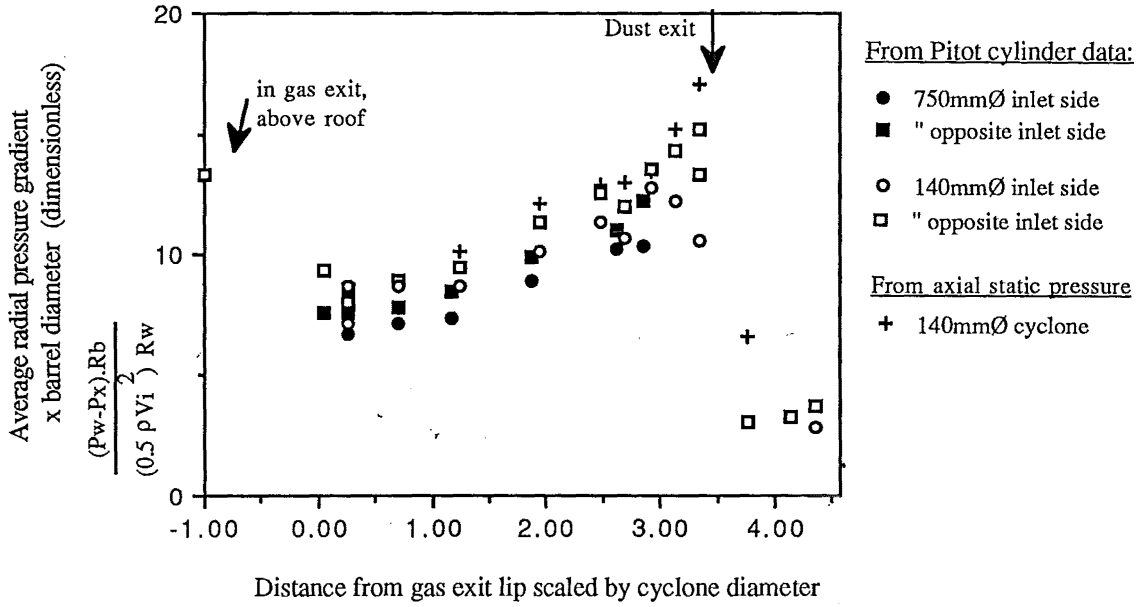

Figure 5.G.15: Average radial pressure gradient in 140mmØ and 750mmØ standard Stairmand High Efficiency geometry cyclones.

This could also be calculated for the 2090mmØ cyclone for the two traverse locations closest to the end of the cone. These values were both 20.5, considerably above the values in the other cyclones. The 2090mmØ cyclone had a non-standard dust exit arrangement, with a cylindrical extension of the dust exit for 2 diameters before the expansion. There was also a small draw off of air through the bin during the runs.

The difference between the normal and extended dust exit geometries was also evidenced in the axial static pressure profiles, which are presented in the following section. Refer in particular to Figures 5.H.5 and 5.H.6 compared with the standard geometry profile in Figure 5.H.2. The bin pressure was also affected by the dust exit geometry, as shown in Figures 5.H.7 and 5.H.8 for the difference between the bin sidewall and base pressures. These will often be easier to measure than pressures at the cone wall and axis.

5.H. AXIAL STATIC PRESSURE

5.H.1. Axial Static pressure profiles

Although the axial probe had negligible effect on the bin side wall reference pressure, flow visualisation with the helium bubble tracers showed there was some disturbance to the flowfield. The bin trap was present only when the base of the bin was flush to within +/- 1mm, and as the probe was inserted the gas exit trap moved downstream. With less than 50mm inserted the gas exit trap was within 5.4DX of the gas exit flange, by the time the probe reached the neck of the bin the trap had moved to 7.5DX downstream from the gas exit lip.

For the Longest geometry there were two distinct profiles - Type A (exemplified by the profiles at 7.9 and 17.6m/s) had a definite minimum in the bin, while for Type B (all the other profiles) the pressure (in the corresponding region in the bin) is approximately constant. The flowfield seems to switch between these two states without a change in the geometry or flowrate. There was no evidence of stabilisation of the profiles by inserting a plate in the gas exit. The type A profile is the only type found in shorter geometries than this.

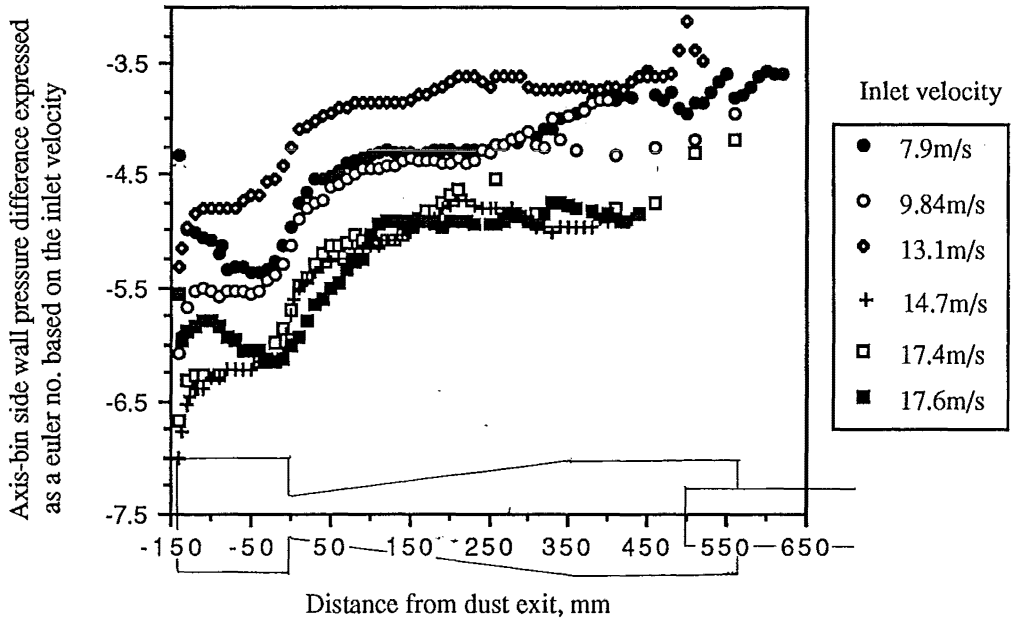

Figure 5.H.1: Profiles of static pressure along the axis of the 140mmØ "Longest" geometry at various flowrates.

Despite the conversion of the measurements to the dimensionless Euler number, there is a difference between profiles at different flowrates. The low flowrate profiles are grouped separately from high profiles, and an intermediate profile (the one at 9.8m/s) seems to be switching between the two. This switching is also shown in the Standard geometry (10.9m/s in figure 5.H.2) below.

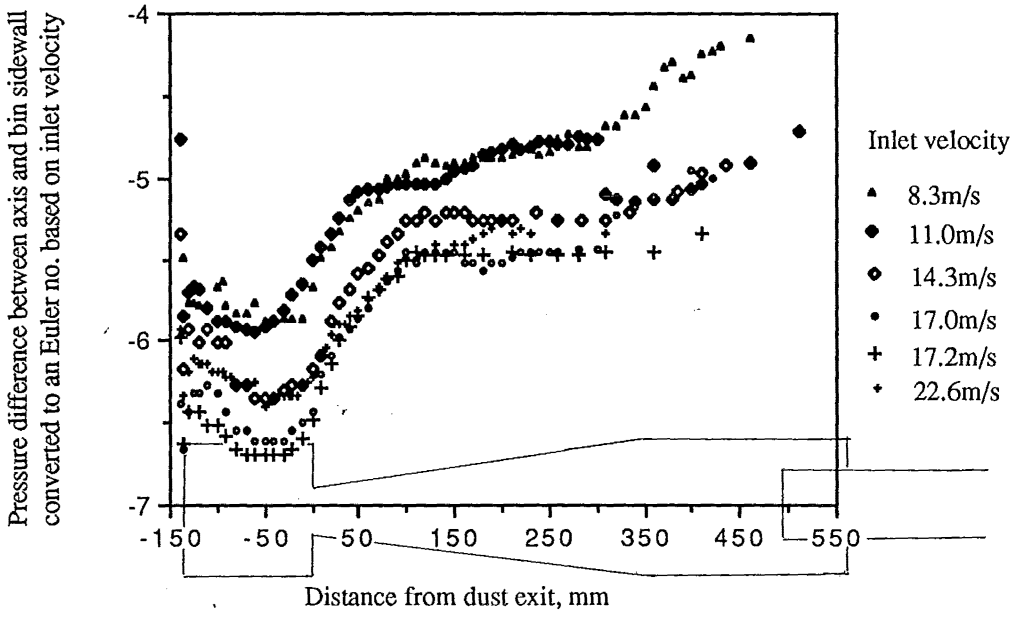

Figure 5.H.2: Profiles of static pressure along the axis of the 140mmØ Standard Stairmand high efficiency geometry at various flowrates.

For both of these the switch from the low flow profile to the high flow profile occurs near the cone/barrel junction. This could be related to the change in slope of the Euler number vs inlet velocity plot, which also occurred at around 10m/s, as shown in figures 5.H.1 - 5.H.4

The dominant feature of the profiles is the sharp rise in pressure in the lower cone. When the barrel was lengthened this pressure rise remained across the bin entrance, as shown in Figure 5.H.3 for a range of barrel lengths from 68-243mm (0.5 to 1.7 barrel diameters), with the same cone length of 355mm, as well as the "Extra long" geometry with a 383mm long barrel and 498mm cone. This could be a result of the cone stabilising the position of the breakdown, or the effect of the dust exit expansion on the static pressure at the axis. This was investigated in the previous section, which seemed to suggest that the distance from the gas exit is the important dimension rather than the distance from the gas exit lip. The rise in the axial pressure in leaving the bin is about 1 to 1.5 Euler numbers. This can be compared with the change in the wall pressure with length in Figure 5.J.4, which also increases in that direction, by a similar amount.

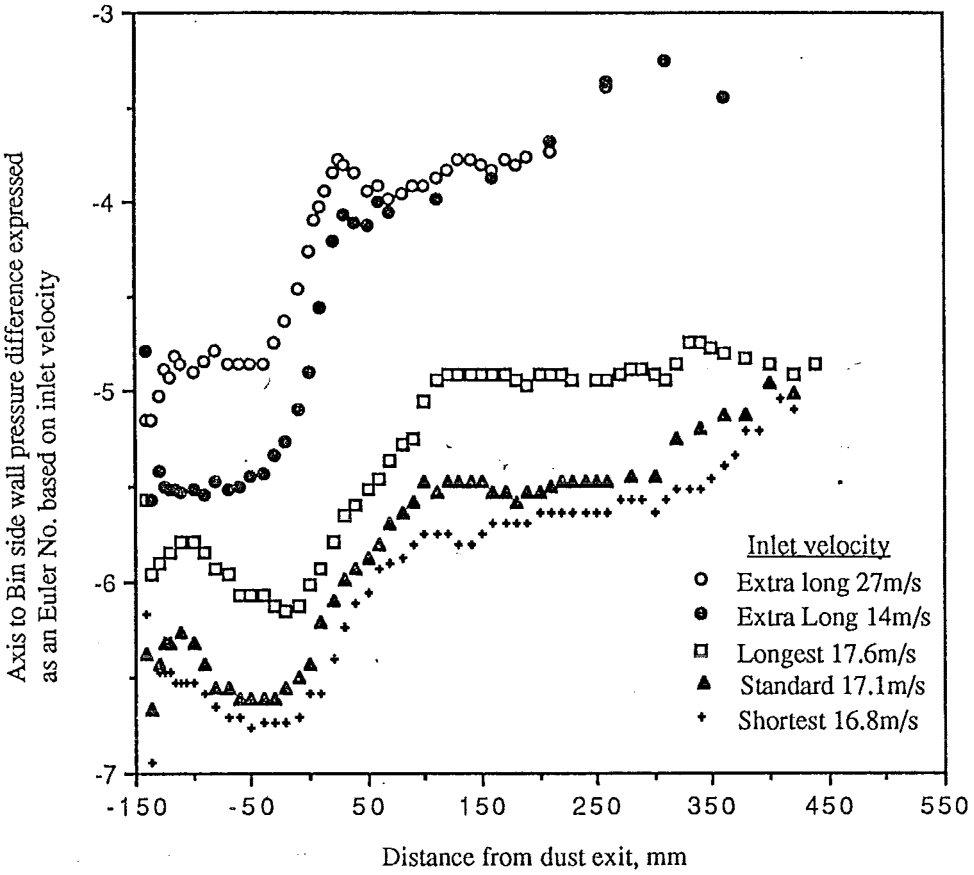

Figure 5.H.3: Axial static pressure profiles for varying overall length

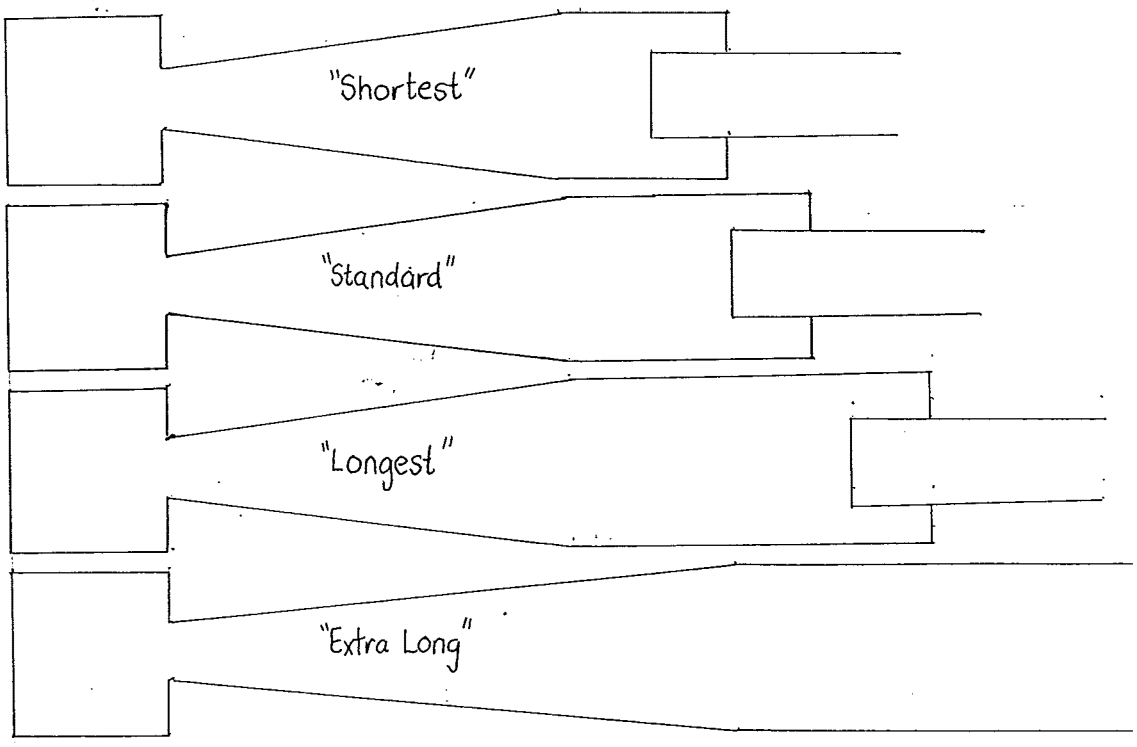

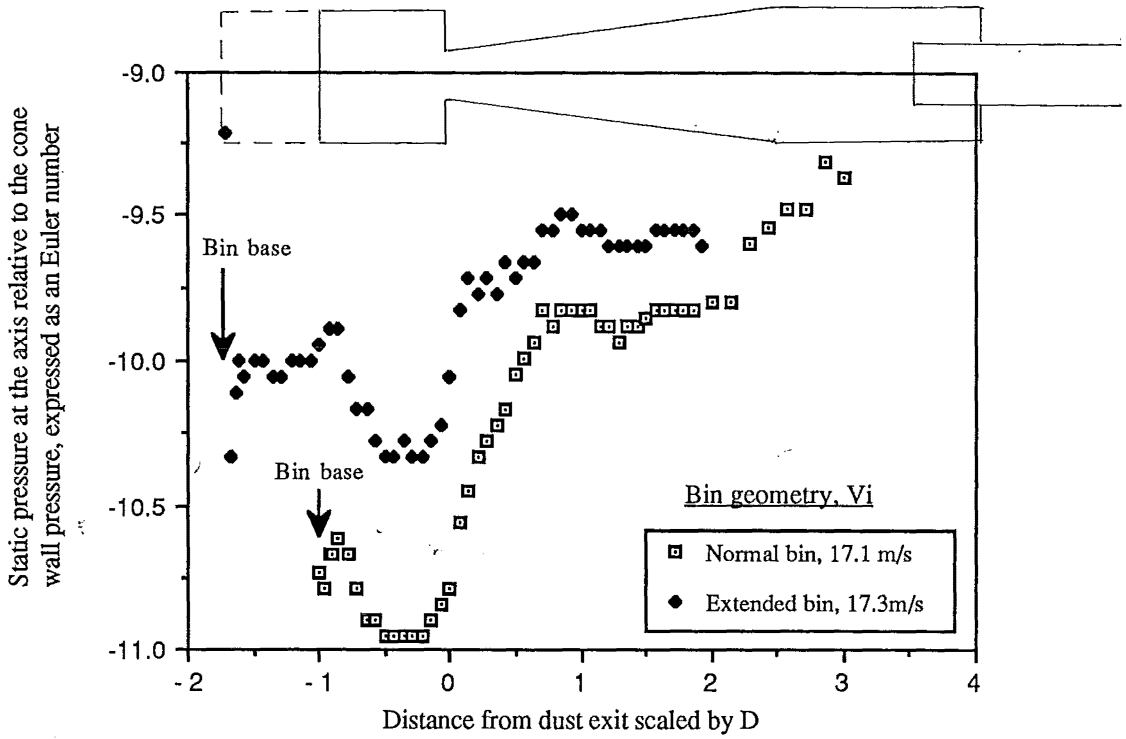

Figure 5.H.4: Effect of extending the bin on the axial static pressure profile in the 140mmØ standard geometry

Lengthening the bin also had no effect on the location of the pressure minimum in the bin or the sharp pressure rise across the bin entrance as shown above in Figure 4.H.4. Since the bin pressure would be different, the pressure along the axis is given relative to the cone wall pressure at Port 9, at the upper end of the cone. The minima in the pressure in the bin could indicate the sealing off of the vortex core after the wall flow separates at the dust exit, which appears in this figure to occur at a constant distance from the dust exit expansion.

When the cone was lengthened by extending the dust exit a very different profile resulted as shown in Figure 5.H.5 below. In the cone the value of the axial pressure is comparable to that found in the normal cyclone. However, instead of decreasing further as the bin is entered, the axial pressure actually rises as the bin is entered. Within the bin the pressure difference between the bin side wall and the axis was very low. The vortex has a low pressure core, which results in a large pressure difference between the wall and the axis. The small difference between the wall and the axis pressures in the bin suggests that the vortex there is weak. The pressure difference remains small as the axial probe is advanced from the bin into the cone until it encounters the end of the vortex.

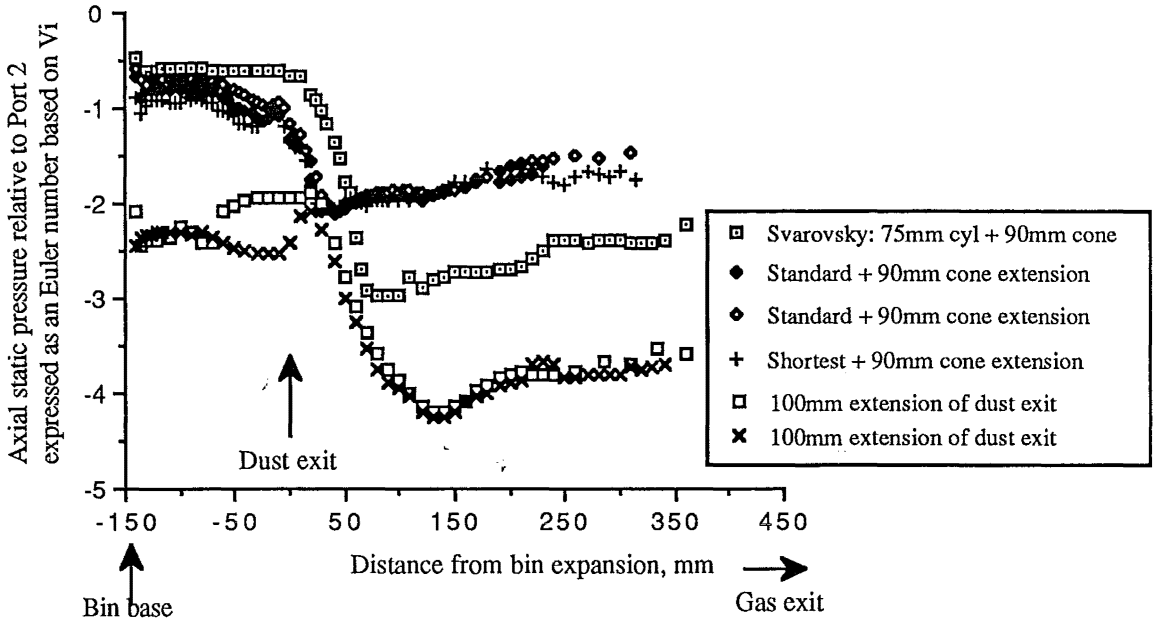

Figure 5.H.5: Axial static pressure profiles relative to the bin side wall for various dust exit configurations in the 140mmØ cyclone.

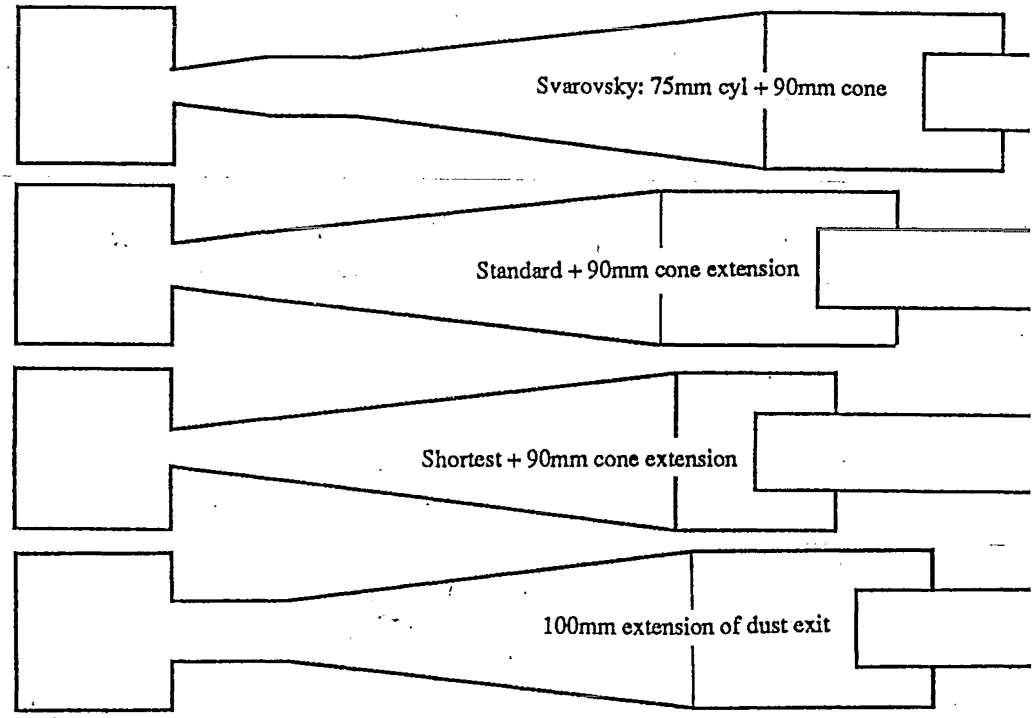

Three different extensions to the cone were examined and are presented in figure 5.H.5. They show the same feature of an increase in axial pressure as the bin is entered, but the point at which the increase starts varies between the types of extensions. Repeat runs show good reproducibility of this location, as indicated. Figure 5.H.5 shows that the length of the cyclone before the dust exit does not have an influence on the position. The Standard and Shortest geometries show the same position and magnitude of the pressure difference relative to the bin side wall when the cone is extended by 90mm to a smaller dust exit diameter. When the standard geometry has a 100mm cylindrical extension to the dust exit the start of the increase occurred much earlier - before the start of the extension piece. The 'Svarovsky' type extension

consisted of a 75mm cylinder followed by the 90mm cone extension. This gave an intermediate position for the increase. Abrahamson and Allen (1986) suggest that the bin and cone wall pressures are equal for short cyclones with large dust exits. This does not appear to be the case in these results. Jackson (1963) cites the negative pressure of the bin as evidence of a direct connection with the inner core of the vortex.

The axial static pressure profiles have been presented relative to the pressure at the side wall of the bin. The bin pressure is obviously affected by the geometry of the dust exit, therefore the results are re-plotted in Figure 5.H.6 with the axial static pressure relative to the wall pressure at Port 9, near the top.of the cone. This shows that the standard geometry has a similar pressure at the end of the normal cone, regardless of the geometry of the dust exit.

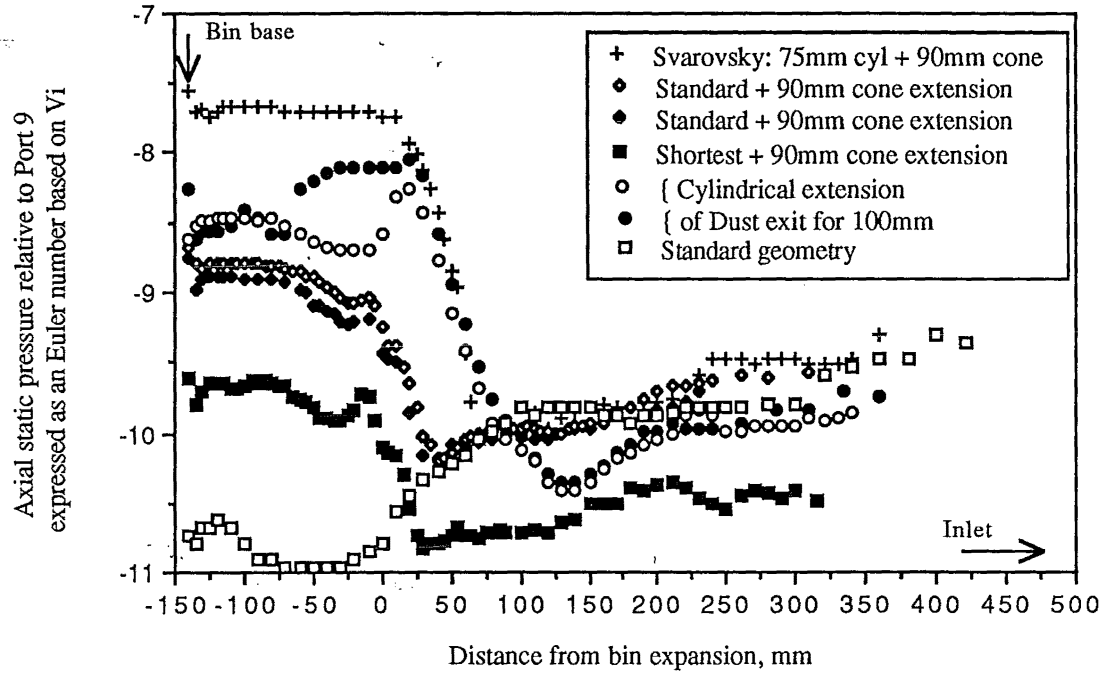

Figure 5.H.6: Axial static pressure profiles relative to the wall of the upper cone for various dust exit configurations in the 140mmØ cyclone.

The standard geometry has a lower bin pressure, but the pressure in the cone is very similar. The change in pressure across the standard dust exit is less than found with the extended versions.

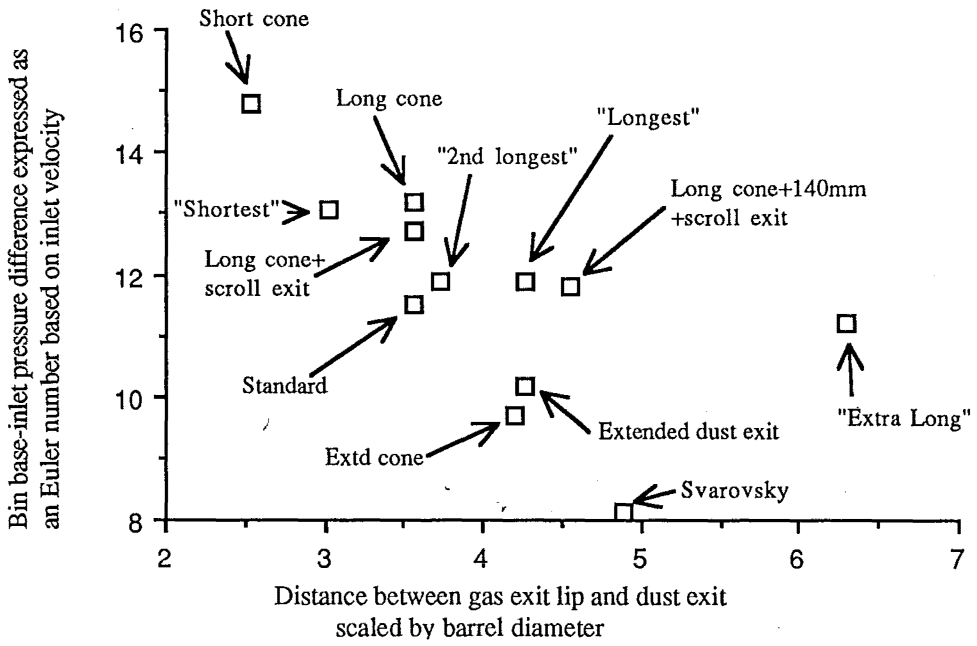

Figure 5.H.7: Pressure difference between bin base and inlet, for 140mmØ geometries.

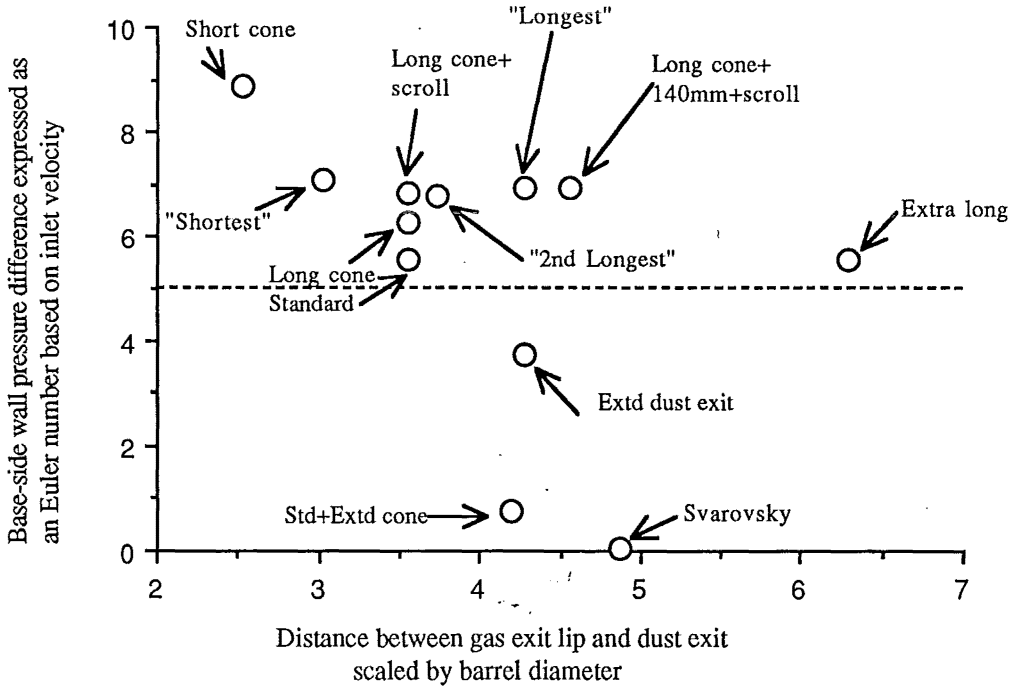

Figure 5.H.8: Bin base and side wall pressure difference in 140mmØ geometries

The effect of the dust exit geometry and cyclone length on the bin pressure is further shown in the above two graphs. The bin base pressure increases as the cyclone is lengthened and as the dust exit diameter is decreased. For the same changes the difference in pressure between the side wall and the base of the bin decreases.

The near-axis reverse flow on the axial static would be expected to have an influence on the bin pressure. By inserting a small body onto the cyclone axis in the lower cone and moving it on

and off the axis, the near-axis reverse flow could be switched on and off. When this was done there was no accompanying change in cyclone ΔP, gas exit pressure, or bin side wall pressure. The only change observed was in the bin base pressure, which increased when the near-axis reverse flow was disrupted.

5.I. PRESSURE-VELOCITY INTEGRAL

Ogawa (1987) approached the calculation of the pressure drop by applying the mechanical energy balance to a finite control volume. He expressed the nett change in the pressure-velocity area integral of the flow between the inlet and outlet as equal to the rate of energy dissipation within the volume. This analysis is outlined in Abrahamson (1991) where the steady state equation is given as:

$$\int_{S_i} P_i V_i . dS - \int_{S_x} P_x V_x . dS = \mu \int_{vol} \gamma^2 . d(vol) \qquad \text{--- (5.I.1)}$$

(i denotes inlet; x denotes the exit, and s denotes surface).The symbols μ and γ are the viscosity and vorticity respectively.

Ogawa assumed that the substantial derivative D/Dt was the same as the partial derivative $\partial/\partial t$, hence he ignored the integration of the flux of kinetic energy over the surface of the control volume. Thus the kinetic head should be added to the static pressure in the integration over the inlet and exit crosssections and the component of velocity perpendicular to the surface, and the total pressures rather than the static pressures (as given by Ogawa) are appropriate. The corrected equation given by Abrahamson (1991) is:

$$\int_{S_i} (P_i + 1/2.\rho_i.|V_i|^2)\mathbf{V_i}.dS - \int_{S_x} (P_x + 1/2.\rho_x.|V_x|^2)\mathbf{V_x}.dS = \mu \int_{vol} \gamma^2 . d(vol) \qquad \text{--- (5.I.2)}$$

Ogawa assumed a constant static pressure across the inlet and exit of the cyclone which simplified the expression, and furthermore assumed that the major dissipation occurred in the core. A simple combined Rankine-type vortex was used to represent the flow. Abrahamson (1991) divided the cyclone into many small control volumes,(each of which contributes to the energy dissipation) and used the Burgers vortex to model the vortex. Both of these studies calculated the energy loss by using the right hand side of equation 5.I.1. The left hand side of equation 5.I.1 can be calculated from the experimental velocity and pressure profiles for the series of control volumes between the traverse locations. This has been done for the profiles from the 750mmØ cyclone and the results are presented here.

The balance is simplified by assuming that the radial flow between the outer and inner vortex is negligible. In addition the outer surface at the cyclone wall can be neglected as there is no flow normal to it. The four remaining surfaces are the axial and tangential planes. The total pressure multiplied by the axial velocity is integrated across the upper and lower surfaces while the total pressure multiplied by the tangential velocity is integrated across the vertical surfaces.

The surface integral of the total pressure multiplied by the velocity component normal to the surface was calculated for the inner and outer vortices over each surface for the inlet and opposite inlet sides. The control volumes are depicted in exploded view in Figure 5.I.1 below.

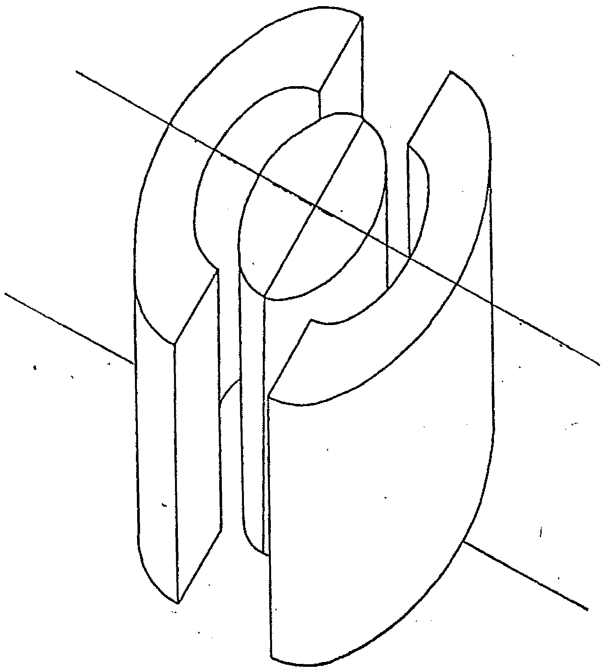

Figure 5.I.1 One slice of the Control volume for the Pressure-velocity integral in the cyclone

OUTER VORTEX, OPPOSITE INLET SIDE

PORT:	$\int P_T V_X dA$	$\int P_T V_T dA$ per metre	height of C.V.	$\int P_T V_T dA$ Actual value	$\int P_T V_T dA$ Average
12LOI	-68.5	1435.7	0.161	230.6	
					208.1
11LOI	-8.9	1156.0	0.161	185.7	
			0.321	371.5	
					363.6
10LOI	-26.5	1106.4	0.321	355.6	
			0.349	386.1	
					383.1
9LOI	-10.2	1088.9	0.349	380.0	
			0.536	583.2	
					668.1
8LOI	-28.1	1406	0.536	753.1	
			0.402	564.9	
					449.0
7LOI	-14.4	829.0	0.402	333.1	
			0.161	133.2	
					118.4
6LOI	-3.6	644.7	0.161	103.6	
			0.161	103.6	
					92.5
5LOI	-2.2	506.8	0.161	81.5	

OUTER VORTEX, INLET SIDE

$\int P_T V_T dA$ Average	$\int P_T V_T dA$ Actual value	height	$\int P_T V_T dA$ of C.V.	$\int P_T V_X dA$ per metre	PORT:
	360.9	0.161	2247.3	-78.4	12LI
307.9					
	254.9	0.161	1587.5	-60.9	11LI
	510.2	0.321			
530.4					
	550.7	0.321	1713.4	-42.6	10LI
	598.0	0.349			
548.0					
	498.1	0.349	1427.1	-40.8	9LI
	764.4	0.536			
641.0					
	517.7	0.536	966.6	-13.1	8LI
	388.4	0.402			
377.2					
	366.1	0.402	911.2	-15.5	7LI
	146.4	0.161			
184.4					
	222.4	0.161	1383.9	-22.1	6LI
	222.4	0.161			
219.0					
	215.6	0.161	1341.6	-25.4	5LI

INNER VORTEX, OPPOSITE INLET SIDE

PORT:	$\int P_T V_X dA$	$\int P_T V_T dA$ per metre	height of C.V.	$\int P_T V_T dA$ Actual value	$\int P_T V_T dA$ Average
12LOI	96.3	3247.5	0.161	521.5	
					526.0
11LOI	71.9	3303.7	0.161	530.6	
			0.321	1061.8	
					1027.4
10LOI	76.3	3089.6	0.321	993.0	
			0.349	1078.2	
					1062.3
9LOI	55.5	2998.29	0.349	1046.4	
			0.536	1605.9	
					1219.1
8LOI	24.5	1553.9	0.536	832.3	
			0.402	624.4	
					539.3
7LOI	17.4	1130.5	0.402	454.2	
			0.161	181.7	
					181.7
6LOI	15.5	1130.4	0.161	181.7	
			0.161	181.7	
					166.8
5LOI	12.6	945.3	0.161	151.9	

INNER VORTEX, INLET SIDE

$\int P_T V_T dA$ Average	$\int P_T V_T dA$ Actual	height of C.V.	$\int P_T V_T dA$ per metre	$\int P_T V_X dA$	PORT:
	437.8	0.161	2725.8	58.9	12LI
447.4					
	457	0.161	2845.5	51.2	11LI
	914.5	0.321			
911.3					
	908	0.321	2825.0	43.6	10LI
	985.9	0.349			
1015.8					
	1045.7	0.349	2996.4	47.3	9LI
	1604.9	0.536			
1337.5					
	1070	0.536	1997.9	36.4	8LI
	802.7	0.402			
617.1					
	431.5	0.402	1074	15.9	7LI
	172.6	0.161			
141.6					
	110.6	0.161	688.2	8.5	6LI
	110.6	0.161			
88.0					
	65.4	0.161	406.8	4.1	5LI

The values of the surface integrals for the tangential and axial surfaces of each control volume are given in the table. The axial surface integral is evaluated at each traverse location and presented in the column labelled $\int P_T V_X . dA$. The tangential surface lies between the traverse locations hence the integral is calculated using both the upper and lower tangential velocity profiles and the average of them taken. The control volumes vary in height according to the spacing of the traverse locations. To enable comparisons of the relative strength of this tangential surface integral at different levels in the cyclone the integral is calculated for a 1 metre high control volume. This is then multiplied by the actual height of the control volume to give the actual integral value. The values for the integral from the upper and lower traverse locations are then averaged.

It will be noticed that the tangential surface integral dominates the axial surface integral, both in magnitude and rate of change. The surface integrals decrease down the cyclone which is consistent with the decrease of flow down the cyclone length. Although the radial surface integral was assumed to be negligible, the decrease in flow must occur through a radial inflow. The nett change in the surface integral for each control volume is compared between adjacent control volumes, and a gradient of this change is calculated. The sign convention that was adopted was that an increase (in the integral balance) in the direction of the flow is positive. The results are presented below in the table and overleaf in the graph, which makes the trend more obvious.

	Opposite Inlet Side		Inlet side		
PORT	Gradient of the $\int P_T . V_n$ dA balance over the control volume				Distance of midpoint
	OUTER	INNER	OUTER	INNER	from gas exit lip, mm
12L					
	-992.7	+641.3	-441.5	512.5	123.3
11L					
	-464.2	+347.5	-337.6	+461.9	364.3
10L					
	-519.1	+192.8	-143.8	+467.3	699.5
9L					
	+84.0	-163.2	+241.4	-102.3	1141.8
8L					
	+144.5	-175.9	+244.6	-172.6	1610.5
7L					
	-477.9	+261.4	-203.5	+452.1	1891.8
6L					
	-795.9	+508.4	-462.7	+808.2	2052.5
5L					

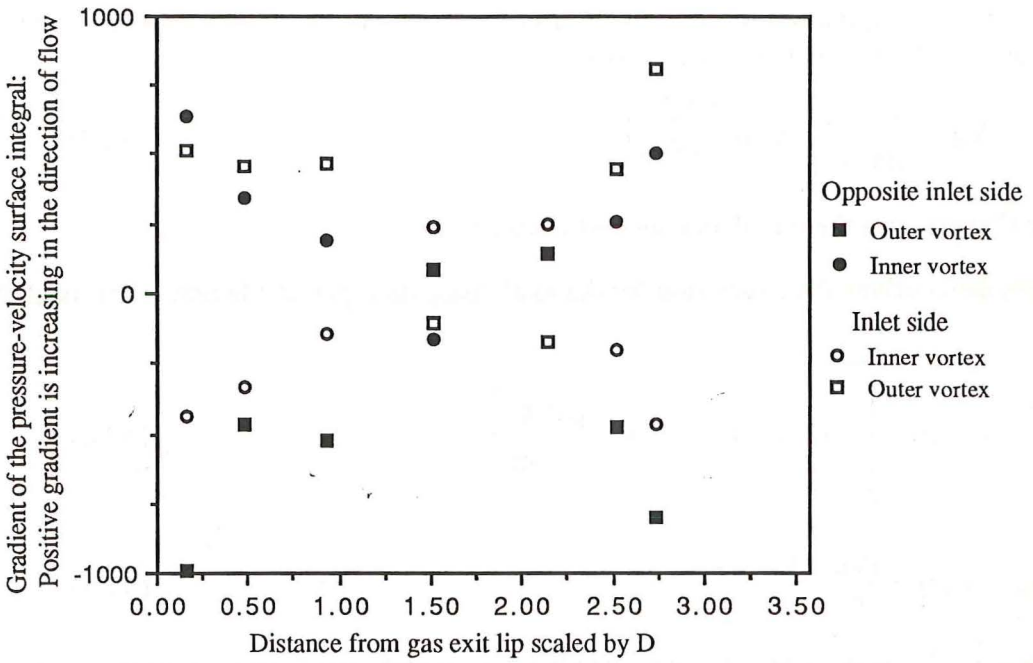

Figure 5.I.2: Gradient of the Pressure-velocity surface integral for the 750mmØ cyclone

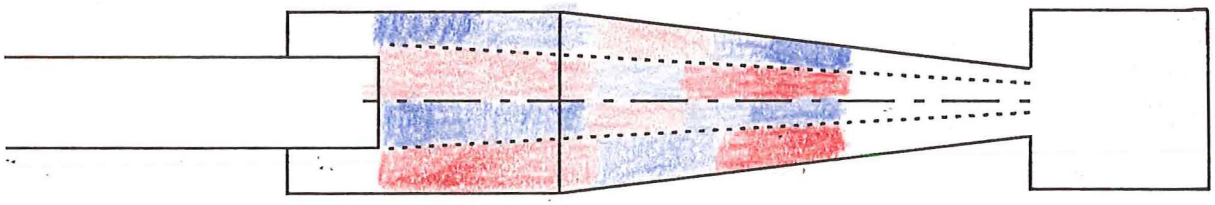

Figure 5.I.3: Schematic representation of the positive and negative regions of the surface integral, red being a decrease in the surface integral value, blue being a gain.

The remaining surface that needs to be taken account of is the radial surface. This has been assumed to be negligible because of the low radial velocities. The radial velocities calculated from the difference between the profiles of axial velocity integrated at each level could be used to calculate the remaining surface integral to see if this accounts for the differences in the balance above.

The integral $\int\gamma^2 d(vol)$ could be evaluated by equating to the final balance of the surface integrals, and thus calculate another estimate of ν_T. This would give a check against the Burgers vortex assumptions that were used in the empirical estimate of the turbulent viscosity in section 6.B1.

Burgers (1948) expression for the axially symmetric vortex with radial and axial velocity components of $V_r = -A.r$ and $V_x = 2A.z$ is :

$$V_\theta = \frac{C}{2\pi}.\left(1 - \exp\left[\frac{-A.r^2}{2\nu}\right]\right) \qquad \text{--- (5.I.3)}$$

where C represents the circulation around the vortex.

Burgers then derives the expression for the total dissipation per unit length in the axial direction:

$$= \rho\nu \int_0^\infty dr\ 2\pi.r.\gamma^2 = \frac{\rho A C^2}{4\pi} \qquad \text{--- (5.I.4)}$$

The vorticity $\gamma = \frac{\partial V_\theta}{\partial r} + \frac{V_\theta}{r}$ --- (5.I.5)

(The loss of the velocity and pressure data files in a mainframe computer crash has prevented the completion of this analysis).

5.J. VORTEX LENGTH ESTIMATE:

This section presents observations that are relevant to the determination of the natural length of the vortex.

5.J.1. Value of Γo near wall vs length

The circulation of the vortex at large radius, Γ_o, is estimated from the tangential velocity profiles in the cyclone. Values of the circulation ($\Gamma = V\theta.r$) are calculated near the wall and the asymptotic limit as r increases is taken as Γ_o. In general this is equal to the maximum value of Γ. The value of Γ_o decreases down the cyclone length, but for most geometries there is a local increase superimposed on this decay in the lower cone. In order to compare different geometries and flowrates the distance from the gas exit is scaled by the barrel diameter D. The circulation at the wall is scaled by dividing by Vi x R_B where V_i is the average inlet velocity and R_B is the barrel radius, and the result is then squared.

As an example, the profiles of the wall circulation in the standard 140mmØ geometry for both the inlet and opposite inlet sides are shown below in Figure 5.J.1:

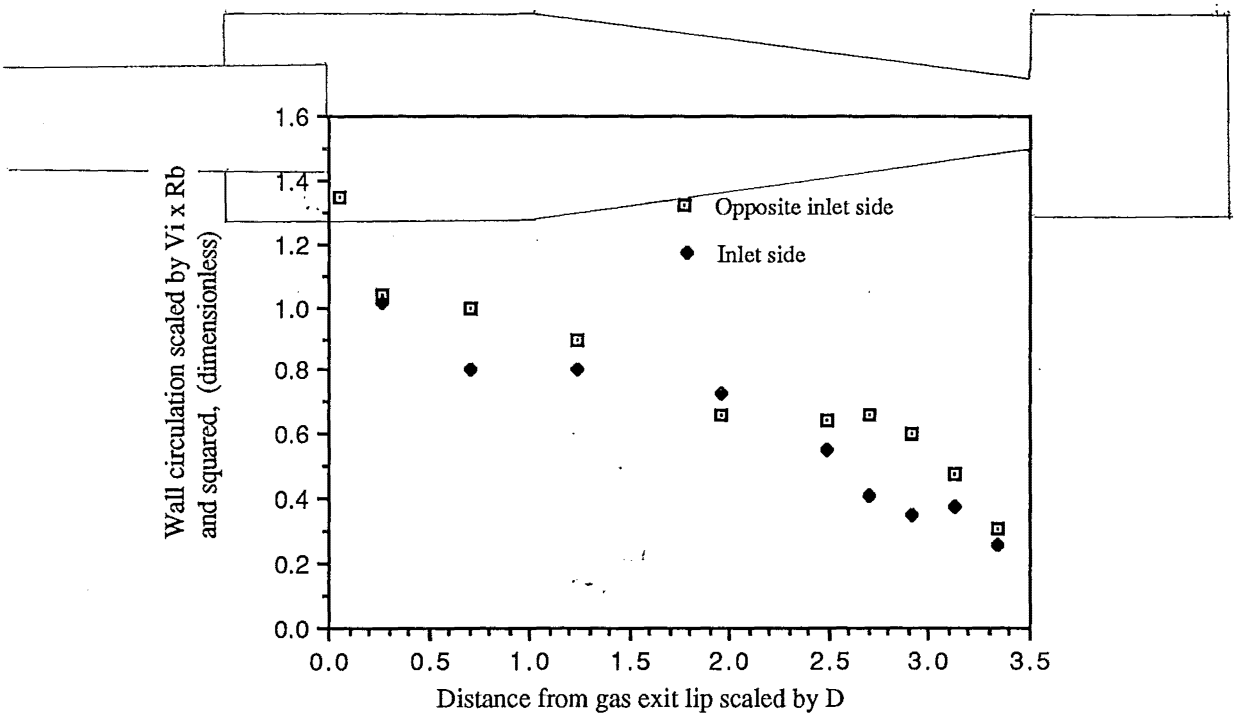

Figure 5.J.1: Decay in the circulation at the wall along the cyclone length in the 140mmØ standard geometry at an inlet velocity of 22m/s

The 750mmØ cyclone traverses for the two ports nearest the dust exit were not able to be done, so the lower cone trends are not clear.

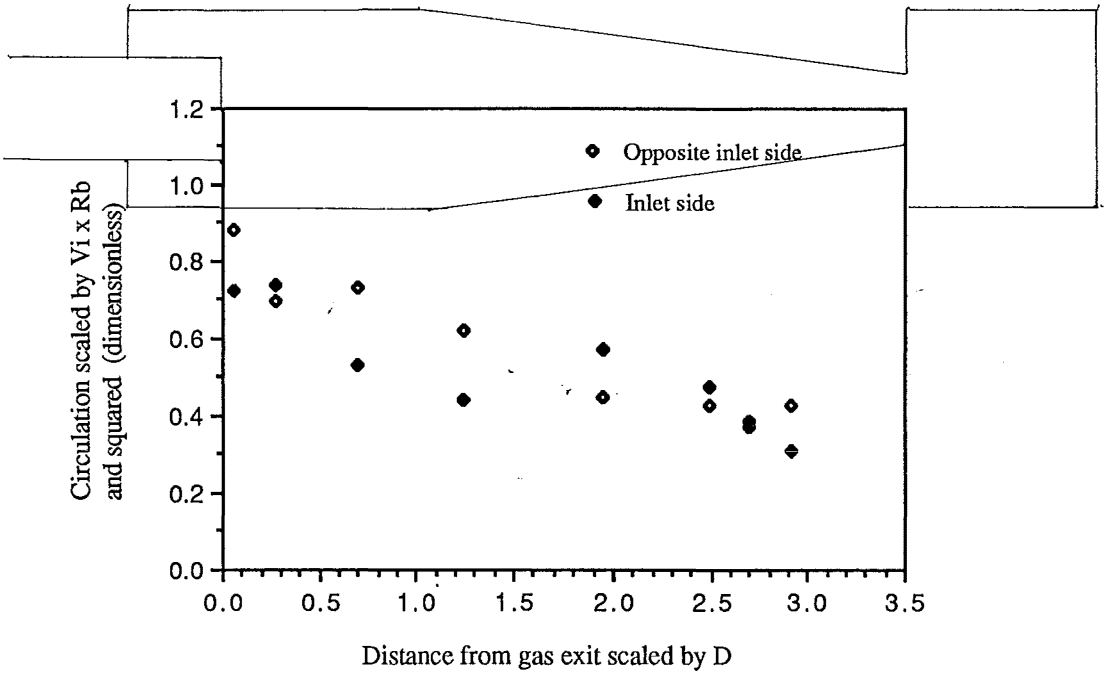

Figure 5.J.2: Decay in the circulation at the wall along the cyclone length in the 750mmØ standard geometry at an inlet velocity of 18m/s

There is a large difference between the inlet and opposite inlet sides for the 140 & 750mmØ standard and the 140mmØ Long cone geometry results, which appears to take the form of the opposite inlet side lagging the inlet side. This is discussed further in chapter 6.A.

The positions of the local increase in Γ_o for various geometries are given below as the distance from the gas exit lip in millimetres and as the number of barrel diameters. The measurements are for the opposite inlet side unless stated:

Longest	420mm	3.0D
Shortest	300mm	2.1D
Extralong	450mm	3.2D
Standard 140Ø	370mm	1.9D,3.1D; (inlet side)
		2.7D; (opposite inlet side)
Standard 750Ø		0.7D, 2.0D
Standard 2090Ø		3D
LongCone (no barrel)		1.9D; (inlet side)
		2.6D; (opposite inlet side)
LongCone+140 barrel		2.9D
Extended cone	450mm	3.2D

5.J.2. Angle of the flow at the wall:

The pitch of the helix of the flow at the wall, as measured by the pitot cylinder, varied in a reproducible manner down the cyclone. This has been mentioned by Pen'kov & Vedernikov (1984) - they found that the vortex in cylindrical cyclones had a constant pitch, while the pitch of the flow in conical cyclones varied along the length.

As shown below in Figure 5.J.3 the flow was steepest around Port 6 on the inlet side, and port 3 on the opposite inlet side for the 140mmØ Standard geometry. This difference between the inlet and opposite inlet sides was also observed in the Γ_o^2 vs L plots such as in Figure 5.J.1 above.

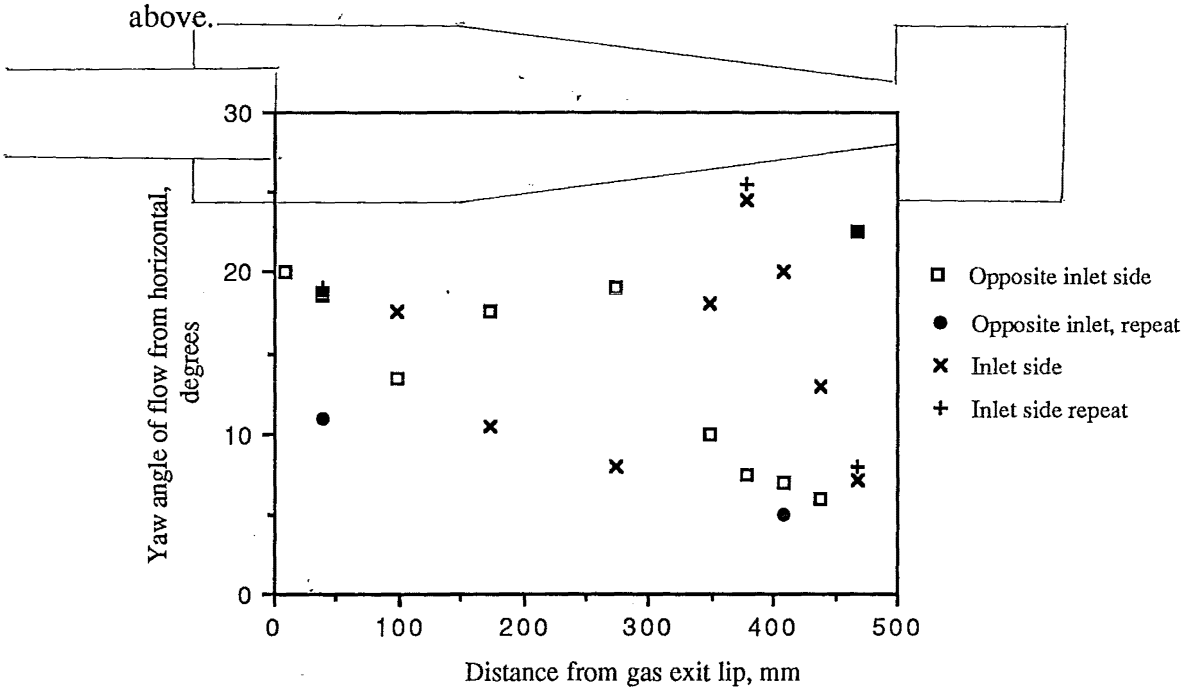

Figure 5.J.3: Variation of the angle of flow to the axial plane near the wall along the length in the 140mmØ standard geometry.

When the flow is disturbed by probe insertion (in this case at Port 11 on the inlet side) there is a change in the angle of the flow elsewhere in the cyclone. The probe insertion causes the flow near the wall to become steeper, but as the probe reaches the centreline the angle of the flow at the wall lessens. The exception to this was low in the cone, where the effect was for the flow near the wall to become less steep upon probe insertion. There was little effect on the flow angle in the core at locations below Port 9 in the cone. In the barrel, probe insertion caused the angle of flow in the core to become steeper in a region just below the gas exit lip, but less steep just above the cone/barrel junction.

5.J.3. Bin pressure and the vortex position

The pressure in the bin is thought to be a useful indicator of the vortex position. Jackson (1963) cites the negative pressure as evidence of a direct connection between the bin and the vortex core. For the standard geometry the pressure at the base of the bin was very low while the side wall pressure was moderate. This suggested that the vortex was well into the cyclone bin. The narrower dust exit and longer length of the extended cone is thought to prevent the vortex from entering the bin, and keeps the bin pressure similar between the base and side wall. For the case of the 2090mmØ cyclone where the dust exit has been extended by 1.5 diameters before the start of the bin the result was intermediate to the above two, suggesting that the vortex entered and left the bin periodically.

The nature of the pressure profiles in the region of the dust exit expansion has been examined in several of the earlier sections. The profile of the static pressure along the axis as described in section 5.H shows a marked difference between geometries with the normal dust exit, and geometries with an extension to the cone. This appears to be largely independent of the cyclone barrel length.

The difference between the pressure at the wall and the axis shown in Figures 5.G.11 and 5.G.12 shows that this difference is more consistent with the distance from the gas exit. This included the wall-axis difference recorded in the bin just below the dust exit expansion. This was reinforced by the average radial pressure gradients shown in Figures 5.G.13 and 5.G.14. The position of a sharp decline in the average radial occurs in nearly the same position (with respect to the distance from the gas exit lip) for a wide range of geometries. Since the balance of the radial pressure gradient depends on the tangential velocity (through $\rho V_\theta^2/r$) this is taken as an indication of the strength of the vortex. It was expected that this gradient would become much less upon the expansion of the flow into the bin, but the occurrence of the start of the decline was before this for the cone extension piece. This supports the observations of the axial static pressure profile, and the bin pressure in suggesting that the vortex tends not to enter the bin when the cone is extended at the dust exit.

The pressure difference between the bin base and the side wall, or the bin pressure relative to the inlet are more easily measured quantities, and they also show the split between geometries with the normal dust exit, and those with extensions to the cone. Since the type of dust exit affects the bin pressure, the axial static pressure profiles for the non-standard dust exits are shown relative to the wall pressure in the upper cone. This shows that the pressure on the axis upstream of the dust exit is largely the same regardless of the type of extension.

5.J.4. Wall pressure profiles in cone

All plots show a steeper wall pressure profile low in the cone. The position of this change in slope (with respect to the gas exit lip) varied slightly between geometries. This is summarised below as the distance from the gas exit lip. An example of the wall pressure profile is given for the Standard geometry at a range of velocities.

Geometry	Distance from gas exit lip mm	# Barrel diam	Geometry	Distance from gas exit lip mm	#Barrel diam
Standard	390	(2.8D)	Shortest	330	(2.3D)
Longest	370	(2.6D)	Extended Dust exit	350	(2.5D)
2nd Longest	390	(2.8D)	Svarovsky B	300	(2.1D)
Long cone	350	(2.5D)			

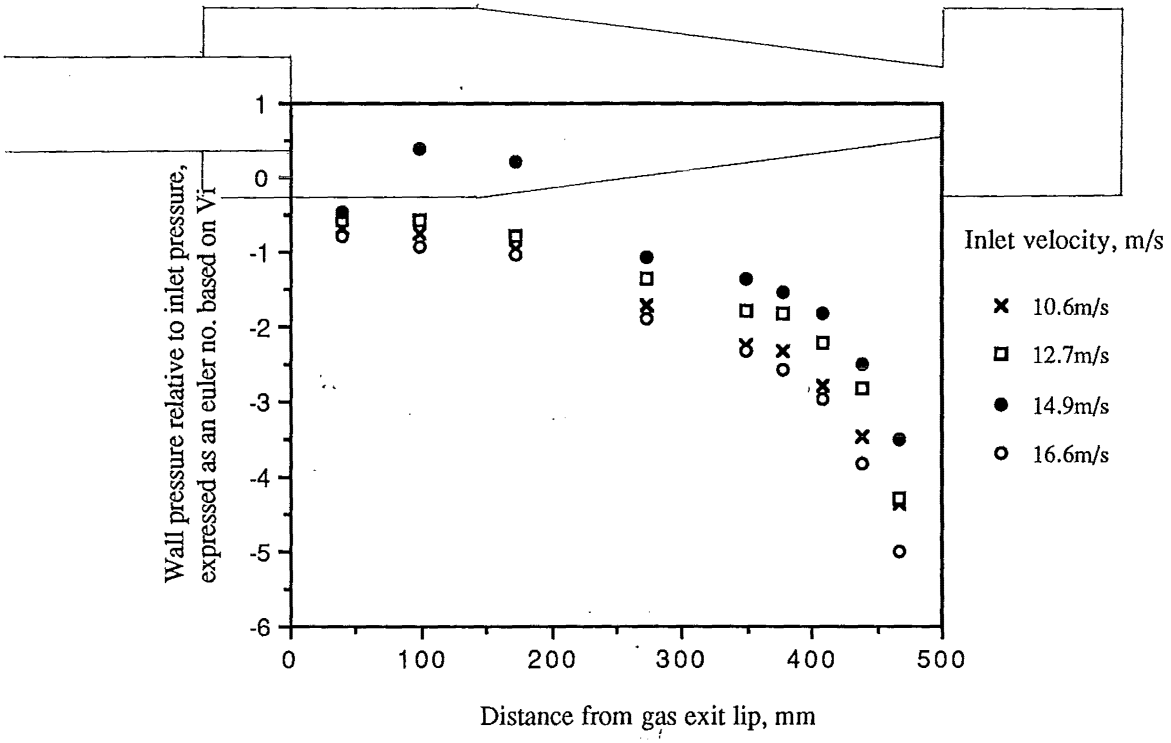

Figure 5.J.4: Profile of the static pressure at the cone wall for 140mmØ cyclone

The position of the change of slope corresponds with the kink in the Γ_0 vs L plots. The difference in wall pressure between the cone/barrel junction and the bin is the driving force for the boundary layer flow. The wall pressure was measured relative to the inlet pressure.

The change in the wall pressure between Ports 8 and 3 is from -1.5 to -4 Euler numbers. In the same range the static pressure along the axis changes very little. Across the dust exit expansion the reduction in the wall pressure is less than the axial static pressure change as shown in section 5.H. The effect of these on the pressure difference between the wall and the axis is shown in section 5.G.

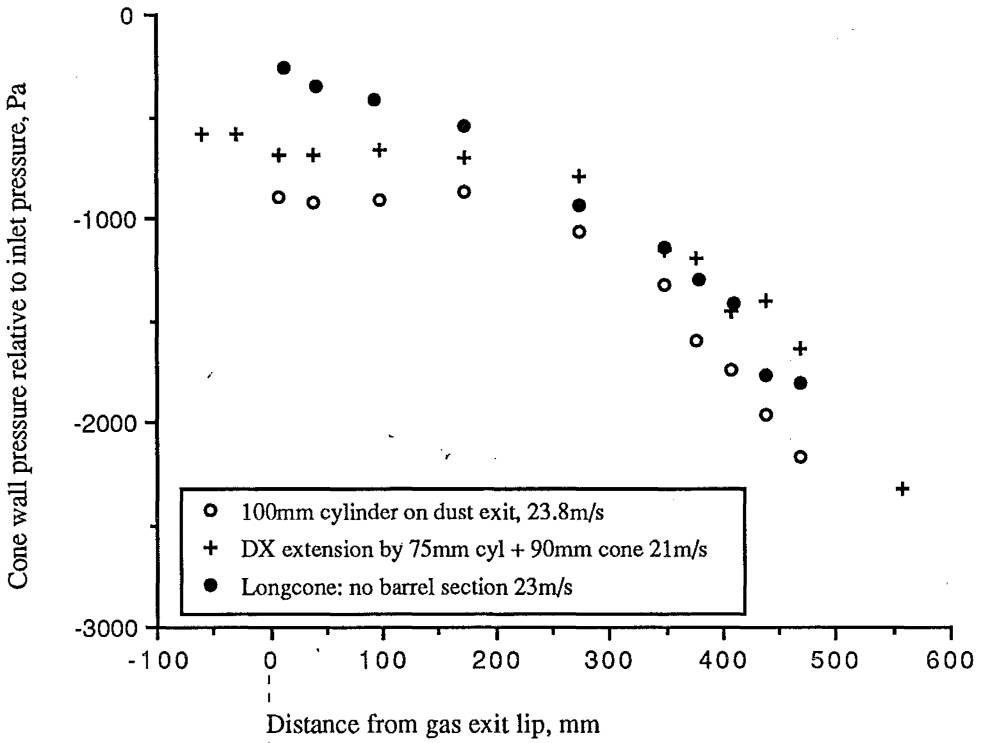

Figure 5.J.5: Profiles of cone wall pressure in 140mmØ cyclones with various cone configurations

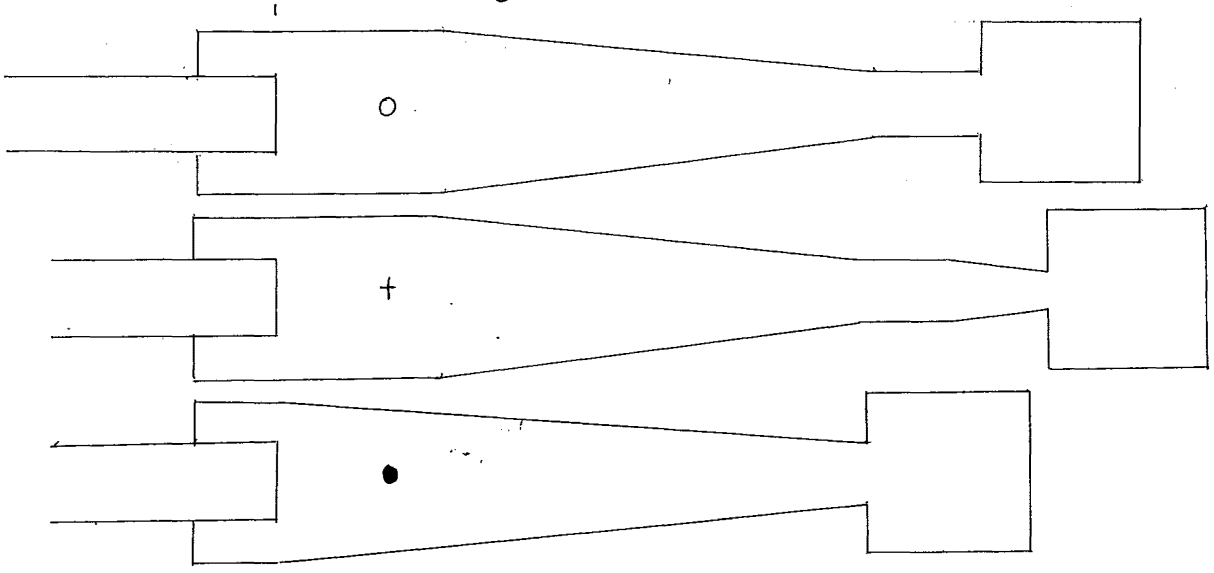

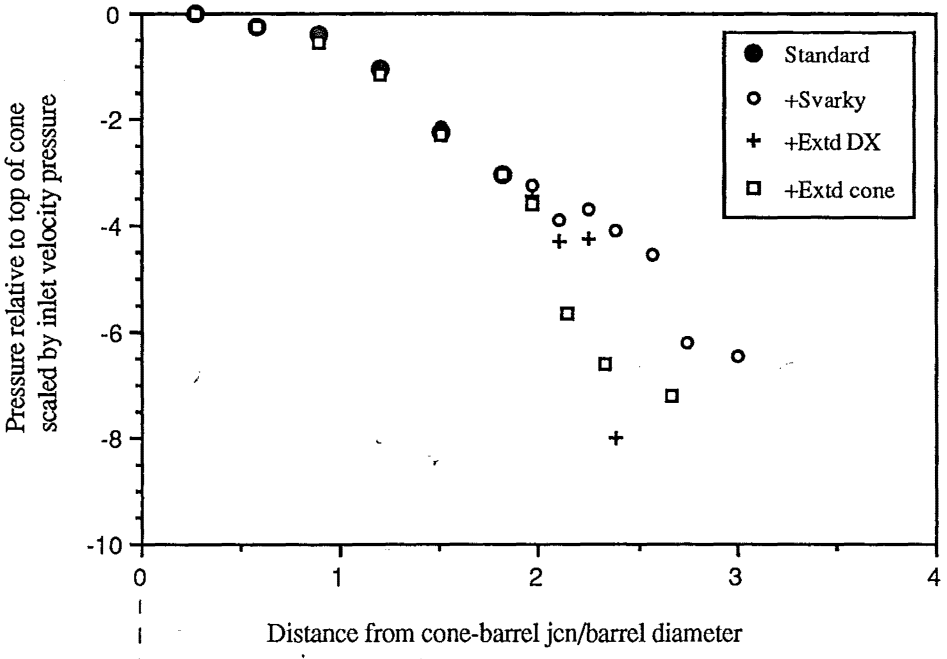

Figure 5.J.6 : Cone wall pressures in a 300mmØ cyclone, various cone lengths

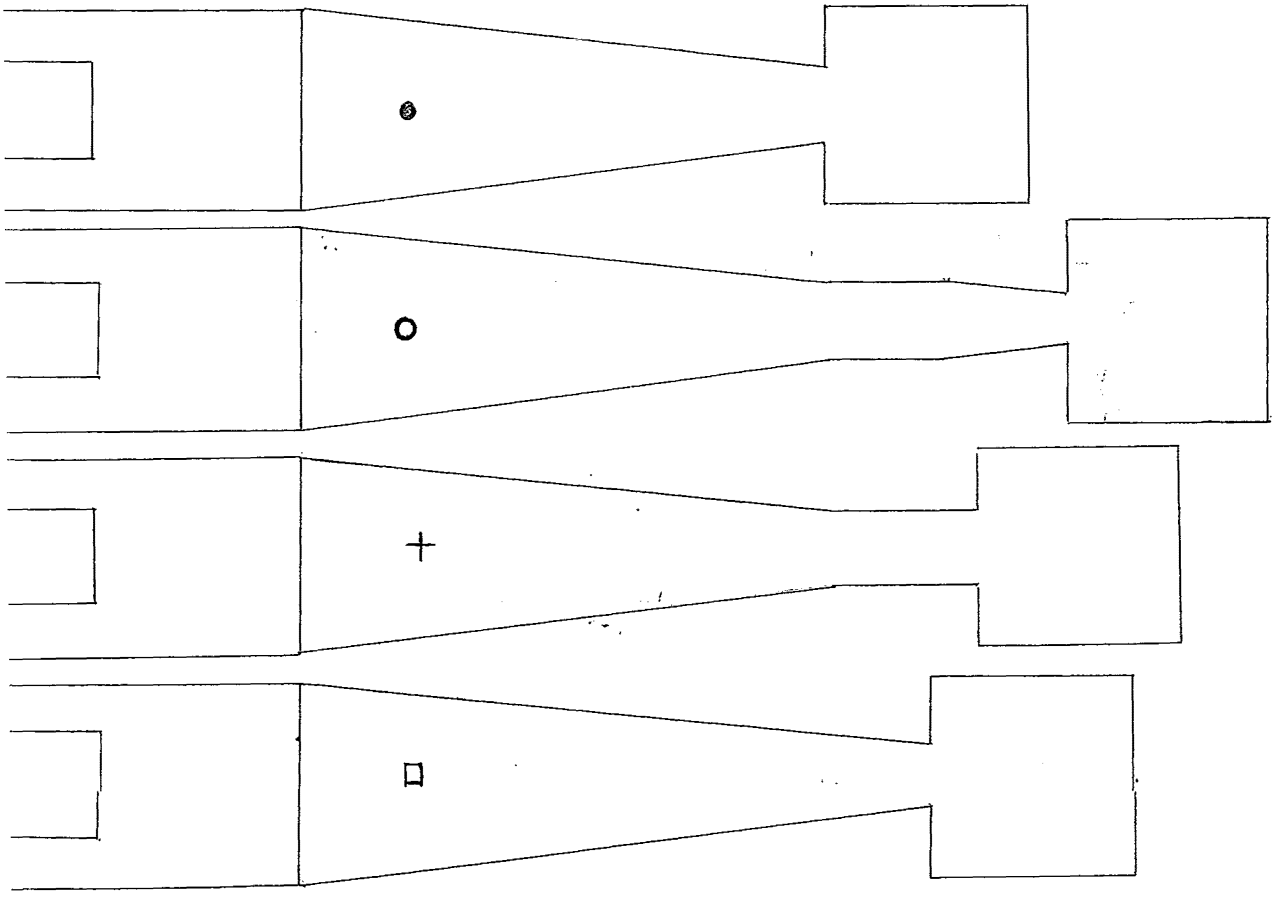

Note that both geometries that have a cylindrical extension on the dust exit showed a rise in the wall pressure just inside the extension, and the sharp drop occurred before the expansion for the extended dust exit geometry, the Svarovsky geometry appears to be able to draw the vortex further into the extension piece.

5.J.5 Helium tracer recirculation zones

The helium bubble tracers are held in recirculation zones or 'traps' that occur repeatedly in certain parts of the cyclone. The most stable zones are just off the bin base, and just downstream of the cyclone roof in the gas exit while more transient traps occur in the cone. The stable zones correspond to local pressure maxima in the axial wall pressure profiles.

When the Pitot cylinder probe is inserted to the centreline, the position of the traps shift, which suggests a link between these traps and the vortex breakdown, which is reported to be sensitive to disturbance by probes. Although the position of the helium bubble tracer traps shift the most when the probe insertion touches the core, this has little effect on the pressure drop, compared with the effect of the probe on the outer vortex - which in turn has little effect on the trap positions.

The simplest case to examine is the insertion of a probe into the "no cone" cyclone, which is just a cylinder of length 3.7 barrel diameters below the gas exit lip. In the undisturbed state there is a recirculation zone centred on the gas exit lip. When the probe is inserted into the outer vortex, this gas exit trap shifts to the base, then moves far downstream in the gas exit when the probe touches the core.

5.J.6. Stabilising the flow

The collection efficiencies for these different geometries now need to be determined, from which it should be possible to determine what position is preferred for the vortex, thus indicating the preferred geometries

Designs that show attempts to stabilise the vortex include the inverted cone in neck used by Gloger & Hanke (1971), and Muschelknautz, (1972) and a solid body on the axis described by Zhou & Soo (1990). Both of these will serve to prevent the vortex reversal on the axis towards the bin that was indicated by the helium bubble tracers. The inverted cone in the neck of the bin was very unstable and needed to be securely fastened to stop the vortex dislodging it

5.K. THE PROBE INSERTION EFFECT:

When the 10mmØ Pitot Cylinder probe was inserted radially into the 140mmØ cyclone there was a marked effect on the flow - the overall pressure drop was reduced (as well as the inlet velocity increasing due to the reduced resistance to the blower) and the recirculation zones as shown by the helium bubble tracers moved large distances. This effect was further investigated by inserting a 10mmØ rod into the flow at various positions in the cyclone.

The overall cyclone pressure drop was measured between the inlet and the base of a 0.5m Ø barrel placed in the gas exit, 6 exit diameters downstream of the gas exit lip. The inlet tapping was on the inlet wall 100mm upstream from where the inside inlet wall met the cylinder. The Euler number was reduced significantly at any level in the cyclone with as little as 10mm of the rod inserted, with a minimum value reached when the rod reached approximately $r/R_b = 0.4$. Beyond this the Euler number stayed relatively constant.

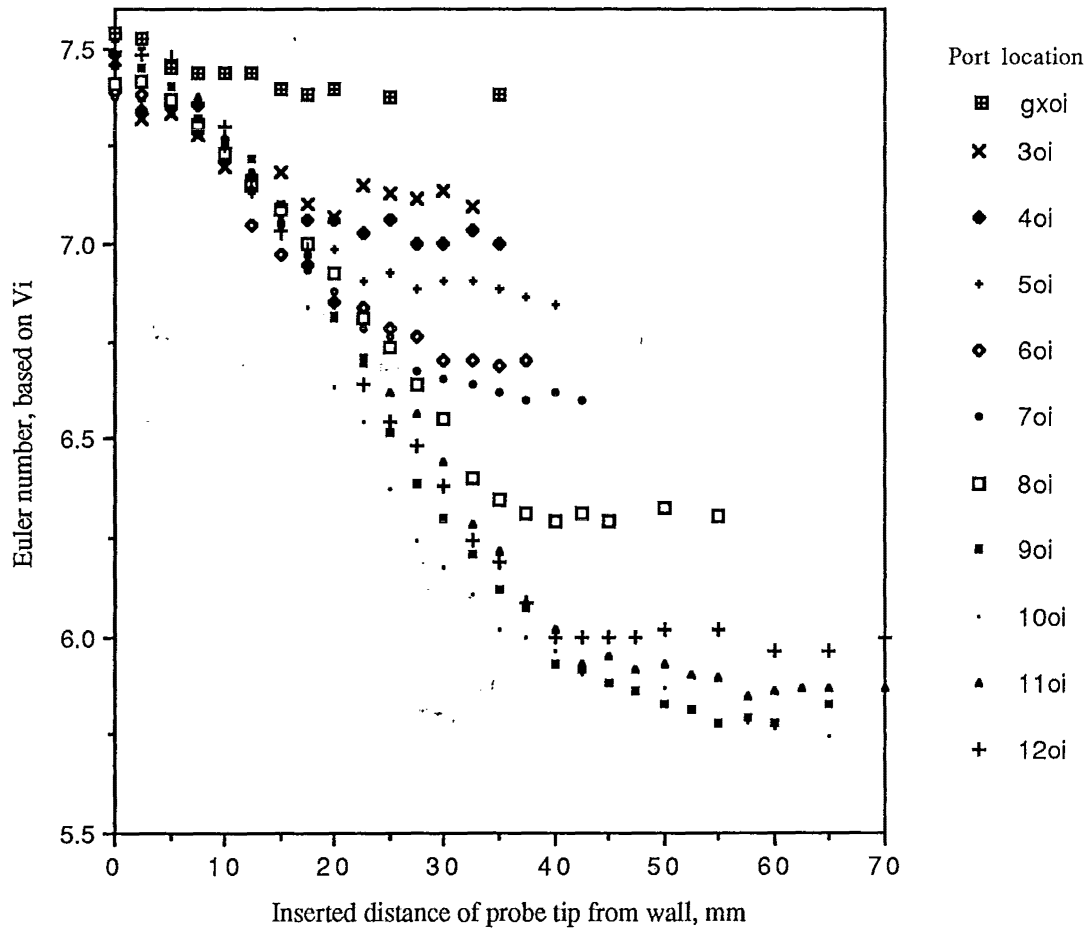

Figure 5.K.1: The reduction in the cyclone pressure drop upon radial insertion of a rod at various axial positions in the 140mmØ standard geometry cyclone.

Inserting the Pitot Cylinder in the gas exit had the least effect followed by the ports in the lower cone. Insertion at Ports 9 and 10 , on either side of the cone/barrel junction had the greatest effect on the Euler number, with insertion at Port 12 (near the gas exit lip) having a similar effect to ports in the upper cone. Most of the observations were made when the probe was

inserted from the opposite inlet side wall of the cyclone, but the same results were obtained for inserting it from the same side as the inlet.

The disturbance of the flow by the probe insertion showed up in many measurements:

- The cyclone pressure drop was reduced significantly, as shown by the Euler number plot above.
- Measurements with the hotfilm anemometer at various positions in the cyclone showed that the rod insertion caused the total velocity to increase in some regions, and decrease in others. When the probe was inserted near the gas exit lip it decreased the flow in the cone below Port 10 and made the boundary layer thinner. The hotfilm traverse was made on the same side of the cyclone as the rod insertion, hence this may be due to the flow moving into the centre when it encountered the probe. However, the hot film total velocity in the gas exit was lower than for the undisturbed case

  The example shown below in Figure 5.K.2 illustrates the effect on the total velocity profile, just below the gas exit lip (Port 12), when the 10mmØ rod was inserted at Port 10 . The velocity profile recorded by the pitot cylinder at Port 12 is also shown - the pitot cylinder being the same size as the rod.

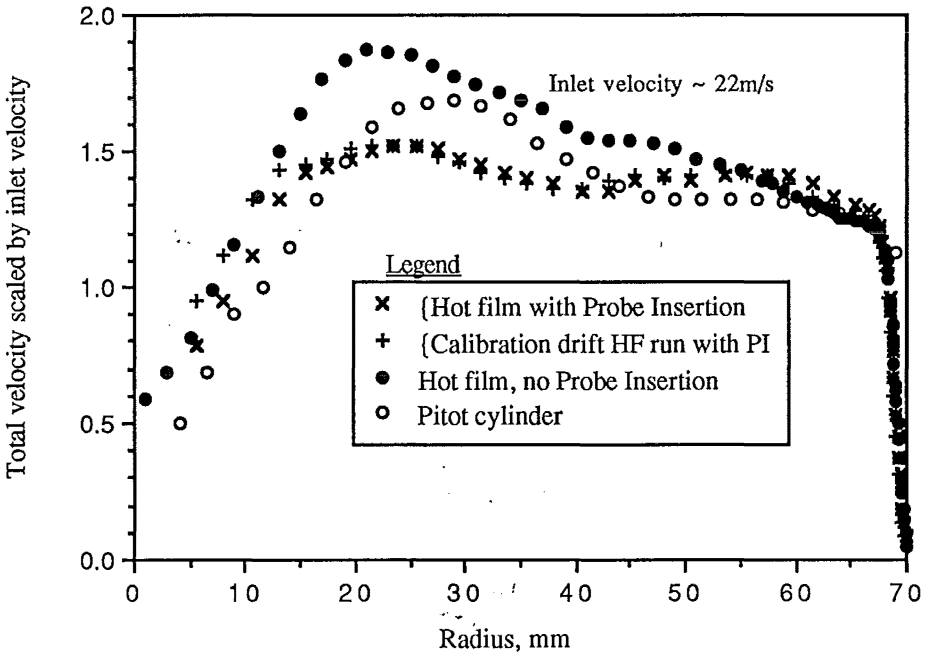

Figure 5.K.2: The effect on the total velocity recorded by the hot film anemometer when a 10mmØ rod is inserted a radial distance of 40mm into the 140mmØ cyclone at Port 10

When the rod was inserted just above the cone junction, the total velocity recorded by the hot film anemometer in the upper barrel region (above the rod) was higher in the outer flow than for the undisturbed case, but lower in the core. The crossover roughly corresponded to the boundary between the outer and inner vortices. The wall boundary layer was thicker when disturbed by the probe.

- The insertion of the probe caused a steepening of the pitch of the outer vortex flow in the cone.
- A similar reduction in the overall pressure drop was recorded when the walls were roughened by lining with grade 80 sandpaper. This supports the theory that the lowering of the pressure drop is due to the slowing of the vortex by the protruding probe (or wall roughness).
- For the helium bubble tracers, when the rod was inserted into Port 12 on the opposite inlet side the position of the gas exit recirculation zone (at 3.2 D_X from the gas exit lip), moved closer to the gas exit lip, staying about the level of the roof (1 to 1.4D_X from the gas exit lip). The new recirculation zone was a tighter formation with less spread of tracers axially and radially. When the probe touched the core the recirculation zone moved well down the gas exit (to 12 D_X from the gas exit). This large movement had little additional effect on the pressure drop.
- The cotton streamers in the gas exit just above the level of the roof were observed to fluctuate between the forward and reverse directions, while at the downstream end of the gas exit (17 exit diameters away) there was a steady reverse flow near the axis of the exit. The rod insertion at Port 11 did not affect the latter reverse flow, but the fluctuations near the roof was virtually stopped. When the probe was inserted to the centreline the helium tracer recirculation zone in the exit moved to occupy a position midway along the gas exit.
- Measurements of the fluctuating velocity in the cone by the Hot film anemometer while the probe was inserted showed little change in the cone when the flow was disturbed at Port 12. With the probe inserted at Port 10, the fluctuating velocities just below the gas exit lip showed **reduced** fluctuations just inside the gas exit when the PC was inserted, but not at centreline or barrel wall. Above the roof in the gas exit, the fluctuations seemed greater upon probe insertion into the barrel section.
- Measurement of the axial static pressure profiles when the 10mmØ rod was inserted near the gas exit shows the features of the axial static pressure profiles remain in the same position relative to the dust exit. The centreline pressure is increased and the pressure minimum in the bin is less marked when the probe is inserted, supporting the theory that the swirl is weakened by the interference of the rod.

The size of the probe had some influence, but the increase in the inlet velocity (caused by the reduction of the cyclone pressure drop) was still observed with the insertion of the Hot film probe, which was at most 3mmØ.

5.L. VORTEX DYNAMICS

The velocity profiles as recorded by the Pitot cylinder and hotfilm probes are time-averaged. Periodic motions were observed while the cyclone was collecting particles and techniques were sought to reveal the nature of this.

5.L.1. Axial static pressure flopping

The Standard and Longest geometries show a flopping between two states at an inlet velocity of around 10m/s. For identical conditions, some profiles for the longest geometry have a bin minima, while some do not as shown in graphs 5.H.1 and 5.H.2. These changes were stable enough to show up in time averaged static pressure measurement, which took up to 30 minutes to record. The axial static pressure profile further up in the cone is also seen to swap between two profiles, with alternate data points falling on different profiles in Figure 5.H.1 for an inlet velocity of 9.8m/s

5.L.2. Wall pressure fluctuations & Fast Fourier Transforms

The bin pressure fluctuations were compared between the side wall and the bin base - to investigate the frequency of the vortex entering and leaving the bin as mentioned in section 5.J.3. It was found in the laboratory set-up of the 140mmØ cyclone that there was a strong beat in the suction line of about 71Hz even when the cyclone was not connected. When the pressure in the cyclone bin was observed this fluctuation showed up in the bin to varying degrees for different geometries. Some split it up into frequencies of 24, 48, 71, 97,114 Hz while the Long-cone, Short-cone and Probe-disturbed cases showed a single, pure fluctuation at 71Hz.

The pressure fluctuations in the 750mmØ Stairmand HE cyclone were also recorded with the Macquisition sampling unit at the centre of the bin base, and the gas exit centre. This cyclone did not have the same problem with fluctuations in the supply. The Fast Fourier Transform spectra for the fluctuations is presented below in Figure 5.L.1

The traces have been offset for clarity, the upper trace is Channel A, the centre of the gas exit. There are dominant frequencies at 13 and 25Hz in the gas exit, and at 10 and 25Hz in the bin. A short section of the time-domain fluctuations for the same sample is shown in Figure 5.L.2. The lower trace is for the bin base and this shows larger, slower fluctuations than found in the gas exit.

Figure 5.L.1: Pressure fluctuations in the frequency domain, 750mmØ cyclone

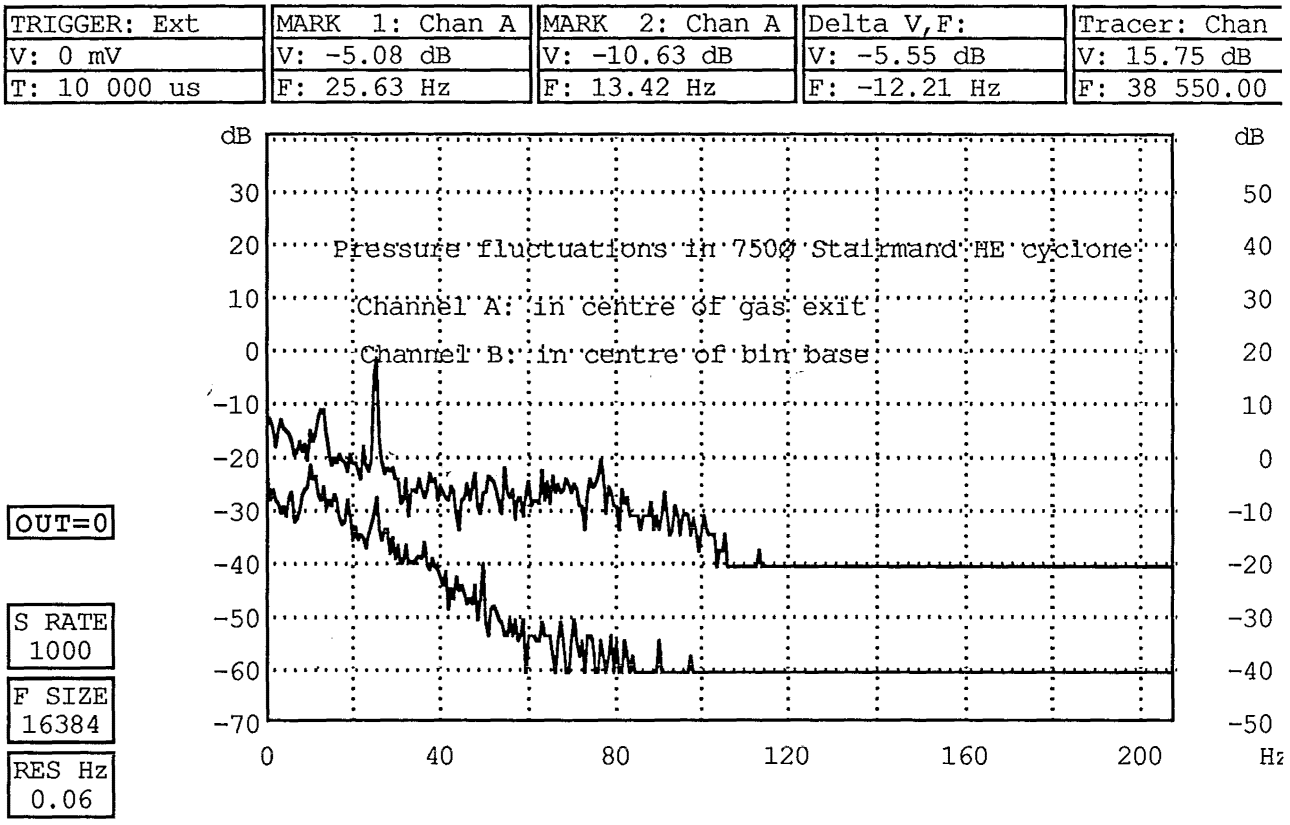

Figure 5.L.2 Pressure fluctuations in the frequency domain, 750mmØ cyclone

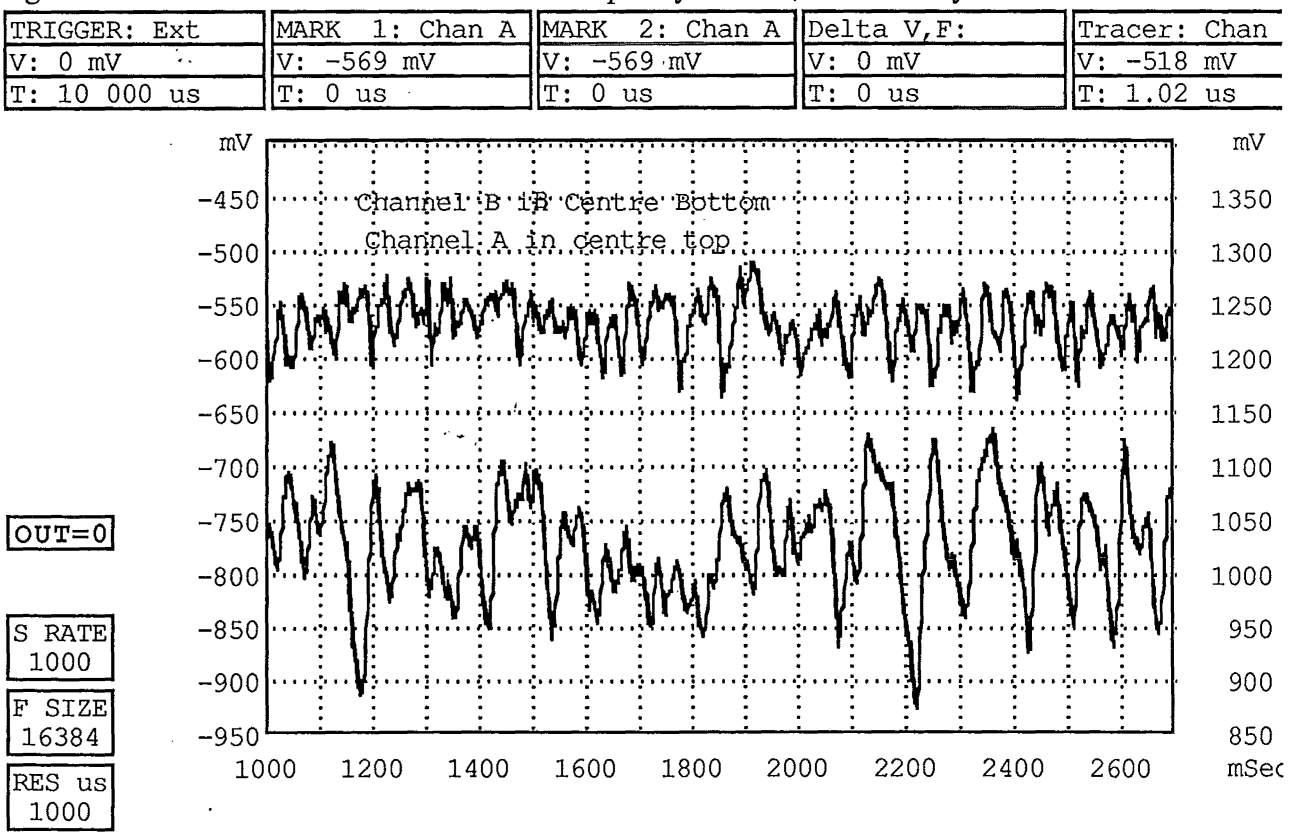

5.L.3. Resonance/Whistling

In order to support the probe the 140mmØ cyclone the ports has sleeves, which are 70-120mm long with a 10mmØ bore. When ports in certain parts of the cyclone were left open on the inside surface (and corked from the outside) a pure and loud tone was produced, typically of about 300Hz. The tone changed pitch when the length of the 'pipe' was varied by moving the cork. Different cyclone geometries affected which ports produced the whistle. Quiet cyclones could be induced to produce whistles or a roar by inserting a probe into the flow. The presence of the whistle had no effect on the movement of the tracers - there was still a reverse core flow and the gas exit recirculation did not shift. Theories have been published (Chanaud, 1965) that relate the phenomena of Vortex whistles to perturbations on the vortex core, but there does not appear to be agreement on the cause.

5.L.4. Flow reversal sensor

The hot film probe was used to sense when the flow reversed at the centreline. A heating element was placed downstream of the hot film probe such that in normal flow the heat would be carried away from the Hot film. When the hot film is contacted by heat from the element the apparent velocity drops. However, the highly fluctuating velocity signal swamped the heat signal, so the Hot film probe had to be de-sensitised by running it at a lower probe current.

When this was done, distinct drops in the output signal could be observed for both upstream and downstream heating, though of course the effect was more marked with upstream heating. However, when the heating element was on the axis the reverse flow of helium bubble tracers on the axis was interrupted, indicating a disturbance of the flow. For this reason, this technique was not pursued further.

5.L.5. Particle collection

With the cyclone in a horizontal position it was fed with samples of shredded paper, and wood fibre. It was observed that when the bin was partly filled, particles from the bin base were periodically re-entrained and escaped from the bin. These movements were fast, but occurred at less than 1Hz frequency. The escaped dust was usually recaptured near the cone/barrel junction.

The dust rope that is commonly reported was observed in the transparent 140mmØ cyclone. Of particular note was the difference in the behaviour between geometries with the normal dust exit and those with some form of extension that delayed the expansion into the bin. The normal dust exit showed the dust to be concentrated in a clear, well defined spiral that maintained a

roughly uniform helical angle all of the way to the dust exit. In the geometries with an extended dust exit the dust rope became more diffuse as it approached the start of the extension - spreading out on the wall.

5.L.6. Helium bubble tracer observations

It was found that the movements of the helium bubble tracers on the axis in the Standard Stairmand geometry were often towards the dust exit. The paths of the tracers in the outer vortex could be seen tightening and spiralling towards the centre. Different bubbles moved into the centre at different points, and once at the axis some bubbles moved towards and some away from the gas exit. Of those that moved initially towards the gas exit some encountered a recirculation zone and reversed the direction of the travel to join the path towards the bin. Even when moving towards the dust exit there were recirculation zones that trapped the bubbles for short periods of time. On the axis the reverse flow consisted of a series of fast spirals connecting 'pauses' where the tracer became trapped for a while, doubling back on itself several times before moving on quickly to the next pause

As the tracers were not always produced of the necessary buoyancy the reverse flow on the axis appeared to be intermittent. However, on occasions there were continuous streams of bubbles and these indicated that the reverse flow was long-lasting, at least of the order of 30 seconds. These continuous chains of tracers also showed the axis flow to be off axis and helical, and footage of this is contained in the video.

The tracer movements were fast, which made it difficult to record. The cyclone was illuminated axially with a slide projector to give a streak path, and also strobed with a triple flash unit to allow the velocity to be estimated. The example shown in Figure 5.A.2 is typical and suggests that the tracer spent a total of 0.2 seconds in the cone, travelling between the cone/barrel junction and the dust exit. Of this time, 90% is estimated to have been spent in the two recirculation zones shown.

Sometimes the axial reverse flow only reached partway down the cone, on the other occasions tracers would reach the bin where they would become trapped just above the base - either until they burst or until a periodic flushing, which carried tracers out of the bin and up the axis to the gas exit. This occurred infrequently - perhaps with a return rate of 30 seconds.

Many tracers short-circuited into the gas exit without being observed in the cone, and there was always a diffuse trap of tracer bubbles close to the axis in the gas exit, about 3 D_X from the gas exit lip. This gas exit trap moved backwards and forwards in the exit over a distance of about 1 D_X. Some tracers escape independently from this trap. Tracers that escaped travelled further down the gas exit in large loops, describing a helical path of larger diameter than the original trap. The tracers were usually recaptured by a reverse flow that featured several hesitations along the axis before reaching the trap near the roof. Movements of tracers out of the gas exit and into the cyclone body on the axis appear to be synchronised with this reverse/recapturing flow observed in the exit pipe - suggesting a large scale movement of air from far down the gas exit (>11 D_X) into the cone and even as far as the bin.

The major influences on the position of the tracer traps and the presence of the axial reverse flow in the cone were disturbances to the flow (such as leaks in the bin or the insertion of a probe) and changes in geometries, with longer cyclones less likely to exhibit axial reversals in

the cone. Leaks in the gas exit or at the cone walls seemed to have little effect, but a leak into the centre of the bin base resulted in the disappearance of all tracer traps/recirculation zones on the axis

Changing the inlet flow had little effect, apart from the bubbles becoming harder to see as the flow increased. Most observations were made at V_i =15 m/s The bubble tracers on the axis were much more visible than when in the outer vortex - partly because the illumination was better on the axis but also because the velocity of the axis reverse flow (particularly in the recirculation zones) was significantly slower than the outer vortex flow.

The presence of the tracer trap just off the bin base is thought to be related to the type A Axial static pressure profile, with the flow swapping between this type and the type B (as shown in figures 5.H.1 & 5.H.2). The point of interest between the two types of Axial static pressure profile is the presence of a pressure minimum just off the base for Type A, while the type B shows a steady rise in pressure up the axis. The intermittency of the bin base trap, and the occasional flushing out of tracers on the axis could be related to the switching between the two states. The tracers moved to a lower pressure from the outer vortex to the core, and the pressure minimum in the minimum may stabilise the movement along the axial pressure gradient. The bin base trap of the helium tracers is slightly off the base (by 5-20mm), as is the position of the pressure minimum. The progress of the tracers along the axis may be hesitant because of the flat portion of the axial pressure profiles in the cone, which does not afford a pressure gradient down which the tracers travel.

The presence of the bin trap depended on the base being smooth to within 1mm , which the axial static measurements will obviously have disrupted. This meant that it was not possible to measure the pressure at the bin base at the same time as observing the bubble flow. The presence of the axial reverse flow and bin base trap features depend on the bin volume as well as the vortex length, despite only 10% of the inlet flow entering the bin. Extending the bin removed the bin trap. These observations suggest that the trap is formed from boundary layer flow across the bin base.

Probes could be inserted radially into the flow from the wall without upsetting the reverse flow on the axis, until the centreline was reached - then the tracers would only travel as far as the probe before returning to the gas exit. When slightly off the centreline the axis reversal could divert around the obstruction. This meant attempts to measure the speed or duration of the reversals with hot film probes and heated elements failed. The heating element was a coil of nichrome wire, in the shape of a cone about 20mm long with a base diameter of 10mm. This presented a small, diffuse obstruction to the flow on the axis. When the element was on the axis, the tracers travelled right up to the tip of the element before stopping and returning to the gas exit. When the element was on the axis the gas exit trap was 3.3 exit diameters from the gas exit lip whereas shifting the element to the side of the core shifted the trap to 6 gas exit diameters downstream from the gas exit lip.

The movements of the helium bubble tracers were recorded on a video which accompanies this thesis. Some notes on the features that are visible in the video are to be found in Appendix 10.J

Helium bubble tracer observations for different geometries.

These are summarised in Table 5.L.1 on the following page . For each geometry the following is indicated:

- The position of the gas exit tracer trap, in terms of the number of gas exit diameters downstream from the gas exit lip. This is the first column, the "undisturbed" state (*Undist*)

- The position of this trap when a 10mmØ probe is inserted radially into the cyclone barrel from the wall. The second column (*PI in outer*) is for the probe inserted only into the outer vortex. The third column (*PI in core*) is for the probe inserted into the core vortex

- The presence (or absence) of the tracer trap in the bin

- The approximate location in the cone where the tracers are seen to move from the outer to the inner vortex. This may be affected by changes in the buoyancy of the bubbles being produced.

- The amount of activity of tracers along the axis in the reverse direction.

Summary of Helium Bubble Tracer Observations

	Position of Gas exit trap: distance from gx lip (in gas exit diameters)			Bin trap presence	Position of HBT inflow to core	Flow reversal behaviour on axis
Geometry:	Undisturbed	PI in outer	PI in core			
Standard	3.1D_X	1D_X trap tightens	11.7D_X	Yes - just off base		YES
Standard + extended bin	3.1 D_X			Rarely, unless via outer vortex	Ports 3-9	NO ?
Standard + Extended cone	3.1D_X	closer to lip	11D_X	None, unless fed by outer vortex at low flow	Port 8	NONE
LC+140: 499mm cone +100mm barrel	3.1D_X			Not often		Infrequent
"Longest" 243mm barrel, 355mm cone	3.1D_X			Less frequent		YES often only as far as Port 7
"No Cone" barrel only, 523mm from base to gx lip	0 D_X on lip	for pi near gx or base the trap moved to just off the base	pi touching the core moves the trap to 3D_X	Only when probe is inserted into outer vortex		NO, tracers enter the core at thebase Hesitant flow along axis towards gx
Standard + short (100mm) bin	< 3D_X			Yes, but swept out more often		YES Strong, less hesitant
Standard + gas exit plate	6D_X	7.4D_X pi to core in gx	9-11D_X to 12oi core	Yes, more via outer vortex	Ports 8-9	Less frequent
Shortest + extended bin	3.5-5D_X				Ports 6/7	NONE
Long cone: 499mm cone, no barrel	5.3D_X			Yes - for the few that make it	Ports 5-8	Infrequent - almost all go to gas exit
Svarovsky type	3-6D_X	4.5D_X	11D_X		Ports 6/7	

	Position of Gas exit trap: distance from gx lip (in gas exit diameters)			Bin trap presence	Position of HBT inflow to core	Flow reversal behaviour on axis
Geometry:	Undisturbed	PI in outer	PI in core			
Shortest	$5.3D_X$				Port 7, sometimes from gx	YES, Strong, less hesitation
Standard + Extended cone + No bin				Trap attaches to end of cone at side wall		
Shortest + extd cone + no Bin	$3\ D_X$?			No bin,the trap attaches to the base side wall		
Long cyclones + No bin				Trap forms against base for all lengths of barrel		
Standard + gas exit expansion	$>4D_X$			Yes, if supplied by outer vortex	Port 4/6	Occasional, at times only as far as Port 7
Standard + Scroll Exit	$8.4D_X$			Yes, occasionally	Ports 5/7	Short reversals in cone

5.M. COLLECTION EFFICIENCY:

5.M.1. Observations of dust collection

Particles such as shredded paper, wood fibre and polystyrene were fed to the perspex cyclone and the collection was observed. There was some difficulty with particles becoming charged from the plastic and from choking when particles were fed too quickly. As the cyclone was operated in a horizontal position there was a tendency for the dust exit to choke as the bin became full.

Leaks into the bin had a dramatic effect on the collection, with particles being quickly carried out up the axis. A periodic pulse of dust out of the bin up the centre vortex was observed when there was an appreciable amount of dust in the bin. This escape flow moved rapidly but occurrences were less than 1 Hz in frequency. The escaped dust was usually recaptured in the cone and delivered to the bin again.

Larger matter fed to the cyclone sometimes stayed circulating in bands in the cone - often just below the cone-barrel junction. There were also particles trapped in recirculating bands around the roof after entering. Most of this eventually carried on down the cyclone but some was seen to travel down the gas exit outer wall and escape.

Descriptions of the variation of the collection efficiency with geometry are being collected from the literature, also for the geometries used here measurements have been made by a final year student at Canterbury (Kevern, 1991), and the results are indicated overleaf. The efficiencies were measured in a 350mmØ cyclone that exhausted to atmosphere, with $CaCO_3$ powder in the range 2 - 80μm (d_{p50} 10μm). It was not possible to collect the exit dust and hence a mass balance was not possible.

There is little difference between the performance of the Standard Stairmand HE cyclone, and a cyclone of the same dimensions, but with a cone extending from the level of the gas exit lip to the dust exit. The difference between the curves was stated to be significant compared with the experimental uncertainty. Both curves appear to show the beginning of a decrease in efficiency at high flowrates, as has also been observed by Svarovsky (1984), Kalen & Zenz (1974) and Stairmand (1951)

The few trials made for the variations on the dust exit geometry again show very little difference in the collection efficiency. This is more surprising considering the major differences in axial pressure profiles and bin pressures shown by these geometries compared with the standard geometry. It suggests that the cyclone may have a self-correcting mechanism that negates the effect that large changes in flow pattern have on the efficiency.

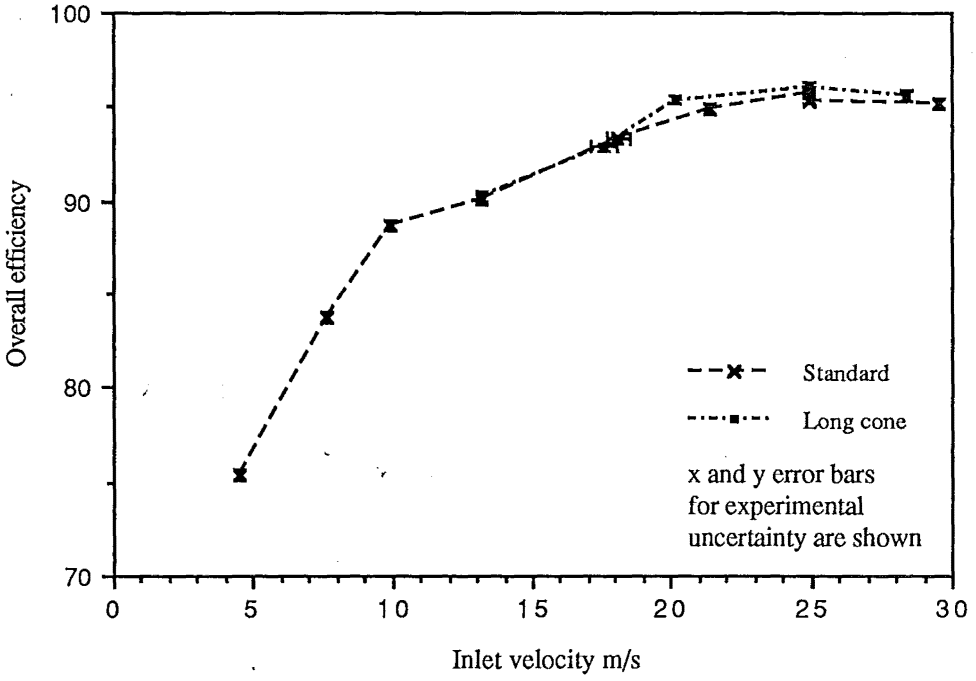

Figure 5.M.1: Cyclone gross efficiencies for 300mmØ Long cone and standard cyclones (from Kevern (1991).

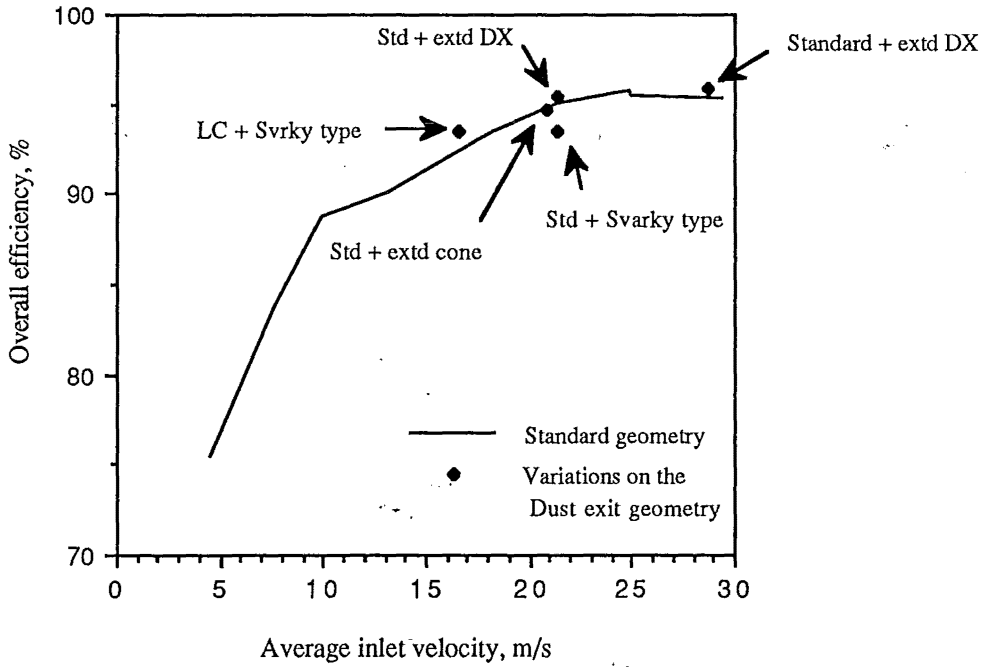

Figure 5.M.2: Cyclone gross efficiency for various dust exit configurations from Kevern (1991)

Chapter

6

DISCUSSION

6.A MEASUREMENT PROBLEMS

Some discussion of the significance of the measurements has been included in chapter 5, alongside the result in question. In this chapter some of the problems encountered with the use of the various measurement techniques are discussed and the significance of the results obtained is considered.

6.A.1 Disturbance of the flow by probe insertion

Harvey (1962), and Green & Acosta (1991) among others have stated that intrusive measurements in vortices are not reliable because of the sensitivity of the vortex to disturbance by probes. Extensive use has been made of probes in this study, and some justification is required for this.

The most marked effect that probe insertion has on the vortex is shown in the pressure drop, which is significantly lowered upon insertion. This decrease in the Euler number (the number of inlet velocity heads in the pressure drop) is as much as 25%, which is comparable to the difference between different geometries. However, the reduction in the case of the probe insertion is thought to be related to the slowing of the vortex by the probe interference rather than a wholesale structural change. The greatest reduction was recorded for insertions near the cone/barrel junction in the standard geometry. A similar reduction in the pressure drop was achieved by lining the cyclone barrel wall with rough sandpaper. If the spin of the outer vortex is slowed down the pressure drop is reduced by the square of the spin ratio.

To check the theory that the probe insertion causes a slowing of the spin, total velocity profiles were measured with a Hot film anemometer near the cone/barrel junction, with a 10mmØ probe inserted just below the gas exit lip. This showed a significant reduction in the total velocity from 38.6m/s to 34m/s when the probe was inserted. The expected reduction in the Euler number is $(34/38.6)^2$ or 77%. The Euler number in the undisturbed case was 7.4, reducing to 5.8 upon probe insertion, a reduction of 78%. Bradley (1965) also observed the reduction of the pressure drop by probe insertion, with a 1mmØ probe inserted 20mm into a 75mmØ hydrocyclone. Retardation of the tangential flow would be compensated for by increased vertical or radial flows, with a decrease in efficiency expected to result.

The effect of probe insertion has been claimed by Iozia and Leith (1989) to be insignificant in the 250mmØ cyclones that they examined. They based this on the finding that the efficiency was unaffected by the insertion of their probe, a TSI model 1650. The diameter of this probe appears less important than the diameter of the probe support, which would presumably be 3-5mm. The effect would therefore be less noticeable than the 10mmØ probe in the 140mmØ cyclone. Experimental measurements on a 300mmØ cyclone by third year students in this department gave inconclusive results as to the effect of probe insertion on the efficiency, with some finding an increase, and others finding a decrease in efficiency. The pressure drop decrease was still observed in this larger cyclone.

The reduction in the cyclone pressure drop number resulted in an increase in the average inlet velocity as the Pitot cylinder was advanced. The extent of the change was 5% for traverses near the cone-barrel junction and less elsewhere, becoming negligible in the lower cone. In later traverses the inlet velocity was continually adjusted to keep the inlet velocity at the same value, but for the earlier results adjustments were made to the velocity profiles during the scaling that was undertaken before they were plotted. This was done by scaling each velocity data point by the actual inlet velocity that was recorded with that amount of probe insertion, rather than the nominal inlet velocity recorded at the start of the run with no probe inserted.

A further check on the extent of the interference of the probe on the flow was the comparison of the static pressure profile along the axis obtained with the axial probe, and from the Pitot cylinder. The diameter of the axial probe was 5mmØ compared with the 10mmØ of the Pitot cylinder, and the former had no observed effect on the cyclone pressure drop. The agreement between the profiles is good: for example, the wall-axis pressure difference calculated from measurements by the two probes are shown in Figure 5.G.15. Other techniques for determining the velocity profiles are also subject to problems. Any method involving intrusive probes is obviously subject to error, and even the Hot film probe (two prongs of 1-2mmØ on a body of 3mmØ) showed the effect of reducing the cyclone pressure drop, although to a lesser degree (about 95% of the undisturbed value, as opposed to 80% of the undisturbed value for the 10mmØ rod). Other velocity measurement methods, such as the Laser Doppler Anemometer also suffer from complications, such as the vortex centreline being off axis.

The movement of tracers along the axis was affected dramatically by the insertion of probes. While the probe was still in the outer vortex the location of the recirculation of the helium bubble tracers in the gas exit moved slightly closer to the gas exit lip. This was associated with the lowering of the pressure drop. As the probe entered the inner vortex there was a lessening of the rate of change of the cyclone pressure drop, but the tracer recirculation zone moved 5 tube diameters downstream. This appears to show two separate mechanisms of probe interference at work. The first is the slowing of the outer vortex and consequent lowering of the pressure drop. The second is interference with the third vortex stream thought to be present along the axis. This was supported by observations made with a slender probe with a large head. This probe could be introduced to the axis without causing a large reduction in the pressure drop, and the interference with the tracer flow was observed only when the probe head was directly in the path of the tracers.

6.A.2 Velocity Profiles

As shown in Figure 6.1 there is a large difference between the relative scale of the pitot cylinder probe in the various cyclones. This suggests that the extent of the interference would vary between the 750mmØ and 140mmØ cyclones. In addition, the 7.5mm spacing of the Pitot cylinder tappings in the radial direction is more significant in the 140mmØ cyclone which has radial pressure gradients an order of magnitude greater than those found in the 750mmØ cyclone. This spacing was corrected for, and generally good agreement is shown for the tangential and axial velocity profiles obtained in different sized cyclones by the 4-hole Pitot cylinder in Figures 5.B.3 to 5.B.4 The profiles of total velocity obtained with the hotfilm probe in the 140mmØ cyclone also show reasonable agreement with the pitot cylinder probe. The velocities are time-averaged, and this may mask some of the disturbance.

Comparing the velocity component profiles obtained in corresponding positions in the 140mmø and 750mmØ cyclones shows larger differences than found between profiles obtained in cyclones of different cone lengths. It was thought that the difference between the 140mmØ and 750mmØ cyclone velocity profiles could be attributed to the difference in their exit configurations. The 750mmØ cyclone had a shorter exit tube (of $2D_X$) that exhausted to open air, and this would present less resistance to axial movements of the core than the long ($17D_X$) straight gas exit of the 140Ø cyclone. Since the 140mmØ cyclone operated under suction it was difficult to arrange a similar expansion. A 0.5 metre diameter expansion barrel was placed in the exit of the 140mmØ cyclone, however this gave a length of 6 exit diameters from the gas exit lip to the expansion, and hence did not match the 750mmØ cyclone configuration. No difference was observed in the 140mmØ profiles for the addition of the expansion barrel. The inlets of the 2090mm and 750mmØ cyclones also had sharp bends 3-4D before the cyclone body, whereas the 140mmØ had a straight entrance.

Radial velocity profiles:

Unfortunately the radial velocity component could not be accurately determined. It is expected that at the prevailing turbulence level of 10% the fluctuating velocity will be of the same order of magnitude as the radial component, which will make the measurement of the radial velocity by any means difficult. For the standard Stairmand high efficiency geometry, the average radial inflow velocity calculated from the inlet flowrate and the surface area of the core boundary is equal to 0.0182 times the average inlet velocity. Since the 2090mmØ and 750mmØ cyclones were operated at V_{in} = 18m/s and the 140mmØ cyclone at V_{in} = 22m/s the respective average radial velocities would be expected to be 0.33 and 0.4 m/s.

The radial velocities measured in the 140mmØ and 750mmØ cyclones were directed radially outwards for most of the radius, which contradicts the mass balance. The magnitude of the measured value reduced as the scale of cyclone increased. The variation in the radial velocity measured with the Pitot cylinder between the different scales of cyclone could be due to the change in the degree of turbulence in the cyclone, or to the reduction in the extent of the disturbance caused by the probe as the cyclone diameter increases. The latter is thought to be

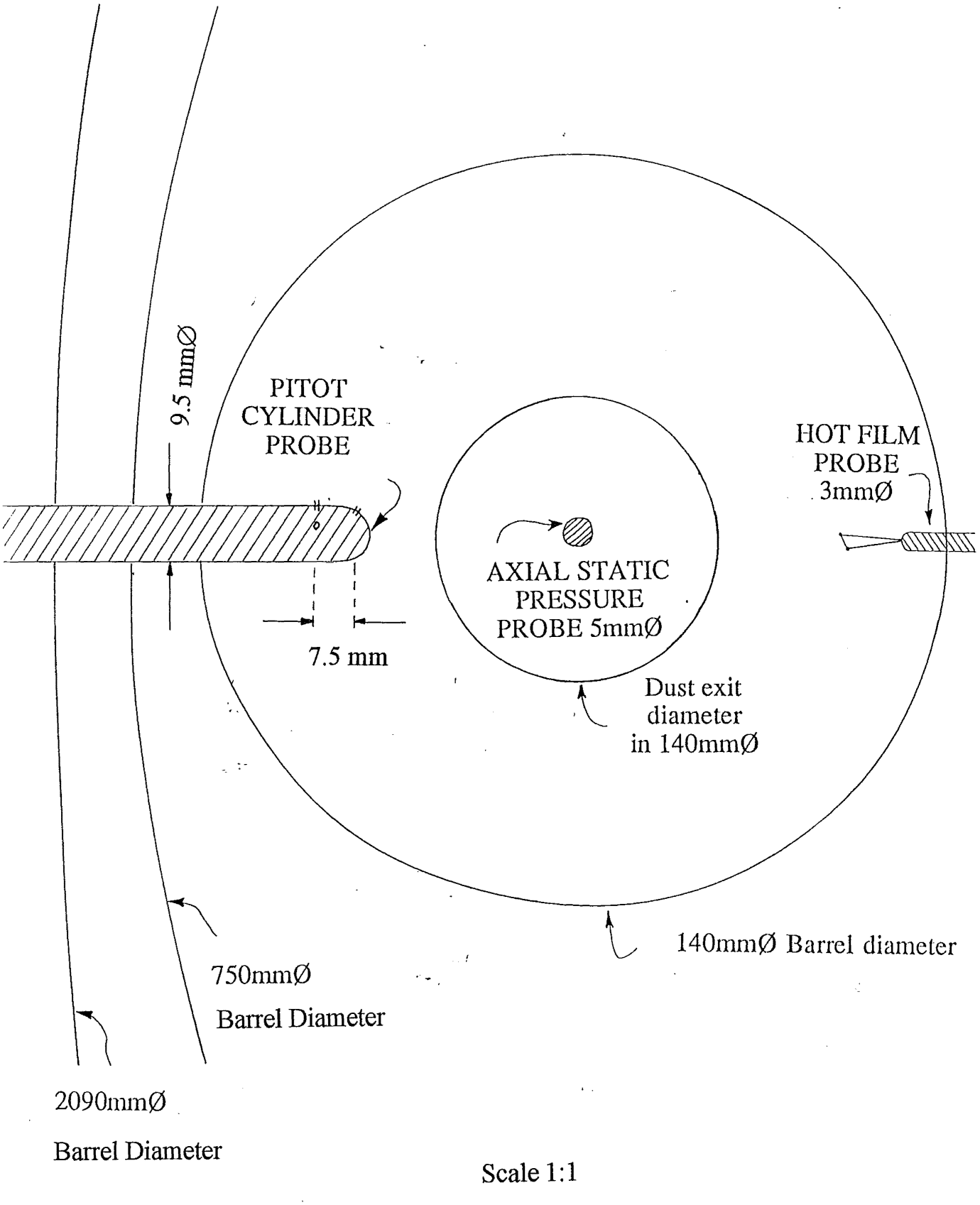

Figure 6.A.1: Relative sizes of the cyclones and probes used in this study

most likely, as measurements of the probe response in different turbulent intensities showed no significant change (Appendix 10.F), and the scatter in the radial velocity estimate increases lower in the cyclone cone.

6.A.3 Pitot cylinder measurement uncertainties

The largest uncertainty in the velocity calculated from the pitot cylinder was contributed by the curve fitting and interpolation that was required to correct for the radial displacement of the tappings. The pressure reading made across the radially displaced tappings was adjusted by fitting a 4 or 5 point curve through the data points to smooth the errors before interpolating to find the static pressure or the P3-PR pressure at the correct location. This could not cope with large errors, and any error in the P1-P2 reading was not corrected for. The results could be improved by fitting curves through all pressure readings to smooth out the random measurement errors. The measurement technique was adapted to ensure that the measurements were taken at spacings of 7.5mm (or sub-multiples of 7.5mm) so that the correction could be made directly. However there is still a difference between these measurements as the probe tip is not located as far into the flow when the tip pressure is read, and the effect of this could not be quantified.

Another possible problem that was identified was the response of the pitot cylinder to fluctuating flows. The probe was calibrated in a wind tunnel with low turbulence, whereas the cyclones featured high levels of turbulence, and the scale of this could be expected to change between the cyclones. Pressure probes are sensitive to the orientation to the flow, and outside the calibrated angle the response of the probe can be highly non-linear. A large fluctuating velocity component coupled with a bias in response can result in a large error in the pressure reading as detailed by Christiansen and Bradshaw (1981). The response of the pitot probe to different levels of turbulence was tested in a duct with different grids placed a short distance upstream. Turbulence intensities of 5% were achieved, with no significant alteration to the pitch or yaw angles obtained from the Pitot cylinder.

An error analysis for the velocity components obtained from the Pitot cylinder has not been performed. Repeat measurements were made at some locations and these generally agreed well. In particular, traverse results that appeared to fall outside the trend exhibited by the other locations were repeated, but this generally confirmed the initial result rather than improved the agreement with the trend.

In the calculation of the velocity from the pitot pressure readings, the determination of the pitch angle contributes the most error. This is partly due to the radial spacing of the pressure tappings in a large pressure gradient, but there appear to be other problems. The determination of the radial velocity component is not possible because of the large scatter in the pitch angle obtained even after correcting for the radial spacing of the tappings. The scatter is reduced in the larger cyclones which have smaller pressure gradients as well as lower turbulent intensity.

Bosley & Negus (1984) found good agreement between the velocity vectors obtained with a LDA and those from a 5 hole Pitot cylinder in a spray drier. The pressure probe diameter was 8mm and the drier diameter varied from 750mmØ to 95mm.

The results from the Pitot cylinder probe gave a large variation in the pitch angle which was at times outside the calibration range of the probe. The radial velocity is the component that is most affected by the pitch angle, and a large scatter in the values was found. The cause of the scatter could not be determined, but it was considerably less in the larger cyclones. The radial velocity obtained was directed outwards, which is in conflict with mass balance requirements.

6.A.4 Flow asymmetry

The vortex centreline determined from the Pitot cylinder measurements did not coincide with the cyclone centreline. In some locations traverses from opposite sides of the cyclone both went beyond the centreline, which appeared to show that the probe was able to push the vortex off the axis Where the vortex axis was well off the geometrical axis problems were encountered in calculations involving the radius. Using the geometrical radius underestimated quantities such as the circulation, but the vortex radius could not be applied to the semi-circle, as obviously the radius had to stay within the cyclone walls. It would be useful to make further traverses across the diameter that is at right angles to the one used. An indication of the variation between different orientations of the traverse diameter with respect to the inlet is given in the profiles presented in Ogawa et al (1990). Discussion has also been made of the phenomenon of vortex asymmetry (in spray drying chambers: Reydon & Gauvin, 1981), the causes and effects of it (Chanaud, 1965) and means of accounting for it in the analysis of velocity profiles (Escudier, Bornstein & Zehnder, 1980). The asymmetry and fluctuations of the core have thwarted attempts to measure radial velocities with a laser Doppler anemometer by Hsieh & Rajamari (1991), who found the flow was most asymmetric near the inlet and dust exit.

Smith (1962a) measured profiles of axial and tangential velocity in a 140mmØ cylindrical cyclone. He used probes with slender heads on 1mmØ tubes that were stretched across the diameter. This allowed the probe to be accurately aligned along the diameter and kept the area symmetrical about the axis. He found that an asymmetric probe caused a strong asymmetric disturbance in the flow. and recommended the use of radially symmetric probe arrangements rather than cantilever probes. The flow in the confined vortex apparatus is commonly acknowledged to be asymmetric. Schowalter and Johnstone (1960) described the form of the asymmetry as a dynamic centreline with a helical shape.

Iozia & Leith (1989a) also found a (statistically significant) difference in the tangential velocity profile between the opposite sides of the cyclone. When the axial velocity profiles are compared with the time-averaged axial velocity model of Bloor and Ingham (1987) (as shown in section 5.C in this study) it can be seen that there is an oscillation in the closeness of fit of the model between opposite sides of the cyclone in the lower cone. The experimental points are below the model for Ports 6 & 7 on the inlet side, but well above the model on the opposite side. Port 5 shows good agreement for both sides but then the opposite trend is shown for Ports 3 & 4 with the experimental points being higher than the model on the inlet side but lower

on the opposite inlet side. Improvements were made to the agreement between the experimental profiles and model profiles by allowing for the vortex centreline being off axis. The locations that were the most asymmetric (Ports 5 & 9) actually gave the best agreement between the model and the experimental points once the model vortex axis was shifted to coincide with the experimental centreline. However, this did not account for the difference in all locations.

The stagnant gas regions that are thought to cap the ends of the vortex could be located off the axis in a precessing fashion with respect to axial distance, or alternatively could be axially aligned with the vortex precessing around them. Particularly with the Long cone cyclone the vortex centreline was found to be precessing off the geometrical axis. .

Apart from in the velocity profiles and with the vortex centreline, the eccentricity differences have shown up in our study in the Γ_0 vs L plots; the variation of the best fit parameters for Γ_0 and the turbulent viscosity; the wall flow yaw angles as well as in visualisation experiments with helium bubble tracers and cotton streamers.

There was a significant difference between profiles of the wall circulation between the opposite sides of the cyclone. This suggests that the hump could be due to a streamwise vortex derived from the asymmetry of the inlet. Most measurements were made on the side opposite to the inlet, but where both sides of the cyclone were studied, there was a difference between them. The opposite inlet side is effectively half a revolution behind the inlet side, and the hump of the Γ_0 was 100mm behind the inlet side in the axial direction. Assuming an average diameter of 100mm, this would make the angle of the flow to the axial plane: $\tan^{-1}(0.100/\pi \times 0.100\text{m}) = 17°$
which is close to the pitch of the vortex that is measured with the Pitot cylinder yaw.

The angle of the flow to the axial plane varied down the cyclone in a different manner for opposite sides of the cyclone. The angle on the inlet side was steepest at 120mm from the dust exit, whereas on the opposite inlet side steeper flow was found 30mm and 225mm from the dust exit. The vortex was observed to be off axis which could promote the unevenness of the flow. Reydon & Gauvin (1981) observed an asymmetry due to the single inlet persisting as far as the cone region. A stagnation bubble would be expected to have a similar effect on each side of the vortex, unless the vortex, or the bubble itself was off axis. A further possibility is that the vortex is attaching itself to the wall; but this was not observed with any visualisation techniques.

6.A.5 Pressure drop

The overall pressure drop was measured for different geometries and was found to vary significantly with cone or barrel length. The measurement of the pressure drop requires the location of the tappings to be specified, particularly the exit tapping. Some studies measure the exit pressure after the spin has been arrested, others use the wall pressure just above the roof. For many runs the pressure drop was measured between the side wall of the inlet just above the entry to the cyclone; and the wall of the gas exit 30mm above the roof. In the latter the presence of spin would obviously affect the measured pressure, but the cyclone operated by drawing air

in at the inlet and the exit did not expand to atmosphere. To correct the problem most measurements in the exit were made to the base of the large expansion barrel that was placed downstream in the exit. Those measurements that were referenced to the gas exit wall may vary because of the effect of the cyclone length on the strength of the spin in the gas exit. The Euler number has been shown to vary slightly with flowrate, so the inlet velocity needs to be stated as well. Zhou & Soo (1990) suggest that the pressure drop is proportional to ρV_{in}^{n} where $2 < n < 3$.

Apart from the location, the position and size of the tapping needs to be considered. Measurements were generally made as close to being flush with the wall as possible, using 1mmØ holes expanding into 3mmØ tubes after 2-3mm.

6.A.6 Axial static pressure profiles

As pointed out by Pauley (1989) the measurement of static pressure in the interior of turbulent laboratory flows is known to be subject to large uncertainties. These are mainly attributed to cross-flow fluctuations and axial flow fluctuations, and the effect is a tendency to lower the mean static pressure. Pauley measured the axial static pressure in a tornado simulator and found no significant differences between different sized tubes or opposing orientations of tubes. This was taken as evidence that the errors due to axial flow fluctuations, and those due to viscous effects (which depend on the size and shape of the probe) are not very large.

Reasonable agreement was found in this study between the estimates of axial static pressure from the axial probe in the 140mmØ cyclone, and those obtained from the Pitot cylinder readings near the axis in the 140mmØ and 750mmØ cyclones.

Effect of radial movements of the probe:

The axial pressure gradients are at least two orders of magnitude lower than the radial pressure gradients over much of the cyclone length. This indicates a problem with the accuracy of the positioning of the axial probe. The 1 metre long probe was supported only at the bin base, and when inserted well into the cyclone there was a tendency for it to droop off the axis. Even if the probe was kept well aligned with the geometrical axis, the variation of the vortex centreline would cause large deviations in the pressure. Even small errors in the radial direction would greatly affect the pressure reading. The radial pressure gradients in section 5.G on page 174 are of the order of 20 000 to 60 000 Pa/m near the core of the 140mmØ cyclone, but the gradient drops steeply in magnitude as the axis is approached. If the gradient was 20 000 Pa/m and the probe moved 5mm from the axis, the pressure could increase by 100 Pa. However, when the probe was significantly off the axis it started to rotate or precess, and readings were taken only while the probe was kept stable. This would tend to keep the probe on the vortex axis rather than the geometrical axis - this was desirable.

The pressure was expected to decrease in the direction of the flow along the axis, but in fact the pressure was reasonably constant, or even rose slightly in the direction of the gas exit. This could be due to the probe being off the vortex axis as it is inserted further, or to the effect of the near axis reverse flow.

6.A.7 Dynamics and Hysteresis

Hystereses in the axial static pressure profiles were observed when the traverses were repeated with no change in flowrate or geometry. There was a difference between measurements made while the probe was progressively inserted, and when it was being withdrawn. Repeat traverses made in the same direction would show the same features, but be displaced by a uniform amount to generally a higher pressure. When the axial static pressure profiles were expressed as Euler numbers the profiles at low (< 10m/s) inlet velocities were grouped separately from higher profiles and intermediate profiles were observed to switch between the two. The pressure drop characteristics of the cyclone also showed a change as the velocity was increased.

The majority of measurements were time-averaged, which given the dynamic nature of the flow, is a source of error. The averaging is expected to indicate the dominant position, and the conflict in the position indicated by different techniques could be due to different response biases to the fluctuating flows. The evidence of the length of the vortex is derived mainly from the time averaged measurements.

Analysis of the fluctuations in the pressure and velocity readings requires further work, since elimination of the pulsations in the inlet air was not achieved. Figure 5.L.2 shows the Fast Fourier Transform spectra for the 750mmØ cyclone at the centre of the bin base and gas exit, which show dominant frequencies of 13 and 25 Hz in the gas exit and 10 and 25 Hz in the bin. Garg & Leibovich (1979) found the wakes of vortex breakdown always contained peaks corresponding to energetic low frequency (under 10 Hz). Their flow visualisation study suggested that these oscillations were associated with non-axisymmetric disturbances.

The phenomenon of confined vortices producing audible frequencies has been linked by Chanaud (1965) to perturbations on the vortex core and associated with vortex breakdown states. The whistle heard when some ports were open on the inner surface could provide information about the dynamics of the cyclone.

6.A.8 Flow visualisation:

Helium Bubble tracers:

The high velocities in the cyclone are an impediment to obtaining good results from flow visualisation. For a typical inlet velocity of 25m/s the tangential velocity in the outer vortex could reach 40m/s (144km/hr) this means that a tracer will complete half a revolution in the cyclone barrel in 6 milliseconds, or less than 3 ms in the lower cone. While photographic methods were developed that could record the tracer movements, the main problem remained triggering the photograph, as the well-buoyant tracer 'events' were relatively infrequent and the human reaction time was too long.

The brightness of the helium bubble tracer image in the flow visualisation photographs depended on the speed and location of the tracer. The best records were obtained for the region near the axis, as the tracers appeared to be moving slower and the illumination from the flashes and projector was concentrated near the axis. It was difficult to obtain uniformly high illumination in the outer region. The determination of the speed of the tracers was also difficult because of the tight spirals and reversals of the tracer path. The fast flash rates required also lowered the amount of light available, so that velocities could not be determined easily.

To get around these problems the inlet velocity was kept low, between 8 and 13 m/s. These lower velocities still appeared to show the same general flow characteristics as the higher velocities that the time-averaged velocity profiles were determined for. As figures 5.B.1 and 5.B.2 show, the time-averaged velocity profiles scale well between 8 and 22m/s.

Buoyancy: The lack of sufficiently tight control over the buoyancy of the helium bubble tracers meant that they could not be used for determining the radial velocity in the cyclone. The high buoyancy forces were greater than the drag forces, resulting in the lighter bubbles being driven into the centre. Gravity separation of the heavier and lighter tracers was not feasible to the accuracy demanded by the magnitude of the centrifugal effect in the cyclone, which could be 3 orders of magnitude higher than gravity. A commercial classifier of tracer buoyancy (based on a vortex) was used by Kessler & Leith (1991) also apparently without successfully removing the lighter tracers.

It has been assumed that once on the axis with a low axial pressure gradient, the tracer movements will reflect the actual air movements. Certainly the pressure gradient is much less steep along the axis. The effect of the gradient of the static pressure along the axis on the tracer movements is expected to be slight. The largest axial gradient occurs across the bin entrance and is less than 3000Pa/m. Elsewhere along the axis the gradient is two orders of magnitude less than this. The radial pressure gradients in the 140mmø cyclone are typically greater than 20 000 Pa/m. Even if the vortex centre oscillates about the geometric axis this wouldn't explain the extensive axial movements. The axial static pressure profile in the cone was generally in the 'well-formed' vortex region. This was characterised by a nearly constant pressure along the axis. This could account for the hesitant nature of the movement of the tracers and the multiple stagnation points.

The recirculation zones observed with the helium bubble tracers in the reverse flow near the axis formed and dispersed at different points along the axis. The range of the locations of these tracer recirculation zones corresponded with the flat portion of the axial static pressure. After the tracers reached within 30mm of the dust exit, no further recirculation zones were seen, but the tracers moved directly to the recirculation zone that was centred on the bin base. This was travelling down the steep pressure gradient along the axis.

At low flowrates (V_i = 5m/s) bubble tracers were observed to make it into the bin via the outer flow. These would be tracers that were slightly heavier than air, with the low flow the separation effect was only 4% of the flow at V_i = 25m/s, which may prove insufficient to cause collision with the wall for some slightly less than buoyant tracers. The cylindrical cyclone (with no cone) showed bubbles appearing at the base in the outer flow before moving into the centre and returning up the centre flow.

Cotton streamers:

Problems were experienced with the cotton streamers becoming tangled with adjacent spacer beads. Moving the position of the bead slightly in the radially direction could also cause quiescent streamers to start fluctuating reversals, which would continue if moved back to the original position. At the axis the cottons often were spinning continuously between the forward and reverse direction

Despite these problems, some regions were found to be quiescent (including zones on the axis), while others fluctuated strongly. Streamers in the outer vortex were generally steady, and some appeared to indicate steep inflow angles. Near the axis, streamers would alternate between the forward (towards the gas exit) and backward (bin-wards) directions. Photographs, taken to 'freeze' the motion showed opposing flows on the axis in adjacent streamers that were 30mm apart, as is shown in figure 5.A.6 on page 142. The extent of the instantaneous reverse flow was often less than 60mm or over 120mm in an axial direction, and around 10mm in the radial direction. It was always located near, although not always on, the axis rather than in the region of the maximum tangential velocity. The frequency of the fluctuations was difficult to estimate from photographs, but appeared to be about 10 Hz from photographs with strobe and triple flash lighting.

The streak photographs of the Helium bubble tracers, such as in Figure 5.A.2 explain the intermittency of the reversals of the cottons. The recirculation zones formed and dispersed, and moved in the axial direction. Inside the zone the flow direction reversed frequently. The response rate of the cotton may not be fast enough for the flow changes, and its inertia may result in an average flow being presented. Jackson (1963) claimed (without giving the source) that "it is now known that in a vortex, flow streamers are an unreliable guide to the flow direction". It is not known what this is based on.

The strongest fluctuations in the cottons were observed low in the cone and around the Alexander natural length, for a range of vortex lengths, again suggesting a stabilising effect of the cone (or dust exit expansion). In fact, the region of most fluctuation activity moved towards the dust exit as the cyclone was lengthened from the 'Shortest' to the 'Longest'. Both the standard and 'Shortest' geometries showed no reversals near the axis in the cone when the bin was extended. The flow reversal near the axis shown by the Helium bubble tracers was also absent with the extended bin.

Fog Tracers:

The high velocities combined with the high turbulence and diffusivity in the cyclone to make this method untenable at normal operating velocities. Experiments were done at an average inlet velocity of 8m/s with a fog produced by heating of an ethanol/water based fluid in a hypodermic tube. This enforced a limit on the velocity of air that the fog could be operated in due to the cooling effect of the air on the tube.

ter Linden (1949) cited the high Reynolds number and considerable turbulence in the cyclone as a practical difficulty in determining flow patterns by smoke tracers, as the smoke was found to quickly spread throughout the cyclone.

6.B. FITTING THE VELOCITY MODELS :

The measurements of the velocities represent the most comprehensive survey reported, both in the axial and radial spacing of measurements, and the range of scales of cyclones that were examined. The previous studies of the velocity profiles were reviewed in section 3.B.

The assumption that the tangential velocity does not vary significantly over the height is supported by the profiles measured in this study. This has been frequently reported, such as by Vatistas, Lin and Kwok (1986), Ogawa (1990) and Reydon and Gauvin (1981). The decrease in the circulation (at the wall) along the cyclone length has received less attention, although it has been commented on by Alexander (1986), and used by Abrahamson (1992) in his pressure drop study. The asymmetry of the velocity profiles that was found has also been mentioned by many workers, such as Knowles et al (1973).

In Chapter 5 the experimental velocity profiles were compared with the tangential velocity component profiles of Burgers (1948) and Phillips (1990); and the axial velocity component profile of Bloor and Ingham (1987). These were considered to be the most promising models found in an initial survey. The performance of these, and possible refinements are examined in this section.

A distributed parameters approach was used to fit the Burgers tangential velocity profile to the radius and magnitude of the experimental maximum tangential velocity. This involved allowing the parameters to vary between each location to achieve the best fit. Simple functional relationships are desired to enable the parameters to be predicted, and the existence of these will be examined here.

The axial velocity model of Bloor and Ingham was shown to be unrealistic near the axis, and to only approximately predict the zero axial velocity boundary. The reasons for this and the possibilities for correcting this will be discussed in section 6.B2. Other axial velocity models will also be considered, such as the polynomial used by Tran (1981), and the exponential profiles derived from the analysis of Batchelor (1964).

6.B.1: Tangential velocity modelling.

Since the purpose of modelling the velocity components is to yield an expression for the velocity that can be used in further calculations a simple form is desirable, preferably with parameters that are uniform throughout or described by universal expressions. The Burgers (1948) equation is of a suitably simple form, with three parameters required to describe the profile, two of which can be combined. This equation was described in section 3.B, and the expression is:

$$V_\theta = \frac{\Gamma_o}{r}\left[1 - \exp\{\frac{-ar^2}{2.\nu_T}\}\right] \qquad \text{--- (6.B1.1)}$$

The parameter 'a' was shown in section 3.B to be given by the radial gradient of the radial velocity, such that:

$$a = \frac{2.Q}{\pi D_x^2 L} \qquad [s^{-1}] \qquad \text{--- (6.B1.2)}$$

The exponential parameters can be combined to give a single parameter α_θ:

$$\alpha_\theta = \frac{a}{2\,\nu_T} \qquad [m^{-2}] \qquad \text{--- (6.B1.3)}$$

and the Burgers vortex can then be written as:

$$V_\theta = \frac{\Gamma_o}{r}\,[1 - e^{\{-\alpha_\theta r^2\}}] \qquad \text{--- (6.B1.4)}$$

The experimental profiles would have some scatter due to experimental error, and would also deviate from ideal behaviour near the wall and axis. Hence, it was not suitable to find parameters by forcing a least-squares-error fit to the entire traverse profile. Instead the model was forced to agree with the value and location of the maximum tangential velocity for each location. Deviations from the ideal profile can be allowed for by the addition of modifications to the model profile. It was shown in section 3.B that the parameter $\alpha_\theta = \frac{a}{2.\nu_T}$ determines the radial location of the model tangential velocity maximum and Γ_o determines the magnitude - and the two can be varied independently.

To achieve a constant value of $\alpha_\theta = \frac{a}{2\nu_T}$ requires that the radius $r(V_{\theta max})$ is constant over the length of the cyclone. The variation of this is shown in figure 5.B.13 for the 750mmØ cyclone. The variation of this in the 140mmØ cyclone was considerably greater than this, possibly due to an increase in the interference caused by the larger relative probe size.

An initial investigation was made by calculating the discrepancy between the model and the experimental data for a range of values of the parameters α and Γ_o. Contour plots were prepared of these and the values corresponding to the global minimum(s) were noted. The parameter values that correspond to the best fit of the $V_{\theta max}$ location and value were not at the global minimum of these contour plots, indicating that some closeness of fit was sacrificed in order to obtain the correct position of the $V_{\theta max}$. This would be largely due to the deviations from the ideal near the wall). The global minima from the contour plots for different axial

locations in the cyclone did not all overlap, which suggested that universal values of the parameters would not be possible. Since the wall radius varies along the cone, and the vortex centreline describes a helix, it was expected that a universal value for each of the parameters might not necessarily be the case. Thus a 'distributed parameters' approach was used, which allowed the parameters to vary between different axial locations, as well as between opposite sides. Each location was fitted independently to allow local differences to show up. These best fit values will now be compared with various methods of predicting the parameters.

Accounting for the variation of the parameters

Garg and Leibovich (1979) found, when modelling a trailing vortex flow with a version of the Burgers equation similar to equation 6.B1.1, that the position of the centreline had a major effect on the exponent parameter 'a' but not on the circulation parameter. Their least square curve fitting was optimised by allowing for small shifts in the centreline. The velocity profiles obtained in the cyclones in this study showed significant asymmetry of the vortex, particularly in the 140mmØ cyclone. The variation of the radial positions along the length of the 750mmØ cyclone is shown in Figure 5.B.13.

The effect of the variation in the position of the tangential velocity maximum caused by the off axis centreline was investigated by using the vortex centreline instead of the geometrical centreline to calculate the radius. The adjustment of the radius obviously improved the fit near the axis, but did not account for all of the differences.

6.B1.1 Explicit scaling of the radius by the local wall radius:

It was thought that the fit of the model to the data might be improved if the radius was scaled by the wall radius, in order to keep the outermost radius constant rather than reducing by 60% from the barrel to the dust exit. This would give a uniform value of $[1 - \exp(-\alpha.r^2)]$ at the wall and keep the same profile shape along the cyclone length. The effect of this is examined next to see if the combination of the apparent variation of 'α', and the actual variation of the R_W would cancel to give a uniform value of 'α'

The effect of this change can be examined without recalculating the flow models, as the parameter in the exponent can be converted from one form to the other.

The parameter 'α_θ' in equation 6.B1.4 has units of m^{-2}, when r is entered as the radius in metres. The parameter 'α' can be seen as implicitly including the scaling radius $(1/R_w^2)$ but this may result in larger values of 'α' being required in the lower cone. If r is explicitly scaled by R_W, the dimensionality and magnitude of 'α' would change. Hence, for ease of comparison, the dimensionless form of the exponent was taken as "$\alpha_2.R_B^2.\left(r/R_w\right)^2$", where R_B is the cyclone barrel radius and R_W is the local wall radius at the location being modelled. The parameter "α_2" again has units of m^{-2} and a similar magnitude to α. It can be seen that $\alpha = \alpha_2.\left(R_B^2/R_w^2\right)$ and thus the corresponding best fit value of α_2 can be easily obtained from α, the two being identical in the cyclone barrel region where $R_W = R_B$. Similarly for the Phillips

2-term equation that was given in equation 3.B.11:

$$\frac{a}{0.7\nu_T} = \frac{a_2.R_B^2}{0.7\nu_T.R_w^2}.$$

The model equations for the explicit scaling by Rw are given below:

Burgers 1 term form: $$V\theta = \frac{\Gamma_o}{r}\left(1 - e^{-\alpha.(R_B)^2.\left(\frac{r}{R_w}\right)^2}\right) \quad \text{--- (6.B1.5)}$$

Phillips 2 term form: $$V\theta = \frac{\Gamma_o}{r} \times \left(1 - \frac{1}{2}\left(\exp\left(\frac{-a.R_B^2.r^2}{0.7R_w^2.\nu_T}\right) + \exp\left(\frac{-a.R_B^2.r^2}{7.R_w^2.\nu_T}\right)\right)\right)$$
--- (6.B1.6)

The variation of the best fit parameters 'α' and 'α_2' found for equation 6.B1.4 by fitting the position of the maximum tangential velocity is shown below in Figures 6.B1.4 and 6.B1.4 for the 140mmØ and 750mmØ cyclones.

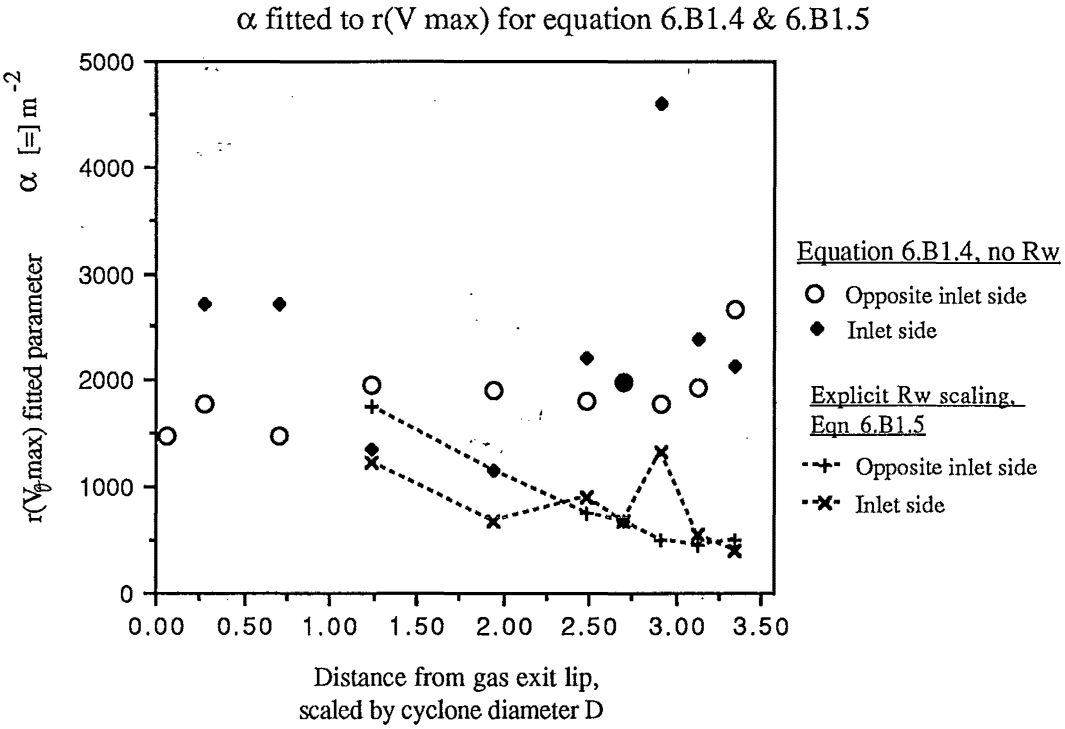

Figure 6.B1.1: The 1-term Burgers model parameter α for the 140mmØ cyclone

The following graph shows the values of the parameters 'α' and 'α_2' obtained when the 750mmØ profiles were modelled with the 1 term equation (Equation 6.B1.4) by fitting the position of the maximum tangential velocity.

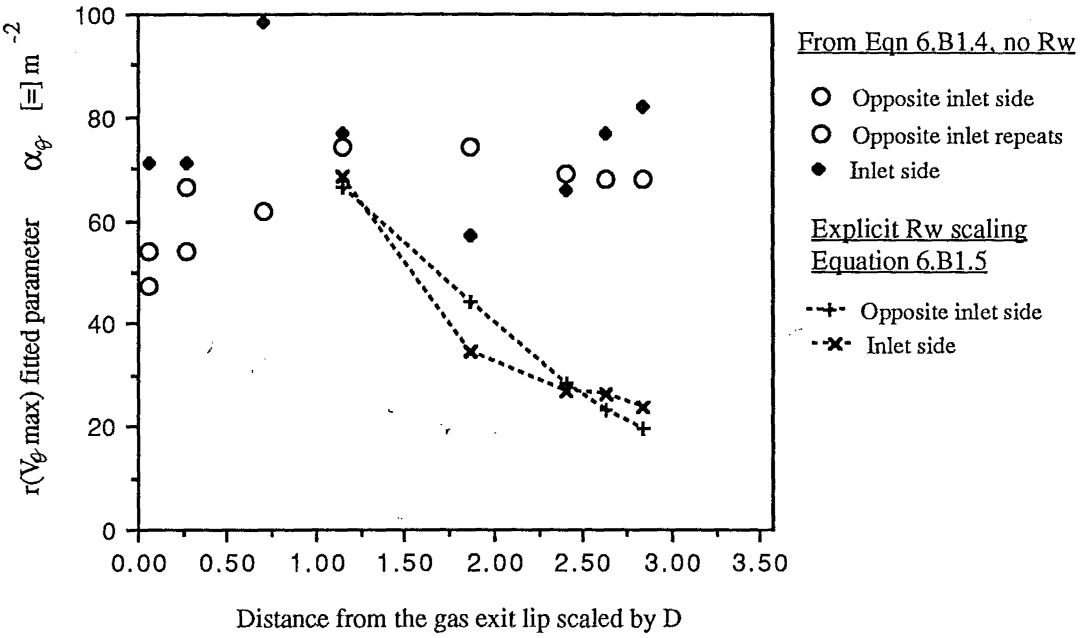

Figure 6.B1.2: The 1-term Burgers model parameter α for the 750mmØ cyclone

The results shown in figures 6.B1.1 and 6.B1.2 show that the variation of 'α' or 'a' along the length was increased by explicitly scaling r by the wall radius. Hence the original forms of the exponent parameters in the equations are preferred. This can also be deduced by observing that although $V_{\theta max}$ remains reasonably constant along the length, the value of the tangential velocity at the wall increases. This is consistent with a uniform profile being truncated at the wall rather than the profile being compressed to fit the changing distance between wall and axis.

The average magnitude of the exponential parameter α_θ in equation 6.B1.4 varies with the cyclone scale, from approximately 1950 m^{-2} in the 140mmØ cyclone, through 72 m^{-2} for the 750mmØ cyclone, to 20.4 m^{-2} for the 2090mmØ cyclone. Converting α to a dimensionless parameter by multiplying by the square of the barrel radius is equivalent to scaling the radius by the barrel radius.

$$\alpha_u = \alpha . R_B^2.$$

Average values of this 'universal' parameter α_u were 9.6, 10.1 and 11.1 for the 140mmØ, 750mmØ and 2090mmØ cyclones. This compares well with a survey of values mentioned by Abrahamson (1981).

6.B1.2 Relation of the α parameter to the core radius:

Another means of estimating the value of α is to compare the Burgers equation with the model used by Zhou & Soo (1990). They used the radius of the core of solid body rotation to scale the radius in the equation:

$$V_\theta = \frac{\Gamma}{r}\left(1 - e^{-\left(\frac{r}{R_c}\right)^2}\right) \qquad \text{--- (6.B1.7)}$$

with the radius of the core of solid body rotation, R_C, given by:

$$R_C = \left(\frac{4\, w_o\, \nu_{eff}}{1 - \left(\frac{\partial \bar{P}}{\partial z}\right)/Pa}\right)^{\frac{1}{2}} \qquad \text{--- (6.B1.8)}$$

As discussed in Chapter 3.B, dimensional considerations show that this equation must contain some typographical errors, and the correct form is thought likely to be:

$$R_c = \sqrt{\frac{4\, \rho_g\, w_o\, \nu_{eff}}{(\partial \bar{P})/\partial z}} \qquad \text{--- (6.B1.9)}$$

where the parameters are (with a value given for the standard 140mmØ Stairmand H.E. cyclone at 21m/s inlet velocity) :

w_o = the average axial velocity in the gas exit = $\frac{V_{in}\, A_{in}}{A_{exit}}$ (=10.7m/s)

$\nu_{eff} = \nu + \nu_T$ the effective viscosity

= kinematic viscosity + eddy viscosity, (= 0.003 m^2/s)

$\frac{\partial \bar{P}}{\partial z}$ = $\Delta p/L$, the pressure drop divided by the cyclone length.

L is taken as the distance between the dust exit and the roof of the cyclone, but it is not detailed where the pressure drop is measured between. For the Standard Stairmand cyclone at an inlet velocity of 21m/s, the pressure drop between the inlet and the gas exit wall just above the roof is 1400Pa. The length L is 568mm. The value of the core radius obtained is 7.9mm for the Stairmand cyclone. The value of the turbulent viscosity used was only 30% of the value used by Zhou and Soo (1990), who were studying a cyclone that was 300mm in diameter. Using their value of $\nu_T = 0.01 m^2/s$ a core radius of 14.4mm is obtained. Repeating the calculation for the 750mmØ cyclone yields an estimate of the core radius of only 35mm. If the dimensionless α_v parameter is taken as 10

$$10 = \alpha . R_B^2$$

This suggests that the radius of the core occurs at 32% of the barrel radius. This value is too close to the axis, and hence this approach is judged to be unsuitable.

Escudier and Zehnder (1982) defined two dimensionless groups necessary to define the onset of criticality in vortex flows. One group was reported to give an invariant measure of the core radius: $r_C = \sqrt{\frac{\nu . L}{w_e}}$ where L is the length of their tube geometry; w_e is the average axial velocity, and ν is the viscosity, presumably the turbulent viscosity in this case. Substituting values for the 140mmØ cyclone gives an estimate of 22.7mm for the core radius in the cyclone barrel, which is of similar magnitude to the values observed (circa 30mm)

The core radius can be approximated by the location of the zero axial velocity or the maximum tangential velocity. As shown in Figure 5.B.13, the former appears to decrease down the cyclone from 0.3 to 0.15, while the latter is approximately constant at 0.15m for the 750mmØ cyclone. These are equivalent to values of 'α' of 11 to 44 m^{-2} and 44 m^{-2} respectively. The values required to fit the experimental profiles are approximately 60 m^{-2}, hence of the two, the better estimate for the R_C parameter is the radius of the maximum tangential velocity.

6.B1.3 Fitting of model to core and wall properties:

The previous method of fitting the tangential velocity profiles ensured the model fitted the position and value of the tangential velocity maximum, and the other regions follow. Deviations at the wall and core may be allowed for by further adjustment of the modelled profile. An alternative method of fitting the profiles is detailed here using the same model equations.

The Burgers vortex model given by equation 6.B1.4 can be simplified by using the 3rd order Taylor series expansion for $e^{-\alpha r^2}$, which for small radius r is approximately $1 - \alpha r^2$. (The next term in the 5th order expansion is $(a^2.r^4/2)$. The characteristic rotation rate of the core, Ω_C, is the limit of V/r as the radius tends to zero. For the simple Burgers vortex given by equation 6.B1.4 and using the expansion above, this can be shown to be:

$$\Omega_C = \lim_{r \Rightarrow 0} \left(\frac{V}{r}\right) = \alpha.\Gamma_O = \frac{a.\Gamma_O}{2\nu_T} \qquad \text{--- (6.B1.10)}$$

This suggests that the parameter in the exponent of the simplified Burgers equation (equation 6.B1.4) can be estimated by $\alpha_c = \frac{\Omega}{\Gamma_O}$. This gives an estimate for α that is dependent on parameters that are characteristic of the core and wall regions respectively; rather than just the region of the maximum tangential velocity.

Γ_O was taken from the experimental values for the wall circulation, the values of which are graphed in Figures 5.J.1 and 5.J.2. The core rotation rate Ω_C was estimated from the slope with respect to radius of the experimental tangential velocity profiles near the axis. The tangential velocity profiles near the axis generally were a good fit to a straight line (r = 0.999). The values of the core rotation rate, Ω_C, obtained in the 140mmØ and 750mmØ cyclones are shown below in figures 6.B1.3 and 6.B1.4 respectively. Both show an approximately linear increase along the cyclone in the direction of the dust exit.

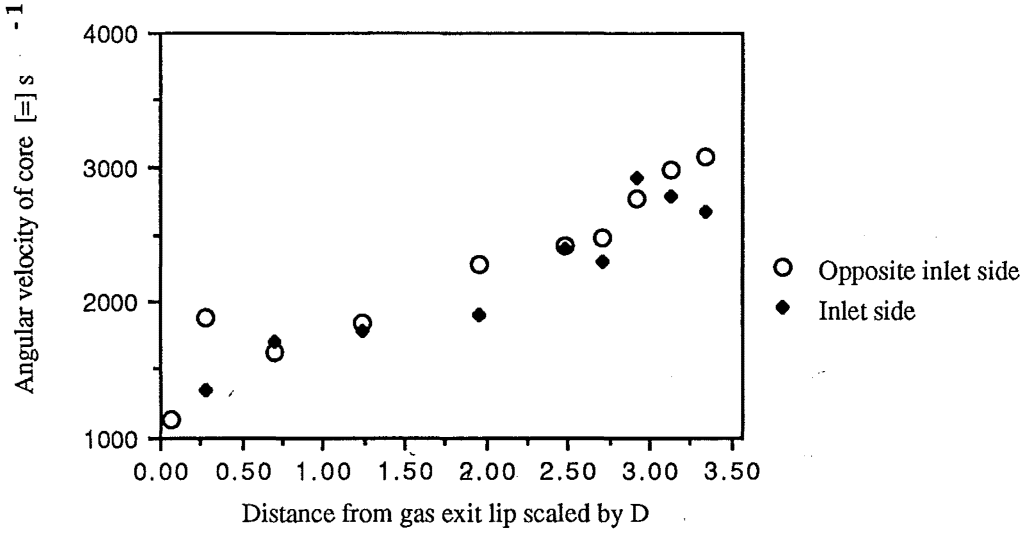

Figure 6.B1.3: Angular velocity in the core for the 140mmØ cyclone

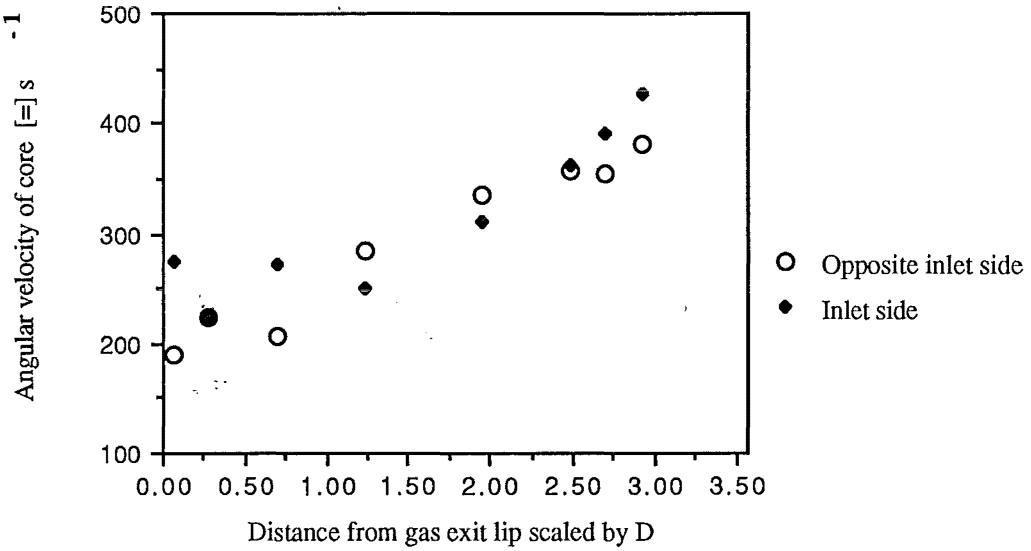

Figure 6.B1.4: Angular velocity in the core for the 750mmØ cyclone

The angular velocity near the axis shows an approximately linear variation with the cyclone length. Since the Γ_0 parameter decreases down the length of the cyclone, (from 2.0 to 1.0 m^2s^{-1} in the 140mmØ cyclone), while the Ω Parameter increases down the length (from 1000 to 3000s^{-1}) the value of 'α' fitted by Ω/Γ_0 will increase down the length from 500 to 3000 m^{-2}.

The full tangential velocity profiles were not replotted with the α_c parameter. Instead, a selection of velocity profiles is given in Section 6.B1.4 showing the variation between the profiles obtained with different parameters. To show how well the two estimates for the exponent parameter α agreed, the values fitted by each method are plotted in Figures 6.B1.5 and 6.B1.6:.

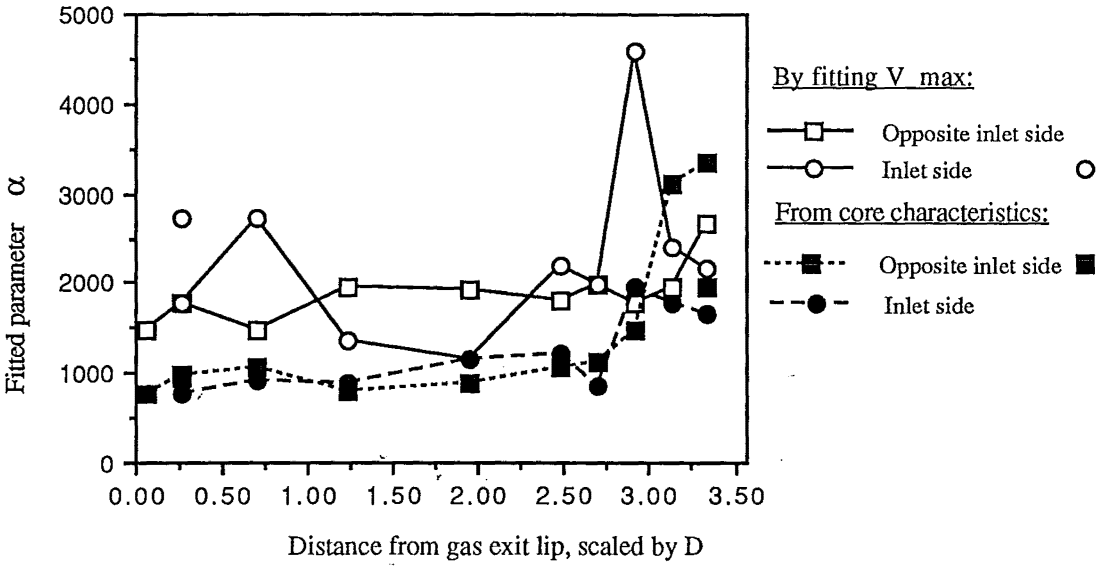

Figure 6.B1.5: Comparison of α_θ calculated from the $r(V_{\theta max})$ and Ω/Γ_o methods for 140mmØ cyclone

For the 750mmØ cyclone the data was less scattered, as shown in the graph below:.

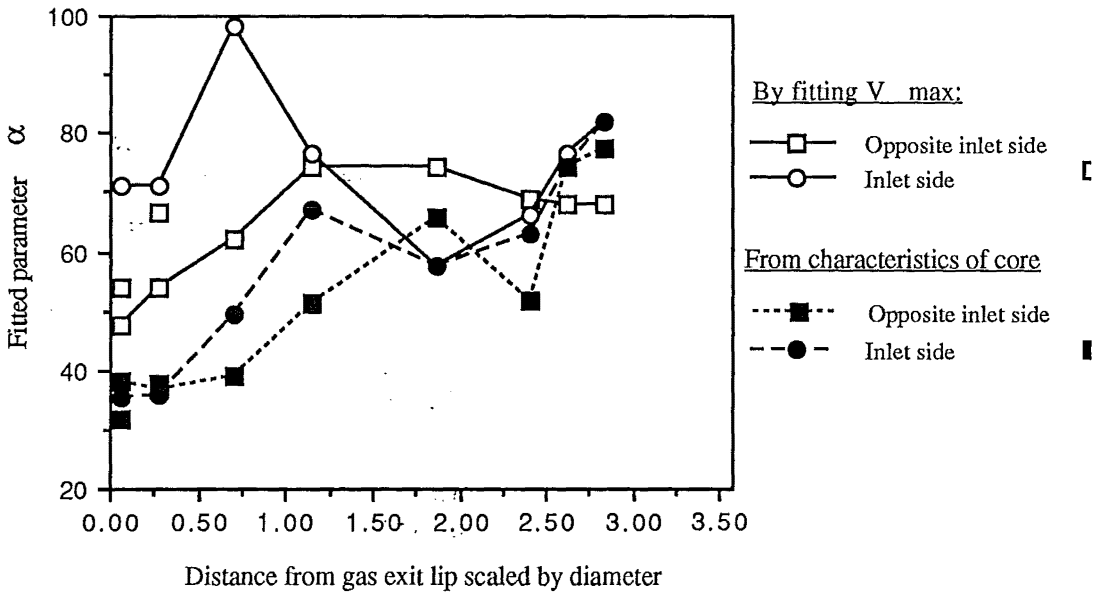

Figure 6.B1.6: Comparison of α_θ calculated from the $r(V_{\theta max})$ and Ω/Γ_o methods for 750mmØ cyclone

6.B1.4 Comparison of 2-term and 1-term equations:

The two term equation uses an average of two different exponential terms to provide a slightly different profile from the 1-term equation. The following graph shows the value of "1 minus the exponential", that is obtained for each variation of the form of the exponential term.

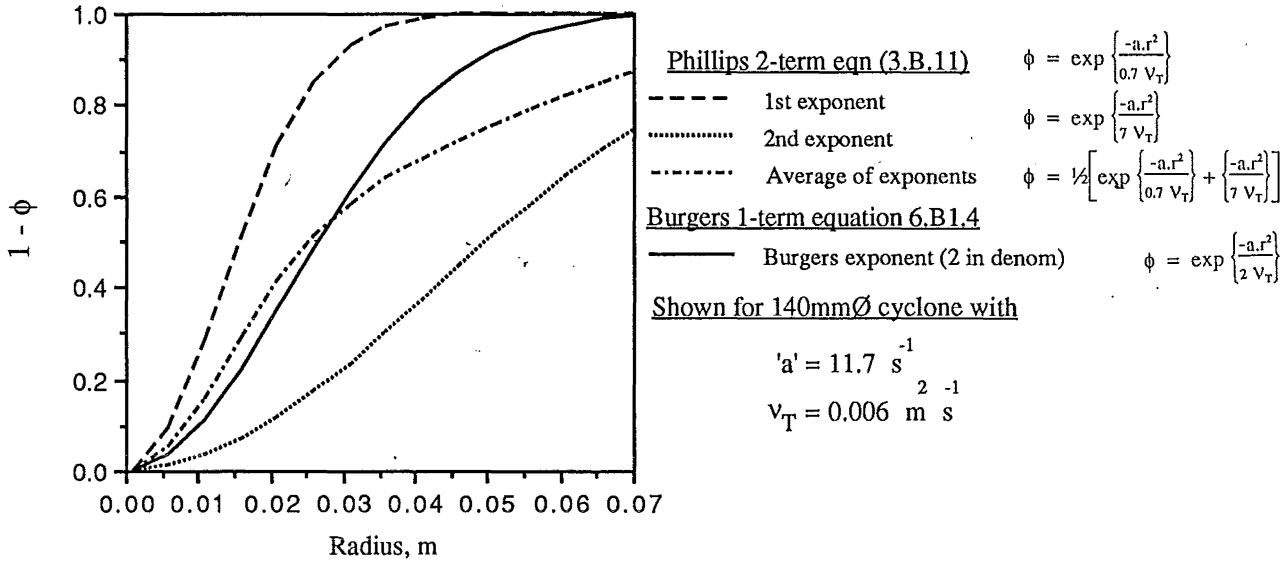

Figure 6.B1.7: Comparison of the exponential in the 1 & 2 term model equations

The $1 - \exp\frac{-a\,r^2}{(0.7*\nu)}$ and $1 - \exp\frac{-a\,r^2}{(7*\nu)}$ terms are extremes, and the average of them :

$1 - \frac{1}{2}\left[\exp\frac{-a\,r^2}{(0.7*\nu)} + \exp\frac{-a\,r^2}{(7*\nu)}\right]$ that is used in the Phillips 2-term equation (eqn 3.B.11) is somewhat less steep in the outer vortex region than the $1 - \exp\frac{-a\,r^2}{(2*\nu)}$ that is used in the 1-term Burgers equation. The effect of this will be to reduce the tangential velocity in the outer vortex, and increase it in the core compared with the 1-term model.

The model profiles that result from the two equations (the Burgers 1 term and the Phillips 2 term) can be compared in the graphs in Section 6.B1.8. Profiles for both equations are fitted by adjusting the turbulent viscosity to provide the best agreement with the position and value of the maximum tangential velocity. Profiles for uniform values of the parameters are also shown.

6.B1.5 Fitting ν_T to the cyclone Pressure drop

For the models that incorporate the turbulent viscosity as a parameter (equations 6.B1.1 and 3.B.11) the value of 'a' was predicted by equation 3.B.9, which is determined by the average radial inflow. An empirical expression based on the work of Ogawa (1987) could then be used to estimate the turbulent viscosity.

Ogawa's expression was developed to fit experimental pressure drops in cylindrical vortex chambers with reverse flow, assuming a Rankine vortex type flow existed. The original form of the expression (Ogawa, 1987) was:

$$\frac{\nu_T}{\nu} = 0.0068 \,.\, Re_C^{1.25} \qquad \text{--- (6.B1.11)}$$

The Reynolds number was defined as: $Re_C = \dfrac{Q_O}{L.\nu}$

where Q_O = the total volume flow
L = the cyclone height below the gas exit lip, m

The substitution of $Q_O = 0.1\ V_i D^2$; L = 3.55 D and a suitable relation between V_W and V_i results in the form of equation 6.B1.12, which was the form used by Phillips (1990).

$$\nu_T = \nu \times 0.0001841 \times \left(\frac{V_W D}{2\nu}\right)^{1.25} \qquad \text{--- (6.B1.12)}$$

This latter form suggests that a local Reynolds number could be used, to allow for the variation of the wall diameter in the cone, and the increase in the tangential velocity at the wall (V_W) that was found experimentally. However, the original equation was based on a universal Reynolds number, and the added complexity of a local Reynolds number did not improve the agreement between the model and experimental profiles, hence these changes were not warranted.

This empirical estimate was compared with the fitted value of ν_T that was needed to achieve the best fit to the position of the maximum tangential velocity. The empirical equation predicted a uniform value throughout the cyclone, and apart from some high values near the inlet/gas exit the fitted ν_T was roughly constant along the cyclone length. However the predicted value is well above the value of the viscosity needed in the 1 term model in the 750mmØ cyclone, as shown below. The 2 term Phillips model requires a higher value of viscosity than the 1 term model because of the differences mentioned in the previous section, but this is still below the value of the prediction. The values of the fitted viscosity from the one and two term models are shown for the 750mmØ cyclone in figure 6.B1.8 below.

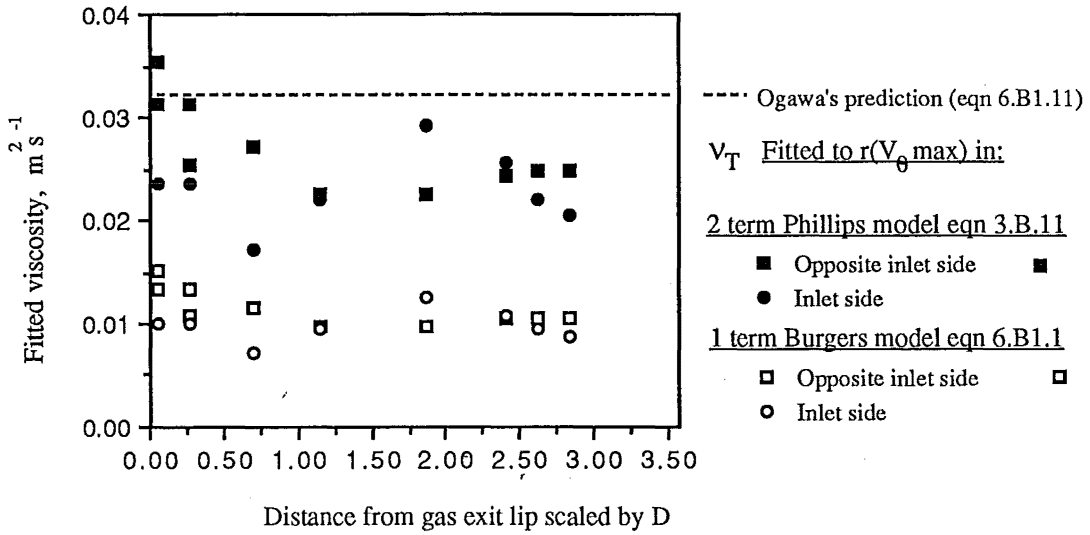

Figure 6.B1.8: Effective viscosity from fitting tangential velocity with 1 & 2 term equations in 750mmØ cyclone

This can be compared with the results from the 140mmØ cyclone:

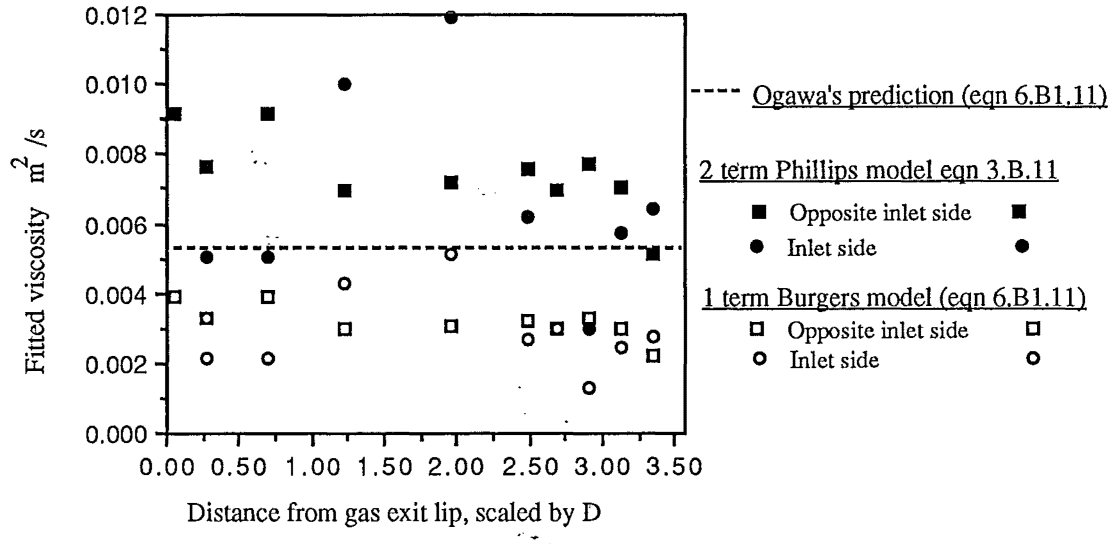

Figure 6.B1.9: Effective viscosity from fitting tangential velocity with 1 & 2 term equations in 140mmØ cyclone

The equation 6.B1.11 clearly overestimates the turbulent viscosity. Since the discrepancy becomes greater in the larger cyclone it seems that the exponent of 1.25 is too large.

6.B1.6 Fitting ν_T to the maximum tangential velocity

The empirical expression for the turbulent viscosity of Ogawa (1987) was based on fitting the pressure drop in reverse flow vortex chambers, and assumed that the flow could be described by a Rankine-type vortex. The estimates agreed reasonably with point measurements made by Ogawa in the core region, but values near the radius of maximum tangential velocity were three times the core values. A similar expression can be proposed based on the value of the turbulent viscosity needed to model the location of the maximum tangential velocity with the 1 term Burgers model (equation 6.B1.1).

Squire (1965) assumed that a vortex with a turbulent core had a turbulent viscosity proportional to Γ_o (the value of the circulation at large radius).

Hall (1966) reports the work of Owen (1964) who summarised attempts to fit the Burgers profile to turbulent swirling flow by assuming a constant value of turbulent viscosity.

Measurements on unconfined trailing vortex cores (for Reynolds numbers 2×10^{-3} to 10^{7}) were correlated with moderate success by:

$$\frac{\nu}{\nu_T} = \Lambda.\left(\frac{\Gamma_o}{\nu}\right)^{\frac{1}{2}} \qquad \text{where the Reynolds number} = \frac{\Gamma_o}{\nu}$$

The constant Λ ranged from 0.2 to 0.6 for the trailing vortices studied, but the results for the one leading edge vortex studied gave a value of 0.035. Abrahamson (1981) found that values of Λ an order of magnitude larger were required in order to fit estimates of the turbulent gas diffusivity in a gas cyclone. This suggests that the result should be applied to other types of vortex core with caution. Nevertheless, this correlation supports a dependence on the Reynolds number that is less than the 1.25 power found by Ogawa.

Retaining the same form for the Reynolds number as was used by Ogawa (1987), the turbulent viscosity can be correlated by:

$$\frac{\nu_T}{\nu} = C_1\,(Re)^n \qquad \text{--- (6.B1.13)}$$

where $Re = \frac{Q}{L\nu}$; for L = height of vortex chamber below gas exit lip, and 'C_1' and 'n' are fitting constants to be determined from results from the 140, 750 and 2090mmØ cyclones. Observing the fitted viscosity values in Figures 6.B1.8 and 6.B1.9, the best fit viscosity can be approximated over the length by values of 0.003 and 0.01 m^2s^{-1} for the 140 and 750mmØ cyclones respectively. In the 2090mmØ cyclone there was only one traverse (at Port 4) that reached as far as the maximum tangential velocity, enabling the fitted turbulent viscosity for this location to be found (and this is 0.0307 m^2s^{-1}). The data obtained was:

Diameter [m]	Volume flow [m^3s^{-1}]	Reynolds no. [-]	Fitted ν_T [m^2s^{-1}]
0.140	0.043	5612	0.003
0.750	1.02	24735	0.010
2.09	7.86	68549	0.0307

Taking the logarithm of both sides of equation 6.B1.13 results in :

$$\log\left(\frac{\nu_T}{\nu}\right) = \log C_1 + n \log Re \qquad \text{--- (6.B1.14)}$$

The fitted values from the three cyclones are plotted below:

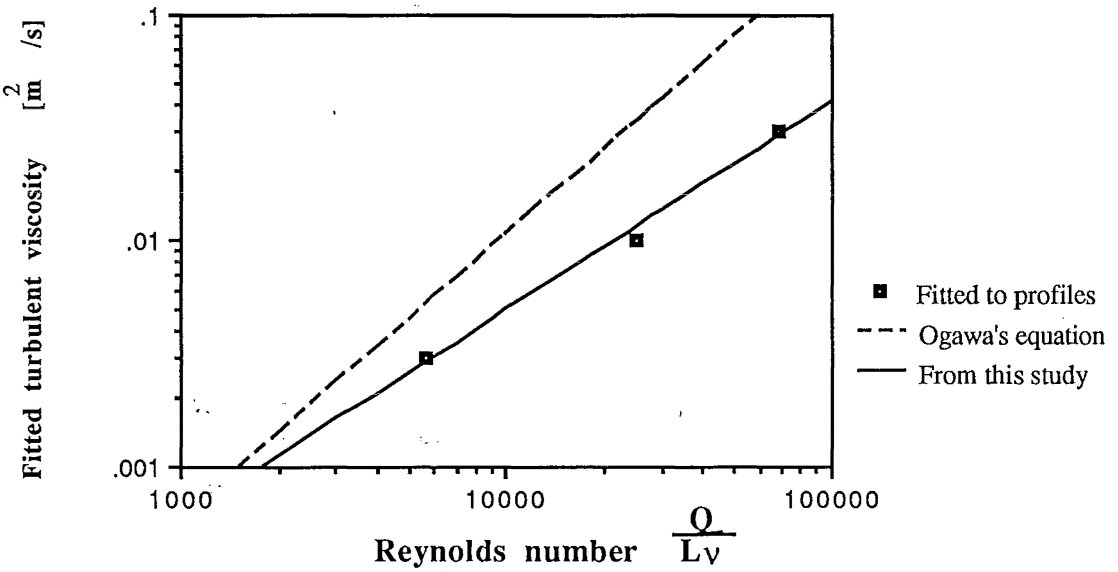

Figure 6.B1.10: Turbulent viscosity obtained by fitting the radius of the maximum tangential velocity to the Burgers model

Using the fitted turbulent viscosity ν_T and the known Reynolds number Re, this can be solved for n and C_1. Linear regression on the data from the three cyclones (r=0.996) yields the following values of the parameters: $n = 0.9206$ & $C_1 = 0.0645$

Thus the suggested form of the turbulent viscosity in the cyclone is :

$$\left(\frac{\nu_T}{\nu}\right) = 0.0645 \times (Re)^{0.921} \qquad \text{--- (6.B1.15)}$$

Apart from experimental error, the variation in the viscosity down the cyclone could also be due to the interaction of the near axis core movements, as a form of coherent structure. The Hot film anemometer was used to measure the average R.M.S. velocity fluctuation intensities at different levels in the cyclone. These seem to remain reasonably constant up the height of the cyclone for a given radius.

Garg and Leibovich (1979) found that 'α', as in equation 6.B1.4 increases approximately linearly with Re. Squire (1965) used an effective turbulent viscosity that was proportional to the wall circulation Γ_0. Uberoi states that this "allowed far too much angular momentum to escape to infinity" and gave other estimates for the turbulent viscosity.

In the Q-vortex model commonly used to examine vortex breakdown stability, $V_\theta = \frac{\Gamma_0}{r}(1 - e^{-\alpha r^2})$ it is reported (Leibovich, 1982) that Γ_0 and 'α' vary slowly with axial distance.and that the variation of the vortex centreline from the axis has little effect on Γ_0 but a large effect on the value of 'α'.

The prediction for the turbulent viscosity from equation 6.B1.15 can be used to obtain an expression for the parameter α_θ in terms of the geometrical parameters.

$$\alpha_\theta = \frac{a}{2\,\nu_T} = \frac{2\,Q\,.(L.\nu)^{0.921}}{\pi\,R_B^{\,2}\,L\,.0.0645\,\nu\,Q^{0.921}} = \frac{4.935}{R_B^{\,2}}\cdot\left(\frac{Q}{L\,\nu}\right)^{0.079} \quad \text{--- (6B1.16)}$$

This demonstrates the slight dependence on the Reynolds (to the 0.079th power) of the ($\alpha_\theta R_B^{\,2}$) parameter, as mentioned in section 3.B. For an inlet velocity of 22 m/s the value varies from 9.76 m^{-2} in the 140mmØ cyclone to 12.08 m^{-2} in the 2090mmØ cyclone.

6.B1.7 Fitting of the wall circulation:

The values of the wall circulation ($\Gamma_W = V_{\theta W}.R_W \approx \Gamma_0$) that were measured in the 750mmØ cyclone are presented along with the values needed to fit the 1 term Burgers equation and 2 term Phillips equation to the value of the maximum tangential velocity.

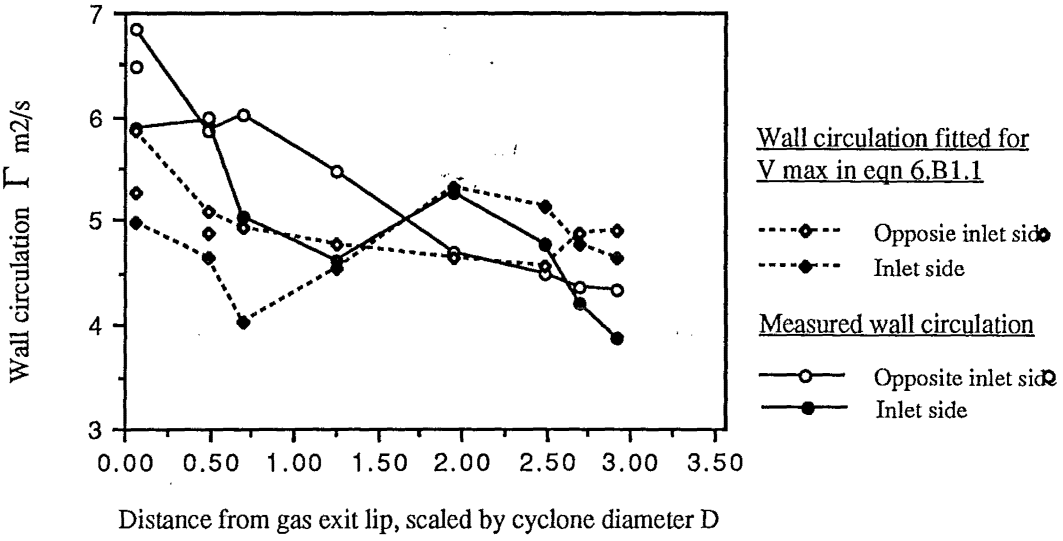

Figure 6.B1.11: The measured wall circulation in the 750mmØ cyclone compared with the value fitted with equation 6.B1.1

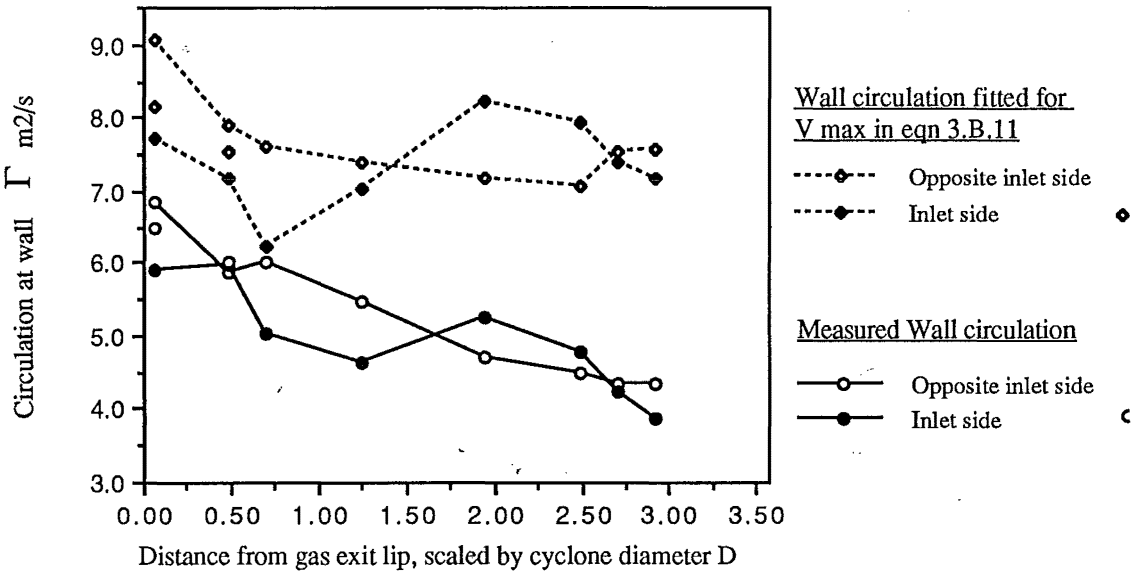

Figure 6.B1.12: The measured wall circulation in the 750mmØ cyclone compared with the value fitted with equation 3.B.11

It can be seen that the values required by the Phillips model equation are almost twice the value of the actual measurements. The 1 term equation results in values of similar magnitude to those measured. Because of the better agreement with the measured values, this section will examine only the modelling of the circulation parameter Γ_o used in the 1 term equation.

As detailed in Section 6.B1.1, applying the Burgers 1 term equation (equation 6.B1.1) to fit the position and location of the maximum tangential velocity results in a value of the circulation parameter that depends on the radius (r^*) and the value ($V_{\theta max}$) of the tangential velocity maximum:

$$\Gamma_o = 1.398 \times (r^* . V_{\theta max}) \qquad \text{--- (6.B1.17)}$$

In the previous section, it was shown that a universal value of the turbulent viscosity could be used to achieve an approximate fit to the location of the maximum throughout the cyclone. This value of ν_T thus determines the value of r^* that is used in equation 6.B1.17 above:

$$r^* = \sqrt{\frac{\nu_T}{0.398.a}} \qquad \text{--- (6.B1.18)}$$

Substituting the empirical expression for ν_T from equation 6.B1.15 and the expression for 'a' from equation 6.B1.2, results in the following expression for the circulation parameter:

$$\Gamma_o = 0.7054\, R_B . V_{\theta max} . \left(\frac{L.\nu}{Q}\right)^{0.0395} \qquad \text{--- (6.B1.19)}$$

The value of the maximum tangential velocity increases slightly along the length of the cyclone (about 3%), but can be taken as constant for this purpose. The empirical expression for the value of the maximum tangential velocity presented by Iozia and Leith (1990) can be simplified for the Stairmand H.E. geometry to:

$$V_{\theta max} = 1.654\, V_{in} \qquad \text{--- (6.B1.20)}$$

The values predicted by this agree well with the measurements made in the 140mmØ and 750mmØ cyclones. The inverse Reynolds number to the 0.0395 power has a value ranging

from 0.64 in the 2090mmØ cyclone to 0.71 in the 140mmØ cyclone, both for an inlet velocity of 22m/s.

Substitution of equation 6.B1.20 into 6.B1.19 along with the appropriate value of the $(Re)^{-0.0395}$ term gives an expression for predicting the circulation parameter for the 1 term Burgers equation.
For the 140mmØ cyclone at V_{in} = 22m/s:

$$\Gamma_o = 0.82956.\ V_{in}.\ R_B. \quad = \quad 1.228$$

With the approximations made (in particular that ν_T doesn't vary over the length), this is a constant value over the height of the cyclone, with a value of 5.24 m^2/s for the 750mmØ cyclone and 1.27 m^2/s for the 140mmØ cyclone. The fitted values in Figure 6.B1.1 were obtained without forcing the radius r^* to be constant over the height, hence these are best fit values. It can be seen that the value of 5.24 m^2/s for the 750mmØ cyclone represents a reasonable average for most of the cyclone.

The fitted parameter Γ_o may be viewed as the virtual circulation (at large radius), whereas the measured circulation is altered by the contracting wall. However a more generalised prediction for Γ_o would allow for the observed decay in the vortex strength down the cyclone, as proposed by Abrahamson (1993). The decay of the wall circulation in a number of different cyclone geometries has been measured, and fitted to the following relationship:

$$\Gamma_o^{\,2} = \Gamma_{oe}^{\,2}\left[1 - g.\frac{z}{R_B}\right] \qquad \text{--- (6.B1.21)}$$

Γ_{oe} is the initial wall circulation at the level of the gas exit lip and 'g ' is the fractional decrease in the circulation with distance, z from the gas exit lip. The results are presented in the table below.

Geometry:	Diameter	Length/ height	V_{in}	Γ_{oe}	g	g.D	g.L
	D, mm	L/R_B	m/s	m^2/s	m^{-1}	[-]	[-]
Stairmand	2090	7	18.8	631	0.108	0.227	0.793
Stairmand oi	750	7	18	39.2	0.252	0.189	0.662
Stairmand i	750	7	18	35.7	0.225	0.168	0.589
Stairmand oi	140	7	22	2.87	1.404	0.197	0.702
Stairmand i	140	7	22	2.52	1.527	0.214	0.764
Stairmand oi	140	7	8	0.4	1.64	0.230	0.805
Stairmand i	140	7	8	0.41	1.37	0.1912	0.685
'Long cone' oi	140	7	22	3.9	1.600	0.224	0.800
'Long cone' i	140	7	22	3.9	1.592	0.223	0.796
'Long cone+140'	140	9.11	22	3.55	1.295	0.181	0.829
'Short cone'	140	5.1	22	3.33	1.976	0.277	0.707
'Shortest'	140	6.0	22	2.3	1.704	0.239	0.721
'Longest'	140	8.5	22	3.19	1.244	0.174	0.746
'Extra long'	140	10.5	22	2.3	1.122	0.157	0.830
'Extended cone'	140	8.4	22	3.04	1.523	0.213	0.898
'Svarovsky B'	140	9.8	22	2.79	1.401	0.196	0.967

The results show good agreement over a range of barrel diameters (from 0.14 to 2.09 metres), inlet velocities (from 8 to 22m/s) and lengths (from $5R_B$ to $10.5R_B$) when the parameter 'g' is made dimensionless by multiplying by either the barrel diameter or the cyclone length (the distance between the gas exit lip and the dust exit). The results in the table are graphed below, showing the variation of the dimensionless numbers against the length in figure 6.B1.13 and against the diameter in figure 6.B1.14. The geometries are sketched in Appendix 10.A.4

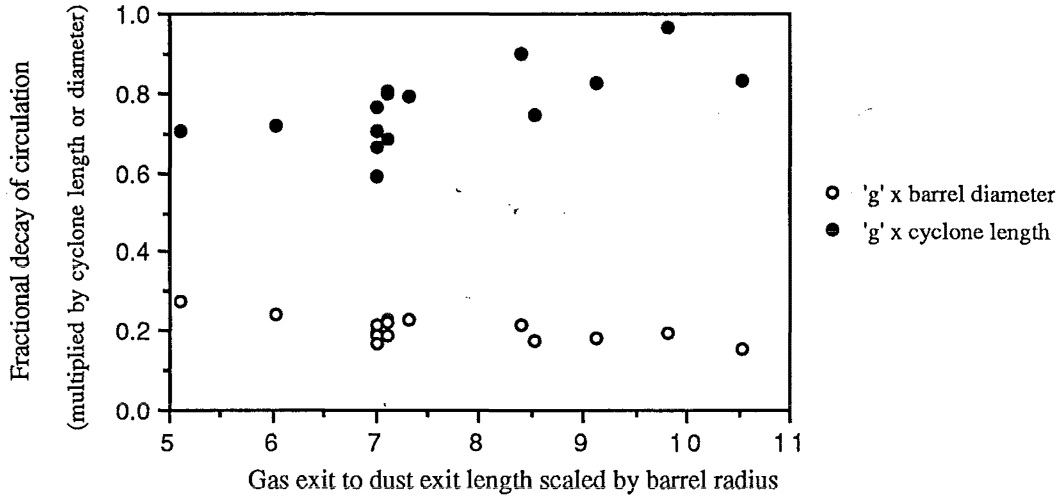

Figure 6.B1.13: Circulation decay parameter plotted against cyclone length

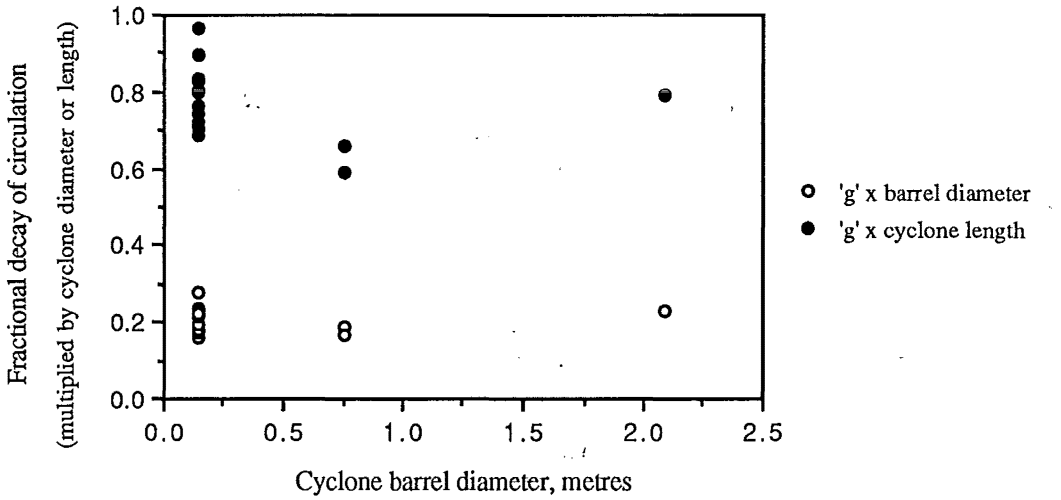

Figure 6.B1.14: Circulation decay parameter plotted against cyclone diameter

A value of gD = 0.2 appears to cover the range of values obtained for the Stairmand H.E. cyclone geometry. The values of the initial circulation Γ_{oe} were scaled by $V_{in}.R_B$ but this showed a wide variation: from 1.05 in the 140mmØ cyclone, to 0.90 in the 750mmØ cyclone to 1.28 in the 2090mmØ cyclone. The expression for the circulation could be generalised for the 140mmØ cyclone by using $\Gamma_{oe} \sim 0.83V_{in}.R_B$ and the value of gD = 0.2. The resulting expression is:

$$\Gamma_o^2 = (0.83V_{in}.R_B)^2 \left[1 - 0.1 \frac{z}{R_B}\right] \qquad \text{--- (6.B1.22)}$$

6.B1.8 Comparison of the models and parameter estimators

To illustrate how well the models for the tangential velocity compared with the experimental profiles, a selection of locations were plotted. The tangential velocity is presented against the radius scaled by the local wall radius for the following models:

1. The Burgers 1-term vortex model as given by equation 6.B1.4. The parameters α and Γ were selected by forcing a fit to the location and value of the maximum tangential velocity.
2. The Phillips 2-term version of the Burgers vortex model, as given in equation 3.B.11. The parameter 'a' was found from equation 6.B1.2, but the turbulent viscosity ν_T and the wall circulation Γ_0 were again found fitting the profile to the location and value of the maximum tangential velocity.
3. The 1-term Burgers equation, equation 6.B1.4, was used, but this time with the parameter 'α_θ' estimated by the ratio of the core rotation rate to the wall circulation: Ω/Γ_0. The values of these were determined from the experimental velocity profiles.
4. The 1-term Burgers vortex as given by equation 6.B1.1 was used, with 'a' and ν_T fitted by the equations 6.B1.2 and 6.B1.11, respectively. The latter is from the work of Ogawa (1987) and is an empirical correlation for ν_T based on fitting the pressure drop. The wall circulation was fitted again by forcing agreement between the model and the experimental profile at the maximum tangential velocity.
5. The 1-term Burgers equation was used again for the final plot, but with the turbulent viscosity ν_T was fitted by equation 6.B1.15, which was an empirical correlation for ν_T from this study based on fitting the location and value of the maximum tangential velocity.

The following comparisons can be made from the graphs:
(a) The 1 term Burgers, and 2 term Phillips equation versions of the models, (#1 & #2)
(b) The difference between fitting the 1 term Burgers model to the location of the tangential velocity maximum, and selecting the parameters on the core characteristic rotation rate, (#1 & #3)
(c) The comparison between profiles from the 1 term Burgers equation when the parameters are fitted to the maximum tangential velocity, as opposed to using empirical correlations for ν_T (#1, #4 & #5).

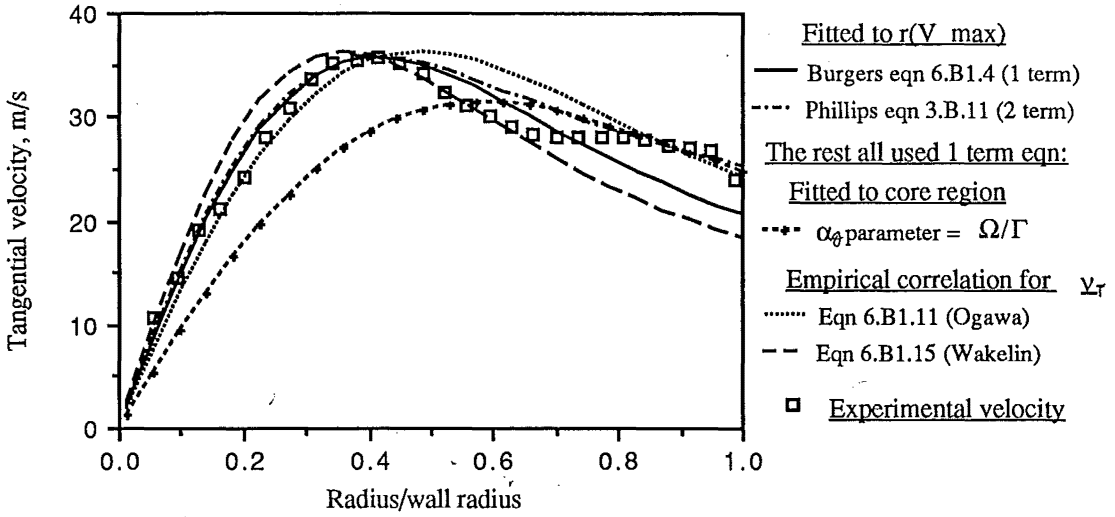

Figure 6.B1.15: Comparisons of tangential velocity from different models and parameters at Port 12oi in the 140mmØ cyclone

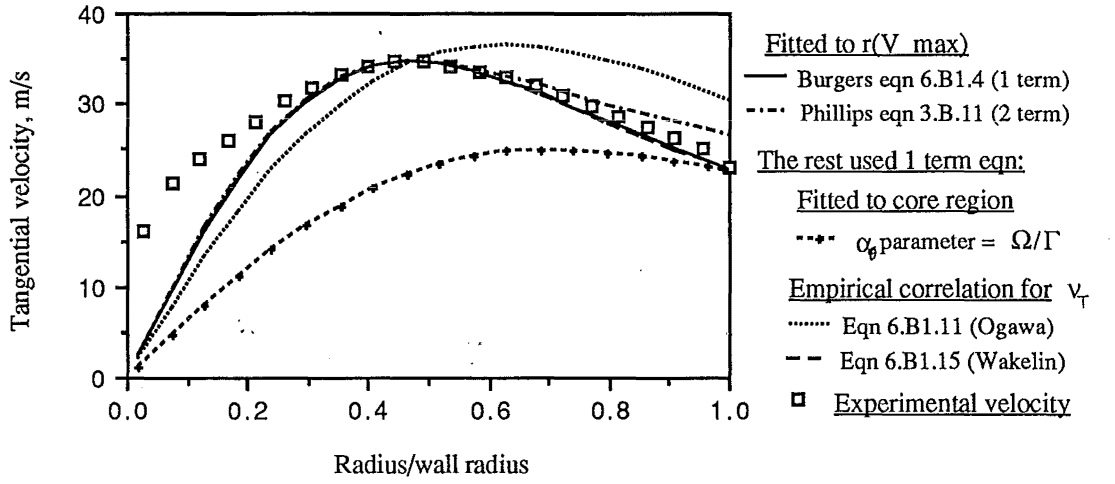

Figure 6.B1.16: Comparisons of tangential velocity from different models and parameters at Port 8oi in the 140mmØ cyclone

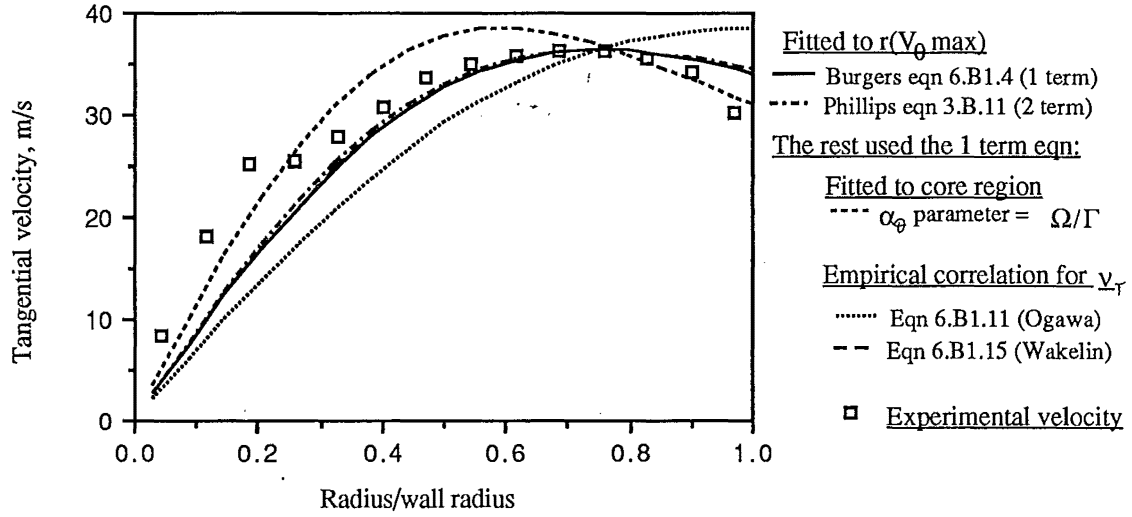

Figure 6.B1.17: Comparisons of tangential velocity from different models and parameters at Port 4oi in the 140mmØ cyclone

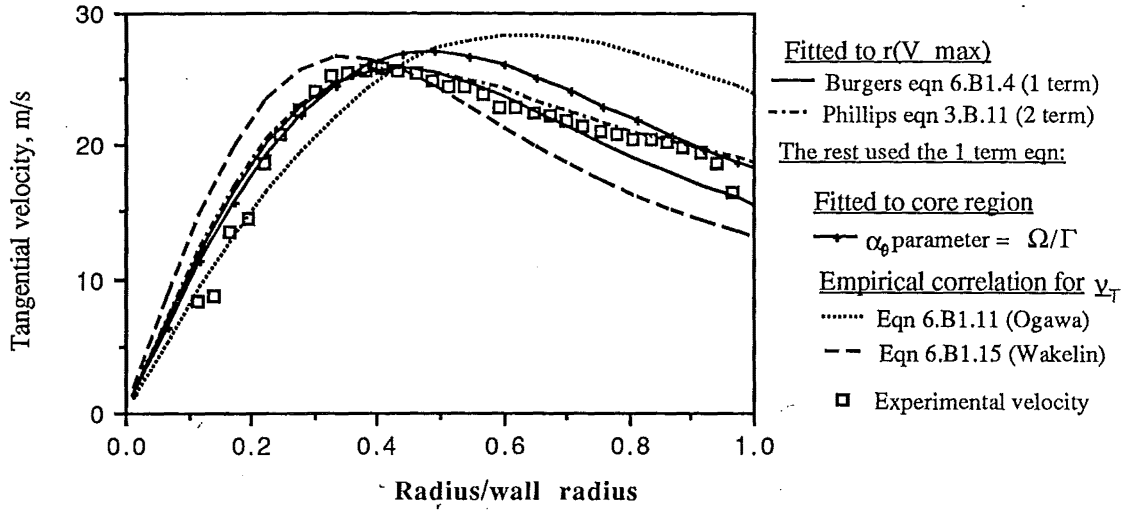

Figure 6.B1.18: Comparisons of tangential velocity from different models and parameters at Port 12oi in the 750mmØ cyclone

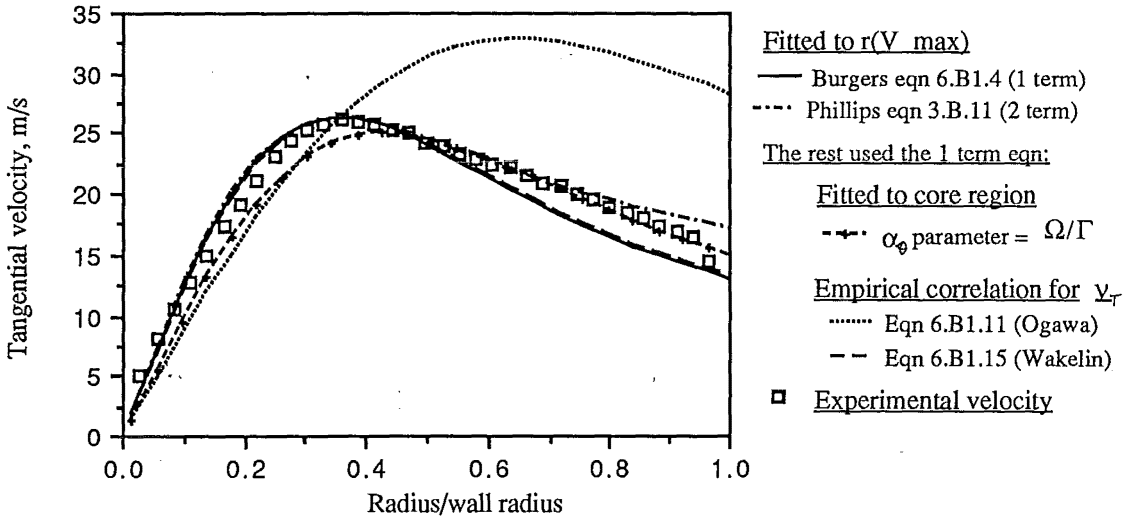

Figure 6.B1.19: Comparisons of tangential velocity from different models and parameters at Port 9oi in the 750mmØ cyclone

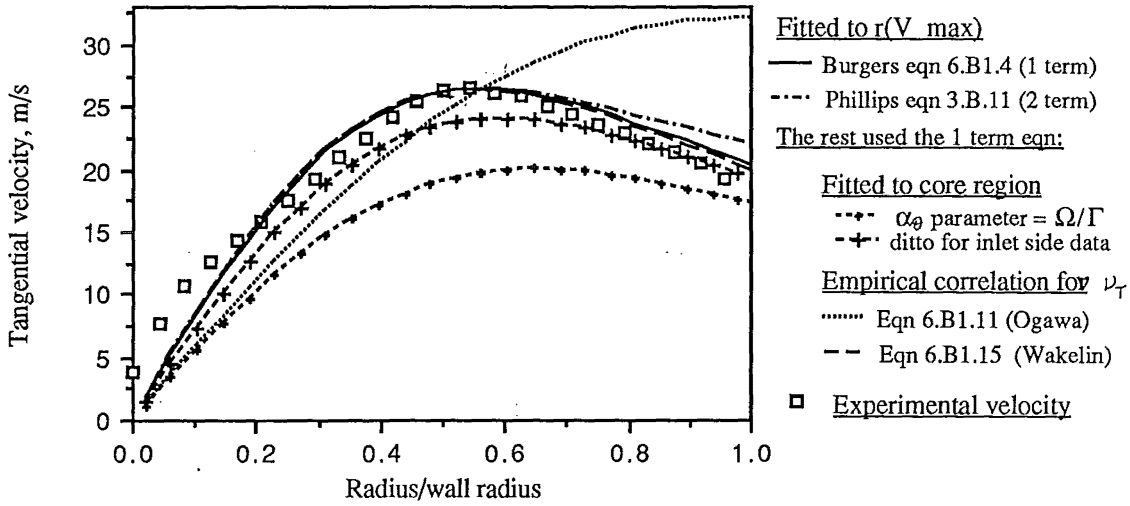

Figure 6.B1.20: Comparisons of tangential velocity from different models and parameters at Port 7oi in the 750mmØ cyclone

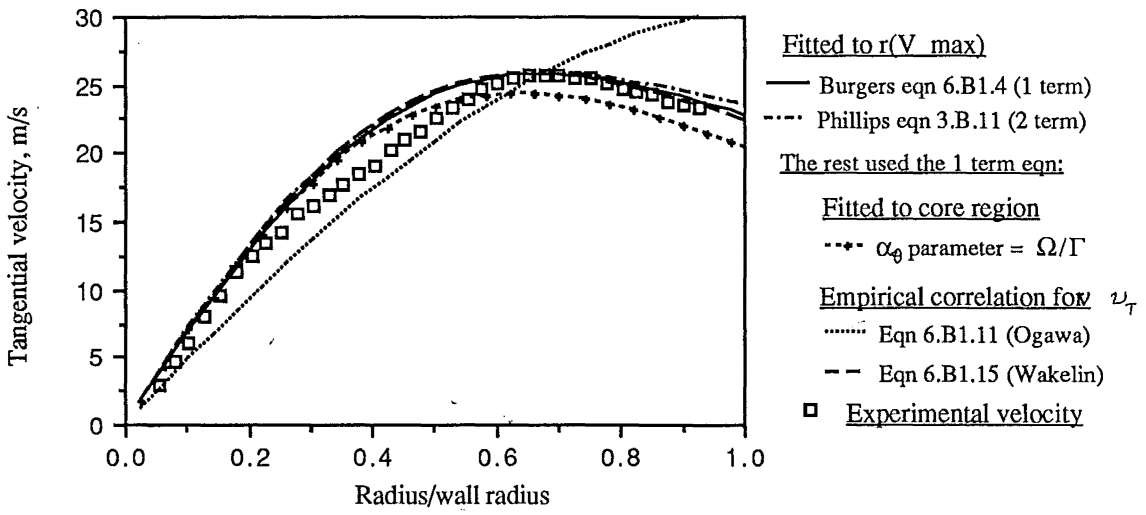

Figure 6.B1.21: Comparisons of tangential velocity from different models and parameters at Port 5oi in the 750mmØ cyclone

6.B1.9 Gas exit tangential velocity profile:

The modelling of the tangential velocity in the gas exit was able to successfully use the same correlation for the turbulent viscosity that was found for the main chamber. The experimental profiles measured in the gas exit were at an inlet velocity of 23.76 m/s , which yielded the following values of the parameters:

'a' = 12.15 s^{-1} ν_T = 0.003 m^2/s Γ_o = 1.36 m^2/s.

The agreement between the Burgers model and the experimental data obtained 1.6 exit diameters downstream from the gas exit lip is shown below:

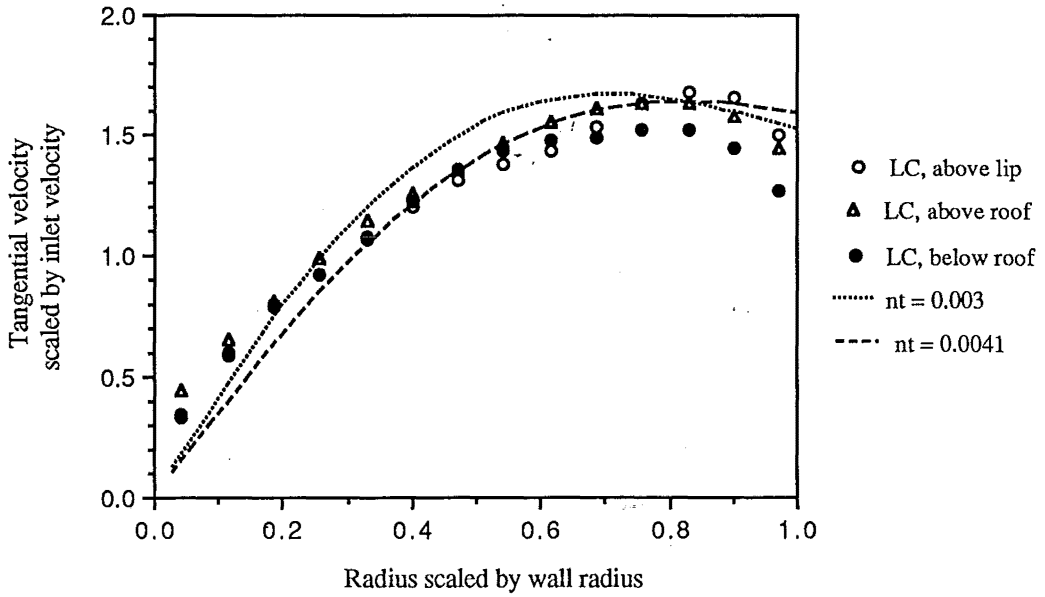

Figure 6.B1.22: Tangential velocity profile in gas exit above roof, with Burgers model

6.B1.10 Summary of tangential velocity modelling:

The modelling of the tangential velocity in the Stairmand H.E. cyclone can be summarised as follows:

The 1 term Burgers equation fits the profiles adequately in the body of the cyclone.

$$V_\theta = \frac{\Gamma_o}{r} \cdot \left[1 - \exp\left(\frac{-a\, r^2}{2.\nu_T}\right) \right] \qquad \text{--- (6.B1.1)}$$

The value of: $\alpha_\theta . R_B^2 = \frac{a}{2\nu_T} . R_B^2$

is approximately equal to 10 over a range of cyclone sizes from 0.14mØ to 2.09mØ.

The parameter 'a' can be better estimated from equation 4.C.4:

$$a = \frac{2Q}{\pi D_X^2 L} \qquad \text{[with units of } s^{-1}\text{]} \qquad \text{--- (6.B1.2)}$$

and the turbulent viscosity estimated from the correlation of equation 4.C.9, which is based on fitting the Burgers vortex to the position of the maximum tangential velocity profile:

$$\left(\frac{\nu_T}{\nu}\right) = 0.0645 \times (Re)^{0.921} \qquad \text{--- (6.B1.15)}$$

where the Reynolds number is based on the cyclone length between the gas exit lip and the dust exit:

$$Re = \frac{Q}{L\,\nu}$$

The equations for 'a' and ν_T can be combined to show the dependence that α_θ has on the cyclone scale. The resulting expression is:

$$\alpha_\theta = \frac{4.935}{R_B^2} \cdot \left(\frac{Q}{L\,\nu}\right)^{0.079} \qquad \text{--- (6.B1.23)}$$

The Reynolds number term varies only slightly with the cyclone scale: for an inlet velocity of 22m/s it varies from 2.45 for the 2090mmØ cyclone, to 1.98 for the 140mmØ cyclone. The corresponding values of the α_θ parameter for the Stairmand High efficiency cyclone at an inlet velocity of 22m/s are:

Barrel diameter:	140mmØ	750mmØ	2090mmØ
$\alpha_\theta . R_B^2$:	9.76	11.14	12.08

This agrees with the range of values of α reported earlier in section 3.B

The wall circulation parameter Γ_o can be taken as constant over the cyclone length for modelling purposes:

$$\Gamma_o = 1.398 \times (r^* . V_{\theta max}) \qquad \text{--- (6.B1.17)}$$

This can be simplified by using the results from equation 6.B1.2, 6.B1.15, 6.B1.18, and 6.B1.20 to give:

$$\Gamma_o = 1.167 \times V_{in} \times R_B \times \left(\frac{L\,\nu}{Q}\right)^{0.0395} \qquad \text{--- (6.B1.19)}$$

Equation 6.B1.1 gives a constant value for Γ_o along the cyclone length. To allow for the decay in the circulation the following expression may be more suitable:

$$\Gamma_o = \sqrt{\Gamma_{oe}^{\,2}\,(1 - 0.1.^{z}/R_B)} \qquad \text{--- (6.B1.21)}$$

The parameter Γ_{oe} is the value of the wall circulation at the level of the gas exit lip. This could be approximated by the value from equation 6.B1.19:

$$\Gamma_{oe} = \gamma\, V_{in}.R_B$$

where $\gamma = 1.167\left(\frac{L\,\nu}{Q}\right)^{0.0395} = 0.75$ to 0.83, for the range of cyclone sizes investigated in this study. The final form of the expression for Γ_o is:

$$\Gamma_o^{\,2} = (\gamma.V_{in}.R_B)^{2}[1 - 0.1.^{z}/R_B] \qquad \text{--- (6.B1.22)}$$

6.B2: Axial velocity modelling:

One experimental observation from this study that was particularly important in testing and developing theories was the discovery by flow visualisation of a third cell of the vortex flow, which is labelled the 'near-axis reverse flow' (or the narf). It consisted of a third vortex that travelled towards the bin, inside (and opposite to) the core vortex. This near-axis reverse flow extends the understanding of the structure of the vortex flow, and may also prove useful in interpreting other observations of the cyclone vortex.

The possibility of mean axial velocities along the axis that oppose the general flow direction in the core have been reported in various studies, such as ter Linden (1953), where a dimple occurs in the axial velocity profile near the axis. Barth (1956) made measurements of the axial velocity just within the exhaust lip. These showed that the gas exited the cyclone in an annulus around a stagnant or reversing core, which was also observed by Pervov (1975).

The visualisation studies of Smith (1962a) can be interpreted as support for the existence of a reverse central flow in cylindrical cyclones. Smith (1962a) injected smoke at the base of a cylindrical reverse flow cyclone that exhausted through its roof to the atmosphere. This smoke was observed to fill the cyclone, except for a zone near the axis which remained clear. Although Smith interpreted this as the separation of smoke by the cyclone it seems likely that the zone was caused by the influx of clean air through the gas exit along the axis. The clear zone was not present for large gas exit diameters at high (30°) swirl angles. The 750mmØ cyclone that was examined in this study showed that there was a strong downdraft at the exit, near the axis where the cyclone exhausted to the atmosphere. Particles that were released there were sucked into the cyclone body and some were found to be collected in the cyclone bin. Smith also showed a reduction in the axial velocity near the centre, and nearest the gas exit a downwards axial velocity was found on the axis.

Browne and Strauss (1978) measured velocity profiles in a Stairmand high throughput cyclone of 200mmØ barrel diameter. An axial reversal was present near the axis, but this was reported to represent only 0.7% of the throughput. The majority of the total throughput (95%) left the cyclone in the outer annulus at a radius greater than 50% of the wall radius. Browne and Strauss (1978) installed a deswirling device five diameters downstream that reduced the pressure drop by 22% with reportedly no effect on the velocity profiles. This consisted of vanes mounted on a centrebody, which would be expected to prevent a reverse flow from returning from far downstream in the exit. Other observations of reversal flow in vortices include those in tornado simulators (Pauley (1989), Church and Snow (1985, 1979)), and notably in hydrocyclones by Dabir and Petty (1986), Hsieh and Rajamani (1991) and Ohtake et al (1987).

6.B2.1 The Bloor & Ingham (1987) axial velocity model

A flaw in the Bloor and Ingham (1987) model (equation 3.B.46) is obvious from Figures 5.D.1-3 - the axial velocity tends to infinity as the axis is approached. This theory was developed for hydrocyclones, which also feature a conically confined vortex, with a reversal

flow, hence it was expected to apply well to the cyclone profiles. Bloor and Ingham attribute the high velocities near the axis to neglecting the air core (that is present in hydrocyclones). Davidson (1988) suggests that the viscosity cannot be neglected in the regions near the wall or axis, and this is the cause of the unrealistic velocities. The inclusion of the air core in the analysis would result in a formulation of the problem in which no simple analytical solution is possible and a full numerical solution would be required. The gas cyclone does not have the problem of an air core, and as the theory is inviscid the same velocities are predicted.
If these explanations are accepted, the high velocities in the near axis region can be ignored. To check this, the mass balance between the outer and inner vortices was calculated by numerically solving (on a HP48SX) the following integral:

$$\int_{r_{ax}}^{r_{zav}} W.2\pi r.\,dr + \int_{r_{zav}}^{R_w} W.2\pi r.dr \qquad \text{for } r_{ax} \to 0 \qquad \text{--- (6.B2.1)}$$

where W is the axial velocity predicted by the Bloor and Ingham model. Since W changes sign at r_{zav} the answer to this should be zero.
Support for the existence of very high axial velocities near the axis comes from the studies of Knowles et al (1973) and Dabir and Petty (1986), but the velocity in the cyclone did not appear to reach these values. It was found that the high velocities near the axis are necessary in order to satisfy the mass balance that is assumed. Typically the contribution to Q was negligible only for $r_{ax}/R_w \approx 0.001/0.07$, whereas the region of unrealistic velocities (those over 10m/s) extended to 10 to 40% of the wall radius, being greater near the gas exit lip. The contribution to the axial volume flow of the core by the region of 'unrealistic' velocities (taken as W > 10m/s) varied from 14% near the dust exit, to over 50% near the gas exit. At the gas exit, the axial velocity in the core reached 10m/s at a radius of 0.45Rw.

This illustrates that the high velocities can not be dismissed as an artefact of the assumptions, but are a consequence of the functional form of the equation. To reduce these values and still satisfy the mass balance requires the position of the zero axial velocity boundary to be moved closer to the wall. This would improve the agreement with the position indicated by the Pitot cylinder in the 750mmØ cyclone. The results from the larger cyclone are expected to be more reliable than those obtained in the 140mmØ. In the model the boundary between the vortices (where the axial velocity is zero) occurs at a constant fraction of the wall radius over the cyclone length: rzav/Rw ~ 0.609. This is determined by the functional form of the equation and cannot be adjusted.

6.B2.2 The position of the zero axial velocity boundary

The position of the zero axial velocity boundary is crucial for the mass balance requirements. The zero axial velocity boundary is usually approximated by a cylindrical surface, whereas it was found by experiment to be asymmetric and approximately conical. In the upper barrel it can be larger than the gas exit diameter.

Bloor and Ingham (1987) compared the axial velocity predictions of their model with the experimental results of Kelsall (1952) and Knowles et al (1973). Kelsall (1952) measured velocity profiles in a 76mmØ hydrocyclone operating with an air core by observing the tracks of particle tracers in the flow. The inlet velocities were varied from 2.3 to 5m/s and three geometries were examined:

- Series I with a dust exit diameter one quarter of the gas exit diameter and the zero axial velocity boundary at 55-63% of the wall radius;
- Series II with the dust exit four times the gas exit diameter and the boundary at 50-56% of the wall radius; and
- Series III with the two diameters equal, for which the position was 50-59% of the wall radius.

The mass balance between the axial flows in the outer and inner vortices was reported by Kelsall (1952) to agree to within 5% for the Series I cyclone, for which the underflow was zero.

Knowles et al (1973) also studied a 76mmØ hydrocyclone, but operated it without an aircore. Measurements were made using a cine camera and tracers, at an inlet velocity of 1.3m/s. The consistency of the axial velocity profiles was checked by carrying out a mass balance. The zero axial velocity boundary was found to vary between 53 and 66% of the wall radius. A comparison between the Bloor and Ingham axial velocity model and the data of Knowles et al (1973) is shown in figure 6.B2.1 for two different axial levels in the hydrocyclone:

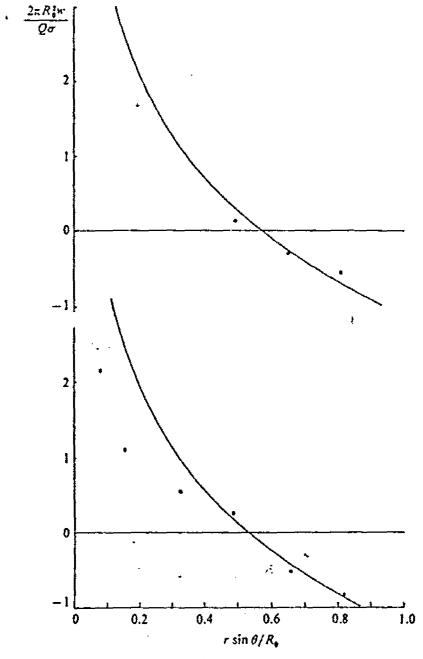

Figure 6.B2.1: Bloor & Ingham's axial velocity prediction compared with the data of Knowles et al (1973), from Bloor & Ingham (1987).

More recently, use has been made of the Laser Doppler Anemometer to measure the axial velocity in hydrocyclones. Dabir and Petty (1986) used the same geometry and flow conditions as Knowles et al (1973)and similarly found agreement of the axial flow mass balance to within 5%, with the position of the position of the crossover at 60% of the wall radius. The axial profile was complicated by the presence of an annular reversal flow (towards the dust exit) in the region between 6 and 14% of the wall radius. Inside this there were very high axial velocities recorded, of about 3.2m/s, compared with the inlet velocity of 1.3m/s. Another Laser Doppler anemometer flowfield survey was made by Fanglu & Wenzhen (1987) in a

hydrocyclone operating with an air core. For an inlet velocity of 3.9m/s the zero axial velocity boundary was found to be between 60 and 71% of the wall radius.

The most thorough presentation of velocity profiles in a hydrocyclone were presented by Hsieh & Rajamani (1991). The axial velocity profiles from Laser Doppler anemometer measurements and numerical simulations are shown below in figure 6.B2.2. The position of the experimental axial velocity crossover varies from 56% to 70% of the local wall radius.

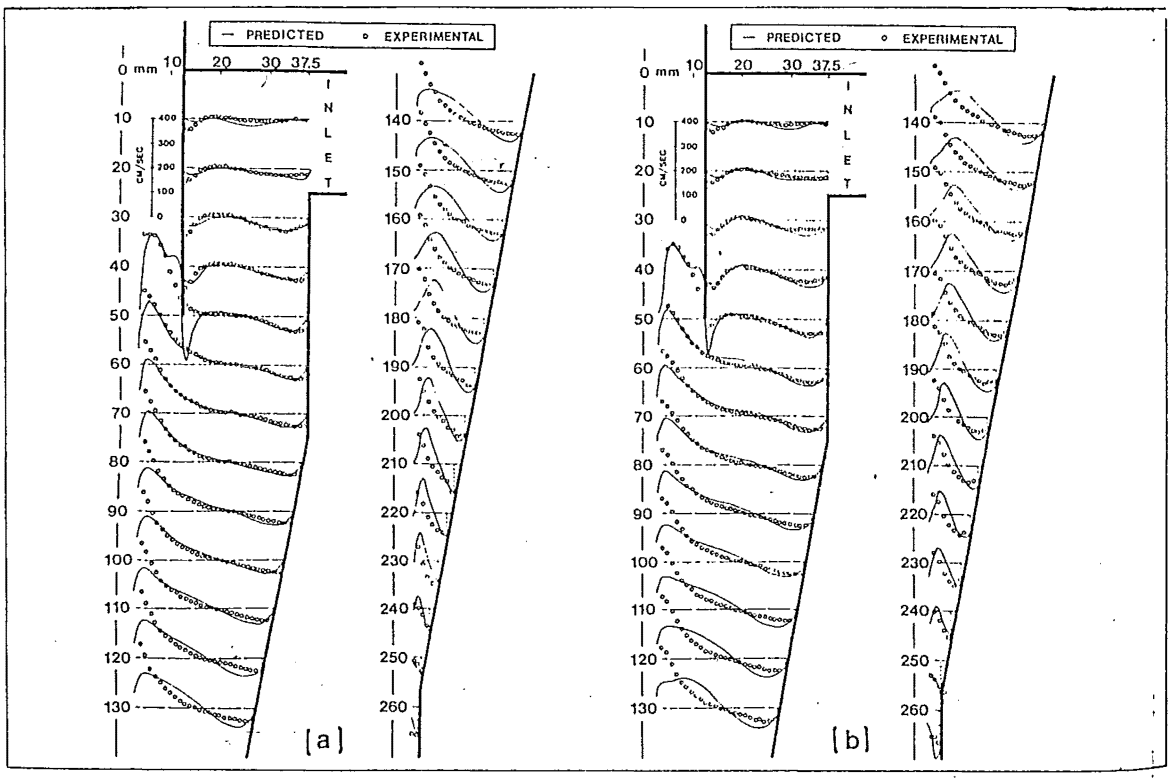

Figure 6.B2.2: Measured (LDA) and predicted (numerically) axial velocity profiles for a hydrocyclone running with (a) water; (b) Glycerol/water mixture

In cyclones operating with air as the fluid the reported values of the axial velocity crossover appear to be closer to the wall than in the hydrocyclone. Smith (1962a) measured velocity profiles in a cylindrical 143mmØ cyclone operating with air at an inlet velocity of 22m/s. The inlet height was varied from 12mm to 50mm. The zero axial velocity boundary was approximately constant over the cyclone height, and was 69% of the wall radius for the 50mm inlet, and 72% of the wall radius for the 12mm inlet. Ogawa (1984) also examined a 140mmØ cylindrical return flow cyclone, and found that the zero axial velocity boundary occurred at 67% of the wall radius.

Zhou and Soo (1990) made measurements of the velocity components in a 150mmØ cyclone using a Laser Doppler anemometer. This was compared with the polynomial analytical expression mentioned in section 3.B (equation 3.B.50), and the results of numerical modelling using the SIMPLE algorithm. The estimates of the axial velocity crossover location obtained from the three methods were reported to agree well, and appear to give the position as 57% of the wall radius in the barrel, and 60–66% of the radius in the cone.

The numerical calculation of the cyclone flow made by Yoshida et al (1991) showed asymmetries, which included radially outwards flow at some circumferential angles just below the gas exit lip. The position of the axial velocity crossover under turbulent flow conditions appeared to be further from the wall than the corresponding predictions for laminar conditions. The position of the zero axial velocity boundary estimated from the graphs of Yoshida et al (1991) for turbulent flow conditions at various azimuthal angles θ were:
θ = 3.8°: 60 to 66% Rw; θ = 67.5°: 50 to 70% Rw; θ = 183.8°: 68 to 79% Rw;
θ = 273.7°: 63 to 75% Rw

Based on measurements of 11 different geometries, Iozia and Leith (1989a) presented an empirical expression to predict the 'core diameter', but this appears to relate to the radius of the maximum tangential velocity, rather than the zero axial velocity boundary. The core diameter depended on the inlet area, as shown:.

$$d_c = 0.52D \left(\frac{a\ b}{D^2}\right)^{-0.25} \left(\frac{D_e}{D}\right)^{1.53} \qquad \text{--- (6.B2.2)}$$

where a, b are the dimensions of the inlet; D is the barrel diameter; and D_e is the exit diameter.

For the 140mmØ Stairmand high efficiency cyclone geometry this predicts a value of 22.4mm for the core radius, or 32% of the barrel radius, which is considerably less that the observed position. Many models equate the core radius to the radius of the zero axial velocity and assume that this is the same as the radius of the maximum tangential velocity.

The axial profiles presented by ter Linden (1953) for a cyclone with a scroll inlet show axial velocity crossovers varying down the length of the cyclone:

Barrel region: 66 -74% of the wall radius; Upper cone: 75% Rw;
Mid cone: 60%Rw; Near dust exit: 50%Rw

The results obtained from the 750mmØ cyclone suggest that the position of the zero axial velocity boundary is at least 70% of the wall radius, as shown in figure 5.B.13. The 140mmØ cyclone indicates a smaller diameter, but the scatter is greater, and the data from the 750mmØ cyclone is expected to be of better quality because of the reduction in the extent of the interference from the probe. Visualisation of the position of the axial flow crossover using the cotton streamers was difficult, and the photograph in figure 5.A.6 can indicate only that it occurs between 47 and 77% of the wall radius. It was decided to use the results obtained with the Pitot cylinder in the 750mmØ cyclone as the best estimate of the axial velocity crossover position for the reverse-flow air cyclone.

6.B2.3: The polynomial model of Tran (1981)

To obtain a model of the axial velocity that incorporates the desired position of the crossover a quartic polynomial was fitted, following the approach used by Tran (1981), which was described in section 3.B (equation 3.B.49). It was applied to the cyclone vortex using different boundary conditions, including one that specified the position of the crossover. In addition, Tran only applied the profile to the region just below the gas exit lip, whereas in this case it is desired to apply it throughout the cyclone. Boundary conditions were therefore added that

specified the volume flow that remained at any given axial location, and the position of the axial velocity crossover.

The variation of the axial flow remaining at any level in the cyclone is assumed to vary linearly between the value at the gas exit lip ($Q = Qin = 0.4.R_B^2.Vin$) and the value at the dust exit, which is assumed to be 10% of the inlet flow. This is approximate, since it is not known how much of the 0.1Qin that enters the bin is contributed by the boundary layer flow. However, this is not expected to affect the resulting profiles greatly. Assuming that the wall radius varies linearly from the gas exit to the dust exit is equivalent to the "Long cone" geometry, for which velocity profiles have been measured in the 140mmØ cyclone. The linear function for the variation of the flow along the cyclone is:

$$Q = A.Rw + B \qquad Qin = A.RB + B$$

$$0.1\,Qin = A.\left(\frac{26.5}{70}.\,RB\right) + B$$

The resulting equation is: $$Q_z = Qin.\left[1.4483\,\frac{Rw}{RB} - 0.4483\right] \qquad \text{--- (6.B2.3)}$$

The boundary conditions used were:

(1) $$\left(\frac{dW}{dr}\right)_{r=0} = 0 \qquad \text{--- (6.B2.4)}$$

(2) $$\left(\frac{dW}{dr}\right)_{r=Rw} = 0 \qquad \text{--- (6.B2.5)}$$

(3) The axial velocity crossover is to occur at a specified r/Rw = 0.70, (or 0.75)
--- (6.B2.6)

(4) The total axial flow between the axis and the wall is zero, that is the total axial outer and inner vortices at any level in the cyclone has the same magnitude but opposite sense.

$$\int_0^{r_{zav}} 2\,\pi r\,W.dr = -\int_{r_{zav}}^{R_w} 2\,\pi r\,W.dr \qquad \text{--- (6.B2.7)}$$

(5) The axial flow in the outer vortex (and hence the inner) is equal to the axial flow as given by equation 6.B2.3

$$\left|\int_0^{r_{zav}} 2\,\pi r\,W.dr\right| = \left|\int_{r_{zav}}^{R_w} 2\,\pi r\,W.dr\right| = Q_z \qquad \text{--- (6.B2.8)}$$

The parameters are then specified as:

$$a = 17.8724.\frac{RB}{Rw} - 5.5319.\left(\frac{RB}{Rw}\right)^2$$

b = -1.9746 c = 0.96195
d = 0 e = -0.024456

The shape of the resulting profile is shown below firstly for the axial velocity crossover specified at rzav/Rw = 0.7, and then at 0.75. The different curves correspond to different axial levels in the cyclone, with the indicated ratio of wall radius to barrel radius:

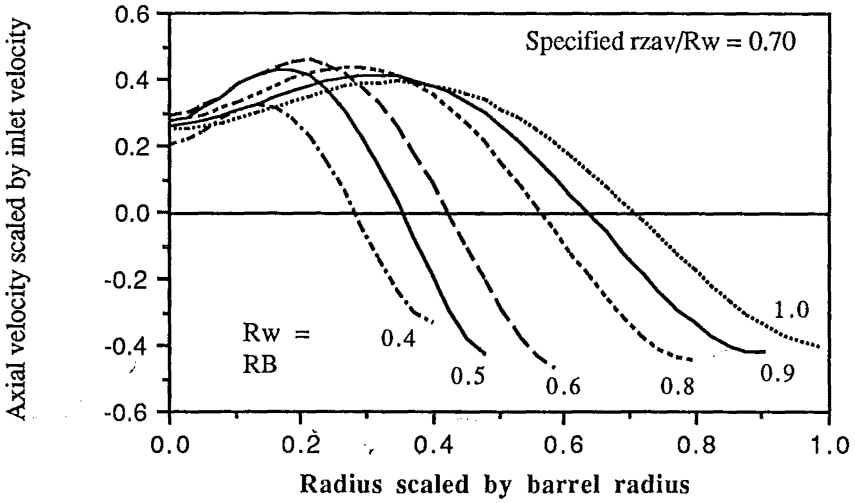

Figure 6.B2.3: Axial velocity profile from polynomial model, (rzav/Rw = 0.70).

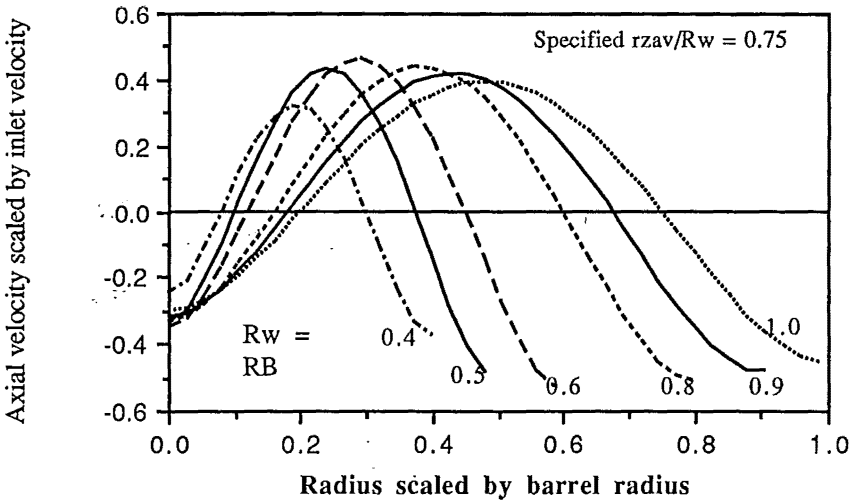

Figure 6.B2.4: Axial velocity profile from polynomial model, (rzav/Rw = 0.75).

Interestingly, the specification of the crossover radius at $r_{zav}/R_w = 0.75$ results in a reversal of the core flow near the axis. The drawbacks of the polynomial are the difficulty of manipulating the model because of the cumbersome form of the equation. Also it is in effect an empirical fit, not based on the equations of motion and need not represent the actual velocity. Instead the trailing vortex axial velocity model proposed by Batchelor (1964) (equation 3.B.25) will be investigated. This takes the form of an exponential profile, and the theoretical basis for it was outlined in section 3.B.

6.B2.4: Batchelor's (1964) model for the axial velocity

The general exponential axial velocity profile was originally developed to describe unconfined trailing vortices, but it has been applied successfully to confined vortices by Faler and Leibovich (1977), Garg and Leibovich (1979) and Lopez (1988). In particular, Garg and Leibovich (1979) found that it gave good agreement to the profiles obtained at high Reynolds numbers (c. 10^4) both upstream and downstream of a vortex breakdown. The following section will examine how the parameters can be selected to fit the model to the experimental profiles.

Different forms of Batchelor's (1964) model have been used by various researchers, based on the simplification proposed by Lessen et al (1974). The form that will be used here for the axial velocity is:

$$W = W_\infty\left(1 + W_{ex}e^{-\alpha r^2}\right) \qquad \text{--- (6.B2.9)}$$

the other commonly used form $W = W_1 + W_2\, e^{-\alpha r^2}$ uses $W_1 = W_\infty$ and $W_2 = W_\infty W_{ex}$. The two are therefore interchangeable, but the form given by equation 6.B2.9 results in simpler expressions in the analysis that follows. Garg and Leibovich (1979) report that the same value of α was used for both the axial and tangential velocity profiles, but this assumption will be examined more closely in the following analysis.

In Burgers' vortex model, the expression for the exponential parameter is: $\alpha = (a/2\nu_T)$, where ν_T is the turbulent viscosity. The value of 'a' for the Burgers vortex can be found from the expressions for the radial or axial velocities. The radial velocity at the boundary between the vortices ($r=r_{zav}$) is estimated by assuming that the total flow Q is uniformly distributed over this boundary surface, which has an area ($2\pi r_{zav}.L$). If r_{zav} is approximated by $D_x/2$ then

Radial: $u = a.r$, therefore $a = \dfrac{u(r_{zav})}{r_{zav}}$ $\Rightarrow$ $a = \dfrac{2Q}{\pi D_X{}^2 L}$. --- (6.B2.10)

The total axial velocity in the Burgers' vortex can be estimated as zero at $z = 0$ and Q at $z = L$. Calculating the average axial velocity at each location by dividing by the cross-sectional area $A=\pi D_x^2/4$ gives the same expression for the value of 'a'. This should not be surprising, since the Burgers' vortex forces the mass balance between the axial and radial velocity components.

Axial: $w = 2\,a\,z$, therefore $a = \dfrac{w}{2\,z}$ $\Rightarrow$ $a = \dfrac{2Q}{\pi D_X{}^2 L}$. --- (6.B2.11)

The exponential parameter 'α' is given by Batchelor (1964) as:

$$\alpha = \frac{W_o}{4\,\nu\,z} \qquad \text{--- (6.B2.12)}$$

where W_o is the freestream axial velocity, which appears to have no physical significance in the case of the cyclone. When equation 6.B2.12 is rewritten as $\alpha = (a_z/2\nu_T)$, as used for the Burgers vortex parameter it can be seen that the parameter 'a_z' has the same form as the Burgers axial velocity profile. This suggests that the same value of the parameter 'a' can be used for both the tangential and axial velocity profiles. The turbulent viscosities will also be the same for the two profiles if isotropic turbulence can be assumed. However, there is evidence in the literature that swirling flows modify the turbulence characteristics in the azimuthal and axial

planes, and the modelling will be kept general by allowing the two values of the turbulent viscosity to be different, but in a constant ratio to each other, with $\alpha_z/\alpha_\theta = p$. Garg and Leibovich (1979)'s contention is therefore that $p = 1.0$.

The value of α_θ is related to the position of the maximum tangential velocity, r^*. To find this relation the equation for the tangential velocity profile (3.B.8) is differentiated and set to zero. This reduces to the form detailed earlier in section 3.B:

$$e^k - 2k - 1 = 0 \qquad (k = \alpha r^2)$$

This has a root at $k = 1.2564$. Therefore given the location of the maximum tangential velocity (r^*), to force a fit between the equation and the profile requires a value of

$$\alpha_\theta = \frac{1.2564}{r^{*2}} \qquad \text{--- (6.B2.13)}$$

This was done in the previous section, and values for the turbulent viscosity and hence α_θ were estimated for the three cyclones examined in this study, resulting in an empirical relationship to predict the turbulent viscosity from the Reynolds number of the flow. This value will be compared with the value required for the axial velocity model. It should be noted that this value of α_θ has only been fitted to the location of the maximum tangential velocity.

Fitting the axial velocity profile

The position of the axial velocity crossover is an important characteristic of the axial velocity profile, and it can be found by setting $w = 0$ in equation (6.B2.9) at the radius of the core, r_{zav} :

$$W_{ex}\, e^{-\alpha_z r_{zav}^2} = -1 \quad (\text{at } r = r_{zav})$$

$$\text{---> } \quad r_{zav} = \sqrt{\frac{-1}{\alpha_z}\ln\left(\frac{-1}{W_{ex}}\right)} = \sqrt{\frac{1}{\alpha_z}\ln(-W_{ex})} \qquad \text{--- (6.B2.14)}$$

So for there to be a real value of the crossover radius, W_{ex} must be less than -1. Only one crossover is allowed, so the axial velocity cannot be zero at the axis as well as at $r=r_{zav}$

The two methods of determining the 'α' parameters can be extracted from (6.B2.13) and (6.B2.14)

$$\alpha_\theta = \frac{1.2564}{r^{*2}} \text{ --- (6.B2.13)} \quad \text{and} \quad \alpha_z = \frac{\ln(-W_{ex})}{r_{zav}^2} \qquad \text{---(6.B2.15)}$$

If these are combined with $\alpha_z/\alpha_\theta = p$ then an expression for the required value of W_{ex} is obtained:

$$W_{ex} = -\exp\{1.256.p.\left(\frac{r_{zav}}{r^*}\right)^2\} \qquad \text{--- (6.B2.16)}$$

$$\text{or} \quad \left(\frac{r_{zav}}{r^*}\right) = \sqrt{\frac{\ln\{-W_{ex}\}}{1.256.p}} \qquad \text{--- (6.B2.17)}$$

The graph below of the ratio r_{zav}/r^* versus values of W_{ex} shows that if p=1, the ratio of the characteristic radii must be close to 1.0 for reasonable values of W_{ex} to be allowable. Figure 5.B.13 shows that the zero axial velocity boundary for the 750mmØ Stairmand High efficiency cyclone is in fact well outside the position of the maximum tangential velocity. There is a wide range in the values, meaning that the results of figure 5.B.13 will be used. The hydrocyclone profiles selected by Bloor and Ingham (1987) to compare with their model featured a crossover at $0.6R_W$, as shown in figure 6.B2.1.

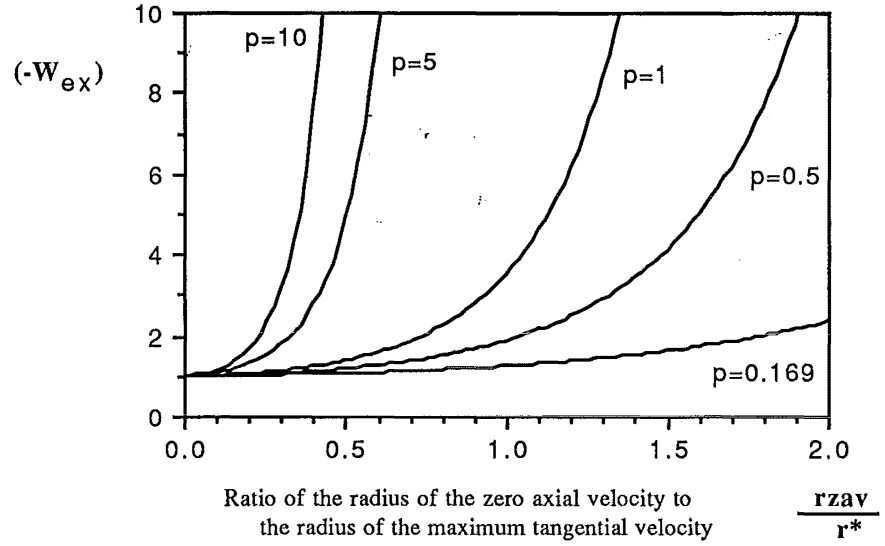

Figure 6.B2.5: Relationship between the characteristic radii and the core axial velocity parameter W_{ex}

A further requirement, which is more binding than those given above, is that the axial flow in the outer vortex must equal the axial flow in the core, to satisfy the mass balance.

$$Q = \int_{r_1}^{r_2} W_\infty\{1 + W_{ex} \exp(-\alpha_z r^2)\}.\ 2\pi\ r.\ dr \qquad \text{--- (6.B2.18)}$$

Integrating the profile results in:

$$Q = \pi W_\infty\left[r^2\right]_{r_1}^{r_2} - \left[\pi \frac{W_\infty . W_{ex}}{\alpha_z}(\exp\{-\alpha_z r^2\})\right]_{r_1}^{r_2} \qquad \text{--- (6.B2.19)}$$

When the profile is integrated between the axis and the wall (that is $r_2 = R_W$ and $r_1 = 0$) the net flow Q must be zero. Setting equation 6.B2.19 to zero with these limits, and rearranging it, yields the following relation between W_{ex}, α_z and the wall radius R_W that is required to satisfy the mass balance:

$$W_{ex} = \frac{\alpha_z R_W^2}{\left[\exp(-\alpha_z R_W^2) - 1\right]} \qquad \text{--- (6.B2.20)}$$

This can be simplified to $W_{ex} = -\alpha_z R_W^2$ when $\alpha_z R_W^2$ is greater than about 3.0, but the full form is required in many cases, and hence will be retained. The mass balance requirement of

6.B2.20 can be substituted into equation 6.B2.14 to calculate the position of the zero axial velocity crossover.

$$r_{zav} = \sqrt{\frac{1}{\alpha_z} \ln\left[\frac{-\alpha_z R_w^2}{(\exp(-\alpha_z R_w^2) - 1)}\right]} \qquad \text{--- (6.B2.21)}$$

The ratio of the crossover radius to the local wall radius R_w is then given by:

$$\frac{r_{zav}}{R_w} = \sqrt{\frac{1}{\alpha_z R_w^2} \ln\left[\frac{-\alpha_z R_w^2}{(\exp(-\alpha_z R_w^2) - 1)}\right]} \qquad \text{--- (6.B2.22)}$$

This gives the position of the crossover that is consistent with the mass balance requirement. It will be observed that the position of the crossover depends on the parameter $\alpha p R_w^2$. This dependence is shown below for various ratios of $p = \alpha_z/\alpha_\theta$.

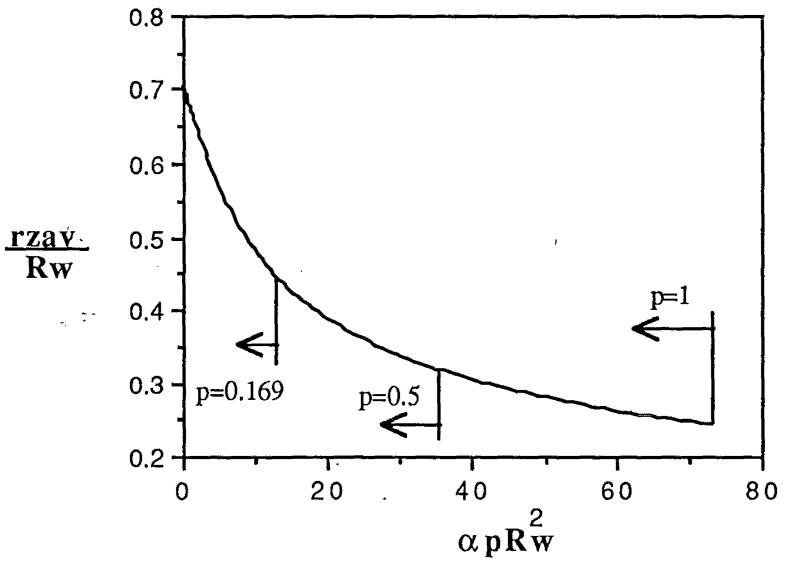

Figure 6.B2.6: Position of zero axial crossover as a function of the exponential term

For the 750mmØ cyclone $\alpha_\theta = 71.78\ m^{-2}$ and the wall radius varies from 0.375 to 0.142m. From these values it can be calculated that for $p = 1$ the $\alpha p R_w^2$ parameter varies from 1.44 to 10; for $p = 0.5$ it varies from 0.72 to 5 and for $p = 0.17$ values between 0.246 and 1.71 are possible. Thus as the value of p is reduced, the crossover is moved closer to the wall. This is shown in the graph below, which shows that for constant values of α and p along the cyclone length, the variation of the wall radius results in the crossover being predicted closer to the wall.

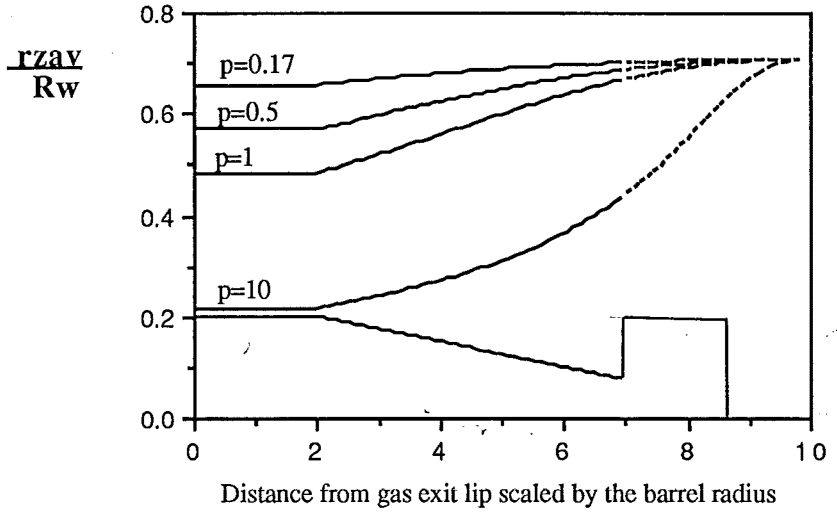

Figure 6.B2.7: Variation of zero axial crossover position along the cyclone length

It is found that the functional form of the velocity profile precludes the ratio r_{zav}/R_w from exceeding 0.7. In practice the crossover occurs at a larger radius than this, and therefore the core velocity that is required by the model in order to satisfy the mass balance is considerably greater than the velocities found in practice. To solve this problem it appears necessary to allow for a different value of α to be used for the axial velocity profile. Substituting $p = \alpha_z/\alpha_\theta$ and equation (6.B2.20) into equation (6.B2.17) for the ratio r_{zav}/r^* gives the relationship between p and the relative positions of the axial crossover and the tangential velocity maximum, when the mass balance is satisfied.

$$\frac{r_{zav}}{r^*} = \sqrt{\frac{1}{1.256.p} \ln\left[\frac{p\alpha R_w^2}{(\exp(-p\alpha R_w^2) - 1)}\right]} \qquad \text{--- (6.B2.23)}$$

Here $\alpha = \alpha_\theta$, the value fitted to the tangential velocity maximum. The variation of p with the radius ratio is shown below:.

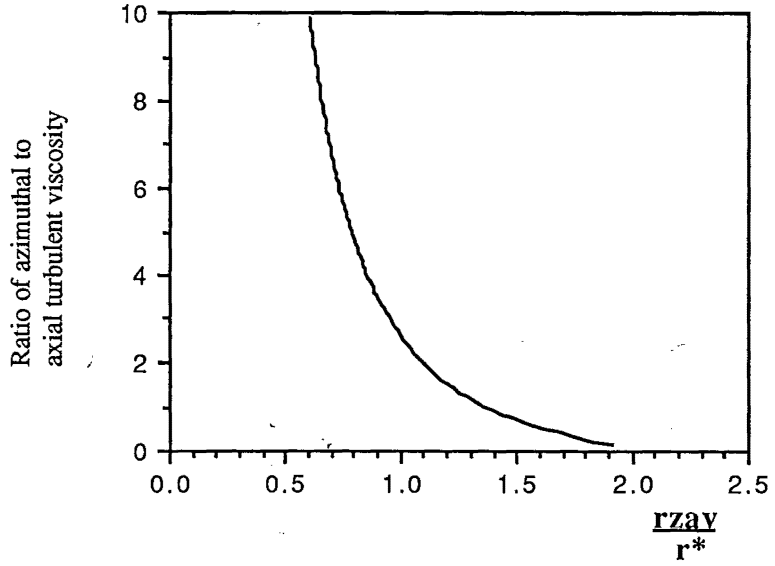

Figure 6.B2.8: Dependence of the viscosity ratio on the ratio of the characteristic radii

The wide range in the values for the characteristic radii that are reported in the literature makes it difficult to determine the correct value. From figure 5.B.13 it appears that in the 750mmØ cyclone the value of r_{zav}/r^* is 1.86, suggesting that a value of p of 0.17 is required in order to satisfy the mass balance requirements. Although the previous studies that used these profiles to model vortex flows (such as Faler & Leibovich, 1978) reported that the same value of α was used for each profile, the graph above suggests that different values are needed for the tangential and axial profiles. The α parameter depends on the 'a' and turbulent viscosity parameters. The 'a' parameters are expected to be constant between the two profiles, but there is considerable support for a variation in the turbulent viscosity in swirling flow between the tangential and the meridional directions. These are reviewed below.

6.B2.5: Anisotropy of the turbulent viscosity in swirl flows:

To fit the exponential axial velocity profile to the experimental profiles it appears to be necessary to vary p, the ratio of the 'α' parameters. It was shown at the start of this section that the α parameter can be expressed as the ratio of an average radial velocity gradient 'a' and a turbulent viscosity ν_T. The average radial velocity gradient (parameter 'a') derived from the velocity models of Burgers (1948) and Batchelor (1964) were shown to be equivalent, leading to the belief that the variation in the α parameter ratio is due to a variation in the turbulent viscosity. Some literature studies of the variation of the turbulent viscosity in swirling flows are mentioned in the following paragraphs.

The estimate of the turbulent viscosity relies on assumptions about the nature of the turbulence in the flow. If the turbulence can be assumed to be isotropic, then the viscosity will be uniform and not depend on the direction considered. In practice, for swirling flows there is a strong anisotropy reported for the turbulence in different directions. The experimental studies of the effect of curved streamlines on the turbulence has been reviewed by Bradshaw (1973), Lilley (1976) and Launder et al (1977). The experimental studies showed that the effect of curvature

is to diminish turbulent transport in flows where the angular momentum increases with radius, and enhance it in the opposite case. Turbulent models developed for non-curved flow do not give accurate predictions for curved flows.

Duggins and Frith (1987) found in their attempts to numerically model the flow in hydrocyclones that the turbulent viscosity had to vary in magnitude across the radius, a feature that was also found by Pericleous and Rhodes (1984). This was explained by a reduction in the net energy transfer from large to small eddies, which has the effect of decreasing the rate of dissipation of turbulence and increasing the length scales - especially along the axis of rotation.

Frith and Duggins (1986) used two different turbulent viscosities to take account of the anisotropy in the numerical model of a swirling flow. The axial and radial momentum equations used a viscosity calculated from the two-equation k-ε model, and the tangential momentum equation used a viscosity calculated from a mixing length formulation. The mixing length model was adequate for the tangential velocity since the tangential velocity profiles remain similar throughout the chamber, but the marked changes in the axial and radial velocity profiles required the more complicated formulation. This model was found to slightly underpredict the radial position and magnitude of the maximum tangential velocity.

Bloor and Ingham (1975) use the Prandtl mixing length model which gives the eddy viscosity by: $$\mu = \rho \lambda^2 \left|\frac{dv}{dy}\right|. \qquad \text{--- (6.B2.24)}$$

This is applicable to unidirectional flows, and λ is the mixing length, which is equal to the length scale of the turbulent eddies. For swirling flow the viscosity was found to be better estimated from:

$$\mu = \rho \lambda^2 \left|\frac{dv}{dr} - \frac{v}{r} + K\right| \qquad \text{--- (6.B2.25)}$$

where K is a term added to ensure that the turbulence does not vanish at the axis. Thwaites (1960) associates the length scales associated with the eddies in a turbulent flow with the boundary layer thickness, in recognition of the boundary layer acting as the source of turbulence. In the cyclone the boundary layer originates at the entry, and the development of it with the distance into the cyclone has been investigated by Rott and Lewellen (1966), giving a maximum value of the thickness in the middle region, after which it decreases. This would suggest that the length scale alters down the length of the cyclone. However it is dubious whether the cyclone boundary layer does actually show this decrease. Bloor and Ingham (1975) observe that the maximum value of the viscosity occurs in the vicinity of the maximum tangential velocity. The Burgers model was successfully fitted to the tangential velocity by adjusting the turbulent viscosity to match the location of the maximum tangential velocity. The good agreement achieved at other radii with this same value of the viscosity could be taken as evidence that the tangential viscosity does not vary greatly across the radius.

Elsner and Kurzak (1987) present radial profiles of the axial and tangential eddy viscosity coefficients measured in slightly heated free swirling jets. The tangential viscosity coefficient was an order of magnitude greater than the axial coefficient, and showed considerable variation across the radius. This would suggest a value of p = 10. The two figures are reproduced below in figure 6.B2.9.

Lilley (1976) acknowledges the anisotropy of the turbulence in swirling flows and expresses the variation in the turbulent viscosities by viscosity numbers such as:

$$\sigma_{r\theta} = \mu_{rz}/\mu_{r\theta} \qquad \text{--- (6.B2.26)}$$

The α parameter ratio used earlier in this section was defined as $p = \alpha_z/\alpha_\theta = \nu_\theta/\nu_z$. Hence the viscosity number in equation 6.B2.26 is the inverse of 'p'.

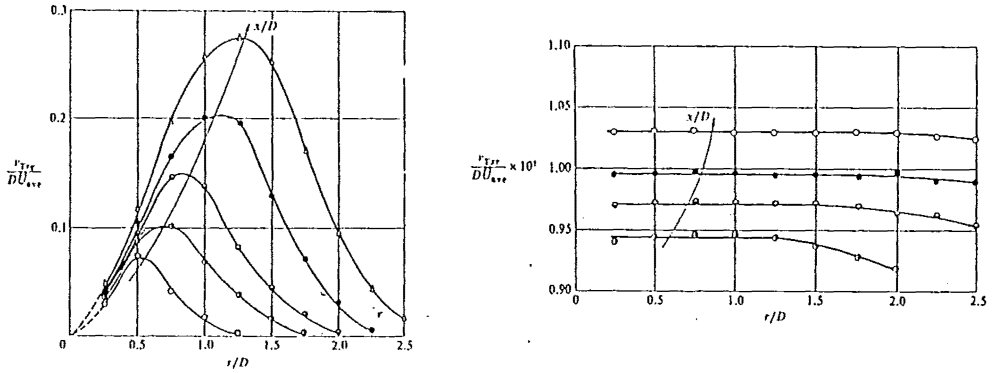

Normalized radial distributions of eddy-viscosity coefficient $\nu_{Tr\theta}$ at $\bar{\theta}_{ave} = 40°$ and $s = 0.31$: ○, $x/D = 7$; ◑, 9; ◒, 11; ●, 13; △, 15.

Figure 6.B2.9: Radial profiles of the axial and tangential viscosity coefficients (from Elsner and Kurzak, 1987)

It is noted by Lilley (1976) that for weakly swirling flows the momentum equations can be simplified by boundary layer approximations, and the six viscosity coefficients of the original axisymmetric swirling flow can be reduced to two: μ_{rz} and $\mu_{r\theta}$. The experimental results of Fejer et al (1968) for swirling flow in a pipe are presented, and are reproduced below in figure 6.B2.10. Other studies are cited by Lilley (1976), all featuring values of the viscosity ratio as defined in equation 6.B2.26 that are greater than unity, especially near the axis ($\sigma_{r\theta} > 1$). This supports the fitting of p~0.17.

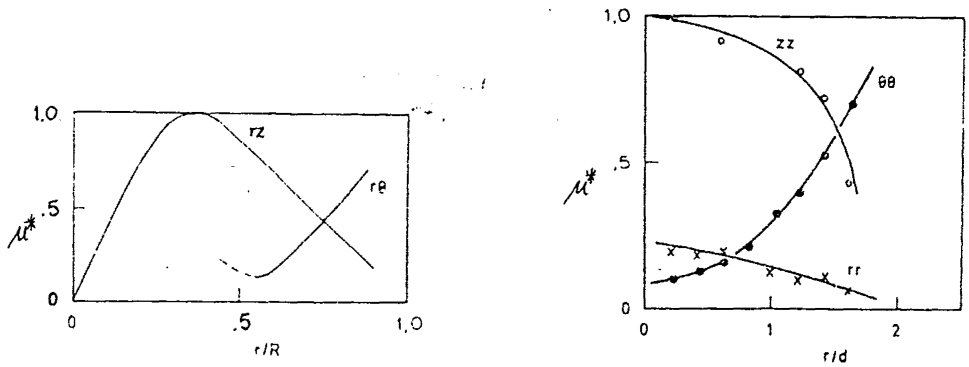

Swirl number S = 1.0 Swirl number S = 0.6

Figure 6.B2.10: Turbulent viscosity components in a swirling pipe flow (from Fejer (1968) in Lilley (1976)

Lilley (1976) suggests that the viscosity number $\sigma_{r\theta}$ is predicted by:

$$\sigma_{r\theta} = 1 + 5\,S^{1/3} \qquad \text{--- (6.B2.27)}$$

where S is the local swirl number. Since S is a positive quantity the result will be greater than unity. The predictive equations reviewed by Lilley (1976) are chiefly valid for low swirl conditions.

Lilley and Chigier (1971) present a method by which the distributions of μ_{rz} and $\mu_{r\theta}$ can be determined from mean axial and tangential velocity profiles, and these distributions are found to be a function of the swirl intensity and the radial position. The Prandtl mixing length models for the non-isotropic eddy viscosities are used:

$$\mu_{rz} = \rho\, l_{rz}^2 \sqrt{\left(\frac{\partial V_z}{\partial r}\right)^2 + \left(r\frac{\partial}{\partial r}\frac{V_\theta}{r}\right)^2} \qquad \text{--- (6.B2.28)}$$

$$\mu_{r\theta} = \rho\, l_{r\theta}^2 \sqrt{\left(\frac{\partial V_z}{\partial r}\right)^2 + \left(r\frac{\partial}{\partial r}\frac{V_\theta}{r}\right)^2} \qquad \text{--- (6.B2.29)}$$

An approach that is commonly used to account for the curvature is to make the mixing length a linear function of a turbulent Richardson number, which is given by Launder et al (1977) in the following form, which differs slightly from the version given in section 3.C.

$$Ri_t = \frac{k^2}{\varepsilon^2}\,\frac{V_\theta \cos\alpha}{r^2}\,\frac{\partial(rV_\theta)}{\partial r} \qquad \text{--- (6.B2.30)}$$

When Ri_t is negative the turbulent viscosity increases, while a positive Ri_t will decrease the turbulent viscosity.

The ratio of the turbulent viscosities, p, may not necessarily be constant across the radius. Allowing for a turbulent viscosity ratio that is a function of the radius complicates the analysis given above, and the effect of this on the fitting of the profiles has not been calculated. The turbulence will be assumed to be non-isotropic and a suitable value of 'p' selected in order to satisfy the mass balance.

6.B2.6: Fitting the velocity values at the centreline and wall

For a realistic axial velocity profile it is desired that the crossover be correctly predicted, and reasonable velocities be obtained near the axis and the walls. The position of the axial crossover can be found from equation (6.B2.21). The position of the crossover has a large influence on the velocities needed to balance the core and outer vortex axial flows. The value of the axial velocity at (or near) the axis can be estimated by examining equation (6.B2.9) at r = 0:

$$W_{(r=0)} = W_\infty\,(1 + W_{ex}) \qquad \text{--- (6.B2.31)}$$

The ratio of the axial velocity near the wall to that near the axis is :

$$\frac{W|r->0}{W|r->R_W} = \frac{(1+W_{ex})}{(1+W_{ex}.e^{-\alpha.p.R_w^2})} \qquad \text{--- (6.B2.32)}$$

For $\alpha = 71.78$; $p = 10$; $R_W = 0.375$ and $W_{ex} = -92.1$ this ratio will be $= (1+W_{ex}) = -91.1$. Experimentally, the velocities are found to be of comparable magnitude, hence this value of p is not consistent with the cyclone velocity profiles. Instead, the value of p will be taken as 0.17, consistent with the observed r_{zav}/r^* ratio of 1.86 and which gives a value of $W_e = -2.08$. The ratio of the velocity at the axis to that at the wall is then:

$$\frac{W|r->0}{W|r->R_W} = \frac{1 - 2.08}{1 - 2.08 \times 0.182} = -1.75 \qquad \text{--- (6.B2.33)}$$

The value of the parameter W_∞ is determined from the mass balance, equation 6.B2.19, using limits of $r_2 = r_{zav}$ and $r_1 = 0$ and equating the integral to the flow Q_Z at that location. The equation for the variation of Q_Z with length is expressed as a function of axial location z, and the fraction F of the inlet flow entering the bin:

$$Q_Z = \Phi(z,F).\, Q_{in} \qquad \text{--- (6.B2.34)}$$

The mass balance requirement, equation (6.B2.19), can then be rearranged to give:

$$\frac{W_\infty}{V_{in}} = \frac{0.1273 \,.\, \alpha.p.R_B^2 \,.\, \Phi}{\left[\ln\{-W_{ex}\} + 1 + W_{ex}\right]} \qquad \text{--- (6.B2.35)}$$

from the mass balance, $$W_e = \frac{\alpha.p.R_W^2}{1 - e^{-\alpha.p.R_W^2}} \qquad \text{--- (6.B2.36)}$$

Hence: $$\frac{W_\infty}{V_{in}} = \frac{0.1273 \,.\, \alpha.p.R_B^2 \,.\, \Phi}{\left[\ln\left\{\frac{\alpha p R_w^2}{1 - \exp\{-\alpha p R_w^2\}}\right\} + 1 - \frac{\alpha p R_W^2}{1 - \exp\{-\alpha p R_W^2\}}\right]} \qquad \text{--- (6.B2.37)}$$

For example, a simple functional form for Q_Z is to assume a linear decrease of Q_Z with length, with a fraction F remaining at the entrance to the bin. If the cyclone diameter is assumed to vary linearly from the gas exit to the dust exit then the dependence of the remaining flow Q_z/Q_{in} on the axial location can be written as a function of the wall radius:

$$\Phi = \frac{Q_Z}{Q_{in}} = 1.6092.(1\text{-}F).\left[\frac{R_W}{R_B} + \frac{(F\text{-}0.37857)}{1\text{-}F}\right] \qquad \text{--- (6.B2.38)}$$

This equation can be substituted into equation 6.B2.29 to yield an expression for the variation of the parameter W_∞ along the cyclone length. Since the zero axial velocity boundary is conical rather than cylindrical, the area reduces as the cone contracts, and a linear decrease of Q along the cone results in a rise in the radial velocity in the lower cone region. A better estimate for the variation of the total axial flow down the cyclone length might be to allow for a constant radial velocity, and allow the volume inflow to be higher in the barrel, where the surface area is greater. This is done by estimating the surface area of the zero axial velocity boundary for the barrel and the cone, assuming that the zero axial velocity crossover is 70% of the wall radius. This indicates that 36% of the area is contributed by the barrel, and 64% by the cone. The average radial velocity is $0.0149\ V_{in}$, if the fraction of flow that enters the bin is 10%. The variation of the remaining flow along the length does not vary greatly from a linear decrease, and is described by the following expressions:

$$\text{For } {}^{z}/_{R_B} < 2.0: \quad \Phi = \frac{Q_z}{Q_{in}} = 1 - \frac{(1-F)\,{}^{z}/_{R_B}}{\left[2 + \dfrac{0.42834\ r_{zav}/R_w}{\sin(\theta_{zav})}\right]} \qquad \text{--- (6.B2.39a)}$$

$$\text{For } {}^{z}/_{R_B} > 2.0:$$

$$\Phi = \frac{Q_z}{Q_{in}} = \left(1 - \frac{2(1-F)}{\left[2 + \dfrac{0.42834\ r_{zav}/R_w}{\sin(\theta_{zav})}\right]}\right) - \left(\frac{(1\text{-}F)}{\left(\dfrac{4\sin(\theta_{zav})}{r_{zav}/R_w} + 0.8567\right)}\right)$$

$$\times\left(1 - \left[\frac{(1 - {}^{z}/_{R_W})\tan(\theta_{zav})^2}{r_{zav}/R_w}\right]\right) \qquad \text{--- (6.B2.39b)}$$

The equations describing the variation of the axial flow along the length (equations 6.B2.38 and 6.B2.39) are substituted into equation 6.B2.29, yielding the following graph. This shows that for p=0.17 there is a significant variation of the parameter W∞ over the length, and in the lower cone values are twice the magnitude of the inlet velocity.

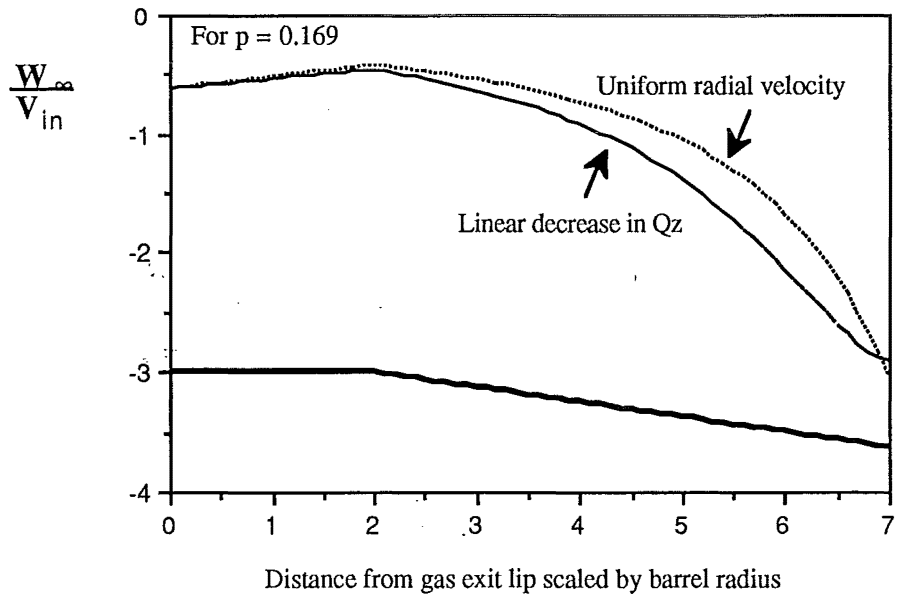

Figure 6.B2.11 Variation of the W_∞ velocity parameter along the cyclone length

There is little difference between the two assumed forms for the decrease in the axial flow along the length. The uniform radial velocity assumption was then used to check the variation of the W∞ parameter with different values of the turbulent viscosity ratio p, as shown in the following graph:

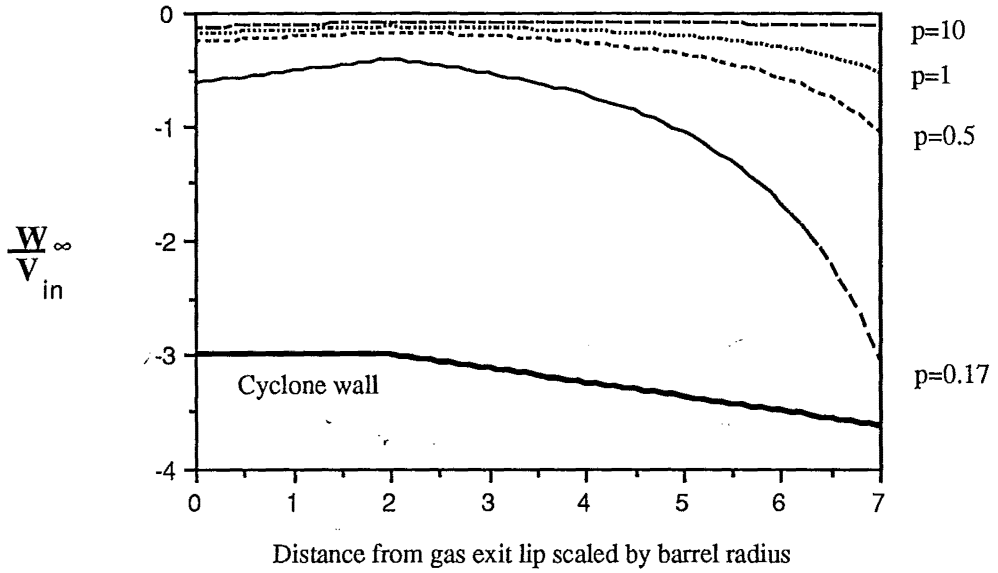

Figure 6.B2.12: Variation of W∞ parameter along length, for different viscosity ratios

This shows that larger values of p result in more uniform values of the W_{∞} parameter along the length. The W_{∞} parameter is the axial velocity at infinite radius, which has a physical meaning in the case of unconfined vortices, where it is the freestream axial velocity of the flow that the vortex is embedded in. In the cyclone, the walls truncate the profile well before it reaches its asymptotic limit, and the seemingly large values of W_{∞} are countered by a decrease in the W_{ex} parameter. Hence a value of p = 0.17 is suitable for describing the velocity profiles in the cyclone vortex.

6.B2.7 Summary of axial velocity modelling

The most suitable form of the axial velocity model of Batchelor (1964) is:

$$W = W_\infty\left(1 + W_{ex}e^{-\alpha_z r^2}\right) \qquad \text{--- (6.B2.9)}$$

The exponential parameter α_z is taken to be related to the exponential parameter α_θ obtained from the tangential velocity modelling by:

$$p = \alpha_z/\alpha_\theta = \nu_{T\theta}/\nu_{Tz}$$

The results reported by Lilley (1976) suggest that the viscosity ratio p will be less than one. The value of p is selected by examining the ratio of the characteristic radii:

$$\frac{r_{zav}}{r^*} = \sqrt{\frac{1}{1.256.p}\ln\left[\frac{p\alpha R_w^2}{(\exp(-p\alpha R_w^2) - 1)}\right]} \qquad \text{--- (6.B2.23)}$$

which is graphed in Figure 6.B2.6. For this study a value of $r_{zav}/r^*$was desired, which resulted in a value of p = 0.17.

The parameter W_{ex} is found by applying the mass balance between outer and inner vortices, giving:

$$W_e = \frac{\alpha_z R_w^2}{\left[\exp(-\alpha_z R_w^2) - 1\right]} \qquad \text{--- (6.B2.20)}$$

The parameter W_∞ is found by fitting the profile to the volume flow at the particular location. This requires the description of the decrease in the volume flow down the cyclone length: $Q_z = \Phi(z).Q_{in}$. Using an assumption of a uniform radial velocity, and 10% of the inlet flow reaching the bin, the expression for W_∞/V_{in} is obtained:

$$\frac{W_\infty}{V_{in}} = \frac{0.1273\ .\ \alpha.p.R_B^2\ .\ \Phi}{[\ln\{Wex\} + 1 - W_{ex}]} \qquad \text{--- (6.B2.35)}$$

A comparison between the experimental data and the axial velocity profiles from equation 6.B2.9 with the fitted parameters is presented in figures 6.B2.15-18. The parameters from the fitting of the exponential model to seven locations in the 750mmØ cyclone are given below:

Port	z/R_B	Q_z/Q_{in}	R_w/R_B	p	αpR_w^2	W_{ex}	W_∞/V_{in}	r_{zav}/R_w
12	0.115	0.9812	1.0	0.17	1.865	-2.207	-0.561	
11	0.543	0.9113	1	0.17	1.865	-2.207	-0.521	
9	2.331	0.6202	0.96	0.17	1.719	-2.094	-0.415	
8	3.75	0.4172	0.773	0.17	1.114	-1.659	-0.649	
7	4.83	0.2898	0.64	0.17	0.764	-1.43	-0.951	
5	5.7	0.2049	0.536	0.17	0.536	-1.292	-1.361	
3	6.7	0.1254	0.4311	0.17	0.347	-1.183	-1.986	

The mass balance between the outer and inner vortices resulted in agreement to within 0.1%. Wl_o/Wl_w is the ratio of the velocity at the axis to the value at the wall. The axial velocity profiles are plotted below against the radial location scaled firstly by the barrel radius (Figure 6.B2.13); and then by the local wall radius (Figure 6.B2.14)

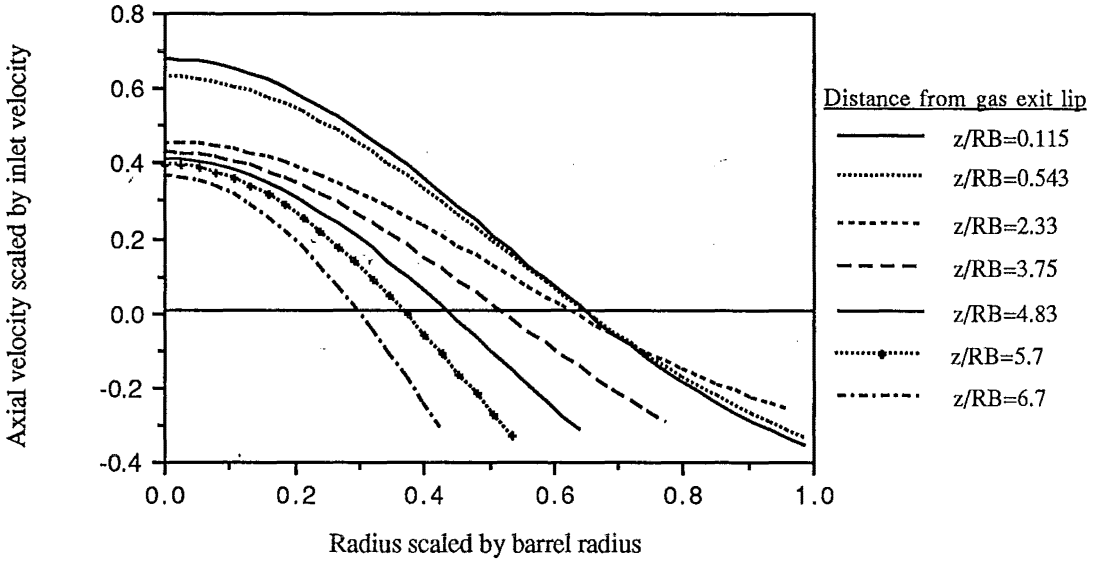

Figure 6.B2.13: Variation of fitted Batchelor (1964) model along cyclone length

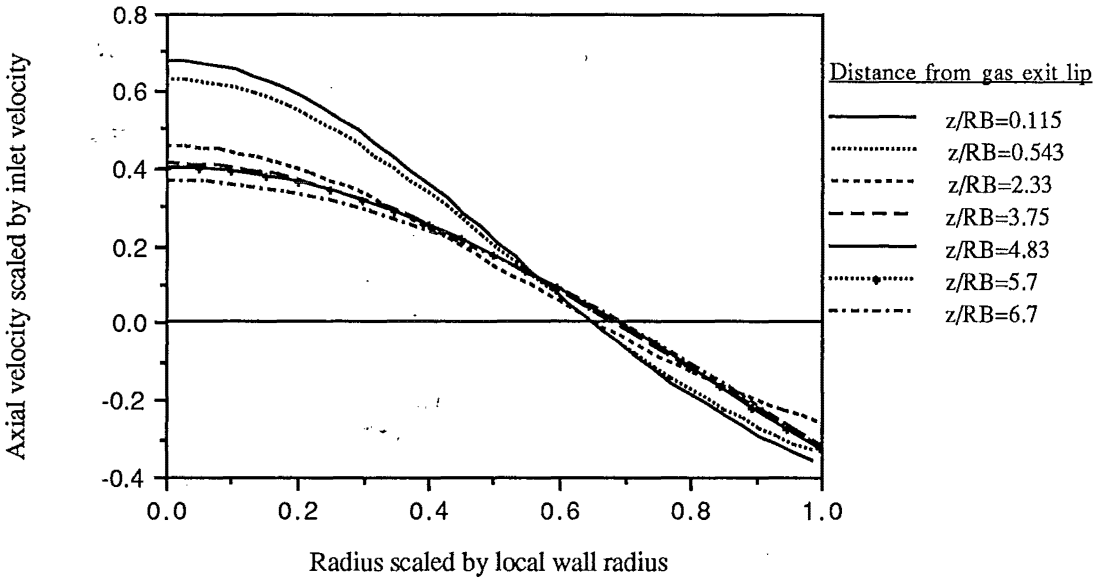

Figure 6.B2.14: Variation of fitted Batchelor (1964) axial velocity model along length when scaled by local wall radius

The fitted Batchelor (1964) (equation 6.B2.9) and Polynomial (equation 3.B.49) models are compared with the experimental axial velocity profiles from the 750mmØ cyclone in the following graphs:

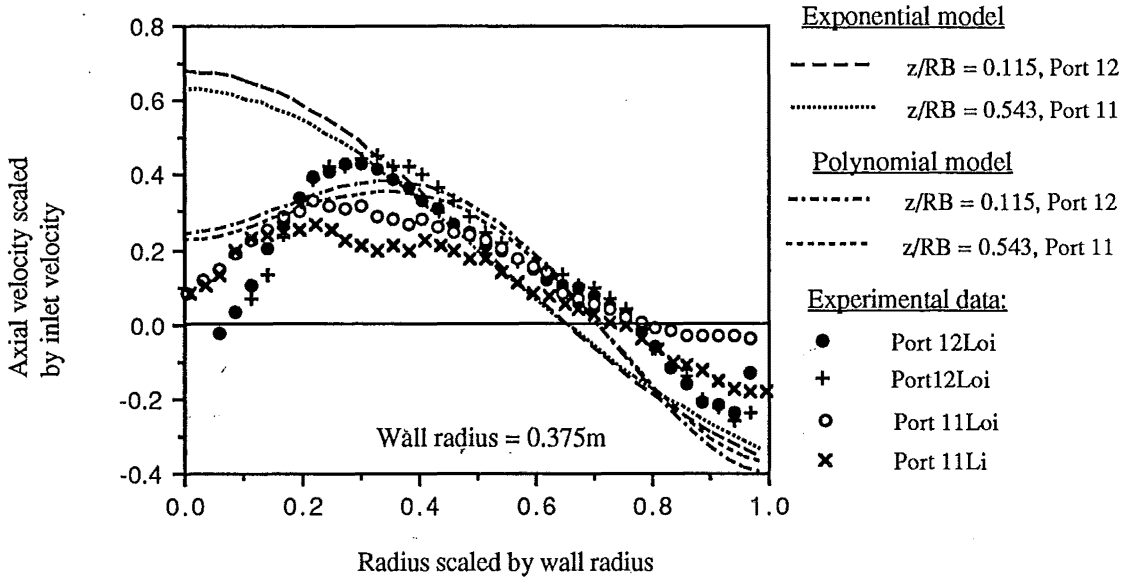

Figure 6.B2.15: Comparison of exponential model with data in upper barrel

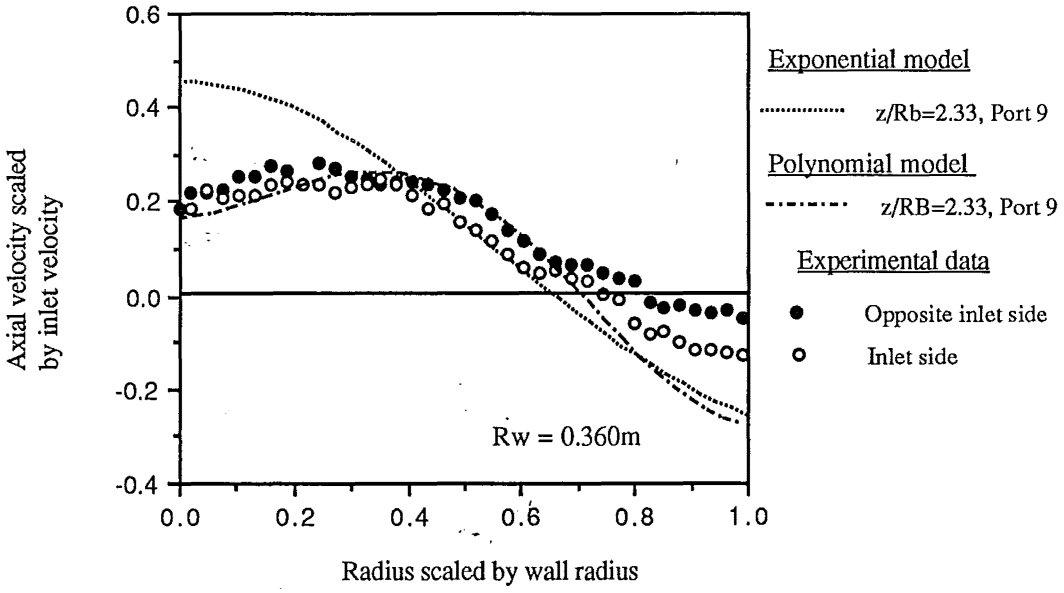

Figure 6.B2.16: Comparison of exponential model with upper cone data

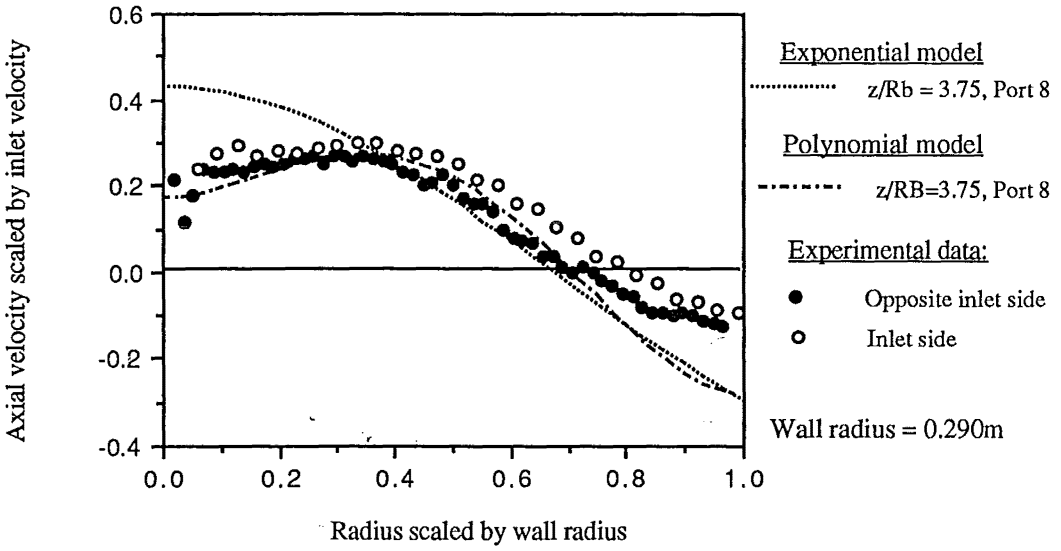

Figure 6.B2.17: Comparison of exponential model with mid cone region data

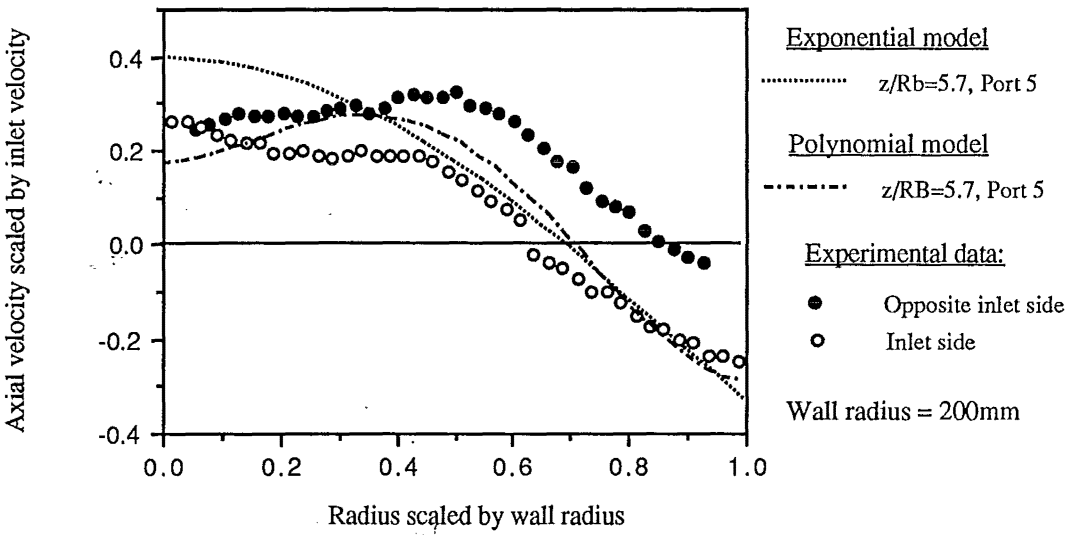

Figure 6.B2.18: Comparison of exponential model with data in lower cone

6.B2.8: Modelling the axial velocity in the gas exit:

The modelling of the axial velocity in the gas exit requires some modifications to the boundary conditions that are used to specify the parameters. Once again equation 6.B2.9 will be used, and it will be assumed that the same turbulent viscosity applies as in the body of the cyclone. This may not necessarily be the case, as the smaller diameter and larger flow may alter the turbulence properties.

In the gas exit the mass balance requirement is simply that:

$$\int_0^{R_w} 2\,\pi\, r\, W.dr \quad = \quad Q_{in} \qquad \text{--- (6.B2.40)}$$

This simplifies to:

$$\frac{W_\infty}{V_{in}} = \frac{0.4/\pi \;.\; R_B^{\,2}/R_w^{\,2}}{\left(1 - W_{ex}\,\dfrac{\exp\{-\alpha_z R_w^{\,2}}{\alpha_z R_w^{\,2}}\right)} \qquad \text{--- (6.B2.41)}$$

The α_z parameter is again taken as a constant fraction of the tangential exponential parameter α_θ, given by: $\alpha_z = p \,.\, \alpha_\theta$

and α_θ is estimated as in equation 6.B1.15

$$\alpha_\theta = 4.935 \left(\frac{Q}{L\nu}\right)^{0.079} \frac{1}{R_B^{\,2}} \qquad \text{--- (6.B2.42)}$$

For the 750mmØ cyclone at an inlet velocity of V_{in} = 22 m/s this simplifies to:

$$\alpha_\theta = \frac{11.14}{R_B^{\,2}} = 79.2\ m^{-2} \qquad \text{--- (6.B2.43a)}$$

However, the only data in the gas exit was obtained in the 140mmØ cyclone, and hence the following derivations will use the value of α_θ appropriate for this scale:

$$\alpha_\theta = \frac{9.807}{R_B^{\,2}} = 2001.5\ m^{-2} \qquad \text{--- (6.B2.43b)}$$

Further simplification of equation 6.B2.41 is possible by substituting equation 6.B2.43b and noting that in the Stairmand High efficiency cyclone the gas exit diameter is 50% of the barrel diameter, hence $R_w = 0.5\ R_B$. This results in:

$$\frac{W_\infty}{V_{in}} = \frac{0.5093}{(1 + 0.81777\ W_{ex})} \qquad \text{--- (6.B2.44a)}$$

If the expression is to allow for variable values of the viscosity ratio p it can only be simplified as far as:

$$\frac{W_\infty}{V_{in}} = \frac{0.5093}{1 - W_{ex}\left[\dfrac{(0.08613)^p - 1}{2.45185\ p}\right]} \qquad \text{--- (6.B2.44a)}$$

The axial velocity at the axis, W_{CL} is determined by the parameter W_{ex}, as shown by setting r = 0 in equation 6.B2.9.

$$W_{CL} = \quad W_\infty(1 + W_{ex}) \qquad \text{--- (6.B2.45)}$$

$$= \left(\frac{0.5093\ (1 + W_{ex})}{1 + 0.81777\ W_{ex}}\right) . V_{in} \qquad \text{--- (6.B2.46)}$$

The average axial velocity in the gas exit is given by

$$\frac{\overline{W}}{V_{in}} = \frac{0.4\ R_B^{\ 2}}{\pi\ R_w^{\ 2}} = 0.50929 \qquad \text{--- (6.B2.47)}$$

This value results in a value of zero for the parameter W_{ex}, since the flow is then in plug flow and has no exponential dependence. The variation of the centreline velocity with the parameter W_{ex} is shown below in figure 6.B2.19:

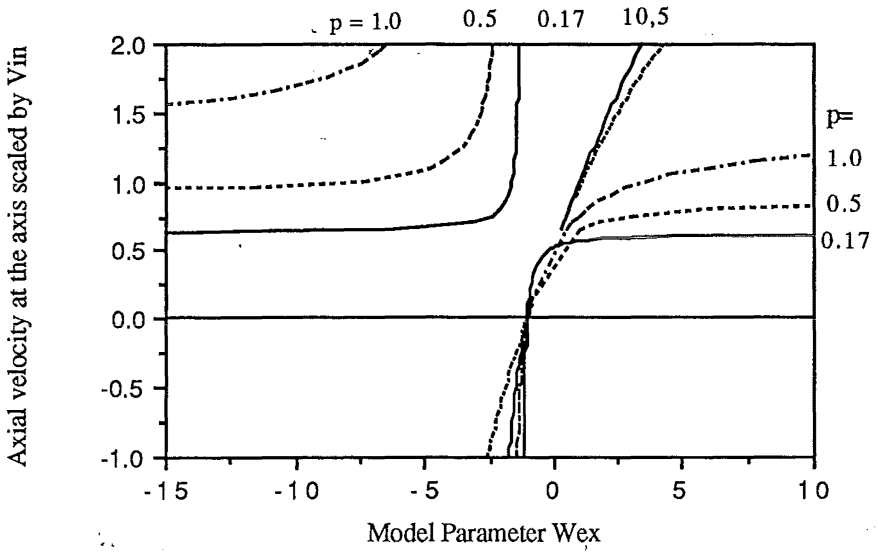

Figure 6.B2.19: Dependence of the centreline velocity on the W_{ex} parameter

The value of the parameter W_{ex} that is required to give a certain W_{CL} value is:

$$W_{ex} = \left(\frac{W_{CL}}{W\infty} - 1\right) \qquad \text{--- (6.B2.48)}$$

$$W_{ex} = \left(\frac{1 - 1.9635\ W_{CL}/V_{in}}{1.60568\ W_{CL}/V_{in} - 1}\right) \qquad \text{--- (6.B2.49a)}$$

Inverting this gives the expression for the centreline velocity as a function of the parameter W_{ex}:

$$\frac{W_{CL}}{V_{in}} = \frac{(1 + W_{ex})}{(1.9635 + 1.60568\ W_{ex})} \qquad \text{--- (6.B2.49b)}$$

It will also be noted that at the ratio $W_{CL}/V_{in} = 0.6227$, the parameter W_{ex} tends to infinity. This value of the centreline velocity may be related to a critical axial velocity above which the form of the flow changes.

The expression for the W_{ex} parameter can be used to simplify equation 6.B2.44 and give an expression for the $W\infty$ parameter in terms of the centreline velocity:

$$\frac{W\infty}{V_{in}} = 2.794739 - 4.4874\ \frac{W_{CL}}{V_{in}} \qquad \text{--- (6.B2.50a)}$$

Allowing for variable values of the viscosity ratio p, gives the ratio as:

$$\frac{W\infty}{V_{in}} = \frac{0.50929 + \frac{W_{CL}}{V_{in}}\left[\frac{(0.08613)^p - 1}{2.45185\ p}\right]}{1 + \left[\frac{(0.08613)^p - 1}{2.45185\ p}\right]} \qquad \text{--- (6.B2.50b)}$$

This is shown below in figure 6.B2.20:

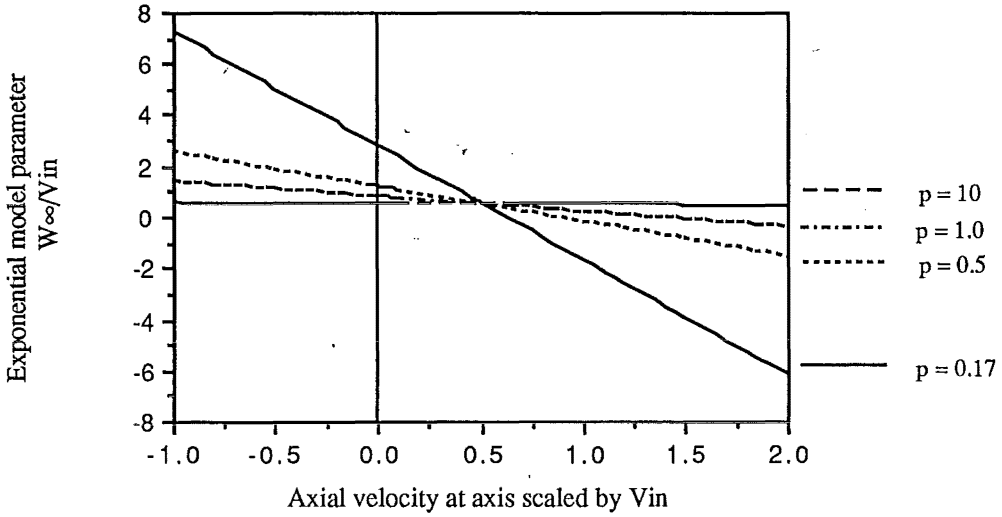

Figure 6.B2.20: Variation of the W∞ parameter with the centreline velocity

As previously noted, the W∞ parameter is the axial velocity as the radius tends to infinity, but in the confined cyclone flow this state is not reached. The velocity at the wall W_w depends on the relative magnitude of α_z and R_w^2 and substituting $r = R_w$ in equation 6.B2.9 results in:

$$\frac{W_w}{V_{in}} = \frac{W\infty}{V_{in}}\left(1 + W_{ex}.0.08613^p\right) \qquad \text{--- (6.B2.51)}$$

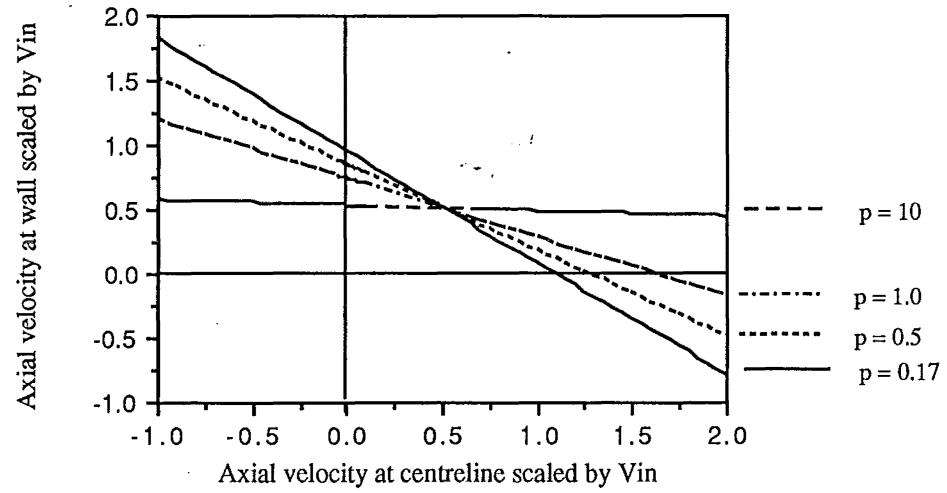

Figure 6.C2.21: Variation of the velocity at the wall with the velocity at the axis

For p = 0.17 the expression for the axial velocity at the wall rearranges to:

$$\frac{W_w}{V_{in}} = 0.952606 - 0.87044\ \frac{W_{CL}}{V_{in}} \qquad \text{--- (6.B2.52)}$$

If the core is stagnant, with zero axial velocity on the axis, then the velocity at the wall must be 95% of the inlet velocity. If the core reverses, then the velocity at the wall will be higher, as would be expected from conservation requirements. If the velocity becomes greater than 1.09 V_{in} the the velocity at the wall will become negative, and an annular reversal results. The wall velocities measured with the pitot cylinder in the gas exit of the 140mmØ cyclone were about 70% of the inlet velocity. This would result in axial velocities along the axis of 0.29 V_{in}.

The position of the zero axial velocity crossover is found by setting 6.B2.9 to zero at $r = r_{zav}$. Using the relationships above to simplify the expression, the position of the crossover as a fraction of the gas exit wall radius R_{gx} is given by:

$$\frac{r_{zav}}{R_{gx}} = 1.5489 \sqrt{\ln[-W_{ex}]} \qquad \text{--- (6.B2.53)}$$

The ratio r_{zav}/R_{gx} is graphed below as a function of the W_{CL}/V_{in} ratio:

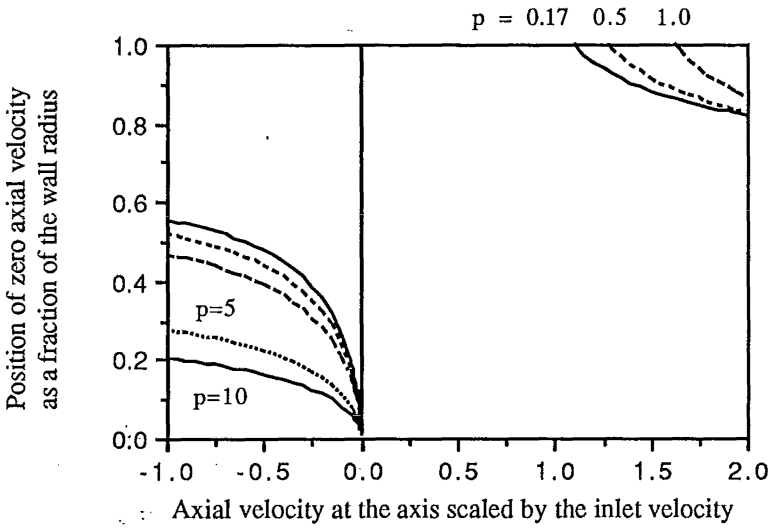

Figure 6.B2.22: The variation of the axial velocity crossover position with the centreline velocity.

The negative velocity at the axis cannot extend to greater than 40% of the wall radius, and for low centreline velocities $0 < W_{CL}/V_{in} < 0.8$ no crossover is possible at all. For centreline velocities greater than $0.8V_{in}$ an annular reversal of the axial flow is possible at radii greater than 79% of the wall radius.

The axial velocity profiles measured with the 5 hole pitot cylinder in the 140mmØ cyclone showed that the axial velocity at the wall was 70% of the inlet velocity. Using the relationships above the parameters consistent with this value can be determined:

$W_{ex} = -0.8053$; $W_\infty = 1.4925\ V_{in}$

for which the centreline velocity was 29% of the inlet velocity. If the wall velocity increases to 90% of the inlet velocity the parameters change to:

$W_{ex} = -0.9761$; $W_\infty = 2.5235\ V_{in}$

and the centreline velocity reduces to 6% of the inlet velocity.

These two model profiles are presented in the graph below, along with the experimental axial velocity profiles. These were obtained at different levels in the gas exit. For both the Standard Stairmand High Efficiency geometry, and the 'Long cone' geometry, a traverse was made 0.57

exit diameters above the roof of the cyclone. In the 'Long cone' geometry further traverses were made 30mm below the roof, and 30mm above the lip. All four profiles are shown in the graph below:

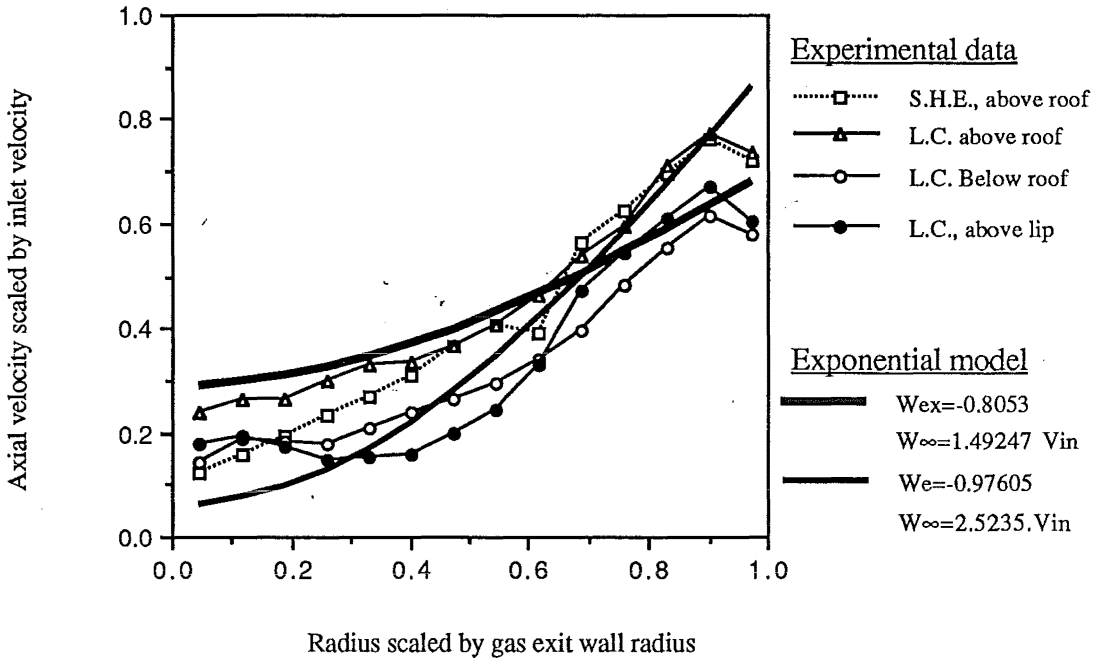

Figure 6.B2.23: Gas exit axial velocity profile with fitted model (140mmØ cyclone).

The absence of a reversal along the core in these measurements is to be expected. The insertion of the probe resulted in the region of recirculating tracers moving well downstream in the gas exit. Velocity measurements in a diffusing gas exit (cone half angle of 7° and length 500mm) with the same pitot cylinder did show reverse velocities in the core. The velocities at the wall appear to be too low to allow a reversal to occur.

Chapter 6.C: Vortex stability

Introduction:

The various criteria that have been proposed in the literature to predict the stability of vortices have been reviewed in Section 3.C.6. Using the models fitted to the velocity components in sections 6.B1 and 6.B2, this section will apply these stability criteria to the cyclone vortex.

Many experimental studies of vortex breakdown have been made, both in unconfined flows and in tubes and these have been compared with the various stability criteria that have been proposed. The results indicate that the understanding of the phenomenon is far from complete, and other factors or mechanisms may be involved. Escudier and Zehnder (1982) reported that the vortex can be unstable and not undergo breakdown, and in other cases undergo breakdown without being unstable. Uncertainty of the theoretical understanding suggests that experimental/empirical criteria are preferable to theoretical developments. For modelling a detailed knowledge of the internal structure of the vortex breakdown may be required, but for design the position of it alone may be sufficient. The form of the breakdown may not necessarily be of the core-type form that has been described in the literature, in which case many of the criteria presented will not apply.

Qualitative explanations for vortex breakdown:
It is important to consider that in the reverse-flow cyclone the only path for the gas is out the gas exit, and hence the flow must undergo a reversal. If there was a draw off of gas elsewhere the flow would be quite different, although possibly not as stable. The reverse flow may be forced to happen as there is no other path for the gas to escape the cyclone and the flowfield results from taking a least resistance path. As a suggestion for saving space, Bohnet (1983) shows a cyclone with the gas outlet tube inserted through the dust exit, and this arrangement has been found to give satisfactory collection efficiencies in a sampling cyclone. However, the reversal of the vortex is observed in unconfined vortices, and the cyclone may represent just such a vortex with confining walls put around it.

Belousov & Gupta (1986) suggest that the axial reversal of the vortex in cyclone type devices comes about due to a natural instability caused by the pressure gradients. The radial pressure gradient yields flow reversal on the axis so as to form a vortex core that behaves like a solid body on the axis, with V_θ/r = constant. This suggests that the vortex is naturally susceptible to reversal of the vortex, wherever the exit is located.

6.C.1 Empirical criteria

The empirical criteria of Escudier & Zehnder (1982) and of Kuroda & Ogawa (1987) for the instability of the vortex were satisfied by the cyclone geometry and inlet flows. The Kuroda & Ogawa criterion for the appearance of a third reversal was also satisfied, with a value of the $Re.Re_\theta^{0.4}$ parameter of 39×10^5 compared with the critical value of 7.5×10^5. The bubble

number proposed by Abrahamson (1985) suggested that the cyclone was unable to fill the cyclone length for values of BUB less than 50 to 150. The values of the BUB number for the 140mmØ and 750mmØ cyclones were 340 and 1450 respectively. The Rossby number criterion of Spall et al (1987) was applied to the cyclone in Chapter 5.D, and showed that the vortex was unstable at all axial locations, and would be for any of the choices for the characteristic axial velocity based on the actual flow. The application of many of the criteria is hampered by the effect of the reversal of the vortex on the axial velocity. The theoretical criteria that are consistent with high swirl being destabilising indicate that the swirl in the cyclone vortex is sufficiently high to be destabilised.

6.C.1 (b) Closed cylinder breakdown criteria.

The experiments of Escudier (1984) on the breakdown of the vortex in a closed cylinder with rotating endwall were summarised in a stability diagram as a function of the rotational Reynolds number and the ratio of the length to the radius of the cylinder. The ratio of the length to the radius for the cyclone is 7, but the value of the Reynolds number is open to interpretation. Lopez (1990) uses a value of $Re = \Omega.R^2/\nu$, where Ω is the constant angular velocity of the rotating lid, R is the radius of the cylinder and ν is the kinematic viscosity. In the cyclone, the angular velocity varies slightly along the core length, as shown in figures 6.B1.3 and 6.B1.4. In the 750mmØ cyclone Ω varies from 200 s^{-1} at the level of the gas exit lip, to 400 s^{-1} at the dust exit end. In the 140mmØ cyclone Ω varies from 1000 s^{-1} at R_w=0.07 m to 3000 s^{-1} at R_w= 0.03 m. If the kinematic viscosity for air is taken the Reynolds numbers are of the order of 10^6, well off the scale of the stability diagram. If the viscosity is instead taken as the turbulent viscosity that was found in section 6.B1 to fit the Burgers tangential velocity profile (equation 6.B1.15), then the Reynolds numbers are in the range of 1000-4220. The turbulent viscosity obtained from the axial velocity modelling in section 6.B2 gives Reynolds numbers of 5300 to 25 000, and these parameter values place the cyclone in line with the instability envelope. In summary:

	Rotational Reynolds number $Re = \frac{\Omega.R^2}{\nu}$			
Estimate of Viscosity used:	750mmØ cyclone at Dust exit	at gas exit	140mmØ cyclone at dust exit	at gas exit
Kinematic $\nu = 1.568\times10^{-5}$ m^2/s	1.8×10^6	2.7×10^6	0.17×10^6	0.31×10^6
Turbulent, θ direction $\nu_{T\theta} = 0.0645\ (Re)^{0.921}$	4220	2810	1630	900
Turbulent, z direction $\nu_{T\,z} = \nu_{T\,\theta}/0.17$	24800	8100	9610	5300

Table 6.C.1: Values of the Rotational Reynolds number for various assumed viscosities

These parameter values are plotted on an extended version of the stability diagram presented by Lopez (1990):

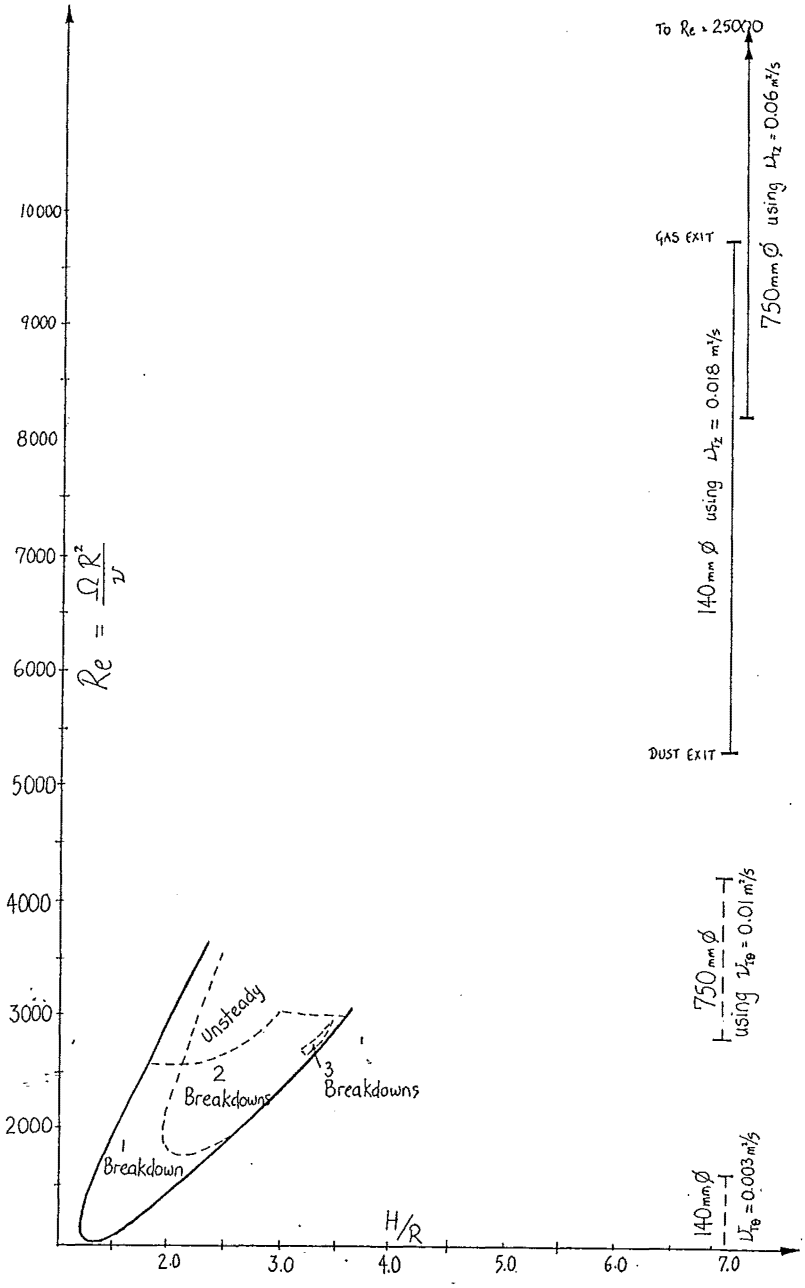

Figure 6.C.1: Stability diagram for vortex breakdown in confined rotating flow.

6.C.1(c) The Rossby number criterion of Spall et al (1987)

The Rossby number stability criterion proposed by Spall et al (1987) has been outlined in section 3.C (see equation 3.C.30 and figures 3.C.13 and 3.C.14). The Rossby number is the ratio of characteristic axial and tangential velocities, defined by $Ro = \frac{w}{\Omega r^*}$, with breakdown predicted for Rossby numbers below 0.65. As mentioned in section 3.C, the presence of a reversal of the axial velocity near the characteristic radius can give spurious results. This was more of a problem in the 140mmØ cyclone, and to avoid negative values of the Rossby number, the maximum axial velocity in the core was used instead of the axial velocity at the radius of the maximum tangential velocity. For the 140mmØ cyclone values of the Rossby number at different levels varied from 0.25 to 0, as depicted below in Figure 6.C.2:

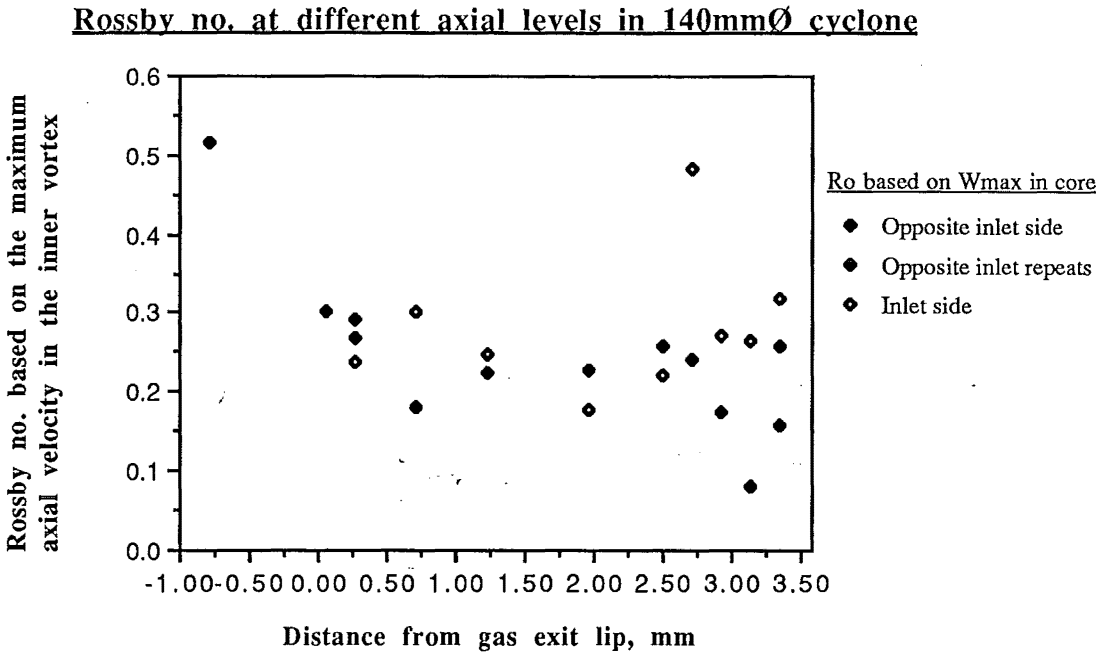

Figure 6.C.2: Rossby number values along the length of the 140mmØ cyclone

The data obtained in the 750mmØ cyclone generally had the axial velocity cross-over away from the tangential velocity maximum position, hence the Rossby numbers show less scatter. The points marked correspond to Rossby numbers calculated with two different characteristic axial velocities. "Ro *" uses the value of the axial velocity at the radius of the maximum tangential velocity, whereas "Ro max" uses the maximum axial velocity in the core. There is little difference between these two approaches for the 750mmØ cyclone profiles. The plot of the local Rossby number against the distance from the gas exit lip for the 750mmØ cyclone is given below:

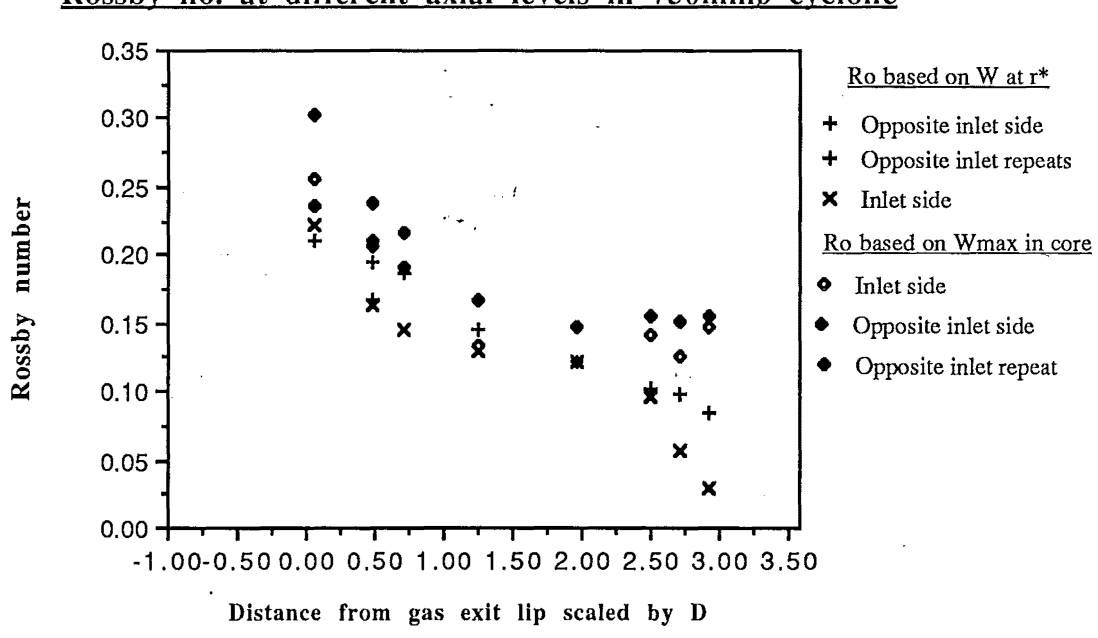

Figure 6.C.3: Rossby number values in the 750mmØ cyclone

Two traverse locations in the 2090mmØ cyclone went sufficiently into the core to allow the estimation of the Rossby number. Both were near the end of the cone, where the cyclone has been modified by adding a cylinder between the cone end and the dust exit. The Rossby number obtained were Ro = 0.083 for Port 4, 0.37 barrel diameters above the end of the cone; and Ro = 0.1 for Port 3, 0.024 D above the end of the cone/start of the dust exit cylinder.

Since the Rossby number is less than 0.65 at all levels the entire cyclone is sub-critical. Hence breakdown would be predicted at the entrance to the cyclone. However as a prediction of breakdown it is inappropriate to use post-breakdown velocity profiles to calculate the Rossby number. The axial velocity that would have been present before breakdown was estimated by the average value of the flow divided by the cross sectional area. As can be anticipated, this results in a lower value of the axial velocity and hence an even more subcritical value.

6.C.2 Applying the theoretical criteria:

The characteristic swirl of the cyclone can be estimated from the geometry and the inlet flowrate, and this may be used to determine whether or not the flow is prone to vortex breakdown. To determine the location of the vortex breakdown a detailed knowledge of the internal structure is needed. Obtaining the velocity profiles in the flow is difficult, and the measurement may disturb the flow or trigger the vortex breakdown. To simplify the calculations, models that describe the velocity across the radius and along the length are desired, and if possible the criteria should be simplified to mean flow parameters that can be easily measured.

Local stability of the cyclone vortex:

The following sections investigate the variation of the stability parameter along the cyclone length, using the modelled velocity profiles obtained from sections 6.B1 and 6.B2. The axial locations corresponded to Ports 12, 11, 9, 8, 7, 5 and 3 in the 750mmØ cyclone to enable comparison with the experimental profiles. The parameters selected are summarised in Table 6.C.2 below:

Location [units]	z/R_B [–]	Q_z/Q_{in} [–]	Rw [m]	W_{ex} [–]	W_∞/V_{in} [–]	Γ_o [m^2/s]	α_θ [s^{-1}]
Port 12	0.115	0.981	0.375	-2.207	-0.561	6.79	78
Port 11	0.543	0.911	0.375	-2.207	-0.521	6.64	78
Port 9	2.33	0.620	0.360	-2.094	-0.415	5.98	78
Port 8	3.75	0.417	0.290	-1.659	-0.649	5.40	78
Port 7	4.83	0.290	0.240	-1.430	-0.951	4.91	78
Port 5	5.70	0.205	0.201	-1.292	-1.361	4.48	78
Port 3	6.70	0.125	0.162	-1.183	-1.986	3.922	78
Gas exit	–	1.000	0.035#	-0.976	+2.524	1.376#	2025#

Table 6.C.2: Parameter values for Axial and tangential velocity modelling

Since the only data available for comparison with the gas exit velocity profiles was from the 140mmØ cyclone the model was fitted for the smaller cyclone. The results will be comparable with the profiles in the larger cyclone when scaled by the wall radius.

6.C.2(a) The Richardson number criterion:

A number of breakdown criteria have been proposed based on the requirement that the local Richardson number of the vortex should be greater than 0.25 for stability of the vortex to perturbations. The Richardson number was given by Howard and Gupta (1962) as :

$$J(r) = \frac{r^{-3}\,\frac{d(r^2.V^2)}{dr}}{(dW/dr)^2} \quad \text{which can be written: } J(r) = \frac{r^{-3}\,2\,\Gamma\frac{d\Gamma}{dr}}{(dW/dr)^2} \qquad \text{--- (6.C.1)}$$

The velocity profiles were modelled in the previous sections using the Burgers and Batchelor models for the tangential and axial velocity components respectively. Substituting these equations for the circulation Γ and the axial velocity W results in the following expression:

$$J(r) = \frac{\Gamma_o\, e^{-\alpha_\theta r^2(1-2p)}}{r^4\,\alpha_\theta.p^2.W_\infty{}^2.W_{ex}{}^2} \qquad \text{--- (6.C.2)}$$

The following plot shows the radial profile of the Richardson number for various axial locations along the cyclone length using values of the parameters from Table 6.C.2.

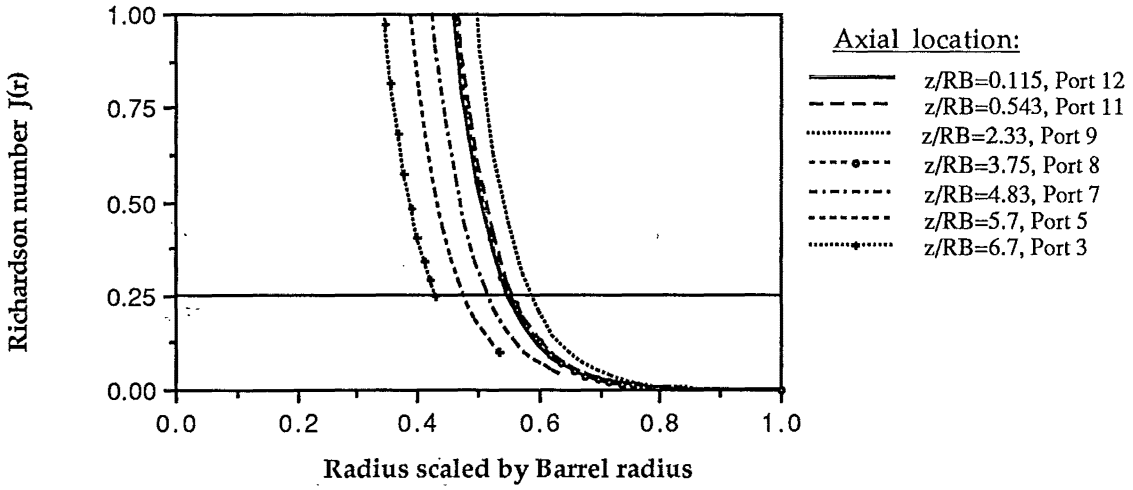

Figure 6.C.4: Variation of Richardson number with radius for different axial locations

It will be noted that the Richardson number predicts that increasing the swirl will be stabilising, with respect to the instability to perturbations. This is in qualitative disagreement with the experimental observations, as vortices are observed to be destabilised by increasing the swirl. It is possible that the criterion fails because the assumption of a columnar vortex is inappropriate, but the perturbation instability theory has been rejected in the literature (Leibovich, 1984) as a plausible explanation of the mechanism of vortex breakdown. The Richardson number in the gas exit was an order of magnitude larger than the values in the main body of the cyclone.

6.C.2(b) The instability criterion of Lessen et al (1974):

The instability of vortex flows to infinitesimal, non-axisymmetric disturbances was examined by Lessen et al (1974) using profiles that can be related to those used in sections 6.B1 and 6.B2. The non dimensionalised profiles were given in section 3.C, page 73 as:

$$V_\theta = q\frac{(1 - e^{-r^2})}{r} \qquad \text{--- (6.C.3)}$$

$$W = \frac{W_o}{W_s} - e^{-r^2} \qquad \text{--- (6.C.4)}$$

Where $q = \frac{\Gamma_o}{W_s.r_s}$ and $r = \frac{r_o}{r_s}$

Comparing these equations with those in section 6.B1 and 6.B2 it can be seen that it has been assumed that $\alpha_z = \alpha_\theta$ and that $r_s = 1/\sqrt{\alpha}$. W_s is equal to $W_\infty W_{ex}$. These relationships agree with the interpretation given to the parameters by Garg and Leibovich (1979), who used other variants on the Burgers and Batchelor velocity models. Substituting these values gives the expression for the q parameter that is frequently used as a measure of the stability of the flow:

$$q = \frac{\Gamma_o.\sqrt{\alpha}}{W_\infty W_{ex}} \qquad \text{--- (6.C.5)}$$

This can also be expressed as $q = 1.57\ V_{max}/Ws$, from which similar values of q are obtained. The variation of this stability parameter along the cyclone length is shown below:

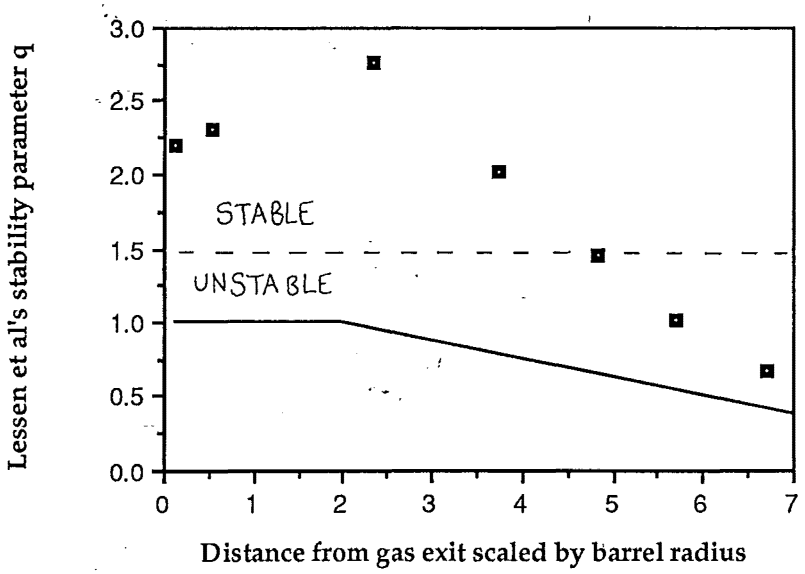

Figure 6.C.5: Variation of the q-stability parameter along the cyclone length.

6.C.2(c) Leibovich & Stewartson's extension of q-stability

Leibovich and Stewartson (1983) extended the analysis of Lessen et al (1974) and found a sufficient condition for the instability of columnar vortices to three dimensional perturbations in unbounded domains. The criterion took the form of a local Richardson number calculated for arbitrary inviscid profiles V(r) and W(r). Instability is predicted if:

$$N_{LS} = V.\frac{d\Omega}{dr}\left(\frac{d\Omega}{dr}\frac{d\Gamma}{dr} + \left(\frac{dW}{dr}\right)^2\right) < 0 \qquad \text{--- (6.C.6)}$$

This can be calculated using the profiles modelled in sections 6.B1 and 6.B2. For the axial locations summarised in Table 6.C.2 the following profiles of the N_{LS} number were obtained:

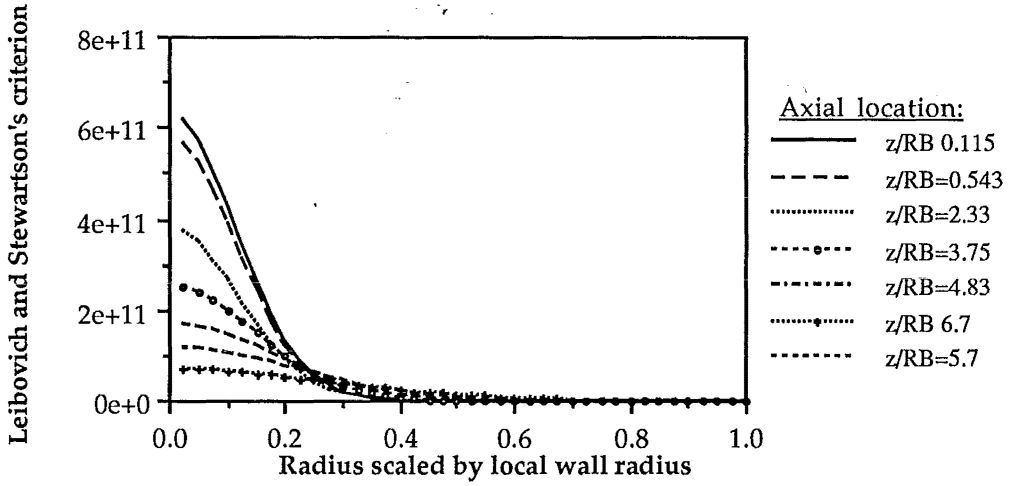

Figure 6.C.6: Radial profiles of the Leibovich-Stewartson criterion

The values are very large in the core, but decrease and pass through zero at larger radii. The values are largest at the gas exit end of the cyclone and reduce by almost an order of magnitude by the dust exit end. The approach to the stability limit of $N_{LS} = 0$ occurs closer to the wall in the direction of the dust exit, as shown in the following close-up of the previous figure:

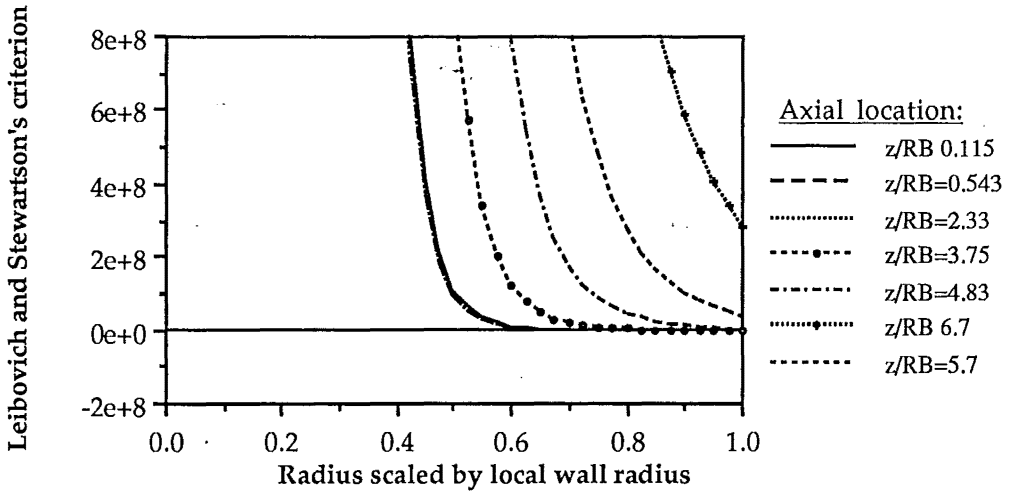

Figure 6.C.7: Detail of the approach of the N_{LS} number to zero

The locations closest to the dust exit do not feature negative values of the N_{LS} number and hence are considered stable. The axial locations that exhibit negative N_{LS} values are shown below in a further enlargement of the previous figure. The scaling radius of the ordinate has been changed to the barrel radius, which shows that the crossover to instability occurs at a constant radius despite the decrease in the wall radius. The effect of the contracting wall is to cut off the decreasing trend. The axial location z/RB =4.83 is grouped with the other locations, but the value of $N_{LS}(Rw)$ is still >0.

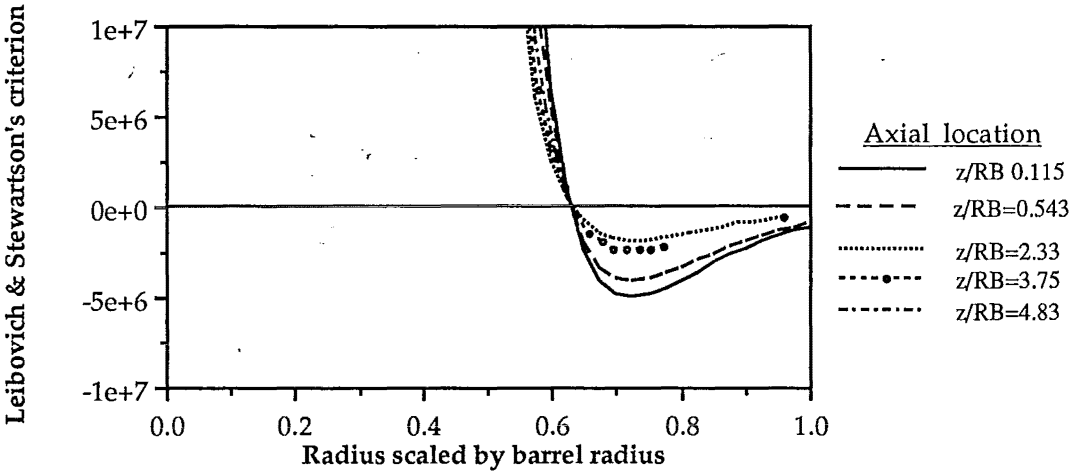

Figure 6.C.8: Detail of the negative region of the N_{LS} number

Leibovich and Stewartson (1983) use the same dimensionless velocity profiles as Lessen et al (1974) and relate the q parameter to the 'maximum pitch angle of the helices on which the fluid particles move in the flow', or $q = \tan^{-1}\{V/W\}$. In the 140mmØ and 750mmØ cyclones the pitot cylinder measurements of the angle of the outer flow to the axial plane were never more than 30° and hence the pitch of the helix near the wall is greater than 60° and q > 1.73. Typical values were less than 20° at the wall (q > 2.7). Larger angles were found in the core, approaching 60° near the axis (q = 0.6). Leibovich and Stewartson (1983)'s analysis predicted that q < 1.41 was a sufficient condition for the instability of the swirling flow.

6.C.2(d) The streamline divergence criterion of Brown and Lopez

The theory that vortex breakdown is a result of streamline divergence has gained favour again recently, and a criterion has been proposed by Brown and Lopez (1990). This predicts that breakdown will occur if the ratio of the helical angles of the velocity to the vorticity is greater than one at some upstream location.

The velocity and vorticity components are:

Tangential velocity: $$V_\theta = \frac{\Gamma_o}{r}\left[1 - e^{-\alpha_\theta . r^2}\right] \qquad \text{--- (6.C.7)}$$

Axial vorticity: $$\xi = 2\,\Gamma_o\,\alpha_\theta\, e^{-\alpha_\theta . r^2} \qquad \text{--- (6.C.8)}$$

Axial velocity: $W = W_\infty(1 + W_{ex}\, e^{-p.\alpha_\theta.r^2})$ --- (6.C.9)

Azimuthal vorticity: $\eta = 2W_\infty W_{ex}\, p.\alpha_\theta.r.e^{-\alpha_\theta.r^2}$ --- (6.C.10)

The ratio used by the criterion is: $\dfrac{\alpha}{\beta} = \dfrac{V_\theta/W}{\eta/\xi}$ --- (6.C.11)

and the vortex is unstable if α/β is greater than one. Substituting the expressions given above for the modelled velocity and vorticity components yields the expression for the criterion ration α/β in terms of the model parameters:

$$\frac{\alpha}{\beta} = \frac{\Gamma_o^2\,(1 - e^{-\alpha_\theta r^2}).\, e^{-(1-p)\alpha r^2}}{r^2.W_\infty^2 W_e.p.\,(1 + W_e\, e^{-p\alpha_\theta r^2})} \qquad \text{--- (6.C.12)}$$

The vortex breakdown will be associated with the development of a negative azimuthal vorticity component. The azimuthal vorticity given by equation 6.C.10 will always be positive, for the values of the parameters used. The Brown and Lopez (1990) theory predicts that the azimuthal vorticity will decrease and become negative if the α/β ratio is greater than one. The approach taken by Brown and Lopez (1990) does not involve calculating values of the azimuthal vorticity as the flow develops, nor does it calculate the value of α_o/β_o at different axial location until the criterion $\alpha_o/\beta_o > 1$ is satisfied. Instead, equation (6.C.12) is evaluated at some upstream location (where the flow is quasi-cylindrical) and if the criterion is satisfied, then breakdown is predicted to be possible at some downstream location.

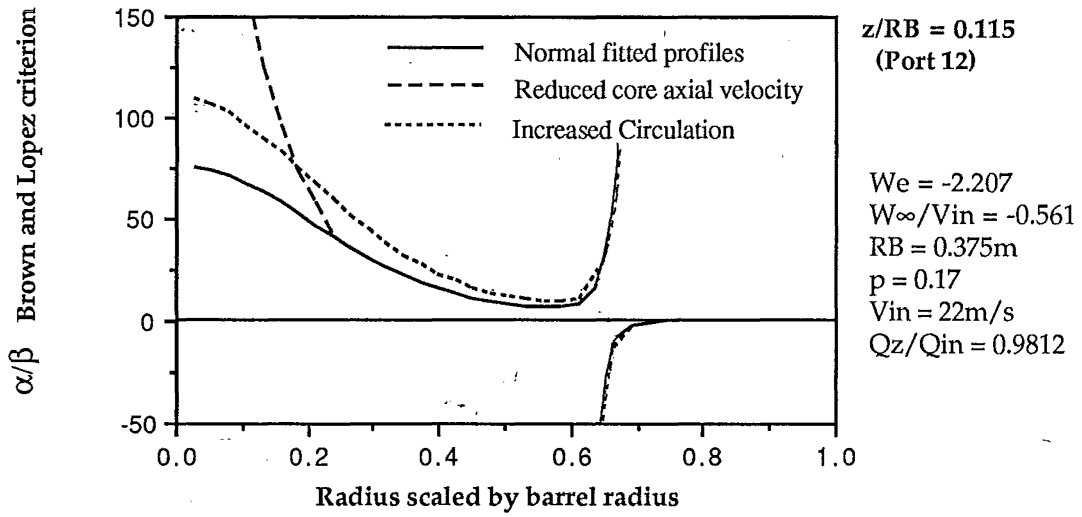

Figure 6.D.9: Radial profile of the Brown and Lopez α/β criterion for z/RB = 0.115, (Port 12)

The values of α/β are greater than one for all of the inner vortex region. The pole at r/Rw = 0.65 is due to the axial velocity crossing through zero. The effect of the circulation strength on the ratio was investigated by increasing the Γ_o parameter by 20%. This resulted in higher values of the ratio being obtained, particularly towards the vortex axis, consistent with increasing swirl being destabilising. The axial velocity model tended to overpredict the velocity near the axis, so the effect of reducing the axial velocity on the α/β ratio was

investigated. The axial velocity within r/Rw < 0.25 was reduced to W_r = W 10.r. This resulted in a sharp increase in the α/β ratio.

The radial profiles of the α/β ratio were then calculated for a range of axial locations in the cyclone, and the results are presented in the graphs below. The axial location of the positions is given as the number of barrel radii from the gas exit lip, and the total axial flow is assumed to decrease smoothly down the cyclone length, with 10% entering the bin. The graphs show the profile at the following locations:

z/R_B = 0.115, 0.543, 2.33, 3.75, 4.83, 5.7, 6.7

and the parameter values are as given in table 6.C.2.

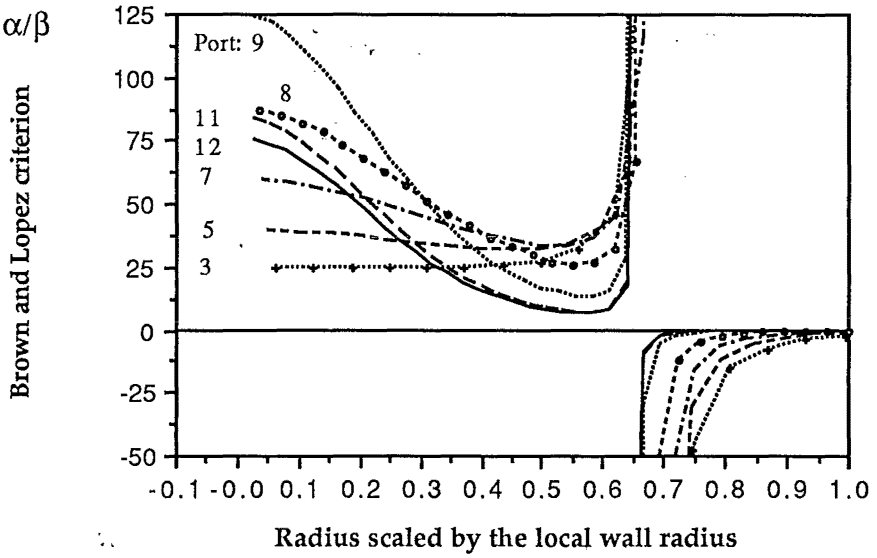

Figure 6.C.10 Brown and Lopez α/β criterion for various axial levels

In the outer vortex all locations gave negative values of the α/β ratio. The α/β ratio is again greater than one everywhere in the inner vortex, with a pole to infinity at the location of the zero axial velocity. The value of the ratio near the axis increased from Port 3 near the dust exit towards the gas exit. However, the highest values of α/β were not obtained at the gas exit, but at Port 9 . This trend was also shown in the effect of probe insertion on the cyclone pressure drop, with the greatest effect being found near the cone/barrel junction. At Port 9 the cross sectional area is the same as just at the level of the gas exit lip, but the flow has been reduced by the radial inflow.

In all regions of the cyclone the tangential velocity is positive and increases with radius, hence the axial vorticity ξ will be positive. The axial velocity in the outer vortex is negative and decreases with increasing radius, hence the azimuthal vorticity will be positive. For the outer vortex the α/β value will be negative. In the core of the cyclone the axial velocity is positive, and decreases with increasing radius, hence the azimuthal vorticity and the α/β value will be positive.

Waviness of the stream surface :

Brown and Lopez (1990) also present an inviscid analysis that enables a prediction to be made of the wavelength of the radial displacement of the stream surface. This is of interest since it may be related to the spacing of the recirculation regions observed with the helium bubble tracers, such as in figure 5.A.2. Equation 14 from Brown and Lopez (1990) is derived from consideration of the radial acceleration balance that leads to the divergence and contraction of the stream surface. This equation is reproduced below:

$$\lambda = 2.\pi.\sqrt{W_1}.\left(\frac{\Gamma}{\sigma_1^2}.\frac{d\Gamma}{d\psi} + \frac{dH}{d\psi}\right)^{-1/2} \qquad \text{--- (6.C.13)}$$

where W_1 is the axial velocity at a radius r_1 and σ_1 is the dimensionless radius at that location.

The gradient of the total head, H along the streamline can be expressed in terms of the gradients of the circulation and the azimuthal vorticity, resulting in :

$$\lambda = 2.\pi.\sqrt{W_1}.\left(\frac{2\,\Gamma}{\sigma_1^2}.\frac{1}{\sigma_1 W_1}.\frac{d\Gamma}{dr} - \frac{1}{r}\eta\right)^{-1/2} \qquad \text{--- (6.C.14)}$$

This was evaluated at three arbitrary values of the initial radius: of 0.028, 0.075 and 0.122m, for the 750mmØ cyclone profiles. The choice of the initial radius does not have a major effect on the wavelength that is predicted to be developed, as is shown below. Note that the wavelength is scaled by the initial radius, and the wavelengths are very short in the inner vortex, but rise rapidly in the outer vortex.

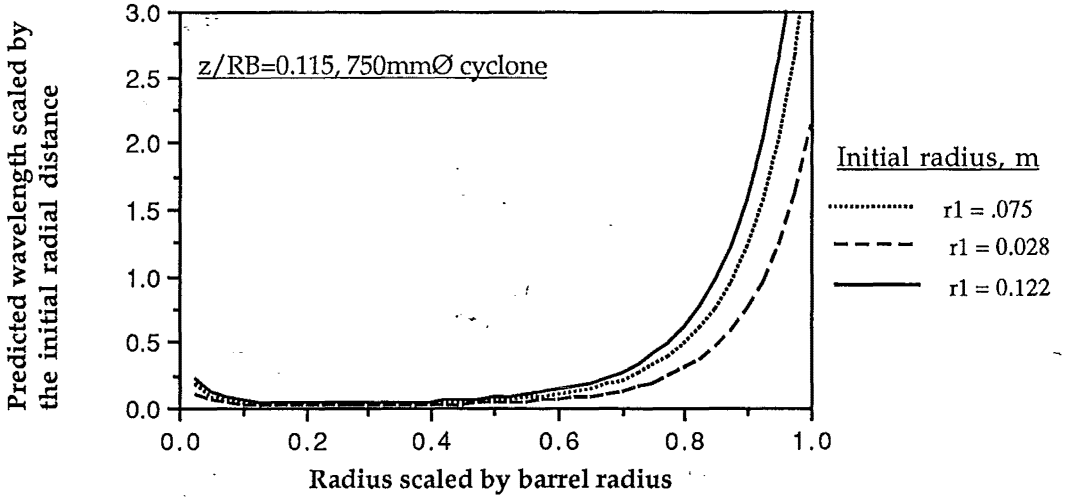

Figure 6.C.11: Dependence of wavelength prediction on choice of initial radius

Different axial locations show the same variation of the wavelength prediction across the radius:

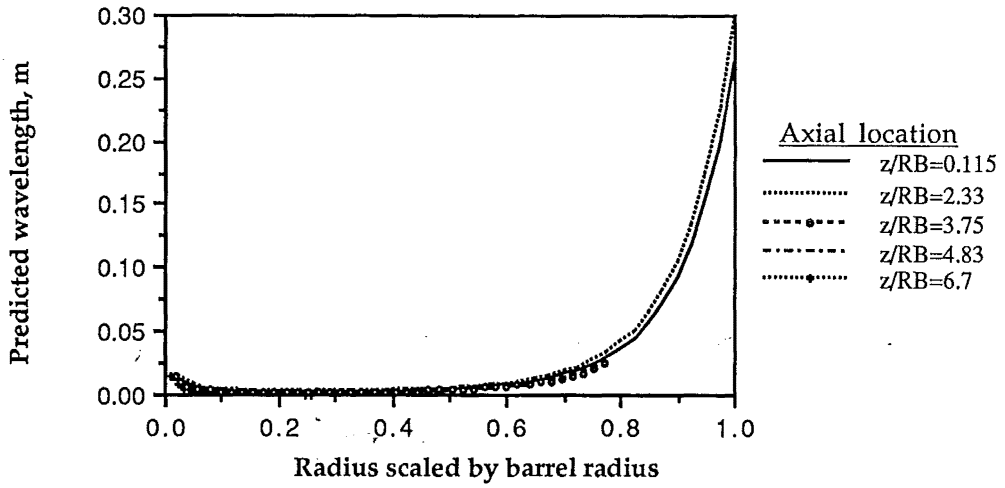

Figure 6.C.12: Detail of the predicted wavelength

and this similarity is continued right down into the fine structure of the small wavelengths. The oscillations in the stream surfaces of the cyclone vortex are predicted to be very small except near the axis and wall, which are regions where the agreement between the model and the velocity measurements is poor.

6.C.3 Stability of the flow inside the gas exit:

The gas exit flow has a different character from that of the main cyclone. The occurrence of a vortex breakdown in the gas exit was supported by the observation of a reversed flow near the axis, and a region at the level of the roof where the tracers were observed to recirculate. In addition, the profile of the wall pressure along the gas exit wall in the same area showed a localised regain in pressure similar to that observed by Kirkpatrick (1964) and Sarpkaya (1971) opposite to a breakdown in a tube.

The Rossby number can be used to examine the tendency of the core vortex to breakdown. In this case, there is evidence from the flow visualisation experiments that a breakdown does occur in the gas exit. By assuming that a breakdown occurred in the exit and resulted in a stagnant core, Abrahamson (1992) worked backwards from the Rossby number to give the magnitude of the axial velocity in the annulus around the bubble that was required for breakdown. Given the flow, the annular area was then defined, and hence the diameter of the core (which was assumed to have zero axial velocity) could be estimated. The size of the breakdown bubble could then be estimated.

Since the core vortex has to contract as it enters the gas exit, the Rossby number criterion predicts that the core vortex is stabilised against breakdown when it enters the gas exit, relative to the conditions in the cyclone body. However it is expected that the effect of the drag on the walls will modify the velocity components and result in unstable conditions at some distance downstream.

Measurements were available only for the 140mmØ cyclone with an inlet velocity of 23.8m/s so the parameters were selected to fit these profiles. The axial and tangential velocity profiles in

the gas exit were modelled in section 6.B1 and 6.B2, and the parameters determined were:

$R_B = 0.07$ m $R_w = 0.035$ m $\alpha_\theta = 2025\ s^{-1}$

$W_{ex} = -0.97605$ $W_\infty = 2.5235.V_{in}$ m/s $\Gamma_o = 1.367\ m^2/s$

The agreement with the tangential velocity profiles measured in the gas exit was good.

The profiles of the velocity and vorticity components are shown below:

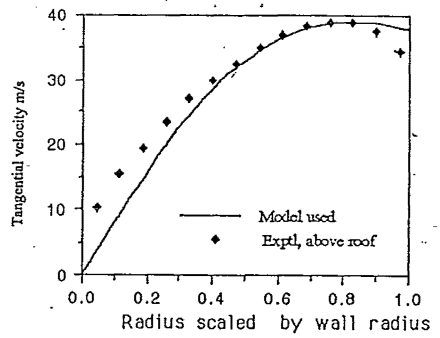

Figure 6.C.13: Tangential velocity profile

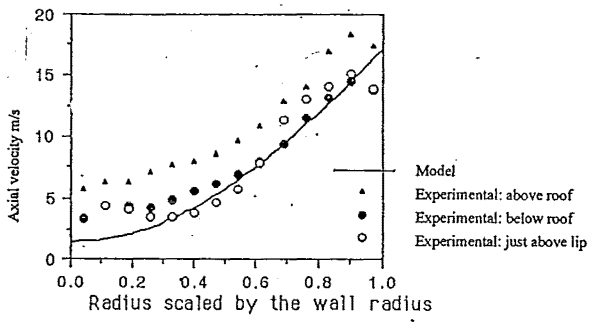

Figure 6.C.14: Axial velocity

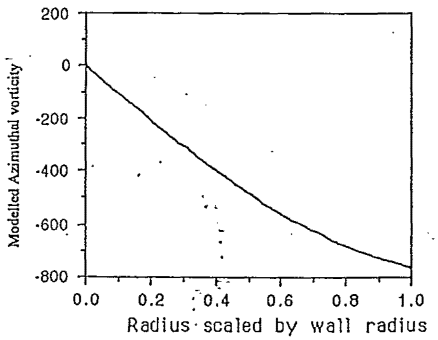

Figure 6.C.15: Azimuthal vorticity

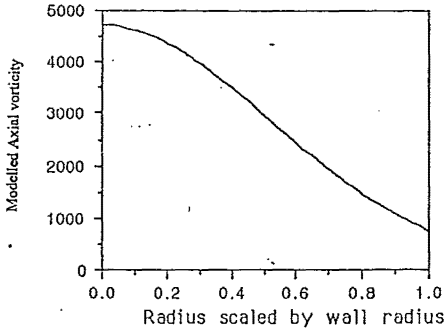

Figure 6.C.16: Axial vorticity

The resulting profile of the α/β criterion parameter for the gas exit is shown below:

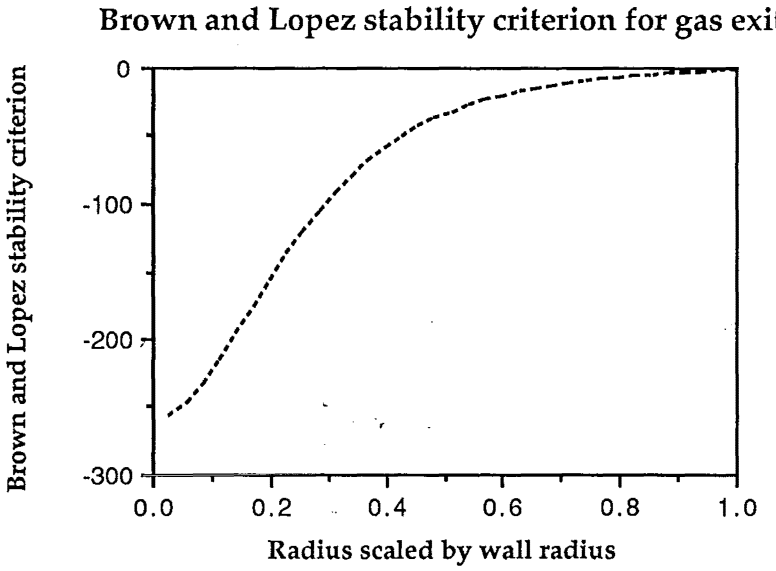

Figure 6.C.17: Brown and Lopez stability criterion in the gas exit.

It will be noted that the value is nowhere greater than 1, hence the Brown & Lopez stability criteria predicts that the gas exit flow is stable to vortex breakdown. This is expected to be generally true for the gas exit flow, since the α/β ratio will only be positive if all, or an even number of the components are positive. The tangential velocity profile in the gas exit are the same as those in the main body of the cyclone, but the axial velocity is positive and increases with increasing radius. The azimuthal vorticity will therefore be negative, and the α/β value will be negative at all radii in the gas exit, as is demonstrated by Figure 6.C.17 above. The development of the flow in the downstream direction would be expected to create a peak in the axial velocity at the axis, which may change the sign of the α/β ratio.

The Brown and Lopez (1990) α/β ratio is a necessary, but not sufficient criterion for the occurrence of vortex breakdown. The initial divergence of the streamlines is thought to be a result of viscous diffusion of vorticity, but the subsequent growth of the divergence requires an inviscid instability. This is provided by an imbalance in the radial force balance:

$$F_r = \rho\frac{V_\theta^2}{r} - \frac{dP}{dr} \qquad \text{--- (6.C.15)}$$

Brown and Lopez (1990) present contour plots of the regions of positive and negative F_r from their numerical calculations. The sign of F_r was estimated from plots of the radial pressure gradient, such as those presented in section 5.G. The regions of positive, neutral and negative values are presented in Figure 6.C.18:

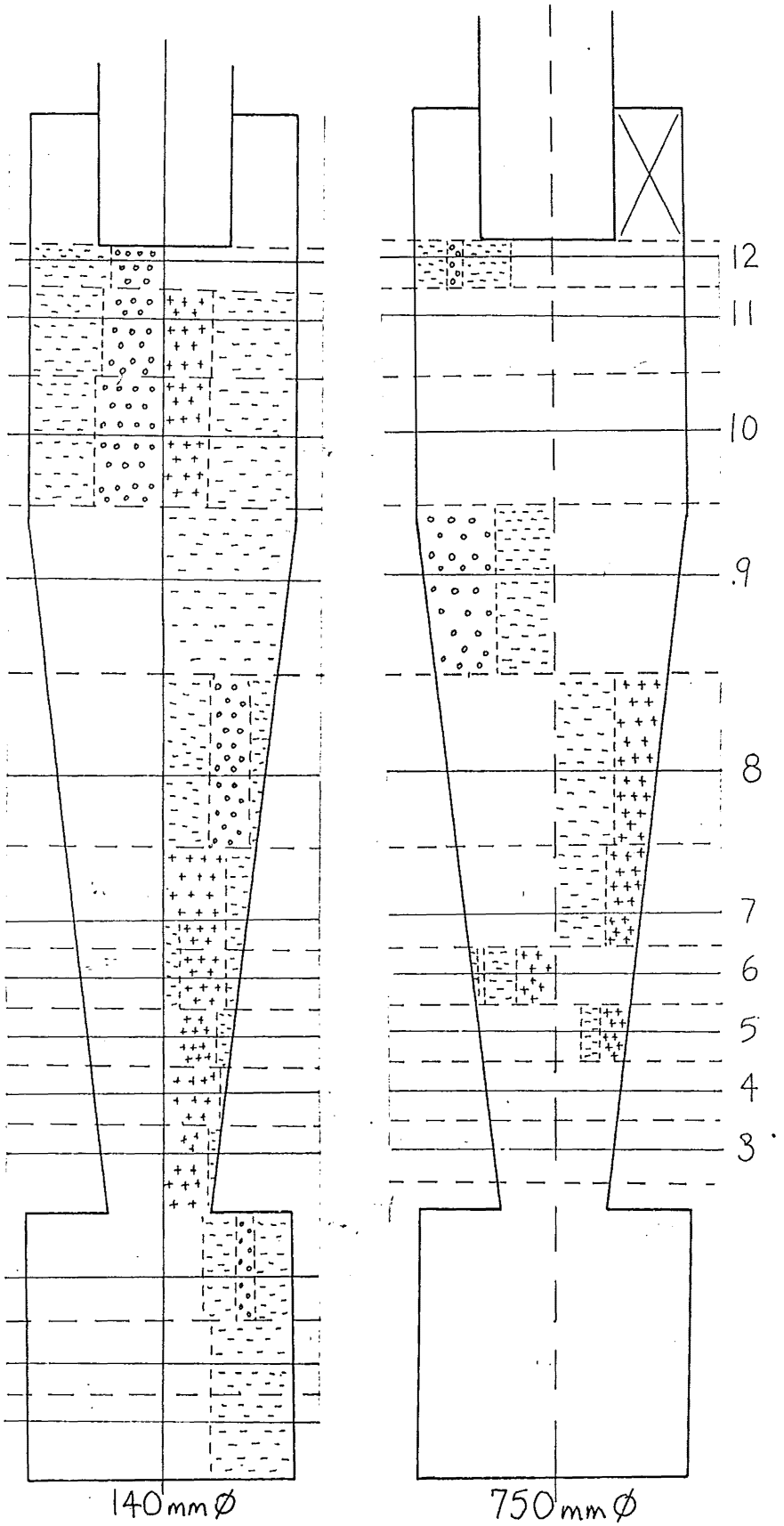

Figure 6.C.18: Regions of positive and negative values of the balance between $\rho\frac{V_\theta^2}{r}$ and $\frac{dP}{dr}$

Summary of stability criteria:

The existing criteria for determining the stability of the vortex have been evaluated using the velocity component models that were fitted in section 6.B1 and 6.B2. The criteria resulting from the perturbation instability analyses suggest that increasing swirl stabilises the vortex, which contradicts the large number of experimental observations that have been reported in the literature. Nevertheless, Garg & Leibovich found that the q parameter obtained from Lessen et al's perturbation instability analysis did drop below the critical level at the vortex breakdown location, and figure 6.C.3 shows this occurring in the cyclone in the lower cone region.

The criterion of Brown & Lopez (1990) shows the entire core vortex in the body of the cyclone to be unstable to vortex breakdown by the streamline divergence mechanism, but the different form of the velocity profiles in the gas exit resulted in a stable result for the gas exit. The stable/unstable predictions are not expected to be affected by changes of the order expected from errors in the velocity components, as the instability is determined more by the gross features of the profile such as the sign and slop.

As with the Rossby number criterion, there are problems in applying the vortex breakdown criteria to a flow that features a flow reversal and which may be viewed as being in the post - vortex breakdown state. In addition, the time-averaged velocities used mask some of the features, such as the presence of a reverse flow near the axis.

6.C.4: Dynamic stability of the vortex

The flow was also investigated in terms of the dynamic stability. Although this thesis has concentrated on the time-averaged behaviour, it was apparent that the flow was subject to rapid, large-scale changes in the flow, such as the reversal of the axial flow direction near the axis.

Photographs of the cottons using a fast triple flash indicated that the frequency of reversals of the cottons near the axis was of the order of 10Hz. This is comparable with the observations and calculations presented by Garg and Leibovich (1979). Using a Laser Doppler anemometer they measured the velocity in a confined swirling flow generated by swirl vanes in a through-flow tube. The continuous velocity signal was analysed for coherent low frequency oscillations downstream of the vortex breakdown, at conditions of Ω = 1.07 and Re = 11480 (based on the average axial flow and the tube diameter). The fluctuations were concentrated in the region near the axis, although the maximum axial fluctuations occurred off the axis at 13% of the wall radius.

Immediately downstream of the breakdown there were two peaks in the power spectra of 13.3 and 23.4 Hz, which could be harmonics within the experimental uncertainty. The coherent fluctuations contained a large fraction of the total energy contained in the flow fluctuations. Further downstream the peaks of the coherent fluctuations were not as prominent and contained a lower proportion of the fluctuating energy.

Both the bubble and spiral types of breakdown were examined by Garg & Leibovich,, and the coherent fluctuations were found to be more energetic for the axisymmetric form of breakdown than the spiral. The dominant frequencies for the spectra of the axial velocity fluctuations were

found to be the same as those for the azimuthal velocity spectra, but the location of the maximum azimuthal fluctuations were observed to occur near the axis. The presence of large oscillations in the tangential velocity at the axis is taken by Garg and Leibovich (1979) as evidence that the oscillations are associated with |m| = 1 wavenumbers, possibly a precessing vortex core.

Garg and Leibovich (1979) apply the linear stability results of Lessen et al (1974) to the mean flow in the wake, using the exponential equations discussed in section 6.B2. The frequency f of oscillations corresponding to a given normal mode of wavenumber is given by:

$$f = \frac{1}{2\pi r_t} k\left(\frac{1}{|W_{ex}|} - c_r\right)|W_\infty W_{ex}|\sqrt{\alpha} \qquad \text{--- (6.C.16)}$$

where c_r is a radial component of the wave speed, r_t is the tube radius, and k is a factor associated with the growth rate. The other parameters are fitted to the axial velocity profile as in section 6.B2. Garg and Leibovich (1979) calculated the frequencies expected for the m = –1 mode, and obtain reasonably good agreement with the experimentally observed frequencies. This is despite the theory being strictly valid only for linear disturbances, whereas the breakdown region is highly non-linear.

Hopfinger (1982) reported that typical vortex cores contain many propagating waves. In the flow examined by Hopfinger, there were 5.2 waves/sec travelling upstream and 2.8 waves travelling downstream. The waves were thought to be responsible for the stationary breakdown if a strong axial flow counters the forward propagation or drift of the breakdown in the direction of wave propagation.

Lopez (1990) observed that at high Reynolds numbers the breakdown recirculations in a closed cylinder with a rotating endwall did not settle down to a steady position, but oscillated back and forwards on the axis, as shown in the figure below

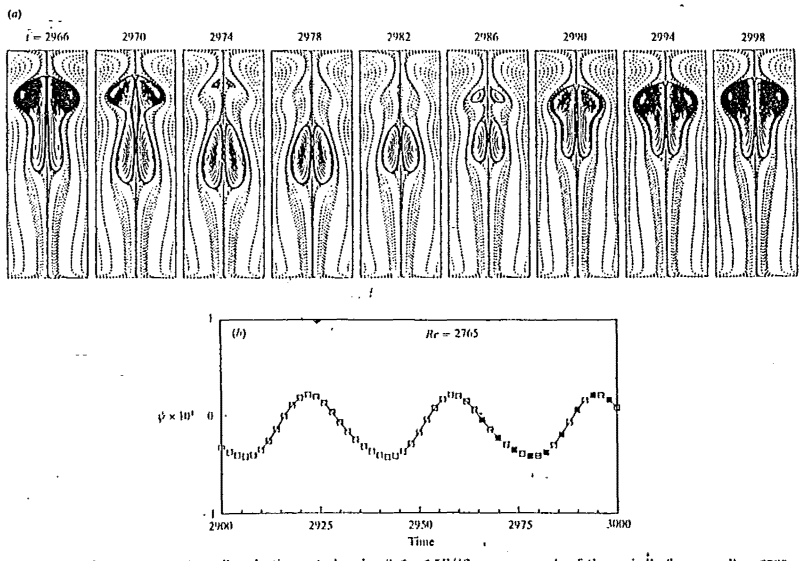

(a) Instantaneous streamlines in the central region $0 \leq r \leq 5R/12$ over one cycle of the periodic flow case $Re = 2705$, $H/R = 2.5$ at the indicated times. (b) Detail of the time history of $\psi \times 10^3$ in figure 5(b). The filled squares correspond to the figures in (a).

Figure 6.C.19: Periodic motion of the breakdown in closed cylinder from Lopez (1990)

This diagram shows the nature of the oscillations, and indicates that the period of one cycle is 36 dimensionless time units. The time is made dimensionless by multiplying by the

characteristic angular Ω, which is Ω = 13.8 s^{-1} for the results shown, at a Reynolds number of Re = 2765. Converting this to the conditions in the 140mmØ cyclone, where Ω = 2500s^{-1} indicates that the oscillations are expected to have a period of 14.4 milliseconds, or 70 Hz.

Lopez (1990) regards the breakdown flow as essentially inviscid, hence no adjustment should be needed to account for the change from liquid to the air in the cyclone. If a scaling is made using the turbulent viscosity for the cyclone from section 6.B.1 (rather than the kinematic viscosity used above) then the frequency of oscillations is predicted to be 30Hz.

6.C.5 Boundary layer stability:

The mean velocity profiles used to calculate the stability criteria earlier do not fit the flow in the boundary layer near the wall. It is also known that boundary layer flows are subject to rapid fluctuations and can contribute to vortex instability. The separation of the boundary layer could take place as well as, or instead of the core vortex breakdown. At present there is no criterion to predict the occurrence of the separation from the wall. It is possible that it is related to competition between the axial flow in the boundary layer and the swirl in the main flow, which would suggest a similar criterion to the Rossby number of Spall, Gatski & Grosch (1987), with suitably defined characteristic velocities.

The possible mechanisms for the development of instability in the cyclone were introduced in section 3.D, and the applicability of these will be examined further here. In summary, four possible causes of instability in the boundary layer of the rotating flow are identified:

- The Rayleigh instability due to the velocity profile
- Separation due to positive pressure gradients in the direction of flow
- Sharp changes in the wall angle
- The action of Gortler vortices on the curved surfaces, and the more general case of quasi-streamwise vortices such as hairpin and horseshoe vortices and other coherent structures of the boundary layer (such as typical eddies).

1. Radial pressure gradient and centrifugal instability:

The centrifugal instability described by Rayleigh predicts that low speed fluid is unstable if it is located at a greater radius than high speed fluid. This is shown by considering the effect of small radial displacement of an element of the fluid. In a stable fluid there is a restoring force to return the element to the original position, while in an unstable fluid the initial displacement leads to further displacement. The approximate pressure distribution resulting from the swirl motion is given by the reduced form of the radial momentum equation (with the turbulence terms omitted). This is $dP/dr = \rho.V_\theta^2/r$. Leibovich (1982) states that for the approach flows observed in experiments the pressure is in approximate balance with the centrifugal forces. If the centrifugal force is reduced, for example by a reduction in the tangential velocity through wall drag then the pressure gradient can drive the element of fluid inwards.

Ustimenko and Bukhman (1968) observed a sharp intensification of the fluctuating motion and turbulent transfer in the wall adjacent region. This was attributed to the decrease in tangential velocity with increasing radius in this region, which causes a hydrodynamically unstable flow zone, and the imbalance in the radial forces. The plots of the radial pressure gradient in section

5.G show that the radial pressure gradient is not always in balance with the centrifugal force, notably in some regions near the wall.

2. Axial static pressure gradient:

Like the vortex breakdown, the separation of the boundary layer would be promoted by positive pressure gradients in the direction of flow. In fact, as shown in Figure 5.J.4 the wall pressure gradient in the axial direction is negative between the inlet and dust exit. It could however become locally positive in the region of the local increase of the circulation versus length plot of figure 5.J.1, or the reverse core may provide an adverse pressure gradient inside the flow. The stability of the boundary layer is also dependent on the presence of a driving force provided by the pressure gradient. If the pressure gradient in the direction of the flow is positive it can cause the fluid to slow, and may form a stagnation point and separation of the fluid from the wall.

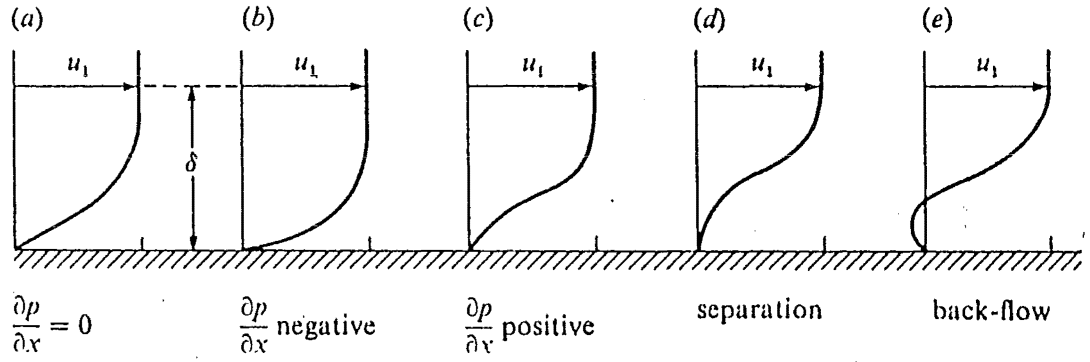

Figure 6.C.20: Effect of axial pressure gradient on the boundary layer velocity profile

3. Sharp change in the wall angle:

This is the most simple mechanism to describe the separation, and it fits in well with the theory of a vortex breakdown occurring at the dust exit. It is however restricted to the dust exit, and cannot explain apparent breakdown observations in regions without a sudden expansion.

4. Streamwise vortices and other coherent structures:

The theoretical and experimental research that has been carried out on the coherent structures in the boundary layer was reviewed in section 3.D. Although the research has concentrated on flat plate boundary layers, this has chiefly been for convenience, and the same features are expected to be present in curved surface boundary layers. However concave surfaces have been shown to be susceptible to the formation of a special type of quasi-streamwise vortices termed Görtler vortices, and these were reported by Swearingen & Blackwelder (1987) to have a much larger physical scale than the quasi-streamwise vortices that are formed in a turbulent flat plate boundary layer. The streamwise extent of the Görtler and hairpin vortices is reported to be similar, of the order of 1000 viscous length scales ($\sqrt{\nu x/U}$). The effect of the Görtler vortex is expected to be more significant than the hairpin or horseshoe vortices because of the larger size,

but the most significant contribution of either phenomenon is the destabilisation of the boundary layer by the creation of unstable layers of slow fluid above faster fluid.

The quasi-streamwise vortices in flat plate boundary layers are associated with the ejection of fluid from the boundary layer in a periodic fashion, and Sabry & Liu (1991) have shown that the Görtler vortices can transform into hairpin vortices and result in ejections from the wall. The dust rope on the wall has been related to the action of Görtler vortices on the wall by Abrahamson (1981). Mothes et al (1981) report that there is increased wall deposit formation for long cyclones and those with large cone angle (although this was reported to result in no major change in the collection efficiency). Meissner (1977) reports that a change in cyclone height and slope angle implies a change in the conditions of the cone boundary layer flow.

The Görtler number that is used to characterise the susceptibility of the vortex to this type of instability is satisfied by the conditions in the cyclone.

$$G\ddot{o} = \left(\frac{U_1\,\theta}{\nu}\right)\left(\frac{\theta}{r}\right)^{1/2} \qquad \text{--- (6.C.17)}$$

Although Floryan & Saric (1984) specify that ν is the kinematic viscosity, Tani (1961) stated that the turbulent viscosity should be used when dealing with turbulent boundary layers, and a constant value could be applied across the boundary layer. The turbulent viscosity that was fitted in 6.B2 was used, and the external velocity near the wall is taken as approximately equal to the inlet velocity of 22m/s. The momentum thickness is estimated as 5mm for the 140mmØ cyclone and 24mm for the 750mmØ cyclone. The values of the Görtler number are then:

140mmØ cyclone Gö = 10 at the Barrel rising to 16 at the dust exit
750mmØ cyclone Gö = 13 at the Barrel rising to 22 at the dust exit.

If the kinematic viscosity was used the values in the barrel rise to 1900 and 8500 for the 140mmØ and 750mmØ cyclones respectively. The estimate of the momentum thickness was made by examining the velocity profiles from the pitot cylinder and the hotfilm anemometer. The former obviously suffers from a lack of resolution, but the hot film also had problems in this regard, due to the significant length (in the radial direction) of the 45° probe used. As the probe was traversed out from the wall recess, the amount of the probe that was exposed to the airstream increased and this sharp rise in the velocity masked the true boundary layer velocity profile. The boundary layer thickness in the 140mmØ cyclone that was estimated from the hot film velocity profile was of the order of 3mm or 4% of the barrel diameter, similar to the radial extent of the probe. Examining the Pitot cylinder velocity profiles in the 750mmØ cyclone suggests that the boundary layer was 15mm or 4% of the radial profile. The momentum thickness was estimated from the hotfilm profile for Port 7, midway down the cone in the 140mmØ cyclone. This involved integrating equation 3.D 10 for the discrete data. The resulting momentum thickness was 1/7 th of the estimated boundary layer thickness.

The spacing of the Görtler vortices in the spanwise direction (λ_c) is shown by Floryan & Saric (1984) to be given by the Görtler wavelength parameter Λ :

$$\Lambda = \frac{U_1\,\lambda}{\nu}\left(\frac{\lambda}{R}\right)^{0.5} = 44.29 \qquad \text{--- (6.C.18)}$$

$$\lambda_c = \left(\frac{44.29\,\nu\,\sqrt{R}}{U_1}\right)^{2/3} \qquad \text{--- (6.C.19)}$$

The change in the Görtler vortex behaviour between different scales of cyclones, and along the length of the cyclone is of interest. As seen above, the spacing is predicted to be dependent on the radius of curvature, the viscosity and the freestream velocity. The latter has been shown to be similar between different scales of cyclones of the same geometry, and also between different axial positions in the cyclone. The radius of curvature is proportional to the cyclone diameter, while the turbulent viscosity has been shown to be proportional to the diameter to the (-0.921) power (although this was a turbulent viscosity fitted to the properties in the body of the cyclone). Given the same velocity outside the boundary layer, the dimensional spacing of the Görtler vortices will be proportional to $D^{-0.3}$. This suggests that the smaller the cyclone, the larger the spacing will be. On the other hand, in a given cyclone the turbulent viscosity is approximately constant over the cyclone length, leaving the radius of curvature as the dominant variable and the spacing proportional to the 1/3 power of the local radius. As the dust exit is approached, Görtler vortices are established with smaller spacings.

For the 140mmØ cyclone with $U_1 = 22$m/s, $\nu_T = 0.003$ and R ranging from 0.07 to 0.0265 the critical wavelength is 14mm in the barrel and 9.8mm at the dust exit. In the 750mm cyclone the wavelengths are 53mm in the barrel, reducing to 39mm at the dust exit. The wavelengths are a smaller fraction of the radius in the larger cyclone. It is found that the spacing of the Görtler vortices is determined by the conditions that prevail at the initiation of the vortex, and this spacing is maintained in the downstream direction. Note that this wavelength prediction specifies the lower bound, and larger wavelengths are possible. Hence a spacing determined at an upstream location is still viable when the Görtler vortices move to a location with a smaller radius of curvature. It is postulated that the combination of boundary layer growth and the reduction in the surface area in the cone results in a strengthening of the Görtler vortex phenomenon towards the dust exit. This is supported by the increase in the value of the Görtler number with decreasing radius of curvature. Larger values of the Görtler number are associated with higher amplification rates.

The Görtler vortices result in the pumping of fluid alternately away from and towards the wall. This has been linked with the formation of the dust rope in the cyclone. This loss of boundary layer fluid and dust from the wall is an important consideration in modelling the dust collecting process in the cyclone.

There is a limit to the streamwise extent of the Görtler vortices, after which they breakdown and are replaced by another set. The length is reported to be of the order of 1000 viscous lengths, or roughly 1000 times the thickness of the boundary layer. This suggests that at least one such occurrence is expected along the cyclone length. By themselves the Görtler vortices represent a small but important fraction of the boundary layer flow. However Hall (1988) found that the major effect of the Görtler vortices is to make the boundary layer highly receptive to rapidly growing Rayleigh modes of instability. This could result in the destabilisation of the boundary layer to the point where it separates from the wall, and flows inwards. This would provide a much larger inflow than the pumping action of paired vortices. Criteria to predict the position at which this would occur are not available, but it is a tendency that increases in the downstream direction, and presumably if it is to occur it will be within the order (1000 viscous lengths) lifetime of the Görtler vortices. Further destabilisation of the boundary layer flow is reported to be caused by the presence of cross flow, which will also be present in the cyclone due to the change in the helical angle of the flow away from the wall.

The ejections from the boundary layer are expected to occur along the entire vortex length at irregular spacings. The order in which the inrush and ejections occur has been debated in the literature for a number of years. A recent review by Smith et al (1991) indicated that the current theories support the occurrence of the inrush after the eruptive events. The ejections are localised but the balancing inflow may be spread over a larger area by the boundary layer. For example, Tran (1981) reported that the dust rope "bounced like a spring in tension", which could be due to axial accelerations of the boundary layer to fill the gap left by an ejection.

It is proposed that the boundary layer separation and ejections become more likely or prevalent as the dust exit is approached. This is supported by the increase in the Görtler number at smaller radii of curvature. In conjunction with the increased occurrence the amount of inflow will become more significant compared with the axial flow that remains at that level. Tran (1981) and Bloor & Ingham (1976) show that the volume flow in the boundary layer can account for all of the flow that enters the bin, hence the flows become more significant in terms of the volume rate. In addition, the distance between the wall and core is less.

Experimental evidence in support of boundary layer separation:

Any of these mechanisms could be sufficient to form a type of vortex breakdown by capping the low pressure vortex centre and effectively ending the vortex. The flow visualisation measurements did not show any conclusive examples of the boundary layer separating possibly because it has a less coherent form than the breakdown bubble. Little information about the outer vortex flow was revealed by photographs of the helium bubble tracers in the cyclone. This was partly due to the tracers moving into the axis quickly, and also because the combination of the low illumination and the high velocities in the outer flow precluded a bright trace in the negative. The injection of 'fog' at the cone wall indicated high inflows in some regions, and low inflows elsewhere, particularly at 60mm above the dust exit. Some cotton streamers also appeared to show localised high radial flows.

Radial velocities due to the boundary layer separation will be distinguished from the natural radial inflow of gas that occurs down the whole length by a matter of location and scale. The Boundary layer separation will result in high radial velocities in that region of the cyclone. This could be the cause of the inflows observed with the fog injected at the wall. For some locations the inflow of the fog took the form of 'fingers' peeling inwards, while in others the inflow was more uniform. Near the dust exit (at Port 4) the fog appeared to be kept against the wall. The high inflows could be explained by gas moving into the core after separating from the wall, or alternatively the high inflows could be the normal case, which is suppressed in some areas by the intermittent ejection of gas from the core flow, as observed by Bandyopadhyay et al (1991).

The best test of the boundary layer separation theory would be measurements of the boundary layer thickness at different heights in the cyclone. These measurements have been carried out with a hotfilm probe, but it appears that the resolution of the probe may be insufficient to give conclusive results. In any case the time-dependent thickness would be required, whereas most techniques will only be able to yield the time-averaged thickness. An example of the boundary layer profile, and the variation of the estimated thickness along the cyclone length are given in figures 5.B.10 - 5.B.12.

Chapter

7

PROPOSED VORTEX STRUCTURE THEORY

"For testing explanatory theories it is a necessary but not sufficient condition that there should be correspondence with the known facts. A 'good' explanation will also have a high degree of explanatory power, will deal with the interesting and relevant aspects of the problem, will proceed from some simple, unifying idea, and above all, will have a high degree of refutability or testability".

paraphrased from "Conjectures and refutations" Karl Popper,
Routledge & Kegan, London (1969)

"Science is nothing without generalisations. Detached and illassorted facts are only raw materials, and in the absence of a theoretical solvent, have but little nutritive value".

Lord Rayleigh (1884).

In this section the theories that have been published in the literature are examined, with regard to the observations and results from this study. As stated in the introduction, the main aim of this thesis is to investigate the structure of the cyclone vortex and the mechanisms responsible for forming it. The experimental results from this study will be used to test for support of the existence of a natural length or vortex breakdown, as proposed by the theories of Alexander (1949) and Abrahamson & Allen (1986).

7.A: Examination of the structural theories:

As mentioned earlier, the existing theories of the structure of the cyclone vortex assume a flowfield of convenience without explanation of the formative mechanisms. Most theories have utilised the "Natural vortex length" that was proposed by Alexander (1949) as the longest distance that the vortex can persist for, and have assumed that this length is measured from the lower lip of the gas exit. The Alexander Natural vortex length (L_{Al}, as given by equation 2.1) is independent of velocity, and for the Stairmand High efficiency design it is equivalent to 2.5 barrel diameters, thus the vortex is predicted to extend no closer than 1 barrel diameter to the dust exit, or between Ports 6 and 7 for the standard geometry. Although the efficiency predicting models of Dietz (1981) and Leith & Licht (1972) assume a finite length of the vortex as predicted by the 'Natural vortex length' of Alexander (1949), there is no attempt to explain the mechanism responsible for the termination.

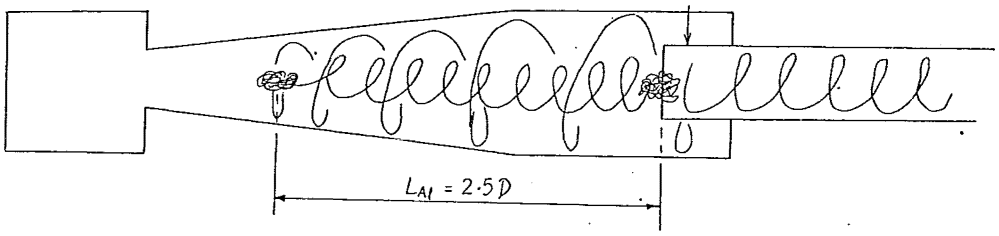

Figure 7.1: The application of Alexander's natural vortex length to the Stairmand High Efficiency geometry.

The initial application of the concepts of vortex breakdown to the description of the cyclone vortex structure was by Abrahamson & Allen (1986). They proposed that the vortex was capped at each end by breakdowns with a recirculating region of gas (or 'gas bubble'), with the upper breakdown stabilised at the gas exit lip and the spacing between the two breakdowns determined by Alexander's 'natural' length, which depended on the geometry, and swirl strength. The position of the lower breakdown relative to the dust exit would then vary as the cyclone geometry was varied, and for short lengths and large dust exit diameters (relative to the gas exit diameter) the breakdown could enter the bin.

Abrahamson & Allen (1986) used this theory to account for the effect of cyclone geometry on the classification number (a measure of the steepness of the grade efficiency curve). The results presented in this thesis suggest that the actual gas exit vortex breakdown is 1 - 1.5 barrel diameters downstream from the gas exit lip, and hence the position of the lower breakdown would be predicted to be higher in the cone - level with the cone/barrel junction.

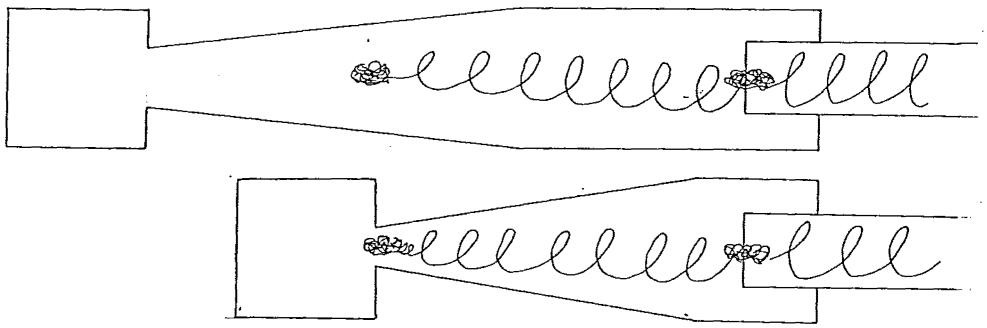

Figure 7.2: Constant spacing of vortex breakdowns in cyclones of varying length

This eliminates one of the reservations about the applicability of the Alexander Natural vortex length: namely that it was found for what was effectively a cylindrical cyclone - as this position is at the end of the cylindrical section. However, Alexander measured the vortex length from the lip of the gas exit, and presumably did not intend the reference location to be moved further down the gas exit.

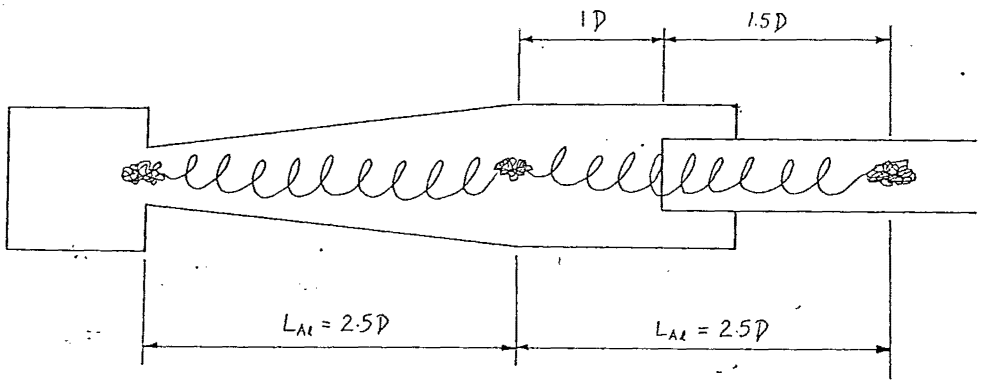

Figure 7.3: Possible breakdown position predicted by Alexander's length

As shown in figure 2.9 Alexander (1949) used cyclones that exhausted to atmosphere as well as those that operated under vacuum. Care is needed when using predictions of vortex length on cyclones with a different exit arrangement to the original study. Studies that have been made to examine the natural length of the vortex (such as Alexander (1949) and Bryant et al (1983)) have varied the cyclone body length, but have kept the same inlet and exit configuration. The results presented in this thesis suggest that the position of the breakdown is strongly affected by the cyclone geometry, particularly the exit geometry.

Vortex breakdown at the cone/barrel junction:

There are several interesting features about the possibility of a vortex breakdown being situated at the junction of the cone and the barrel, as is predicted by the Alexander natural length. Since the barrel section has a constant area, the radial inflow will weaken the vortex by lowering the average axial velocity, and cylindrical walls are found to destabilise vortices compared with conically reducing walls. The effect that inserting a probe had on the pressure drop was the

greatest in this region. The wall pressure profiles shown in figures 5.J.4-5.J.6 all showed a change to a steeper gradient just below Port 9, at the start of the conical section.

The helium bubble tracers were often recorded moving into the centre around or just below this position, as shown in Figure 5.A.2. The tracers started from the outer vortex, appeared to start to move in the direction of the gas exit, and then reversed to travel towards the bin near the axis. A vortex breakdown could account for high radial inflows that took the tracers in to the centre. When the cyclone bin had dust in it there were pulses of dust ejected from time to time. These pulses seemed to slow down and be re-collected when they reached the barrel section, although some dust passed out the exit. Larger particles were collected to the wall, and were observed to remain rotating around the wall at the cone/barrel junction for long periods (of the order of 20 seconds) until dissipated by the gradual loss of dust to the boundary layer flow. The position of this recirculation was not always right at the junction, for example with the 'Shortest' geometry the circulation path was near to port 8.

However, the normal dust rope that was observed when dust was being fed continuously to the cyclone showed no deviation from its normal helical path in this region. This is an important observation, as Alexander developed the theory based on the behaviour of streaks of water on the wall. In addition, the flow visualisation was not able to show the sort of long-lived structure that was observed in the gas exit, and the angle of the flow near the wall measured by the Pitot cylinder does not show any change in this region. Hence the existence of a vortex breakdown involving the outer flow, that is paired with the gas exit vortex breakdown is ruled out.

A vortex breakdown in the lower cone region could be expected if Alexander's natural vortex length was measured from the gas exit lip, or if the vortex length was extended beyond that predicted by equation 2.1 because of the contracting walls of the cone.

7.B: The proposed Vortex structure theory

The shortcomings of the paired vortex breakdown theory of Abrahamson and Allen (1986) required the proposal of modified and alternative structures and mechanisms. Some of the experimental observations that a successful flow theory needs to allow for include:
- The slope of the grade efficiency curve. (see Abrahamson & Allen, 1986)
- The effect on the Pressure drop of increasing the cyclone length. (Abrahamson, 1985)
- The varying influence of leaks into the bin on different geometries (Tengbergen, 1955)
- The two concentric axial reversals of the vortex
- Axial non-uniformities in the radial inflow between the outer and inner vortices.
- The asymmetry of the velocity profiles
- The effect of geometrical changes on the performance.
- The sharp change in profiles of the axial static pressure and wall-axis pressure gradient.
- The recirculating zones along the axis indicated by the Helium bubble tracers
- The absence of visual evidence of recirculating regions involving the outer flow in the cone or at the dust exit.

This study aimed to look for evidence of vortex breakdown in the cyclone, and its position compared with that predicted by Alexander's equation, in conjunction with recent theoretical developments and reports of experimental studies of vortex breakdown. Different types of breakdown were considered, and other explanations for the structure of the cyclone vortex were advanced. The rest of this chapter will outline the proposed vortex structure and the supporting arguments and results.

Flow visualisation of the cyclone geometries examined in this research showed no indication of multiple vortex cores (such as described by Church et al (1979)) being present in the cyclone. These would be expected to show up as disturbances to the helium bubble tracer paths or the cotton streamers away from the axis. It is possible that the constriction of the small angled cone does not provide enough room for this to develop, or the form of the multiple core is disguised (such as by being twisted around each other). Previous observations showing multiple cores have been in short, squat spray driers (Reydon & Gauvin, 1981) or tornado simulators (Ward, 1972; Church et al, 1979). As many as five concentric changes in axial direction in squat swirl chambers have been reported, and as the length to diameter was increased the flow changed to being directed completely downwards. Similarly, the attachment of the vortex core to the wall (Muschelknautz & Krambrock, 1970) was not observed in this study, and it seems that previous observations of this phenomenon were made for cylindrical cyclones of lengths in excess of those typically used in cyclones.

7.B.1: Basic structure of the proposed model:

The tangential inlet to the cyclone produces a strongly swirling flow in the outer annular region of the cyclone with an axial component directed towards the dust exit. The axial flow measured with the pitot cylinder and shown by the visualisation experiments is in agreement with the commonly assumed structure viz: an outer vortex directed towards the bin, with an inner (or core) vortex with the axial component directed towards the gas exit. The visualisation experiments with the helium bubble tracers also showed a third cell to the vortex structure, travelling inside the core vortex, near the axis, in the direction of the bin. This "near-axis reverse flow" will be examined in more detail in later sections.

At the level of the dust exit approximately 10% of the inlet flow remains in this flow; the remainder has moved inwards and joined the core vortex. The core vortex starts from this region with 10% of the flow and accumulates extra flow with height until it reaches the gas exit, through which all of the inlet flow leaves the cyclone.

The radial velocity of the gas is usually calculated by assuming that the inflow is uniformly distributed along the cyclone length. This is supported in general terms by the velocity profiles, as if there was no inflow in the upper region of the cyclone, the axial velocity would increase as the area reduced along the cone. Since the profiles are approximately uniform there must be a reduction in the total flow along all of the cyclone length. The radial inflow is a natural feature that is also observed in cylindrically confined, and unconfined, vortices. Despite the reduction in the total axial flow, the contracting walls of the cone serve to keep the axial velocity approximately constant along the cyclone length, as shown in section 5.B. The average inflow velocity would be expected to vary between different cyclone geometries depending on the cyclone length. As pointed out by Abrahamson (1981) there may exist an optimum length, where the uniform radial inflow matches the required supply of angular momentum. The amount of flow that reaches the bin could be self-regulating - with a balance between the resistance to the inflow, and that incurred by the axial flow towards the bin.

The visualisation of the flow with the fog tracer showed radial inflow velocities or radial diffusivities that varied along the cyclone length, and had values that were an order of magnitude greater than the calculated average flow. At Port 8, near the cone/barrel junction, the fog showed a uniformly high inflow. In the mid cone region, the fog tended to move inwards in fingers in a ragged fashion, while near the dust exit there appeared to be very little inwards movement over the half revolution that was visible. These three extremes are shown in figures 5.A.8 -5.A.10 (Plate 4), and are summarised below:

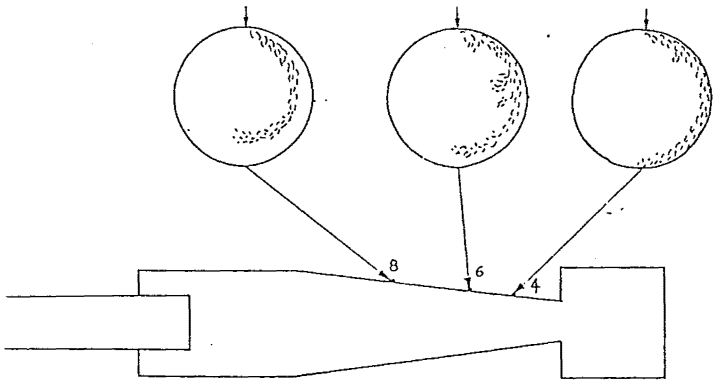

Figure 7.4: Radial inflow behaviour shown by fog tracer, summarising plate 4.

The rapid inwards movement suggested that the average convective inflow was dominated by the turbulent diffusion or localised ejections from boundary layer instability. Either of these would transport particles from the wall into the centre and hence the region of lower inflow near the bin entrance is of interest.

The non-uniformity of the radial inflow has been considered by Stairmand (1951), who noted that local values may exceed the mean by a factor of 2 or 3. The effect of a doubling of the inward drift velocity would result in some particles 40% larger than the cut size reaching the exit. Pervov (1974) mentioned the use of an 'unswirling device' in the gas exit to smooth the 'large radial non-uniformities that were present in high capacity cyclones, but suggested that in high efficiency cyclones these radial flows were already smoothed over the length. High capacity cyclones are generally shorter and squatter than high efficiency cyclones.

The observations of vortex breakdown in a tube reported by Escudier, Bornstein and Maxworthy (1982) included features that are apparently related to the radial inflow. Their apparatus introduced water tangentially to a tube, in which the following two features of interest were observed:-

1. The outer flow, outside the core appeared to consist of a series of vortex-ring structures spaced more or less equidistantly along the length of the tube and spanning the annular gap between the outer wall and the vortex core. The rings appeared to be driven "by the centrifugal instability of the boundary layer at the outer wall"
2. There was a sharp transition between the core and the outer fluid. Pieces of fluid were seen to be torn from the core in a manner reminiscent of that observed by Maxworthy (1974, 1977) for turbulent vortex rings.

Escudier et al (1982) suggest that the core interface acts a source for very weak vorticity in the outer region, which is then mixed by the large scale ring vortices.

7.B.2: Boundary layer separation mechanisms:

The non-uniformity in the radial inflows is thought to be related to ejections of boundary layer fluid from the wall, and the transport of these inwards due to an imbalance in the radial forces. The instability of the boundary layer was considered in Chapters 3.D and 6.C, and four mechanisms identified for the loss of fluid from the boundary layer. Under normal conditions, the axial and radial gradients of the vortex would be expected to give stable boundary layers, but sharp changes in the wall angle and the presence of quasi-streamwise vortices in the boundary layer can result in the separation of the boundary layer.

Both forms of quasi-streamwise vortices (Görtler vortices or hairpin/horseshoe vortices) result in ejections of low speed fluid away from the wall, and although these would not reach far from the wall, it has been shown that this can lead to unstable inflexional velocity profiles in the boundary layer that lead to its separation from the wall. Slow moving fluid at large radius would not be in balance with the radial pressure gradient. The radial force profiles outside of the boundary layer were shown in section 5.G and figure 6.C.18. Some regions were shown to be out of balance, which could assist the inward movement of ejections.

Any ejection, whether the initial boundary layer ejection, or the large-scale inflow must be balanced by an inrush. At present there is no consensus in the literature about the source of the inrush into the boundary layer. Offen and Kline (1975) consider that it originates from within the boundary layer in the log law region, while Kline and Robinson (1989) hold that it originates from further out, from the outer region. It has been suggested by Gad el Hak & Hussain (1986) that the ejections are the consequence of inrushes. This was found by creating inrushes by applying suction to the boundary layer on a flat plate. However, more recent research (reviewed by Smith et al, 1991) supports mechanisms in which the inrush follows the ejection.

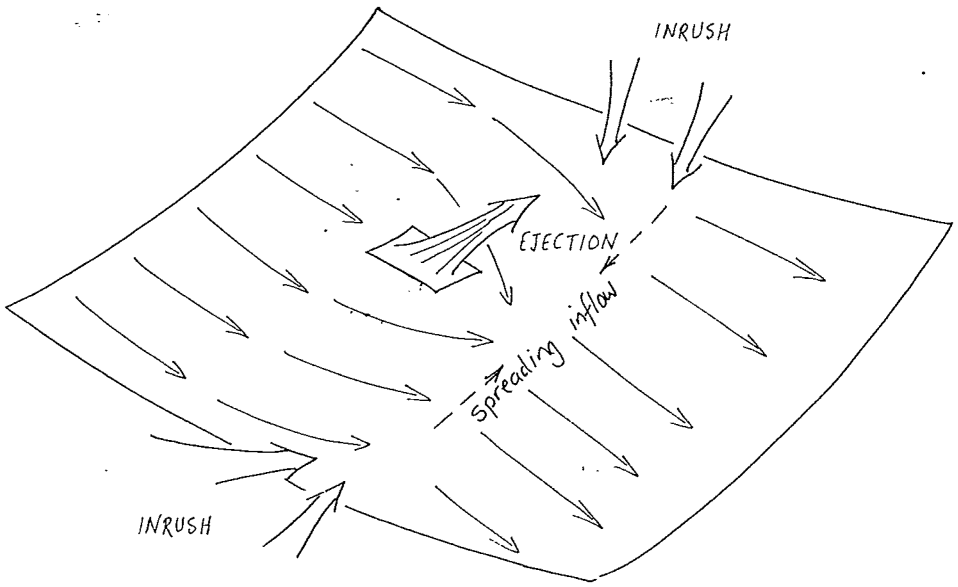

Figure 7.5: Spreading of the boundary layer to balance the ejection.

In the cyclone the ejection is postulated to be balanced by an acceleration (or stretching) of the upstream boundary layer to fill the gap. This is consistent with the observation of Tran (1981) that the dust rope acts like a coiled spring. This inrush from the adjacent region of the

boundary layer would itself need to be balanced by a flow from the outer vortex into the boundary layer. The boundary layer spreads the area that the inflow is acquired over, hence the ejection is a more localised flow than the inflow.

Radially outwards velocities were indicated in some areas by experimental measurements including the pitot cylinder radial velocity and the mass balance on the integration of the axial velocity. In addition, the visualisation experiments with fog filaments showed regions where the radial inflow was reduced. The regions of low radial inflows were in the same regions that low mean yaw angles at the wall were found.

Theory from the literature, such as Floryan (1984) predicts that both the Görtler vortices and the hairpin vortices strengthen as the radius of curvature decreases, that is towards the small end of the conical section in the cyclone. In the case of the Görtler vortices, the spacing of the vortices is determined by the conditions at their initiation, and this spacing is reported to be maintained downstream. Hence the wall curvature was thought to be only of importance in the incipient development of the vortices. It should be remembered that the vortices will be breaking down and reforming along the cyclone length, so that the change in wall curvature will alter the characteristics of the boundary layer flow.

The Boundary layer must separate at the bin entrance, and it is possible that the flow will also separate in the cone, and the boundary layer will rebuild to some extent before separating again at the bin entrance. This would allow the theory to account for the changes in the wall profiles observed in the cone (in measurements such as the wall circulation, the wall static pressure or the pitch of the flow at the wall). The critical condition for separation should allow for a dependence on the flow, the cone angle and the cyclone length. If the mechanism for the separation is the breakdown of the Görtler vortices then the approximate lengthscale according to Swearingen & Blackwelder (1987) is of the order of 1000 viscous lengths, or 1-3m in the 140mmØ cyclone. This is measured along the helical path, so several growth and breakdown cycles are possible along the cyclone length.

7.B.3: Observations of Vortex length

The flow visualisation experiments carried out in the course of this research did not reveal any structure in the lower cone that resembled a vortex breakdown bubble, or clearly showed the termination of the vortex. Other researchers using transparent conical cyclones have also failed to observe any such structures, including van Schaick (1970), who specifically set out to investigate the existence of a natural vortex length. Kessler & Leith (1991) appear to be the only other study to have made use of helium bubble tracers, but they too did not report any unusual motion.

7.B.3a: Measurements indicating possible discontinuities of the vortex

Some measurements and observations made in the course of this study could be interpreted as evidence of discontinuities in the lower cone, and many occur at a distance from the gas exit lip that corresponds approximately with that predicted by the Alexander Natural vortex length. A selection of these have been presented in section 5.J, and they will be only briefly highlighted here.

It was thought that the presence of a vortex breakdown bubble would result in disruptions to the radial velocities, with increased radially inward velocities at the fore and aft of the bubble, and reduced or even outwards radial velocities around the bubble. The radial velocity is very difficult to measure, and the problems associated with the three techniques used yield results that are inconclusive.

Changes in the vortex behaviour were noted in some time-averaged measurements in the lower cone. The profile of the static pressure at the wall was used by Kirkpatrick (1964) and Sarpkaya (1971) to characterise the location of a vortex breakdown in a diverging tube, with the profile changing from a positive to a negative gradient opposite the breakdown. In the case of the converging cone of the cyclone, the prevailing pressure gradient is negative, but a change to a steeper gradient was observed in the cone, between the cone/barrel junction and the dust exit, as shown in figures 5.J.4 - 5.J.6. Assuming constant spin and axial velocities, a steeper profile corresponds to a steeper gradient of the pressure-velocity integral, and hence a greater dissipation loss, which would be expected to occur at a vortex breakdown. For the standard geometry and longer variations this occurred between 2.5 and 2.8 barrel diameters from the gas exit lip. Shorter geometries as well as extensions of the cone on the standard geometry had the steeper gradient beginning between 2.1 and 2.3 barrel diameters from the gas exit lip.

The circulation at the wall showed a decay in strength from the inlet towards the dust exit. Previously, this has not been allowed for in the published literature with the vortex assumed to have constant strength. In addition, superimposed on the gradual decay with length, almost all plots show a local increase in the strength in the lower cone. This kink could be due to the restriction of the vortex to a smaller flow area, either by precession of the vortex axis bringing it closer to one wall, or by the diversion of flow around the outside of the recirculation zone or 'gas bubble' that caps the vortex breakdown. The local maximum in the wall circulation occurred between 2.1 and 3.0 barrel diameters from the gas exit lip for a range of barrel lengths.

The observations quoted above of anomalous behaviour in profiles of vortex properties in the lower cone region are based on measurements near the wall, suggesting that they could be explained by reference to the behaviour of the boundary layer region. The Alexander Natural Vortex length was also developed from observations of the wall flow: in the angle of water streaks on the wall. Observing the dust rope that was formed when dust was fed to the cyclone confirmed what other workers (Tran (1981) and van Schaick (1970)) had found: that the helical pattern of the dust rope on the wall is uniform down the cone. It is possible that the converging walls of the cone delay the onset of vortex breakdown until the dust exit is reached. This thesis contends that the radial inflow is not uniform over the cyclone length, but rather, localised radial inflows occur due to the ejection or separation of boundary layer fluid from the wall, and these can explain the behaviour in the near-wall region in the cone.

7.B.3b Vortex strength indicated by pressure profiles.

It was considered that the strength of the vortex at any axial position could be characterised by the gradient of the pressure between the wall and the axis. Under normal conditions the radial pressure gradient is balanced by the centrifugal force that is generated by the tangential velocity.

$$\frac{dP}{dr} = \frac{\rho V_\theta^2}{r} \qquad \text{--- (7.1)}$$

A decrease in the radial pressure gradient is thought to be related to a slowing or weakening of the spin of the vortex, hence the expansion into the bin, (with resulting drop in the tangential velocity) is expected to result in a sharp drop in the radial gradient. A plot of the average $\Delta P/\Delta r$ against the distance from the dust exit expansion (as in figure 5.G.13) was expected to show a sharp decrease at the location of the expansion, regardless of the overall length. Instead it was found that in geometries in which the cone was extended at the dust exit end, this decrease began as much as one barrel diameter upstream of the dust exit expansion, suggesting that the vortex weakens and possibly terminates before the expansion.

A further check was made in a 300mmØ cyclone with wall tappings of 1mmØ spaced along the length of the cone as well as the various dust exit extensions. The results shown in Figure 5.J.6 suggest a slight increase in the wall pressure for the cylindrical extension of the dust exit, and as noted previously, such an adverse pressure gradient is often associated with a vortex breakdown or boundary layer separation. Similar profiles are obtained with either conical, cylindrical or cylindrical/conical extensions of the dust exit.

The hypothesis that the extension of the dust exit leads to the termination of the vortex before the dust exit expansion was supported by observations of the dust behaviour. Kevern (1991) observed deposits of dust on the walls of the extension piece when the cyclone was dismantled at the end of a run. The rest of the cyclone wall was comparatively dust free, but below where the termination was predicted to occur there was a sharp transition to a smooth coating of dust, as shown in figure 7.5 below. Other studies have also mentioned abrupt changes in the patterns of wall deposition of dust, such as Bryant et al (1983), but these are usually observed higher in the cone.

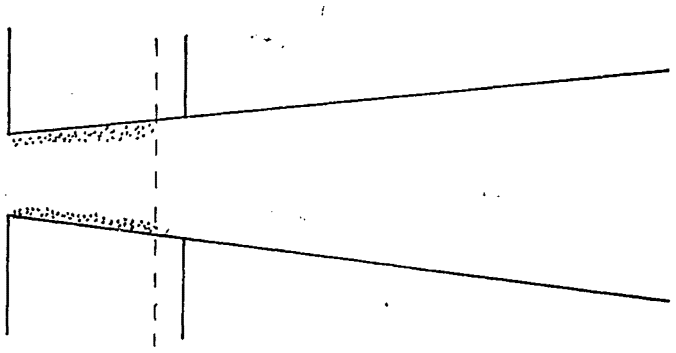

Figure 7.6: Dust deposits observed by Kevern (1991)

When dust was fed to the perspex cyclone the formation of the dust rope could be seen clearly, as mentioned in section 5.L. The helical angle of the dust rope was approximately constant for cyclone with the normal dust exit, but with the extended dust exit geometries the angle of the dust rope reduced, and the rope became more diffuse and spread out on the wall.

These results suggest that the cyclone geometries could be divided into one of two classes: those with the standard dust exit configuration, and those with the expansion delayed by conical or cylindrical extensions. The difference between these two types was more clearly demonstrated by the profile of the static pressure along the axis, as plotted in section 5.H.

7.B.3c: Axial static pressure profiles

Referring to the graphs in section 5.H, it can be seen that the profiles were axially located with respect to the dust exit expansion for a range of barrel lengths, but the two types of exit configuration displayed opposite trends. Cyclones with a normal dust exit had a bin pressure that was lower than the pressure on the axis in the cone, and these regions were connected with a sharp change in pressure across the dust exit expansion. This steep pressure gradient remained located at this position for a range of barrel lengths of 0 to 2.74 barrel diameters (with the standard or long cones), and for different bin depths. The pressure at the base of the bin was generally considerably less than the pressure at the side wall of the bin. On the other hand, cyclones with extensions to the dust exit had a more uniform bin pressure, and this pressure was higher than the pressure on the axis in the cone. Again, these regions were connected with a steep pressure gradient, but in some cases this was located on the cone side of the expansion, inside the extension section.

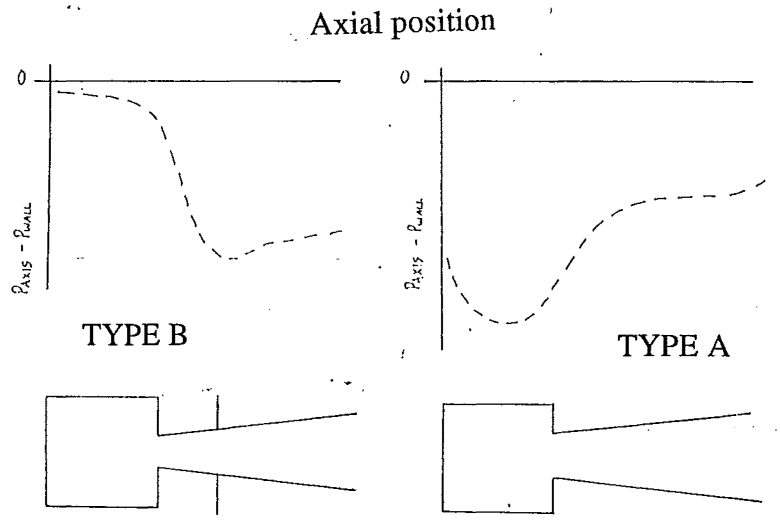

Figure 7.7: Types of static pressure profiles along the axis.

Sharp changes in pressure such as this cannot be sustained by a normal vortex, and must be associated with an axial stagnation point. The interpretation that is attached to these observations is that the vortex breaks down at the dust exit expansion for the normal geometry, but a termination may occur earlier for geometries where the expansion is delayed by an

extension of the dust exit end of the cone. In the latter case the vortex does not reach into the bin.

The association of a low bin pressure with a vortex core that enters the bin is supported by the results of Bryant et al (1983), shown in figure 2.11 . The pressure difference between the bin side wall and base offers a convenient method of characterising the position of the vortex end. The largest difference between the bin side wall and bin base in this study was found for the "shortest geometry" with the normal dust exit. The large pressure difference between the bin side wall and base is presumably due to the vortex core reaching the bin base, while the bin side wall registers the pressure of the outer vortex. The geometries with a conical extension of the dust exit to a smaller diameter showed the smallest difference between the bin side wall and the base. The cylindrical extension of the dust exit showed an intermediate value of this pressure difference, suggesting that the vortex was able to enter and leave the bin periodically.

7.B.4: Cause of Vortex breakdown at the dust exit expansion:

Returning to the case of the normal dust exit configuration, the occurrence of the vortex breakdown at the dust exit is accounted for by the effect of the expansion on the flow. The vortex breakdown phenomenon is known to be promoted by positive pressure gradients and diverging streamlines. The inability of the flow to follow the sudden expansion of the wall would cause a separation of the boundary layer and allow the outer layers to turn into the centre, capping the vortex.

The expansion of the flow into the bin would normally be expected to result in an increase in pressure, giving a positive pressure gradient in the direction of the flow. In fact the static pressure along the axis shows a sharp decrease as the bin is entered. This sharp change in pressure suggests the presence of a stagnation point, as normal vortex cores are unable to sustain a substantial pressure gradient. The axial static pressure profile only indicates the pressure at the axis and there may still be a positive gradient in the outer flow. Different dust exit geometries gave different axial pressure gradients across the dust exit, but this may be a result of where the recirculating gas bubble is located after breakdown, with different geometries stabilising it in different positions. It should be kept in mind that the insertion of the probe may disturb or precipitate the vortex breakdown.

7.B.5: Location of the dust exit vortex breakdown

Experimental support for the breakdown of a swirling flow at a sudden expansion can be found in the studies by Dixon et al (1983) and Leuckel & Fricker (1976) of the swirling jet in combustion chambers. The upstream tip of the vortex breakdown recirculating zone (or 'bubble') was observed to be level with the lip of the expansion, which would allow the flow to enter the bin in the annulus around the bubble. The axial flow is also able to penetrate through the centre of the recirculation bubble, as shown in the 'flame type 1' diagram. Hence the location of the vortex breakdown bubble across entrance to the bin need not impede the entry of the outer region boundary layer nor the near axis reverse flow into the bin.

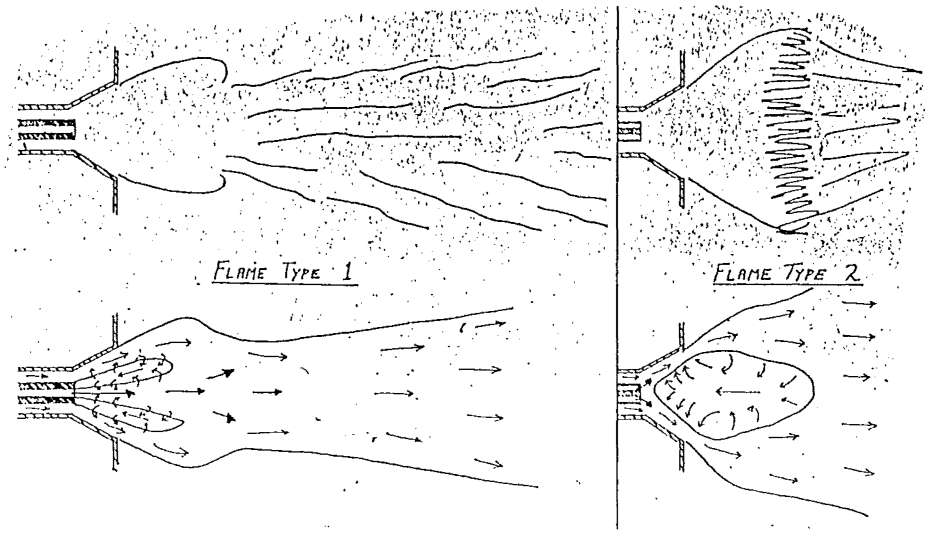

Figure 7.8: Vortex breakdown at an expansion in a burner jet from Leuckel & Fricker (1976).

The studies of vortex breakdown flows reported in the literature have found that the position of the breakdown depends on the flow parameters as well as the geometry. In particular, at sufficiently high swirl the breakdown is observed to move upstream, drawing a columnar reverse vortex behind it. Usually the vortex breakdown involves the core region only, which is well away from the tube walls. The outer regions of the flow continue to flow in the original direction, towards the exit. In the cyclone the flow must turn to leave the cyclone through the gas exit, and the turning of the remaining flow in the outer vortex is presumably achieved in the bin. The flow visualisation experiments did not reveal any coherent structure resembling a vortex breakdown recirculation zone near the dust exit, which suggested the possibility that the breakdown had moved upstream.

However, the geometry of the reverse flow cyclone means that the flow differs significantly from the simpler case of a swirling flow in a straight-through tube. The location of the gas exit ensures that the core flow reverses towards the gas exit, and this core flow is largely supplied by the radial inflow from the outer vortex that takes place along the cyclone length. This is expected to alter the properties of the core and prevent the vortex breakdown from moving upstream from the dust exit to the gas exit.

Escudier & Keller (1985, 1983) observed a breakdown moving upstream and taking an annular form in an annulus, until it 'disappeared' at the upstream end wall. This is considered unlikely to occur in the cyclone, as the vortex breakdown is thought to be caused by the bin expansion, which would then oppose the breakdown moving upstream. The annular breakdown moving upstream was considered as a possible explanation for how the audible tones of a vortex whistle (described in section 5.K) came to be transmitted upstream to the inlet. If the vortex breakdown moved to the inlet annulus, the entire vortex would be subcritical according to the theory of Squire (1960), and wavelike disturbances would be able to travel upstream (which is the definition of the subcritical flow). However, the velocity of soundwaves is sufficiently greater than the velocity of the cyclone vortex to enable them to propagate upstream even in a supercritical vortex.

This thesis proposes that for the normal dust exit configuration the vortex breakdown is stabilised at the dust exit expansion. The helium bubble tracers was the only flow visualisation technique that was sufficiently robust to show the recirculations in a breakdown. The failure of the tracers to reveal any coherent structure in the dust exit region may be due to the tracers reaching this region via the near-axis reverse flow, which passed straight through to the bin base, presumably punching through the centre of the vortex breakdown. If the outer flow could be seeded with tracers just before the expansion the structure may be able to be revealed.

Support for the stabilisation of the cyclone vortex breakdown on an expansion was found with the expansion of the gas exit, which will be discussed later. In brief, the helium bubble tracers revealed a recirculation zone just downstream of a sudden expansion in the gas exit, and this recirculation showed no tendency to move upstream into the straight walled tube that led to the expansion.

The axial velocity profiles obtained by Wong (1973) in different bins of a Stairmand high efficiency cyclone showed evidence of a recirculation of air in the bin, and this was more pronounced close to the dust exit. The sharp change in the static pressure along the axis is taken as further evidence of the vortex breakdown being located in the dust exit region.

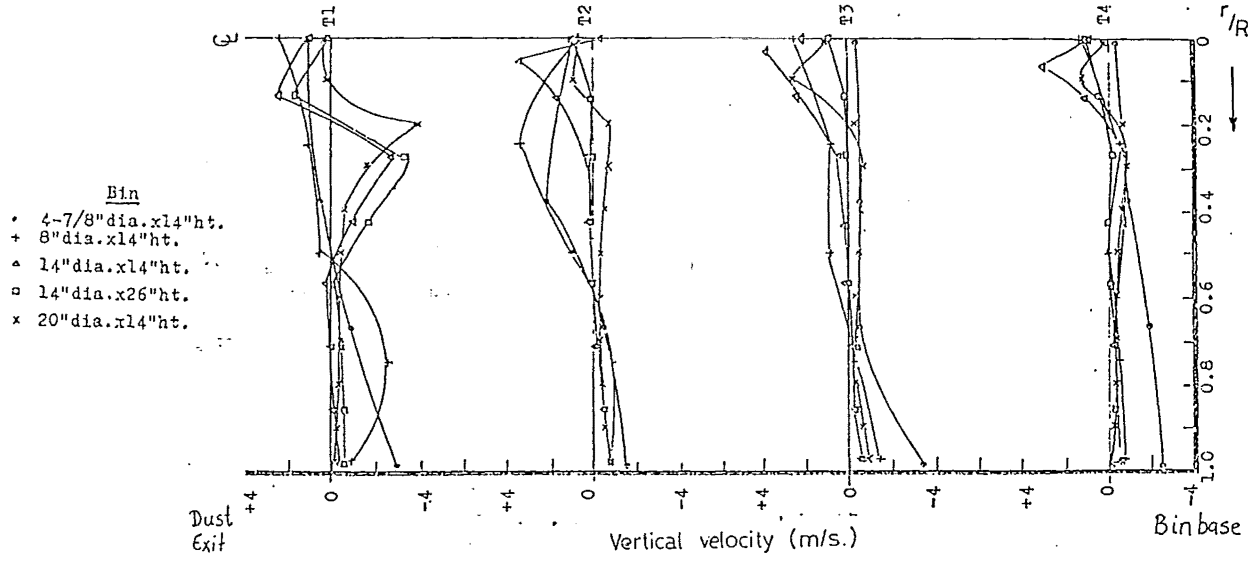

Figure 7.9: Axial velocity profiles in the bin of a Stairmand H.E. cyclone from Wong (1973)

The previous discussion has concentrated on the occurrence of vortex breakdown at the dust exit for cyclones with the normal dust exit geometry. It was noted earlier that when the expansion into the bin is delayed by an extension of the dust exit, different behaviour is observed, and the vortex appears to terminate before the expansion, suggesting that some mechanism apart from (or as well as) the expansion is responsible. It is proposed that this premature termination is due to a separation of the boundary layer from the wall, and some supporting arguments for this will be briefly presented here.

The mechanisms for boundary layer separation have been discussed earlier, in Chapter 6.C. The ejections of fluid from the wall by the Görtler or quasi-streamwise vortices is promoted by

smaller radii of curvature, and at the dust exit these ejections will become more significant with respect to the remaining flow and will be more able to reach the core. The presence of the vortex breakdown at the expansion is thought to result in an axial deceleration of the approaching flow, which enhances the boundary layer instability and the propensity to separate and flow inwards. It should be noted that the steep gradient in the axial static pressure extends to either side of the expansion even for the normal dust exit.

All of these causes of increased instability apply equally to the normal dust exit configuration, but the extended dust exit geometries are more affected since they feature a greater length at the smaller diameter. The boundary layer separation mechanism explains why the barrel length has comparatively little effect. In addition it is known that vortices are stabilised by the contracting walls of a cone, relative to a cylindrical or diverging tube. The cylindrical extension of the dust exit appeared to promote the termination earlier than the conical extension did, suggesting that the mechanism was not solely based on the proximity of the wall to the core, but also involved the stability of the flow. The cylindrical extension may promote the boundary layer separation because of the change in the wall angle. An understanding of this would be useful, as cylindrical extensions to the dust exit are commonly used to connect the cyclone to the bin.

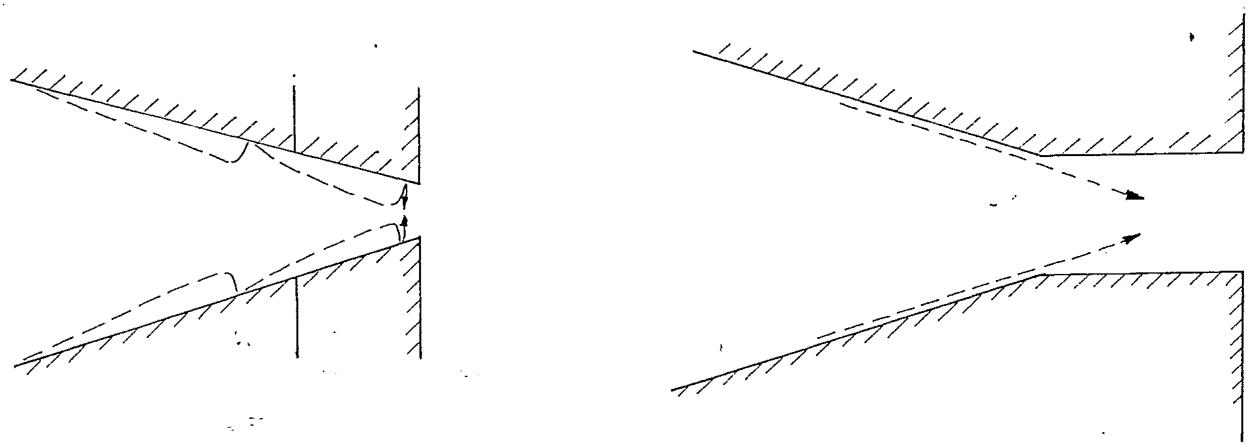

Figure 7.10: Separation induced by the dust exit extension section

A change in the character of the reverse flow was reported by Ustimenko and Bukhman (1968) when a neck was fitted to the dust exit, apparently forcing the boundary layers to meet. Steffens (1988) examined the stability of a two dimensional vortex (that is neglecting the axial component of velocity), and found that transitions in the behaviour occur as the ratio of the swirl to the volume inflow increases. For low inflows compared with the circulation, a two-celled vortex formed with a central downflow.

Although the cylindrical extension used with the 140mmØ cyclone was roughly made, which could have contributed to the separation, the same features were observed in the measurements in a carefully made extension to a 300mmØ cyclone. The higher bin pressure that was found in the case of the extended dust exits is thought to be a consequence of the termination, and it would further destabilise the boundary layer flow by reducing the pressure difference that provides the driving force.

The effect of the barrel length on the vortex length was examined to the extreme of the "Extra long" geometry, which had a cylindrical section of 2.74 barrel diameters, and the 'long cone' with a length of 3.5 barrel diameters, giving a total length from the gas exit lip to the dust exit of 6.24 barrel diameters. Although the bin and axial static pressures showed a normal vortex

structure for almost all of the time, on one occasion the axial static pressure profile showed a clear indication that the vortex had not entered the bin, until the probe reached the mid-bin region whereupon the flow pattern switched to the normal mode with an audible and visible change in the flow. This observation suggested that there was a limit to the overall length that the vortex could be stretched over, but this limit is far in excess of the normal cyclone lengths.

The termination of the vortex may be characterised by a vortex length number which incorporates aspects of the boundary layer stability, the relative strength of the ejection to the remaining flow, the length of the cyclone, and the length of the cyclone below a critical exit diameter. However, the limited number of extension geometries that were examined make it difficult to propose a criterion to predict under what conditions the vortex will terminate before the dust exit expansion. More carefully made extension pieces of different lengths need to be examined.

7.B.6: The inner vortex breakdown in the gas exit:

Although the inner or core vortex starts at the bin, 90% of the flow at the level of the gas exit lip has arrived in the core via the radial inflow from the outer vortex. For this reason the characteristics of the core vortex will be determined more by the inflow behaviour than from how the vortex turns at the dust exit or bin. This study has found some support for the occurrence of a classic bubble-type breakdown in the gas exit, as predicted by Abrahamson and Allen (1986).

The most obvious and stable structure of the vortex was that revealed in the gas exit by the flow visualisation with the helium bubble tracers. Once the tracers had passed through the cyclone and entered the gas exit (which took 1-2 seconds) they were then held in a recirculating region for periods of the order of minutes at an axial position between 2 and 3 gas exit diameters downstream from the gas exit lip. The tracers were constrained to a narrow chain along the axis of the exit tube, which moved axially to and fro, about the level of the roof. The extent of the trap was 100mm in the axial direction and up to 20mm in diameter (about 0.57 of the exit diameter). The large number of tracers that were collected in this region, and the erratic nature of the paths meant that a good representation of this phenomenon could not be obtained with still photographs. A better representation is contained in the video, which contains footage of the movement of the tracers, and the effect of upstream disturbances to their behaviour.

This trapping of the tracers was thought to be due to the action of a vortex breakdown bubble at or near this location. The tracers are thought to be either caught inside the recirculating gas bubble that caps the vortex, or be held at the upstream end of the reversal. The gas exit tracer trap has a long, thin structure compared with the more bubble-like shape reported in the experimental investigations of vortex breakdown in tubes. When the trap came near the gas exit lip the trap spread away from the axis, but contracted again as it moved back downstream, as if to avoid a 'solid' object on the axis near the gas exit lip. The tracers may be trapped between the reverse flow from the far end of the gas exit, and the vortex breakdown itself.

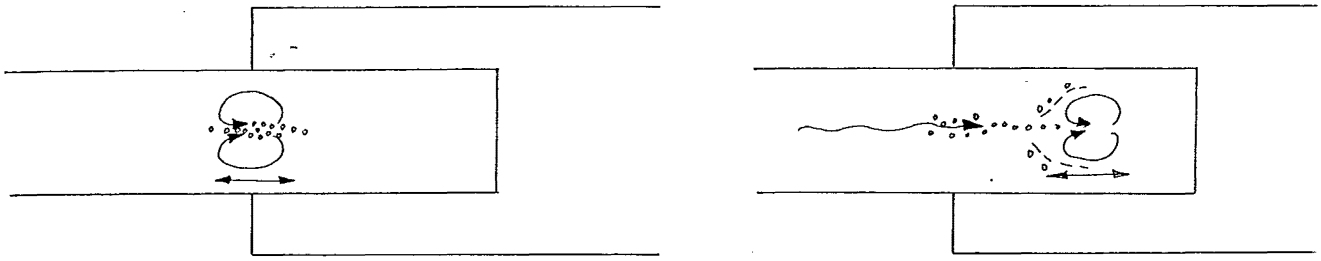

Figure 7.11: Relation of gas exit tracer trap to position of vortex breakdown.

The mean position of the trap coincided with a localised region of steep positive pressure gradient that was found in the gas exit wall pressure (see figure 5.F.6), within the more general negative pressure gradient that extended over the rest of the gas exit. This regain in pressure would promote the vortex breakdown, or may be the result of the presence of the breakdown, similar to the wall pressure profiles shown by Sarpkaya (1971) and Kirkpatrick (1964) opposite a vortex breakdown (see figure 3.C.5). Other short regains in pressure occurred down the length of the straight gas exit suggesting further breakdowns.

The occurrence of vortex breakdown in the gas exit is supported by theoretical and experimental results in the literature. Lavan et al (1969) found that when a rotating fluid enters a stationary tube a region of reversed flow forms on the axis, and the shear at the wall is larger than in a flow without rotation. When a non swirling flow enters a rotating tube a region of separated flow tends to form near the tube wall, and the shear at the wall is smaller than in straight flow. The axial extent of the disturbance increases with the Reynolds number. The case of the rotating tube corresponds to the core vortex in the main body of the cyclone, surrounded by the co-rotating outer vortex. The entry into the stationary tube corresponds to the core vortex entering the gas exit.

The Rossby number criterion of Spall et al (1987) suggests that the occurrence of breakdown depends critically on the ratio of the axial to the tangential velocity. The core vortex must contract as it enters the gas exit, according to the estimates of the core radius from this and other studies. This will increase the axial velocity, but by the conservation of angular momentum the tangential velocity must also have increased. The action of the wall drag will reduce the axial velocity at the wall, and at some distance downstream of the gas exit lip the condition for breakdown is expected to be met.

Escudier, Bornstein and Maxworthy (1982) found a breakdown occurred as a vortex entered an abrupt contraction. This exit vortex breakdown is attributed by Leibovich (1984) to disturbances set up in the core vortex as it crosses the vortex lip. Brown & Lopez (1990) mention the wavy nature of vortex flows, where overshoots occur. The contraction of the streamlines as the gas exit is entered would result in the centrifugal acceleration being greater than the radial pressure gradient. The flow diverges, but overshoots before converging again, and this 'waviness' initiates the vortex breakdown according to Brown & Lopez (1990). In conjunction with this the wall friction slows the outer region of the vortex.

The influence of changes in the cyclone geometry on the location and behaviour of the gas exit tracer trap gives some insight into possible mechanisms for its formation. When a long straight gas exit was used the trap was observed as described above. Tracers were observed to escape and be carried as much as 10 exit diameters downstream, but they usually would be recaptured and returned to the 2-4D_X position. The cotton streamers revealed a steady reversal of the gas exit flow at the axis at the far (downstream) end of the straight exit tube (17D_X from the gas exit lip), but a fluctuating reversal at the level of the roof. The video shows clearly an exchange of tracers from the gas exit into the body of the cyclone.

It was observed in positive pressure cyclones (such as the 750mmØ) that the reverse flow at the axis of the exit was stronger when the exit was short (about 1D). It is thought that the shorter exit length before expansion gave less resistance to the recirculation flow, so the front of the stagnation zone could move further upstream into the cyclone. When the dust exit was extended the gas exit trap appeared to be located closer to the lip.

When an expansion was placed in the gas exit (within about 6 exit diameters of the gas exit lip) the tracer trap was not present in the straight section. By using one of the inlet sections as an expansion/scroll exit the effect of the expansion on the position of the tracer trap could be observed. With the expansion/scroll exit the tracers were located just downstream of the expansion, and the trap showed no tendency to move upstream.

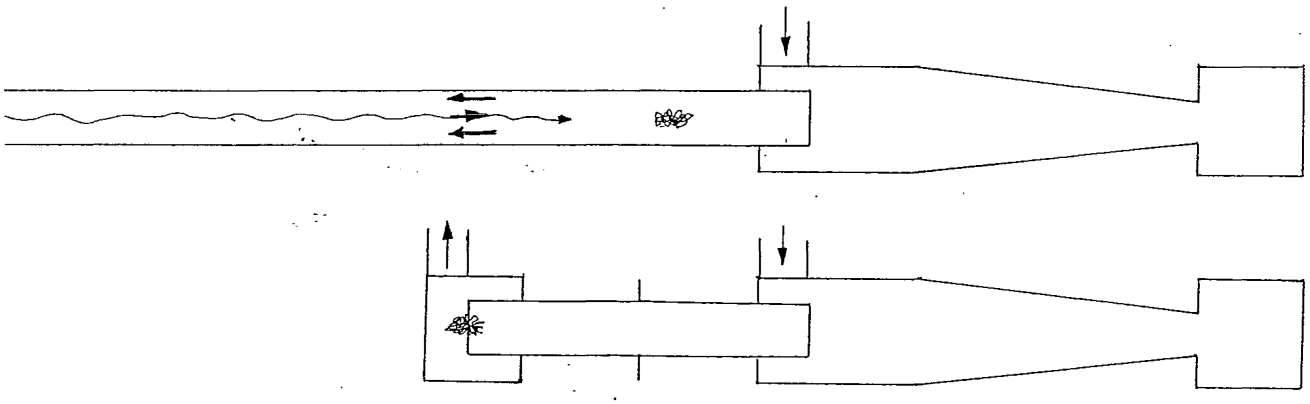

Figure 7.12: Variation of the tracer trap position with the gas exit configuration

The insertion of a rod into the cyclone body initially resulted in the gas exit recirculation becoming more clearly defined in a narrower region along the axis and moving towards the gas exit lip. Further insertion of the probe into the core region resulted in the recirculation of the tracers moving well downstream, as shown in figure 7.13. A similar behaviour has been observed by So (1967) in a conical diffuser as the velocity was taken through critical states, as shown in figure 3.C.4.

The cyclone pressure drop was markedly reduced by the initial insertion, but the insertion of the rod into the core region brought about very little further change in the pressure drop despite the large movement of the tracer trap. The reduction in the pressure drop was consistent with that

expected from the reduction in the tangential velocity that was measured with a hot film anemometer.

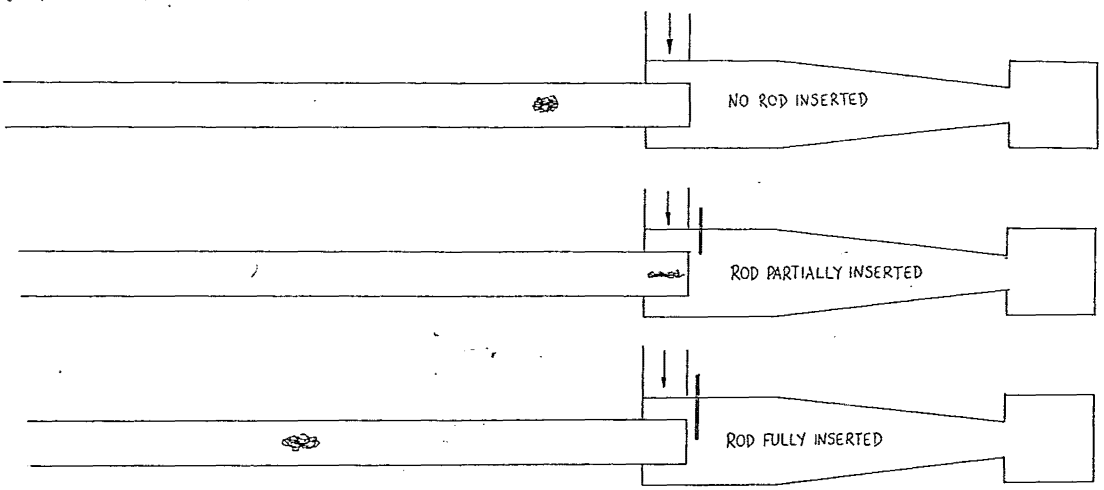

Figure 7.13: Effect of rod insertion in cyclone barrel on the tracer trap position

From the different behaviour exhibited with the scroll exit and long straight gas exit tube it would appear that the gas exit breakdown prefers to be stabilised on the expansion, as is thought to be the case at the dust exit. With the long straight gas exit the breakdown occurs well downstream and is not stabilised, and consequently moves upstream against the core flow, forming a reverse flow near the axis. It is thought that the available pressure drop places a limit on the distance that this reverse flow can penetrate, as the presence of the reverse core results in higher axial velocities in the annular exiting flow.

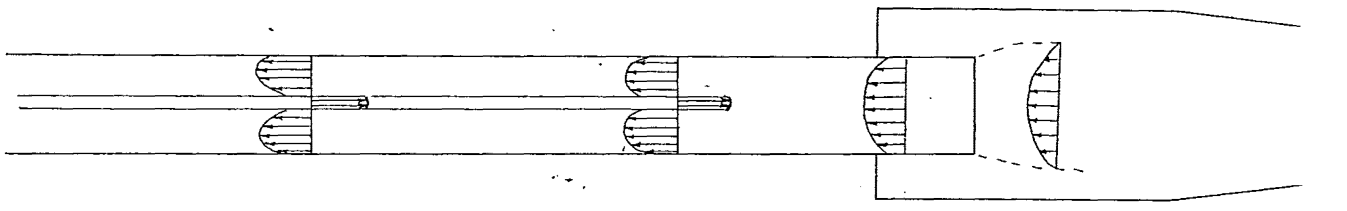

Figure 7.14: The reverse flow in the gas exit opposes the exiting flow

The reverse flow appears to extend further upstream than the tracer trap. Tracers were observed to be carried into the body of the cyclone, and in positive pressure cyclones with a very short gas exit length before the expansion strong downdrafts were observed near the axis of the gas exit. Particles inserted into the centre of the gas exit were found to be collected in the cyclone bin suggesting a connection to the bin (although this could be due to reseparation of the particles once inside the cyclone body).

7.B.7: The near axis reverse flow:

7.B.7a: The importance of this feature

The existence of a reverse flow near the axis, extending from the gas exit to the bin was an important finding from this study. It will prove useful for testing simulations of the cyclone flowfield, as the dynamic features (such as vortex breakdown recirculations) have been identified by Lopez (1990) as being much more demanding tests of the validity of flow simulations than the ability to reproduce details of the mean flow. Theories proposed to describe the cyclone flowfield will need to be able to account for the formation of this reverse flow (henceforth referred to as the 'near-axis reverse flow').

The near-axis reverse flow appears to contribute a significant proportion of the bin flow, with figure 5.A.2 suggesting an axial velocity of 60m/s, or four times the average inlet velocity. The helical path of the tracer has a diameter of 20mm, and if the tracer velocity is representative of the air velocity across this diameter then the reverse flow could comprise as much as 60% of the cyclone throughput!. When a plastic bag was attached at the centre bottom of the 750mmØ cyclone bin, distinct pulsations were observed in the bag. These were low frequency (one or two cycles per second) and presumably followed pressure fluctuations, or the entry of the near-axis reverse flow into the bin.

To what extent this feature needs to be allowed for in models used to predict the dust collection performance depends on how much influence the rapid fluctuations have on the collection efficiency or pressure drop. It is likely that estimates of core properties such as the turbulent viscosity may need to be adjusted. Although the near-axis reverse flow had a very high axial velocity, the residence time of tracers in the region near the axis was increased by localised recirculations. For the example shown in figure 5.A.2 the tracer is estimated to spend as much as 90% of its time in the recirculations.

The apparent intermittency of the near-axis reverse flow could be due to the visualisation method used, in particular - the small number of tracers of the correct buoyancy. The helium bubble tracer visualisation experiments involved feeding a large number of approximately neutral density tracers into the cyclone. Since the buoyancy could not be exactly controlled many of these impacted on the walls in the entrance to the cyclone, or short-circuited to the gas exit. However, at times a continuous chain of tracers travelling towards the bin near the axis could be obtained.

7.2.7b: Mechanism of formation of the near axis reverse flow

It is proposed that the near-axis reverse flow is the result of a vortex breakdown moving upstream from the gas exit towards the bin, in accordance with the observations of Harvey (1962) and Escudier et al (1982). The vortex breakdown is not fully stabilised at the bin base, and both the feature and the mechanism should be viewed in dynamic and intermittent terms because of this meta-stability. The following section outlines the proposed theory and shows how it is consistent with the experimental results and observations.

The video clearly shows an exchange of tracers from the gas exit into the body of the cyclone, but this occurs sporadically, and only involves a few of the tracers - the majority remain in the gas exit trap. If the gas exit vortex breakdown moved upstream to the bin the trap of the helium bubble tracers in the gas exit would be expected to move into the cyclone as well. The permanence of the gas exit trap suggests that the gas exit vortex breakdown moves upstream no further than the gas exit lip. It is accepted that the gas exit vortex breakdown is permanently located in the gas exit, but it is proposed that at irregular intervals there is a separation of the vortex breakdown, and part moves upstream into the cyclone, while the original vortex breakdown is maintained in the gas exit. This is consistent with the reports of the formation of multiple vortex breakdowns along vortex cores.

The vortex breakdown that moves upstream along the core into the cyclone, travels towards the bin and the near-axis reverse flow forms behind it. The movement of the breakdown is very fast at typical cyclone flowrates (faster than four times the inlet velocity), and the vortex breakdown and near-axis reverse flow would have no difficulty in penetrating through the vortex breakdown recirculation at the bin entrance, and reaching the base. The observation of a trap of helium bubble tracers just above the bin base (for the standard Stairmand High Efficiency and shorter geometries) suggests that the breakdown is preferentially located on the bin base.

The near axis reverse flow exists while the vortex breakdown is stabilised on the bin base. Tracers can (and are observed to) join this near-axis reverse flow at locations that are spread along the cyclone length - figure 5.A.2 is a good example of this. At irregular intervals there is a purging of the bin trap, with all of the tracers moving quickly in the direction of the gas exit. The period until a bin base trap was re-established varied widely, and presumably depended on the quantity and quality of the helium bubble tracers being produced. The interval was of the order of several seconds, which was similar to the return period of the pulsing movements of the gas exit trap towards the gas exit lip.

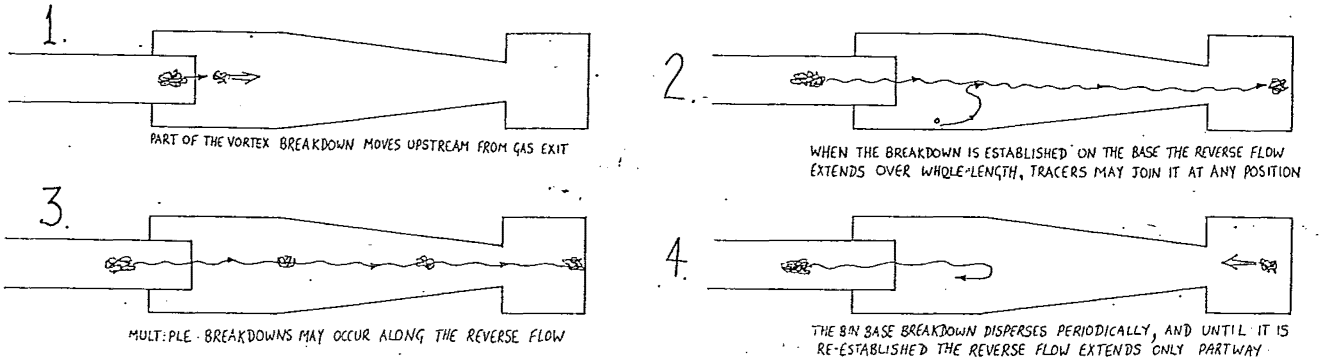

Figure 7.15: The formation of the near-axis reverse flow

There appeared to be fewer full length reverse flow events during the period when no bin trap was visible, compared with when the bin trap was present. The partial reverse flows observed, where the tracer travelled partway along the cone axis towards the bin before returning to the

gas exit, are consistent with the failure of the vortex breakdown to reach the bin base. This dynamically varying mechanism is needed to account for the near-axis reverse flow, which appeared intermittent at times, but at other times showed chains of tracers travelling continuously towards the bin.

7.B.7c: The recirculations of the tracers within the near-axis reverse flow

Velocities inside the breakdown bubble are reported by Leibovich (1982) to be small - around 4 to 15% of the axial velocity in the approach flow. The tracer path as recorded in figure 5.A.2 consists of regions of approximately constant axial velocity, interspersed by regions of sharp reversals of flow direction, in the form of recirculation zones. The velocities estimated in these two regimes vary considerably, but in the uniform flow the velocity appears to be four times higher than the inlet velocity. This suggests that the near-axis reverse flow phenomenon is due to a columnar reversal behind a breakdown that has moved upstream (to the dust exit or bin), rather than being due to the reversals inside a breakdown itself.

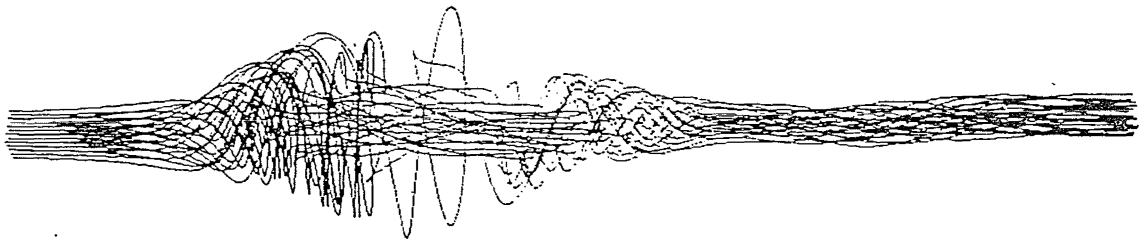

Vortex lines for flow with vortex breakdown.

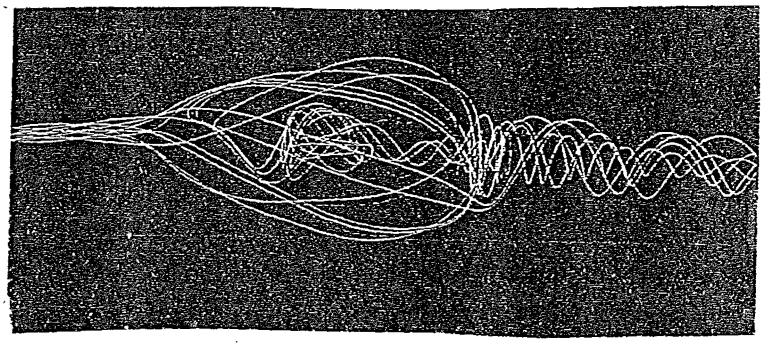

Figure 7.16: Vortex lines and particle paths from numerical simulation of vortex breakdown flow (from Spall et al, 1990)

The pathlines of the helium bubble tracers in the recirculations in the near axis reverse flow shows a similarity to the observations of the vortex breakdown by Faler and Leibovich (1978). Spall et al (1990) have also computed numerical simulations of the vortex breakdown and

present particle path diagrams of a low Reynolds number bubble-type breakdown, which again shows a similar structure.

Lopez has computed numerical simulations of vortex breakdown both in closed cylinder flow (Lopez (1990)) and swirling through-flow in pipes (Lopez (1986)) and Salas & Kuruvila (1989) have obtained similar results in their numerical simulation of vortex breakdown. These all show multiple recirculation zones along the axis, which increase in number as the swirl or velocity is increased. Examples are shown below:

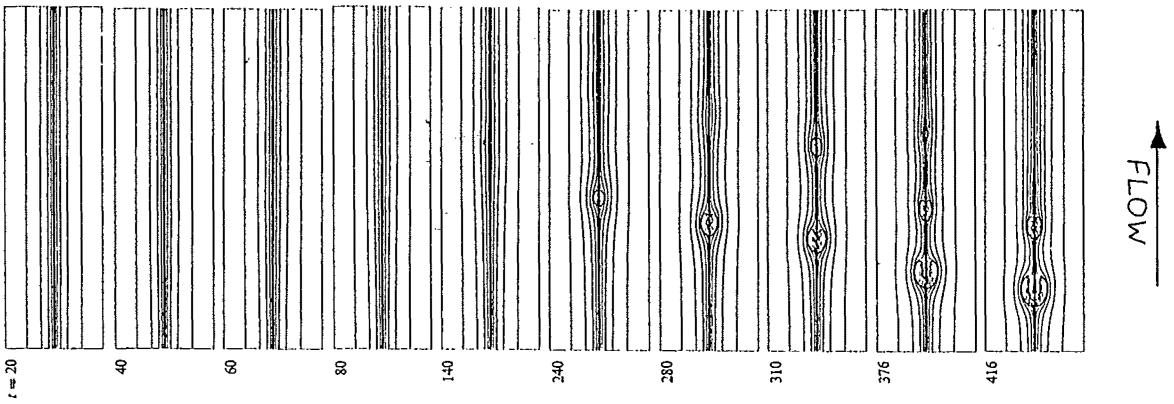

Figure 7.17: Evolution of numerically computed streamlines of swirling flow in tubes, from Brown & Lopez (1990)

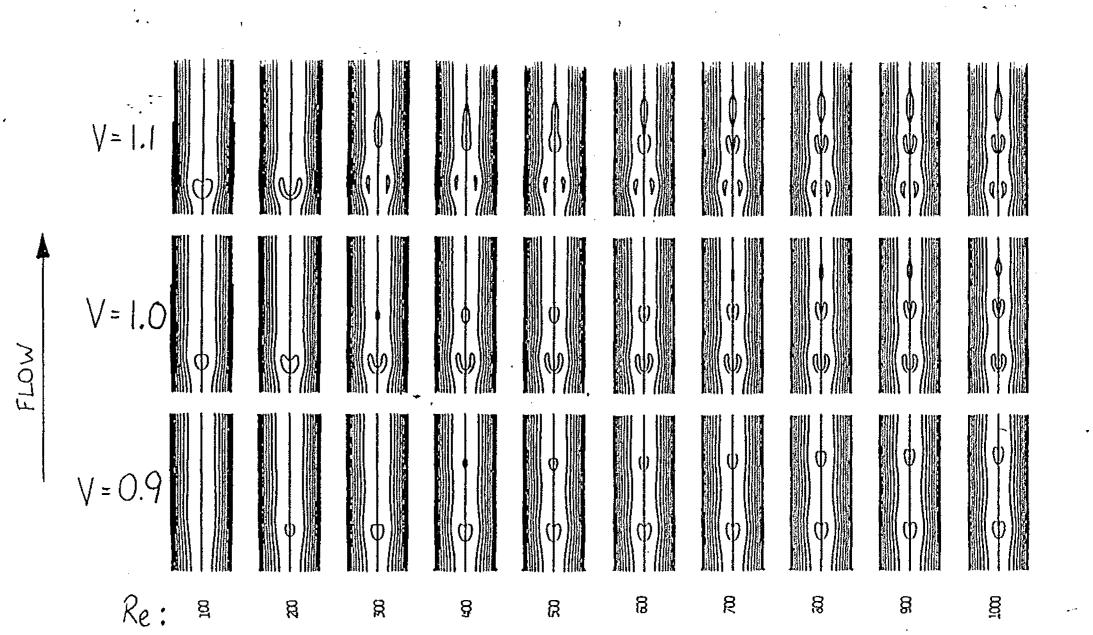

Figure 7.18: Development of multiple breakdowns on the axis in swirling flow in a tube with increasing Reynolds number and swirl parameter V. Numerically computed streamlines, from Salas & Kuruvila (1989)

The position of the recirculations observed in the cyclone near-axis reverse flow varied between successive photographs (see figures 5.A.2 to 5.A.5), and these recirculations are thought to be temporary disruptions to the flow since the tracer eventually passed through the recirculation, and in some photographs the tracer did not encounter any recirculation zones at all.

Lopez (1990) found that at high length to diameter ratios and high Reynolds numbers, multiple breakdowns occurred along the axis in a closed cylinder with rotating endwall. This was preceded by the development of wavy motion on the envelope of the vortex core. The distance between the recirculation zones reduced as the Reynolds number was increased. The mechanism involved the overshoot of the divergence of the streamlines caused by an initial viscous diffusion of vorticity. The numerical simulation of swirling flow in pipes was initially in cyclostropic balance and did not develop vortex breakdown without the presence of viscosity. The wavy nature of rotating fluids ensured that the subsequent development of the flow was essentially inviscid. The breakdowns moved upstream and did not reach a steady state in high Reynolds numbers flows, which is in accordance with the observations of the tracers. Examining the path of the tracers in the near-axis reverse flow, the envelope seems to contract rather than diverge just before the region of recirculations. The divergence of the streamlines is an important part of the mechanism, but the tracer pathlines do not necessarily coincide with the streamlines.

The presence of a reversal near the axis was also demonstrated by the cotton streamers, which also showed rapid changes in direction. These directional changes could be induced by the variation of the vortex axis off the centreline, which has been reported by Dabir & Petty (1986) and others; or by the disruption of the cottons by the presence of one of the recirculating zones that are indicated by the helium bubble tracers

7.B.7d: The bin base boundary layer

The possibility that the bin base tracer trap was related to the vortex breakdown of the bin base boundary layer was considered, but rejected on the basis of the experimental evidence available from this study.

Considerable attention has been given in the literature to the investigation of the interaction between a vortex and a plane placed at right angles to the axis of rotation. This interest is largely because of the applicability to the interaction between tornadoes and the ground. Theoretical and experimental studies have been reported by Phillips (1984, 1987), Burgraaf et al (1971),Church et al (1979, 1985) and Pauley (1989).

The boundary layer induced by the vortex spirals inwards on the plane, and the collision at the axis of rotation results in an eruption of the boundary layer fluid into the main body of the fluid, forming the core. The laboratory simulations of the flow feature low angular momentum fluid at large radius being convected radially inwards across a base, and also have a contraction aloft, through which the core vortex flows, similar to the contraction of the dust exit that is present in the cyclone. Church et al (1979) found that the core vortex in the Tornado Vortex Chamber (TVC) underwent a vortex breakdown further aloft, and this breakdown moved upstream towards the plane as the swirl was increased, eventually merging with the lower surface. A reverse flow followed the breakdown right to the surface. The photograph of the vortex

breakdown in figure 5 of Church et al (1979) resembles the bin base tracer trap observed with helium bubble tracers in the cyclone bin. Further increases in the swirl in the TVC resulted in multiple vortices being formed, entwined around each other. This was not observed in the cyclone, and its occurrence in the literature appears to be restricted to devices with large diameter to length aspect ratios.

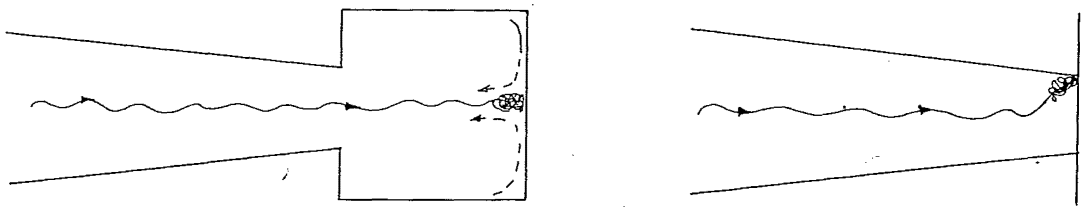

Figure 7.19: Location of base tracer trap in bin, and with blanked off dust exit.

The importance of the bin base boundary layer to the stabilisation of the vortex breakdown was investigated by blanking off the dust exit with a glass plate. The strong near-axis reverse flow was observed to end at a tracer trap that was located against the wall/plate junction, rather than on the axis, which would have been expected by the boundary layer breakdown mechanism. This suggested that the tracer trap in the lower cone/bin region was derived from the gas exit rather than the bin base boundary layer.

This mechanism whereby a vortex breakdown has moved upstream from the gas exit to the bin is able to explain the absence of the bin base trap from longer geometries (particularly those of longer barrel length). The theory that longer geometries had a weaker vortex in the bin that was unable to induce the boundary layer flow necessary for vortex breakdown was not supported by the observations of the rate of spin of tracer particles in the bin.

7.B.7e: Dependence of the near-axis reverse flow on the geometry:

When the cyclone was lengthened by adding sections to the barrel or the dust exit the near-axis reverse flow was less frequently observed, and the bin trap was absent. This is consistent with the vortex breakdown being unable to reach the bin from the gas exit because of the extra length. The near-axis reverse flow and bin trap were also absent from the standard geometry when the bin was extended. Apart from the increase in the distance to the bin base, the extensions to the dust exit and bin may affect the near-axis reverse flow by altering the properties of the core, in particular an increase in the core pressure may result from the inflow of low velocity, high pressure fluid from the wall. Although the near-axis reverse flow is able to punch through the vortex breakdown at the expansion into the bin, when the vortex breakdown occurs in the dust exit extension the constraint placed on the spreading of the vortex breakdown by the walls may prevent the reverse flow from penetrating it.

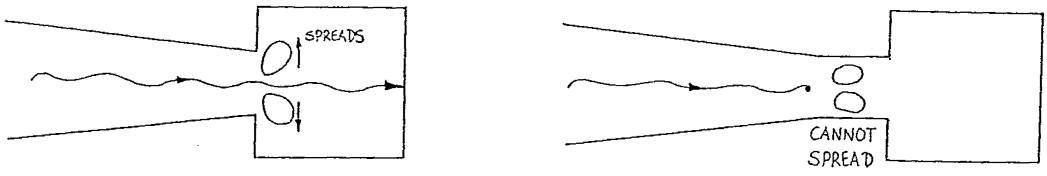

Figure 7.20: Obstruction of the reverse flow by the different vortex ending

The near-axis reverse flow was resilient and tracers could divert around an obstruction placed near the axis, but when the obstruction reached the centre the tracers were prevented from going further. Even then they travelled right up to the obstruction before turning and travelling back to the gas exit.

The cyclones with increased barrel length but normal dust exit and bin feature less frequent occurrences of the near-axis reverse flow simply because the distance between the gas exit and bin base is further than the near-axis reverse flow vortex breakdown is capable of moving upstream over.

Although the near-axis reverse flow is an essentially dynamic phenomenon, there was support in the time averaged measurements for the near-axis reverse flow switching between failing and succeeding to reach the bin base. The profile of the axial static pressure was shown to differ markedly depending on whether the outer vortex entered the bin or not (see figure 7.7). There were also more subtle differences observed in the axial static pressure profiles near the bin base that were obtained for cyclones with extra barrel length. For no change in the flowrate either a type A or type B profile could be obtained, as shown in figure 5.H.1. The essential shape was:

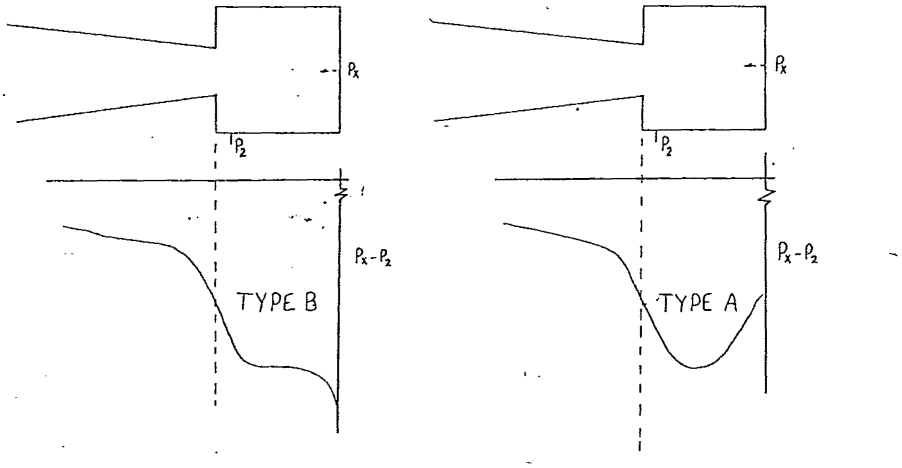

Figure 7.21: Types of profiles of static pressure along the axis near the bin base

The type A profile was more common, and was the type obtained in shorter cyclones, while the type B profile was only found in the extended barrel geometry and was only occasionally observed. The insertion of the axial static pressure probe disturbed the tracer trap, so it was not

possible to directly relate these profiles to the presence or absence of the bin trap of tracers. The profile of the static pressure deficit has been measured in the TVC apparatus by Church & Snow (1985) and Pauley (1989). Church & Snow made time dependent measurements by taking the maximum value over a 200 second sample. The profile shows a distinct minimum just above the surface at low swirl, which corresponded to the position of the vortex breakdown bubble, and as the swirl was increased the reverse flow was reported to become firmly attached to the surface and the deficit decreased.

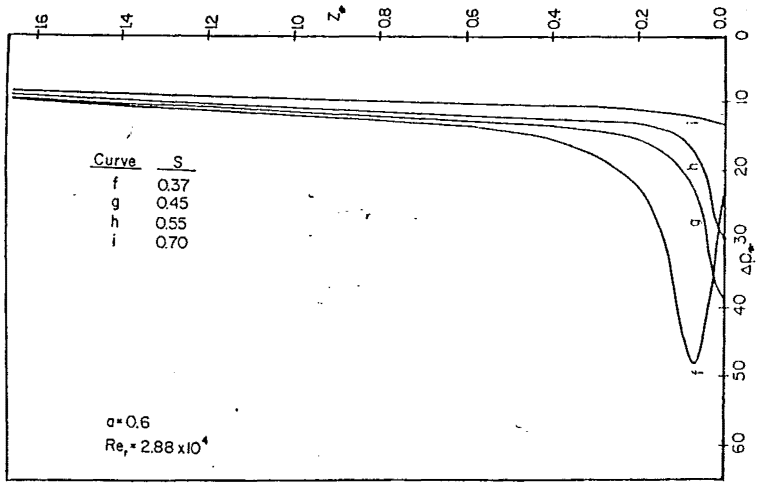

Figure 7.22: Time dependent profile of the TVC static pressure along the axis from Church & Snow (1985)

In the cyclone the trap of the helium bubble tracers was observed to be located just above the bin base, and a distinct minimum in the static pressure deficit was found at the same position, as in the case of curve f in Figure 7.22

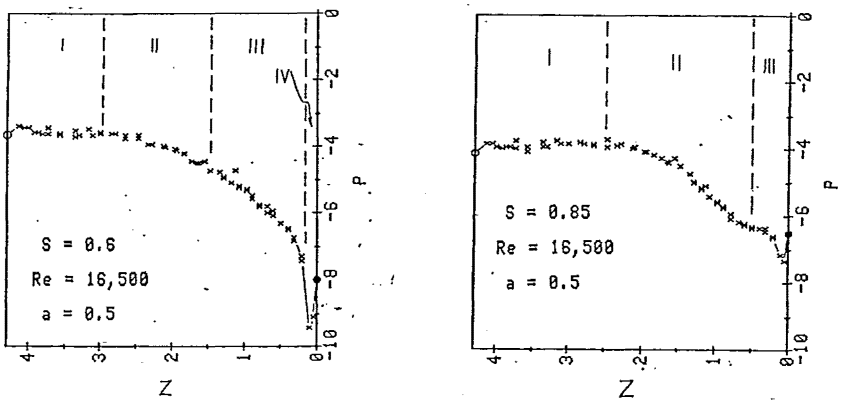

	S = 0.6	S = 0.85
I Nearly stagnant or weak downflow	Z > 3	Z > 2.5
II Accelerating and/or strong downflow	1.5 < Z < 3	0.5 < Z < 2.5
III Decelerating and/or moderate downflow	0.1 < Z < 1.5	Z < 0.5
IV Intermittent upflow and downflow	Z < 0.1	—

Figure 7.23 Time averaged axial static pressure profile and associated velocity regimes on axis in TVC (from Pauley, 1989)

The time-averaged pressure deficit measurements made by Pauley (1989) in the TVC matches the measurement technique used in this study more closely. Pauley reports a "pronounced

pressure minimum near the surface in the vicinity of the vortex breakdown" and identified four regimes of axial velocity near the axis including weak downflow, strong downflow and intermittent upflow and down flow. A very abrupt change in the pressure was identified at the vortex breakdown.

At higher swirl in the TVC a profile similar to type B was obtained. This flow featured entwined multiple vortices, but Pauley considered that these were not close enough to the axis to affect the measurements. In addition the flow was transient and changed between the multiple vortices and endwall vortex breakdown conditions.

Apart from the change in the profiles near the bin base in the cyclone there was also a switching found further aloft, for example the profile obtained at V_{in} = 9.8m/s in the extended barrel geometry, shown in figure 5.H.1. Away from the base the profile matched the dimensionless pressure obtained at V_{in} =7.9m/s, which had a type A profile. In the mid cone region however the readings start switching between values that match the V_{in} = 7.9m/s profile, and lower deficits that are closer to profiles obtained at higher velocities. A similar switch is also shown in figure 5.H.2 for the standard Stairmand High Efficiency geometry. This also involves a profile at an intermediate inlet velocity that initially matches a profile made at a lower velocity but then switches to pressures that are more consistent with a higher velocity profile.

These results suggest a velocity dependence, which is explained by the near axis reverse flow being unable to extend to the full cyclone length at low inlet velocities, but slightly higher velocities becoming meta stable and switching between the high and low flow states. Further measurements are required to clarify whether the disturbance caused by the probe insertion has an effect on this behaviour, and measurements of the axial static pressure profiles in larger cyclones are needed. A velocity dependence was also observed in the plots of the Euler number (dimensionless pressure drop of the cyclone) versus the inlet velocity. Initially the Euler number increased rapidly with inlet velocity, but above a certain velocity (that varied between cyclone geometries, but was in the range of 10-20m/s) the Euler number became more constant.

Chapter

8

IMPACT ON CYCLONE DESIGN

It is believed that the results of this research have yielded some insight into the relationship between the geometry and the vortex behaviour. The previous chapter outlined a possible theory to describe the vortex structure and the mechanisms that form it. This theory is thought to be consistent with the results obtained in this study and the theory from the literature, but as Popper (1969) points out, correspondence with the known 'facts' is not sufficient for a 'good' explanatory theory. This chapter will examine the implications for improving the understanding of cyclone performance and design, particularly the effect on the collection of dust. The theory offers itself to further testing, such as a closer examination of the occurrence of boundary layer separations and the effect of the dust exit configuration on the vortex termination.

8.A: The Vortex structure and dust collection:

This section considers in general terms the relationship between the efficiency and the vortex structure in terms of the theory presented in Chapter 7. This study was commenced with the expectation that the vortex structure consisted of bubble-type vortex breakdowns, which would have a strong influence on the performance in terms of the collection efficiency and also have some influence on the pressure drop. Only the location of this feature was thought to vary between different geometries. The results obtained have suggested the actual vortex structure is more complicated than this, and different forms of the breakdown need to be considered as well.

The standard Stairmand high efficiency design as the name suggests has a high collection efficiency, but it has a low sharpness of classification (the slope of the grade efficiency curve) and is reported (Stairmand, 1951) to suffer from a reduced efficiency at higher flowrates, as are some other designs. The reduction in the efficiency at high velocity can be countered by the extension of the dust exit according to Svarovsky (1984) (see figure 2.5). The effect of this on the slope of the grade efficiency curve needs to be determined.

The results presented by Abrahamson & Allen (1986) in figure 2.4 suggested that where it is difficult for the vortex to enter the bin, the sharpness of classification increased. The degree of difficulty was characterised by the length of the cyclone and the ratio of the exit diameters. The results of this study have shown that the overall length is less important than the length of the small diameter end of the cone, and the plot of Abrahamson and Allen (1986) could be reinterpreted in terms of this.

It is thought that the vortex strength is sufficient to reach the bin for the range of barrel lengths examined in this study, but if the dust exit is constricted or extended at the small radius the vortex may stop before the dust exit. If the vortex ends in the cone it may interfere with the dust flow at the wall, especially if the form of the vortex termination is the attachment of the vortex to the wall. The transport of dust to the bin can still be achieved, as the boundary layer is driven by the pressure gradient, which appeared to be favourable even for the geometries with an apparent termination before the expansion.

8.A.1: Boundary layer transport of dust:

If the vortex breaks down before the dust exit, there must still be some airflow to the bin to carry the dust. Velocity profiles with the Pitot cylinder show that by the level of the lowest traverse location (30mm above the dust exit) only 10% of the inlet flow remains in the outer vortex flow. As this is comparable with the strength of the boundary layer that is expected along the wall it is possible that the vortex could end in the cone, and the transport of the dust to the bin be achieved by the boundary layer. This was suggested by Tran (1981) who compared measurements of the volume flow into the bin with theoretical calculations of the flowrate, and found them to be approximately equal.

The driving force for the boundary layer flow is the pressure gradient along the wall between the cone/barrel junction and the bin. The lower the bin pressure relative to the upper cone wall

pressure, the stronger the flow. The bin presumably provides a connection between the core and the outer vortex, through the air that enters from the boundary layer and the near axis reverse flow and leaves it via the core. The bin may have an influence on the core pressure by providing the core with slow-moving air. If the bin and core are connected, the low bin pressure required for a large boundary layer flow driving force would also require a low core pressure. However the radial pressure gradient resulting from a core pressure much less than the wall pressure can result in the boundary layer becoming unstable and moving inwards. The restoring force due to the centrifugal action from the tangential velocity is required to balance this tendency.

Measurements of the cone wall and bin pressures in the 140mmØ cyclone for inlet velocities from 10 to 16 m/s, such as in figure 5.J.4 on page 201 and in section 5.H show that the wall - bin gradient is favourable for the boundary layer flow. There is a steady decrease in pressure along the cone wall towards the bin, and the bin pressure is lower still. The experimental radial pressure gradients are compared with the centrifugal restoring force in section 5.G and some areas are apparently unstable.

The vortex structure theory proposed from the results of this study suggest that there will be continual removal of dust from the boundary layer and recirculation of dust from the bin and gas exit. Although the separation and radial inflow of the boundary layer decreases the effective residence time of the particles, the recirculation of large, already-collected particles from the wall into the core would improve the chance of agglomeration for the finer particles that would otherwise leave in the core flow. As the large particles move outwards from the core they can 'sweep' finer particles to the wall. This was reported by Mothes et al (1981) to be the most effective means of agglomeration.

If, as is suggested by the results, the higher inflows are concentrated in the lower cone region, a design modification is suggested: consisting of a short cylindrical sleeve placed around the vortex core in this region to prevent the inflows carrying dust into the core vortex, while still allowing dust to be reseparated from the core vortex into the outer vortex higher in the cyclone.

8.A.2: Airflows in the bin

It would seem preferable for the vortex to enter the bin to assist the transport of dust to the bin and enhance the agglomeration of particles, by the agglomeration mechanisms described by Abrahamson et al (1978), Mothes et al (1981) and Tackie et al (1989). The positive pressure gradient that would be caused by the sharp dust exit expansion would act against the entry of the vortex onto the bin, as theory given in the literature indicates that this will stabilise or promote the vortex breakdown. Wong (1973) (see Abrahamson et al (1978)) found that a recirculating flow extended well into the bin, which is thought to be part of the capping of the vortex. The sudden expansion and slowing of the swirl will allow the dust to disengage and settle. The entrainment of dust from the bed surface in a rotary kiln was found experimentally by Tackie et al (1989) to be due primarily to collision with saltating particles on the solid bed. Even if the main vortex flow is prevented from entering the bin, entrainment from the bin may still occur with the near axis reverse flow, which has been observed to reach into the bin, and return from there.

If the velocity is too high however, the entrainment from the bin may rise to detrimental levels. Stairmand (1951) stated that this 'base pick-up' had been shown to be the chief cause of

excessive emission in a poorly designed cyclone. In this situation longer cyclones are preferred as they allow more time for this dust to be re-separated from the core before it leaves the cyclone. This recirculation of dust from the bin and cone boundary layer appears to account for the increased capture of fines through agglomeration, and the loss of larger particles that would have been expected to have been collected.

The re-entrainment of dust from the bin may be beneficial to the collection efficiency. Abrahamson et al (1978) and Mothes et al (1981) contend that the agglomeration of particles is not just an important part of the collection process, but for fine particles it may be a necessary step, as the fine particles are too small to settle out by themselves. Mothes et al (1981) suggest that the major cause for the improvement in the total efficiency with increasing feed dust concentration is the increased agglomeration. Apart from the saltation mechanism, the agglomeration is most likely to occur near the wall, because of the higher concentrations of particles in that region, and the higher fluid shear rate. However, Abrahamson (1981) found that very few agglomerates existed close to the wall due to their breakup in collisions with the wall.

The size of the dust exit affects the performance in several different and possibly conflicting ways. The ratio of the exit diameters determines the resistance to the flow leaving the cyclone - a relatively larger gas exit is thought to increase the inflow of the vortex in the upper cyclone to the detriment of the efficiency. A small dust exit increases the possibility of loss of the boundary layer and dust inwards to the core, while a larger dust exit may permit too much air to enter the bin, resulting in increased entrainment. The optimum size of the dust exit is expected to depend on the inlet velocity.

8.A.3: Form of the vortex 'breakdown'

The attachment of the vortex core to the wall would have a severe effect on the efficiency by removing the boundary layer carrying the dust along the wall. This was not observed in the cyclone geometries examined in this study, but the separation of the boundary layer from the wall will clearly have a similarly large effect on the dust transport. The paired streamwise vortices in the boundary layer (Görtler vortices) would serve the same function on a smaller scale with the 'pumping' of boundary layer fluid away from the wall.

The proposed theory does not involve a bubble-type vortex breakdown in the lower cone or bin, as there were no supporting observation for this from the visualisation experiments. However, the vortex must separate from the walls, and will turn inwards after the initial expansion, forming a recirculation that differs from the tight bubble-type vortex breakdown described in chapter 3.C. The tracers were able to penetrate through this recirculation and the dust flow into the bin may well be enhanced rather than impeded by the presence of this sort of breakdown at the dust exit. The near axis reverse flow may result in some back-mixing of dust from the gas exit, although the reverse flow has not been proven to exist while dust is being fed to the cyclone. It is well known that the flowfield in the cyclone is modified by the presence of dust.

8.A.4: Influence of geometry on the efficiency

As previously stated the Stairmand High Efficiency cyclone was chosen as the starting point for this study because the slope of its grade efficiency curve is markedly less steep than other designs. This suggests that the vortex is interfering with the dust flow to the bin, with enhanced loss of coarse particles and some recapture of fines. The plot of the sharpness of cut for a variety of cyclones given by Abrahamson & Allen (1986) (reproduced in figure 2.3) shows that where the vortex is predicted (by Alexander's equation) to end well down in the cone the classification is markedly less sharp than for shorter or longer versions. As well as the cyclone length, the ratio of the dust exit to gas exit diameters had an influence, which was attributed to the stabilisation of the vortex breakdown bubble or the ease with which the vortex enters the bin. The steepest classification in Abrahamson & Allen's study was found for cyclones with a large dust exit, and a short cyclone length.

The only observation of a structural change induced by the geometry that has been reported in the literature is the attachment of the vortex core to the wall in cylindrical cyclones of length/diameter ratios that are greater than normally used in industrial cyclones. This study has revealed evidence of differences in the vortex structure between different geometries, and it is assumed that these translate into differences in the dust collecting performance.

Modifications are frequently made to the dust exit to suit the location of the bin and cone, and also to modify the bin pressure. It was shown that the extension of the dust exit had a dramatic effect on the flowfield, whereas an increase in the barrel length had little impact. The collection efficiency of these geometries were examined by a final year student (Kevern, 1991), but no significant difference was found despite the difference in the flow structure. If there is to be any improvement in cyclone design, there must be an observable difference in collection efficiencies between geometries. The optimum vortex structure may turn out to be a compromise between opposing trends.

From experience with the van Tongeren AC850 cyclone, Svarovsky (1984) states that large dust exits expanding into large bins result in the vortex being able to reach into the bin, with a consequent decrease in the efficiency at higher flowrates. This was reported to be avoided by extending the cone at the dust exit end, an arrangement that was examined in this study as the 'Svarovsky design' and which was found to have a markedly different vortex structure at the dust exit end. The decrease in efficiency at higher flowrates was also reported by Stairmand (1951). Tengbergen (1955) reports improved efficiencies in some cases by increasing the dust exit diameter. He found a more significant difference when air was leaked into the bin, with the cyclones with large diameter dust exits showing a smaller decrease in collection efficiency than those with smaller dust exits. The dust exit diameter was varied by extending the length of the cone, which again introduces another factor - an increase in the cyclone length.

The previous means of estimating the vortex length was the empirical equation of Alexander (1949), which had no dependence on velocity. Bryant et al (1983) similarly found no change in their observations of vortex length in a return flow cyclone for velocities ranging from 16 to 35 m/s. The theory that was proposed in Chapter 7 predicts that higher velocities will result in an increased instability of the boundary layer to the ejections and separations due to the embedded streamwise vortices. The effect of increasing the diameter of the dust exit is also accounted for, as the greater distance of the core from the wall reduces the likelihood of the

ejections or separation reaching the core. A large diameter dust exit also gives more protection of the boundary layer from precession of the core vortex.

The reduction in efficiency at higher velocities was attributed by Stairmand (1951) to bouncing of particles off the wall, to the extent that 6000μm particles escaped a d_{50} = 10μm cyclone. Kalen & Zenz (1974) found quantitative support for the saltation theory, but since different behaviour is obtained for different cyclone geometries with the same speeds and particle densities it would appear that something other than saltation is contributing.

The other new features of the proposed vortex structure theory were the vortex breakdown in the gas exit, and the near axis reverse flow from the gas exit to the bin. The position of the gas exit breakdown was well down the gas exit, suggesting that it would have no effect on the collection efficiency. However, the near axis reverse flow is thought to originate from the gas exit, and this may result in a recapture of dust from the gas exit. The significance of this depends on the amount of flow that is contained in the reverse flow, and also on the amount of dust that is present in the source region near the axis. It is observed that most of the air leaves the cyclone in a narrow annulus near the gas exit wall, and the majority of the dust is expected to be in this region. Sampling dust in the exit of the 2090mmØ cyclone (unpublished work, Abrahamson) revealed an order of magnitude larger concentration of the dust next to the wall of the gas exit, then uniform concentration in the core.

The improvement in collection efficiency achieved by Zhou & Soo (1990) by inserting a probe with a cross section of '*' along the axis would appear to be due to the modification of the near axis reverse flow. The reverse flow behaviour near the axis will be modified by this probe suggesting that control of the motion on the axis could help to improve the efficiency. The near-axis reverse flow has also been shown in this study to be affected by changes in the geometry, such as the cyclone length, the dust exit diameter, and the bin depth, and also to disturbance by bodies on the axis. It does not appear to be present with cyclone lengths longer than the standard Stairmand H.E. design. The insertion of the probe by Zhou & Soo (1990) may also have resulted in a slowing of the axial velocity close to the axis, which would allow the particles to move to larger radii. The efficiency is also predicted to be improved (in an analytical study by Zhou & Soo, 1991) if the gradient of tangential velocity near the wall is reduced, as this reduces the particle turbulence near the wall.

A common approach to the study of cyclones has been to measure the collection efficiency for small variations of the geometrical parameters about the standard design. The proposed theory can be applied to the changes in geometry to examine if it can account for the changes in the efficiency. The variation of one geometrical parameter can have several effects, which complicates the result. Iozia and Leith (1989b) used the efficiency predictions of Iozia & Leith (1989a) and the pressure drop predictions of Stairmand (1949) and Barth (1956) to optimise the cyclone design, based on the Stairmand geometry. The optimised designs were longer than the Stairmand High efficiency design, and had inlet areas 10% larger, and exit areas 24-64% smaller .

Zhou et al (1987) made an experimental study that varied the cyclone dimensions in a 2^4 factorial manner. This showed that the lowest pressure drop and highest efficiency was achieved by a cyclone that had the cone angle decreased, and increased ratios of $S/_{de}$ (the length of the gas exit inside the cyclone relative to the exit diameter), $d_o/_D$ (the ratio of the gas exit outer diameter to the barrel diameter - that is a smaller inlet annulus, keeping the inner diameter

constant), and $^{Hk}/_{D}$ (the height of the cone, as expected from the decrease in the cone angle). These correspond to a longer cyclone with thicker gas exit wall and longer cone, but the design that was started with is not detailed.

Although the existing theoretical models suggest that the efficiency should increase with increasing height, Mothes et al (1981) report that in fact the measured grade efficiency curves are almost the same for different cyclone heights. This supports the concept that the vortex has a natural length, beyond which the additional length has little effect. The results of this study suggest that vortex reaches the bin for a wide range of barrel lengths, as long as the dust exit is not constricted. If the vortex is assumed to be stabilised on the dust exit then increasing the length of the cyclone should decrease the average radial inflow, with a resulting improvement in the efficiency. The observation of Mothes et al may be due to a balancing of gains and losses.

8.B The impact of geometry on the Pressure drop:

The position of the vortex breakdown could also have an influence on the cyclone pressure drop depending on whether the vortex enters the bin or not. The pressure drop is thought (Ogawa (1987), Abrahamson (1992)) to be dominated by the core dissipation, and longer vortex lengths would reduce the dissipation by the weighting of the dissipation to lower spin values. Changing the geometry will also have an effect on the core dissipation by altering the core reversal activity. Zhou & Soo (1990) found the pressure drop was reduced to 1/3 of the original value by inserting a fluted probe axially into the cyclone. This is consistent with the above view as it would severely reduce spin in the core region.

Abrahamson (1992) reports the results from a study of the pressure drops of 54 geometries which showed "the Euler number to linearly decrease with increasing vortex length". The results presented in Figure 5.F.2 suggest a limit to this is reached around the standard Stairmand HE geometry, and beyond this length additional barrel length has little effect on the pressure drop. It is thought that the vortex reaches the dust exit regardless of the barrel length, suggesting that there is another factor countering the effect of the increased length. It was observed that the near-axis reverse flow was less common for geometries that were longer than the standard Stairmand High efficiency geometry. It was not expected that the near-axis reverse flow would be a large enough fraction of the flow to have a significant influence, but it may modify the turbulent viscosity of the core. The absence of the reverse flow in longer geometries may be associated with other changes that were not observed.

The measurements of pressure drop reported by Abrahamson (1992) for a variety of barrel and cone lengths, and exit diameters all fitted to a Stairmand H.E. type entry show two stable lines in the Euler number vs Vortex length plots. The split between the lines occurred at the same vortex length (about 1.5 barrel diameters) for a range of exit diameters. The upper line persisted for longer due to stabilisation by the cone. This had a higher Euler number, and was thought to be associated with a single straight vortex with less spin decay and hence less turbulent mixing with the boundary layers. The lower line was thought to be due to a distorted vortex, possibly an off axis precessing vortex or a multiple core. Further explanation of the significance of this Euler number versus cyclone length plot is given in Abrahamson (1992).

Ayer & Hochstrasser (1976) report two inlet/outlet pressure drop-flow regimes in their study of Stairmand HE cyclones of barrel diameter 19mm. Geometries with shorter versions of the cone length exhibited a smooth increase in pressure drop with flow, but the standard cone length had two stable pressure drop-velocity profiles: for exit pipe Reynolds numbers below 2000 (laminar) and above 4000 (turbulent). Between these, pressure drops were observed on either profile, but the turbulent condition was more stable, and showed a lower pressure drop. They proposed that the normal flow was the turbulent condition, and in the laminar case the vortex ended partway down the cone at a 'zone of stagnation'. This was confirmed by a ring of particles deposited at the wall with none below, and the fact that there was no further change of pressure inside the cyclone below this plane.

The flow in all the cyclones examined in our study was well into the turbulent region. It is possible that the effect observed by Ayer & Hochstrasser was due to a factor other than the turbulent transition. The effect is certainly related to the vortex length, as the shorter cone length showed no such change with Reynolds number. At higher flowrates the vortex is given enough energy to run the full length, and below 5m/s it tends to end in the mid-cone region. The shorter cone stabilises the vortex and prevents the short-circuiting.

Pervov (1975) reports modifications to the gas exit that were found to lower the pressure drop. For high capacity cyclones this was achieved with no effect (or a slight improvement) on the efficiency. The modifications consisted of 'unswirlers' that extended the gas exit well down into the lower cone region, and allowed gas to enter through longitudinal apertures. This was reported to smooth out the radial velocity and give a uniform inflow over the length of the cyclone, as well as reducing the rotational velocity somewhat. The smoothing of the radial inflow was an advantage for the high capacity cyclones where the radial flow non-uniformities were reported to be large, this advantage balanced the loss of separating capacity due to the reduced rotational velocity. It was further suggested that the high efficiency cyclones already had a uniformly distributed radial velocity and consequently the decrease in the rotational velocity was not compensated for by evening out of the radial flow. This is an interesting result, although it is not clear how much of it is based on conjecture, and how much is based on measurements. The concept of longer, slender cyclones having a more uniform radial inflow which results in a lower pressure drop and a higher collection efficiency is presumably related to a change in the vortex structure. The more slender cone has a slower change in the radius of curvature along the length. It is possible that the Görtler vortices are less stable when the curvature changes rapidly, as the spacing of the vortex pairs is determined at their initiation, and maintained downstream.

The "Long cone" geometry that was examined in this thesis had no barrel but was the same overall length as the standard Stairmand High Efficiency geometry. It had a slightly higher pressure drop than the standard geometry, but when a barrel section of 140mm was added to the long cone, the pressure drop was reduced to below that of the standard. The "Long cone" geometry combines the lack of constriction afforded by the barrel in the upper cyclone with the stabilising effect of the long cone, apparently enabling the vortex to be held in a stretched out form. This was confirmed by the axial static pressure profile, which was consistent with the profiles obtained in geometries with unconstricted dust exits. This was examined to the extreme length of the "Extra Long" geometry, which appeared to be near the limit of the vortex length, with a single set of measurements indicating that the vortex did not reach into the bin, while the rest indicated the vortex did reach the bin.

The 'Shortest' geometry had the highest pressure drop of the four basic lengths studied. When the extended cone piece was added, (which resulted in a smaller dust exit and a length slightly greater than the standard geometry) the pressure drop was reduced. The pressure drop for the standard geometry with the extended cone increased slightly. It is suggested that the extension of the cone with the shortest geometry gives a longer vortex length, which is useful to reduce the dissipation loss, whereas the extra cone length is again redundant in the standard geometry. Other variations of extending the length of the standard geometry, such as a constant diameter extension of the dust exit also had no effect on the pressure drop. Figures 5.G.13 and 5.G.14 appear to show the vortex penetrating further for the 'shortest' geometry when the extension is added. The radial inflows in the standard geometry as shown by the fog tracers in figures 5.A.4 to 5.A.6 appear to be far from uniform along the length.

The Euler number increased with increasing flowrate, with a steeper rise at low flowrates. The standard geometry indicated a levelling off at an inlet velocity of about 20m/s, with longer geometries this tended to happen earlier - at about 12m/s. The flowrate of 12m/s in the longer cyclones is the region where the switching between axial static pressure profiles takes place. This switching involved two types of profiles near the bin base - one with a distinct pressure minimum just off the base, and another with a plateau in the axial pressure at the same location. The pressure minimum could be related to the structure that caused the trapping of tracers at the bin base, which was thought to be a bubble-type vortex breakdown. The bin base trap was observed to be intermittently present for long geometries, possibly due to a limit in the length that the near-axis reverse flow could travel from the gas exit.

Disturbance of the core flow caused the movement of the gas exit recirculation zones seven diameters downstream, yet had little effect on the pressure drop. From this it appears that the dynamic movements near the axis or the reversal flow at the axis have little influence on the pressure drop. Features such as the scroll exit or the plate on the axis in the gas exit may help to stabilise and locate the axial movements of the vortex but these also appear to have little effect on the pressure drop in the main body of the cyclone. The pressure drop in cyclones with a scroll exit cannot be directly compared because of the different exit loss.

8.C Velocity Profiles and modelling

As discussed earlier, the models that supply cyclone grade efficiency curves make assumptions about the form of the velocity components in the cyclone. The discrepancy between the theories and experiments is largely due to the simplified flow models on which they are based. The reason for studying the flows in the cyclone is to provide more realistic estimates, and in order for these to be easily applied to a design model a simple analytical form is desired.

Previously the zero axial boundary surface has been assumed to be a cylindrical extension of the gas exit tube, and the tangential velocity given by:

$$V_\theta \propto 1/r^n \qquad \text{with n often taken as 0.5.}$$

The 1 term Burgers vortex equation gives a satisfactory fit to the tangential velocity components with predicted parameters (from empirical equations that fit the Stairmand H.E. geometry, at least). The Burgers tangential velocity model was fitted by adjusting the turbulent viscosity parameter. In the absence of any obvious trend in the scatter of the fitted values an average

value was then taken as an approximation for the turbulent viscosity throughout the cyclone. It has been suggested (Abrahamson, 1992) that 'the turbulent viscosity should be based on the cyclone dimension in the direction of the important direction of transport, which is the wall radius'. The wall is the boundary for the oscillations and these could wash across the whole section. Adjusting for the variation of the wall radius along the cone length did not reduce the scatter in the fitted viscosity. The core diameter is the alternative dimension, but this is approximately constant over a great height.

It has been shown in section 5.D that the axial velocity model of Bloor & Ingham (1987) can not satisfy the mass balance without resorting to unrealistic values of the axial velocity near the axis. If the exponential axial velocity profile of Batchelor (1964) is to satisfy both the mass balance and the position of the zero axial velocity boundary then different values are required for the axial and tangential turbulent viscosity. Swirling flows are commonly reported to feature anisotropic turbulent viscosities.

Abrahamson (1992) also suggested that: 'the stability of the core and hence rate of radial transport of angular momentum depends more on the length of the vortex than the outer diameter'. The lower cone region could be expected to be subject to more instability than elsewhere because of the ending of the vortex. Hence if the parameter is affected by the stability of the vortex then large variations could be expected in the lower cone - the variation in the best fit values was greater in the cone region. Allowance may need to be made for the effect of the vortex breakdown, boundary layer separation and the reverse flow at the axis as these would be expected to influence the turbulent viscosity as well as the stability of the vortex.

The flow model will need to allow for the effect of the near-axis-reverse-flow on core properties such as the turbulent viscosity. These dynamic movements may not be visible in the mean velocity profiles, but may still have a significant effect on the efficiency or pressure drop. The flow models also need to make allowance for the asymmetry of the vortex, which has a helical variation of the vortex centreline along the axis. Improvements were made to the agreement between the experimental profiles and model profiles by allowing for the vortex centreline being off axis. For some purposes, it will also be necessary to allow for the differences found between opposite sides of the cyclone.

Iozia & Leith (1989a) also found a (statistically significant) difference in the tangential velocity profile between the opposite sides of the Stairmand H.E. cyclone. Apart from in the velocity profiles and with the vortex centreline, the eccentricity differences have shown up in our study in the Γ_0 vs L plots; the variation of the best fit parameters for Γ_0 and the turbulent viscosity; the wall flow yaw angles as well as in visualisation experiments with helium bubble tracers and cotton streamers. The results from this study show it to be more pronounced in the cone.

The tangential velocity profiles are reasonably constant along the cyclone length. Although the value of the maximum tangential velocity at each level is similar, the value close to the wall decreases down the length, presumably as the boundary layer builds up. The similarity of the gradient of the tangential velocity near the axis suggests that there is an exchange of momentum along the axis. This similarity appears to be influenced by the rapid vertical pulses in the core. At the lower end of the cone, some vorticity is expected to be supplied from the bin flow, and this is probably spread up through the core. The distance from the cone to the bin base seems to affect the behaviour of the vortex in the lower cone, which is consistent with the boundary layer from the bin base being a source of vorticity for the core.

Dynamic simulations of the flow

The use of the steady state profiles to predict the cyclone efficiency may fail because of the lack of account taken of the dynamic behaviour of the vortex. Some progress on the dynamic modelling of the cyclone flow is reported in the literature. Boysan et al (1982, 1983) developed a computer model of the flow with an algebraic turbulence model and were able to reproduce 'all the features of experimentally observed gas flow in a cyclone'. The model was used for a stochastic particle tracking simulation of the collection efficiency. Spall et al (1991) have numerically modelled the breakdown bubble of a vortex flow and showed details of the internal structure that resembled the experimental observations of Faler and Leibovich (1978).

Vortex dynamics are more often incorporated as add-ons or corrections to the steady-state theory. Zhou & Soo (1991) incorporated the effect of particle and gas turbulence into the formulation of particle motion and collection in a cyclone separator. Ranz (1985) developed a dynamic description of the dust ropes in the boundary layer on the cyclone wall.

The development of a realistic simulation of the cyclone flow is still some way off being able to reliably predict the efficiency. The observations from this study, such as the near axis reverse flow shown by the helium bubble tracers (Figure 5.A.2), and the boundary layer movements shown by the fog tracer (figures 5.A.8 - 5.A.10) will prove useful as means of verifying the simulations.

8.D Simple diagnostics and cyclone design:

In order to diagnose problems with existing cyclones, techniques are needed by which the position of the vortex can be determined. These need to be quick and simple and involve a minimum of disruption to the cyclone. Obviously many of the techniques used in this study are unsuitable for use on an existing cyclone in an industrial situation, such as the need for transparent walls or time consuming traverses. The determination of the circulation at the wall requires a series of holes to be drilled in the walls of the cyclone, but full traverses need not be carried out, which represents a considerable time saving as well as a minimisation of the disturbance of the flowfield. However because of the discrepancy between the opposite sides of the cyclone more thorough measurement surveys would be needed to establish the vortex location. The axial static pressure measurement would prove difficult because of lack of head room with vertical cyclones, but this has clearly shown a difference between geometries with the extended cone piece and those with the standard dust exit.

A clear indication of the position of the termination of the vortex could be obtained reasonably simply by graphing the profile of the average wall-axis pressure gradient, however this still required measurements of the pressure at the axis, albeit at larger spacings. The measurement of the pressure at the axis can be criticised on the grounds of disturbance of the flowfield. Instead, the profile of the static pressure along the cone wall can be used by itself, as this shows a slight rise in the case of the cylindrical extension of the dust exit, at the same position indicated by the wall-axis pressure gradient.

A simpler technique is to measure the bin pressure at the side wall and base. A large pressure difference between these two locations appears to indicate that the vortex core reaches into the

bin. Apart from the effect of having the vortex entering the bin the detrimental effect of leaks into the bin should also be considered. This suggests that a design which operates with the average bin pressure near atmospheric pressure is preferable. It was found that the extension of the dust exit at constant diameter, or an extension of the cone to a smaller dust exit diameter raised the bin pressure. Tengbergen (1955) has also mentioned the manipulation of the bin pressure by altering the diameter of the dust exit, which appears to have been achieved by extending the cone. The bin pressure is also increased by increasing the bin volume.

Presuming that the cyclone performance is shown to be affected by the position of the vortex structure or breakdown position, and that the position can be determined, then some means of altering the position is required. Often this will mean modifications to an existing cyclone to improve its performance, with corresponding restrictions on the extent of the changes that can be made. Many modifications to the geometry have been suggested to improve the efficiency of the cyclone. An improved understanding of the flow patterns could help to explain why (or whether) these work. The inverted cone in the entrance to the bin described by Krambrock (1979) would be expected to prevent the near-axis reverse flow from entering the bin, and may also help to stabilise the end of the vortex at the dust exit. The path of the air leaving the bin is also extensively modified. The observations of localised regions of high radial inflow in the lower cone (such as shown in Figures 5.A.4 - 6) suggests that the efficiency could be improved by the axial insertion of a sleeve around the core in the lower cone to prevent the flow separated from the wall from reaching the core.

8.E Development of a new design method

The results of this report have not yet been extended to the development of a design method for predicting the efficiency and pressure drop. The velocity profiles and fitted models can be used to adjust the assumptions made about the flow pattern, and the mechanism of interference on the secondary flows carrying the dust can be taken into account.

Models that have been proposed to predict the grade efficiency generally fall into either those based on residence time concepts (Leith & Licht, 1972) or on the concept of a separation area. The best performed of these design models are the original approach of Muschelknautz (1972) (who developed the ideas of Barth, 1956), and this has been refined by Dietz (1981) and Mothes & Loffler (1984). These models all concentrate on the imaginary surface formed by the extension of the exit tube, and differ in their estimates of the flow and particle behaviour within the cyclone. A description of the features of the models has been presented by Abrahamson (1985) and will not be repeated in detail here.

The reduction of the collection efficiency as the inlet velocity is increased is contrary to the prediction of the simple models, and this is usually attributed to an increase in turbulent re-distribution and entrainment from the walls by bouncing. Leith & Licht used the concept of instantaneous redistribution of dust across the cyclone cross section to approximate the effect of turbulent mixing. This yielded a grade efficiency curve that had a similar shape to experimental curves but the assumed velocity of redistribution was found by Abrahamson et al (1978) to be much higher than can be accounted for by the turbulence. The localised radial inflows proposed in Chapter 7 could have a role in this.

The dust is re-entrained from the cone walls and bin and re-separated higher in the cyclone. This re-separation of dust is supported by the measurements of ter Linden (1949) who found that the particles were still collected even when introduced to the core of the cyclone, with no reduction of collection efficiency if the dust was fed no higher than halfway from the gas exit to the dust exit. Abrahamson et al (1978) found that sand of 180-250μm was entrained from the bin when the deposited dust surface was 70mm from the dust exit, but the cyclone length was sufficient to re-separate the particles. This may not be the case for shorter cyclones or for finer particles. The pulsing of dust from the bin was observed in this study (see section 5.L**) with the dust appearing to reach the wall around the top of the conical section. Abrahamson (1981) noted that the dust rope could be formed with no dust fed to the inlet, simply by the recirculation from the bin.

The particle cut size d_{50} can be predicted by theory, but the slope of the grade efficiency curve requires an explanation for the increased collection of finer particles, and reduced collection of larger particles. Abrahamson et al (1978) have shown that collection of the finer particles could be achieved only by agglomeration. The evidence cited in support of this includes the increase in collection efficiency with humidity and with increasing dust loading.

The modelling of the velocity as detailed in section 6.B can be used to improve the estimates of the flow behaviour. Hoffman et al (1992) summarises the methods of calculating the tangential velocity at the radius of the gas exit, which is used as the control surface. Muschelknautz-Barth assumes an average geometry, whereas the other two approaches can relate the grade-efficiency curve to different geometries. Muschelknautz (1972) requires the knowledge of the sink velocity of the particle w_p and the inflow velocity of gas (v_r), expressed as the ratio $S = \frac{w_p}{v_r}$. The tangential velocity U_x at the radius of the gas exit lip is used to estimate the w_p.

Dietz (1981) assumes that particles are mixed instantaneously by turbulence across each of three regions of the cyclone. The parameters needed to define the grade efficiency curve are then S, T and l_{en}/l. Where T is the ratio of the values of $w_p r$ at the gas exit radius and at the barrel surface. For Stokes drag this is simply the equivalent ratio of the tangential velocities. The form of the tangential velocity assumed by Dietz is $V_\theta . r^m$ = constant.

Mothes & Loffler limit the turbulent diffusion of particles in the radial direction, and consider a bin region. In addition to the parameters in the Dietz model this requires parameters Δ and $\frac{Q_{bin}}{Q}$, representing the dimensionless diffusivity, and the fraction of the inlet flow entering the bin, respectively. The flow assumptions of the Mothes-Loffler model allow for:
(a) an entrance correction to the inlet velocity V_{en} to obtain the wall tangential velocity
(b) a tangential velocity profile related to a wall friction factor
(c) a radial inflow velocity averaged over the actual exit-to-exit distance.

The form of the cyclone tangential velocity profiles found by the present author will be used to develop a cyclone design model. The influences of the secondary flows and vortex dynamics will also be incorporated. In particular, attention will be paid to the disruption of the cone boundary layer by boundary layer separation. The magnitude of the radial turbulent diffusivity needs to be examined as well.

Chapter

9

CONCLUSIONS

This thesis presents two major contributions to the study of the flowfield in the return-flow cyclone. The first is the measurement of the time-averaged velocity profiles in three scales of cyclones, and the identification of suitable time-averaged models to describe these profiles as well as equations to predict the model parameters. The second contribution is the investigation of the existence of a 'natural' vortex length and its relation to vortex breakdown phenomena. A wide range of measurement techniques have been utilised and interpreted to build up a theory that accounts for the vortex structure and explains the mechanisms by which the structure is formed. The proposed theory is consistent with the results from this study and other experimental and theoretical studies from the literature. The validity of the theory may be tested by further experiments.

This study has revealed a number of features of the flowfield that will prove useful in testing other models or simulations of the flow. In particular the existence of a second reversal of the vortex near the axis, travelling from the gas exit towards the bin, will be useful for testing time-dependent simulations.

It was shown that the 'natural vortex length' prediction of Alexander (1949) does not apply to the length of vortex in conical or cylindrical/conical cyclones, at least in the range of conventionally used cyclone lengths. This is due to the stabilising effect of the contracting walls of the cone compared with the cylindrical cyclones that the occurrence of a natural length is most commonly observed in.

The vortex appeared to reach the entrance to the bin under normal conditions and then breakdown by a combination of the expansion and separation of the boundary layer from the wall, resulting in a recirculation of the fluid from the outer region in to the axis to cap the vortex, just inside the bin. For geometries with constrictions or extensions to the dust exit end of the cone (relative to the Stairmand High Efficiency geometry design) the vortex may terminate before reaching the dust exit due to the instability and separation of the boundary layer. Radial inflows resulting from these instabilities occur along all of the cyclone length, but it is the smaller radius of curvature and the proximity of the boundary layer to the core that makes the dust exit location particularly susceptible to the termination. Further work is needed to investigate more closely the conditions and geometries under which the termination occurs. The length of the barrel section was found to be much less important than the dust exit configuration.

According to the proposed theory, the core vortex undergoes a core-type vortex breakdown as it leaves the cyclone through the gas exit, and the position at which this is stabilised depends on the exit geometry. For exits with expansions a short distance above the start of the gas exit the vortex breakdown is stabilised on the lip of the expansion. In sufficiently long, straight exits the vortex breakdown moves upstream and is stabilised a short distance downstream of the gas exit lip. A subsidiary vortex breakdown moves further upstream into the cyclone body and can reach the bin under favourable conditions, becoming stabilised just off the bin base.

The majority of measurements made in this study were time-averaged, which tended to result in a steady-state view of the vortex structure. Fast, dynamic behaviour of the vortex was noted, but the increased complexity required by a model to allow for this should be balanced against the effect that short term events have on the time-averaged performance. From preliminary measurements, the gross efficiency and the overall pressure drop do not appear to be significantly different between geometries with or without the near-axis reverse flow or the termination of the vortex before the dust exit. The contribution of such features to the residence time and recirculation of dust may have more influence on the agglomeration of dust and hence be more apparent in the grade efficiency behaviour.

Models for predicting the cyclone efficiency use several assumptions that are founded more on expedience than experience. The existence of a natural length of the vortex, and the uniformity of the radial inflow are contradicted by the results of this study. The observations of the dynamic features of the cyclone flow may help to refine the turbulence and dust redistribution aspects of the models. The identification of the models of Burgers (1948) and Batchelor (1964) as being suitable for the description of the tangential and axial velocity components will improve the predictions of the velocities that are used in the models. The empirical relationships that were developed to predict the model parameters over the range of industrial sized cyclones will be useful, particularly the expressions for the turbulent viscosity components.

REFERENCES

Abraham, F.F.: "Functional dependence of drag coefficient of a sphere on Reynolds number". Physics of fluids 13 p2194-5 (1970)

Abrahamson, J.: "Collision rates of small particles in a vigorously turbulent fluid" Chem. Eng. Sci 30 p1371-1379 (1975)

Abrahamson, J.: "Mechanisms of dust collection in cyclones", in "Progress in filtration and separation" Vol 2. ed R.J. Wakeman, Elsevier, Amsterdam 1981.

Abrahamson, J.: "Cyclone design models and procedures". report to Separation Processes Service, unpublished (1985).

Abrahamson, J.: "The performance of an air ejector". Consultant report to Addington Engineering Ltd unpublished (1988)

Abrahamson, J. Note on corrections to Bloor & Ingham's 1987 paper unpublished (1989)

Abrahamson, J. "Cyclone pressure drop" report to S.P.S. unpublished (1992)

Abrahamson, J & Allen, R.W.K. "The efficiency of conventional Return-flow cyclones at high temperatures". Proc. I.Chem.E. Symp. Ser. no.99 p30, (1986).

Abrahamson, J.; Martin, C.G. & Wong, K.K. "The physical mechanisms of dust collection in a cyclone". Trans. I. Chem. E. 56 p168 (1978)

Acarlar, M.S. & Smith, C.R. "A study of hairpin vortices in a laminar Boundary layer, Parts 1 & 2 " J. Fl. Mech 175 p1-41, 43-83 (1987).

Aidun, C.K. "Principles of hydrodynamic instability: application in coating systems Part 1 Background" Tappi J p213 Feb (1991).

Aihara, Y. & Koyama, H. "Secondary instability of Görtler vortices: formation of periodic three-dimensional coherent structure". Trans Japan Soc Aero Sci 24 p78-94 (1981)

Alexander, R.McK. "Fundamentals of cyclone design and operation" Proc. Austr. Inst. of Min. & Metall. N.S. Nos. 152-153 p203-228 (1949)

Alexander, R.McK. Pers comm. to D. Leith (June, July 1986)

Antonia, R.A.; Danh, H.Q. & Prabhu, A. "Bursts in turbulent shear flows". Phys Fluids 19 n11 p1680 (1976).

Aslami, M & Licht, W. "Concept of effective residence time applied to cyclone-type particle collectors" A.I.Ch.E. Sympos. Ser. 74 no175 (1978)

Ayer, H.E. & Hochstrasser, J.M. "Cyclone discussion" in 'Proceedings of Aerosol Measurement Workshop' Gainsville, Fla. (March 1976)

Bandyopadhyay, P.R.; Stead, D.J. & Ash, R.L. "Organised nature of a turbulent trailing vortex" AIAA J. 29 no10 (1991)

Barth, W. "Design and layout of the cyclone separator on the basis of new investigations" Brenn. Warme Kraft 8 p1-9 (1956)

Bassom, A.P. "On the effect of crossflow on nonlinear Görtler vortices in curved channel flows" Q. J. Mech. Appl. Maths 42 495-510 (1989)

Bassom, A.P. & Hall, P. "Vortex instabilities in three-dimensional boundary layers: the relationship between Görtler and crossflow vortices". J. Fluid Mech 232 p647-680 (1991)

Batchelor, G.K. "Axial flow in trailing line vortices". J.Fl. Mech 20 p645 (1964)

Batchelor, G.K. "An introduction to Fluid dynamics". Cambridge Univ. Press London, (U.K.). (1967)

Beeckmans, J.M. "A steady-state model of the reverse-flow cyclone".
Aerosol Sci. 3 no6 p491 (1972)

Beeckmans, J.M. "A two dimensional turbulent diffusion model of the reverse flow cyclone"
Aerosol Sci. 4 no4 p329-336 (1973)

Beeckmans, J.M. & Kim, C.J. "Analysis of the efficiency of reverse-flow cyclones"
Can. J. Chem. Engg. 55 p640 (1977)

Bellamy-Knights, P.G. "An unsteady two-cell vortex solution of the Navier-Stokes equations"
J. Fl. Mech 41 p673 (1970)

Belousov, A.N. & Gupta, A.K. "PVC and instability in swirl combustors"
Chem. Eng. Commun. 47 p363-380 (1986)

Benjamin, T. B. "Theory of the Vortex Breakdown Phenomenon"
Journal of Fluid Mechanics 14 p593 (1962)

Benjamin, T.B. "Significance of the vortex breakdown phenomenon"
Trans ASME J. Basic Eng 518 (1967)

Beranek, L.L. "Noise reduction". 1st edition, McGraw-Hill New York (1960)

Bidlake, K.M. "The influence of air pumping, about vaned rotary Atomisers on spray drying air swirls"
unpublished B.E. project report (1989)

Bippes, H. "Experimentelle untersuchung des laminar-turbulenten Umschlags an einer parallel angestromten konkaven Wand" Sitaungsberichte der Heidelberger akademie der Wissenschaften Math. Klasse 3 Abhandlund p103-180 Jahr (1972).
(Cited in Floryan & Saric (1984)).

Blackwelder, R.F. & Haritonidis, J.H. "Scaling of the bursting frequency in turbulent boundary layers"
J. Fluid Mech. 132 p87 (1983)

Bloor, M.I.G. & Ingham, D.B. "Theoretical investigation of the flow in a conical hydrocyclone"
Trans. Instn. Chem. Engrs. 51 p36-41 (1973)

Bloor, M.I.G. & Ingham, D.B. "Turbulent spin in a cyclone".
Trans. Instn. Chem. Engrs. 53 p1-6 (1975a)

Bloor, M.I.G. & Ingham, D.B. "The leakage effect in the industrial cyclone"
Trans. Instn. Chem. Engrs. 53 p7-11 (1975b)

Bloor, M.I.G. & Ingham, D.B. "Boundary layer flows on the side walls of conical cyclones"
Trans. Instn. Chem. Engrs. 54 p276-280 (1976)

Bloor, M.I.G. & Ingham, D.B. "The flow in industrial cyclones"
Journal of Fluid Mechanics 178 p 507-519 (1987)

Bohnet, M. "Cyclone separation of gas/solids mixtures".
Ger. Chem. Eng. 6 (or 4?) p211-220 (1983).

Bosley, R.B. & Negus, C.R. Airflow studies in a spray dryer chamber using the LDA technique".
AERE-R11400; U.K. Atomic Energy Authority, Harwell, U.K. (1984)

Bossel, H.H. "Vortex breakdown flowfield" Phys Fluids 12 (3) p498-508 (1969)

Bossel, H.H. "Stagnation criterion for vortex flows" Phys Fluids 12 (3) p498-508 (1969)

Bottaro, A. "Spatially developing flow in a curved duct" in Numerical methods in laminar and turbulent flow Vol VII pt1 ed Taylor, Chin & Homsy. Proc 7th Intl Conf Stanford July (1991). Pineridge Press, Swansea, UK

Boysan, F; Ayers, W.H.& Swithenbank, J. "A fundamental mathematical modelling approach to cyclone design". Trans. I. Ch. E 60 p 222- (1982)

Boysan, F; Ewen, B.C.R.; Swithenbank, J & Ayers, W.H. "Experimental and theoretical studies of cyclone separator aerodynamics" Powtech'83 Particle technology. Proc. I.Chem.E. Symposium series no.69 (1983)

Bradley, D. "The hydrocyclone". Pergamon Press, Oxford (1965)

Bradley, D. & Pulling, D.J. "Flow patterns in the hydraulic cyclone and their interpretation in terms of performance". Trans. Instn. Chem. Eng. 37 p34 (1959)

Bradshaw, P. "An introduction to turbulence and its measurement ". Pergamon Press, Oxford, (1971)

Bradshaw, P. "The effects of streamline curvature on turbulent flow". AGARDOgraph 169 (1973)

Briggs, L.W. "Effect of dust concentration on cyclone performance". Trans. A.I.Ch.E. 42 p511 (1946)

Brown, G.L. & Lopez, J. "Axisymmetric vortex breakdown. Part 2 Physical mechanisms" J. Fl. Mech. 221 p553-576 (1990).

Browne, J.M. & Strauss, W. "Pressure drop reduction in cyclones" Atmospheric Environment 12 p1213-1221 (1978)

Breuer, M. & Hanel, D. "Solution of three-dimensional incompressible Navier-Stokes equations for the simulation of vortex breakdown". In 8th GAMM Conf, Delft in Notes on numerical fluid dynamics, Viewerg-Verlag (1989)

Bryant, H.S.; Silverman, R.W. & Zenz, F.A. "How dust in gas affects cyclone pressure drop" Hydrocarbon Process June p87 (1983)

Burgers, J.M. "A mathematical theory illustrating the theory of turbulence" Advances in Appl. Mech 1 p 198 (1948)

Burggraf, O.R.; Stewartson, K. & Belcher, R. "Boundary layer induced by a potential vortex" Phys Fluids 14 (9) p1821 (1971)

Burkholz, A. "Approximation formulae for particle separation in cyclones" Ger. Chem. Eng. 8 p351-358 (1985)

Cantwell, R. "Organised motion in turbulent flow" Ann. Rev Fluid Mech. 13 p457 (1981)

Chanaud, R.C. "Observations of oscillatory motion in certain swirling flows" Journal of Fluid Mechanics 21 p 111 (1965)

Chedaille, I & Brand, Y. "Industrial Flames" Vol 1: Measurements in flames E. Arnold (1972)

Chigier, N.A. & Chervinsky, A. "Experimental investigation of swirling vortex motion in jets" J. Appl. Mechs. Trans ASME 89 p443 (1967)

Christiansen, T & Bradshaw, P. "Effect of turbulence on pressure probes" J. Phys. E.: Sci. Instrum 14 (1981)

Chu, C.C. & Falco, R.E. "Vortex ring/viscous wall layer interaction model of the turbulence production process near walls". Experiments in Fluids 6 p305 (1988)

Church, C.R. & Snow, J.T. "Measurements of axial pressures in tornado-like vortices" J. Atmos. Sci 42 n6 p576-582 (1985)

Church, C.R.; Snow, J.T.; Baker, G.L. & Agee E.M. "Characteristics of Tornado-like vortices as a function of swirl ratio: a Laboratory investigation". J. Atmos. Sci 36 (1979)

Clauser, F.H. "The turbulent boundary layer" Advances in Appl. Mech 4 p1-51 (1956)

Clift, R.; Ghadiri, M & Hoffman, A.C.Appendix: "Critique of cyclone models of Leith and Licht, and of Dietz" unpublished SPS report. (pers com to J. Abrahamson) (1985)

Clift, R.; Ghadiri, M & Hoffman, A.C. "Critique of two models for cyclone performance" A.I.Ch.E J. 37 n2 p285 (1991)

Coleman, P. "Ball Lightning" M.Sc thesis, Physics Dept, University of Canterbury (1990)

Coles, D. "Transition in circular Couette flow" J. Fl. Mech 21 p385 (1965)

Comas, M; Comas, J; Chetrit, C & Casal, J. "Cyclone pressure drop and efficiency with and without an inlet vane" Powder Tech. 66 p143 (1991)

Crowe, C.T. & Pratt, D.T. "Analysis of the flow field in cyclone separators" Computers and Fluids 2 p249-260 (1974)

Dabir, B. & Petty, C.A. "Measurements of mean velocity profiles in a hydrocyclone using laser Doppler anemometry". Chem Eng Commun. 48 p377 (1986)

Danckwerts, P.V. "Continuous flow systems: distribution of residence times" Chem. Eng. Sci. 2 p1-11 (1953)

Daniels, T.C. "Investigation of a vortex air cleaner" The Engineer p358 Mar (1957)

Daudpota, Q.I.; Hall, P & Zang, T.A. "On the nonlinear interaction of Görtler vortices and Tollmien-Sclichting waves in curved channel flows at finite Reynolds numbers" J. Fluid Mech. 193 p569-595 (1988)

Davidson, M.R. "Similarity solutions for flow in hydrocyclones" Chem. Eng. Sci. 43 n7 p1499-1505 (1988)

Denier, J.P.; Hall, P & Seddougui, S.O. "On the receptivity problem for Görtler vortices: vortex motions induced by wall roughness".Phil Trans. Roy. Soc. Lond A 335 p51-85. (1991)

DeOtte, R.E. "Characterisation of the velocity field in a small, cylindrical, low Reynolds Number Aerosol sampling cyclone". Aerosol Sci. & Tech. 12 p1037 (1990a)

DeOtte, R.E. "A model for the prediction of the collection efficiency characteristics of a small, cylindrical aerosol sampling cyclone". Aerosol Sci. & Tech. 12 p1055 (1990b)

Dietz, P.W. "Collection efficiency of cyclone separators". A.I.Ch.E. J 27 p 888-892 (1981)

Dirgo, J.A. & Leith, D. "Cyclone collection efficiency: comparison of experimental results with theoretical predictions". Aerosol Sci. Tech. 4 p401-415. (1985a)

Dirgo, J.A. & Leith, D. Filtration & Separation 22 p 119-125 (1985b)

Dixon, T.F.; Truelove, J.S & Wall, T.F. "Aerodynamic studies on swirled co-axial jets from nozzles with divergent quarls" J. Fluids Eng 105 p 197 June 1983.

Donaldson, C.duP. & Sullivan, R.D. in Proceedings of the 1960 Heat Transfer Fluid Dynamics Inst Stanford Univ Press, Stanford, CA (1960)

Drabner, M.; Schaue, A & Steudner, G. "Untersuchengen zum einfluss der Tachrohrgeometrie auf die Leistungsparameter von Fliehkraftabscheidern". Luft und Kaltechnik 2 p69-73 (1988)

Duggins, R.K. & Frith, P.C.W. "Turbulence effects in hydrocyclones". BHRA 3rd Int. Conf. on Hydrocyclones, Oxford. p75-81 ed P.A. Wood, Elsevier (1987)

Elsner, J.W. & Kurzak, L. "Characteristics of turbulent flow in slightly heated free swirling jets". J. Fluid Mech 180 p147-169 (1987)

Enevoldsen, S.S. & Werner, C. "An investigation of the influence from the air pumping on the drying air swirl in a spray drying chamber". Thesis presented for Civilingenior degree, Instit. Kemitecknik, Danmarks Tekniske Højskole, Lyngby, Danmark (1988)

Escudier, M.P. "Confined vortices in flow machinery". Annual Reviews of Fluid Mechanics 19 (1987)

Escudier, M.P. & Merkli, P. "Observations of the oscillatory behaviour of a confined ring vortex" AIAA J 17(3) p253-260 (1979)

Escudier, M.P. & Keller, J.J. "Vortex Breakdown". AGARDO-graph CP342 (1983)

Escudier, M.P. & Keller, J.J. "Recirculation in Swirling flow: a manifestation of Vortex Breakdown". AIAA J 23 Jan 1985

Escudier, M.P; Bornstein,J. & Maxworthy, T. "The dynamics of confined vortices" Proc. Roy. Soc. Lond. A 382 p335 (1982)

Escudier, M.P; Bornstein,J & Zehnder, N. "Observations and LDA measurements of confined vortex flow" J. Fl. Mech 98 p49-63 (1980)

Escudier, M.P.& Zehnder, N. "Vortex flow regimes" Journal of Fluid Mechanics 115 p105 (1982)

Eskinazi, S & Yeh, H. "An investigation on fully developed turbulent flows in a curved channel" J. Aeronaut. Sci 23 p 23-34 Jan (1956)

Falco, R.E. "A coherent structure model of the turbulent boundaryt layer and its ability to predict Reynolds number dependence" Phil. Trans. Roy. Soc. A336 p103-129 (1991)

Falco, R.E. "Structural aspects of turbulence in Boundary layer flows" in "Turbulence in liquids" ed GK Patterson & JL Zakin p1-14 Univ Missouri-Rolla (1980)"

Faler, J.H. & Leibovich, S. "Disrupted states of vortex flow and vortex breakdown" Phys. Fluids 20 p1385-1400 (1977a)

Faler, J.H. & Leibovich, S. "An experimental map of the internal structure of a vortex breakdown" J. Fluid Mech. 86 p313-335 (1978)

Fanglu, G.U. & Wenzhen, L. "Measurement and study of velocity field in various cyclones by use of laser doppler anemometry" p65 Paper C2 3rd Intl Conf Hydrocyclones, Oxford, England. ed P.A. Wood. Elsevier (1987)

Fejer, A.; Lavan, Z & Wolf, L. "Study of swirling flows". ARL-68-0173 Aerospace Research Laboratories USAF Wright-Patterson AFB, Ohio. (1968)

First, M.W. "Fundamental factors in the design of cyclone dust collectors" Doctoral thesis, Harvard Univ. (1950)

Floryan, J.M. "Görtler instability of wall jets" AIAA J 27 n1 p112 (1989)

Floryan, J.M. "Görtler instability of boundary layers over concave and convex walls". Phys Fl. 29(8) Aug p2380 (1986)

Floryan, J.M & Saric, W.S. "Wavelength selection and growth in boundary layers" AIAA J 22 n11 p1529 (1984)

Floryan, J.M. & Saric, W.S. "Stability of Görtler vortices in boundary layers" AIAA J 20 (3) p316 (1982)

Franko, "Centricleaning", Chapter XVI in "Pulp & Paper manufacture" Vol2: Mechanical Pulping ed MJ Kocurek & RA Leask (Tappi/CPPA) (1987)

Frith, P.C.W. & Duggins, R.K. "Flow modulation in turbulent vortex chambers" 9th Austr Fl. Mech Conf Aucklans p338-341 (1986)

Friedlander, S.K.; Silverman, L.; Drinker, P. & First, M.W. "Handbook on Air cleaning" U.S.A.E.C. Washington AECD-3361; NYO-1572 (1952)

Gad el Hak, M. & Hussain, A.K.M. "Coherent structures in a turbulent boundary layer 1. Generation of artificial bursts". Phys Fluids 29 (7) p2124-2139 (1986)

Garg, A & Leibovich, S. "Spectral characteristics of vortex breakdown flowfields" Phys Fluids 22 (11) (Nov 1979)

Gloger, J. & Hanke, S. "Der Einfluß der Wiederaufwirbelung des Staubes und der Grenzschichtabsaugung auf den Absheidegrad und Druckverlust von Zyklonabscheidern".Energietechnik 21 Jg Heft 4 April 1971

Goldshtik, M.A. "A paradoxical solution of the Navier-Stokes equations" Prik Mat Mekh 24 p610-621 translated in J Appl. Math. Mech 24 p913-929 (1960)

Görtler, H. "Uber eine dreidimensionale Instabilitat laminairer Grenzschichten an konkaven Wänden". Nachrichtung Gesellschaft Wessenschaftlich, Göttingen, Mathematik-Physik 1 p1 (1940)

Govindaraju, S.P. & Saffman, P.G. "Flow in a turbulent trailing vortex". Phys Fluids 14 n10 p2074 (1971)

Grabek, & Meirzwinski, . "Application of the LDA to industrial problems" DISA Information no 25 Feb (1980)

Grabowski, W.J. & Berger, S.A. "Solutions of the Navier-Stokes equations for vortex breakdown" J. Fluid Mech. 75 p525 (1976)

Green, S.I. & Acosta, A.J. "Unsteady flow in trailing vortices". J. Fluid Mech. 227 p107-134 (1991)

Guezennec, Y.G.; Piomelli, U & Kim, J. "On the shape and dynamics of wall structures in turbulent channel flow". Phys Fluids. A 1 (4) p764-766 (1989)

Gupta, A.K; Lilley, D.G. & Syred,N. "Swirl Flows" Abacus Press (1984)

Hall, M.G. "The structure of concentrated vortex cores". Ch 4 in progress in Aeronautical Sciences v.7 (1966)

Hall, M.G. "A new approach to vortex breakdown". Proc, Heat Transf. Fluid Mech. Inst p319-40 (1967)

Hall, M.G. "The structure of Vortex Breakdown". Annual Review of Fluid Mechanics 4 1972

Hall, P. "Taylor-Görtler vortices in fully developed or boundary layer flows: linear theory" J. Fluid Mechanics 124 p475-494 (1982)

Hall, P. "The linear development of Görtler vortices in growing boundary layers" J. Fluid Mechanics 130 p41-58 (1983)

Hall, P. "The non-linear development of Görtler vortices in growing boundary layers" J. Fluid Mechanics 193 p243-266 (1988)

Hall, P & Horseman, N.J. "The linear inviscid secondary instability of longitudinal vortex structures in boundary layers". J. Fluid Mech. 232 p357-375 (1991)

Harris, C.M. "Harris' handbook of Noise control" McGraw Hill, New York 2nd ed (1979)

Harvey, J.K. "Some observations of the vortex breakdown phenomenon" Journal of Fluid Mechanics 14 (1962)

Hatton, L. "Stagnation point flow in a vortex core". Tellus 27 (3) p269 (1975).

Head, M.R. & Bandyopadhyay, P. "New aspects of turbulent boundary layer structure" J. Fl. Mech 107 p297-338 (1981)

Hejma, J. "Influence of turbulence on the separation process in a cyclone" Staub-Reinhalt. Luft 31 no7 (1971)

Herbert, T. "Secondary instability of boundary layers". Ann Rev. Fluid Mech 20 p487 (1988)

Hinze, J.O. "Turbulence: an Introduction to its mechanism and theory" McGraw-Hill N.Y. (1959)

Hoffman, E.R. & Joubert, P.N. "Turbulent line vortices". J. Fl. Mech 16 p395 (1963)

Hoffman, A.C.; van Santen, A. & Allen, R.W.K. "Effects of geometry and solid loading on the performance of gas cyclones". Powder Tech. 70 p83-91 (1992).

Hon, T.L & Walker, J.D.A. "Evolution of hairpin vortices in a shear flow". Computers Fluids 20 (3) p343-358 (1991).

Hopfinger, E.J.; Browand, F.K. & Gagne, Y. "Turbulence and waves in a rotating tank". J. Fl. Mech. 125 p505-534 (1982)

Howard, L.N. & Gupta, A.S. "On the hydrodynamic and hydromagnetic stability of swirling flows" J. Fluid Mech 14 p463-76(1962)

Hsieh, K.T. & Rajamari, R.K. "Mathematical model of the hydrocyclone based on physics of fluid flow" A.I.Ch.E. J. 37 no.5 (1991)

Hultgren, L. "Stability of swirling gas flows". Phys. Fluids 31 (7) p1872 (1988)

Hutchinson, C.A. "Turbulence Intensity and flowfield measurements in a spray dryer". unpublished B.E. report (1991)

Ince, E.L. "Integration of ordinary Differential equations". 7th ed Oliver & Boyd, Edinburgh (1956)

Iozia, D.L. & Leith, D. "Effect of cyclone dimensions on Gas flow patterns and collection efficiency" Aerosol Science & Technology. 10 p491 (1989a)

Iozia, D.L. & Leith, D. "Cyclone Optimisation". Filtration & Separation July/Aug (1989b)

Iozia, D.L. & Leith, D. "The logistic function and cyclone fractional efficiency" Aerosol Science and Technology 12 p598 (1990)

Ito, Suematsu, Hayase, Mem. Fac. Eng Nagoya Univ. 37 117 (1985a)

Ito, H, Watanabe, Y & Shoji, Y. "A long-radius inlet nozzle for flow measurement" J. Phys E.: Sci Instrum. 18 p88 (1985b)

Jackson, R. "Mechanical equipment for removing grit and dust from gases" Chapter V, High efficiency cyclones: return flow types p164-168 British Coal Utilisation Research Assn. (1963)

Jones, "The breakdown of vortices in separated flow" Rept 140, Univ. Southampton, Aeronautics & Astronautics Dept (1960).

Kalen, B & Zenz, F.A. "Theoretical-Empirical approach to saltation velocity cyclone design" in Recent advances in Air Pollution Control. AIChE Sympos Series no 137 70 (1974)

Karman, Th. v. "Some aspects of the turbulence problem". Proc. 4th Intl Cong. Appl. Mech Cambridge 54-9 1934.

Kasagi, N. & Hirata, M & Nishino, K. "Streamwise pseudo-vortical structures and associated vorticity in the near wall region of a wall-bounded turbulent shear flow" Exp. Fluids 4 p309-318 (1980)

Kay, J.M. & Nedderman, R.M. "Fluid mechanics and transfer processes". Cambridge Univ. Press, Gt Britain (1985)

Keller, J.J. & Escudier, M.P. "Theory and observations of waves on hollow core vortices" J. Fl. Mech. 99 pt 3 p495 (1980)

Keller, J.J; Escudier, M.P. & Bornstein, J. "The physics of Vortex breakdown" unpublished report, February (1983)

Kelsall, D.F. "A study of the motion of solid particles in a hydraulic cyclone" Trans. Instn. Chem Engrs. 30 (1952)

Kelsall, D.F. "A further study of the hydraulic cyclone". Chem. Eng. Sci. 2 p254 (1953)

Kendall, W.M. "Unsteady two-cell similarity solution to a convective atmospheric vortex model" Tellus 30 p376-382 (1978).

Kentfield, J.A.C. & Barnes, R.W. "The prediction of the optimum performance of air ejectors" Proc. Inst. Mech Engrs 186 p54/72 (1972)

Kessler, M. & Leith, D. "Flow measurement and efficiency modeling of cyclones for particle collection" Aerosol Sci. & Tech. 15 p8-18 (1991)

Kevern, R. "Cyclone Efficiencies" unpublished B.E. final year project report Univ. Canterbury (1991)

Kim, J.C. & Lee, K.W. "Experimental study of particle collection by small cyclones" Aerosol Sci. & Tech. 12 p1003-1015 (1990)

Kirkpatrick, D.L.I. "Experimental Investigation of the breakdown of a vortex in a tube" Aeronaut. Res. Counc. CP 821 RAE Tech. Note no. Aero 2963 (1964)

Kline, S.J.; Reynolds, W.C.; Schraub, F.A. & Runstadler, P.W. "The structure of turbulent boundary layers". J. Fluid Mech 30 p741 (1967)

Kline, S.J. & Robinson, W.C. "Quasi-coherent structures in the turbulent boundary layer Part 1: status report on a community wide summary of the data" in 'Near wall turbulence Proc Zaric Meml Conf ed Kline & Afgan p200-217 Hemisphere, NY (1988)

Knowles, S.R; Woods, D.R. & Feuerstein, I.A. "The velocity distribution within a hydrocyclone operating without an air core". Can. J. Chem. Eng. 51 p262 (1973)

Kopecky, R.M. & Torrance, K.E. "Initiation and structure of axisymmetric eddies in a rotating stream" Computers & Fluids 1 p289-300 (1973)

Korteweg & de Vries, Phil. Mag. 39 (5) p422 (1895)

Krambrock, W. "Kritische Anmerkungen zur Untersuchung" Chem Ing Tech 51 n5 p493 (1979)

Krause, E. "A contribution to the problem of vortex breakdown" Agard Conf. Proc no. 342 p 26-1 April 1983

Kuchemann, D. "Report on the IUTAM symposium on concentrated vortex motions in fluids" J. Fluid Mech 21 p1 (1965)

Kuroda, C & Ogawa, K. "Characteristic flow behaviour of high swirling jet in a circular vessel" J. Chem. Engg. Japan 20 no2 p 188 (1987)

Kuroda, C.; Ogawá,K & Inoue, S. "Axial velocity distribution - an approximate equation" J. Chem. Eng. Japan 14 (1981)

Lamb, H. "Hydrodynamics", 6th edition, Cambridge The Univ. Press (1932)

Lambourne, N.C. & Bryer, D.W. "The bursting of leading edge vortices - some observations and discussion of the phenomenon". Aero. Res. Counc R & M 3282 . (The photo was reporduced in Hall (1972).

Lapple, C.E. "Processes use many collector types". Chem. Eng. 58 p144 (1951)

Launder, B.E. & Rodi, W. "The turbulent wall jet - measurement and modelling" Ann. Rev. Fluid Mech. 15 p429 (1982)

Launder, B.E. & Spalding, D.B. "The numerical computation of turbulent flow". Comp Meth in Appl. Mech and Engr 3 p269 (1974)

Launder, B.E.; Priddin, C.H. & Sharma, B.I. "The calculation of tubulent boundary layers on spinning and curved surfaces". J. Fluids Eng p231 March (1977).

Lavan, Z.; Nielsen, H. & Fejer, A.A. "Separation and flow reversal in swirling flows in circular ducts". Phys Fluids 12 (9) p1747-1757 (1969)

Leibovich, S. "The structure of Vortex Breakdown". Annual Review of Fluid Mechanics 10 1978

Leibovich, S. "Vortex stability and breakdown" AGARD-CP-342 p23-1 (1983) (also in AIAA. J. 22 (1984))

Leibovich, S. "Vortex stability and breakdown: Survey and Extension". AIAA J. 22 p 1192-1206 (1984)

Leibovich, S. & Holmes, P. "Global stability of the Burgers' vortex". Phys. Fluids 24 (3) p548 (1981)

Leibovich, S & Kribus, A. "Large amplitude wavetrains and solitary waves in vortices" J. Fluid. Mech. 216 p459 (1990)

Leibovich, S & Randall, J.D. "Amplification and decay of long nonlinear waves" J. Fl. Mech 58 p481 (1973)

Leibovich, S & Stewartson, K. "A sufficient condition for the instability of columnar vortices" J. Fluid Mech. 126 p335 (1983)

Leith, D & Licht, W. "The collection efficiency of cyclone-type particle collectors - a new theoretical approach". A.I.Ch.E. Symp. Ser 68 no 126 (1972)

Leoutsakos, G. "Boundary layer transition on concave surfaces" PhD thesis, London Imperial Coll of Sci & Techm (1987)

Leslie, F.W. "Surface roughness effects on suction vortex formation - a laboratory simulation" J. Atmos. Sci 34 p1022 (1977)

Leslie, F.W. & Snow, J.T. "Sullivan's two-celled vortex" AIAA J. 18 p1272 (1980)

Lessen,M.; Singh, P.J. & Paillet, F. "The stability of a trailing line vortex. Part 1. Inviscid theory" J. Fluid Mech 63 p 753 (1974)

Leuckel, W & Fricker, N. "The characteristics of swirl stabilised natural gas flames - Part 1" J. Inst. Fuel 49 p 103-112 (1976)

Li, P.M.; Lin, S. & Vatistas, G.H. "Predicting collection efficiency of separation cyclones: a momentum analysis". Can. J. Chem. Eng. 65 (1987)

Liepmann, H.W. "Investigations of laminar boundary layer stability and transition on curved boundaries" NACA Wartime report W 87 (1945)

Lilley, D.G. "Nonisotropic turbulence in swirling flows". Acta Astronautica 3 p919-933 (1976)

Lilley, D.G. & Chigier, N.A. "Nonisotropic turbulent stress distribution in swirling flows from mean value distributions". Int. J. Heat Mass Transfer 14 p573-585 (1971)

Lindgren, E.R. "Vorticity and rotation" Am J. Phys 48 p465 (1980)

Loffler, F. & Meissner, P. "Pressure drop determination in cyclone separators". Proc 1st Iranian Congress Chem Eng ed P. Dalavoo, Elsevier, Amsterdam, p405-413 (1973)

Lopez, J. "Numerical investigation of axisymmetric vortex breakdown" 9th Australasian Fluid Mechanics Conference. Auckland, N.Z. (1986)

Lopez, J. "Axisymmetric vortex breakdown Part 1.: Confined swirling flow" J. Fluid Mech 221 p533-552 (1990)

Lu, L.J. & Smith, C.R. "Use of flow visualisation data to examine spatial-temporal velocity and burst-type characteristics in a turbulent boundary layer" J. Fluid Mech. 232 p303-340 (1991)

Ludwieg, H. "Zur Erklarung der Instabilitat der uber ange stellten Deltaflugeln auftretenden freien wirbelkerne".Z. Flugwiss 10 p242-249 (1962)

Ludwieg, H. "Erklarung des wirbel aulf-platzens mit Hilfe der Stabilitat stheroriefur Stromungen mit schraubenlinien formigen Stromlinien" Z. Flugwiss 13 p437-442 (1965)

Ludwieg, H. "Vortex breakdown" Dtsch. Luft Raumfahrt Rep 70-40 (1970)

Lugt, H.J. "Vortex breakdown in atmospheric columnar vortices". Bull. Am. Meteorological Soc. 70 n12 p1526 (1989)

Lugt, H.J. "Vortex flows in Nature and technology" Wiley New York (1983)

Lugt, H.J. & Abboud, M. "Axisymmetric vortex breakdown with and without temperature effects in a container with a rotating lid". J. Fluid Mech 179 p179-200 (1987)

Lundgren, T.S. & Ashurst, W.T. "Area-varying waves on curved vortex tubes with application to vortex breakdown". J. Fluid Mech. 200 p283-307 (1989)

Mager, A. "Dissipation and breakdown of a wing-tip vortex". J. Fluid Mech. 55 p609-28 (1972)

Maslowe, S.A. & Stewartson, K. "On the linear stability of rotating Poiseuille flow" Phys. Fluids 25 n9 p1517 (1982)

Maxworthy, T J. Fl. Mech 64 p227 (1974)

Maxworthy, T J. Fl. Mech 81 p465 (1977)

Meaden, T. "Circles in the corn" New Scientist p47 23 June (1990)

Meek, R.L. & Baer, A.D. "The periodic viscous sublayer in turbulent flow" AIChE J 16 n5 p841 (1970)

Meißner, P. Dissertation, Universität Karlsruhe (1977)

Miller, J.A. "A simple linearised hot-wire anemometer". J. Fl. Eng. Dec (1976)

Moore, D.W. & Saffman, P.G. "The rise of a body throug a rotating fluid in a container of finite length" J.Fl. Mech 31 pt4 p635-642 (1968)

Moore, D.W. & Saffman, P.G. "Motion of a vortex filament with axial flow" Phil T. Roy. Soc A 272 p403 (1972)

Mothes, H & Löffler, F. "Zur Berechnung der Partikelabscheidung in Zyklonen" (A model for particle separation in cyclones) Chem. Eng. Process. 18 p 323-41 (1984) (also in Proc. Partech '84, Nurnberg 1984)

Mothes, H. & Löffler, F. "Motion and deposition of particles in cyclones" Ger. Chem. Eng. 8 p223-233 (1985)

Mothes, H.; Sievert, J. & Loffler, F. "Investigation of the cyclone grade efficiency curves using a light-scattering particle size analyser" In Proc. Powtech Conf. I.Chem.E. Symposium series no. 63 (1981)

Muschelknautz, E. "Design of cyclone separators in the engineering practice" Staub. Reinhalt Luft 30 (5):1 (1970)

Muschelknautz, E. "Die berechnung von Zylonabscheidern fur Gase" Chem. Ing. Tech. 44 p63-71 (1972)

Muschelknautz, E & Brunner, K "Untersuchungen an zyklonen". Chem.-Ing. Tech 39 p531 (1967)

Muschelknautz, E & Krambrock, W. "Aerodynamic factors of some cyclone separators" Chem.-Ing. Tech 42 n5 p247 (1970)

Nakamura, Y. & Uchida, S. "Breakdown condition of an axisymmetric swirling flow" AIAA J. 19 no8 p1083 (1981)

Nissan, A.H. & Bresan, V.P. "Swirling flow in cylinders". AIChE J. 7 No. 4 p 543 (1961)

Offen, G.R. & Kline, S.J. "A proposed model of the bursting process in turbulent boundary layers" J. Fl. Mech 70 pt2 p209-228 (1975)

Ogawa, A. "Theoretical consideration of the pressure drop of the cylindrical cyclone dust collectors" Nihon University publication, Japan 1987

Ogawa, A. "Estimation of the collection efficiencies of the 3 types of cyclone dust collectors from the standpoint of the flow patterns in the cylindrical cyclone" J.S.M.E. Bull 27 n222 p64 (1984)

Ogawa, A.; Kato, T.; Hironaka, A & Nagabayashi, H. "Detailed flow patterns in the cylindrical cyclone dust collector" in Advances in fine particles Processing ed J. Hanna & Y. Attia Elsevier (1990)

Ohasi, H. & Maeda, S. "Motion of water in a hydraulic cyclone" Chem Eng Japan 22 p200 (1958)

Ohtake, T.; Usuda, M & Kadoya, T. "A fundamental study of hydrocyclones Part 1: Flow pattern in the hydrocyclone". Japan Tappi 41 (2) p60 (1987).

Oseen, C.W. Ark. Met. Astr. Fys 7 (1911)

Parker, R; Jain, R; Calvert, S.; Drehmel, D & Abbott, J. "Particle collection in cyclones at high temperature and high pressure". Environment Sci. Tech 15 p451 (1981)

Pauley, R.L. "Laboratory Measurements of axial pressures in two-celled tornado-like vortices" J. Atmos. Sci 46 n21 (1989)

Peckham D.H. & Atkinson, S.A. "Preliminary results of low speed wind tunnel tests on a Gothic wing of aspect ratio 1.0" British Aeronautical Res Council CP508 (1957)

Pen'kov N.V. & Vedernikov, V.B. "Calculation of the efficiency of dust collection in cyclones" Zh. Prikl Khimii 57 No 5 p1057-1061 May 1984

Pericleous, K.A.& Rhodes, N. "The hydrocyclone classifier - a numerical approach". Int J. Mineral Processing 17 p23-43 (1986)

Pericleous, K.A.; Rhodes, N. & Cutting, G.W. "A mathematical model for predicting the flow field in a hydrocyclone classifier". Proc Int. Conf. on Hydrocyclones 2 p27 (1984)

Pericleous, K.A.; Rhodes, N. & Cutting, G.W. "A mathematical model for predicting the flow field in a hydrocyclone classifier". BHRA 3rd Int. Conf. on Hydrocyclones, Bath, U.K. p27-40 (1987)

Pervov, A.A. "Comparitive tests of cyclones with unswirling devices"Khimi. i Nefty. Mash. 1 p12-14 (1975) (translated in Chem. & Petrol. Eng. 1 p24-27 (1975)

Pervov, A.A. Chem. & Petrol. Eng. 10 p898 (1974)

Peterson, C.M. & Whitby, K.T. "Fractional efficiency characteristics of unit type collectors" ASHRAE J. 7 (5) p 42-49 (1965)

Petroll, J & Langhammer, K. "Vergleichsversuche an Zyklonabscheidern" Freiberger Forschungsheft A220 p175-196 (1962)

Phillips, H. "Modified Burgers equation for tangential velocity modelling". pers comm from SPS Harwell to J. Abrahamson (1990)

Phillips, W.R.C. "The effusing core at the centre of a vortex boundary layer" Phys Fluids 27 (9) p2215 (1984)

Phillips, W.R.C. "On vortex boundary layers". Proc. Roy. Soc. Lond A400 p253-261 (1984)

Phillips, W.R.C. & Khoo, B.C. "The boundary layer beneath a Rankine-like vortex" Proc. Roy. Soc. Lond A 411 p177-192 (1987)

Prandtl, L. "Essentials of Fluid dynamics with applications to hydraulics, aeronautics, meteorology and other subjects". Blackie, London (1952)

Praturi, A.K. & Brodkey, R.S. "A stereoscopic visual study of coherent structures in turbulent shear flow". J. Fluid Mech. 89 p251-272 (1978

Ramachandran, G.; Leith, D.; Dirgo, J. & Feldman, H. "Cyclone optimization based on a new empirical model for pressure drop" Aerosol Sci. & Tech. 15 p135-148 (1991)

Randall & Leibovich, S. "The critical state in a trapped wave model of vortex breakdown" J. Fl. Mech 53 p495-515 (1973)

Ranz, W.E. "Wall flows in a cyclone separator: A description of internal phenomena" Aerosol Sci. and Tech. 4 p417 (1985)

Rao, K.N.; Narasimha, R & Badri Narayanan, M.A. "The bursting phenomenon in a turbulent boundary layer". J. Fl. Mech. 48 p339-352 (1971)

Rayleigh, Lord. "On the dynamics of revolving fluids". Proc. Roy. Soc Lond. A 93 p148-154 1917

Rayleigh, Lord. Proc Lond. Math Soc 11 p57 (1880)

Reydon, R.F. & Gauvin, W.H. "Theoretical and Experimental studies of confined vortex flow" Canadian J. Chem Eng 59 (Feb 1981)

Reyna, L.G. & Menne, S. "Numerical prediction of flow in slender vortices". Computers Fluids 16 (3) p239-256 (1988)

Rhodes, N; Pericleous, K.A. & Drake, S.N. "The prediction of hydrocyclone performance with a mathematical model". Proc. Int. Conf. on hydrocyclones p51 (1987)

Richmond, M.C & Patel, V.C. "Convex and concave surface curvature effects in wall-bounded turbulent flows" AIAA J 29 n6 p895 June (1991)

Rietema, K. "Performance and design of hydrocyclones". Chem. Eng. Sci. 15 p298-325 (1961)

Roach, P.E. "The generation of nearly isotropic turbulence by means of grids". Heat & Fluid Flow 8 n2 p82 June (1987)

Robinson, S.K. "Coherent motions in the turbulent boundary layer". Ann. Rev. Fl. Mech. 23 p601-639 (1991)

Rodi, W. "Examples of turbulence models for incompressible flows". AIAA J 20 n7 p874 (1992)

Rott, N. "On the viscous core of a line vortex" ZAMP 9 p543 (1958) (or 10 p73 (1959)

Rott, N & Lewellen, W.S. "Boundary layers in rotating flows"
in Progress in aeronautical sciences 7 p111 (1966).

Rotunno, R. "A study in tornado-like vortex dynamics" J. Atmos. Sci p140 (1979)

Runstadler, P.G.; Kline, S.J. & Reynolds, W.C. "An experimental investigation of flow structure of the turbulent boundary layer". Rep. No. MD-8, Dep Mech Eng Stanford Univ, Stanford, California (1963)

Sabry, A.S. "Görtler vortices". was to appear in Ann. Rev Fluid Mech (1992), (but possibly now 1993)

Sabry, A.S. & Liu, J.T.C. "Longitudinal vorticity elements in boundary layers: nonlinear development from initial Görtler vortices as a prototype problem"
J. Fluid Mech 231 p615-663 (1991)

Saffman, P.G. "The lift on a small sphere in a slow shear flow". J. Fluid Mech 22 p385 (1965).

Sage Action Inc. "Bubble Generator Systems - Air flow Visualisation and Measurement". Product brochures sent 1986, dated 1976. P.O. Box 416 Ithaca, New York

Sakao, F. "Two point calibration of the linearisers for a hot-wire anemometer"
J. Phys.E: Sci Instrum 13 (1980)

Salas, M.D. & Kuruvila, G. "Vortex breakdown simulation: a circumspect study of the steady, laminar axisymmetric model". Computers Fluids 17 (1) p247-262 (1989)

Sarpkaya, T. "On stationary and travelling vortex breakdown" J. Fluid Mech 45 p545 (1971a)

Sarpkaya, T. "Vortex breakdown in swirling conical flows" AIAA J. 9 p1792-1799 (1971b)

Sarpkaya, T. "Effect of the adverse pressure gradient on vortex breakdown"
AIAA J. 12 p602-607 (1974)

Schowalter,W.R. & Johnstone, H.F. "Characteristics of the mean flow patterns and structure of turbulence in spiral gas streams". A.I.Ch.E. J p648 (1960)

Schubert, H. "A hydrocyclone separation model in consideration of the turbulent multi-phase flow". undated manuscript in the collection of Dr Abrahamson (c. 1984)

Schweizer, P.M & Scriven, L.E. "Evidence of Görtler-type vortices in curved film flows"
Phys Fluids 26 (3) p619 March (1983)

Shepherd, C.B. & Lapple, C.E. "Flow pattern and pressure drop in cyclone dust collectors"
Ind. Eng Chem. 31 p972-984 (1939)

Shepherd, C.B. & Lapple, C.E. "Flow pattern and pressure drop in cyclone dust collectors"
Ind. Eng Chem. 32 no.9 p1216 (1940)

Shivamoggi, B.K. & Uberoi, M.S. "Contribution to the theory of vortex breakdown"
Acta Mech. 41 p211-215 (1981)

Shizawa, T. & Eaton, J.K. Turbulence measurements for a longitudinal vortex interacting with a three-dimensional turbulent boundary layer" AIAA J. 30 n1 p49-55 (1992)

Smith, A.M.O. "On the growth of Taylor-Görtler vortices along highly concave walls"
Q. Appl. Mech 13 p233-262

Smith, C.R.; Walker, J.D.A; Haidari, A.H. & Sobrun, U. "On the dynamics of near-wall turbulence"
Phil Trans Roy. Soc Lond. A 336 p131-175 (1991)

Smith, C.R. in Proc. Eigth Symp on Turbulence (ed GK Patterson & JL Zakin) Dept Chem Eng Univ Missouri Rolla (1984)

Smith, J.L. "An experimental study of the Vortex in the Cyclone Separator."
J. Basic Eng. Trans. A.S.M.E. 84D p602, (1962a)

Smith, J.L. "An analysis of the Vortex flow in the Cyclone Separator."
J. Basic Eng. Trans. A.S.M.E. 84D p609, (1962b)

So, K.L. "Vortex Phenomena in a conical diffuser". AIAA J. **5** no 6 p1072 June 1967

So, R.M.C. & Mellor, G.L. "Experiments on turbulent boundary layers on a concave wall" Aero Quart. Feb p25 (1975)

Spall, R.E.; Gatski, T.B. & Grosch, C.E. "A criterion for vortex breakdown". Phys. Fluids. **30** p3434 Nov (1987)

Spall, R.E.; Gatski, T.B. & Ash, R.L.. "The structure and dynamics of bubble-type vortex breakdown" Proc. Roy. Soc. Lond. **A 429** p 613 (1990)

Spall, R.E.; Gatski, T.B. "A computational study of the topology of vortex breakdown" Proc. Roy. Soc. Lond. **A 435** p 321-337 (1991)

Spink, L.K. "Principles and Practice of Flowmeter Engineering" 9th edition, Foxboro, Mass. USA (1972)

Sproull, R.E. "Air pollution and its control" Exposition press, Jericho, N.Y. (1970)

Squire, H.B. "Analysis of the Vortex Breakdown Phenomenon". Miszellanen der Angewandten Mechanik, Akademie, Berlin (1962) p 306-312

Squire, H.B. "Analysis of the Vortex Breakdown Phenomenon" Imp. Coll. Sci. Tech. Lond Rep no.102 (1960)

Squire, H.B. "The Growth of a vortex in turbulent flow". Aero. Quart. **16** p 302 (1955)

Stairmand, C.J. "Pressure drop in cyclone separators". Engineering **168** p409 (1949)

Stairmand, C.J. "The design and performance of cyclone separators" Trans. Instn. Chem. Engrs. **29** (1951) p356

Stefferns, J.L. "The effect of Vorticity-Profile shape on the instability of a two-dimensional vortex" J. Atmos. Sci. **45** No.2 p 254 (1988)

Stern, A.C.; Caplan, K.T.Bush, P.D. "Cyclone dust collectors" American Petroleum Inst Washington (1955)

Stewartson, K. "The stability of swirling flows at large Reynolds number" Phys. Fluids **25** (11) p1953 (1982)

Sullivan, R.D. "A two-celled vortex" J. Aer. Sci **26** p767 (1959)

Suzuki Sci. Pap. Inst. Phys., Chem Res. Tokyo **54** p43 (1960)

Svarovsky, L. "Some notes on the use of gas cyclones for classification of solids" From 'Preprints of European Symposium on Particle Classification in Gases & Liquids' Vol 1 Nurnberg, (1984)

Swearingen, J.D. & Blackwelder, R.F. "The growth and breakdown of streamwise vortices in the presence of a wall". J. Fluid Mech **182** p255 (1987)

Syred, N & Beer, J.N. "Combustion in swirling flows: a review" Combustion and Flame **23** p 143 (1974)

Tackie, E.N.; Watkinson, A.P. & Brimacombe, J.K. "Experimental study of the elutriation of particles from rotary kilns". Can J. Chem Eng **67** (1989)

Tager, S.A. " Calculating the aerodynamic resistance of cyclone combustion chambers" Teploenergetika **18 (7)** p88-91 (1971)

Tani, I. "Production of longitudinal vortices in the boundary layer along a concave wall" J. Geophys Res **67 n8** p3075 July (1962)

Taylor, G.I. Q. J. Mech. Appl. Math **3** p129 (1950)

Taylor, G.I. "Distribution of velocity and temperature between concentric rotating cylinders" Proc. Roy. Soc. **A151** p494 (1935)

Tengbergen, H.J.van E. "Influence of the size of the dust outlet on the efficiency of cyclones" in 'Problems & Control of Air Pollution' Ed. F.S. Mallette. Reinhold N.Y. (1955)

Tengbergen, H.J.van E. "Dust cyclone - law of similarity - influence of the dust concentration" Werktuig- en Scheepsbouw 1 (1965) p W1

ter Linden, A.J."Investigations into Cyclone dust collectors" IME Proc. 160 p233 (1949)

ter Linden, A.J. "Cyclone dust collectors for Boilers" Trans. ASME 75 p433 (1953)

Theodore, L.T. & De Paola, "Predicting cyclone efficiency". J. Air Pollution control assoc. 30 n10 p1132 (1980)

Theodorsen, T. "Mechanism of turbulence". Proc. Midwest Conf. Fluid Mech, 2nd. Columbus, Ohio p1-18 (1952)

Thwaites, B. "Incompressible aerodynamics" p56 Oxford Univ Press Oxford (1960)

Tran, T.V. "Experimental and theoretical studies on gas cyclone separators operating at high efficiency" unpublished PhD thesis, Univ Minnesota (1981)

Troyankin, Y.V. & Baluev, E.D. "The aerodynamic resistance and efficiency of a cyclone chamber" Teploenergetika 16 p29-32 (1969)

Truelove, J.S. & Mahmud, T. "Calculation of strongly swirling jet flows". 9th Australasian Fluid Mech. Conf Auckland p492 (1986)

Tsai,C-Y. & Widnall, S.E. "Examination of group-velocity criterion for breakdown of vortex flow in a divergent duct" Phys. Fluids 23 (5) p 864 (1980)

Turner, J.S. "The constraints imposed on tornado-like vortices by top and bottom boundary conditions" J. Fluid Mech 25 p377 (1966)

Uberoi, M.S. "Mechanisms of decay of laminar and turbulent vortices". J. Fluid Mech. 90 p241 (1979)

Ustimenko B.P. & Bukhman, M.A. "Turbulent flow structure in a cyclone chamber" Teploenergetika 15 (2) p64-67 (1968)

Uspenskii, V.A.; Solov'ev, V.I. & Gur'ev, V.S. "Studying velocity fields in a cyclone separator" Fluid mechanics - Soviet Research 1 no.1 p152 (1972)

van Dyke, M. "An album of fluid motion". Parabolic Press, Stanford, California (1982)

van Schaick, T.E. "Further mathematical modeling of cyclone efficiency based on new experimental investigations". M.S. Thesis, Univ. Cincinnati (1970)

Vatistas, G. "Tangential velocity and static pressure distribution in vortex chambers". AIAA J. 25 n8 p1139 (1987)

Vatistas, G. "A similarity relationship for the pressure drop in vortex chambers". Can J. Chem Eng 647 p540 (1989)

Vatistas, G.H.; Kozel, V & Mih, W.C. "A simpler model for concentrated vortices" Expts in Fluids 11 p73 (1991)

Vatistas, G.H.; Lam, C. & Lin, S. "A similarity relationship for the pressure drop in vortex chambers" Can. J. Chem. Eng 67 p540 Aug (1989)

Vatistas, G.; Lin, S. & Kwok, "Theoretical and experimental studies on vortex chamber flows" AIAA J. 24 n4 p635 (1986)

Vettin, F. "Meteorologische Untersuchungen" Poggensdorfs Ann. der Physik 102 p246. (1857)

Vogel, H.U. "Experimentelle Ergebnisse über die laminaire Strömung in einem zylindrischen Gehäuse mit darin rotierender Scheibe". Max-Planck-Institut für Stromungsforschung, Göttingen, Bericht 6 (1968)

Walker, J.D.A.; Smith, C.R.; Cerra, A.W. & Doligaliski, T.L. "The impact of a vortex ring on a wall" J. Fluid Mech. 181 p99 (1987).

Ward, N.B. "The exploration of certain features of tornado dynamics using a laboratory model" J. Atmos. Sci 29 p1194 (1972).

Ward-Smith, A.J.. "Internal Fluid flow: the fluid dynamics of flow in pipes and ducts" Clarendon Press, Oxford, UK p458-459 (1980)

Weber, H.E. "The boundary layer inside a conical surface due to swirl" J. Appl. Mech. 23 p587-592 Dec (1956)

Weber, H.E. & Keenan, J.H. "Head loss in flow through a cyclone dust separator or vortex chamber". J. Appl. Mech 23 p16 (1956)

Weidman, P.D. & Browand, F.K. "Analysis of a simple circuit for constant temperature anemometry" J. Phys. E.: Sci. Instrum 8 (1975)

Westphal, R.V. & Mehta, R.D. "Interaction of an oscillating vortex with a turbulent boundary layer" Experiments in Fluids 7 p405-411 (1989)

Willmarth, W.W. & Tu, B.J. "Structure of turbulence in the boundary layer near the wall" Phys Fluids 10 pS134-137 (1967)

Winoto, S.H. & Low, H.T. "Transition of boundary layer flows in the presence of Görtler vortices" Expts in Fluids 8 p41-47 (1989)

Winternitz, F.A.L & Ramsay,W.J. "A cantilever pitot cylinder for three-dimensional flow surveys" N.E.L. Report No 77. DSIR National Engg Laboratory, U.K. Jan (1963)

Wohl, P.R. & Rubinow, S.I. "The transverse force on a drop in an unbounded parabolic flow" J. Fluid Mech 62 p185 (1974).

Wong, K.K. "Gas flow and dust collection in cyclone bins". M.E. Report, unpublished, Univ. Canterbury (1973)

Wu, J "Conical turbulent swirling vortex with variable eddy viscosity" Proc. Roy. Soc Lond A403 p235-268 (1986)

Wyngaard, J.C. & Lumley, J.L. "A constant temperature hot-wire anemometer" J. Sci. Instrum. 44 (1967)

Yih, C.S.; Wu, F.; Garg, A.K. & Leibovich, S. "Conical vortices: a class of exact solutions of the Navier-Stokes equations". Phys Fluids 25 (12) (1982)

Yoshida, H; Saki, T; Hashimoto, K & Fujioka, T. "Size classification of submicron powder by air cyclone and 3-D analysis" J. Chem. Eng Japan 24 n5 p640 (1991)

Yuu, S; Jotaki, T; Tomita, Y. & Yoshida, K. "The reduction of pressure drop due to dust loading in a conventional cyclone" Chem Eng Sci. 33 p1573 (1978)

Zhou, L.X. & Soo, S.L. "Gas-solid flow and collection of solids in a cyclone separator" Powder Technology, 63 (1990) p45-53

Zhou, L.X. & Soo, S.L. "On boundary conditions of particle phase and collection efficiency in cyclones" Powder Technology, 64 p213-220 (1991)

Zhou, L.; Zhang, Z. & Yu, K. "A study of Structure Parameters of Cyclones" International Symposium on Multiphase flow Hangzhou, China Aug, (1987)

Chapter

10

EXPERIMENTAL APPENDICES

CONTENTS:

10.A. CYCLONE GEOMETRIES USED

This study concentrated on the flowfield in the Stairmand High Efficiency design cyclone. Four scales of this cyclone geometry were examined: with barrel diameters of 140mmØ, 300mmØ, 750mmØ and 2090mmØ. The largest cyclone was installed in a Medium density Fibreboard mill, and was used during maintenance shutdowns. The 750mmØ cyclone was also an industrial unit, but one that had been retired from service. The 300mmØ cyclone was constructed in this department from steel plate for a final year project (Kevern, 1991). The 140mmØ cyclone was constructed from perspex, and designed in a modular form that allowed the geometry to be varied. The details of the construction of this cyclone are given below.

10.A.1: Construction of the perspex cone for the 140mmØ cyclone:

The 140mmØ laboratory cyclone was constructed from 'perspex' - a transparent polymethacrylate resin. This posed some problems in the manufacture of the cone, and the credit for their solution is due to David Brown, Technical Officer in the Chemical and Process Engineering Department. This section records some notes on the methods employed. The simplest solution would have been to machine the cone from a solid block of perspex, but the cost of that was prohibitive. Instead, the cone was formed from a sheet of 6mm thick perspex, by heating the sheet to the malleable condition, and then forcing it into shape in conical molds until it had set.

Perspex becomes workable at approximately 160°C. The molds (an outer and an inner) needed to be at this temperature as well when the sheet was formed to allow time for the sheet to be worked into position before it cooled and set. This temperature ruled out the use of cones made from laminated wood, and in addition a smooth surface was required to reduce the finishing work required to bring the cone to optical quality. The molds were made from 'plaster of paris' ($CaSO_4$) after some trial and error.

The successful procedure used was as follows:

(i) A wooden former was made to fit the inner surface of the required cone, with additional length. This was machined smooth, varnished, and polished to a smooth surface. Silicone car wax (or vaseline? was used to ensure the mold released from the former. (Vaseline was found to give ridges in the surfaces, and the plaster was able to penetrate the vaseline in some places, allowing it to stick to the wood).

(ii) To make the outer mold, a rough cone of cardboard was made, suitable to give 30mm of clearance around the wooden former. The vertex end was plugged, and a rod inserted axially through the plug on which the wooden former could be located . This was stood upright, with the vertex downwards, and the wooden former clamped in position inside it. The prepared plaster was then poured around the former, and the cardboard vibrated gently to work any air bubbles to the surface. The plaster was sprinkled over the water in a bath/trough. The consistency of the plaster was determined by eye, and varied depending on the other additives that were trialled. Glass fibres, dental plaster and pumice were added to try and improve the strength of the mold at high temperatures, but there was still a problem with the fragility when

hot. (Earlier unsuccessful attempts used medical plaster bandages, and gauze soaked in plaster to layer an outer mold over the wooden former. This did not give an acceptably smooth finish, was slow to construct and was difficult to release. The bandages did not give a significant improvement in the strength of the finished mold).

(iii) Once the mold had set, the wooden former was released by tapping the locating rod through the plug. The mold was then cured for several days in warm conditions to dry out the plaster.

(iv) A plaster replica of the wooden former was then made using the outer mold as the pattern. The problem was again how to ensure the release of the two parts, and in this case, the plaster-plaster was more prone to bonding than the plaster-wood had been. Vaseline and silicone wax could not be used, as the amount needed to ensure release resulted in ridges in the surface. The eventual solution was to use a condom as the separating agent. The plaster was poured into the condom, which stretched under the weight, and was allowed to fill the outer mold from the vertex upwards. Care was needed to avoid contact with sharp edges as the rubber was stretched close to its strength limit. Other sources were investigated, including horse artificial insemination brands, but the thicker rubber was not able to stretch under the plaster weight, and the surface smoothness was not acceptable. Standard chemist brands were used successfully.

(v) The inner and outer plaster molds needed to be heated up slowly over several days to avoid stressing cracks in the plaster. The perspex sheet was cut to the shape of the development of the conical surface, and then heated in a drying oven. Overheating, or holding too long at the soft state results in discolouration of the perspex. When sufficiently heated the sheet could be folded readily into the outer mold, and the inner mold was then inserted to force the sheet into shape. The join of the sheet edges tended to approach an angle rather than a smooth curve and hence needed to be forced out to the wall of the outer mold. The plaster molds were fragile in the hot, dried state, and this limited the number of the attempts that could be made to achieve the desired shape.

(vi) Once cooled below the malleable condition the perspex sheet held the conical shape . The perspex was able to bridge over small imperfections in the plaster mold finish, but did acquire some indentations and protuberances from the plaster. The sheet edges were 'welded' with acetone cement and this joint was sanded to shape. By sanding and polishing the perspex an extremely smooth finish was able to be achieved.

10.A.2: 140mmØ Perspex cyclone

The cyclone was made in modular form to allow a range of lengths to be easily examined. The barrel diameter was 140mmØ, and the cone was 355mm long. The inlet section had 68mm of barrel below the gas exit lip, and two barrel extensions of 75mm and 100mm were made. Two bins were made, both of 140mm diameter and 140mm depth, one with a port in the centre of the bin base, and the other with a removable base, that allowed it to be used as a further barrel section. A 90mm long conical extension piece was made, with the same cone angle as the standard cone. To examine the effect of the barrel sections on the flowfield a long cone and a short inlet piece were made. The new inlet section had a flange 5mm from the gas exit lip, and the long cone covered the standard Stairmand High Efficiency design length without any barrel

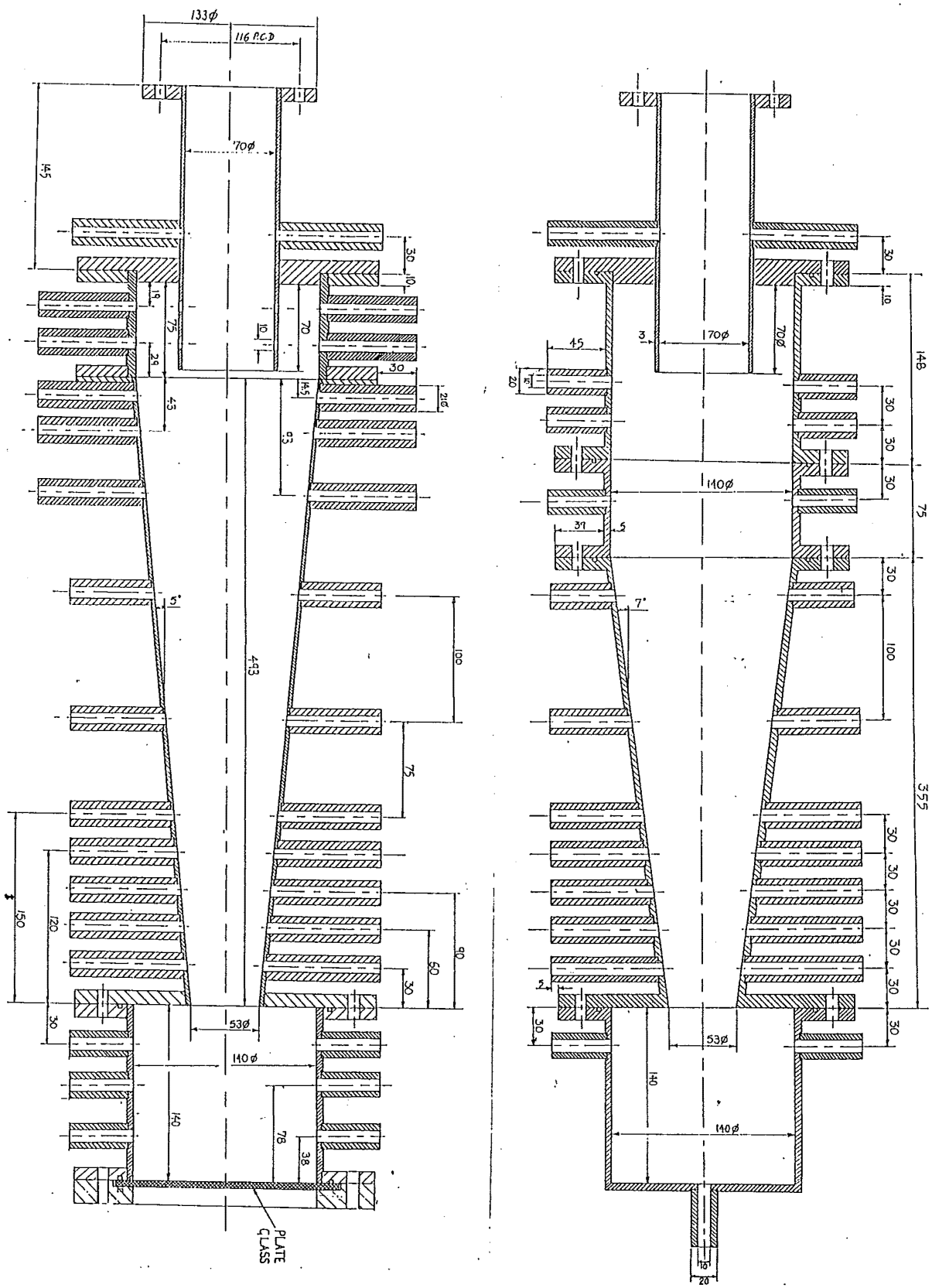

Figure 10.A.1: Dimensions and location of measurement ports in 140mmØ cyclones. Standard and Long cone versions of the Stairmand High Efficiency design

Opposite: Plate 5: Figure 10.A.2: The sections of the 140mmØ laboratory cyclone
Figure 10.A.3 The 750mmØ cyclone, with and without bin.

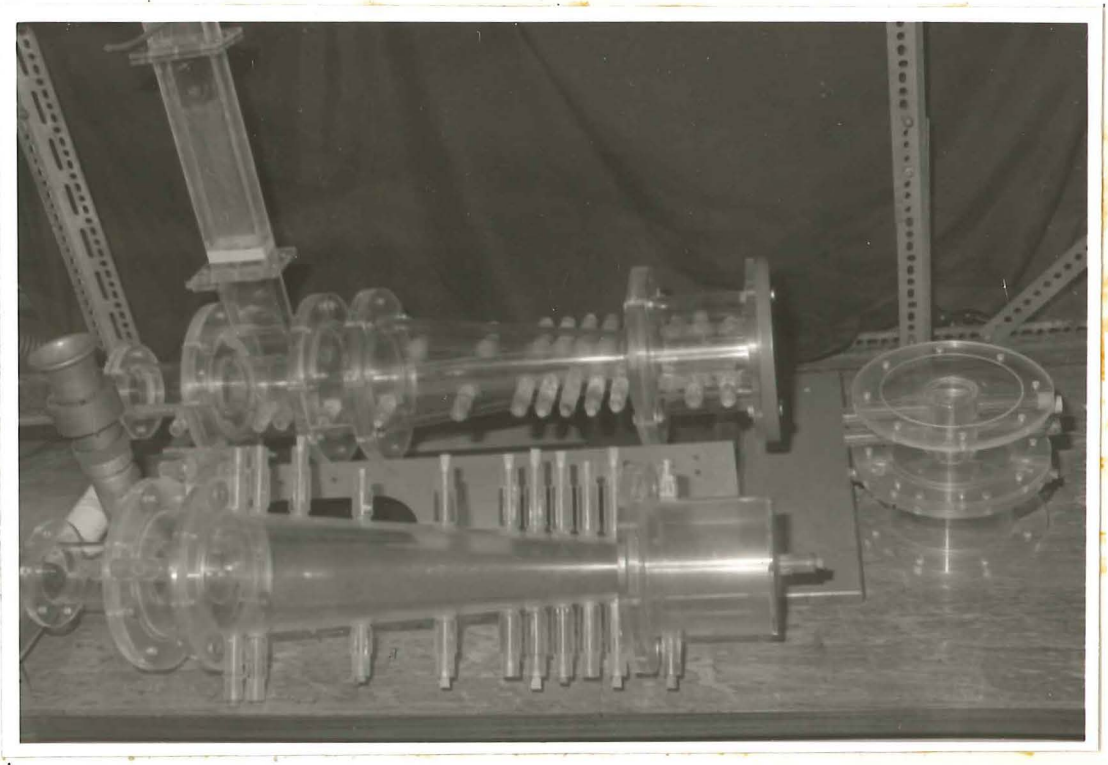

Plate 5A: Figure 10.A.2: The sections of the 140mm∅ laboratory cyclones

Plate 5.B: Figure 10.A.3: The 750mm∅ cyclone with and without the bin

sections, at a cone half angle of 5°, rather than the 7° of the standard cone. All flanges could be connected to each other. The drawings overleaf show the standard geometry, and the 'Long cone' geometry. The inlet section and bin shown attached to the Long cone could be exchanged with the standard pieces. Measurement ports were provided at intervals along the cyclone length

10.A.3: Traverse locations

The locations of the Ports at which the traverses were made in the 140mmØ cyclones are given below as the distance from the gas exit lip, and the distance from the dust exit. The wall radius of the cyclone at that location is also given with all measurements in millimetres. To facilitate comparisons between the different scales of cyclone the position is also expressed as the number of barrel diameters from the gas exit lip.

PORT NUMBER:

GEOMETRY:	12	11	10	9	8	7	6	5	4	3
Standard 140mmØ										
from gx lip	8	38	98	173	273	348	378	408	438	468
(scaled by D)	(0.057)	(0.271)	(0.7)	(1.236)	(1.95)	(2.49)	(2.70)	(2.91)	(3.13)	(3.34)
from dust exit	490	460	400	325	225	150	120	90	60	30
(scaled by D)	(3.5)	(3.29)	(2.86)	(2.32)	(1.61)	(1.07)	(0.857)	(0.643)	(0.429)	(0.214)
Wall Radius	70	70	70	66.3	54.1	44.9	41.2	37.5	33.9	30.2
(scaled by RB)	(1.0)	(1.0)	(1.0)	(0.947)	(0.773)	(0.641)	(0.588)	(0.536)	(0.484)	(0.431)

Long cone 140mmØ										
from gx lip /mm	13	40	93	173	273	349	379	409	439	469
(scaled by D)	(.093) (3.35)	(0.286)		(0.664)	(1.236)	(1.95)	(2.493)	(2.71)	(2.92)	(3.14)
from dust exit	486	459	406	325	226	150	120	90	60	30
(scaled by D)	(3.47)	(3.28)	(2.90)	(2.32)	(1.61)	(1.07)	(0.857)	(0.643)	(0.429)	(0.214)
Wall radius	68.9	66.5	61.9	54.9	46.2	39.6	37.0	34.4	31.7	29.1
(scaled by R_B)	(0.984)	(0.95)	(0.884)	(0.784)	(0.66)	(0.566)	(0.529)	(0.491)	(0.453)	(0.416)

PORT NUMBER:

GEOMETRY:	12	11	10	9	8	7	6	5	4	3
Standard 750mmØ										
from gx lip	43	204	525	874	1409	1811	1972	2132	-	-
(scaled by D)	(0.057)	(0.272)	(0.7)	(1.165)	(1.879)	(2.415)	(2.63)	(2.84)		
Wall Radius	375	375	375	360	290	240	41.2	37.5		
(scaled by R_B)	(1.0)	(1.0)	(1.0)	(0.96)	(0.773)	(0.64)	(0.589)	(0.536)		

The 2090mmØ cyclone traverse locations were at slightly different locations to the 140mmØ & 750mmØ cyclones. In the results the plot of radial velocity at Port 9 in the 140mmØ and 750mmØ cyclones was compared with the results from ports 9 and 10 in the 2090mmØ cyclone, as these were spaced on either side. This cyclone differed from the standard Stairmand design in that it had a shorter cone, that was then extended for $1.5D_{dx}$ at constant diameter.

2090mmØ Cyclone:

Port:	13	12	11	10	9	8	7	6	4	3	2
Distance from the end of the cone, mm											
	7200	6370	5755	4885	4250	3570	2870	2050	765	50	-400
(Scaled by D)											
	(3.44)	(3.05)	(2.75)	(2.34)	(2.033)	(1.71)	(1.37)	(0.981)	(0.366)	(0.024)	(-0.191)
Wall Radius, mm											
	1045	1045	1045	1000	970	891	809	714	546	462	457
(scaled by R_B)											
	(1.0)	(1.0)	(1.0)	(0.957)	(0.928)	(0.853)	(0.774)	(0.683)	(0.522)	(0.442)	(0.437)

The variations on the Stairmand High efficiency cyclone design that were examined in the 140mmØ cyclone are shown in scale drawings on the following pages. The term by which they are referred to in the text are given. It should be noted that the 'Longest' geometry was not in fact the longest one examined, but was the longest of the four variations that were examined initially. Similarly, the short cone design is shorter than the 'Shortest' geometry.

10.A.4: Variations of the geometry examined with the 140mmØ Cyclone.

The following diagrams show the different geometries that were examined using the modular perspex cyclone. All of these have a barrel diameter of 140mmØ.

Standard: 355mm cone, 143mm barrel below gas exit lip, 53mmØ dust exit

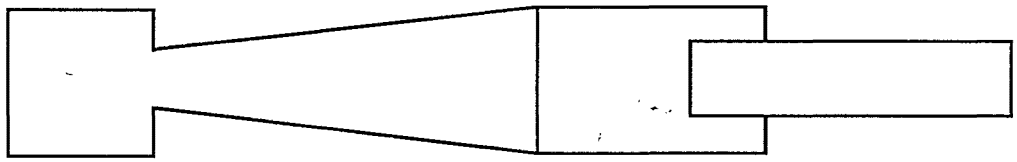

Standard + extended cone:
355mm cone extended a further 90mm, Dust exit 29mmØ,

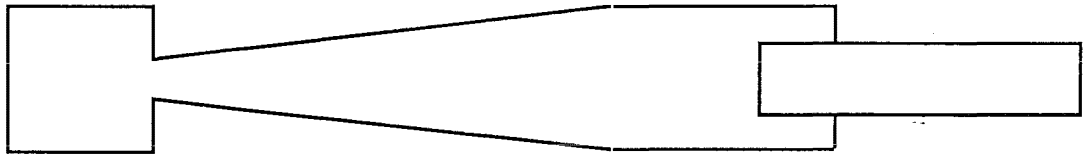

Long cone: 499mm cone, 3mm barrel below gas exit lip, 53mmØ dust exit

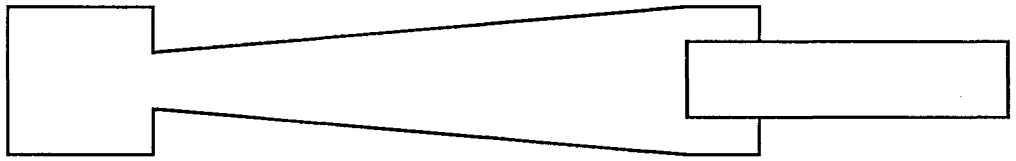

Longest: 355mm cone with 243mm barrel below gas exit lip

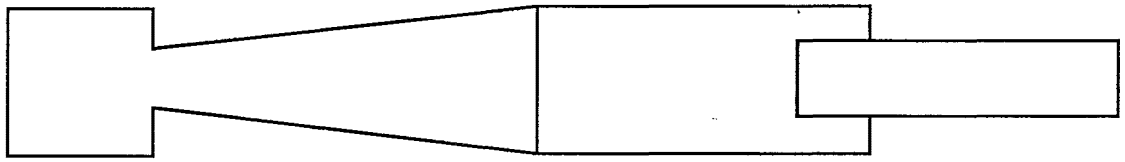

2nd Longest 355 mm cone with 168mm barrel below gas exit lip

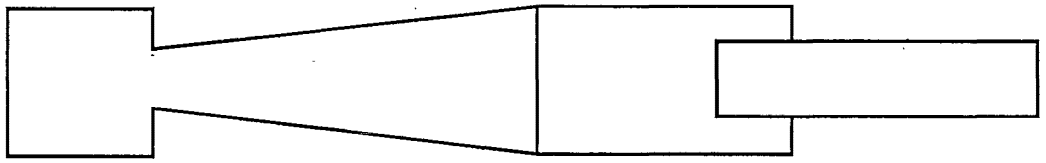

Shortest: 68mm barrel below gas exit lip, 355mm cone, 53mmØ dust exit

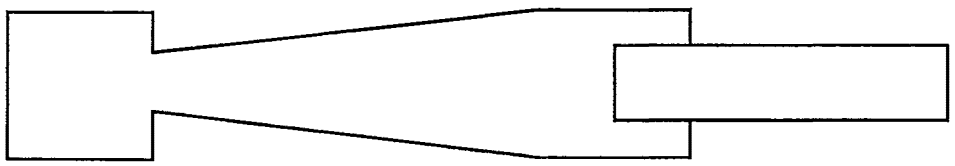

Shortest + Extended cone:

68mm barrel below gas exit lip, 355mm cone + 90mm extension, 29mmØ dust exit

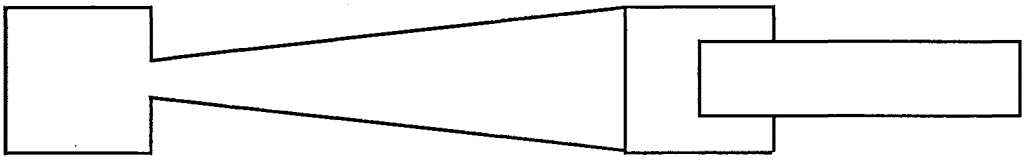

Svarovsky design B

Standard geometry with the dust exit extended for 75mm, then the 90mm cone extension piece added on

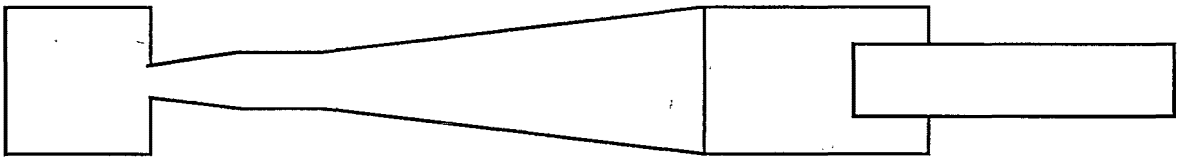

Extended bin 100mm longer bin

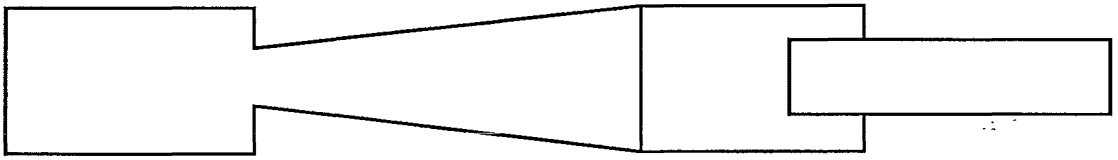

Extended dust exit

Standard geometry with the dust exit extended for 75mm.

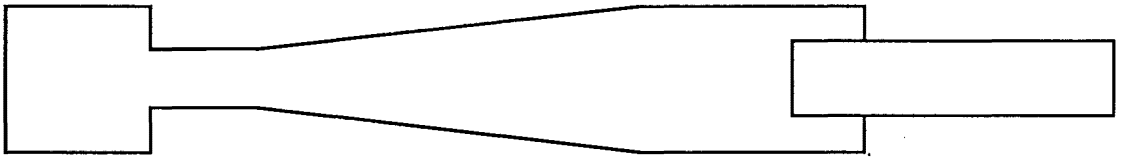

Extra long 523mm barrel below gas exit lip, 355mm cone

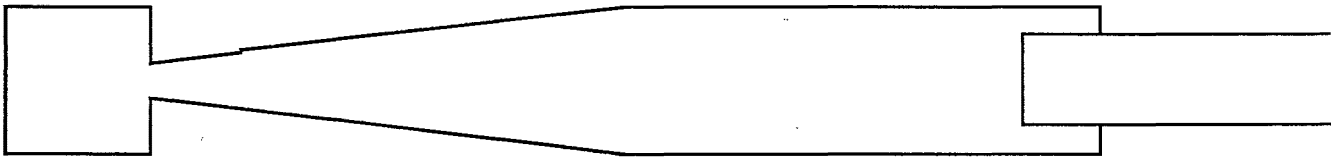

No Cone: 523mm below gas exit lip, all cylindrical sections

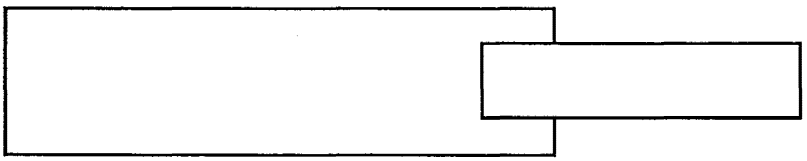

Long cone + 140mm barrel

499mm cone + 140mm barrel below gas exit lip

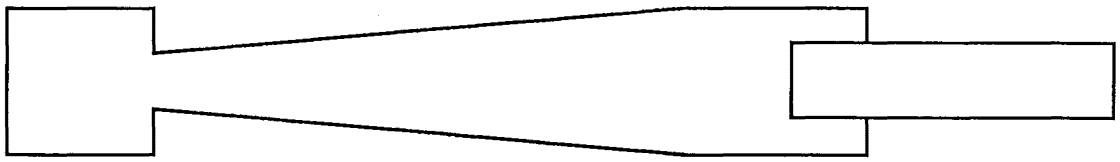

Longest + Extended Cone

243mm barrel below gas exit lip, 355mm cone + 90mm extension, 29mmØ dust exit

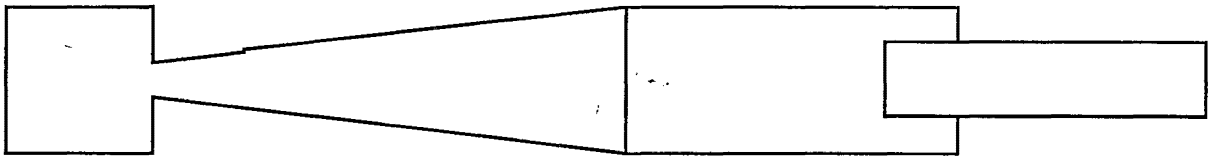

Gas exit plate

Standard geometry with a disc in the gas exit, 225mm from the gas exit lip

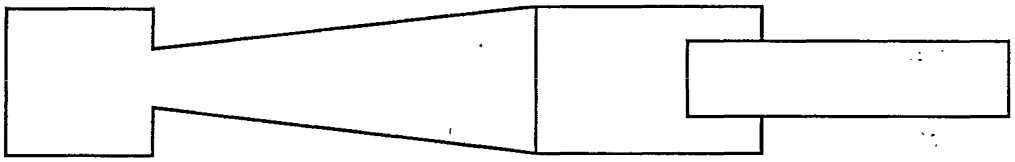

Short cone: 355mm cone, No barrel, 53mmØ dust exit

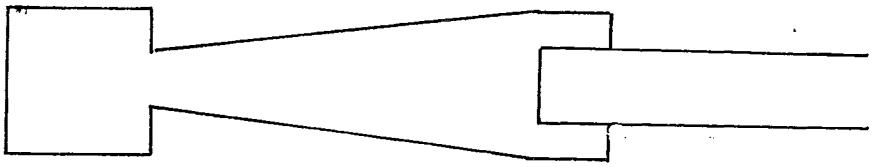

Extra long: 498mm cone, 383mm barrel below gas exit lip, 53Ø dust exit

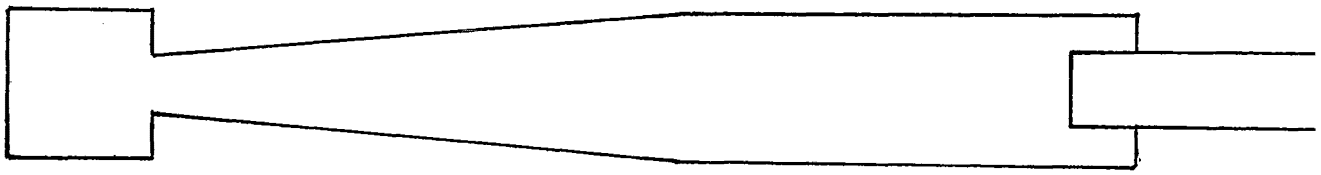

Gas exit Barrel

Standard geometry with a 500mmØ expansion barrel 470mm from the gas exit lip.

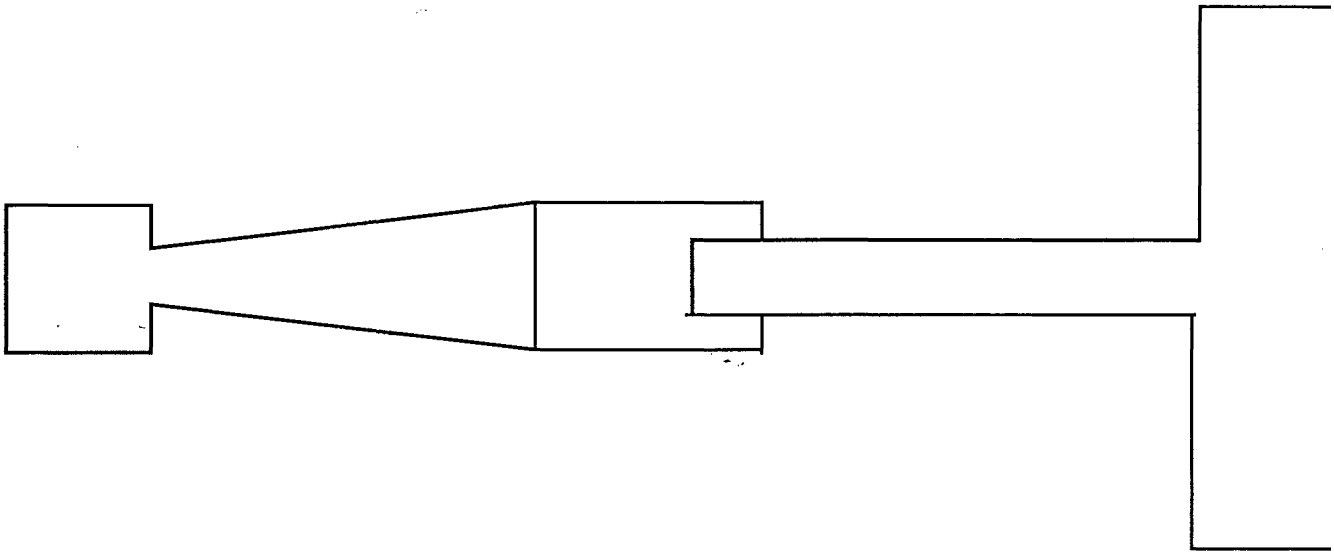

10.B. AIR EJECTOR TO SUPPLY SUCTION TO CYCLONE

In order to be able to easily introduce flow tracers into the cyclone it was desired to operate the cyclone by drawing air from the gas exit. A Rootes Blower fan was available, but this blown air needed to be converted to suction, hence an air ejector was designed, following the procedure of Kentfield and Barnes (1972).

The maximum allowable pressure difference in air pumped by the ejector is $\Delta P = 1psi \cong 7kPa$. The Euler number for the Stairmand High efficiency cyclone is generally taken as 5 (the number of inlet velocity heads in the pressure drop across the cyclone). Hence the maximum inlet velocity in the cyclone achievable from an air ejector would be:

$$\therefore \quad V_{inlet} = \sqrt{\frac{7000}{0.5 \times \rho \times \xi}} = \sqrt{\frac{7000}{0.5 \times 1.2 \times 5}} = 48 m/s$$

and the maximum volume flowrate achievable through the cyclone would be:

$$Q_{max} = V_{inlet} \times A_{inlet} = 48m/s \times 1.96x10^{-3} = 0.095\ m^3s^{-1}$$

The design flow available from the Rootes blower to drive the ejector was taken as $0.222m^3s^{-1}$ (From pump curves and specification sheets). The important dimensions on a typical ejector design are shown below:

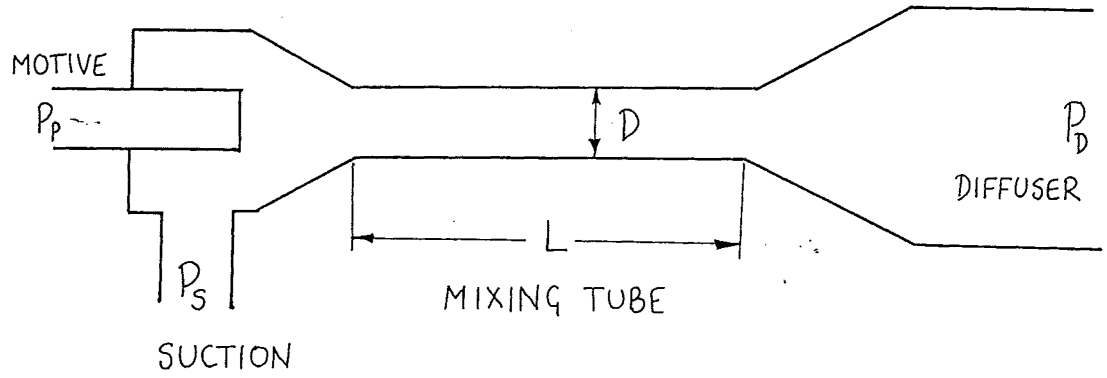

Figure 10.B.1: Geometry of ejector,
showing primary, suction, mixing and diffuser regions

The maximum allowable Δp in air pumped by the ejector = 1 psi ≈ 7 kPa. The parameters specified by the available pressures and the desired flowrates are ratios of the suction side to the motive side density, and mass flowrate. The density is taken to be proportional to the pressure. These ratios are given below:

$$\text{Density ratio } r = \frac{\text{suction side } \rho}{\text{motive side } \rho} \quad \alpha \quad \frac{14.7\ psi}{14.7+3\ psi} = 0.831$$

$$\text{Mass ratio } \beta = \frac{\text{suction mass flow}}{\text{motive mass flow}} \quad \frac{0.095}{0.222} \times 0.831 = 0.355$$

The design chart used was Figure 10 in Kentfield and Barnes (1972), which was said to be 'indicative of the results that could be expected with a very rough mixing tube'. Using the specified ratios from above the pressure ratio is then defined as: $\frac{P_D - P_S}{P_P - P_S} \approx 0.39.$

Given an available pressure difference of 3psi developed by the Rootes Blower, the pressure available to drive cyclone can be calculated as

$$\Delta P_{pumped} = 0.39 \times 3\,\text{psi} \times \frac{10^5}{14.7} = 7.96\,\text{kPa}.$$

Figure 10 in Kentfield and Barnes (1972) also defines a value of the area ratio:
$S = \frac{\text{suction area}}{\text{primary area}} \approx 1.55$ and the ejector efficiency of $\approx 27\%$.

The other design parameters fixed by the figure 10 are:

$c_s = 0.98$ - primary nozzle velocity coefficient
$c_p = 0.96$ - primary nozzle velocity coefficient
$f = 0.03$ - friction factor in mixing tube
$\frac{L}{D} = 6$ - ratio of length to diameter of mixing tube
$\eta = 75\%$ - diffuser effectiveness.

The mixing tube has the same area as the primary and secondary areas combined, and the ratio of the area of the diffuser to the area of the throat is specified as 4, in order to obtain adequate recovery of momentum to pressure. The analysis that the design is based on assumes that the velocity in the diffuser outlet is negligible compared with the

The secondary area, A_S, is then established from the equation below, using the known secondary mass flow $\dot{m}_s$:

$$A_S = \frac{\dot{m}_s}{c_s \sqrt{\frac{2\rho_s (P_p - P_s)}{\left(r \left(\frac{c_s\ s}{c_p\ \beta}\right)^2 - 1\right)}}}$$

$$A_S = \frac{0.1118}{0.98 \sqrt{\frac{2 \times 1.177 \times .(20.684 \times 10^{+3})}{\left(0.831 \left(\frac{0.98\ 1.55}{0.96\ 0.355}\right)^2 - 1\right)}}} = 0.001896\,\text{m}^2$$

The primary area A_p is then calculated using the design area ratio $A_p = \frac{A_S}{1.55} = 0.001308$ m^2 This specifies an internal diameter of the primary nozzle of: 40.8 mm I.D. The nearest diameter available is a 41mm I.D. pipe, hence the actual $A_p = \frac{\pi}{4} \times (41 \times 10^{-3}) = 0.0013203$ m^2. The actual secondary area required is then be adjusted to: $A_S = 1.55 \times A_p =$ 0.0019144 m^2. Assuming a wall thickness of 2mm, the Secondary area can be determined :

$$A_S = \frac{\pi}{4} D^2 - \frac{\pi}{4} \times 0.045^2 = 0.0019144 \text{ m}^2 \text{ -» } D = 66.8 \text{ mm}$$

The nearest suitable piping available was 68mm I.D. and the design dimensions are altered to suit:.
Mixing length 400mm, Diffuser diameter 135mm, Primary nozzle 41mm I.D. and 46.7mm O.D.

The ejector was built with these dimensions, and installed. A reliable means of measuring the cyclone inlet flow was not available, but it appeared that the flow was well short of the $0.095 m^3/s$ ($V_i = 48 m/s$) that was expected. A traverse was made through the gas exit with the 4 hole Pitot cylinder, and the integration of the axial velocity across the diameter suggested that the suction flow was only $0.03 m^3/s$. The orifice plate was designed according to a standard text, but the flowrates shown by this were even lower, at $0.022 m^3/s$. The cyclone overall pressure drop Euler number was well above the accepted value for the Stairmand H.E. design. When the bellmouth entry flowmeter was obtained, the actual inlet flow to the cyclone was found to be $0.04 m^3/s$. This gave a reasonable value for the Euler number, and agreed with other estimates of the suction side flowrate.

This suction side flowrate was found to be well short of the expected flowrate because the motive side flowrate was considerably less than the $0.222 m^3/s$ that was used in the design. This was apparently due to losses incurred in the 52mmØ piping between the Blower and the ejector, as the blower was located in the basement, 2 floors below. .

In April 1987 the flowrate produced by the Rootes blower was measured as $0.083 m^3/s$ in the 52mmØ pipe on level 2. This is well short of the 0.222 m^3s^{-1} that is predicted to be possible from the pump curves. The ejector was found to be performing to the design ratios, with the suction achieved (0.0384 m^3s^{-1}) at this lower primary flow being 44% of the primary flow (compared with the 43% predicted from the design).

The stagnation pressures in the ejector were estimated, as a check on the ejector performance. Relative to atmospheric pressure the motive side pressure was -2640 Pa; the diffuser pressure was -90 Pa; and the suction side pressure was -2190 Pa. These needed to be corrected for the likely contribution from the velocity pressure: In the motive side velocity pressure = 2382 Pa; in the diffuser V.P. = 36.5 Pa and in the suction side V.P. = 53.7 Pa.

These measurements allow a rough estimate for the ejector pressure to be made:

$$\frac{P_D - P_S}{P_P - P_S} \approx \frac{2072}{1878} = 1.10$$

Note that this estimate is not strictly correct, and the design curves show that there is no intersection for the given area ratio (S=1.55) and pressure ratios above 0.38. However this result does suggest that the ejector is operating at a higher pressure ratio than expected. The lower cyclone pressure drop at this lower air flow meant a high pressure ratio was not needed. It was decided to improve the suction flowrate by altering the design to give a lower value of the pressure ratio. This was done by bringing the mass ratio closer to unity, at the expense of the available driven pressure.

To double the cyclone flow requires a four-fold increase in pressure as $\Delta P \propto V_i^2$. Therefore $\Delta P_{secondary} \approx 4 \times 930 = 3720$ Pa.

A correction was found necessary to the figures used in the initial calculation. The bottom line of the pressure ratio ($P_p - P_s$) was better estimated as $P_p \approx 3$ psi available head; and $P_s \approx 1/2$ psi, the negative pressure due to the cyclone. Thus the bottom line is 3 + 1/2 = 3 1/2 psi, which improves the ejector performance. Losses in the piping to the ejector were taken as 1/2psi, which kept the bottom line at 3 psi. In fact the estimated losses for 52mmØ pipe are 1.2 psi, and the diameter of the delivery piping needs to be increased to at least 63 mm to keep the losses below 0.5 psi.

The density ratio $= \frac{\text{suction side density}}{\text{motive side density}}$ is again estimated by taking the density proportional to pressure, with the pressures adjusted as mentioned in the previous paragraph.
The motive side pressure is the atmospheric pressure plus the 3 psi head developed by the blower. The suction side pressure is the atmospheric pressure minus the expected cyclone pressure drop (3720 Pa = 0.54 psi). The desired suction side flowrate is $0.1 m^3/s$ which is to be produced from the $0.085 m^3/s$ motive side flowrate.

$$\text{Density ratio } r = \frac{14.7 - 0.54}{14.7+3} = 0.8$$

$$\text{Mass flow ratio } = \beta = \frac{0.1}{0.085} \times 0.8 = 0.941$$

Using these in Figure 10, the results were :

Pressure ratio $\frac{P_D - P_S}{P_P - P_S} = 0.22$; Area ratio $S = 3.6$; Efficiency = 30%

Now $P_D - P_S = 0.22 \times (3+0.54) \times \frac{101.3 \times 10^{-3}}{14.7} = 5920$ Pa . This doesn't quite meet the cyclone pressure drop, but should result in an increase in the flowrate supplied.

The possible options for altering the dimensions to improve the performance were:
(a) Keep the mixing tube diameter at 68mmØ, Make outside diameter of primary 50.3mm and the inside diameter 24.1mm
(b) Sleeve the mixing tube to reduce its diameter to 64mmØ, and keep the outside diameter of the primary nozzle at 45mmØ, and the inside diameter 24.1mm
(c) Sleeve the mixing tube diameter to 53.7mmØ and make the outside diameter of the primary nozzle 28mmØ and the inside 24.1mmØ.

For ease of fabrication it was decided to keep the mixing tube at the same diameter, and the alterations were made to the primary nozzle. A conical reduction was added to the end of the nozzle, and the end retracted back from the start of the mixing tube to allow the jet more room to expand before the start of the mixing tube. These alterations were made and the flowrate through the cyclone was increased to $0.0416 m^3/s$ ($V_i = 21.2$ m/s). This is an increase of 25% in the cyclone flowrate. Further developments in the air supply arrangements involved the replacement of the 4kw Rootes Blower motor with a 10kw motor, and also the replacement of the Rootes blower with a larger Blower and gear box.

10.C ROOTES BLOWER PERFORMANCE:

The original Rootes Blower motor appeared not to deliver the design flow - measurements showed the flowrate was 0.03 $m^3\ s^{-1}$ (or 64 cfm). The capacity should be :

Pump type : 59AF
The motor turns at 2900 rpm with a reduction of 4.5 in : 7.5 in
Pump rpm = 2900 x 4.5/7.5 = 1740 rpm

From pump curves this is 467 cfm

With the 4kw pump motor the pressure developed is 225mm water head = 2.2kPa = 0.3 psi with no weights on the release valve. With the weight on it could develop 0.55psi, but cuts out as the motor overheats. This was diagnosed as due to failed motor bearings, and the motor was replaced.

With a new 10kw motor the pump could deliver 182cfm. With 6 weights on the pressure release and all the outlets blocked off, the blower developed 4psi. This is more than the blower is rated for, and caused overheating again. The head was measured for each weight to find the safe operating condition.

No. weights	Total weight/g	Head developed/mmHg	Head/psi
0	0.0	55	1.06
1	1627.8	80	1.55
2	3289.0	105	2.03
3	4917.2	130	2.51
4	6546.8	160	3.10
5	8147.1	183	3.54
6	9175.2	205	3.97

Correlation of the total weight versus psi has a regression coefficient of r=0.9995, the equation is $1.05358 + 3.032702 \times 10^{-4} \times$ weight/g

$\Rightarrow$ 3.5 psi requires 8066.8 g. To achieve this use the lightest 5 weights, which total 8054 g
$\Rightarrow$ 3.496 psi. The lightest 4 weights plus the heaviest total 8085.6 g $\Rightarrow$ 3.6 psi

The pressure loss incurred in the piping on level 2 reduced the primary flow available. The line pressure losses were measured between the points marked P1 and P2 on the sketch below, which shows the piping path on level 2 from the well to the ejector. The velocity in the 52mmØ pipe was measured with a 3mmØ pitot probe and found to be 50m/s ($0.106 m^3/s$) when the cyclone inlet flow was 22m/s ($0.0426 m^3/s$). At this flow, the piping pressure drop was 5300 Pa (or 0.8 psi out of the 3.5psi available from the Rootes Blower), giving a fitting loss of $\Sigma K_f = 1.87$, and a friction loss of $4 f L/D = 1.7$. It was clear that by increasing the pipe diameter, the losses could be reduced and more suction flow achieved from the ejector. The 52mmØ piping on level 2 was replaced with 100mmØ piping. With this change made (September 1990) the cyclone flowrate was increased to $0.055 m^3/s$ (V_{in} = 28m/s)

10.D. SILENCER

The noise Rootes Blower was found to be too loud when running so a silencer duct was designed and built, with the aim to reduce the sound level to the level where normal conversation was possible.

A lined duct was chosen, with the size selected on the restriction on the velocity required to avoid erosion (V_{crit} < 12.5m/s). The maximum design flow expected is: 0.24 + 0.1 = 0.34 $m^3 s^{-1}$. To keep the velocity at or below 12.5 m s^{-1} requires an area of 0.0272 m^2. The internal duct dimensions were selected as 200 mm by 140 mm. Using 50mm thick acoustic insulation, the percentage open area can be calculated as: $\frac{200 \times 140}{300 \times 240} = 39\%$

The attenuation expected from the silencer is calculated separately for the vertical sides and the top and bottom surfaces, and these are then added. For each of 6 frequency bands the ratio of the duct width to the average band wavelength is calculated, and this parameter (L_y/λ) is used in Figure 17.2 on p440 in Beranek (1960) to find the attenuation per unit length (AL_y).

Calculation of attenuation for L_y = 200 mm

Mid range Frequency /Hz	125	250	500	1000	2000	4000
Wavelength λ /m	2.75	1.38	0.688	0.344	0.172	0.086
L_y/λ	0.0727	0.1449	0.2907	0.5814	1.163	2.326
AL_y	1.2	2.2	3.0	3.2	2.9	1.3
A per metre	6.0	11	15	16	14.5	6.5

Calculation of attenuation for L_y = 140 mm

Mid range Frequency /Hz	125	250	500	1000	2000	4000
Wavelength λ /m	2.75	1.38	0.688	0.344	0.172	0.086
L_y/λ	0.0509	0.101	0.2035	0.407	0.814	1.628
AL_y	0.8	1.6	2.6	3.2	3.0	2.6
A per metre	5.71	11.4	18.6	22.9	21.4	18.6
Total Attenuation per unit length	11.7	22.4	33.6	38.9	35.9	25

To achieve the desired noise level of NC50 a 1200mm long silencer was specified. The expected noise level was then: 65 57 47 36 39 52 db

The noise levels in the laboratory were measured with the ejector running unsilenced, and then the background noise was measured without the Rootes blower or ejector running.:

Frequency mid range/Hz	125	250	500	1000	2000	4000	A scale
(a) Background noise: Linear scale: 70db	54	58	56	55	55	46	60

(b) Unsilenced ejector:
Linear scale: 92 db

Freq resp/db	79	84	87	83	82.5	82	89.5

The expected attenuation:
(for 1.2m silencer of 50mm Siliner with internal dimensions 200mm x 140mm

		14	27	40	47	43	30
Expected silenced sound levels:		65	57	47	36	39	52

Actual sound levels measured post silencing

Linear scale: 78	Fast	73	68	66	68	65	68	74
Linear scale: 80	Slow	71.5	69.5	69.5	72	68	69	76.5

Although the silencer did not perform to the predictions of the design, the noise levels were reduced to a comfortable level.

The noise levels in the plant room were also measured:

Linear scale: 97	82	89	93	90	86.5	76.5	94

Since these measurements were made a more powerful motor and larger capacity blower have been installed. The noise levels could be reduced further by the addition of a normal muffler, which can also achieve a further 10db of attenuation for frequencies above 1865 Hz from the Random incidence parameter.

10.E. INLET FLOW METERING:

10.E.1: Design of Orifice Plate for flow measurement :

A maximum flowrate of 0.094 $m^3 s^{-1}$ was expected, which equates to an average inlet velocity of 48 m s^{-1} in the inlet duct (which has dimensions of 0.07 x 0.028 m). The problems with the ejector and the Rootes Blower meant that the actual maximum flowrate was initially limited to 0.04 $m^3 s^{-1}$, which was used as the design flow.

The "Universal Calculation" method on p328 of Spink (1972) was used to size the orifice plate. This method also yields a calibration equation relating the flowrate to the orifice differential pressure.

A. The procedure used to calculate the bore for the orifice plate.

1.The proper flow range was selected as 0.04 - 0.01 $m^3 s^{-1}$ (= 374 lb/hr)

2. Using the Universal Calculation, the parameter S is found from:

$$S = K_1\beta^2 = \frac{W_m}{359\, D^2 F_a F_m F_c Y \sqrt{h_m \gamma_f}} \qquad \text{--- (10.E.1)}$$

Given this value the corresponding d/D can be read from tables in Spink (1972). D is the equivalent diameter of the rectangular inlet, which equals four times the hydraulic radius, R_H:

$$4 \times R_H = 4 \times \left(\frac{0.07 \times 0.028}{2 \times (0.07 + 0.028)} \right) = 0.04\text{m} \qquad \text{--- (10.E.2)}$$

Initally assume that:
F_c = Reynolds number correction = 1.0;
Y = expansion factor = 1.0
F_a = temperature expansion ratio ≈ 1.0;
F_m = manometer factor ≈ 1.0
h_m = maximum differential in range of differential gauge, in wg. ≈ 4 inches.
W_m = Maximum rate of flow lb/hr = 317.5 lb/hr

$$\gamma_f = \text{specific weight of gas} = \frac{m_w \rho_f}{10.73\, T_f Z_f} \qquad \text{--- (10.E.3)}$$

m_w = molecular weight = 28.964
ρ_f = flowing pressure psia = $p_{atm} - \Delta p \approx 14.7$
T_f = flowing absolute temperature = 538.8°R
Z_f = compressibility factor at flowing conditions ≈ 1.0

γ_f = 0.07373

Therefore, for a pressure reading of 4" w.g. the parameter S required is: S = 0.65651. This is off the chart for all types of orifice, as Table 13 for full flow taps extends only as far as S = 0.4782. To reduce S allow a greater range of differential pressure - say 12 ".

Then $S = 0.37855$ =» $d/D = 0.7215$ and $d = 28.86$

Orifice hydraulic radius = 7.22mm $= \frac{a_o b_o}{2(a_o + b_o)}$ --- (10.E.4)

Allowing the bore to take the same geometry as the inlet requires $a_o = 20.2$mm $b_o = 50.5$mm

B. Calculation of rate of flow for orifice plate :

Given h_w the orifice plate pressure drop (oppd) in mm water gauge, the mass flowrate can be calculated from :

$$W_h = 359\ S\ D^2\ F_a\ F_m\ F_c\ Y \sqrt{\gamma_f} \times \sqrt{h_w} \qquad \text{--- (10.E.5)}$$

It can be assumed that F_a, F_m, F_c and Y are all ≈ 1.0. S depends only on d/D and is constant at 0.3680. D = 1.57 inches.

$\gamma_f = 0.07373 = \frac{22.07}{T_f}$ for T_f in Kelvins

$W_h = 305.4 \sqrt{\frac{h_w}{T_f}}$ in lbs/hr; for h_w in mm water gauge, T_f in Kelvin.

$Q = 0.0384798 \times \frac{1}{\rho}\sqrt{\frac{h_w}{T_f}}$ in $m^3\ s^{-1}$ for ρ in kgm^{-3}; T_f in K; h_w in mm_{wg}

The values obtained from the orifice plate were found later to be considerably lower than the actual flowrate. A better method of metering the flowrate was obtained by borrowing, and later fabricating a bellmouth entry flowmeter.

10.E.2: Bellmouth entry flowmeter

To obtain a more accurate check on the actual cyclone flowrate, a 52mmØ bellmouth entry flowmeter was borrowed from Andersen Engineering, Christchurch. This had been designed according to the method published by Ito et al (1985b), and calibrated using pitot traverses. The calibration equation was given by :

$$Q = 0.00779\ C_D \sqrt{\Delta P_o} \qquad \text{--- (10.E.6)}$$

where ΔP_o is the pressure drop across the entry, in mm H_2O
C_D is a function of the Reynolds number, from Figure 3 in Ito et al (1985b)
Q is the volumetric flow in m^3/s.

The bellmouth was used to calibrate the orifice plate, by connecting the two in series, with a metre of piping between them. The calibration plot is given below, from several repeat runs.

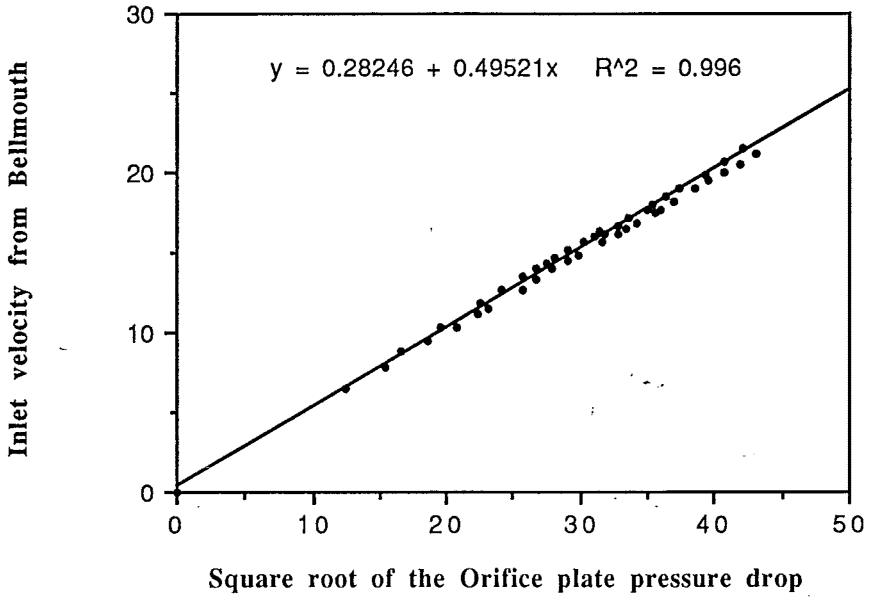

Figure 10.E.2: Calibration of the Orifice plate against the bellmouth.

As the Bellmouth flowmeter was only on loan, a duplicate was made, following the design given in Ito et al (1985b), and using a programable milling machine, which was given the coordinates of the elliptical surface. This was calibrated against the orifice plate, and was found to give 6% higher flows than the original bellmouth, probably due to the more highly polished surface. The calibration curve is given below:

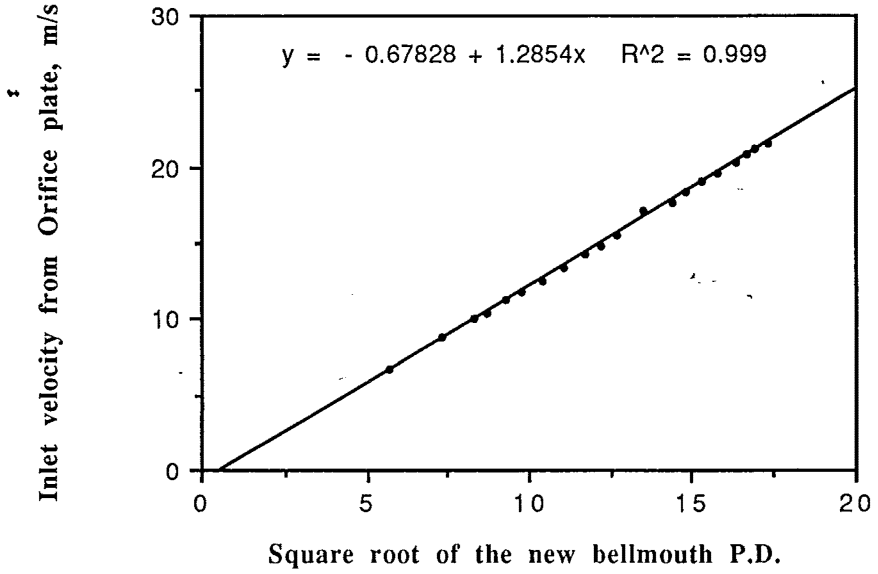

Figure 10.E.3: Calibration of the New Bellmouth flowmeter.

10.F. PITOT CYLINDER ANALYSIS:

The 4 hole cantilever Pitot cylinder that was used to obtain the velocity profiles in the 140mmØ, 750mmØ and 2090mmØ cyclones was built in the Chemical and Process Engineering Department, following the design detailed in Winternitz and Ramsay (1963). The probe had previously been calibrated, and used by Snegirev (1982) but only a rough corection was made for the effect of the radial pressure gradient on the probe readings. For the purposes of this study the probe was re-calibrated in June 1986, and the computer programme used to calculate the velocity and pressure components was expanded. The Pitot cylinder and computer programme have subsequently been used by other workers in the department (Enevoldsen & Werner, 1989; Bidlake 1989; Hutchinson, 1991).

10.F.1: Principles of operation:

The 4 hole cantilever Pitot cylinder can provide the three components of the velocity profile from the measurement of the angle of the flow to the axial plane, and three pressure differences over the hemispherical tip of the probe.

The probe consists of a 9.5mmØ cylinder with a carefully smoothed hemispherical tip. Four pressure tappings are provided in the tip region of the probe and the pressure differences between these are dependent on the flow direction and strength. The probe was constructed according to the principles outlined in the report by Winternitz and Ramsay (1963), who considered the effect of probe size and of the position of the probe tappings. The dimensions and layout of the probe are shown below:

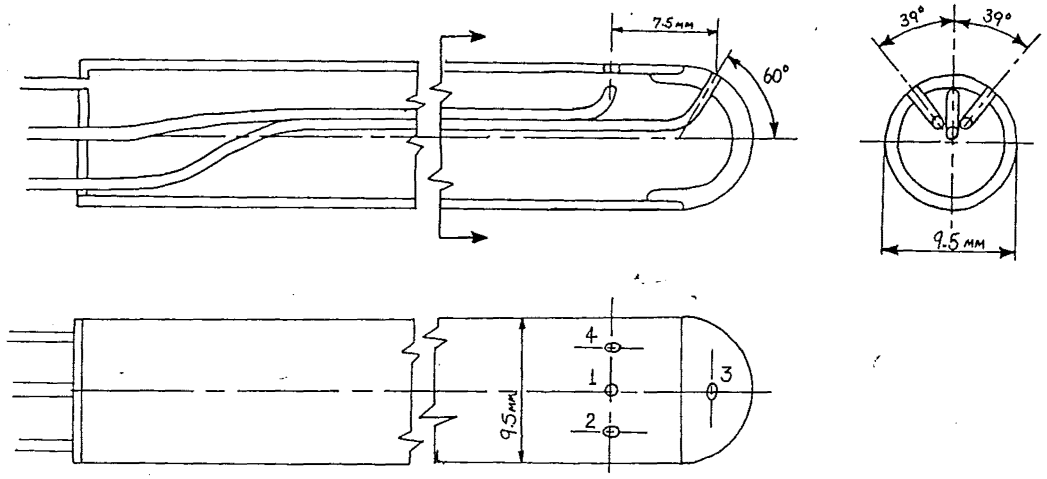

Figure 10.F.1: Pitot cylinder probe dimensions and location of tappings

The distance from the tip orifice to the centre orifice is 7.5mm, while the diameter of the cylinder is 9.5mm. In this respect, the calibration cannot be directly compared with the results of Winternitz & Ramsay (1963), as they used a radial spacing of the tappings of 0.6D. The tip orifice is 60° to the axis of the probe, while the side tappings are located symmetrically 39° on either side of the centre tapping.

During a traverse the probe is inserted progressively from the wall in a radial direction. The tappings 1,2,and 4 are the same distance from the wall, and this distance is kept as small as possible for the first reading. This was typically 1mm in the 140mmØ cyclone, and 10-15mm in the 750mmØ cyclone. The tapping in the probe tip (P3) is always 7.5mm further into the flow, and the effect of this must be corrected for.

Early measurements relied on curve fitting the measured pressure differences and correcting for this 7.5mm spacing. In later experiments the reading P3-PR was measured directly at the same location as the P1-PR by ensuring that measurements were taken at intervals that were multiples of 2.5mm or 7.5mm. This allowed a more direct correction for the radial spacing of the probe tappings.

At each radial position of the probe the following procedure was followed:
- The yaw angle of the probe was altered so that the centre tapping (P1) was pointed directly into the flow. This could be ascertained by examining the pressure difference between the side tappings P2 and P4, which would be zero when they were symmetrically arranged with respect to the flow direction. This difference was displayed on an inclined tube manometer that could be read to 1 Pascal. Since the zero could also be achieved with the probe directed symmetrically away from the flow it was checked that the $P1\text{-}P_{ref}$ reading was at a maximum. (Note that in many cases the P1 pressure was less than the reference pressure and hence the absolute reading |P1-Pref| was minimised).

- The angle between the flow direction and the axial plane (the plane that cuts the cyclone axis at right angles) is given by the yaw angle, and this is measured by the use of the protractor and pointer. When the grub screw is tightened the pointer tip is in line with the tip and centre tappings.

- In turn the pressure differences P1-PR, P1-P2, P1-P3 (and P3-PR) were read, and the position and yaw angle were noted. A switchboard was prepared to simplify the operation of switching between these readings. The Airflow Type 4, 2-limb inclined manometer was used for all experiments. The short limb was used to observe the P2-P4 difference continuously, with the most sensitive setting used, enabling ΔP to be read to within 1 Pa.

The other readings were made on the long limb, which could be read at three settings:

0 to 5000Pa at +/- 10Pa
0 to 1000Pa at +/- 2Pa
0 to 500Pa at +/- 1Pa

A manometer zeroing device was included enabling the long manometer limb to be isolated while changing tappings, or re-zeroing after switching between scales. The connection of hoses was as shown, with the valves open or closed according to the accompanying chart:

The probe is then advanced further into the flow and a further set of measurements were made. The original 1cm markings along the probe (the deep grooves) were found to be only approximately marked. A finer marked is scribed to show the distance along the probe more accurately, and a dot is located 2.5mm from the 10mm mark.

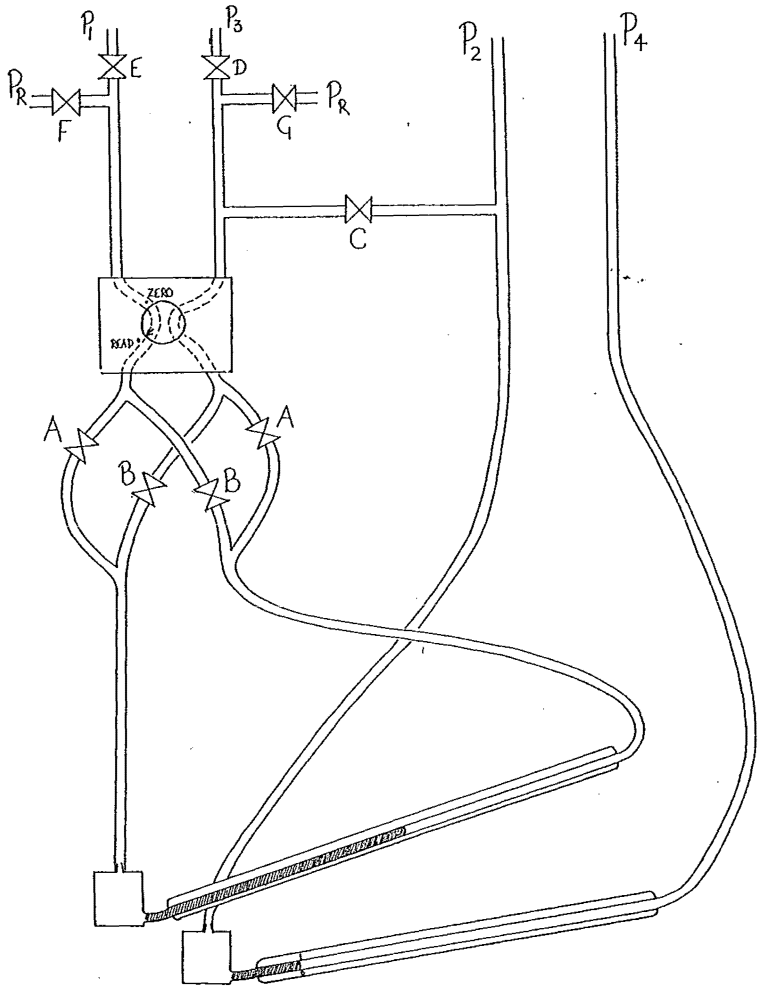

Figure 10.F.2: The manometer switchboard

	G	F	E	D	C	B A	
P1-PR	O	X	O	X	X	TO SUIT	
P1-P3	X	X	O	O	X	THE	O Open
P1-P2	X	X	O	X	O	SIGN OF	X Closed
P3-PR	X	O	X	O	X	THE ΔP	
P2-P4	Using the short manometer limb (all of the time)						

10.F.2: The Pitot Cylinder calibration:

The Mechanical Engineering Department windtunnel was used to provide a uniform airflow of known velocity (20m/s).and direction. The probe was inserted at different angles to the flow (that is varying pitch angles) and the pressure differences noted. The calibration results are presented in terms of ratios of the pressure differences (dimensionless coefficients), as functions of the pitch angle. The use of the pitot cylinder depends on these pressure coefficients for a given probe being dependent on the flow inclination only, and independent of the flow Reynolds number.

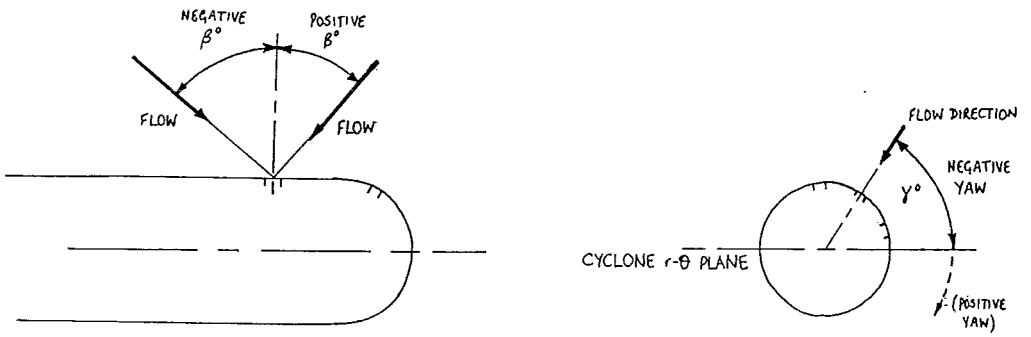

PITCH ANGLE YAW ANGLE

Figure 10.F.3: Sign conventions for the flow angles determined by the Pitot cylinder

The pressure differences are made dimensionless with respect to the centre to side pressure difference (P1-P2) obtained when the probe yaw is zero. The coefficients that characterise the probe performance are then:

Pitch angle coefficient: $$\zeta_\beta = \frac{P_1 - P_3}{P_1 - P_2}$$

Total pressure coefficient: $$\zeta_T = \frac{P_T - P_1}{P_1 - P_2}$$

Static pressure coefficient: $$\zeta_S = \frac{P_S - P_1}{P_1 - P_2}$$

All of the pressure differences are obtained for the probe set to zero yaw angle. P_T and P_S are the Total and Static pressures in the flow, respectively, which are measured in the wind tunnel with a conventional Airflow Pitot Tube.

Winternitz and Ramsay (1963) state that the Total Pressure coefficient may be taken as constant with Reynolds number, down to Re = 4 000. The calibrations carried out for this study were made at 20m/s, giving a Reynolds number in the vicinity of the probe of 12 800, well into the turbulent region. Winternitz and Ramsay made measurements for Reynolds numbers in the range of Re = 1 000 to 5 000.

The calibration curves are presented overleaf. Before starting the measurements for this study a thorough calibration was carried out in July 1986. This calibration was used for all the measurements made up to July 1989. At this time the probe tip was damaged during use in the spray dryer by Bidlake (1989), and the tip had to be rebuilt. The second calibration was carried out to check the effect that this had on the probe performance, and this second calibration was used for all subsequent measurements. There was a slight change in the Pitch angle coefficient, and this combined with a change in the static pressure coefficient to produce radial velocities considerably different to the earlier calibration. The tangential and axial velocities were not affected significantly, as shown in the figure 10.F. In December 1991 the probe was again calibrated (Hutchinson, 1991) with reportedly no significant change in performance.

The calibration data from the initial calibration in July 1986 are presented below.

All pressure readings are in Pa, angles in degrees.

Pitch angle	P_1-P_S	P_1-P_3	P_1-P_2	Yaw	P_T-P_1
-42.5	115	176	121	-2	129.8
-37.5	132	205	137	-2	112.8
-32.5	152	282	157	-2.25	92.8
-27.5	169	311	169	-2	75.8
-22.5	182	326	182	-2	62.8
-17.5	201	332	214	-2	43.8
-12.5	214	327	235	-1.5	30.8
-7.5	226	301	253	-1.5	18.8
-2.5	235	264	257	-1.0	9.81
2.5	242	215	266	-0.5	2.81
7.5	244	174	269	-0.5	0.81
12.5	242	121	271	0.5	2.81
17.5	235	76	262	1.25	9.81
22.5	224	34	248	2.5	20.8
27.5	209	-5	232	3.0	35.8
32.5	190	-47	214	3	54.8
37.5	165	-77.5	190	2.5	79.8
47.5	123	-122	144	2.0	121.8

The P_T-P_1 reading was calculated by adding the known velocity pressure (from a Pitot tube in the windtunnel) on to the P_S-P_1 difference. The yaw angle was noted as a check on the alignment of the probe and flow direction.

The calibration data after the probe tip had been rebuilt (September 1989) are given below. All pressure readings in Pa, angles in degrees.

Pitch angle	P_1-P_s	P_1-P_3	P_1-P_2	Yaw	P_T-P_1
-40.0	116	175	121.5	2.0	128.8
-37.5	130	238	136	2.0	114.8
-37.5	130	238	134	2.0	114.8
-35.0	139.5	252	{143	2.0	105.3
			{144		105.8
-32.5	145.5	260	151	2.0	99.3
	144		149		100.75
-30.0	157	269	158.5	2.5	87.8
-27.5	166.5	272	166	3.0	78.3
-25.0	177	282	175	3.5	67.8
-22.5	179	276	178	3.0	65.8
-20.0	191	287	193	3.0	53.8
-15.0	203	286	214	2.5	41.8
-10.0	213.5	270	233	2.5	31.3
-5.0	222.0	240	244	2.0	22.8
0.0	230.0	204	248.5	2.0	14.8
5.0	234	171	252	2.0	10.8
10.0	237	120.5	260	2.0	7.8
	240	126	259	2.0	4.8
15.0	235	85	261	2.5	9.8
20.0	229	47.5	255	1.5	15.8
25.0	219	9	242	1.0	25.8
30	207	-22	226	0.5	37.8
	203	-26	236	0.5	41.8
35	181	-64	202	0	63.8
40	161.5	-83.5	180.0	0.7	83.3
45	142	-105	162.0	0.7	102.8
50	117	-116	136.5	0.5	127.8
60	68	-135	81	0	176.8

The calibration results were plotted in the form used by Winternitz and Ramsay, with the dimensionless pressure difference ratios as functions of the pitch angle. In the calibration the pitch angle is measured with a protractor as the angle of the probe to the wind tunnel wall. In actual experimental measurements the calibration is used to determine the pitch angle from the measured pressure ratios.

Equations describing the calibration curves were obtained by least squares curve fitting, and these equations can be found in the computer programme. The computer programme includes both the July 1986 and September 1989 calibrations, so that data from either period can be processed. The calibration curves are shown below:

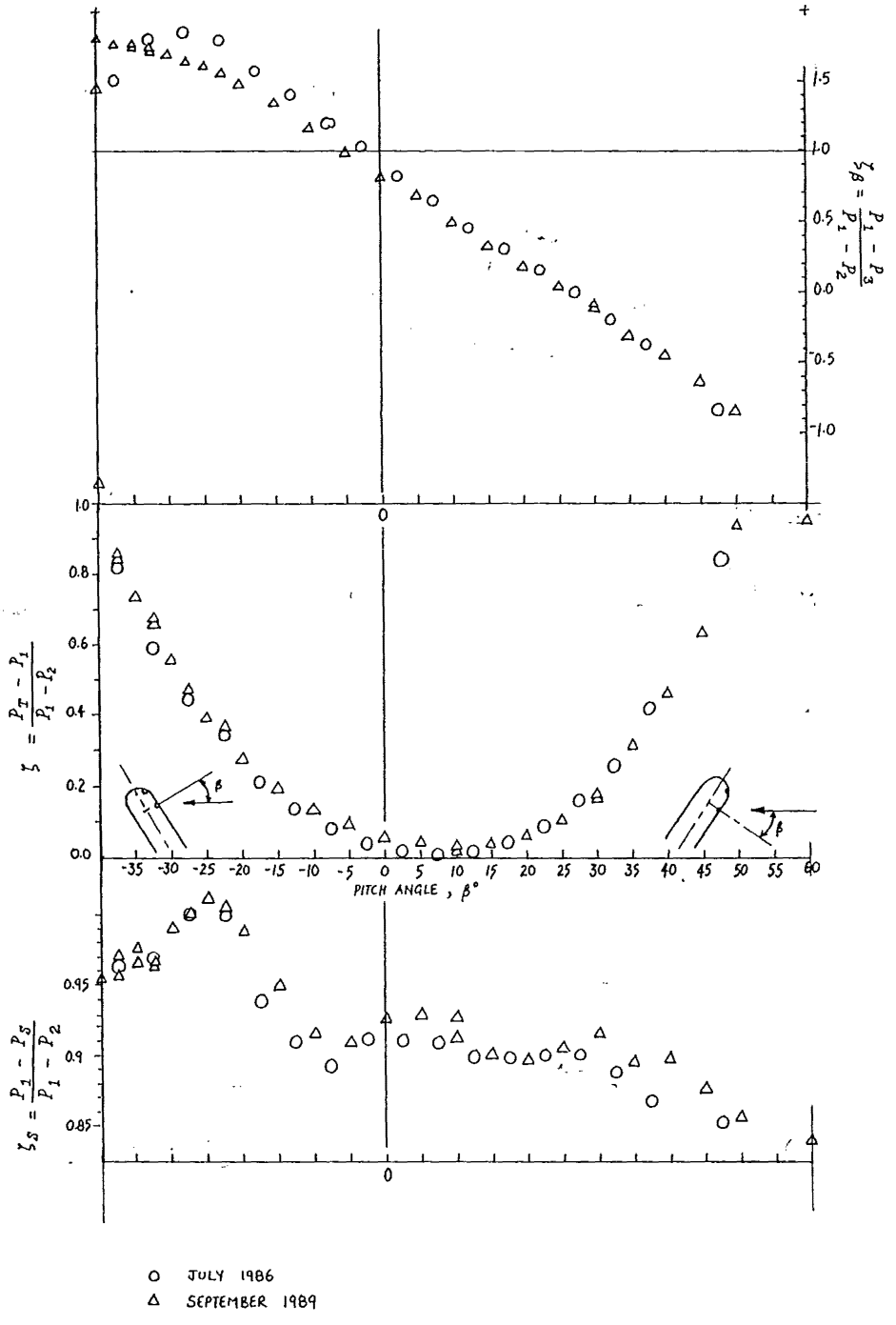

Figure 10.F.4: The Calibration curves for the Pitot cylinder

The effect of the different calibration curves is shown in the following graphs of the velocity components calculated from the same raw data, using the two different calibrations.

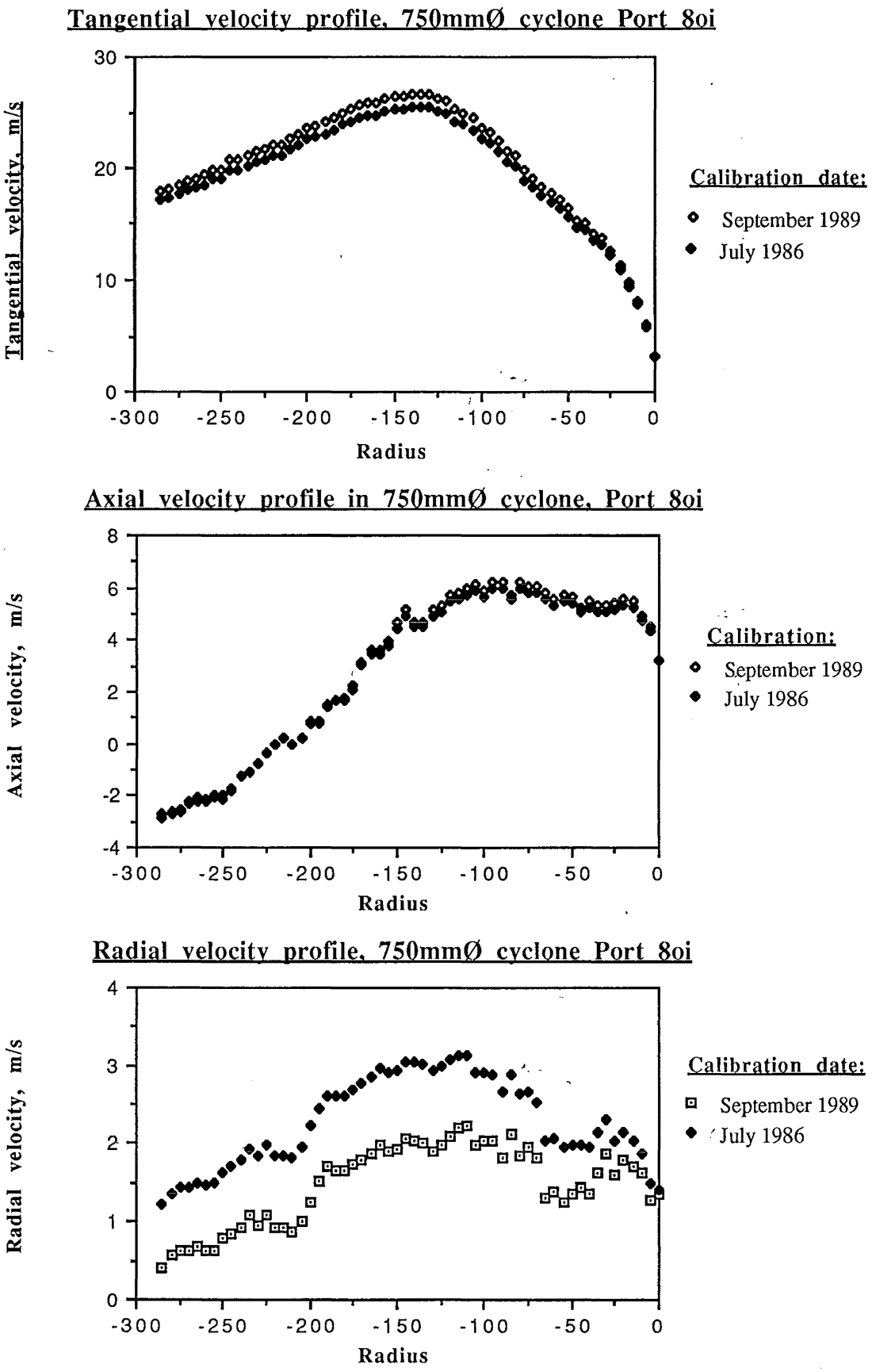

Figure 10.F.6: The difference in calculated velocities from the two calibrations

10.F.3: Calculation of velocities from Pitot Cylinder:

By calculating the pitch angle coefficient ξ_β and finding the pitch angle from the calibration curve, the static pressure coefficient ξ_s and the total pressure coefficient ξ_t can be found from the other calibration curves. The velocity pressure VP is the difference between the total and static pressures, and can be obtained from $\xi_s+\xi_t$ since:

$$\frac{P_T - P_S}{P_1 - P_2} = \frac{P_T - P_1}{P_1 - P_2} + \frac{P_1 - P_S}{P_1 - P_2} = \xi_s+\xi_t$$

that is $VP = (P_1-P_2).(\xi_s+\xi_t)$
and hence the total velocity is given by:

$$V_{total} = \sqrt{\frac{2}{\rho}(P_1-P_2).(\xi_s+\xi_t)}$$

The total velocity can be resolved into components using the yaw and pitch angles:

Tangential = $V_{total}.\cos(yaw).\cos(pitch)$
Axial = $V_{total}.\sin(yaw).\cos(pitch)$
Radial = $V_{total}.\sin(pitch)$

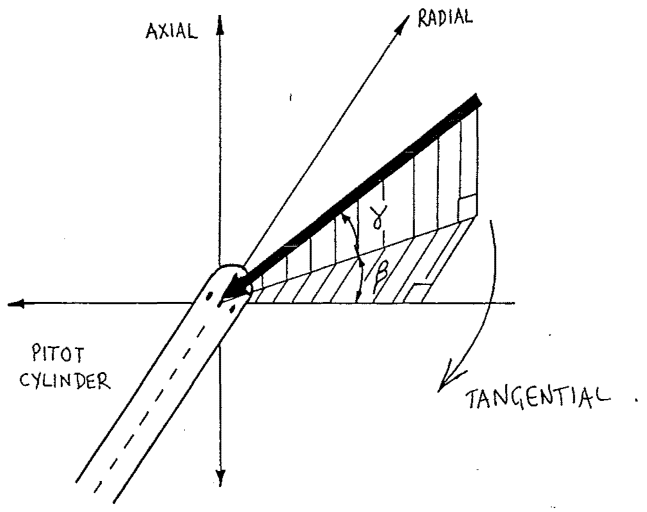

Figure 10.F.7: The resolution of the total velocity into tangential, axial and radial components using the pitch (β) and yaw (γ) angles

For the small pitch angles generally found, the tangential and axial velocity components are largely independent of the pitch angle, whereas the radial velocity is very dependent. The large error in the pitch angle results in a large error in the radial velocity.

10.F.4: Correction of the Tip pressure reading:

The radial distance between the tip pressure tapping and the other three tappings gives rise to an error in the determination of the pitch angle. The error in the pitch angle is given in Winternitz and Ramsay (1963) as:

$$\Delta\beta = \frac{1}{2} d \left(\frac{dP/dr}{dP/d\beta} \right)$$

where d is the linear distance between the tip and centre orifices (= 7.5mm)
dP/dr is the radial pressure gradient
(typically 60 000Pa/m in the 140mmØ, 10 000Pa/m in the 750mmØ)
dP/dβ is the sensitivity of the probe to the flow inclination

The measured pressure difference P1-P3 is comprised of contributions from the static pressure at the two locations, as well as the pressure difference. Since the tappings are radially displaced, any radial gradient in the static, P1 or P3 pressures will introduce an error to the P1-P3 reading.

Snegirev (1982) corrected for this variation in the P_3 pressure reading by:

$$P4 = P3 + 0.0075 . \left(\frac{dP1}{dX} \right)$$

This only corrects part of the problem, as will be shown below.

The measured value of P1-P3 can be broken down according to the location it was measured at, and the contributions due to the static pressure and the dynamic pressure in the tapping can be separated:

$$(P1\text{-}P3)_{meas} = (P_1+P_s)\big|_x - (P_3+P_s)\big|_x$$

$$= P_1\big|_x + P_s\big|_x - P_3\big|_{x+7.5} - P_s\big|_{x+7.5}$$

$$= P_1\big|_x - P_3\big|_{x+7.5} - \left(P_s\big|_{x+7.5} - P_s\big|_x \right)$$

$$= P_1\big|_x - P_3\big|_{x+7.5} - \Delta P_s$$

If the measured P1-P3 is corrected by adding ΔP_s to it then the result $(P_1\text{-}P_3)_k$ only needs to be corrected for the position. The curve of P3-PR is found and adjusted back 7.5mm. P1-PR is comprised of:

$$P_1\text{-}P_R = P_1\big|_x + P_s\big|_x - P_R, \quad \text{so}$$

$$P_1\text{-}P_R - \left(P_1\big|_x - P_3\big|_{x+7.5} \right) = P_1\text{–}P_R - (P_1\text{-}P_3)_{meas} + \left(P_s\big|_{x+7.5} - P_s\big|_x \right)$$

$$= P_1\text{–}P_R - (P_1\text{-}P_3)_k$$

$$= P_1\big|_x + P_s\big|_x - P_R - P_1\big|_x + P_3\big|_{x+7.5} = P_3\big|_{x+7.5} + P_s\big|_x - P_R$$

Hence P_1–P_R must have had the static pressure component removed from it, yielding $(P_1–P_R)_k$. Then: $(P_1–P_R)_k - (P_1–P_3)_k = P_3|_x - P_R = (P_3–P_R)_k$.

A curve can then be fitted through the $(P_3–P_R)_k$ points and the data shifted back 7.5mm. The correct P_1-P_3 can then be reconstructed by reversing the project.

Note:
The subscript k denotes that the pressure has no static pressure component
To subtract the static pressure from the readings it first has to be calculated. This requires an initial guess for P_1–P_3 and subsequent iterations.

The yaw angle also changes with radius, and the P_1-P_3 reading is made with the probe aligned with the yaw angle at the P_1 position, while the P_3 component of the pressure difference may be out of alignment with the yaw at that position. The change in the P_1–P_3 reading caused by the variation in the yaw angle has been checked and found to be acceptably small, given the rate of change of the yaw angle over the 7.5mm distance. The following graph presents the variation of the reading with yaw angle, and the response can be seen to be reasonably flat for variations of less than +/- 10°.

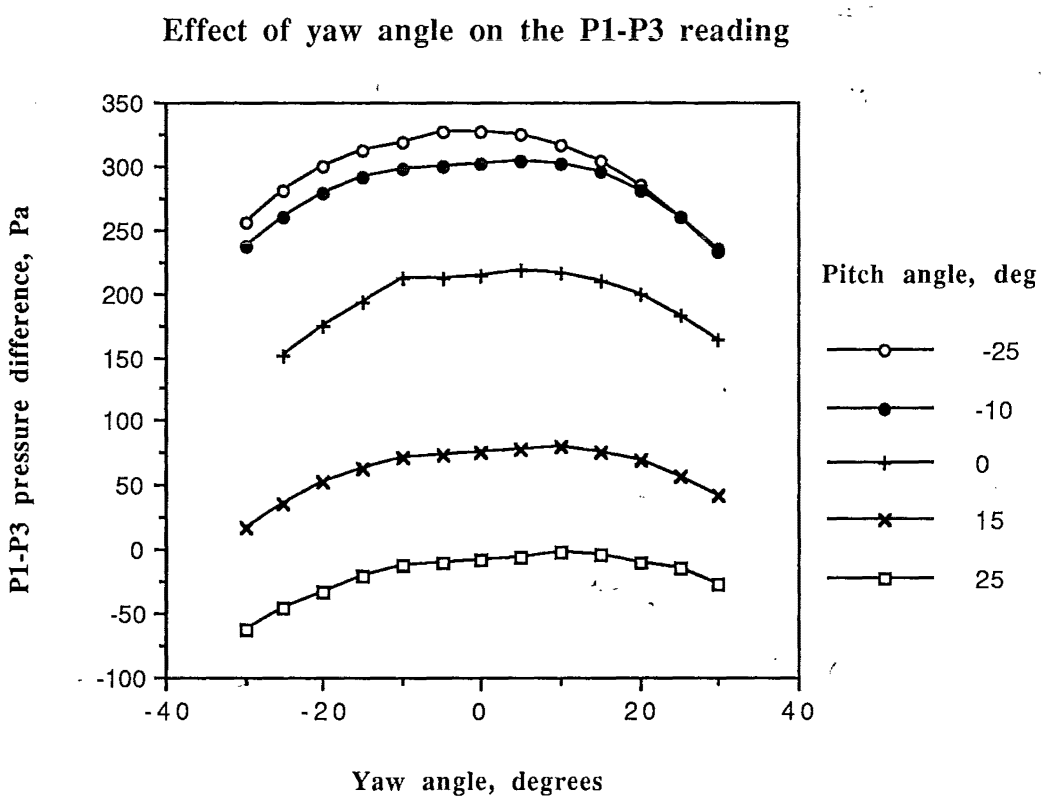

Figure 10.F.8: Variation of P_1-P_3 reading with yaw angle.

The corrections to the pressure readings were made by piecewise fitting parabolic curves to the data, using least squares. A choice of 4 or 5 point curve fitting is allowed in the computer programme, with the data points selected to be spead on either side of the data point that is to be corrected. The curve fitting requires that the measurements are made at equal spacings. The

curve fitting smooths out some of the irregularities in the pressure readings, but sharp changes (or a large error in one point) can lead to misfitting of the curve and magnification of the errors.

An alternative, and preferable method of correcting for the radial spacing of the P_1 and P_3 tappings was used in later experiments. The pressure reading P_3-P_R was measured directly with the probe withdrawn by 7.5mm. This moved the P_3 tapping to the location that the P_1 measurement was made at, giving both pressure differences the same static pressure component, and radial position, and thus allowed the P_1-P_3 pressure difference to be calculated directly, without curve fitting. The computer programme incorporated an option allowing the data to be entered in this form, and the results obtained generally had less scatter in the pitch angle and hence radial velocity. The plot below shows that when the direct measurement method is used the scatter in the P1-P3 pressure difference is less than when the P1-P3 reading is corrected with curve fitting. The smoother profile is reflected in less scattered profiles of the pitch angle and radial velocity, as shown in figure 10.F.10 overleaf.

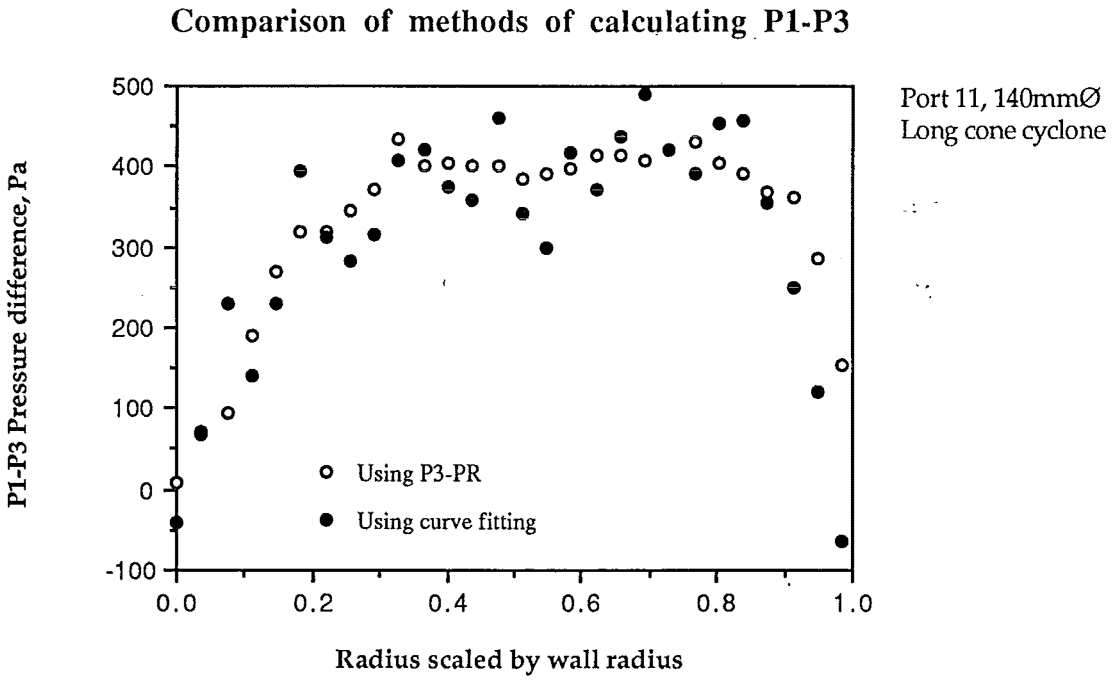

Figure 10.F.9: Comparison of the P1-P3 pressure difference calculated from the direct measurement of P3-PR, and the curve fitted correction.

The differences between the calculated velocity profiles between 4 point and 5 point curve fitting, and the direct measurement of P3-P_R are shown below. "P3ractual" is the velocity obtained when the P3-P_R measurement was made directly, and the other two points are for 5 point and 4 point curve fitting of the data.

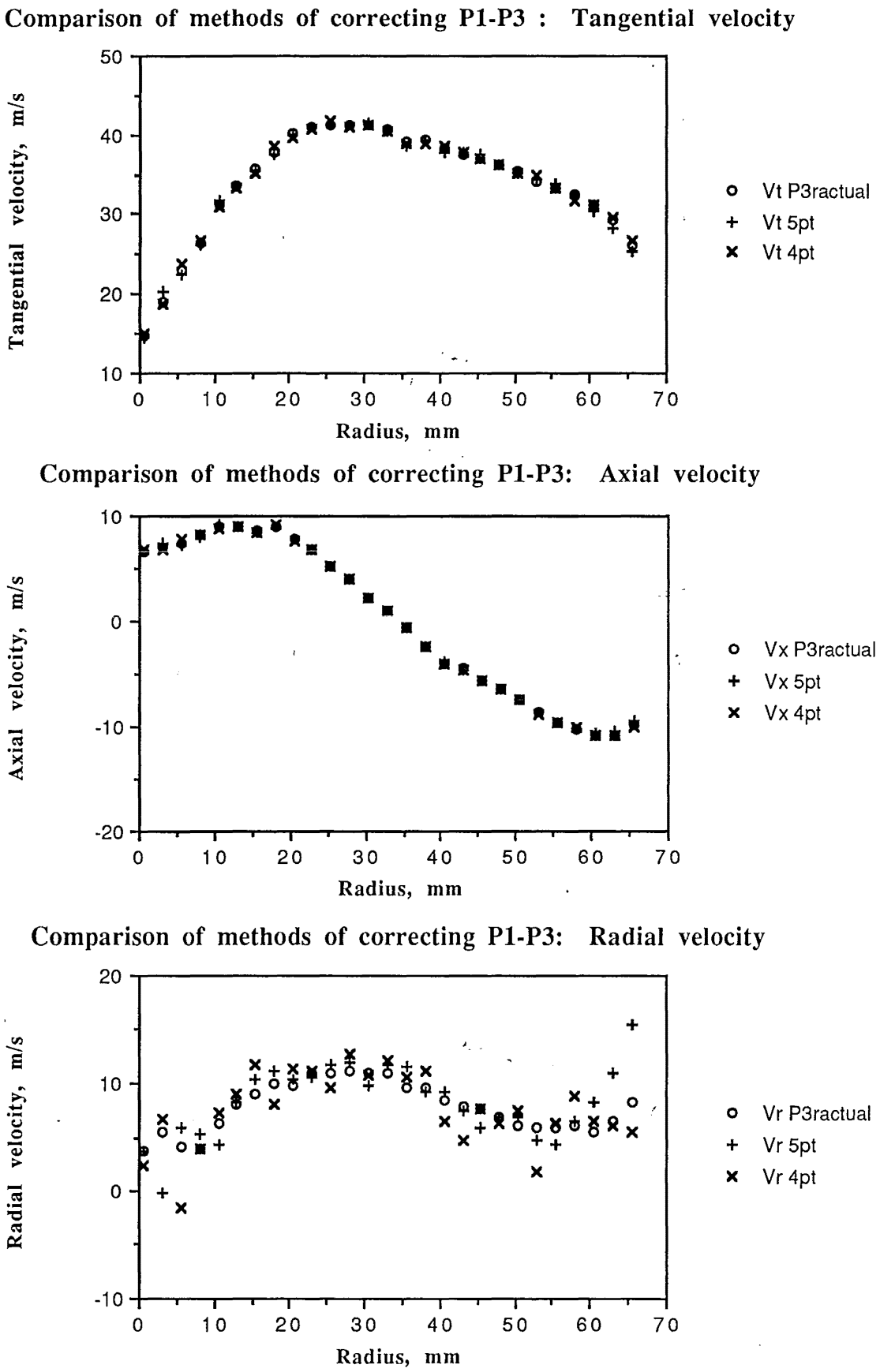

Figure 10.F.10: Velocity profiles calculated with different methods of correcting P1-P3

Errors in the pressure readings could be magnified during the curve fitting, by the data point altering the shape of the curve. This was avoided by fitting the 4 or 5 point curve to points on either side of the point to be corrected. As an example, the data obtained for two pressure readings ((P1-P2) and (P1-P3)) in the Port 8 (opposite inlet side) traverse in the 750mmØ cyclone were found to be recorded incorrectly at two locations. These mistakes are easily identified and corrected when the pressure readings are plotted versus the radius as shown below:

In this case the mistakes were consistent with a transcription error (dropping a decimal place), and not allowing for a change in inclination of the manometer (out by a factor of two). Usually large errors were identified while the computer programme was running, as the difference between the data point and the fitted curve was displayed on the screen for all stages of the iteration, and large differences were checked.

The effect of this sort of error on the tangential velocity is significant, as shown in Figure 10.F.11. However, the error is not propagated into adjacent readings by the curve fitting, despite the iterative nature of the P1-P3 correction process. The error could also be corrected by smoothing the final velocity curves, but the smoothing of the pressure reading before calculating is preferred. Smoothing of the raw data before calculating the velocities could improve the results.

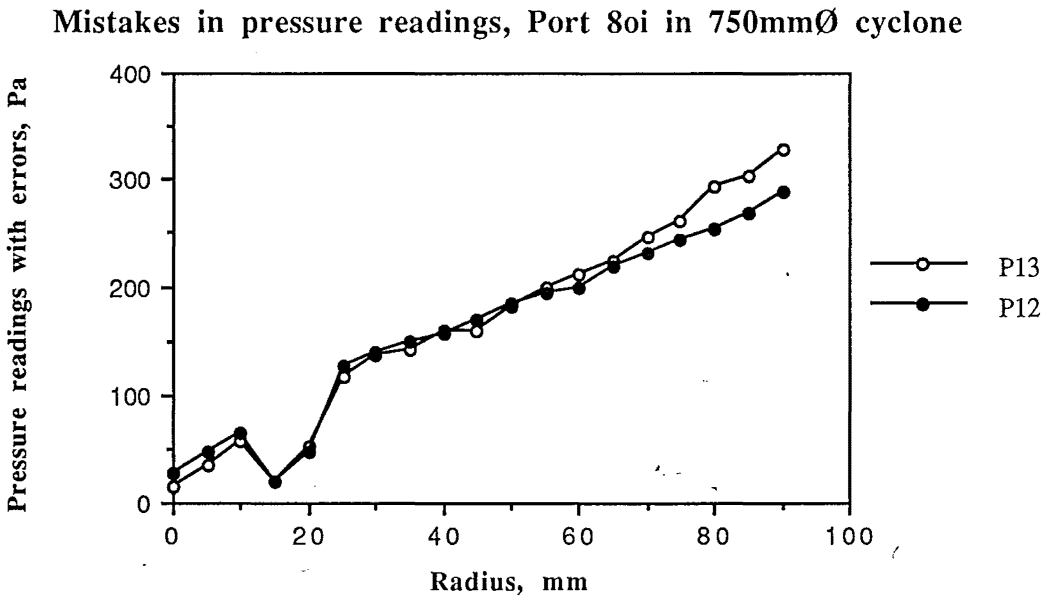

Figure 10.F.11: Error in the pressure readings due to a recording error

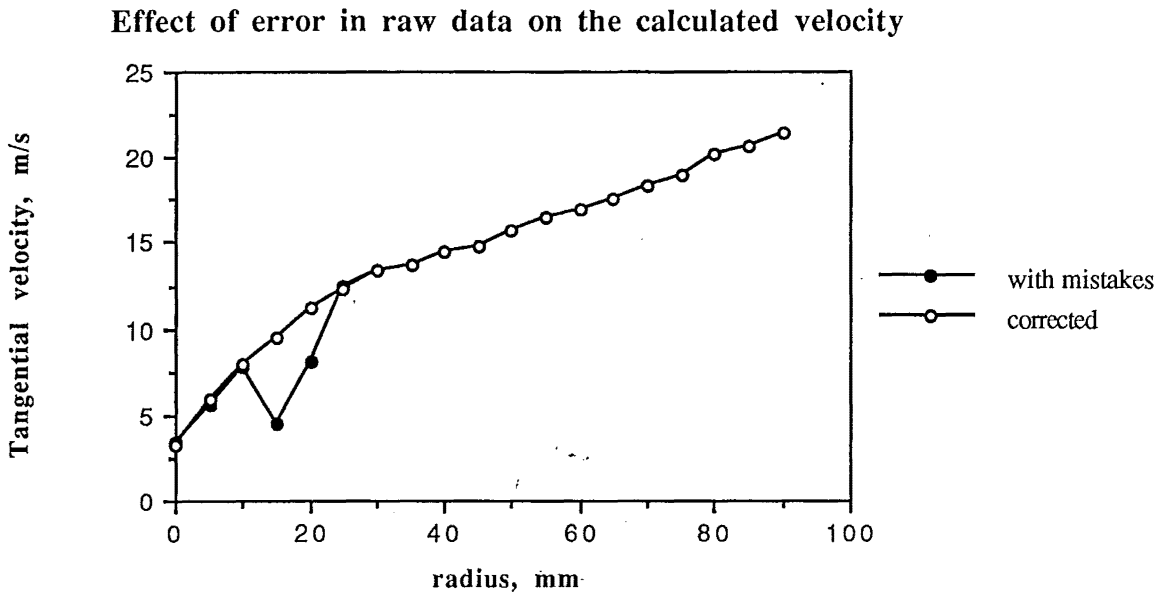

Figure 10.F.12: Effect of measurement error on the calculated velocity

10.F.5: Response of the Pitot cylinder to turbulence:

The calculated pitch angle and radial velocities were still subject to a substantial scatter, even after the correction of the pressure readings for the radial displacement of the tappings. It was thought that this could be due to a response bias to the turbulent fluctuation in the cyclone. The effect of the turbulence on the pitot cylinder was investigated by inserting the probe into a duct downstream of a grid. The mesh size of the grid was varied, and the intensity of the turbulence was varied by increasing the distance of the probe from the grid.

The turbulence produced by grids is reported by Roach (1987) to be isotropic at positions greater than 10 mesh lengths downstream of the grid, and Roach has presented plots of the decay of the turbulence intensity with the position downstream. To check the probe response, a uniform square grid was used with a mesh length of M = 2.5mm, and a round bar diameter of d = 0.6mm, with the probe positioned 25mm, 60mm and 120mm downstream of the grid. From figure 3 of Roach (1987) these correspond to turbulence levels of 5%, 2.8%, and 1.7%. To approach a turbulent intensity of 15%, while still maintaining 10 mesh lengths distance from the grid requires the bar diameter to be equal to the mesh length, which would lead to total blocking. 10% turbulence at 10 mesh lengths distance requires that the bar diameter must be 50% of the mesh length. The minimum eddy size is approximately 1mm, which means that the spacing between the bars (M-d) should be kept to about this dimension, hence a mesh length of 2mm would be needed, with bars of 1mm diameter.

The response of the pitot cylinder to the turbulence levels of 5%, 2.8% and 1.7% showed little change, certainly not of the level needed to explain the pitch angles observed in the cyclone. The probe was aligned to be at zero pitch angle to the mean flow. At a turbulent intensity of 5% the calculated pitch angle was -0.7°, within the uncertainty of the value of the actual pitch angle of the probe to the flow. To increase the turbulence, the probe was positioned 3mm from the

grid, and the pitch angle calculated again. However it was found that shifting the grid slightly (by a fraction of the mesh length) caused a shift in the pressure readings. (This was also a problem when the probe was 25mm, although not as severe). Both P1-P2, and P1-P3 were affected, and taking the extremes would result in pitch angles of +1.6° to -3.3°. This suggested that the angle of the air around the grid bars was affecting the reading, but even in this non-isotropic turbulence the effect on the pitch angle was not as large as was found in the cyclone. It would appear that the scatter in the calculated pitch angle is due to other factors apart from the turbulence.

Since the scatter is observed to decrease in larger cyclones, it may be related to the disturbance of the flow by the probe, which would be expected to decrease in the larger cyclone. The Pitot cylinder suggests radial velocities are directed outwards, which contradicts the mass balance requirements. The build up of a boundary layer on the probe may affect the readings.

10.F.6: The errors associated with the Pitot cylinder

Several factors could contribute to the error in the Pitot cylinder velocities. These include:

- The response time resulting in an averaging of the pressure.
- A bias in the response to fluctuations in the yaw or pitch directions.
- The probe not being aligned with a diameter of the cyclone
- The vortex axis being off the geometrical axis.
- Discrete errors from pressure measurement or calibration
- The change in the axial location of the P_1 tapping as the probe is rotated with the yaw angle.
- The response to the turbulence in the cyclone.

10.F.7: Raw data and calculated velocity components:

The Vax mainframe computer used for the data storage and computation 'crashed' in August 1991, losing all of the contents of the user space. Due to a misunderstanding, back-ups of the data and programmes had not been kept. A rough re-creation of the Pitot cylinder analysis programme is appended. The hard copies of the raw data and computed results are too numerous and bulky to be included in this report in their present form. The data will be re-entered into a suitable computer system and will be available on disk at some time in the future.

FORTRAN PROGRAMME LISTINGS

Data Entry from keyboard: DATASTOR.FOR

```
      DIMENSION A(150),B(150),C(150),D(150),E(150)
      CHARACTER PORTCODE*10
C
020   WRITE(*,030)
030   FORMAT(1X,'IF DATA IS TO BE ENTERED IN IN.WG TYPE 1',/,'IF
     &  TO BE ENTERED IN PASCALS TYPE 0')
      READ(*,035) LD
035   FORMAT(I1)
C
      WRITE(*,050)
050   FORMAT(1X,'ENTER NUMBER OF DATA POINTS ')
      READ(*,194) N
C
      WRITE(*,060)
060   FORMAT(1X,'Enter the Port code eg 10POI')
      READ(*,061) PORTCODE
061   FORMAT(A)
       WRITE(*,070)
070   FORMAT(1X,'Enter the vortex radius - the centre of the data')
      READ(*,071) RDC
071   FORMAT(F8.2)
C
      OPEN(UNIT=8,FILE='PTO'//PORTCODE,STATUS='NEW')
      WRITE(8,080) N,RDC
080   FORMAT(1X,I2,2X,F7.2)
C
      DO 250 I=1,N
C
090   CONTINUE
      WRITE(*,100)
100   FORMAT ('    ENTER DISTANCE, MM ')
      READ(*,195) A(I)
C
      WRITE(*,105)
105   FORMAT('  ENTER Yaw, P1-PR, P1-P2, P1-P3')
      READ(*,*) B(I),C(I),D(I),E(I)
C
C
194   FORMAT(I2)
195   FORMAT(F5.1)
200   FORMAT(F5.1)
210   FORMAT(F12.4)
220   FORMAT(F10.4)
230   FORMAT(F10.4)

240   WRITE(*,260) A(I),B(I),C(I),D(I),E(I)
      WRITE(*,241)
241   FORMAT(1X,'IS DATA CORRECT ? IF NOT TYPE 1 TO START AGAIN')
      READ(*,242) LER
242   FORMAT(I1)
      IF (LER.EQ.1) GO TO 090
            IF (LD.EQ.0) GO TO 248
                  C(I)=248.84*C(I)
                  D(I)=248.84*D(I)
                  E(I)=248.84*E(I)
248         WRITE(8,260) A(I),B(I),C(I),D(I),E(I)
250   CONTINUE
260   FORMAT(1X,F5.1,1X,F5.1,1X,F12.4,1X,F8.4,1X,F8.4)
      END
```

PITOT CYLINDER ANALYSIS:

```
C
C       Pitot cylinder analysis program
C
C       Re-entered in Jan 1992, after the original was lost in The Crash
C       from PTOCALC.FOR;41 dated 23 Oct 1989
C       There may be more recent versions around
C
C       PRESSURE/VELOCITY ANALYSIS
C       The programme takes the pressure measurements from the
C       Pitot cylinder probe and :
C               (a) Calculates the velocities with adjustments for radial
C               pressure gradients and radial spacing of probe holes
C               (b) Dumps the velocities to a file for plotting
C
        DIMENSION X(150), YW(150),P1R(150),P12(150),P13(150),
     &  P1RK(150),PTC1I(150),TC1(150),SC1(150),Z(150),P(150),
     &  Q(150),DSP(150),P13D(150),R(150),S(150),T(150),U(150),P13C(150)
     &  ,SL1(150),SL2(150),AD(150),DU(150),P3R(150),P13K(150),P3RC(150)
     &  ,DT(150),BC1(150),STCP(150),P3RK(150),DV(150),RX(150)
C
        CHARACTER FILNAM*32
C
        WRITE(*,005)
005     FORMAT(1X,'Enter the filename the pressure data is in
     &  PTO-')
        READ(*,006) FILNAM
006     FORMAT(A)
C
C       OPEN(UNIT=8,FILE='PTO'//FILNAM,STATUS='OLD')
        OPEN(UNIT=7,FILE='PVRSLTS.DAT',STATUS='NEW')
        OPEN(UNIT=10,FILE='P.DAT',STATUS='NEW')
C
        ICORR=1
        WRITE(*,010)
010     FORMAT(1X,'Enter the diameter of the cyclone the data
     &  is from - in mm')
        READ(*,011) CDIA
011     FORMAT(F7.1)
        FMS=CDIA/140.0
        WRITE(*,012)
012     FORMAT(1X,'Enter the Port number for the traverse data')
        READ(*,013) LP
013     FORMAT(I2)
C
        WRITE(*,020)
020     FORMAT(1X,'Enter 1 if old calibration is to be used'/,1X,
     &  'Or 2 for the post-Ken Bidlake calibration')
        READ(*,025) NOC
025     FORMAT(I1)
C
C       CALCULATE THE CYCLONE WALL RADIUS
C
        IF(LP.GT.7) GO TO 026
        HDE=(LP-2)*30*FMS
        GO TO 034
026      GO TO (027,028,029,030,031),LP-7
027     HDE=225*FMS
        GO TO 034
028      HDE=325*FMS
        GO TO 034
029     HDE=400*FMS
        GO TO 034
030     HDE=460*FMS
        GO TO 034
031     HDE=490*FMS
034     CONTINUE
C
        IF(LP.GT.9) GO TO 038
        RD=FMS*26.5+HDE*43.5/355
        GO TO 039
038     RD=70.0*MSF
039     CONTINUE
C
        WRITE(*,040)
040     FORMAT(1X,'Enter the desired degree of stiffness: if 1 degree type 4
     &  '/,39X,' if 2 degrees type 5')
        READ(*,041) IDOS
041     FORMAT(I1)
        WRITE(*,042)
042     FORMAT(1X,'Type 1 if the data is in INCHES w.g.')
        READ(*,043)LD
043     FORMAT(I1)
C
        READ(8,*) N,CNTR
        WRITE(7,044)
044     FORMAT(1X,'DATA PROCESSED USING PTOCALCRENT.FOR and
     &  CORRECTING
     &  FOR THE STATIC PRESSURE IN P1-P3 BEFORE ADJUSTING P3R')
        WRITE(7,045) N,RD
045     FORMAT(1X,'NUMBER OF DATA POINTS = ',I2,4X,'WALL RADIUS= ',F7.1)
C
        IF(NOC.NE.1) GO TO 047
        WRITE(7,046) IDOS
046     FORMAT(1X,'The July 1986 calibration for the Pitot cylinder
     &  was used '/,1X,' and the correction
     &  for the radial pressure gradient '/,1x,' used a curve
     &  fitted through',I2,' Points by the least squares method')
        GO TO 049
047     CONTINUE
        WRITE(7,048) IDOS
048     FORMAT(1X,'The September 1989 calibration for the Pitot cylinder
     &  was used '/,1X,' and the correction
     &  for the radial pressure gradient '/,1X,' used a curve
     &  fitted through',I2,' Points by the least squares method')
049     CONTINUE
C
C
        DO 050 I=1,N
050     READ(8,*) X(I),YW(I),P1R(I),P12(I),P13(I)
C
        WRITE(*,051)
051     FORMAT(1X,'ENTER ESTIMATE OF CENTRE OF VORTEX')
        READ(*,052) CNTR
052     FORMAT(F5.1)
C
        DO 053 J=1,N
        IF(X(J).GT.CNTR) GO TO 054
053     CONTINUE
        GO TO 058
054     WRITE(*,055) CNTR
055     FORMAT(1X,'IF DATA AFTER X(I) = ',F5.1,' HAS CORRECT SENSE
     &  THEN TYPE 1'/)
056     READ(*,057) ISNS
057     FORMAT(I1)
058     CONTINUE
C
        IF(LD.NE.1) GO TO 061
C
C       DATA INPUT FINISHED
C       CONVERT PRESSURE READINGS TO PASCALS
        DO 060 LI=1,N
                P1R(LI)=248.84*P1R(LI)
                P12(LI)=248.84*P12(LI)
                P13(LI)=248.84*P13(LI)
060     CONTINUE
C
061     DO 062 I=1,N
                DSP(I)=P1R(I)
                P13D(I)=P13(I)
062     CONTINUE
C
        IW=0
C       <<<<<<<<<<<<<<<<<<<<
C       LOOPS RETURN TO HERE
C       ^^^^^^^^^^^^^^^^^^^^
063     IW=IW+1
C
065     DO 100 I=1,N
070             BC1(I)=P13D(I)/P12(I)
                IF(NOC.EQ.2) GO TO 079
C
C               PRE KEN BIDLAKE CALIBRATION JULY 1986
C
                PTCH(I)=25.686-27.828*BC1(I)
                IF(PTCH(I).LT.-22.5) GO TO 075
                IF(PTCH(I).LT.-2.5) GO TO 076
                IF(PTCH(I).LT.27.5) GO TO 077
                IF(PTCH(I).LT.45.0) GO TO 078
                SC1(I)=0.85
075             SC1(I)=1.00
                GO TO 095
076             SC1(I)=0.893+((4.792E-04)*(PTCH(I)+7.5)**2)
                GO TO 095
077             SC1(I)=0.893+((6.23E-05)*(PTCH(I)-12.5)**2)
                GO TO 095
078             SC1(I)=1.0144-((3.9E-03)*PTCH(I))
                GO TO 095
C
C               POST KEN BIDLAKE CALIBRATION SET 1989
C
079             CONTINUE
                IF(BC1(I).GT.1.76) GO TO 089
                IF(BC1(I).GT.1.487) GO TO 080
                IF(BC1(I).GE.-0.85) GO TO 081
                IF(BC1(I).LT.-0.85) GO TO 089
080             PTCH(I)=(-0.4296844+0.3963306*BC1(I)+0.04408188*
     &          BC1(I)**2-0.13816035*BC1(I)**3)
                GO TO 083
081             PTCH(I)=(0.25905657-0.3111546*BC1(I)-
     &          0.0179743*BC1(I)**2+0.01464028*BC1(I)**3)
C
083             CONTINUE
C
                WRITE(*,*) 100*PTCH(I)
                        IF(PTCH(I).GT.0.5) GO TO 089
                        IF(PTCH(I).GE.0.25) GO TO 084
                        IF(PTCH(I).GE.0.125) GO TO 085
                        IF(PTCH(I).GE.0.0) GO TO 086
                        IF(PTCH(I).GE.-0.15) GO TO 087
                        IF(PTCH(I).GE.-0.325) GO TO 088
                        IF(PTCH(I).LT.-0.325) GO TO 089
C
084              SC1(I)=(0.8488133+0.3269211*PTCH(I)-0.2451663
     &          *PTCH(I)**2-0.75059152*PTCH(I)**3)
                GO TO 090
085             SC1(I)=(0.98292238-0.78390253*PTCH(I)+1.22499
     &           *PTCH(I)**2+2.68205261*PTCH(I)**3)
                GO TO 090
086              SC1(I)=(0.92575109+0.14926654*PTCH(I)-1.88790405
     &          *PTCH(I)**2-1.57367*PTCH(I)**3)
                GO TO 090
```

```
087               SC1(I)=(0.92563552+0.54013385*PTCH(I)+4.2118397
  &               *PTCH(I)**2-2.8266758*PTCH(I)**3)
                  GO TO 090
088               SC1(I)=(0.89520294+0.51090759*PTCH(I)+9.1654*
  &               PTCH(I)**2+21.24240494*PTCH(I)**3)
                   GO TO 090
C
089               WRITE(*,091) X(I)
090               CONTINUE
091               FORMAT(1X,'Outside the PITCH angle calibration for X(I) = ',F)
                  PTCH(I)=PTCH(I)*100
C
095               CONTINUE
C
                  STCP(I)=P1R(I)-(SC1(I)*P12(I))
                  DV(I)=STCP(I)
100       CONTINUE
          NOF=1
C
C         ADJUST READINGS FOR STATIC PRESSURE CHANGE
C
          CALL PARABFIT(N,IDOS,X,DV,NOF,DT,P3RC,ISNS,CNTR)
C
          DO 109 IQ=1,N
                  P1RK(IQ)=P1R(IQ)-STCP(IQ)
                  IF((X(I).GT.CNTR).AND.(ISNS.NE.1)) GO TO 105
                  P13K(IQ)=P13(IQ)+DT(IQ)
                  GO TO 106
105               P13K(IQ)=P13(IQ)-DT(IQ)
106               P3RK(IQ)=P1RK(IQ)-P13K(IQ)
                  DV(IQ)=P3RK(IQ)
109       CONTINUE
C
          IF(IW.GT.15) GO TO 820
C
C         NOW ADJUST THE P3R READING BY 7.5MM
C
          NOF=2
C         ------------------------------------------------
          CALL PARABFIT(N,IDOS,X,DV,NOF,DT,P3RC,ISNS,CNTR)
C         ------------------------------------------------
          TERR=0
          DO 150 I=1,N
          P13C(I)=P1RK(I)-P3RC(I)
150       TERR=TERR+(ABS(P13D(I))-ABS(P13C(I)))
          IF((TERR/N).LE.10.0) GO TO 160
          DO 155 I=1,N
C         WRITE(12,*) P13C(I)
155       P13D(I)=P13C(I)
                  GO TO 063
160       CONTINUE
C
C         P13 IS NOW CORRECTED FOR STATIC PRESSURE AND POSITION
C         NOW CALCULATE PRESSURE AND VELOCITY VALUES
C
          DO 400 I=1,N
                   BC1(I)=P13C(I)/P12(I)
                  IF(NOC.EQ.1) GO TO 190
C
C
C         NEW CALIBRATION
C         POST KEN BIDLAKE CALIBRATION SEPT 1989
C         ======================================
          IF(BC1(I).GT.1.76) GO TO 188
          IF(BC1(I).GT.1.487) GO TO 165
          IF(BC1(I).GE.-0.85) GO TO 166
          IF(BC1(I).LT.-0.85) GO TO 188
165         PTCH(I)=(-0.4296844+0.3963306*BC1(I)+
     &  0.04408188*BC1(I)**2-0.13816035*BC1(I)**3)
          GO TO 167
166         PTCH(I)=(0.25905657-0.3111546*BC1(I)-
     &    0.0179743*BC1(I)**2+0.01464028*BC1(I)**3)
C
167       CONTINUE
C
          IF(PTCH(I).GT.0.5) GO TO 188
          IF(PTCH(I).GE.0.25) GO TO 170
          IF(PTCH(I).GE.0.125) GO TO 171
          IF(PTCH(I).GE.0.0) GO TO 172
          IF(PTCH(I).GE.-0.15) GO TO 173
          IF(PTCH(I).GE.-0.325) GO TO 174
          IF(PTCH(I).LT.-0.325) GO TO 188
C
170         SC1(I)=(0.8488133+0.3269211*PTCH(I)-
     &      0.2451663*PTCH(I)**2-0.75059152*PTCH(I)**3)
          GO TO 176
171         SC1(I)=(0.98292238-0.78390253*PTCH(I)+
     &      1.22499*PTCH(I)**2+2.68205261*PTCH(I)**3)
          GO TO 176
172         SC1(I)=(0.92575109+0.14926654*PTCH(I)-
     &      1.88790405*PTCH(I)**2-1.57367*PTCH(I)**3)
          GO TO 176
173         SC1(I)=(0.92563552+0.54013385*PTCH(I)+
     &      4.2118397*PTCH(I)**2-2.8266758*PTCH(I)**3)
          GO TO 176
174         SC1(I)=(0.89520294+0.51090759*PTCH(I)+
     &      9.1654*PTCH(I)**2+21.24240494*PTCH(I)**3)
176       CONTINUE
C
          PTCH(I)=PTCH(I)*100
          GO TO 200
C
188         WRITE(*,189) X(I),100*PTCH(I)
189         FORMAT(1X,'WARNING!! Outside SC1 calibration range at
     &   X= ',F,2X,'as PTCH = ',F,/,1X,'Calculation proceeding
     & with SC1 = 0.92')
C
          SC1(I)=0.92
          GO TO 200
C
C   OLD CALIBRATION
C
190   CONTINUE
C   PRE KEN BIDLAKE CALIBRATION JULY 1986
C
      PTCH(I)=25.686-27.828*BC1(I)
     IF(PTCH(I).LT.-22.5) GO TO 195
     IF(PTCH(I).LT.-2.5) GO TO 196
     IF(PTCH(I).LT.27.5) GO TO 197
     IF(PTCH(I).LT.45.0) GO TO 198
     SC1(I)=0.85
      GO TO 200
195   SC1(I)=1.00
     GO TO 200
196   SC1(I)=0.893+((4.792E-04)*(PTCH(I)+7.5)**2)
     GO TO 200
197   SC1(I)=0.893+((6.23E-05)*(PTCH(I)-12.5)**2)
     GO TO 200
198   SC1(I)=1.0144-((3.9E-03)*PTCH(I))
     GO TO 200
C
200   STCP(I)=P1R(I)-(SC1(I)*P12(I))
     IF(NOC.EQ.1) GO TO 220
C
C   NEW CALIBRATION
C   ---------------
C   NEW TOTAL PRESSURE COEFFICIENT CALIBRATION
C   ------------------------------------------
C
     PTCH(I)=(PTCH(I)/100)
     IF(PTCH(I).GT.0.5) GO TO 205
     IF(PTCH(I).GE.0.1) GO TO 201
     IF(PTCH(I).GE.-0.325) GO TO 202
     IF(PTCH(I).LT.-0.325) GO TO 205
C
201         TC1(I)=(0.05541862-0.31624466*PTCH(I)+0.04903051
     &*PTCH(I)**2+8.11142063*PTCH(I)**3)
      GO TO 219
202         TC1(I)=(0.06155076-0.49486541*PTCH(I)+1.9563*
     &PTCH(I)**2-6.66435*PTCH(I)**3)
       GO TO 219
C
205   WRITE(*,206) X(I),PTCH(I)
206   FORMAT(1X,'OUTSIDE TC1 CALIBRATION RANGE AT X(I) =
     & ',F,' WITH PITCH= ',F)
C
219   CONTINUE
C
     PTCH(I)=100*PTCH(I)
      GO TO 230
C
C   ============================
C   OLD CALIBRATION
220   CONTINUE
     IF(PTCH(I).LT.32.5) GO TO 221
      TC1(I)=0.0412*PTCH(I)-1.115
     GO TO 230
221     TC1(I)=0.003+((3.656E-04)*(PTCH(I)-7.5)**2)
C
230   CONTINUE
C
C   ++++++++++++++++++++++++++++++++++++++++
C    CALCULATION OF VELOCITY COMPONENTS
C   ++++++++++++++++++++++++++++++++++++++++
C
C
330   Z(I)=P1R(I)+TC1(I)*P12(I)
     T(I)=P1R(I)-SC1(I)*P12(I)
     AD(I)=P12(I)/248.84
     P(I)=20.6*SQRT((TC1(I)+SC1(I))*AD(I))
380   S(I)=P(I)*COS(YW(I)/57.3)*COS(PTCH(I)/57.3)
     R(I)=P(I)*SIN(PTCH(I)/57.3)
390   Q(I)=P(I)*SIN(YW(I)/57.3)*COS(PTCH(I)/57.3)
400   CONTINUE
C
C     WRITE(11,405)
C405   FORMAT(1X,'X = ',5X,' BC1 = ',5X,' PTCH = ',5X,
C     &'SC1 = ',5X,' TC1= ')
C     DO 410 KJ = 1,N
C     WRITE(11,408) X(KJ),BC1(KJ),PTCH(KJ),SC1(KJ),TC1(KJ)
C408   FORMAT(1X,F,F,F,F,F)
C410   CONTINUE
C
C
     DO 495 I=1,N
420   IF(NOC.NE.1) GO TO 490
425   IF(BC1(I).LT.-0.2.OR.BC1(I).GT.1.75)  WRITE(7,500) X(I),PTCH(I)
```

```
      GO TO 495
  490 IF(BC1(I).LT.-0.65.OR.BC1(I).GT.1.84) WRITE(7,500) X(I),PTCH(I)
  495 CONTINUE
  500 FORMAT(1X,'CALCULATED PITCH ANGLE OUT OF RANGE OF BC1
     & CALIBRATION AT X = ',F9.3,2X,'PTCH= ',F)
C
C     IF(X(I).GT.CNTR) GO TO 405
C     R(I)=P(I)*SIN(PTCH(I)/57.3)
C     GO TO 408
C 405   R(I)=-1*P(I)*SIN(PTCH(I)/57.3)
C
  510 WRITE(7,525)
  515 WRITE(7,530)
      DO 520 I=1,N
  520 WRITE(7,535) X(I),YW(I),PTCH(I),P1R(I),P12(I),P13(I),P13C(I)
  525 FORMAT(/,1X,'DISTANCE ',3X,'YAW ',10X,'PITCH ',8X,
     &'RELATIVE PRESSURE (PA)')
  530 FORMAT(3X,'(MM)',7X,'(DEG)',7X,'(DEG)',5X,'CENTRE',5X,
     &'SIDE',6X,'TIP',9X,'TIP (CORR)')
  535   FORMAT(3X,F5.1,4X,F7.2,4X,F8.2,3X,F9.2,2X,F8.2,2X,F8.2,2X,F)
C
      WRITE(*,536)
  536 FORMAT(1X,'If traverse is from inlet side type +1',/,
     &' If traverse is from opposite inlet side type -1')
      READ(*,537) ISDE
  537 FORMAT(I2)
C
      DO 538 I=1,N
      RX(I)=ISDE*(RD-X(I))
  538 CONTINUE
C
C
CC    WRITE(7,540)
C540  FORMAT(/,/,1X,'VELOCITIES WITH RESPECT TO PROBE ARE:',/)
C     WRITE(7,545)
C545  FORMAT(1X,'X(I)',4X,'RX(I)',8X,'TOTAL',5X,'RADIAL',
C     &5X,'AXIAL',5X,'TANGENTIAL')
C     DO 550 IH=1,N
C550    WRITE(7,555) X(IH),P(IH),R(IH),Q(IH),S(IH)
C555      FORMAT(1X,F5.1,2X,F8.3,3X,F8.3,2X,F9.3,3X,F8.3)
C
      DO 590 I=1,N
       IF(ISNS.EQ.1) GO TO 560
        ISGN=1
        GO TO 565
  560   ISGN=-1
  565   CONTINUE
       IF(X(I).GT.CNTR) GO TO 580
       GO TO 585
  580   R(I)=ISGN*R(I)
       S(I)=ISGN*S(I)
  585   CONTINUE
  590 CONTINUE
C
       WRITE(7,660)
       WRITE(7,670)
      DO 655 I=1,N
  655   WRITE(7,680) X(I),RX(I),Z(I),T(I),P(I),R(I),Q(I),S(I)
  660     FORMAT(/,18X,'PRESSURE (PA)',24X,'VELOCITY (M/S)')
  670     FORMAT(3X,'X(I)',3X,'RX(I)',4X,'TOTAL',6X,'STATIC',5X,
     &  'TOTAL',7X,'RADIAL',5X,'AXIAL',5X,'TANGENTIAL')
  680       FORMAT(2X,F5.1,2X,F6.1,3X,F8.2,3X,F8.2,2X,F8.2,
     &    3X,F8.2,2X,F8.2,3X,F8.2)
C
      OPEN(UNIT=13,FILE='PTOGRFING.DAT',STATUS='NEW')
      OPEN(UNIT=12,FILE='VELCPT.DAT',STATUS='NEW')
        WRITE(12,688) N
        DO 685 I=1,N
          WRITE(12,689) X(I),R(I),Q(I),S(I)
  685       WRITE(13,690) X(I),RX(I),Z(I),T(I),P(I),R(I),
     &  Q(I),S(I)
  688       FORMAT(2X,I2)
  689         FORMAT(1X,F8.3,3X,F8.3,3X,F8.3,3X,F8.3)
  690         FORMAT(2X,F5.1;2X,F6.1,3X,F8.2,3X,F8.2,2X
     &    ,F8.2,2X,F8.2,2X,F8.2,3X,F8.2,3X,F8.2)
C
C
C
      WRITE(*,750)
  750 FORMAT(1X,'RESULTS ARE PRESENTED IN THE FILE PVRSLTS.DAT')
      WRITE(*,800) CNTR
  800 FORMAT(1X,'CENTRE OF VORTEX IS X= 'F5.1)
  810 CONTINUE
C
      GO TO 830
  820   WRITE(*,821)
  821   FORMAT(1X,'Static pressure is not converging')
  830 CONTINUE
  990 CONTINUE
      END
C     ------------------------------------------------------
C     ******************************************************
C     ------------------------------------------------------
C
C
C     ------------------------------------------------------

C     ******************************************************
C     ------------------------------------------------------
C
      SUBROUTINE PARABFIT(N,IDOS,X,DV,NOF,DT,P3RC,ISNS,CNTR)
C
      DIMENSION X(150),P3RC(150),T(150),DT(150),DV(150)
      DIMENSION DX(5),Y(5),EPS(150),B(150,5)
      REAL*8 B
C
      DO 380 I=1,N
       IF(NOF.EQ.1) GO TO 050
       IF(I.LE.3) GO TO 125
       IF(I.LE.(N-2)) GO TO 126
       IF(I.LE.N) GO TO 127
      GO TO 400
  050   IF(I.LE.2) GO TO 125
      IF(I.LE.(N-3)) GO TO 128
  120   IF(I.LE=N) GO TO 127
      GO TO 400
  125   ID=1
      GO TO 135
  126   ID=I-2
      GO TO 135
  127   ID=N-3
      GO TO 135
  128   ID=I-1
  135   CONTINUE
      IDP=ID
      DO 150 IJ=1,IDOS
        DX(IJ)=X(IDP)/100
        Y(IJ)=DV(IDP)
        IDP=IDP+1
  150   CONTINUE
C
C     Note that the x value has been scaled by 100
C     in order to keep the coefficients of comparable size
C     The effect on the goodness of fit is only slight.
C
C     FIT THE LEAST SQUARE PARABOLA BY SOLVING MATRIX
C
  190   CONTINUE
C     ^^^^^^^^^^^^^^^^^^^^^^
      CALL LSTSQR(IDOS,I,B,DX,Y)
C     ^^^^^^^^^^^^^^^^^^^^^^
C
      EPS(I)=DV(I)-(B(I,1)+B(I,2)*(X(I)/100)
     & +B(I,3)*(X(I)/100)**2)
      IF(NOF.EQ.1) GO TO 200
      IF(NOF.EQ.2) GO TO 220
  200   DT(I)=B(I,2)*0.075+B(I,3)*(((X(I)+7.5)/100)**2
     &  -((X(I)/100)**2))
C
      WRITE(*,202) X(I),EPS(I)
  202   FORMAT(1X,'Error in Pstatic at X(I)= ',F5.1,' equals ',F8.3)
      GO TO 250
C
  220   IF((X(I).GT.CNTR).AND.(ISNS.NE.1)) GO TO 225
        P3RC(I)=B(I,1)+B(I,2)*((X(I)-7.5)/100)+
     &  B(I,3)*((X(I)-7.5)/100)**2
       GO TO 229
  225     P3RC(I)=B(I,1)+B(I,2)*((X(I)+7.5)/100)+
     &  B(I,3)*((X(I)+7.5)/100)**2
  229   CONTINUE
C
C       WRITE(12,230) B(I,1),B(I,2),B(I,3),DV(I)
  230     FORMAT(/,1X,'P3R= ',F14.5,' + ',F11.5,'* X(I)/100 + ',F11.6,
     & ' * (X(I)/100)**2',2X,' P3R =',F14.5)
      WRITE(*,232) X(I),EPS(I)
  232   FORMAT(1X,' P3R ERROR at X(I) = 'F5.1,' equals ',F)
C
  250   CONTINUE
C
  380   CONTINUE
C
  400   CONTINUE
      RETURN
      END
C
C
C     ^^^^^^^^^^^^^^^^^^^^^^^^^^^^^^^^^^^^^^^^^^^^^^^^^^^^
C
C
C
C
      SUBROUTINE LSTSQR(IDOS,I,B,DX,Y)
C
      DIMENSION UL(5,5),DX(5),RHS(3),SUM(5),EM(3,3)
      DIMENSION ALF(5),Y(5),B(150,5),RM(3)
C
      REAL*8 UL,RHS,SUM,EM,ALF,B,RM
C
      RHS(1)=0
      RHS(2)=0
      RHS(3)=0
C
```

```
      DO 080 M2=1,IDOS
        RHS(1)=RHS(1)+Y(M2)
        RHS(2)=RHS(2)+(DX(M2)*Y(M2))
        RHS(3)=RHS(3)+((DX(M2)**2)*Y(M2))
080   CONTINUE
      SUM(1)=IDOS
      SUM(2)=0
      SUM(3)=0
      SUM(4)=0
      SUM(5)=0
C
      DO 120 IZ=2,5
        DO 110 M3=1,IDOS
          SUM(IZ)=SUM(IZ)+(DX(M3))**(IZ-1)
110     CONTINUE
120   CONTINUE
C
      EM(1,1)=SUM(5)
      EM(1,2)=SUM(4)
      EM(2,1)=SUM(4)
      EM(1,3)=SUM(3)
      EM(3,1)=SUM(3)
      EM(2,2)=SUM(3)
      EM(2,3)=SUM(2)
      EM(3,2)=SUM(2)
      EM(3,3)=SUM(1)
C
C     SOLVE BY GAUSSIAN ELIMINATION
C
      RM(1)=EM(2,1)/EM(1,1)
      EM(2,1)=0
      EM(2,2)=EM(2,2)-RM(1)*EM(1,2)
      EM(2,3)=EM(2,3)-RM(1)*EM(1,3)
      RHS(2)=RHS(2)-RM(1)*RHS(3)
      RM(2)=EM(3,1)/EM(1,1)
      EM(3,1)=0
      EM(3,2)=EM(3,2)-RM(2)*EM(1,2)
      EM(3,3)=EM(3,3)-RM(2)*EM(1,3)
      RHS(1)=RHS(1)-RM(2)*RHS(3)
      RM(3)=EM(3,2)/EM(2,2)
      EM(3,1)=0
      EM(3,2)=EM(3,2)-RM(3)*EM(2,2)
      EM(3,3)=EM(3,3)-RM(3)*EM(2,3)
      RHS(1)=RHS(1)-RM(3)*RHS(2)
C
      B(I,1)=RHS(1)/EM(3,3)
      B(I,2)=(RHS(2)-(EM(2,3)*B(I,1)))/EM(2,2)
      B(I,3)=(RHS(3)-(EM(1,2)*B(I,2)+EM(1,3)*B(I,1)))/EM(1,1)
C
C     ------------------------------------------------------
C       This section outputs the data to allow the fitted curve
C     to be compared with the data.  The agreement is good, as
C     long as the curve isnt too far off a parabola
C
C       WRITE(*,970) NOF,IDOS
C       WRITE(12,970) NOF,IDOS
C 970     FORMAT(1X,'ON #',I2,' PASS THROUGH WITH IDOS= ',I2)
C     DO 960 PH=1,IDOS
C       WRITE(*,980) DX(PH),Y(PH)
C       WRITE(12,980) DX(PH),Y(PH)
C 960  CONTINUE
C 980      FORMAT(1X,'AT X = ',F,3X,' Y = ',F)
C        WRITE(*,990) B(I,1), B(I,2),B(I,3)
C        WRITE(12,990) B(I,1), B(I,2),B(I,3)
C
C 990   FORMAT(/,1X,'In the LSTSQR subroutine the coeff are:',/,
C     &  F,2X,F,2X,F,/,/)
C     ------------------------------------------------------
C
      RETURN
      END
```

10.G. HOTFILM ANEMOMETER:

Several velocity profiles were measured in the 140mmØ cyclone with a Hot film anemometer using 45° Hot film probes (Tsi serial numbers 1213-60, 1213-20 and 1263A-10, where the number after the dash represents the nominal size in microns). The Anemometer was one of two (Instrument numbers 1554 and 1574) constructed in 1983 by Gordon Grey, a Chemical and Process Engineering Department technician who has since left the Department. For the majority of the measurements the #1554 instrument was used. The anemometer contains a linearising circuit that can be adjusted to produce an output voltage that is directly proportional to the velocity, by utilising King's equation:.

$$e^2 = A + B.U^n \qquad \text{--- (10.G.1)}$$

where e is the probe voltage, and U the fluid velocity. A, B and n are constants

The lineariser equation is :

$$OUT = F\left[\frac{(IN/C)^2 - E}{D}\right]^N \qquad \text{--- (10.G.2)}$$

where IN is the input voltage (from the 45° probe); OUT is the linearised output voltage; and F,C,E,D and N are constants that can be adjusted by potentiometers.

The linearisation and calibration of the hotfilm anemometer was hindered by the lack of information about the potentiometers that were used in the construction. After much trial and error it was found that the potentiometer for the exponent 'N' had an inverse relationship. The value on the dial of the potentiometer was related to the value actually used by N = 10/dial. Thus to obtain an exponent of N=1 it is necessary to dial up a value of 10, whereas for N = 2 a value of 5 is required on the dial. Two similar versions of the anemometer were built originally. Instrument number 1554 has had a 'chocolate box' wired onto the rear of the anemometer to allow the intermediate voltages in the linearising circuit to be sampled. The effect of the potentiometers on the voltage were examined individully by measuring the voltage before and after the potentiometer, with the following results:

"E" when E = 0.0 on the dial it actually is -0.18. To obtain a value of zero the dial must be turned to a value of +0.28.

"D" is fairly accurate, giving a value of 7.36 when the dial is at 7.46. Likewise "C"

"F" gives values of 1.00, 2.03, 3.00, 4.1, 5.0 when the respective integers are dialled up, hence this potentiometer is also sufficiently accurate

"N" is given by 10 divided by the value on the dial

Without realising the effect that potentiometers "E" and "N" were having on the circuit it was impossible to linearise the anemometer.

The procedure for linearising the anemometer output is as follows:
1. It is important that the current is adjusted to balance the resistances into the LH0061 chip, otherwise the probe may be burnt out. A potentiometer is used to adjust the resistance, and the

number of turns, x, required to do this can be calculated by examining the circuit diagram below:

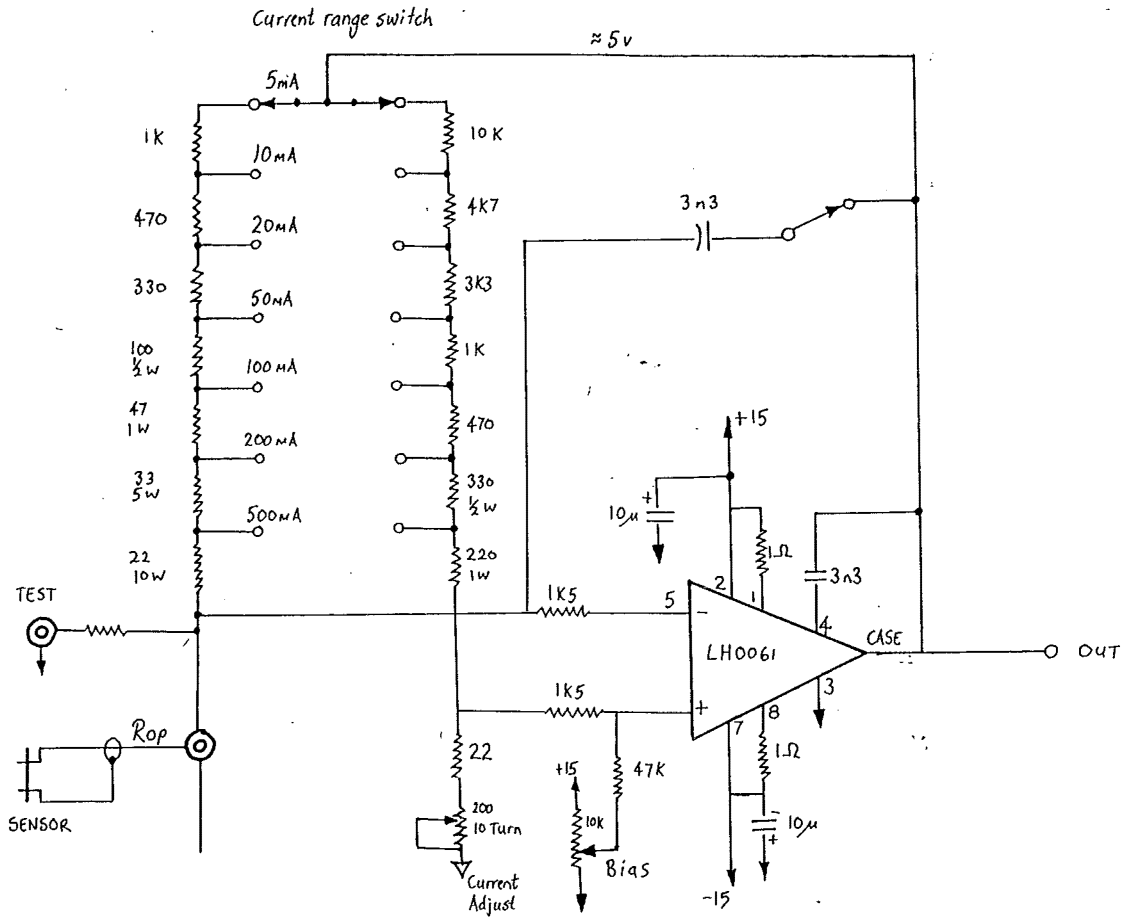

Figure 10.G.1: Hot film anemometer lineariser circuit diagram for #1574.

For example, at a current range setting of 500mA, the probe resistance R_{op} requires a number of turns of the potentiometer (x), that is given by:

$$\frac{R_{op}}{22.28} = \frac{x/10 \times 200}{110.6} \qquad \text{--- (10.G.3)}$$

$$\text{so } x = R_{op} \times 0.2482$$

Similarly the other current settings can be calculated, for both of the anemometers (Instrument numbers 1574 and 1554), which have slightly different resistances. :

Current range:	500	200	100	50	20	10	5
x/R_{op} #1574	0.248	0.291	0.375	0.437	0.476	0.487	0.493
x/R_{op} #1554	0.248	0.290	0.387	0.445	0.478	0.491	0.498

The linearising procedure is that suggested by Sakao (1980), which involves making measurements with the probe at two air velocities, $U_1 > U_2$. These are selected to cover the expected operating range as much as possible. At the setting U_1 the output is measured with the potentiometers set to give "F" = 1, "E"=0, "C"=10, "D"=1,"N" = 1.0. The output voltage

V_1 is then proportional to the square of the lineariser input, and hence is proportional to the square of the probe output.

The flowrate is then changed to U_2, and the new output voltage V_2 noted. The "E" potentiometer is then adjusted until the output voltage at this new velocity is brought to a value V_c, calculated by:

$$V_c = V_2 - E_A = \frac{V_1 - V_2}{\left(\frac{U_1}{U_2}\right)^{0.5} - 1} \qquad \text{--- (10.G.4)}$$

The setting for "N" is then changed to N=2.0, with "E" = the value determined above, and suitable scaling values are chosen for F, C, and D. The output should be linearly related to the velocity.

The proof of the validity of the linearising procedure is based on King's Law, which gives the relationship between the voltage, 'e' and the velocity 'U' as:

$e^2 = A + B.U^n$ with the exponent 'n' approximately equal to 0.5

For velocities U_1 and U_2, for which $\alpha = \left(\frac{U_1}{U_2}\right)^{0.5}$ the square of the output voltages will be:

$$e_1^2 = A + B.U_1^{0.5} = A + \alpha.BU_2^{0.5}$$
$$e_2^2 = A + B.U_2^{0.5}$$

hence: $e_1^2 - e_2^2 = (\alpha - 1).BU_2^{0.5}$

But since $e_2^2 - A = BU_2^{0.5}$

therefore $e_2^2 - A = \frac{e_1^2 - e_2^2}{\alpha - 1}$

By setting A' such that $e_2^2 - A' = \frac{e_1^2 - e_2^2}{\alpha - 1}$ --- (10.G.4)

the value A' obtained is exactly equal to the value A in King's equation, and so $e_2^2 - A' = BU_2^{0.5}$

and $U = \left(\frac{e_2^2 - A'}{B}\right)^2$ --- (10.G.5)

A' is determined from equation 1 with "N" set to a value of 1.0. A' is the value of the potentiometer "E" required to reduce e_2^2 to the value determined by $\frac{e_1^2 - e_2^2}{\left(\frac{U_1}{U_2}\right)^{0.5} - 1}$

The velocity will be linearly related to the output voltage given by the right hand side of equation 2, for which "N" is set to 2.0.

Once linearised the anemometer could be calibrated against the known flowrates obtained in a hot film probe calibrator that was borrowed from the Mechanical Engineering Department. The calibrator consisted of a 100mmØ perspex cylinder with flow straighteners at the bottom and a 25mmØ orifice at the top across which the probe was placed. The air supply was from a compressed air line, and the velocity in the orifice at the top was related to the pressure reading by:

$$Vel = 1.3034.\sqrt{\Delta P} \qquad \text{--- (10.G.6)}$$

where ΔP is the pressure difference (in Pascals) between the cylinder wall tapping (below the orifice) and the atmospheric pressure, to which the calibrator exhausted immediately after the probe. The volume flowrate through the calibrator proved to be a significant fraction of the capacity of the Siemon Building compressor, and velocities above 13m/s could not be obtained steadily. The flowrate was held steady for sufficient time to take readings at high velocities by opening a valve as the flowrate declined. The probes and anemometer had to be re-linearised and re-calibrated every 2-3 hours as the calibration drifted.

The hot film anemometer yields the total velocity, with the probe element perpendicular to the main flow direction. To obtain the three-dimensional velocity components requires the output to be measured at 36 yaw angle positions for each radial position in the traverse. Apart from the excessive time that this requires, the analysis is complicated, and subject to error magnification. Hence the Hotfilm anemometer was used only as a check of the Pitot cylinder total velocity profiles, and was not resolved into components.

The other main use for the Hot film anemometer was to estimate the root-mean-square fluctuations of velocity in the cyclone. The measurement of turbulence is based on the slope B of the bridge voltage versus flow velocity curve.

$$B = \frac{de}{dU}$$

$$B.U = \frac{e^2 - e_o^2}{4\ e}$$

and the percentage turbulence $= 100.e_{RMS} . \frac{4.e}{e^2 - e_o^2}$

where e = the bridge voltage and e_o is the zero flow bridge voltage.

Note that the output voltage of the anemometer was the voltage drop across the probe and a 100Ω resistor in series. It cannot be assumed that the fluctuations in the voltage are proportional to the velocity fluctuations, but they were used as a relative measure of the turbulence level.

10.H. HELIUM BUBBLE GENERATOR:

10.H.1: Construction of the helium bubble generator:

Commercial units to produce helium filled detergent bubbles are produced by Sage Action Inc, Ithaca, New York. These were priced too high for the budget for this research, and since the concept is simple, a unit was constructed in this department. The important components are the generator head which brings the three component streams together, and suitable means of metering and controlling these streams. The generator head is shown below, the dimensions of this were selected on the basis of the external picture of the head given in a Sage Action Inc head, and some consideration of the flowrates that would be required. It does not seem that the sizes are critically important to the operation.

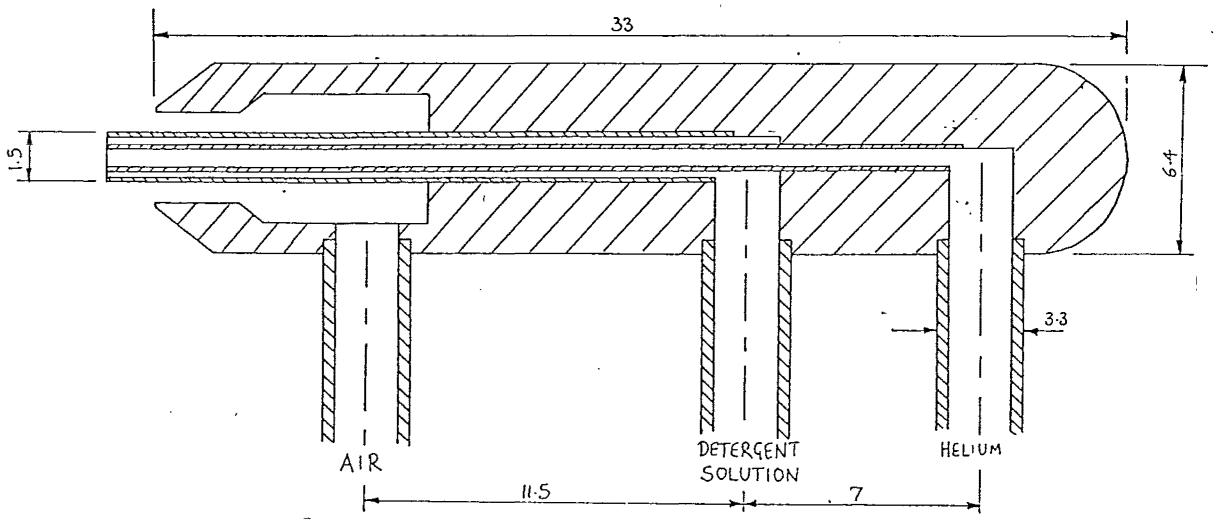

Figure 10.H.1: Layout of the Helium bubble generator head.

The bubble is produced by blowing helium through a detergent solution via concentric tubing. The bubble size is determined by the speed at which it is removed from the generator nozzle, which is controlled by the flowrate of the air in a third concentric pipe. It was found that the flowrates of helium and detergent solution that were required were very low. The detergent solution used was predominantly Teepol, a commercial detergent. It had been found by the Mechanical Engineering department that a mixture of 75% Teepol: 20% Water: 5% Glycerine gave the best results. The glycerol was included to improve the strength, but neither this, nor the water seemed to have a significant effect on the bubble quality that was produced, and in some cases 100% Teepol was found to perform better.

Overleaf: Plate 6, showing the generator and the relation of the bright spots to the outline

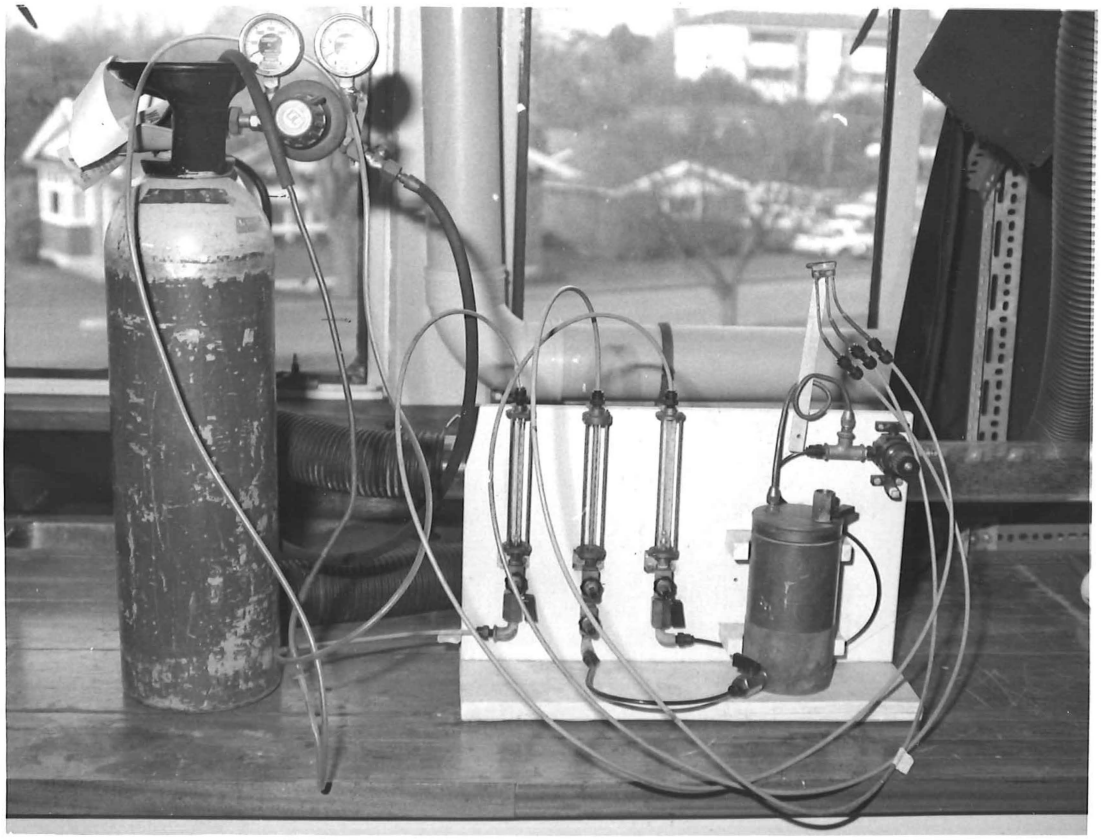

Plate 6.A.: The apparatus for generating the helium bubble tracers

Plate 6.B.: Relation of paired images to the helium bubble outline
Illuminated horizontally from left

The bubble tracer will experience a lift force if it is in a flow with appreciable velocity gradients, which is certainly the case in the cyclone vortex flow. The lift force arises because the velocity at the top and bottom of the bubble differ, causing a pressure difference between the top and bottom. The lift force acts in a direction parallel to the direction of the velocity gradient, and would act to drive the bubble into the centre of the vortex. An expression for the lift force experienced by a sphere is given by Saffman (1965); and updated in Moore & Saffman (1968):

$$L = 6.46\,\mu\,V\,a^2\sqrt{\frac{K}{\nu}} \qquad \text{--- (10.H.1)}$$

μ, ν = dynamic,kinematic viscosity
a = radius of sphere
K = magnitude of velocity gradient

This is for a sphere moving through a very viscous liquid with velocity V relative to a uniform simple shear. As an estimate of the magnitude of the velocity gradient K, look for the greatest slope of the velocity profiles. From the pitot cylinder data, between radial positions of 160mm and 150mm.

$$K = \frac{|\Delta V|}{|\Delta r|} = \frac{(13.5 - 11.45)}{(0.16 - 0.15)} = \frac{2.05}{0.01} = 205\ s^{-1} \qquad \text{--- (10.H.2)}$$

$\nu = 1.568 \times 10^{-5}\ m^2s^{-1}$
$\mu = 1.846 \times 10^{-5}\ kgm^{-1}s^{-1}$
$a = 3.0 \times 10^{-3}$ m.
$V = 35$ m/s (fluid velocity)

$$L = 6.46 \times 1.846 \times 10^{-5} \times (3.0 \times 10^{-3})^2 \times \sqrt{\frac{205}{1.568 \times 10^{-5}}} \times 35 \qquad \text{--- (10.H.3)}$$

$= 1.36 \times 10^{-4}$ N

This is the lift force due to the **velocity gradient.**

The Lift force due to deformable particles is given by Wohl and Rubinow (1974) as :

$$F_l = \frac{19}{10}\,\pi\,\mu\,\varepsilon\,U_o\left(\frac{a}{R_o}\right)^4 b\,F\left[1 + o(\varepsilon)\right] \qquad \text{--- (10.H.4)}$$

ε = ratio of Weber number to Reynolds number. $\varepsilon = \mu\,U_o\,T^{-1}$
U_o = velocity of fluid at centreline of duct.
T = surface tension of drop; typical values : Glycerol/air T = 63.4 dynes/cm
Water/air = 72.8 dynes/cm
5% Glycerol/water = 72.9 dynes/cm.
(Use a value of 70 dynes cm^{-1})

α = ratio of drop and external fluid viscosities. This should be taken as the helium : air ratio, not the detergent : air ratio as this is a calculation for deformable bubbles.

$$\alpha = \frac{194.1 \times 10^{-3}}{182.7 \times 10^{-3}} = 1.0624 \qquad \text{--- (10.H.5)}$$

R_0 = radial distance from position of zero flow to position of maximum flow. a/R_0 gives an indication of the size of the particle compared with size of flow. Say a = 2mm ; R_0 = 40mm. As a maximum value take 0.1.

b = radial vector from flow axis to centre of mass of bubble. This is the offset from the flow.

F = $F_{10} + F_{11} + F_{12}$; each worked out as below:

$$F_{10} = \left(\alpha - \frac{\alpha + 1}{3} \times \left(\frac{R_0}{a}\right)^2 k_0\right) \times \left(\frac{1}{\alpha + 1}\right)^3 \times \left(\frac{1}{\alpha + 2/3}\right) \times [\alpha + 16/15] \times [\alpha^2 - 8/3\,\alpha + 6] \qquad \text{--- (10.H.6)}$$

k_0 is the non dimensional body force parameter given by:

$$k_0 = \frac{K_0 a^2}{\mu U_0} \qquad \text{--- (10.H.7)}$$

where K_0 is the body force per unit volume, and 'a' is the radius of the drop.

$$F_{11} = \left(\frac{1}{\alpha + 1}\right)^3 \left(\frac{1}{\alpha + 2/3}\right) \times [\alpha + 16/19] \times [9/8\,\alpha^2 - 41/672\,\alpha - 3461/168] \qquad \text{--- (10.H.8)}$$

= -4.1828. This is the largest contribution for small α.

$$F_{12} = -\left(\frac{1}{\alpha + 1}\right)^3 \times [\alpha + 10/11] \times \left(13541/3724\,\alpha^2 - 222101/37204\,\alpha - 79002/18620\right) \qquad \text{--- (10.H.9)}$$

= -0.45189

Wohl & Rubinow (1974) show that the magnitude and algebraic sign of F_1 depends only on the viscosity ratio parameter α and the dimensionless parameter $k_0(R_0/a)^2$. The latter parameter implies that the contribution to F_1 due to the body force is negligible compared to that due to deformation when $k_0 << (a/R_0)^2$ and is dominant when $k_0 << (a/R_0)^2$. The parameter F_{10} is always positive according to Wohl & Rubinow (1974), implying that its contribution is always in the outward radial direction. F_{12} is always negative, whereas F_{11} changes sign from negative to positive as α increases. The summation $F_{10}+F_{11}+F_{12}$ is reported to be always negative, implying that the force on a neutrally buoyant drop will always be directed towards the flow axis. To estimate the maximum force, the contribution of F_{10} is disregarded, as it opposes the sign of the summation, and the value is calculated at small α.

$$F_1 = -1.1 \times 10^{-11} \times b \qquad \text{--- (10.H.10)}$$

It can be seen that the effect can be expected to be small, for the values of the parameters assumed. The dominant effect is expected to be the lift force.

Form Drag :

The radial velocity of the bubble will be determined by the balance between the various forces acting on the bubble, (including the centrifugal force) and the fluid drag of the radial inflow. To examine the contribution of the lift force, the other forces will be neglected for the moment, and a balance made between the lift force and the drag on the bubble. This will yield the velocity that the bubble would move if acted on by the lift force alone, and the value of this can be compared with the expected magnitude of the radial velocity. An equation which gives good agreement to numerical predictions of drag on spherical bubbles is

$$C_D = 14.9\ R_e^{-0.78} \qquad \text{--- (10.H.11)}$$

Drag Force $= F_d = {}^1/_2\ C_D\ \rho\ S\ \langle u\rangle^2$ $\qquad S = \pi/4\ a^2$

Lift force $= 1.36 \times 10^{-4}$ N

The radial relative velocity when drag and lift forces are equal :

$$1.36 \times 10^{-4} = {}^1/_2 \times 14.9 \times \left(\frac{u \times d}{\nu}\right)^{-0.78} \times \rho\ \frac{\pi}{4}\ d^2 \times u^2$$

assuming a bubble diameter of d = 2.5mm, and properties for standard air, the radial velocity.

$\langle u\rangle = 65$ m/s

This suggests that this effect may be appreciable. Note that the calculations have been of only order-of-magnitude accuracy, and the calculation of the lift force used an analysis that applies for low Reynolds number flows such as very viscous fluids. The lift force will be directed inwards, regardless of the buoyancy of the tracer, while the centrifugal force will be expected to be directed outwards for tracers that are heavier than air, and inwards for tracers that are lighter than air.

10.H.3. Photographic images of the helium bubble tracers:

When the helium tracers were photographed using flashes, the image consisted of a pair of bright spots. Several experiments were conducted to investigate the cause of these pairs, and to estalish the relationship of them to the bubble centre. For determination of velocity and paths it was essential that the true position of the bubble be known. Several hypotheses rose from observations, and were tested and eliminated.

It was observed that the orientation of the image pair depended on the flash source, with the two images being oriented along the path of the light. This was shown using colour filters on the flashes and shooting colour film, allowing the different flashes to be distinguished. Changing the order of the flashes changed the orientation, and swapping the flashes retained the orientation. The double image was obtained from a single flash, with care taken to avoid multiple reflections from external surfaces. This suggested the pair of images was an optical effect.

The possibility of the curved perspex surface refracting and splitting the light that was reflected or refracted by the bubble was investigated by making a length of perspex tubing with a cut-away section. The bubbles were photographed through the gap, as well as through the perspex while the flash was directed through the gap. This showed there was no effect the image caused by either (a) the light passing through the perspex before illuminating the bubble; and (b) the light leaving the bubble passing through the curved perspex before reaching the camera. It was noted that under conditions of all-around lighting, a single image was obtained.

The solution was found by employing a high voltage arc flash, which gave a very bright flash of short duration. These photographs were able to show the bubble outline as well as the bright spots, and revealed that the double images were located inside the bubble, at positions that would be expected to correspond to the focal point of the bubble. The images were aligned along the light path of the flash, and thus could be used to distinguish between different flashes on monochrome film by keeping the orientation of the flashes different. Most importantly, it was shown that the bright spots were located equally on either side of the bubble centre, allowing the bubble position to be easily determined. An example is shown in Plate 6 above.

The depth of field of the photographs of the tracers was also examined. It was found that the flash of light was able to be recorded past the point where the picture became out of focus for images such as a scale.

The lighting and camera settings varied between the different experiments that were conducted. Early experiments used colour film rated at 1600ASA, and used three flashes with cyan, magenta or yellow filters in front to enable them to be distinguished. This allowed three positions of the bubble to be determined, and hence the velocity magnitude and direction. A map of these discrete velocity results showed a very confusing structure, with velocities directed contrary to what was expected. To obtain a more complete picture of the tracer path, a new bin was constructed with a clear glass plate for the base, and no probe hole in the base. This allowed the illumination of the axis of the cyclone, with photographs taken from the side. A slide projector was used for the light source, and precautions were taken to minimise the refraction from the perspex surfaces. A slide was prepared from black cardboard to restrict the angle of the beam, and the roof of the bin was also covered.

The axial illumination was able to show the complete path of the tracer in the core region, but the combination of the reduced illumination, and seemingly higher velocities in the outer vortex made the recording of the tracer motion in the outer vortex more difficult. In addition, the tracers appeared to move into the axis quickly, and hence there were more tracers there to be observed. In addition to the axial illumination, the triple flash unit was used to illuminate the cone of the cyclone from above, with the three flashes spaced typically 86 microseconds apart, and repeating the cycle every 0.5 milliseconds. This should give a spacing between the flash groups of 5.8 times the spacing between flashes within the group, as shown below.

Since the orientation of the flashes enabled the tracer images to be distinguished, the velocity of the tracer along the illuminated path could also be determined. However, in practice the balance between the amount of light in the axis, and that provided by the strobing flashes was difficult to achieve, and frequently the flash images could not be discerned clearly.

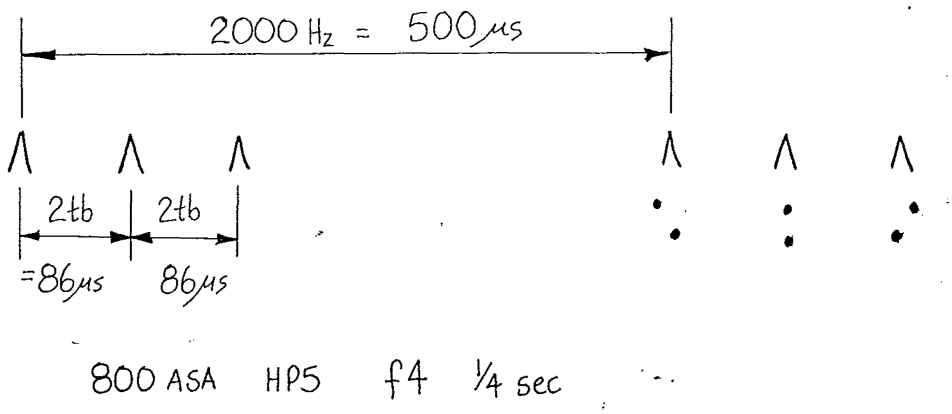

Figure 10.H.3: Flash settings for Helium bubble tracer photographs.

The camera settings were adjusted depending on the lighting arrangements, but were typically as follows. The film used was HP5, developed at 800ASA. Nikon FG and Pentax Spotmatik cameras were used, with 35-70mm lenses. The camera was placed about 500mm away from the axis of the cyclone, with a black background and surrounds. All experiments were carried out after dark, with the laboratory lighting off to give the best contrast. The inlet velocity was restricted to 15m/s and the shutter speed was selected to maximise the chance of recording a tracer 'event' without suffering from multiple 'events'. This was found to be in the range of 1/2 - 1/30 sec, with an f stop of 4. The photographs in Plates 1 & 2 were shot at 2000Hz, with 86μs delay between each of the triple flashes. The HP5 film was developed at 800ASA and the camera settings were f4 and 1/4 second.

10.H.4: Video footage of Helium bubble tracer motions:

The video has been appended to this report as a record of the dynamic movements of the tracers, which are difficult to represent with still photographs or text. The lighting conditions used were the same as for the still photographs, with a slide projector providing a beam of light along the axis. For a few sections of the video the flash unit was strobed to provide extra illumination in the lower cone region. The video was shot on a HandyCam Traveller 8mm video recorder, and subsequently edited and dubbed onto VHS format. Brief explanatory titles have been inserted throughout the video, and these accompanying notes are designed to explain the action more fully.

Video footage notes:

The video that accompanies this thesis shows some of the dynamic features that were revealed by the helium bubble tracers. Most of the footage was shot in the 140mmØstandard Stairmand High Efficiency cyclone at an inlet velocity of 15m/s. The video records at 24 frames per second, which is not fast enough to freeze the motion in one frame, but the features are representative of what is observed with the eye. Unfortunately the editing and duplication process has resulted in some loss of clarity.

The video is broken up into sections with title pages to help with the interpretation of the footage, and further comments are given below. The total running time of the video is approximately 33mins, with the first three and a half minutes consisting of a summary, with 10-15 seconds of footage from each of the sections. The titles in order of appearance are:

"1992 University of Canterbury Christchurch, New Zealand"
"Cyclone Flow visualisation Ross Wakelin"
The opening sequences feature a still shot of the 140mm laboratory cyclone, which was used for the photographs. The slide projector illuminated the cyclone along the axis from the right, through the base of the bin. Strobe flashes were also used at times, directed downwards onto the cone region.

"Preview of contents"
These sections are explained more fully in the main section. The video shows in succession an overall view of the cyclone with the tracers recirculating in the gas exit, then pulsing towards the dust exit, eventually being trapped just off the bin base. Close up shots of the gas exit tracers, and the reverse flow are also shown. The effect of inserting a probe into the cyclone is shown as a large shift in the position of the gas exit trap. Finally, a geometry with a conical extension to the dust exit is examined.

"1. Gas exit trap"
"2. Gas exit recapture"
"3. Gas exit-barrel transfer"
"4. Near axis reverse flow in cone"
"5. "Bin trap"
"6. Gas exit trap close up"
"7. Tracers in cone close up"
"8. Probe insertion in barrel"
"9. Cyclone with extended cone"
"Summary ends"

"Extended footage detailed views"

"Recirculation of tracers in gas exit"
Initially there is no action in the field of view, which was typical of the performance. A helium bubble tracer (henceforth: "tracer") arrives from the main body of the cyclone to the right, and becomes trapped near the flange in the gas exit. Other tracers join the recirculating region, and some escape downstream (to the left) in very fast movements which are not

clearly recorded. Tracers are recaptured from the left.in a reverse flow near the axis. The trap moves back and forth along the axis. The camera moves to show the gas exit lip region. Note the tight form of the gas exit trap when it is located above the cyclone roof, and how this become more diffuse when it moves to the right near the gas exit lip. Tracers can also be seen escaping into the cyclone body. (The summary footage was not a good selection to show this clearly).

"Gas exit close up"
A freeze frame begins this, showing the tangled paths of the tracers in the trap in a single frame. The tracer has described this path in less than 1/24th of a second, which shows the high velocity of the tracer, (the outer diameter of the spirals is about 30mm.

"Gas exit reduced flow 8m/s"
The action was slowed down by reducing the inlet velocity from 15 to 8m/s. The cyclone is out of the picture to the right, and the reverse flow along the axis of the gas exit is shown travelling from the left towards the right.

"Recapture in Gas exit normal flow 15m/s" (Time from start of tape 5min 52sec)
The flow is increased back to 15m/s, showing correspondingly faster tracer movements. The footage is faint at first, and the cyclone is out of the picture to the right.

"Transfer from gas exit to barrel"
The first segment is handheld, and the tracers are not clearly visible in the third generation video copies. The second section of this footage shows the action more clearly, particularly how the gas exit trap becomes more diffuse as it nears the gas exit lip.

"Reduced flow 8m/s"
This shows the transfer from the gas exit to the barrel of the cyclone.

"Near axis reverse flow in cone" (Time from start of tape 14min 17sec)
The normal flow for the core vortex is from the right to the left.
"Reduced flow 8m/s"
As the flow is reduced it appears that the frequency of the reverse-flow events decreases, although the intermittency of the phenomenon makes this difficult to tell for sure.

"Close up of near axis reverse flow"
This is a close up view of the cone - starting with a freeze frame. There are long gaps between the tracer footage, which is due to the difficulty in producing sufficient quantities of tracers of the correct buoyancy. There are also some views of the tracers moving from the right to the left, which is the normal direction for the core vortex.

"Tracers reach bin base"
Again there is a long pause at the start before the first tracer arrives at the bin base, but once the bin trap is established there are other arrivals. At the end the tracers all disperse up the axis in a pulse that purges the bin of the trap

"Reducing flow 5m/s to zero"
The footage starts at the reduced inlet velocity of 5m/s. Note the kink in the almost continous chain of tracers along the axis. Then later in a close up of the action the flow is reduced to zero, and back to 5m/s, then reduced and increased again.

"Probe insertion in gas exit"
When the probe is inserted into the gas exit the tracer trap moves downstream to the left. The probe is left in place for most of this footage, and then withdrawn until the tip is flush with the wall, then inserted again, then withdrawn and removed. The behaviour of the tracers is less erratic when the probe is inserted. The footage closes with footage of the gas exit trap with no probe insertion, before the tracers disappear at the end.

"Probe insertion in barrel"
The probe is firstly inserted about 30-40mm until the tip is just inside the core vortex. At this point the tracer trap in the gas exit has moved closer towards the gas exit lip and tightened into a thinner chain along the axis. Contrast this behaviour with the more diffuse form that was observed as the trap moved towards the gas exit in the undisturbed footage. The probe is then withdrawn and the behaviour reverts to the normal form, with more erratice movements. The probe is then re-inserted and gradually moved further into the core vortex. With sufficient insertion the tracer trap moves downstream to the left, ending up 8 exit diameters downstream of the original position. When the probe is withdrawn the tracers come back to the roof. The speed of the response of the flow to the insertion is then demonstrated by the rapid insertion and removal of the probe - the adjustment of the trap position is practically instantaneous, for both the initial movement and the return to the original position.

"Conical extension of cone"
All of the footage to here was shot in the standard Stairmand High Efficiency geometry. This section shows a view of the cone region for the standard geometry with a 90mm conical extension attached to the dust exit. The tracers appear to come from the gas exit into the main body of the cyclone, but return to the gas exit after travelling only a short distance towards the dust exit. The gas exit trap appears to be of a more stretched out form, between the gas exit lip and the gas exit flange and extending into the body of the cyclone at times.

"Long cone - no barrel"
The Long cone geometry has the same overall length as the standard, but has no barrel section, just a cone of half angle of 5 degrees. There were no measurement ports attached to the cone at the time that this footage was shot, so the cone outline is difficult to see. The trap is visible downstream to the left, but no examples of the near-axis reverse flow are seen, although there were occasional examples.

10.I. FOG TRACER GENERATOR:

The other tracer used for flow visualisation in the cyclone was a fog vapour. This was a commercial product used for stage productions, and was prepared by Trevor Berry, the Chemical & Photographic technician in this department. The vapour is generated by electrical heating of the 'juice', which is thought to be comprised of alcohol and water. The following calculations were performed to check that a suitably opaque fog could be obtained by a gravity feed of the solution through a hypodermic tube with electrical resistance heating of the tube.

10.I.1: Calculation of flowrates for Smoke Generation device

The heating requirement = $\omega.Q$, where ω is the liquid flowrate of fog juice.

Number of drops / m^{-3} $= n = \omega \times \frac{1}{\rho} \times \frac{6}{\pi D_p^3} \times \frac{4}{V_g \pi D_j^2}$ --- (10.I.1)

which can be estimated from the theory from the theory of Wickramansinghe (1973) and Hulst (1957)

The column density of grains (m^{-2}) is N, so that $n = N \times D_j$; where D_j is the maximum path length.

From extinction $\frac{I(\lambda)}{I_0(\lambda)} = 0.02$ (roughly) $= \exp\left(-N\pi a^2 Q_{ext}\right)$ --- (10.I.2)

In the figure, the ordinate $x = \frac{2\pi a}{\lambda}$

λ = wavelength of light $\approx 0.7\ \mu m$

a = the drop diameter $\approx 2\ \mu m$

Q_{ext} = average extinction efficiency = 2 to 2.5 from Hulst for $\frac{1}{x} \approx 0.1$

Using (10.I.2), the column density of droplets can be calculated from:

$$N = \frac{-\ln 0.02}{\pi a^2 Q_{ext}} = 4.981 \times 10^{11} \ \#/m^2 \qquad \text{--- (10.I.3)}$$

hence: $\omega = 4.1 \times 10^{-9}\ kg\ s^{-1} \approx 4.1 \times 10^{-6}\ ml\ s^{-1}$

With this small flow, the opacity is not a problem. The following calculation checks that this flow can be achieved through a 0.5mmØ hypodermic syringe using gravity feed. The tube is sealed at the end, and a hole ground in the tube wall about 50mm from the end, from which the fog vapour escapes. The general arrangement of the fog generator is shown below, for which

the following dimesions have been assumed: $h_1 = 200mm$; $h_2 = 75mm$; $d_1 = 20mm$; $d_2 = 0.5mm$; $l_1 = 500mm$.

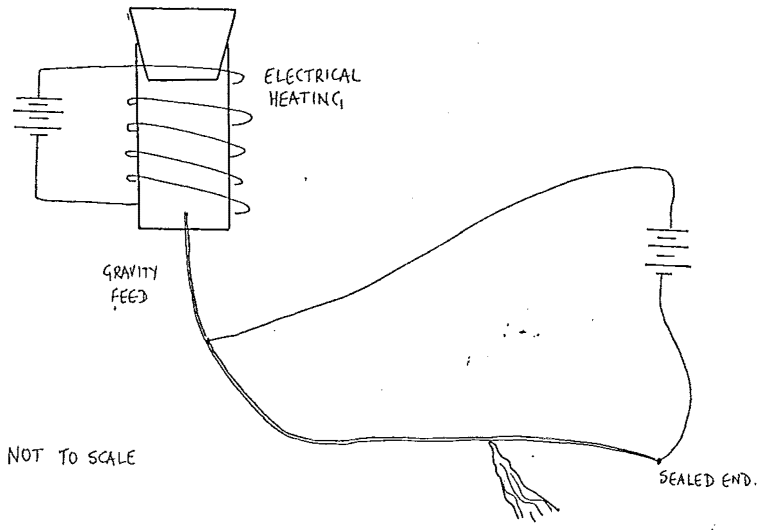

Figure 10.I.1: General concept of the fog generator

As a rough calculation, use the Fanning Equation :

$$H_t = 4 f \frac{L}{D} \frac{\langle u \rangle^2}{2g} \sum K_f \frac{\langle u \rangle^2}{2g} \qquad \text{--- (10.I.4)}$$

Guess a value for the friction factor f at high R_e for $\varepsilon/D = 0.091$ =» $f = 0.018$

$\Sigma K_f = 0.5 + 0.75 + 0.75 = 2.0$ $H_t = 0.275$ m height of gravity feed

$$u = \sqrt{\frac{0.275 \times 2 \times 9.81}{28}} = 0.439 \text{ m s}^{-1}$$

This equates to a flowrate of 5.2 ml min^{-1}, and this flowrate changes by 2% over an hour

The latent heat = 2258 kJ/kg

Heating required $\approx 8.62 \times 10^{-8}$ m^3s^{-1} x 1000 kgm^{-3} x 2258 kJ/kg

≈ 0.195 kW

This assumed the flow properties were the same as water - whereas it is more viscous. Also the fog juice is only 25% water, with some heat retaining heavy components =» the latent heat may not be the same as water. Nevertheless, this value will give an order-of-magnitude value.

This heating can be comfortably supplied by the electrical resistance heating of the tube, as shown by the measurement of the resistance of 20 gauge s/s tube (950mm length)

Current	Voltage	Ω
1A	2.07	2.07
2A	4.25	2.13
3A	9.40	2.35

Electrical Power $P = VI = I^2R$ Watts. Hence to provide 200 W of heating requires a current of 10 Amps. Finer gauge wire was also tested, since it has a higher resistance less current will be needed. For a length of 500mm:

Outside diam /mm	Inside diam. /mm	Voltage at 1A
0.72	0.3	1.75
0.55	0.3	2.58

The fog generator worked satisfactorily. The brass feed tank was conductively heated by a coil of nichrome wire that was electrically insulated from the tank. This preheating of the feed increased the flow in the tube. The hypodermic tube was inserted a distance of 5mm above the base of the tank to avoid clogging with the impurities that settled on the feed tank base. It was found that if the tube was heated over all of its length the fog vapourised before reaching the exit hole, and the fog jet was produced erratically. The correct level of heating kept the juice in the liquid state until near the exit, with the heating applied over the last section of the tube to achieve the vapourisation.

The fog generator was used in the cyclone by stretching the hypodermic tube across the diameter. The tube extended for 50mm past the exit hole, and a tensioning wire was soldered to the end of the tube so that it could be pulled from the other side. Insulating sleeves were required to protect the perpex from contact with the hot wire. The exit could be arranged near the wall, or anywhere across the diameter. It was found that the cooling effect of the airstream hindered the production of the fog, and this restricted the experiments to inlet velocities of around 8 m/s. The fog was best produced by sealing the feed tank with a cork, and giving this a slight squeeze immediately before taking the photograph. This brought warmer fog juice from the upstream section of the tube and gave a more visible jet stream. The squirt was not thought to significantly alter the radial inflow of the tracer.

The injection of the fog tracer at the wall was used to visualise and measure the radial inflow of air in the cone of the cyclone. The fog was swept around from the injection point by the tangential velocity, and by viewing along the axis, the distance that the jet had moved inwards could be seen. This radial movement was related to a radial velocity by using the tangential velocity that had been measured at that location with the pitot cylinder. The radial position of the jet was taken as the centreline position, as the edges of the jet often had a ragged appearance, with 'fingers' of fog showing a much higher inflow.

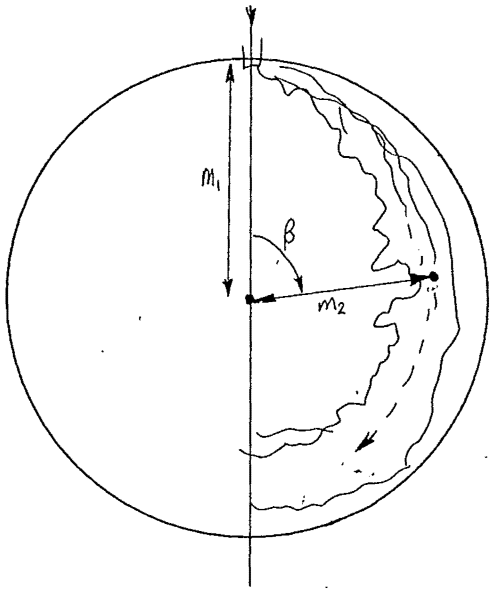

Figure 10.I.2: The radial inflow of the fog tracer, and calulation of the radial velocity

The fog was photographed through the bin base, along the cyclone axis. When these measurements were made only the orginal cyclone bin was available. The presence of the measurement port in the centre of the base meant that the camera could not be aligned with the axis, and different axial locations resulted in different angles between the camera viewing angle and the cyclone axis. The apparent radial position of the bubble had to be corrected for the difference in the angle, which was done as shown in the diagram below:

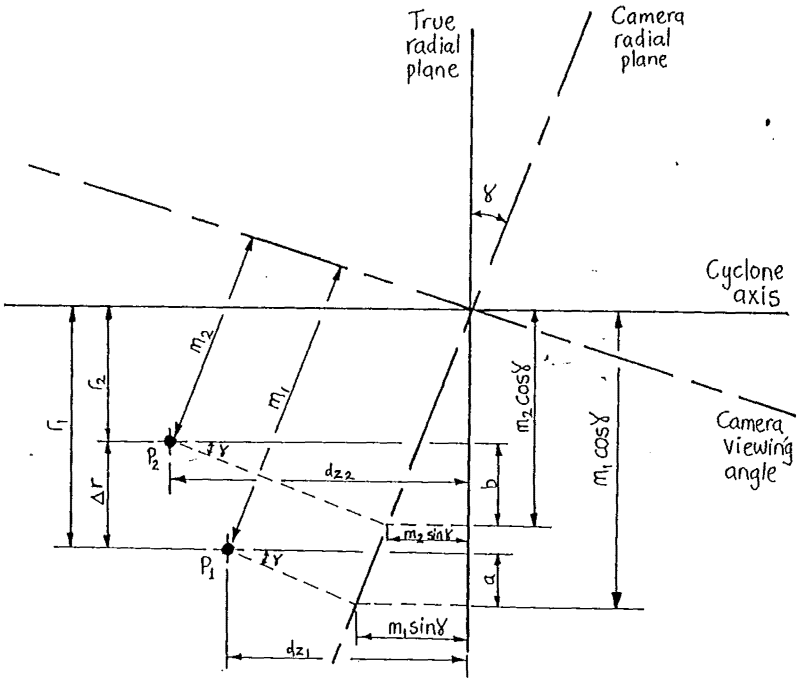

Figure 10.I.4: The calculation of the true radial shift of the fog tracer

The true radial shift Δr is found by

$$\Delta r = (m_1 \cos\gamma - a) - (m_2 \cos\gamma - b) \quad \text{--- (10.I.5)}$$

where: γ is the angle between the camera viewing angle and the cyclone axis,
m_1 and m_2 are the measured radial positions, and

$$\frac{a}{(dz_1 - m_1 \sin\gamma)} = \tan\gamma = \frac{b}{(dz_2 - m_2 \sin\gamma)} \quad \text{--- (10.I.6)}$$

hence $$\Delta r = (m_1 \cos\gamma - \tan\gamma(dz_1 - m_1 \sin\gamma) - (m_2 \cos\gamma - \tan\gamma(dz_2 - m_2 \sin\gamma)) \quad \text{--- (10.I.7)}$$

The distance travelled in the axial direction is estimated from the helical angle of the fog when viewed from the side of the cone. The majority of the photographs were taken with two cameras synchronised - one from the bin base, and one from the side of the cone. The axial travel could be estimated from the angle α of the flow to the axial plane, and the angle β of the arc that the fog described. If the local diameter is D_L, then:

$$dz = \beta/360 \times \pi D_L \sin\alpha \quad \text{--- (10.I.8)}$$

The radial velocity was then found from:

$$V_R = \frac{\Delta r\, V_\theta}{\beta} \times \frac{\cos\alpha}{2\pi r \times 1/360} \quad \text{--- (10.I.9)}$$

These values were found to be considerably higher than expected from the uniform radial inflow. It was thought that the movement of the fog tracer may due to the radial diffusivity rather than the convective velocity. The diffusivity is calculated from:

$$\Delta r = \sqrt{2\,\vartheta\, t} \quad \text{--- (10.I.10)}$$

where $$t = \frac{\Delta r}{v_R} \quad \text{--- (10.I.11)}$$

hence $$\vartheta = 0.5\, V_R.\Delta r \quad \text{--- (10.I.12)}$$

The diffusivity ϑ can be scaled by $V_{in}D$, to facilitate comparison with measurements made in other cyclones, such as Hejma (1971). This showed that the values obtained in this study are 4-7 times greater than previously reported values.

The values of the inflow that were calculated are presented here:

Port number: 3.
Local diameter: D_L = 60.5mm. Camera viewing angle γ = 8.6°;
Helical angle α: not visible, assume 20° (from Pitot cylinder)
Tangential velocity: V_θ = 11.7m/s at 5mm and 10mm from wall; 10m/s at 20mm from wall.

Film:	19/5 2000					25/5 film B					
Frame number:		43A	42A	38A	35A	35A	34A	92	92	99	
Angular posn β		25	55	55	70	90	55	30	30	180	(deg)
Radial posn m_2		25.3	22.9	22.1	30	18.2	22.9	24.5	25.5	18.4	(mm)
Axial shift dz	4.5	9.9	9.9		16.3	9.9	5.4		32.5		(mm)
True radius r	24.9	21.7	20.9		15.9	21.7	23.9		13.7		(mm)
Δr in mm	5.4	8.6	9.4		14.3	8.6	6.3		16.6		
Radial vel V_R	4.2	3.0	3.3	0.0	2.8	3.0	4.1		1.7		(m/s)
time $\Delta r/V_R$ t	1.29	2.9	2.9	-	5.1	2.9	1.5		9.8		(milliseconds)
Diffusivity ϑ	11.3	12.9	15.5	0.0	20.1	12.9	12.92		14.11		(m^2/s)

Port number: 4
Local diameter: D_L = 68mm. Camera viewing angle γ = 9.0°;
Helical angle α: 12° (from photograph)
Tangential velocity: V_θ = 12m/s at 4mm and 12.3 m/s at 9mm from wall.

Film:	22/5 1900					21/5					
Frame number:		96A	95A	95A	92A	92A	57	53	50	50	
Angular posn β		40	90	30	60	90	70	70	150	20 to 60°	
Radial posn m_2		31.0	29.1	33.8	34.8	23.5	31.0	32.9	35.7	34.8	24.4
Axial shift dz	4.9	11.1	3.7	7.4	11.1	8.6	8.6	18.5	2.5	7.4	
True radius r	30.6	27.7	33.7	34.0	22.0	30.0	31.9	33.2	34.8	23.6	
Δr in mm	3.4	6.3	0.3	0	11.9	4	2.1	0.77	0		
Radial vel V_R	1.7	1.4	0.2	0	2.7	1.1	0.58	0.1		5.6	
time $\Delta r/V_R$ t	1.98	4.5	1.5	3.0	4.4	3.6	3.6	7.4		1.07	
Diffusivity ϑ	2.9	4.4	0.03	0.0	16.1	2.2	0.61	0.04		0.032	

Port number: 5.
Local diameter: D_L = 75.6mm. Camera viewing angle γ = 9.3°;
Helical angle α: 15° (from photograph)
Tangential velocity: V_θ = 11.4m/s at 5mm , 12.5m/sb at 12mm from wall; 12.3m/s at 20mm.

Film:	26/5 film C						25/5 film C			
Frame number:	51	51	52	52	53	55	50	74	73	
Angular posn β	90	35	180	90	35	40	180	45	60	
Radial posn m_2	20.8	29.1	18.0	29.1	33.3		24.8	23.4		18.7
Axial shift dz	15.4	6	30.7	15.4	5.9	6.8	30.7	7.7	10.2	
True radius r	18.6	28.5	13.2	27.0	32.7	32.6	20.1	22.5	17.3	
Δr in mm	19.2	9.3	24.6	10.8	5.1	5.2	17.7	15.3	20.5	
Radial vel V_R	3.8	4.7	2.5	2.2	2.4	2.2	1.8	6.2	6.2	
time $\Delta r/V_R$ t	5.05	1.98	9.84	4.9	2.9	2.4	9.8	2.5	3.3	
Diffusivity ϑ	36.5	21.9	30.8	11.9	6.1	5.7	15.9	16.4	63.6	

Port number: 6.
Local diameter: D_L = 83mm. Camera viewing angle γ = 9.7°;
Helical angle α: not visible, assume 20° (from Pitot cylinder)
Tangential velocity: V_θ = 12.5m/s at 5mm from the wall; 13m/s at 15mm; 12.2 m/s at 20mm; 10.9m/s at 25mm.

Film:	26/5 film A											
Frame number:	15A	14A	14A	14A	12A	12A	11A	11A	10A	10A	9A	9A
Angular posn β	45	35	90	140	70	15	50	90	55	110	80	30
Radial posn m	30.2	34.8	30.7	29	33.1	41.8	37.1	29	26.7	26.1	29.0	45.2
Axial shift dz	8.4	6.6	16.9	26.2	13.1	2.8	9.4	16.9	10.3	20.6	15	5.6
True radius r	29.2	34.2	28.3	24.9	31.3	41.9	36.1	26.5	25.3	22.8	26.8	44.9
Δr in mm	12.3	7.3	13.2	16.6	10.2	0.0	5.4	15.0	16.1	18.7	14.7	0.0
Radial vel V_R	4.6	3.5	2.5	2.1	2.5	0.0	1.8	2.9	5.1	2.8	3.2	0.0
time $\Delta r/V_R$ t	2.7	2.1	5.3	7.9	4.1	1.0	3.0	5.2	3.2	6.7	4.6	2.0
Diffusivity ϑ	28.3	12.8	16.5	34.9	12.8	0.0	4.9	21.7	41.1	26.2	23.5	0.0

Port number: 6 continued.

Film:	26/5 film A											
Frame number:	8A	8A	8A	7A	7A	7A	7A	6A	6A	6A	5A	5A
Angular posn β	90	105	180	90	45	35	180	20	115	60	90	180
Radial posn m	25.5	18.6	16.2	26.7	38.3	35.9	23.2	37.7	29.0	30.2	24.4	27.6
Axial shift dz	16.9	19.7	33.7	16.9	8.4	6.6	33.7	3.7	21.6	11.2	16.9	33.7
True radius r	22.9	15.3	10.5	24.1	37.4	35.4	17.8	37.6	25.7	28.7	21.8	22.2
Δr in mm	18.6	26.2	31.0	17.4	4.1	6.1	23.7	3.9	15.8	12.8	19.7	19.3
Radial vel V_R	3.4	3.6	2.4	3.4	1.5	2.9	1.9	3.2	2.4	3.6	3.6	1.8
time $\Delta r/V_R$ t	5.5	7.3	12.9	5.2	2.7	2.1	12.5	1.22	6.6	3.6	5.5	10.7
Diffusivity ϑ	31.6	47.2	37.4	29.1	3.08	8.9	22.5	6.24	19.0	23.0	35.5	17.4

Port number: 7.
Local diameter: D_L = 90.6mm. Camera viewing angle γ = 10.1°;
Helical angle α: 15° (from Photograph)
Tangential velocity: V_θ = 11.8m/s at 5mm from wall; 12.6m/s at 10mm from wall; 13.1m/s at 15mm and 13.0 m/s at 20mm.

Film:	17/5											
Frame number:		70A	69A	69A	69A	68A	68A	68A	66A	65A	65A	63A	63A
Angular posn β		30	30	90	135	15	30	90	40	60	30	180	50
Radial posn m	39.0			21.2	37.7	35.7	29.7	37	29.7	39.7	22.2	39.7	
Axial shift dz	6.14	6.13	18.4	27.6	3.1	6.1	18.4	8.2	12.3	6.1	36.8	10.2	
True radius r	38.5	35.2	23.5	16.6	37.7	35.2	26.9	36.1	28	39.2	15.9	38.5	
Δr in mm	6.7	10.1	21.7	28.7	7.6	10.1	18.4	9.2	17.3	6.1	29.3	6.8	
Radial vel V_R	3.36	5.3	3.8	3.4	7.7	5.3	3.3	3.5	4.5	2.9	2.6	2.0	
time $\Delta r/V_R$ t	1.99	1.9	5.7	8.4	0.99	1.9	5.6	2.6	3.8	2.1	11.3	3.4	
Diffusivity ϑ	11.3	26.9	41.2	48.8	29.3	26.8	30.4	16.1	38.9	8.85	38.1	6.8	

Port number: 7 continued.

Film:	17/5										
Frame number:		63A	62A	62A	61A	61A	61A	60A	59A	60A	60A	59A
Angular posn β		15	15	45	15	70	45	90	20	45	15	50
Radial posn m	38.3	41.0	36.4	39.7	29.7	36.4	26.4	39.0	36.4	39.7	31.7	
Axial shift dz	3.07	3.07	9.2	3.07	14.3	9.2	18.4	4.1	9.2	3.1	10.2	
True radius r	38.4	41.1	35.3	39.7	27.7	35.3	23.6	38.9	35.3	39.7	30.4	
Δr in mm	6.9	4.2	10.1	5.6	17.6	10.0	21.7	6.4	10.0	5.6	14.9	
Radial vel V_R	6.9	4.0	3.4	5.4	4.0	3.4	3.8	4.6	3.4	5.3	4.8	
time $\Delta r/V_R$ t	1.0	1.05	2.97	1.04	4.4	2.9	5.7	1.4	2.94	1.06	3.1	
Diffusivity ϑ	23.8	8.4	17.2	15.1	35.2	17.0	41.2	14.7	17.0	14.8	35.8	

Port number: 7 continued

Film:	16/5											
Frame number:		89A	89A	89A	88A	88A	87A	87A	87A	87A	85A	86A
Angular posn β		45	30	180	60	25	40	135	45	180	70	45
Radial posn m	33.1	38.3	22.2	33.1	35.7	42.3	26.4	42.3	20.2	34.4	38.3	
Axial shift dz	9.2	6.1	36.8	12.28		5.1	8.2	27.6	9.2	36.8	14.3	9.2
True radius r	31.9	37.8	16.0	31.4	35.3	41.5	21.9	41.3	13.9	32.4	37.3	
Δr in mm	13.4	7.5	29.3	13.9	9.9	3.8	23.4	3.97	31.4	12.9	8	
Radial vel V_R	4.8	3.7	2.6	3.7	6.1	1.4	2.7	1.3	2.8	2.9	2.7	
time $\Delta r/V_R$ t	2.8	2.0	11.3	3.8	1.6	2.7	8.7	3.1	11.2	4.5	2.96	
Diffusivity ϑ	32.2	13.9	38.1	25.7	30.5	2.7	31.6	2.6	44	18.8	10.8	

Port number: 7 continued.
Film: 16/5

Frame number:	86A	85A	84A	84A	84A	84A	83A	83A	82A	82A	81A
Angular posn β	20	40	35	90	45	85	105	40	25	120	140
Radial posn m	41.6	41.0	37.0	29.1	36.4	34.4	29.8	36.4	38.3	26.4	19.8
Axial shift dz	4.1	8.2	7.2	18.4	9.2	17.4	21.5	8.2	5.1	24.6	28.6
True radius r	41.6	40.2	36.3	26.3	35.3	31.8	26.4	35.5	38.0	22.5	15
Δr in mm	3.73	5.13	8.98	19.0	10.0	13.5	18.9	9.8	7.3	22.8	30.3
Radial vel V_R	2.7	1.85	3.95	3.4	3.4	2.5	2.9	3.8	4.3	3.02	3.4
time $\Delta r/V_R$ t	1.4	2.8	2.3	5.6	2.9	5.4	6.5	2.6	1.7	7.5	8.9
Diffusivity ϑ	5.04	4.7	17.7	32.3	17.0	16.9	27.4	18.6	15.7	34.4	51.5

Port number: 7 continued
Film: 16/5

Frame number:	81A	81A	81A	79A	79A	77A	77A	77A
Angular posn β	150	40	90	180	170	90	45	180
Radial posn m	29.1	34.4	29.1	21.5	23.8	33.1	38.3	26.4
Axial shift dz	30.7	8.2	18.4	36.8	34.8	18.4	9.2	36.8
True radius r	24.1	33.5	26.3	15.3	17.9	30.3	37.3	20.3
Δr in mm	21.2	11.8	19.0	30.0	27.3	15.0	8.0	25.0
Radial vel V_R	2.2	4.6	3.4	2.6	2.6	2.7	2.8	2.2
time $\Delta r/V_R$ t	9.6	2.6	5.6	11.5	10.5	5.6	2.9	11.4
Diffusivity ϑ	23.3	27.1	32.3	39	35.5	20.3	11.2	27.5

Port number: 8
Local diameter: D_L = 109.4mm. Camera viewing angle γ = 10.9°;
Helical angle α: 12°
Tangential velocity: V_θ = 11.6m/s at 8mm from wall; 12.5m/s at 15mm from wall and 12.8m/s at 25mm

Film:

Frame number:	39A						38A				37A
Angular posn β	35	40	65	90	135	180	40	50	90	180	90
Radial posn m	41.0	36.3	48.9	45.8	37.9	34.9	39.4	33.1	45.0	41.3	36.3
Axial shift dz	6.95	7.94	12.9	17.9	26.8	35.7	7.9	9.9	17.9	35.7	17.9
True radius r	40.4	35.4	47.3	43.2	33.4	28.7	38.6	31.8	42.4	35.2	33.5
Δr in mm	14.3	19.3	7.4	11.5	21.3	25.9	16.1	22.9	12.4	19.5	21.2
Radial vel V_R	5.3	6.3	1.4	1.6	2.1	1.9	5.1	6.0	1.7	1.4	3.1
time $\Delta r/V_R$ t	2.7	3.0	5.5	7.2	10.1	13.6	3.2	3.8	7.3	13.9	6.8
Diffusivity ϑ	37.5	60.7	4.77	9.2	22.4	34.6	41.1	68.7	10.5	13.7	32.9

Port number: 8 continued

Film:

Frame number:	37A		36A	35A	36A	36A	34A	34A	35A	34A	34A	33A
Angular posn β	145	180	35	30	50	145	180	90	135	135	45	60
Radial posn m	35.5		33.1	41.0	37.9	35.5	32.6	39.4	33.1	34.7	41.0	38.7
Axial shift dz	28.8	35.7	6.9	5.95	9.9	28.8	35.7	17.9	26.8	26.8	8.9	11.9
True radius r	30.6	23.1	32.4	40.6	36.7	30.6	26.3	36.7	28.6	30.2	40.1	37.1
Δr in mm	24.1	31.6	22.3	14.1	18.0	24.1	28.4	18.0	26.1	24.5	14.6	17.6
Radial vel V_R	2.2	2.3	8.4	6.0	4.7	2.2	2.1	2.6	2.53	2.3	4.2	3.8
time $\Delta r/V_R$ t	11	13.7	2.7	2.4	3.8	11	13.5	6.9	10.3	10.7	3.5	4.6
Diffusivity ϑ	26.5	36.3	93.7	42.3	42.3	26.5	29.8	23.4	33	28.2	30.7	33.4

Port number: 8 continued

Film:

Frame number:	33A	32A	32A	31A	31A	31A	30A	30A	30A	29A	28A	27A
Angular posn β	100	65	105	90	135	45	90	130	45	100	30	45
Radial posn m	33.1	43.4	39.4	35.5	29.9	36.3	45.8	29.9	45	36.3	39	33.1
Axial shift dz	19.8	12.9	20.8	17.9	26.8	8.9	17.9	25.8	8.9	19.8	6.0	8.9
True radius r	29.9	41.7	36.2	32.7	25.4	29	43.2	25.6	44.0	33.1	40.6	35.2
Δr in mm	24.8	13.0	18.5	22.0	29.3	25.7	11.5	29.1	10.6	21.6	14.1	19.5
Radial vel V_R	3.2	2.5	2.3	3.2	2.9	7.5	1.6	2.9	2.8	2.8	6.0	5.6
time $\Delta r/V_R$ t	7.8	5.2	8.0	6.9	10.1	3.4	7.2	10.0	3.8	7.7	2.4	3.5
Diffusivity ϑ	39.7	16.3	21.3	35.2	42.5	96.4	9.2	42.2	14.8	30.2	42.3	54.6

Port number: 8 continued

Film:

Frame number:		26A		25A	25A	24A
Angular posn β		60–90		45	90	90
Radial posn m	39		33.1	44.9	28.4	
Axial shift dz	12-18		8.9	17.9	17.9	
True radius r	30.8		38.4	42.3	25.5	
Δr in mm	9.2		16.3	12.4	29.7	
Radial vel V_R	3.9		4.6	1.7	4.3	
time $\Delta r/V_R$ t	2.4		3.5	7.3	6.9	
Diffusivity ϑ	17.9		37.5	10.5	63.9	

Port number: 10
Local diameter: D_L = 140mm. Camera viewing angle γ = 3.6°;
Helical angle α: 20°
Tangential velocity: V_θ = 9.8m/s at 10mm from wall; 10.8m/s at 20mm from wall

Film:	8/6 2000									
Frame number:		38A	42A	42A	1	1A	3A	6A	6A	9A	10A
Angular posn β		90	120	45	65	120	90	130	85	90	90
Radial posn m	33.8	31.5	38.3	22.1	45	33.8	36.0	33.8	32.6	40.5	
Axial shift dz	38.1	50.9	19.1	27.5	50.9	38.1	55.1	36.0	38.1	38.1	
True radius r	31.4	28.4	37.1	20.4	41.9	31.4	32.6	31.6	30.3	38.2	
Δr in mm	39.6	42.6	33.9	50.6	29.1	39.6	38.4	39.4	40.7	32.8	
Radial vel V_R	4.2	3.4	6.8	5.8	2.2	4.1	2.8	4.4	4.3	3.3	
time $\Delta r/V_R$ t	9.4	12.5	5.0	8.7	13.2	9.7	13.7	8.9	9.5	9.9	
Diffusivity ϑ	83.2	72.4	115	146	32	81.2	53.8	86.7	87.5	51.1	